Geotechnical and Grain Size Assessment Using Corescan Automated Core Logging and Complementary Microanalytical Techniques

UNIVERSITY OF TASMANIA

Cassady L. Harraden

BSc., Fort Lewis College

Submitted in fulfilment of the requirements for the degree of
Doctor of Philosophy

University of Tasmania, May 2018

TMVC
TRANSFORMING THE MINING VALUE CHAIN

Declaration of Originality

This thesis does not contain any material which has been accepted for the award of any other degree or diploma in any tertiary institution. To the best of my knowledge and belief, this thesis contains no material previously published or written by another person, except where due reference is made in the text of the thesis, and does not contain any material that infringes copyright.

Signed: Date: 11 May 2018

Authority of Access

This thesis is bound by the ARC Industrial Transformation Research Hub Intellectual Property and Confidentiality Deed (signed 29 February 2016) and is not to be made available for loan or copying for two years from the date this statement was signed. After that time, limited copying and communication is permitted in accordance with the Copyright Act of 1968.

Signed: Date: 11 May 2018

Abstract

Careful assessment and modelling of geotechnical and geometallurgical characteristics within an ore deposit are crucial to determining both the viability and profitability of a mining operation. Typically, a geotechnical model is constructed by combining manually collected geotechnical measurements from drill core with other geological observations. While this approach is successfully applied in the mining industry, it is often laborious and has the potential to generate inconsistent results. A geometallurgical model is the synthesis of comminution, liberation, and recovery data. While mineralogical proxies for comminution are widely used, proxy models for predicting liberation and recovery are inadequate for broad-scale implementation. The liberation, and ultimately, recovery of economic minerals is directly linked to the grain size, but current grain size assessment methods are costly and slow.

This research investigates the potential to use data generated by a Corescan hyperspectral drill core logger for geotechnical and geometallurgical applications. Two primary aims are the focus of this thesis: (1) develop protocols to rapidly extract consistent morphological and mineralogical geotechnical parameters from Corescan data, and (2) test a number of currently available microanalytical techniques that could complement the current Corescan system in rapidly determining proxies for copper sulphide and gold grain sizes. These complementary techniques must operate on the same interval as a typical assay (1 to 2 metres) and collect measurements at a rate similar to Corescan data acquisition (3 minutes per metre). Corescan digital drill core data and rock samples from the Cadia East underground mine provide a case study to develop, test, and evaluate the protocols generated to address these aims.

To extract ore, the Cadia East underground mine currently uses the block cave mining method. The site geotechnical model provides the foundation for the construction of stress models, caveability models, ground support design, and fragmentation analysis. While not all industry standard geotechnical parameters can be derived from Corescan data, this research focuses on calculating fracture orientation, fracture roughness, number of fracture sets, fracture spacing, fracture condition, and fracture alteration. A test dataset of 199 fractures from one Cadia East drill hole was used to develop and test a workflow to extract geotechnical parameters from Corescan data. The orientations of the 199 fractures were measured manually prior to Corescan analysis. After Corescan analysis, the

manual measurements were compared to the calculated measurements derived from the Corescan data. Over 75% of the calculated orientations were within 25° of their measured orientation value. Calculated fracture roughness, number of fracture sets, fracture spacing, fracture condition, and fracture alteration results were compared to expected site values and drill core photographs. Overall, the fracture protocols performed well and produced over 90% roughness values within the expected range for Cadia East, slightly underestimated the number of fracture sets and fracture spacing, and produced fracture condition and alteration values consistent with the fracture condition observed in photographs. One advantage of the automated protocols developed in this study is the ability to collect a higher density of data than is feasible by manual methods. This increased data density is collected rapidly and consistently, providing additional advantages over manual geotechnical logging methods.

The second aim of this research is to search for a proxy dataset that would predict grain size at the critical size for recovery (less than 100 microns). The Cadia East geometallurgical model classifies ore types as they relate to mineral processing flowsheets and mill design. One of the key parameters used in the site geometallurgical model is the grain size of chalcopyrite, bornite, and gold. Accounting for the effects of grains size on liberation and recovery can optimise processing design. If rapid and broad-scale assessment of grain size can be utilised, robust proxies for liberation and recovery can be incorporated into the geometallurgical model to improve mine planning and design.

A scoping study was designed to test multiple commercially available microanalytical techniques and determine which methods could provide reasonable proxies for copper sulphide and gold grain sizes. The objective of this study was to identify one or more microanalytical techniques that complement the current Corescan system, since the current sensors cannot directly detect sulphides less than 100 microns. Copper sulphide and gold grain sizes are commonly determined by the mineral liberation analyser (MLA) method. Microanalytical systems were tested using a set of twenty-six, 3 cm by 3 cm rock tile samples from Cadia East. Samples were analysed by portable x-ray fluorescence (pXRF), micro-x-ray fluorescence (μXRF), laser ablation inductively coupled mass spectrometry (LA-ICP-MS), laser induced breakdown spectroscopy (LIBS), and laser Raman. To determine the functionality of each technique, a grain size proxy derived from the microanalytical data was compared to the MLA dataset.

Of the five microanalytical techniques tested, μXRF, LA-ICP-MS, and LIBS were capable of producing reasonable grain size proxies for copper sulphide minerals. Determining grain size proxies for gold proved challenging due to complexities with sampling statistics, but, in general, when a sufficient number of gold grains were analysed, pXRF and μXRF produced reasonable gold grain size proxies. LA-ICP-MS line scan analysis was unable to overcome the challenges of sampling statistics for gold, but this is the only technique with high enough precision to detect sub-micron gold grains (which could have broader geometallurgical applications). The laser Raman system was unable to detect gold and copper minerals under relevant conditions and further testing of this technique was terminated.

Currently available μXRF and LIBS technologies are able to collect a sufficient number of analyses to produce robust copper sulphide grains size proxies at a rate comparable to the Corescan system throughput. Recent developments in core scanning XRF systems indicate that this analysis will have data acquisition rates sufficient for gold grain size proxy calculations to become feasible. At the moment, LA-ICP-MS technology cannot be completed outside of an ablation cell, but, it could be used for the rapid scanning of selected core samples outside of the Corescan sample analysis stream. Of all the methods tested, μXRF and LIBS show the most promising potential for future development and integration into the current Corescan system for geometallurgical grain size assessment.

The use of current data outputs obtained from the Corescan automated core logging system allow for key properties that affect the geotechnical response of a rock mass to be rapidly and consistently estimated. Integration of the existing laser height and hyperspectral derived mineralogical data with a complementary system (such as μXRF or LIBS, to quantify grain size) provides an opportunity to generate large volumes of consistent data. Through the methods developed in this thesis for geotechnical and geometallurgical grain size assessment, the underlying statistical support for rock mass characterisation and liberation and recovery modelling can be greatly increased. These outcomes have the capacity to substantially contribute to better geotechnical and geometallurgical models that will improve mine planning and ore recovery, which in turn will improve mine safety and profitability.

Acknowledgements

This research was funded by the Transforming the Mining Value Chain (TMVC), an Australian Research Council (ARC) Industrial Transformation Research Hub (project #IH130200004) at the University of Tasmania. I would like to thank Newcrest Mining Limited and Corescan Proprietary Limited for providing data, logistical, and financial support throughout this project. Thank you to Anthony Harris and Neil Goodey who were instrumental in developing the research question and discussing future applications of this research.

I would like to thank my supervisors, Sebastien Meffre, Ron Berry, and Matt Cracknell for their support, encouragement, and willingness to read through my many drafts. I thank you all for taking me on when I was an over-enthusiastic, PhD student in need of guidance. I owe a special debt of gratitude to Ron: you pushed me when I needed to be pushed, and reminded me to enjoy this journey when things got too serious. Thank you for dedicating so many of your hard-earned retirement hours to helping me think about geology in a whole new way. I will be forever grateful to count myself as one of your students.

The staff within the TMVC Hub and CODES has provided an immeasurable amount of guidance and support, both directly and indirectly. Thank you to Jane Higgins, Helen Scott, and Karen Huizing for your kindness, patience, and assistance with the logistics that come with PhD research. Many thanks to the analytical team at UTas, including Thomas Rodemann, Karsten Goemann, Sandrin Fieg, Paul Olin, Ivan Belousov, Sarah Gilbert, and Jay Thompson for their guidance in analytical methods, and Al Cuison and Michele Chapple-Smith for their lapidary expertise. Thanks to Dr. Mark Pearce at CSIRO for his assistance with the μXRF analysis. I would like to extend my sincere thanks to Dr. Richard Hark at Juniata College for teaching me about LIBS and his support throughout my two weeks in PA. David Cooke is gratefully acknowledged for his support of this project, and his review of numerous abstracts, papers, and presentations.

The geology and geotechnical teams at the Cadia Valley Operations were instrumental in my understanding of the application of data at site, and the geological and geotechnical aspects of the Cadia East deposit. Thank you to Stephen Guy, Maya Secheny, Matt Faugher, Jo Morrison, Mel Morgan, Chris Chester, Ali Oxbrow, Sarah Stark, and Justin Thrift for showing me the ropes and

making me feel right at home. I would like to especially thank James Lett– you have provided me with so much support and inspiration throughout this project, and I have learned so much from you.

I would like to express my deepest gratitude for the entire team at Corescan, but especially Ronell, Neil, Brigette, Katerina, Erin, and Lionel. Your willingness to discuss ideas and teach me about the Corescan outputs, spectral interpretation, and the power of this incredible technology are much appreciated.

To my colleagues and friends at CODES – thank you for your friendship, Tassie adventures, and tea room chats. There are too many to name you all, but a special thank you to Ben and Georgia, Martin and Doreen, Dave and Paul, Sam, Alex, Laura, Dan and Selina, Matt, Nathan C., Nathan and Anita, and Brett. I would also like to thank my Volleyball Tasmania family (especially Steve, Steph, Mick, and Jess) – you've shown me that it's important to have passions outside of geology.

Thank you to my family and friends back in the US – the emails, cards, and photos of your beautiful families help me feel like I'm not so far away from home. Thank you to my teachers and professors through the years for the encouragement and inspiration, especially Risë McEwen and Vesta Coufal. I would like to extend a special thank you to Dylan, Sy, Lane, and Austin for your encouragement and love. And to Chrissy and Scott who have always been such an important piece of who I am as a person: thank you for the love, support, and adventures through the years.

This thesis would not have been possible without three of the most important people in my life: Mom, Dad, and Brian. To Mom and Dad: you have given me so much support, guidance, and love throughout my entire life, but especially in this Ph.D. adventure. Thank you for being my sounding board, my guides, my editors, and especially my cheerleaders. You've taught me that "once in a while you get shown the light, in the strangest of places if you look at it right". I am so lucky to have you both in my life, and I am eternally grateful for your love and inspiration. Thank you from the bottom of my heart. And finally, to Brian: you have been an incredibly positive and supportive force in my life, especially these past few years. You remind me that I'm never alone, you bring me peace in the chaos, and you make me smile even when I don't want to. You have been there when it's fun, and when it's hard. You are truly my rock. Thank you for taking this journey with me. I can't wait to see where we go next.

To my three rock stars: Brian, Dad, and Mom.

I love you.

Table of Contents

List of Figures

List of Tables

List of Equations

List of Abbreviations

2D	two dimensional
2.5D	two and one half dimensional
3D	three dimensional
AlOH	aluminium hydroxide
AMIRA	Australian Minerals Industry Research Association
Au	gold
Ar	argon
C	carbon
cm	centimetres
cm^2	square centimetres
Ca	calcium
$CaCO_3$	calcium carbonate
CIC	Cadia Intrusive Complex
CSV	comma separated value
CT	computed tomography
Cu	copper
D_{PSSL}	diameter by phase specific surface length
DSM	digital surface model
Fe	iron
FeOH	iron hydroxide
F/m	fracture frequency per metre
FRV	Forest Reef Volcanics
g	grams
g/t	grams per tonne
gm/cm^3	grams per cubic centimetre
GeM	Geometallurgical Mapping and Mine Modelling
GIS	geographic information system
GSI	geological strength index
H_2O^-	water (chemical formula)
HCI-3	Hyperspectral Core Imager Mark-III
Hz	hertz
ICCD	intensified charge-coupled device
ICP-MS	inductively coupled plasma mass spectrometer
ID	identification
IR	infrared
J_a	joint alteration
J_n	number of joint sets
J_r	joint roughness
JRC	joint roughness coefficient
J_w	joint water reduction factor

kcps	kilo counts per second
keV	kilo-electron volt
LA-ICP-MS	laser ablation inductively coupled plasma mass spectrometry
LIBS	laser induced breakdown spectroscopy
ln	natural log
m	metres
m^2	square metres
mg	milligrams
MgOH	magnesium hydroxide
MLA	mineral liberation analyser
mm	millimetres
mm^2	square millimetres
MPa	megapascal
ms	milliseconds
N	nitrogen
Nd:YAG	neodymium-doped yttrium aluminium garnet
nm	nanometres
O	oxygen
OH	hydroxide
PC	panel cave
PCA	principle component analysis
ppb	parts per billion
ppm	parts per million
ppt	parts per trillion
PSSL	phase specific surface length
pXRF	portable X-ray fluorescence
QEMSCAN	quantitative evaluation of mineral by SEM
Q-Index	tunnelling index
R^2	Pearson correlation coefficient
r_s	Spearman correlation coefficient
RGB	red green blue
RL	real length profile
RMR	rock mass rating
RQD	rock quality designation
RSR	rock structure rating
sec	seconds
SE	standard error
SEM	scanning electron microscope
Si	silicon
SRF	stress reduction factor
SWIR	short-wave infrared
XRF	X-ray fluorescence
UCS	uniaxial compression strength

UV	ultraviolet
vol%	volume percent
VNIR	visible and near infrared
wt%	weight percent
YAG	yttrium aluminium garnet
μm	microns
μm^2	square microns
μXRF	microscopic X-ray fluorescence

Chapter 1

General introduction

1.1 Introduction and current knowledge gaps

The ability of mining and mineral processing methods to be successful is directly influenced by the geologic and geotechnical characteristics of the rocks being mined. The variability of geologic and geotechnical features such as rock type, fracture orientation and frequency, mineralogy, and grain size influence the entire mining process from infrastructure development to waste rock disposal. As such, these features need to be carefully considered throughout the mine planning process. Regardless of commodity, initial assessments of the geological and geotechnical characteristics of an ore deposit are largely conducted using drill core-derived data. Mining and exploration companies invest significant financial and workforce resources to the collection and analysis of drill core data. Information from drill core is often collected using a combination of manual observations and measurements in conjunction with geochemical, geophysical, or microanalytical results from selected sub-samples of the drill core. In the past decade, advancements in computer processing capacity, digital data storage, high-precision robotics, and high-resolution analytical methods has resulted in a new generation of high-speed drill core logging systems. The application of multi-sensor automated systems provides the mineral resource sector an opportunity to optimize data collection from drill core and increase the value gained from drill core assessment. Two key datasets that can be extracted from drill core to provide fundamental information regarding the characteristics of a rock mass are the geotechnical parameters and grain size of economic minerals of interest. These two datasets can contribute to informed mine planning and are investigated here.

When designing and developing a mine, characterising the geotechnical parameters of an ore deposit is vitally important. Modelling the geotechnical characteristics of a deposit provides critical information regarding the rock mass and its response to the mining process. Geotechnical models provide data inputs into a range of numerical and empirical analysis methods that make up the foundation for mine design. The data provides input into construction of stress models, caveability models, ground support design and fragmentation analysis.

Standard methods for geotechnical data acquisition and ground condition modelling in hard rock environments rely on the identification of fractures from manual logging of drill core. While this approach has been and is currently applied to mining successfully, it is often laborious and has the potential to generate inconsistent results. Automation of geotechnical data collection from fractures identified in digital drill core data would allow for consistent, rapid assessment of key parameters as they relate to ground conditions.

The size of economic minerals of interest, known as grain size, is vitally important in understanding how mined material will behave in a processing circuit. There is a strong correlation between grain size and the liberation and recovery of economic minerals present in ore (Hunt et al., 2011). This relationship dictates that predictive, geometallurgical models will require quantified grain size data. Grain size assessment is traditionally completed by reflected light microscopy or scanning electron microscopy (SEM) in conjunction with advanced mineralogical interpretation software packages (Fandrich et al., 2007; Goodall and Butcher, 2012; Gu, 2003). These methods have proven reliable for grain size assessment, but they require preparation of a highly polished surface and can be very time consuming. The development of rapid, automated grain size assessment tools is vital to ensuring that grain sizes can be assessed on a statistically significant number of samples to assist in recovery modelling.

1.2 Key research questions

The current data gaps in geotechnical and grain size assessment discussed in the previous section lead to two fundamental questions:

> (1) Can the methods currently used in manual geotechnical data collection be automated using data derived from automated core logging technology?
>
> (2) Are currently available microanalytical methods capable of producing robust grain size proxies at a rate similar to current automated core logging systems?

These research questions are addressed through a series of research aims (outlined in section 1.3) which present the development and testing a series of geotechnical and grain size assessment methods and protocols and comparing the results of these protocols to data collected in the traditional manner.

1.3 Aim and scope

The Cadia East is currently being mined by Newcrest Mining using underground block caving methods. Drill core from the Cadia East deposit was analysed using Corescan technology which allows for automated, continuous downhole data collection over the length of scanned drill holes. This technique provides quick, consistent analysis of a large quantity of drill core in a district where a wide breadth of geotechnical and grain size knowledge already exists for comparison. The data extracted from Corescan's automated core logging technology shows great promise to allow for the rapid, continuous, down hole calculation of key geotechnical and geometallurgical parameters.

This research investigates the potential to use data generated by a Corescan hyperspectral drill core logger for geotechnical and geometallurgical applications. To address the two fundamental research questions proposed in section 1.2, two primary aims are the focus of this thesis: (1) develop protocols to rapidly extract consistent morphological and mineralogical geotechnical parameters from Corescan data, and (2) test a number of currently available microanalytical techniques that could complement the current Corescan system in rapidly determining proxies for copper sulphide and gold grain sizes. These complementary techniques must operate on the same interval as a typical assay (1 to 2 metres) and collect measurements at a rate similar to Corescan data acquisition (3 minutes per metre). Corescan digital drill core data and rock samples from the Cadia East underground mine provide a case study to develop, test, and evaluate the protocols generated to address these aims.

The scope of the geotechnical portion of the PhD research was to develop a methodology that successfully extracts geotechnical index parameters, not to develop computer code that executes this workflow. The reader should keep in mind that the protocols proposed here utilize manual steps, such as manually extracting points associated with each fracture and manually inputting those points into an Excel workbook for orientation processing. It is assumed that someone with computer programming knowledge would be able to code these steps into an automated process, but challenges may be encountered as some of the steps may require advanced data extraction methods. Computer programing aspects of the protocols, as well as the associated challenges, will not be addressed in this thesis. This work is considered to be a proof of concept study only.

The aims of the grain size assessment work were: (1) determine if each microanalytical method could detect gold and copper sulphide minerals adequately for a grain size proxy calculation, (2) compare the calculated grain size proxy to the measured MLA value to assess the performance of the grain size proxy, (3) determine the number of analyses required to obtain a reasonable grain size proxy, and (4) determine if the rate of data acquisition is similar to that of the Corescan rate of 3 minutes per metre. The scope of this research is limited to testing the methodology only, and does not discuss the logistics of implementing this type of system into the Corescan data collection procedures.

The protocols for both geotechnical data extraction and grain size assessment were developed and tested using data from the Cadia East underground resource. To provide a geologic background for the study site, the geologic setting, rock types, and style of mineralisation at Cadia East will be briefly discussed in section 1.4.

1.4 Geology of Cadia East

Porphyry copper deposits are an important global source of metal and account for over 50% of the Cu production worldwide (Sinclair, 2007). The Cadia East Au-Cu porphyry deposit is located approximately 20 km south of Orange, NSW, Australia (Figure 1.1), and is wholly owned and operated by Newcrest Mining Limited. The current resource estimate of 3 billion tonnes at 0.37 g/t gold and 0.26% copper contains over 35 million ounces of gold (Newcrest, 2018).

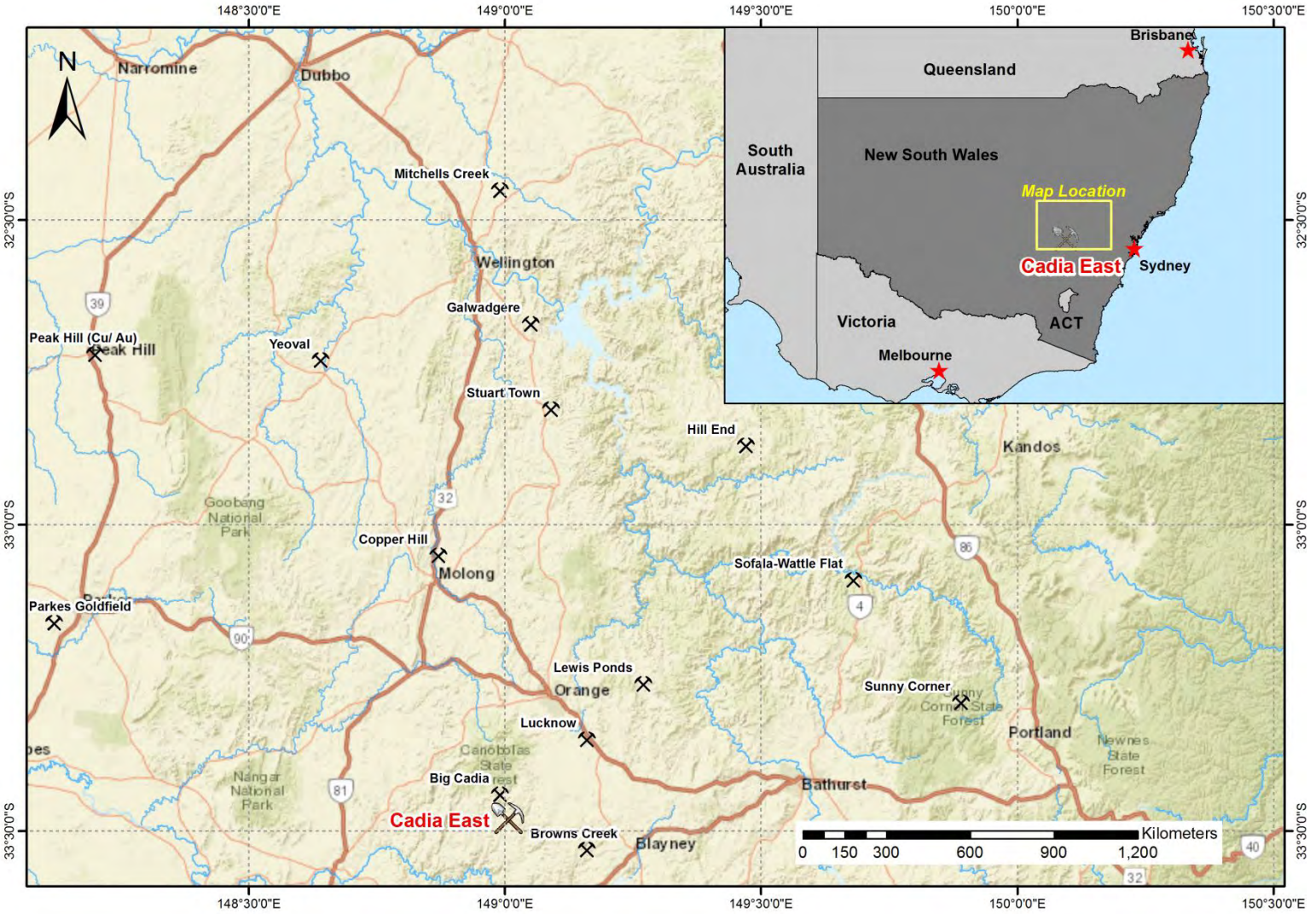

Figure 1.1. *Location of the Cadia East deposit, New South Wales, Australia.*

The chert, feldspathic siltstones, and sandstones of the Ordovician Weemalla Formation represent the oldest strata in the Cadia district and are conformably overlain by the intermediate to mafic volcanic and volcano-sedimentary rocks of the Forest Reef Volcanics (Squire, 2001; Wilson, 2003). The Forest Reef Volcanics are the primary lithostratigraphic unit observed within the Cadia East deposit. The Cadia Intrusive Complex intrudes the Weemalla Formation and Forest Reef Volcanics as a 1.5 km by 3 km composite stock of quartz-monzonite porphyry and hosts a majority of the mineralisation within the Cadia district (Wilson, 2003). Approximately 2.5 km southeast of the Cadia Intrusive Complex, a series of subvertical to steeply-dipping, east-west striking monzonite to quartz monzonite porphyry dykes known as of the Cadia Far East Intrusive Complex intrude the Forest Reef Volcanics (Wilson, 2003). A generalised cross-section through the Cadia East deposit is shown in Figure 1.2 to demonstrate the relationship between these units. Table 1.1 outlines the primary rock types observed in the Cadia East deposit.

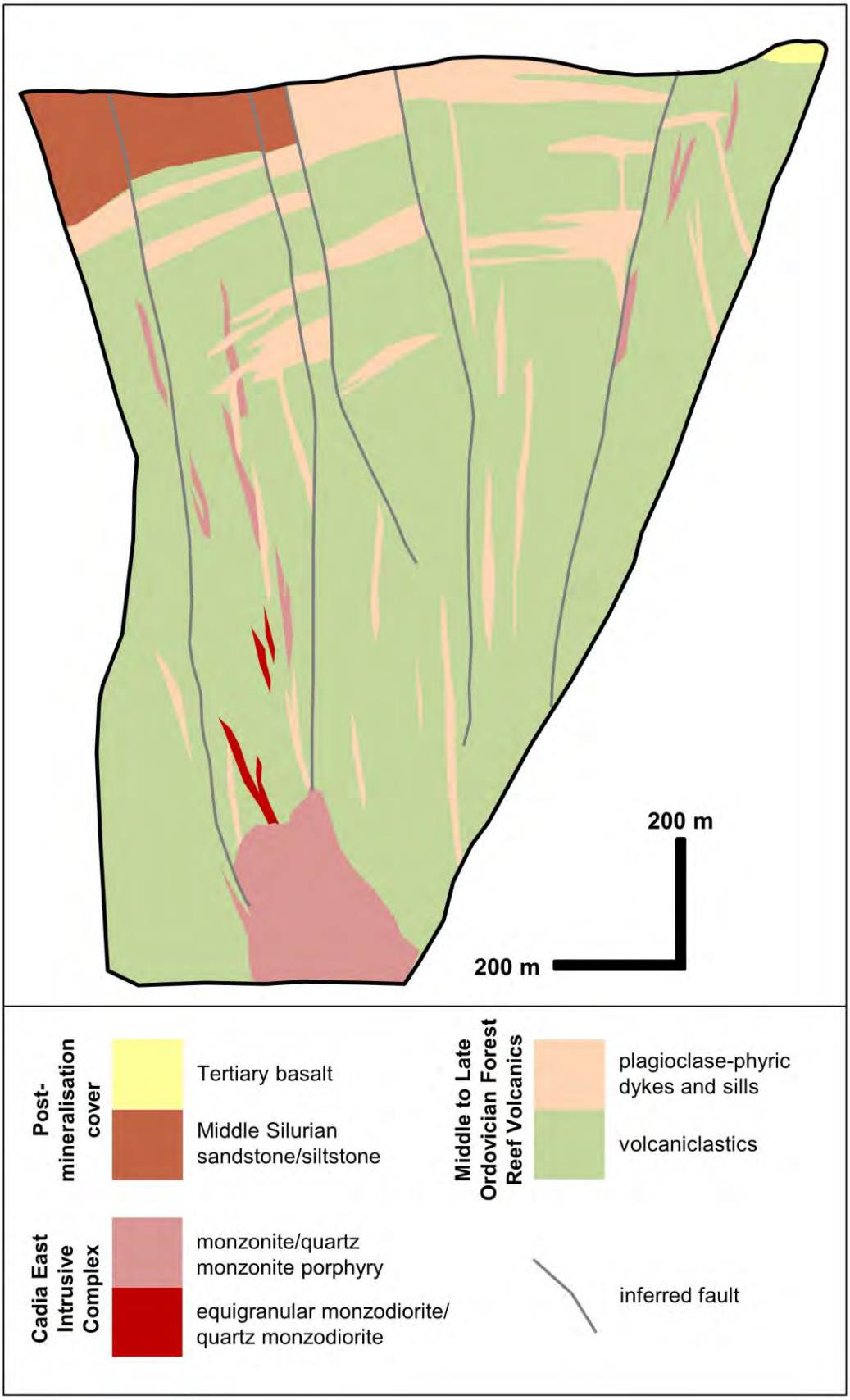

Figure 1.2. *Generalised E-W cross-section (looking north) through the Cadia East deposit. Figure modified from Fox (2012).*

Table 1.1. *Primary rock types present in the Cadia East deposit. Compiled from Kitto (2005); Squire (2001); Wilson (2003).*

Rock Unit Name	Age	Spatial Extent	Description
Weemalla Formation	Middle to Late Ordovician	exposed in the Cadia district; not intersected at Cadia East, but inferred to be present below Forest Reef Volcanics	fine-grained, laminated sediments; likely distal turbitie successions
Forest Reef Volcanics	Late Ordovician	widely distributed in the Cadia district; principle lithostratigraphic unit at Cadia East	greater than 450 m thick; six main facies: (1) polymictic volcanic conglomerate with sandstone matrix, (2) massive clinopyroxene-phyric basaltic andesite, (3) bedded calcareous volcanic sandstone, (4) polymictic volcanic pebble conglomerate with breccia matrix, (5) planar laminated volcanic siltstone, and (6) pyroxene-phyric and feldspar-pyroxene-phyric intrusions; likely represent products of submarine volcaniclastic apron
Cadia Intrusive Complex	Late Ordovician to Early Silurian	intrudes Forest Reef Volcanics at 800 m; present within Cadia East	subvertical to steeply-dipping, east-west striking monzonite to quartz monzonite porphyry dykes, typically < 15m apparent thickness
Wallace Shale	Middle to Late Silurian	overlies Forest Reef Volcanics; partially covers Cadia East	argillite to arenite (minor calc-arenite); basal conglomerate
Canobolas Volcanic Complex	Tertiary	uncomformably overlies Forest Reef Volcanics; partially covers Cadia East	massive to vesicular fine-grained basalt; consists of olivine, pyroxene and plagioclase phenocrysts; accessory magnetite and Fe-Ti oxides in a dark grey, aphanitic groundmass

More than 70% of the total gold in the Cadia district is contained within the ~2 km long, 600 metre wide, and more than1500 metre deep mineralized zone called the Cadia East deposit. This resource is hosted in a zone of steeply north- and south-dipping sheeted quartz-calcite-feldspar veins containing bornite-chalcopyrite ± molybdenite (Harris et al., 2010). Two zones of mineralisation are observed within the deposit area: (1) an upper, copper-dominant zone hosted in a 200-300 metre thick package of volcaniclastic breccia; and (2) a deep, central, gold-rich zone associated with sheeted veins centred on a core of steeply-dipping quartz-sulphide veins (Kitto, 2005). In the upper unit, copper mineralisation occurs as finely to coarsely disseminated chalcopyrite with minor bornite within the Forest Reef Volcanics. The deep, central zone hosts chalcopyrite, bornite, molybdenite, gold, and minor covellite (Kitto, 2005; Wilson, 2003). Copper sulphides typically occur as fine to coarse disseminations, along grain boundaries, in cracks and fractures, within veins, and as intergrowths with each other (Figure 1.3A and B). Gold mineralisation is spatially associated with sulphide mineralisation. Gold occurs along sulphide grain boundaries when hosted in sulphide minerals and as elongated inclusions or along cracks and grain boundaries in silicate minerals (Figure 1.3C) (Kamenetsky and Berry, 2010).

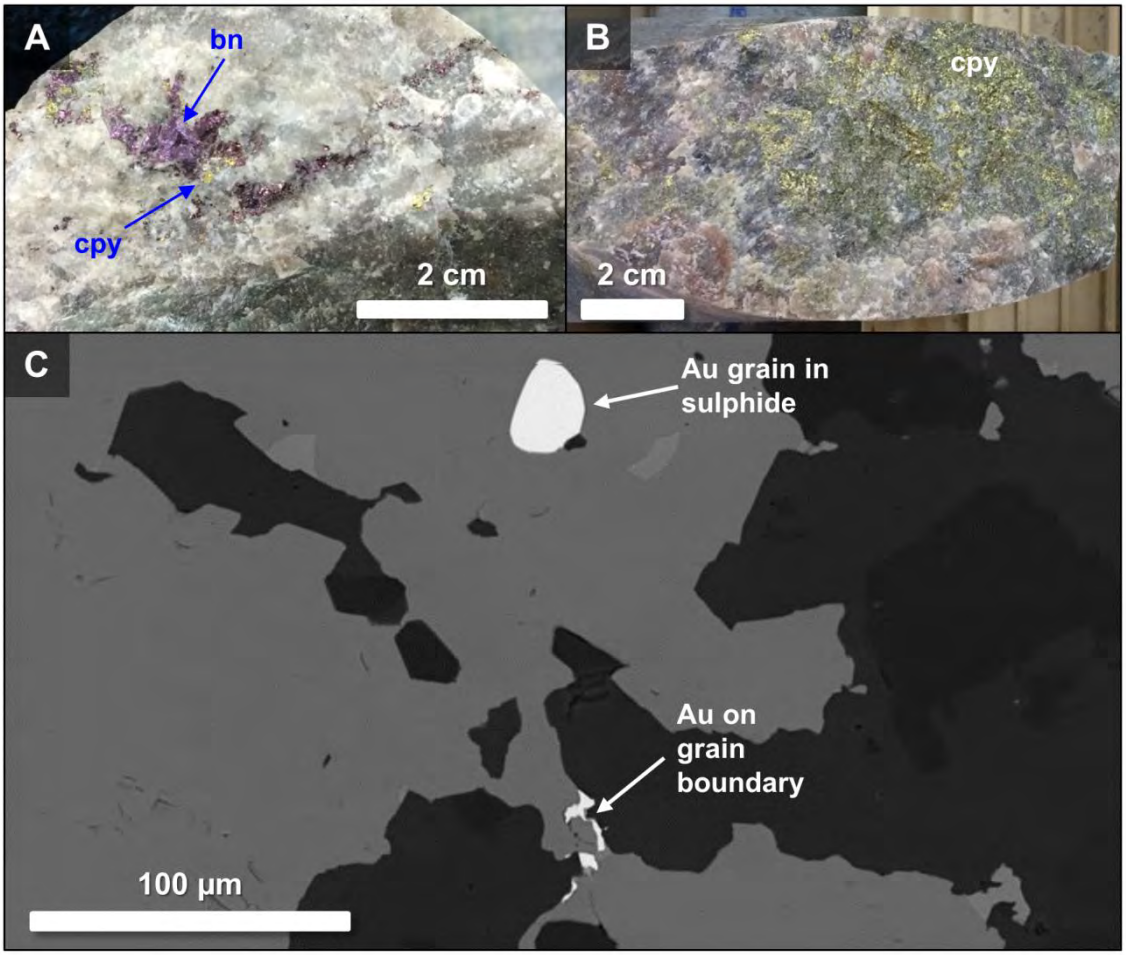

Figure 1.3. *Examples of vein-hosted copper sulphide (A and B, drill core images) and gold (C, SEM backscatter image) mineralisation from the Cadia East deposit. Bn = bornite, cpy = chalcopyrite, Au = gold.*

The structural setting of the Cadia East deposit is long-lived and complex (Wilson, 2003). An intersection of regional-scale faults is interpreted to have localised the Cadia Intrusive Complex and associated gold-copper mineralisation (Newcrest, 2011). The Cadia East deposit is bounded to the north and south by steeply-dipping normal and reverse faults (Kitto, 2005). Mineralisation in the Cadia East deposit is offset by, at least, three major, post-mineral structures including the north-trending Gibb Fault, the east-trending Pyrite Fault Zone, and an unnamed east-trending reverse fault that displaces mineralisation by more than 100 metres in some areas of the deposit (Holliday et al., 2002). The Pyrite Fault Zone is spatially related to the monzonitic intrusions and gold-copper mineralization that occurs at depth in Cadia East (Wilson, 2003).

1.5 Thesis structure

This thesis is comprised of twelve chapters which address the thesis aims. Geotechnical assessment using Corescan is introduced, followed by three chapters outlining the methods and results with the following structure:

- Chapter 2 contains a discussion of geotechnical assessment indices, manual geotechnical data collection methods, key geotechnical characteristics of the Cadia East deposit, scientific principles of VNIR-SWIR hyperspectral analysis, and automated core logging technology (including the Corescan system).

- Chapter 3 outlines the method development and proposed methods used to extract key, morphological (e.g. non-mineralogical) geotechnical index parameters from Corescan data.

- Chapter 4 compares the extracted geotechnical index parameters (outlined in Chapter 3) and the measured or observed values.

- Chapter 5 presents methods to estimate mineralogical-related geotechnical index parameters from Corescan and includes a discussion of the performance of these methods compared to visual estimation and manual core logging.

Grain size assessment by various microanalytical techniques is introduced in chapter 6, followed by a separate chapter for each microanalytical technique with the following structure:

- Chapter 6 introduces the grain size assessment method chapters and includes a discussion of the importance of grain size assessment in recovery modelling, industry-standard grain size assessment methods, and details the experiment designed to test multiple microanalytical techniques for grain size assessment.

- Chapters 7 – 11 detail the individual microanalytical techniques used to assess grain size. These chapters begin with a discussion of the scientific principles of the technology, followed by the methods used to calculate gold and copper sulphide grain size proxies. The results are compared to the measured grain sizes from MLA, and the potential of each technology to be used as a grain size assessment tool at a rate similar to the Corescan

is discussed. The specific chapters addressing each microanalytical technique are:

- Chapter 7: portable x-ray fluorescence spectroscopy (pXRF)
- Chapter 8: microscopic x-ray fluorescence spectroscopy (μXRF)
- Chapter 9: laser ablation inductively coupled mass spectrometry (LA-ICP-MS)
- Chapter 10: laser induced breakdown spectroscopy (LIBS)
- Chapter 11: laser Raman spectroscopy

The thesis concludes with a compilation of the key findings of both the geotechnical and grain size research (Chapter 12). The application of the methods developed in the thesis is also addressed, as well as the potential implementation of these protocols within the Corescan data outputs. Key considerations and recommendations for future work are also discussed.

Chapter 2

Introduction to geotechnical assessment and hyperspectral principles

2.1 Introduction

Careful assessment and modelling of geotechnical characteristics within an ore deposit are vital to determining both the viability and profitability of a mining operation (Hoek et al., 2000). Geotechnical characteristics of rocks are a function of the geological processes that formed both the host rocks and associated mineralisation. Typically, a geotechnical model is constructed by combining manually collected geotechnical measurements from drill core with other geological observations. Observations of rock mass conditions provide critical information in an underground mining scenario, particularly as it relates to ground support requirements (Hoek et al., 2000). Understanding the geotechnical characteristics requires information about the morphological properties of fractures (e.g. fracture spacing, roughness, etc.) as well as the mineralogical properties. Two common geotechnical indices used to characterise groundmass conditions are the RMR and Q-index.

Standard methods for geotechnical data acquisition and ground condition modelling in hard rock environments rely on the identification and classification of fractures from manual logging of drill core. While this manual method is successfully applied to mining, it is often laborious and has the potential to generate inconsistent results. Additionally, inconsistencies in manually collected data require that underground geotechnical observations weigh heavily in determining the geotechnical index values. While these observations are robust, the geotechnical characteristics should be adequately assessed prior to underground development. Automation of geotechnical data collection from fractures identified in digital drill core data would allow for consistent, rapid assessment of key parameters as they relate to ground conditions.

The application of downhole imagery to perform fracture analysis has been used in the oil and gas industry since the 1960s (Prensky, 1999). In mining, acoustic televiewer data acquired from borehole logging is often used to measure the orientation of fractures and joints downhole (Shigematsu et al., 2014; Trofimczyk

and Du Pisani, 2009). While these data are accurate and provide the added advantage of *in situ* measurements, it is expensive and often difficult to acquire in areas with poor ground conditions. Automated core logging systems provides a unique opportunity to automatically capture and record continuous fracture data over large volumes of drill core.

This chapter will introduce common geotechnical assessment indices, as well as, the geotechnical characteristics and considerations for the Cadia East study site. An outline of key geotechnical mineral properties and how these relate to geotechnical assessment is also presented, followed by a discussion of automated core logging systems (including the Corescan system) and hyperspectral data principles. This chapter concludes with an outline of the subsequent geotechnical chapters.

2.2 Geotechnical assessment calculations

The stability and behaviour of rocks within an underground mine are affected by numerous factors, including the sequence of mining, *in situ* stresses, geometry, composition and the nature of an orebody and the surrounding host rocks. Consistent, quantitative rock classification is required to understand both the caveability of an ore body as well as the ground support required for the installation of underground development and extraction infrastructure (Brady and Brown, 2013; Hoek et al., 2000). The first historical record of a formal rock mass classification system was proposed by Ritter (1879). Other early authors designed classification schemes that fit the purpose they were designed for, but did not necessarily apply to engineering applications outside of their intended scope (Lauffer, 1958; Terzaghi, 1946). Since this time, a number of rock mass classification systems have been proposed, including the geological strength index (GSI) proposed by Marinos and Hoek (2000) and the rock structure rating (RSR) proposed by Wickham et al. (1972). Three geotechnical assessment indices commonly used in mining are the rock quality designation (RQD), rock mass rating (RMR), and the tunnelling index (Q-index). These three indices are discussed in sections 2.2.1 through 2.2.3 below.

2.2.1 Rock Quality Designation (RQD)

Rock Quality Designation (RQD) is commonly used to estimate rock conditions from drill core (Deere et al., 1967). The RQD value is calculated by measuring the

percentage of core that is considered to be unbroken (greater than 10 cm in length) as shown by the following equation:

$$RQD(\%) = \frac{(\sum length\ core{>}10\ cm)}{(total\ length\ core\ run)}\ x\ 100\% \qquad [2.1].$$

The relative RQD values and their general rock quality description are outlined in Table 2.1.

Table 2.1. *RQD% values and their indication of relative rock mass quality. From Deere et al. (1967).*

RQD Value	Relative Rock Quality
0 – 25%	Very poor
25 – 50%	Poor
50 – 75%	Fair
75 – 90%	Good
90 – 100%	Excellent

The RQD is a proxy for *in situ* ground conditions, so any fracturing induced by the drilling process needs to be removed from the RQD calculation. The RQD can act as a rock quality description alone, but is also a key component in both the Rock Mass Rating and Q-index calculations.

2.2.2 Rock Mass Rating (RMR)

The RMR classification system was originally developed for civil engineering applications, but has since been modified to account for underground mining conditions (Bianewski, 1989; Hoek et al., 2000). The original RMR classification system was developed using a series of case studies for the behaviour of rock masses in the underground mining environment (Bieniawski, 1976). Over the years, the system had been continuously modified to incorporate more case studies, and significant changes were made between the 1976 and 1989 RMR rock classification systems (e.g. Laubscher (1977), Laubscher and Taylor (1976), Laubscher (1984), Laubscher and Page (1990), Cummings et al. (1982), and Kendorski et al. (1983)) (Hoek et al., 2000).

The RMR as defined by Bieniawski (1989) is calculated by categorizing six parameters: 1) uniaxial compressive strength (UCS); 2) RQD; 3) spacing of

discontinuities; 4) condition of discontinuities; 5) groundwater conditions; and 6) orientation of discontinuities. For each parameter, a range of measured or observed values defines the rating number (Table 2.2). These values are then summed to obtain the final RMR value. Bianewski (1989) defines the relative rock quality based on the range of RMR values calculated (Table 2.3). These values are then used to define the excavation type and ground support requirements (Bieniawski, 1989).

Table 2.2. *Classification of individual parameters associated with the RMR calculations. Modified from Bieniawski (1989).*

RMR Classification Criteria								
Rating Value		15	12	7	4	2	1	0
Strength of intact rock	Point-load strength index	> 10 MPa	4 - 10 MPa	2 - 4 MPa	1 - 2 MPa	UCS preferred		
	UCS	> 250 MPa	100 - 250 MPa	50 - 100 MPa	25 - 50 MPa	5 - 25 MPa	1 - 5 MPa	< 1 MPa
Rating Value		20	15	13	8	3		
Drill core quality	RQD	90 - 100%	75 - 90%	50 - 75%	25 - 50%	< 25%		
Rating Value		20	15	10	8	5		
Fracture spacing		> 2.0 m	0.65 - 2.0 m	200 - 600 mm	60 - 200 mm	< 60 mm		
Rating Value		30	25	20	10	0		
Fracture condition	Rating Value	6	4	2	1	0		
	Length	< 1 m	1 - 3 m	3 - 10 m	10 - 20 m	> 20 m		
	Rating Value	6	5	4	1	0		
	Aperture	None	< 0.1 mm	0.1 - 1.0 mm	1 - 5 mm	> 5 mm		
	Rating Value	6	5	3	1	0		
	Roughness	Very rough	Rough	Slightly rough	Smooth	Slickenside		
	Rating Value	6	4	2	2	0		
	Infill	None	Hard filling < 5 mm	Hard filling > 5 mm	Soft filling < 5 mm	Soft filling > 5 mm		
	Rating Value	6	5	3	1	0		
	Weathering	Unweath	Slightly weathered	Moderately weathered	Highly weathered	Decomposed		
Rating Value		15	10	7	4	0		
Ground-water	Inflow per 10 m tunnel length (l/m)	None	< 10	25-Oct	25 - 125	> 125		
	(Frac water press)/ (Principle stress)	0	< 0.1	0.1 - 0.2	0.2 - 0.5	> 0.5		
	General conditions	Completely dry	Damp	Wet	Dripping	Flowing		

Table 2.3. *Rock mass quality based on the RMR classification system. Modified from Bieniawski (1989).*

RMR Value	Relative Rock Quality
< 21	Very poor
21 – 40	Poor
41 – 60	Fair
80 – 61	Good
81 – 100	Excellent

The application of the RMR system requires that a rock mass be divided into structural regions and that the RMR be calculated individually for each structural region. The boundaries of these regions are typically defined by major structural or lithological boundaries. Some rock types and structural zones display significant heterogeneity with respect to discontinuity spacing or general rock characteristics, and thus must be subdivided further (Hoek et al., 2000).

2.2.3 Tunnelling (Q) Index

The Norwegian Geotechnical Institute's Q-index was developed after examining numerous case studies of rock behaviour in underground mines (Barton et al., 1974). The Q-index is defined as a numerical value on a logarithmic scale from 0.001 to 1000 with the following geotechnical inputs: (1) RQD; (2) number of joint sets (J_n); (3) joint roughness (J_r); (4) joint alteration number (J_a); (5) joint water reduction factor (J_w); and (6) stress reduction factor (SRF). The relationship between these six parameters is given by the following Q-index formula:

$$Q = \frac{RQD}{Jn} \times \frac{Jr}{Ja} \times \frac{Jw}{SRF} \qquad [2.2]$$

where,

RQD/J_n is an approximation of block size, J_r/J_a is an estimate of the inner block shear strength, and J_w/SRF represents a total active stress indicator (Barton et al., 1974). The first quotient in the calculation (RQD/J_n) is an estimate of particle size with the two extreme values of 100/0.5 and 10/20 (separated by a factor of 400) (Hoek et al., 2000). The second quotient (J_r/J_a) is weighted in favour of rough, unaltered fracture surfaces in direct contact with one another. Fractures with thin coatings of clay minerals have significantly reduced strength, so this quotient is vitally important to understanding the failure probability for a rock mass. The third and final quotient (J_w/SRF) quantifies two primary stress parameters: (1) the

stress reduction factor (SRF), and (2) the water reduction factor. The SRF measures loosening loads in an excavation near shear zones and clay-bearing rock, rock stresses of competent rock, and squeezing loads in plastic, incompetent rocks. The water reduction factor accounts for the control that water flow has on shear strength by rock softening and wash-out of soft clay minerals and gouge (Barton et al., 1974). Table 2.4 outlines the classification of individual parameters associated with the Q-index calculations.

Table 2.4. *Classification of individual parameters associated with the Q-index calculations. Modified from Barton et al. (1974).*

Tunnelling Quality (Q) Index Classification Criteria										
Rating Value		90 - 100	75 - 90	50 - 75	25 - 50	0 - 25				
Drill core quality	RQD	Excellent	Good	Fair	Poor	Very Poor				
Rating Value		0.50 - 1.00	2	3	4	6	9	12	15	20
Fracture Set Number	J_n	Massive, few fractures	1 fracture set	1 fracture set + random	2 fracture sets	2 fracture sets + random	3 fracture sets	3 fracture sets + random	4 + fracture sets, heavily fractured	Crushed rock, earthlike
Rating Value		4	3	2	1.5	1.5	1	0.5		
Fracture Roughness Number	J_r	Discontinuous fractures	Rough, irregular, undulating	Smooth, undulating	Slickenside, undulating	Rough or irregular, planar	Smooth, planar	Slicken, planar		
Rating Value		0.75	1	2	3	4				
Fracture Alteration*	J_a	None	< 10	10 - 25	25 - 125	> 125				
Rating Value		1	0.66	0.5	0.33	0.10 - 0.20	0.05 - 0.10			
Fracture Water Reduction	J_w	Dry excavation or minor inflow (< 5 l/min)	Medium inflow , rare outwash of fracture infill	Large outflow in solid rock with unfilled fractures	Large inflow or high pressure	Very high inflow at blasting, decaying with time	Very high inflow or pressure			
Rating Value		2.5	1	0.50 - 2.00	5.00 - 10.00	10.00 - 20.00				
Stress Reduction Factor^	SRF	Low stress, near surface	Medium stress	High stress, very tight structures	Mild rockburst	Heavy rockburst				

*Additional criteria used when mapping larger scale structures (e.g. underground drives). Criteria are used on drill core observations.

^Additional criteria used for different levels of rock competency and rocks stress. Criteria are designed for competent rock with rock stress challenges.

2.3 Manual geotechnical data collection from drill core

Manually logging drill core for geotechnical parameters is common practice for exploration and mining projects. Geologists and geotechnical engineers evaluate the drill core manually and classify key geotechnical parameters within the drill core. Geotechnical information can be collected on both oriented and unoriented drill core. Drill core orientation is typically completed at the drill rig using a series of tools designed to locate the bottom of the drill hole by gravimetric or magnetic means (Ureel et al., 2013). The drilling crew then draws a line on the drill core surface representing the bottom of the drill hole, known as the orientation line or the orientation mark (Holcombe, 2013). Some authors have proposed techniques to orient the drill core after it has been removed from the drill rig using a known fabric orientation (cleavage, bedding, etc.), making the measurement of fracture orientations in unoriented drill core possible (Holcombe, 2013; Scott and Berry, 2004). If the drill core is not oriented, only apparent fracture orientations can be collected. In this case, other parameters not related to the orientation of the drill core such as RQD and fracture roughness can still be assessed.

The objective of measuring fracture orientations from oriented drill core is to characterise the true orientation of fractures in space (Sullivan et al., 1992). To measure fracture orientations from oriented drill core, the industry standard methods outlined in Holcombe (2013) are used. The alpha angle is defined as the acute angle between the long axis of the ellipse and the core axis (Figure 2.1). The angle between the orientation line (representing bottom of the drill hole) and the down hole edge of the ellipse of the apical trace of the fracture (measured clockwise) is defined as the beta angle (Figure 2.1) (Holcombe, 2013). In practice, fracture orientations are collected manually using a protractor to measure alpha angles and a wrap-around ruler to measure beta angles (Figure 2.2).

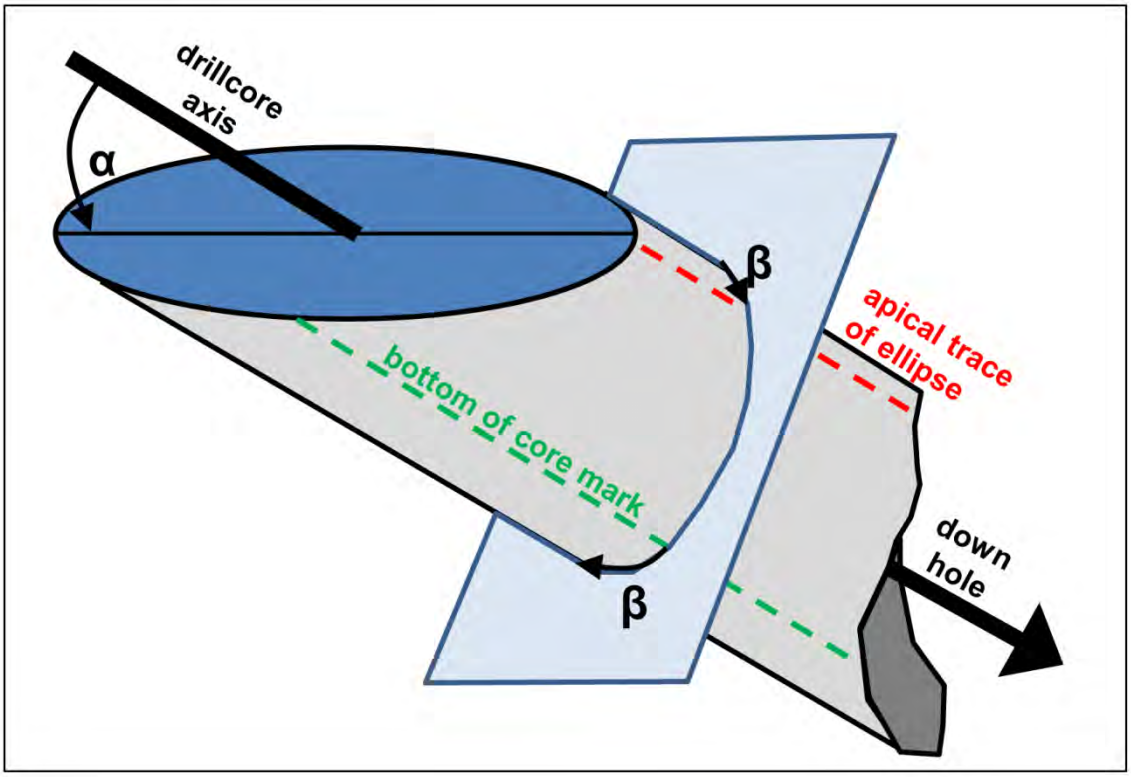

Figure 2.1. *Drill core orientation conventions including the alpha angle and the beta angle. Figure modified from Holcombe (2013).*

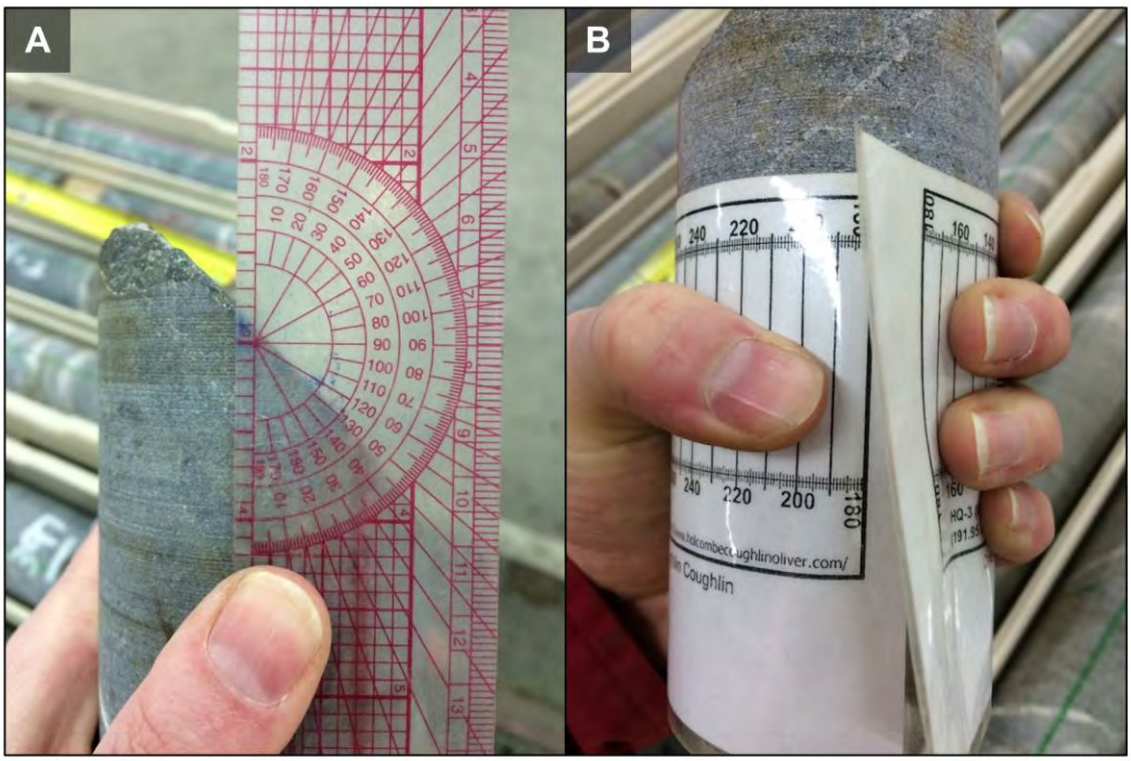

Figure 2.2. *The alpha angle is measured using a placed protractor parallel to the drill core and perpendicular to the fracture (A). The beta angle is measured using a wraparound ruler for the appropriate diameter of drill core (B).*

Since the alpha and beta angles represent the apparent orientations of fractures, the true, measured orientations need to be determined to account for the trend and plunge of the drill hole. This transformation can be manually completed using stereonets, but modern software (such as GeoCalculator®) can quickly perform these transformations mathematically.

Fracture roughness is evaluated manually by comparing the visual profile of the fracture surface to reference profiles outlined in the geotechnical index being used. In the Q-index system, Barton (1976) defines six general roughness classifications (J_r values) based on the geometry and general roughness of the fracture surface. The Joint Roughness Coefficient (JRC) is a similar measure of roughness proposed by Barton and Choubey (1977) to quantify the relative roughness of a fracture surface. The JRC values are directly related to the J_r values required by the geotechnical Q-index, so either of the two parameters can be logged manually using the reference profiles (Figure 2.3).

Description	Reference Profile	J_r	JRC
Stepped			
Rough		4	20
Smooth		3	14
Slickenside		2	11
Undulating			
Rough		3	14
Smooth		2	11
Slickenside		1.5	7
Planar			
Rough		1.5	2.5
Smooth		1.0	1.5
Slickenside		0.5	0.5

Figure 2.3. *Reference roughness profiles used to manually determine the Jr (in the Q system) and JRC for 20 cm drill core samples. Modified from Barton (1987).*

The number of fracture sets is evaluated manually on each core run by assessing the fracture orientation relative to the core axis and the mineralogy within each fracture. A core logging geologist or geotechnical engineer will determine how many different groups (or sets) of fractures are present for a given logging interval. Fracture spacing is measured by determining the average distance between fractures for a given interval and the number of fractures per metre. The RQD is measured by summing the length of core pieces greater than 10 cm over a given interval, then dividing this value by the total meterage for the interval (Deere et al., 1967).

2.4 Geotechnical properties of minerals

The geotechnical behaviour of a rock mass is, in part, determined by the mineralogical properties present within and surrounding fractures. The hardness, swelling potential, and friction potential of the minerals present and the relative abundance of these minerals influence the geotechnical properties of a rock mass. The hardness of minerals can be defined in a number of ways, but the most common geological classification for relative hardness is Mohs scale (Broz et al., 2006). This system was proposed by Mohs (1825) and defines a relative ranking based on a mineral's resistance to scratching compared to other minerals.

The swelling potential of various minerals is well-documented in the geotechnical literature, and is directly related to the crystal structure of the mineral (e.g., Rauh and Thuro, 2007 and Sabtan, 2005). Minerals such as quartz and feldspar are unlikely to absorb water molecules in their crystal structure and, therefore, have no swelling potential. Minerals belonging to the clay subclass of the phyllosilicate group form alternating tetrahedral and octahedral sheet structures. When the ratio of tetrahedral (T) to octahedral (O) sheets is 1:1 (T-O structure), water molecules are unlikely to be absorbed giving these minerals no swelling potential (Figure 2.4A). When the ratio of T to O sheets is 2:1, sequences of T-O-T structures are held together by interlayer cations (Figure 2.4B). Some minerals with the T-O-T structure, such as chlorite, phlogopite, and sericite, do not typically contain interlayer water and are considered to have low swelling potential. Other T-O-T minerals, such as montmorillonite, nontronite, and vermiculite have interlayer cations that can be surrounded by water molecules. When interlayer water is present, the mineral is considered to have high swelling potential and is capable of expanding to many times the original volume. This expansion can cause instability, particularly when present in fractures (Bell, 2013).

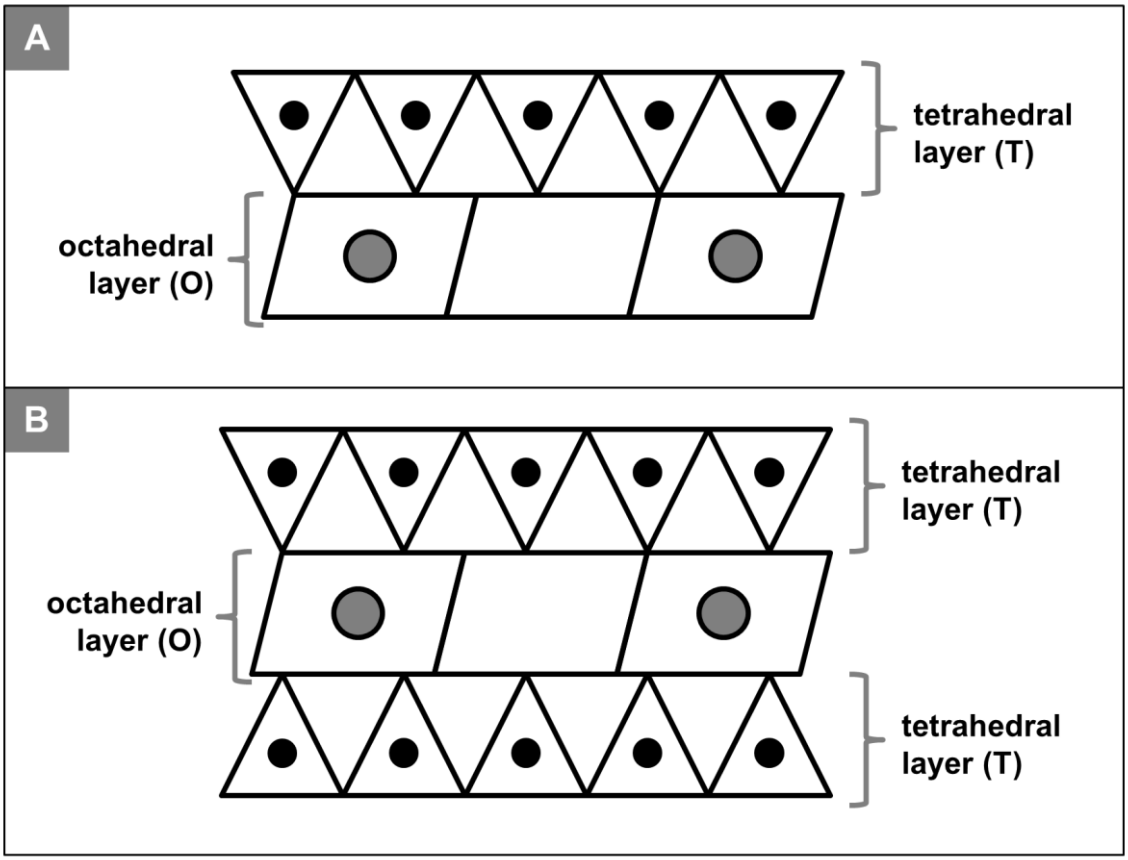

Figure 2.4. *Schematic, simplified tetrahedral-octahedral (TO) mineral structure (A) and tetrahedral-octahedral-tetrahedral (TOT) mineral structure (B) Modified from Railsback (2006).*

Anhydrite is a calcium sulphate mineral that is capable of absorbing water into its crystal lattice to form gypsum. This absorption can increase or decrease the volume of the mineral by up to 60% of the original volume (Rauh and Thuro, 2007). The zeolite mineral group is also capable of absorbing water, but typically this water is absorbed into open pore space and does not cause any major volume changes.

The friction potential of a mineral is based on the inherent internal cohesion defined by the maximum resistance to an applied shear stress (Hoek et al., 2000). While many methods for calculating friction potential have been applied to geotechnical applications (e.g. Coulomb, 1773, Barton, 1973), the relative friction potential for common fracture filling minerals have been calculated by Barton et al. (1974) for use in fracture assessment in the Q-index system. Since only a relative friction potential classification is required for the Q-index parameters, the values defined by Barton et al. (1974) are sufficient.

2.5 Geotechnical assessment at Cadia East

The grade and tonnage contained in the Cadia East deposit are amenable for underground panel caving methods. In contrast to bulk block caving methods, panel cave mining segments the ore body into individual panels to prevent dilution due to bulk extraction (Brady and Brown, 2013). The area immediately below the designed panel is excavated from the undercut level. An extraction level is then developed directly beneath the undercut level to allow for access and removal of ore upon initiation of the panel cave. The rock directly above the undercut level is then preconditioned using hydraulic fracturing techniques, and the ore material begins to naturally cave by gravity into draw points at the extraction level. This particular mining method is known for sustained high rates of production with relatively low production costs per tonne (Brady and Brown, 2013).

Active underground panel cave mining of the Cadia East deposit commenced in January 2013. Within the Cadia East underground operation there are three panel cave areas. Newcrest is currently mining panel cave 1 (PC1) and developing panel cave 2 (PC2), while panel cave 3 (PC3) is being drilled for resource and geotechnical definition (Figure 2.5). In order to safely and effectively develop the Cadia East deposit, a detailed geotechnical model was built on site.

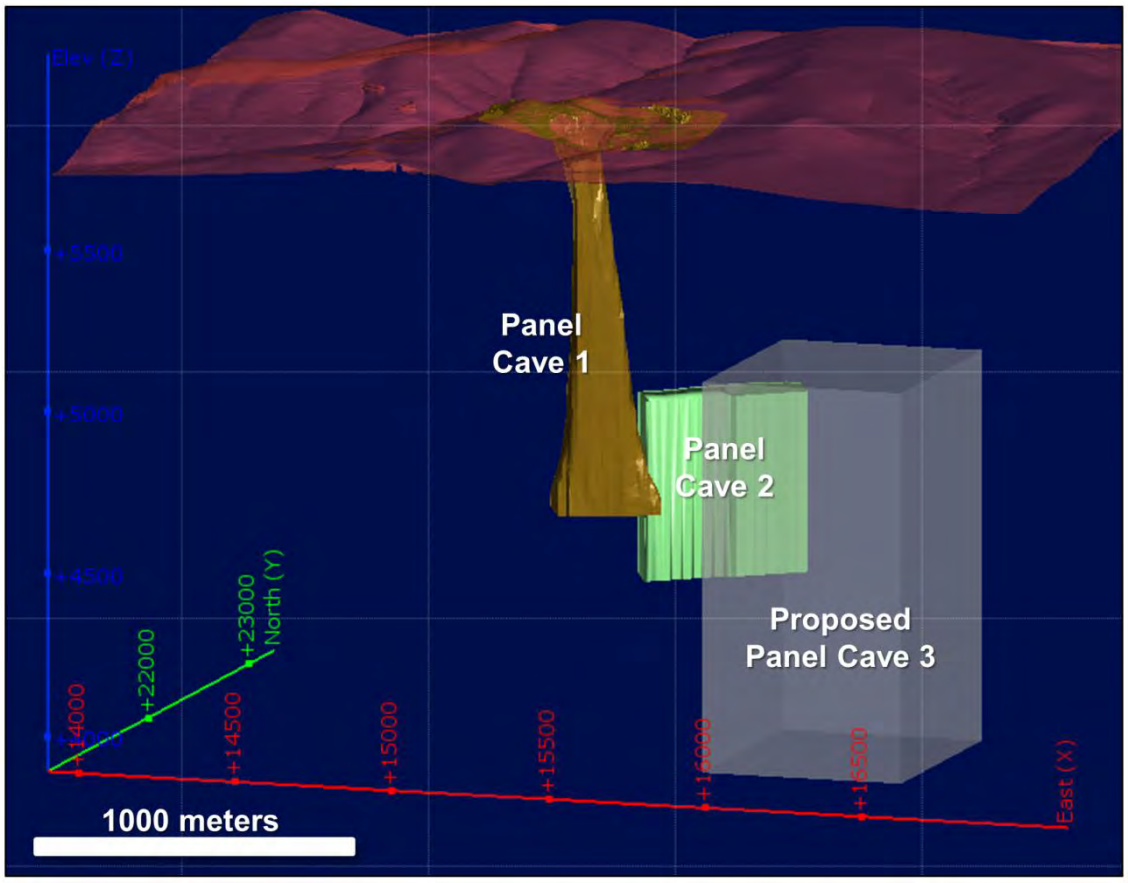

Figure 2.5. *Location and geometry of panel caves 1-3 at the Cadia East Mine. Panel cave 1 is currently being mined, panel cave 2 is in development and panel cave 3 is planned.*

The Cadia East geotechnical model aims to predict the variability of rock mass conditions using slightly modified versions of the RMR and Q-index values (known as the RMR' and Q'-index). The data inputs used to calculate the RMR' and Q'-index are presently collected manually using the geotechnical core logging methodology outlined in section 2.3.

Currently, the Cadia East geotechnical model is built by calculating the RMR' and Q'-index values for each domain from dill core measurements, and then confirming the modelled values using underground observations as development advances (Rossimel and Lett, 2012). The logistics of geotechnically logging drill core manually prevents all holes drilled at Cadia East from being logged from top to bottom for geotechnical parameters. Key drill holes that are expected to intersect challenging rock types as well as areas requiring more data are prioritised for geotechnical logging. This ensures that sufficient data is available for input into the geotechnical model. Unfortunately, inconsistencies in manual core logging techniques mean that not all of the data collected from drill core can be used in the geotechnical model. Additionally, these inconsistencies require that the underground geotechnical

observations weigh heavily in determining the RMR' and Q'-index values. While these observations are robust, ideally the geotechnical characteristics would be adequately assessed prior to underground development.

The Cadia East deposit has been divided into nine distinct geotechnical domains based on structure, rock type, and general rock mass quality. With respect to the geotechnical considerations at Cadia East, the primary rock types that are considered in the geotechnical domains are the volcaniclastics, porphyry dykes, and the monzonite intrusions (Cadia Intrusive) (Rossimel and Lett, 2012). The structures that most influence the geotechnical domains include pyrite faults, carbonate faults, and calcite-laumontite faults. The key geotechnical domains at Cadia East and their general features are outlined in Table 2.5, and discussed in detail in the following sections.

Table 2.5. *Summary of the nine primary geotechnical domains at Cadia East and their typical geotechnical characteristics, RMR and Q-index values (compiled from Rossimel and Lett, 2012).*

Geotechnical Domain	Dominant Features	Typical Fracture Sets	Typical Fracture Spacing (m)	Typical RQD%	Average RMR'	Average Q'-index
Calcite Laumontite (Ca-La) Crunch Central	highly fractured; commonly puggy chlorite shears	3.5	0.1	90 - 100%	36	4.2
Calcite Laumontite Crunch Zone	highly fractured; commonly puggy chlorite shears	4	variable	80 - 100%	33.6	3.5
Pyrite Faults	average 3 metres thick; pyrite infill; clay + rock flour gouge	3.5	variable	80 - 100%	36	5.6
Carbonate Faults	chlorite shearing; can be puggy gouge + iron carbonate	3.5	variable	80 - 100%	40.8	5.9
Porphyry Dyke	5 - 30 metres thick; very strong, brittle rock mass	2	variable	80 - 100%	60.1	16.7
Volcaniclastics	fine-grained massive volcaniclastics to conglomerates	3	0.25 - 0.5	variable	48.4	7.4
Monzonite	very competent, hard rock mass	2.5	0.25 - 0.4	90 - 100%	60.2	16.5

2.5.1 Calcite laumontite crunch and crunch central zones

The Calcite Laumontite (Ca-La) Crunch and Crunch Central fracture zones include highly fractured and veined zones up to tens of metres wide which are characterised by the presence of calcite and laumontite. Laumontite within these zones occurs as pale orange-pink crystals in areas of propylitic alteration. Laumontite is a member of the zeolite family and displays common zeolite characteristics (e.g. soft, hydrous, capable of reversible hydration). Both laumontite and calcite are prone to deterioration when exposed to the elements, so rock mass stability is of particular concern in this domain (Rossimel and Lett, 2012). Photographs of typical calcite laumontite crunch and crunch central drill core are shown in Figure 2.6.

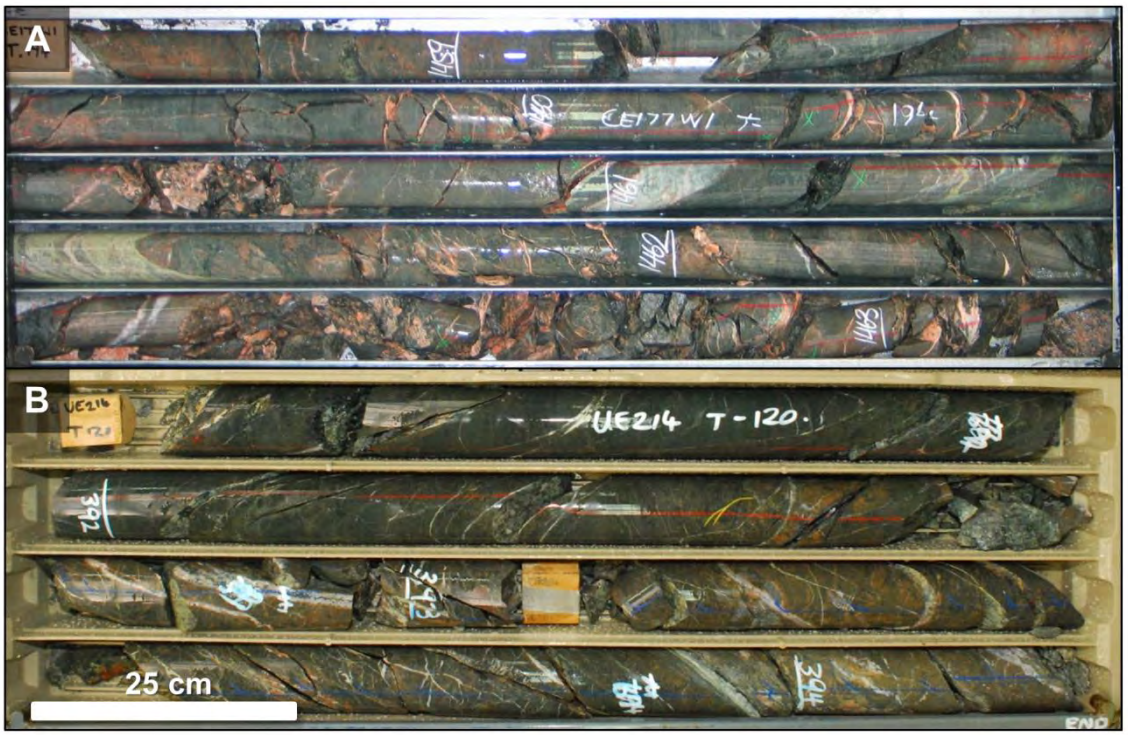

Figure 2.6. *Typical Ca-La crunch and crunch central drill core from the western edge of panel cave 2 (A) and central panel cave 2 (B). Photographs courtesy of Sarah Stark, Cadia East site team.*

2.5.2 Pyrite faults

The pyrite fault zone is cut by a series of twelve pyrite faults within the Cadia East deposit. Pyrite faults are dominated by a stiff, crystalline pyrite infill and selvage with variable, soft phyllic alteration. These faults range from 0.1 metres to 5 metres and average 3 metres in thickness. The P2 Fault is the thickest of these twelve structures at 5 metres thick. Movement along these faults is believed to be tens of metres, creating gouge consisting of both rock flour and clay. Where pyrite faults

intersect a rock mass, pyrite infill of fractures is common (Rossimel and Lett, 2012). Examples of the pyrite fault observed in drill core are shown in Figure 2.7.

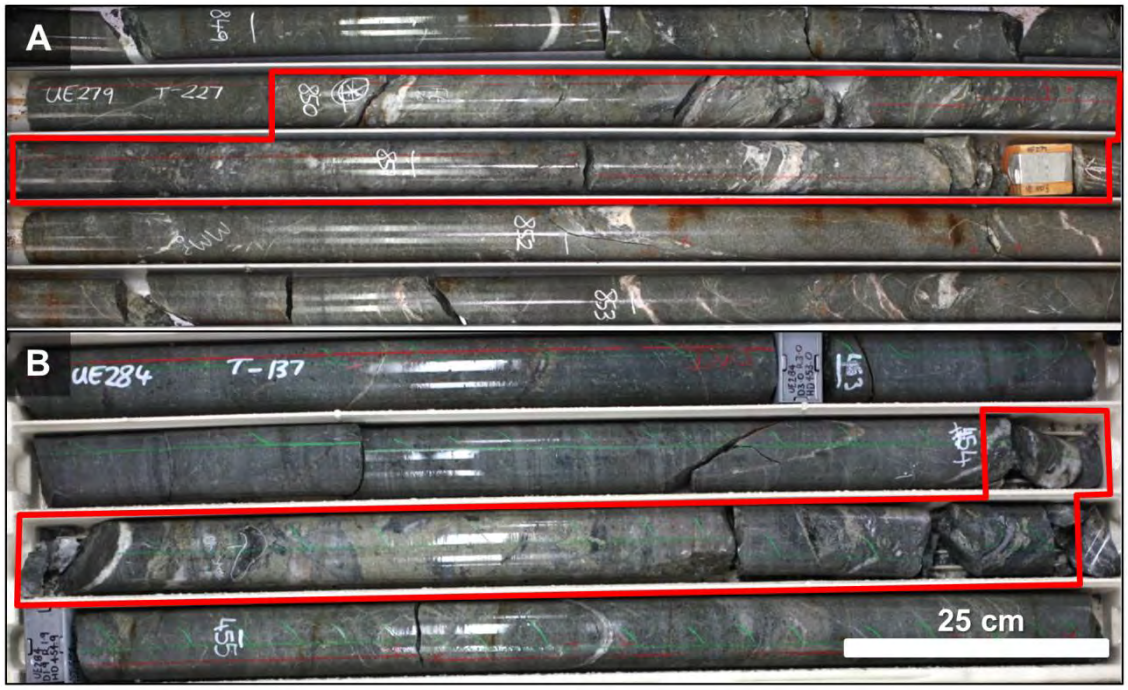

Figure 2.7. *Typical Pyrite fault drill core displaying moderate gouge from panel cave 2 (A, outlined in red), and well healed fault material from panel cave 3 (B, outlined in red). Photographs courtesy of Sarah Stark, Cadia East site team.*

2.5.3 Carbonate faults

The carbonate faults at Cadia East are a series of very shallow-dipping (approximately 30°), east-west striking structures, spaced approximately 50 metres apart. These faults are characterized by zones of yellow-orange iron-carbonate ± albite alteration and sheared chlorite surrounding a zone of cream-yellow calcite veins. Some intervals contain calcite-rich puggy gouge with iron-carbonate selvages. The nature of these structures would indicate that there has been significant movement along the faults, however, this offset has not been quantified (Rossimel and Lett, 2012). Examples of drill core intersections from the carbonate fault are shown in Figure 2.8.

Figure 2.8. *Typical carbonate fault drill core from the eastern part of panel cave 2 (outlined in red). Photographs courtesy of Sarah Stark, Cadia East site team.*

2.5.4 Porphyry dyke

Four main porphyry dykes intersect the Cadia East deposit. These dykes range from 5 metres to 30 metres in true thickness and can exceed 1500 metres in strike length. This rock mass is very strong, but brittle, and must be analysed for rock burst potential. The contacts between the porphyry dykes and host rocks can be highly sheared, but all known contacts have been healed by silica flooding (Rossimel and Lett, 2012).

2.5.5 Volcaniclastics

The volcano-sedimentary sequences of the Forest Reef Volcanics are the host rocks to the Cadia East porphyry system, and therefore represent an important rock type in the deposit. Forest Reef Volcanics within the Cadia East deposit can be divided into five primary lithofacies: (1) upper bedded; (2) volcaniclastic; (3) lower bedded; (4) massive volcanic; and (5) lower sequence (polymictic conglomerates and volcaniclastic sandstones). These five lithofacies differ, primarily, in texture and mineralogy, ranging from fine-grained massive volcaniclastics to volcanic conglomerates. The textural and mineralogical differences do not seem to affect the geotechnical behaviour, but the upper and lower bedded units contain an additional fracture set (Rossimel and Lett, 2012). Examples of typical volcaniclastic drill core are shown in Figure 2.9.

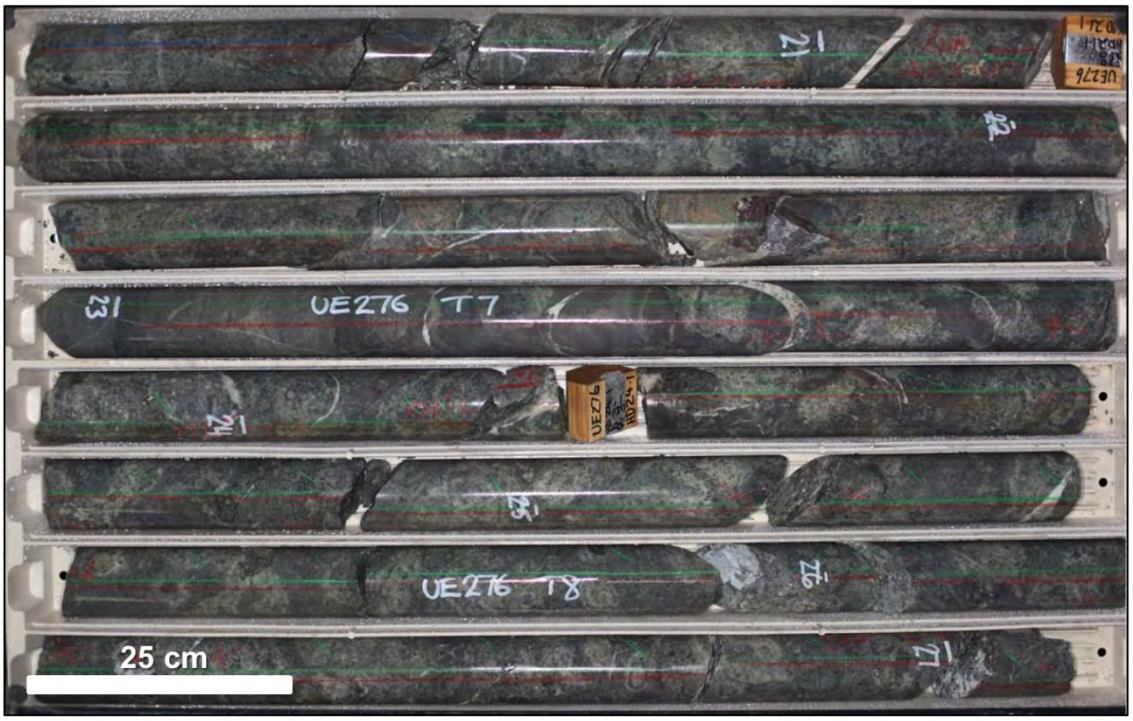

Figure 2.9. *Typical volcaniclastic drill core (volcaniclastic facies) from panel cave 2. Photographs courtesy Cadia East site team.*

2.5.6 Monzonite

The lower facies of the Forest Reef Volcanics within the Cadia East deposit are intruded by a swarm of north-east trending, sheet-like dykes of monzonitic to dioritic composition. These dykes are primarily concentrated in the eastern part of the deposit, but narrow, isolated monzonite dykes occur on the far western end. Paragenetic relationships indicate that a mafic-dominated monzodiorite is the

earliest porphyry phase, followed by a long-lived phase of more intermediate monzodiorite. These monzonite bodies are often associated with higher grades and the grade rapidly changes at the lower contact with the monzodiorite. This intrusive complex is the most competent unit in the deposit with the highest strength values, as indicated by geotechnical testing and drilling penetration rates (Rossimel and Lett, 2012). Examples of typical monzonite porphyry drill core are shown in Figure 2.10.

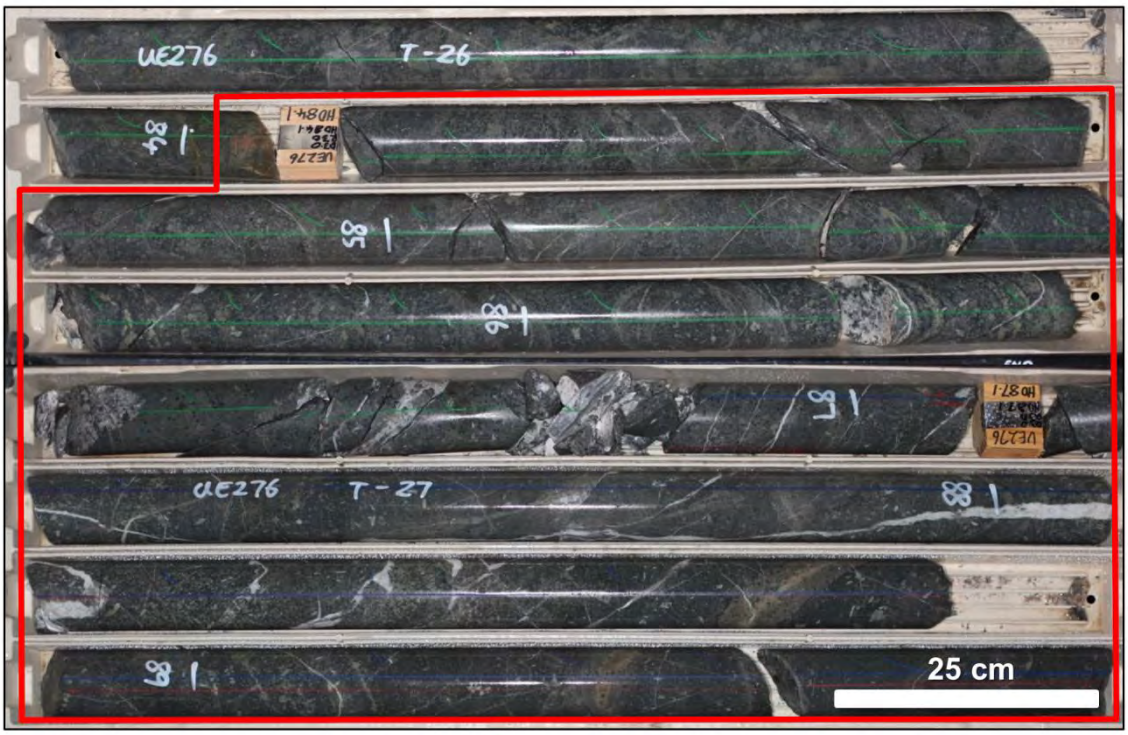

Figure 2.10. *Typical monzonite porphyry drill core from panel cave 2 (outlined in red). Photographs courtesy of Cadia East site team.*

2.6 Automated core logging and fracture analysis

Infrared technology dates back to the 1950s, but modern, automated hyperspectral loggers have only been developed in the past few decades (Mauger, 2014). Automated hyperspectral drill core logging technologies are increasingly important in ore deposit characterisation, particularly in the areas of alteration zonation and geologic modelling. These systems are becoming increasingly popular for geological assessment and logging (e.g., Fresia et al., 2017; Tappert et al., 2011; Huntington et al., 2006; Jackson et al., 2018). Recent studies have proposed that automated core logging technology could be applied to geometallurgical studies for the assessment of mineralogical textures as they relate to processing (e.g., Tiu, 2017; Arqué Armengol, 2015).

Numerous automated and semi-automated fracture detection and orientation techniques have been proposed over the years. Some approaches use imaging data collected using either an optical or acoustic imager such as the Televiewer system which produces 360° images from inside a drill hole (Trofimczyk and Du Pisani, 2009). These images are then "unfolded" and the amplitude of the sine wave fitted to each fracture is used in combination with the orientation of the bore hole to calculate the fracture orientation (Ureel et al., 2013). While these methods produce robust fracture recognition and orientations, it requires suspending drilling operations so that the drill hole imaging tools can be lowered down to collect bore hole images. Additionally, these methods are expensive and often difficult or impossible to acquire in areas with bad ground conditions.

Others have proposed using drill core imagery to identify and orient fractures. Berry and Nguyen (2016) developed a technique for calculating the orientation of features from high-resolution drill core photographs. This method shows good agreement with manually collected fracture orientations, however it requires a user to manually identify and digitise the location of fractures from the photographs. Quiniou et al. (2007) proposed automated methods for identifying and orienting drill core features from core images using a Hough transform technique. This approach produced orientations similar to those measured by a geologist, but also identified a number of false features.

The advantages of automated hyperspectral drill core logging technologies include fast throughput, low running costs and high resolution (Keeling et al., 2004). Automated geotechnical assessment is not a new concept. The mining industry commonly uses acoustic televiewer down hole logging systems to measure fracture orientations *in situ* (Shigematsu et al., 2014; Trofimczyk and Du Pisani, 2009). While the televiewer system provides accurate fracture orientations, it does not provide mineralogical information.

2.7 Corescan technology and data outputs

Numerous core scanning systems incorporating a series of mineralogical, geochemical, and core surface topography sensors are currently on the market including the HyLogger, SisuROCK, and Corescan (Mason and Huntington, 2010; SGS, 2014; Specim, 2014; TerraCore, 2014). These systems incorporate a number of sensors that collect core topography and hyperspectral-based mineralogical information and can analyse large volumes of drill core rapidly and consistently.

The Corescan system utilizes the Hyperspectral Core Imager Mark-III (HCI-3) logging technology to collect high resolution, true colour photography, 2.5D laser height profiles, and high resolution visible near-infrared and short wave infrared (VNIR-SWIR) spectra (SGS, 2014). The photography is collected at a resolution of 50 μm per pixel (Figure 2.11A) while the laser profile data is collected at a pixel size of 200 μm with a vertical resolution of 15 μm (Figure 2.11B). VNIR-SWIR spectra is collected at a 3.84 nm spectral resolution with a 500 μm pixel size (Figure 2.11C). The Corescan system automatically co-registers the pixels of the photography, the laser profiler data, and the hyperspectral image so that the pixels of all three data sets correspond to the same points in space. All three Corescan data outputs are spatially referenced so that the x-, y-, and z-values represent true measurements in metres. In this system, x measures the width of drill core referenced to the centre line, y measures the down hole depth, and z measures the core height and the digital surface topography (Figure 2.12).

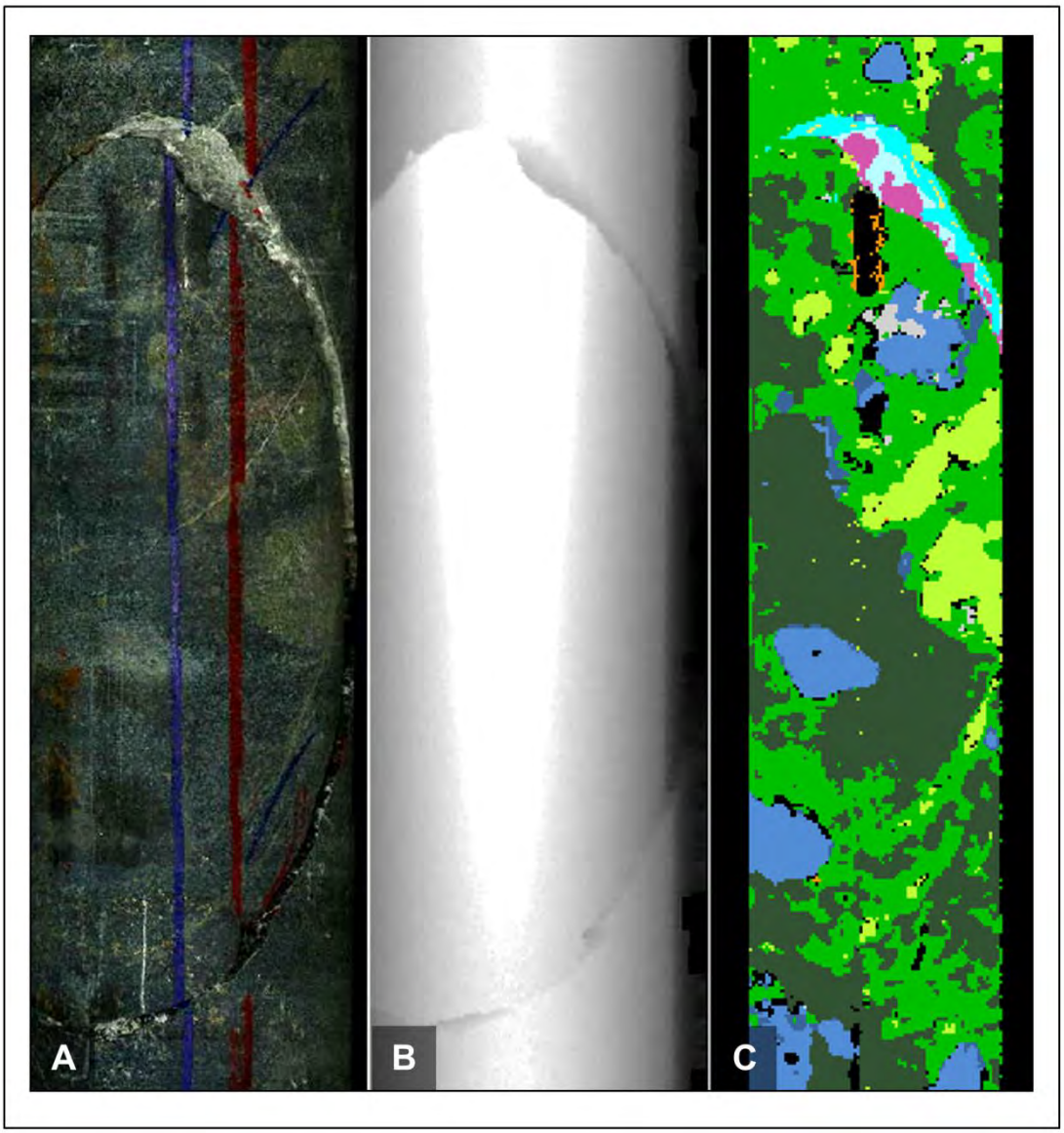

Figure 2.11. *The Corescan system simultaneously collects high resolution photography (A), a laser image of surface topography (B), and mineralogical information (C). Images from Coreshed, courtesy of Corescan Pty Ltd.*

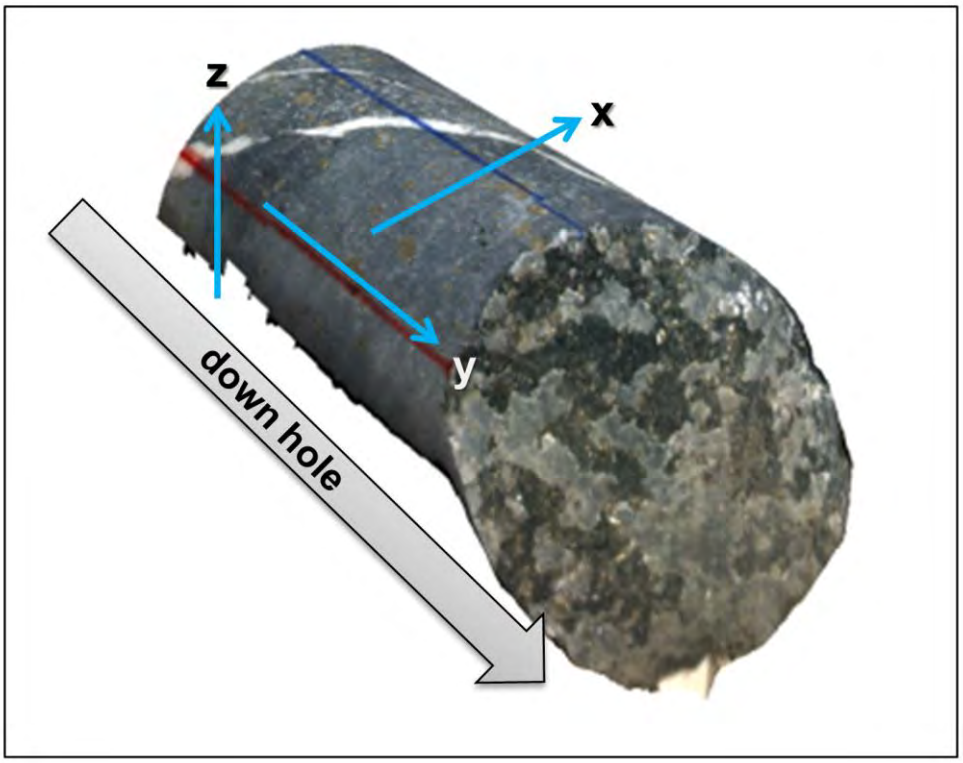

Figure 2.12. *Coordinate conventions automatically assigned to the Corescan data outputs. These coordinates allow the Corescan data to be spatially referenced relative to the drill hole.*

The Corescan proprietary spectral interpretation software compares the collected VNIR-SWIR spectrum for each 0.5 mm pixel to a deposit specific spectral library (Figure 2.13). A spectral match value between 0 and 1 for each library mineral is then assigned to the pixel. This spectral match value represents how well the unknown spectrum fits the library spectrum, with 0 representing no match, and 1 representing a perfect match. A mineral match image is a visual representation of this degree of fit of the collected spectrum to the project library spectrum. The lowest acceptable value (approximately 0.92) returned from the comparison of a sample spectrum to a library spectrum is called the match threshold. The results of the spectral matches are then colour coded using a rainbow colour table, a perfect match is coloured red, a spectral match equal to the match threshold is coloured blue and every match in between follows the RGB gradient as shown in Figure 2.13D.

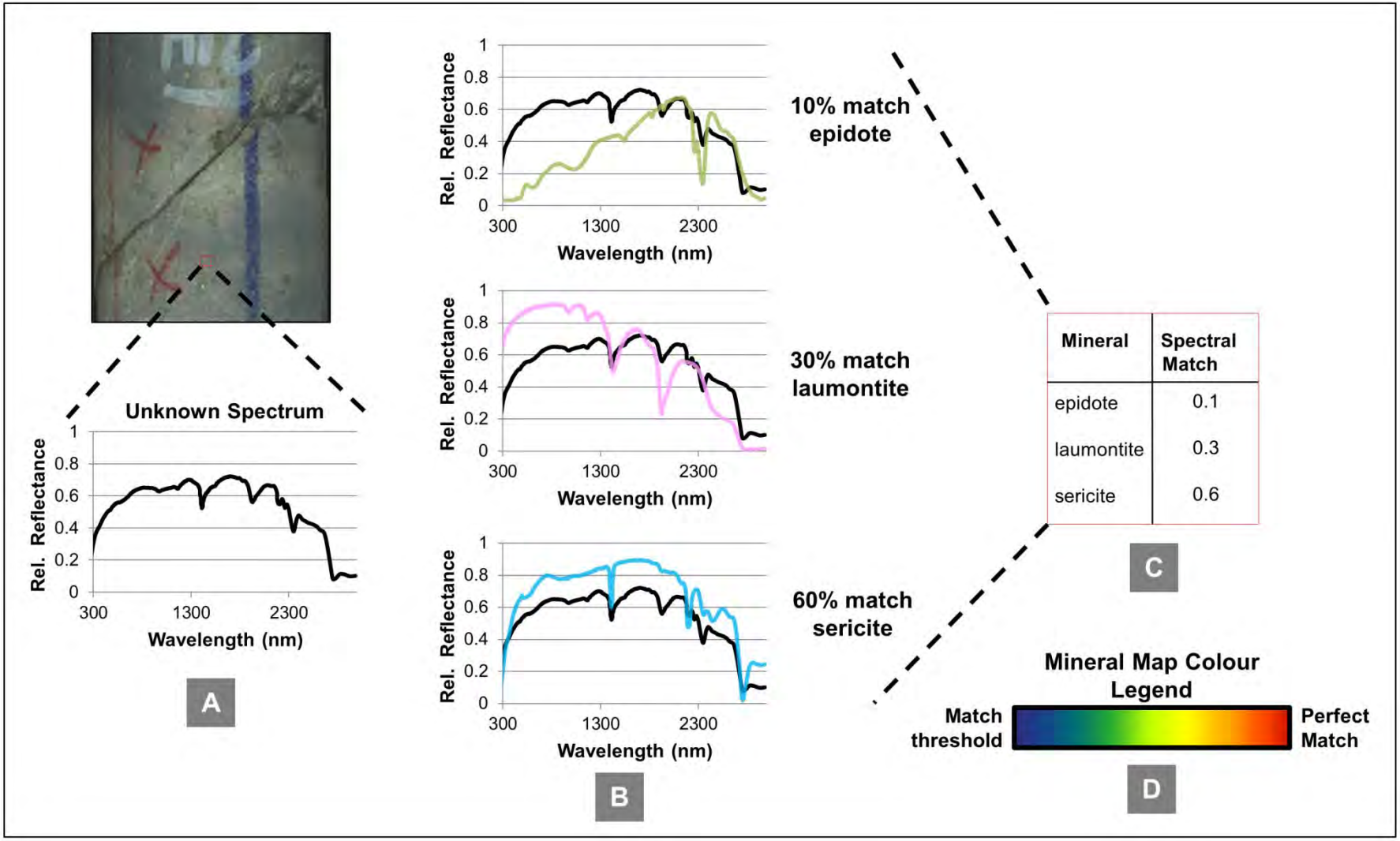

Figure 2.13. *Corescan methods for assigning spectral match values. The unknown spectrum (A) is compared to a library of spectra (B). A spectral match value between 0 and 1 is assigned to the pixel to represent how well the unknown spectrum fits the library spectrum (C). Spectral match values equal to the match threshold are coloured blue, perfect matches are coloured red, and matches between follow the RGB gradient (D).*

The Corescan software also generates images representing the variation of some mineral specific spectral characteristics. For some SWIR active minerals, the wavelength position of the dominant absorption feature is influenced by ionic substitution in certain crystal sites. These shifts in wavelength positions are presented as a pseudo coloured image, using the same rainbow colour table as for the mineral match images, where shorter wavelengths are assigned blue and longer wavelengths red (Figure 2.14B). The VNIR-SWIR spectra also provide information on the relative crystallinity of the white mica mineral group (Figure 2.14C). The mineral class map image considers the minerals matched at each pixel and then allocates a class colour of the mineral with the highest priority for each specific pixel (Figure 2.15). The purpose of the class map is to compile the multi-dimensional hyperspectral mineral images into a single product for a quick visual overview of down hole trends in mineralogy (Figure 2.15).

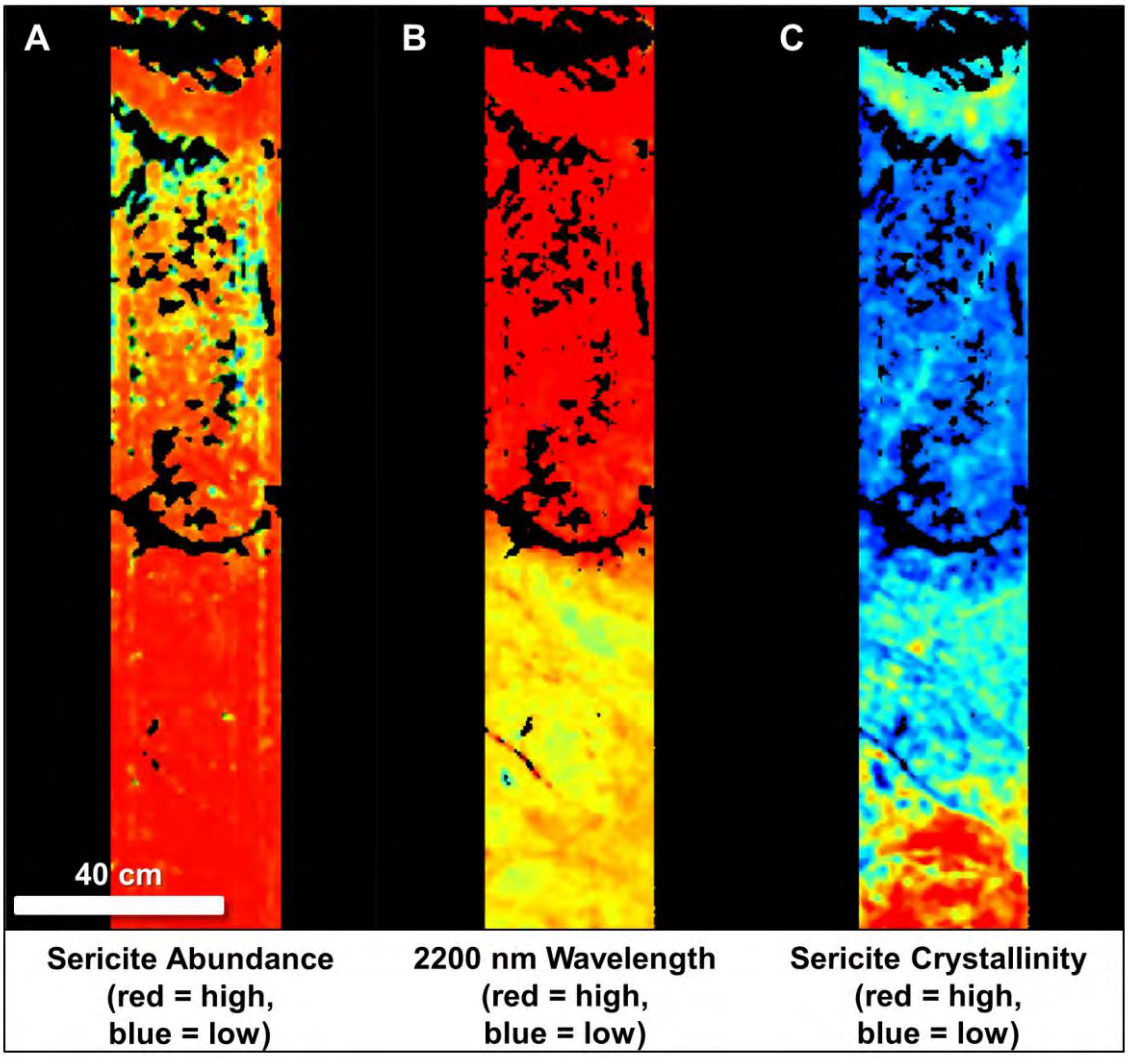

Figure 2.14. *Examples of mineral abundance and spectral characteristics maps produced from the Corescan system: relative abundance (A), AlOH wavelength value (B), and relative white mica crystallinity (C). Images from Coreshed, courtesy of Corescan Pty Ltd.*

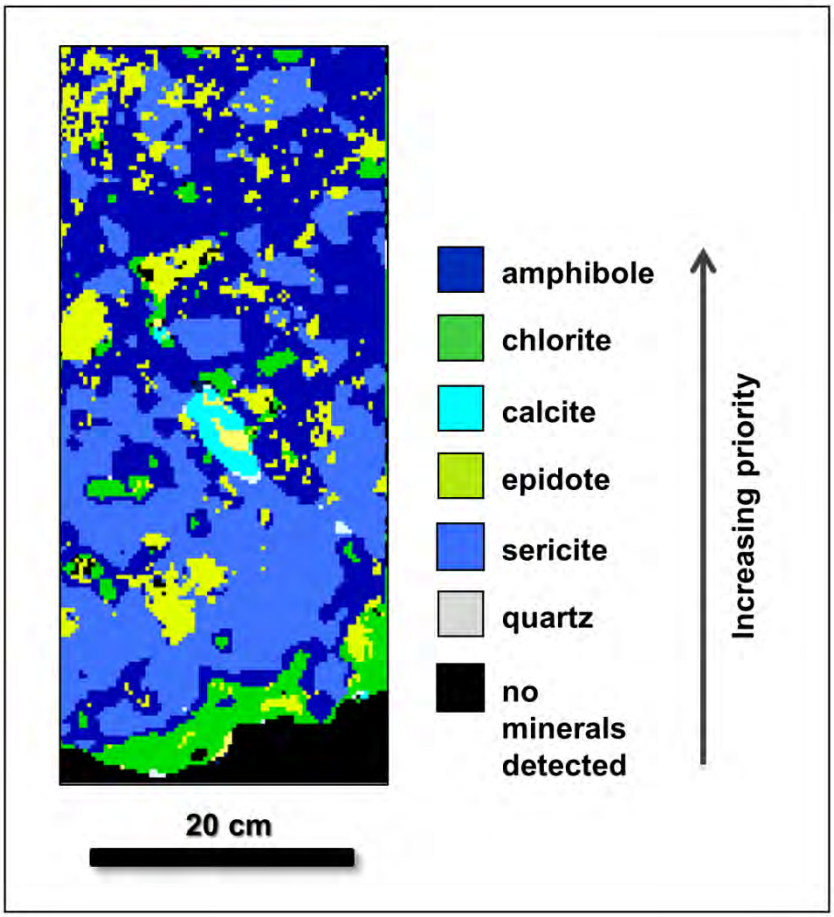

Figure 2.15. *Example of a Corescan mineral map created by taking the highest priority mineral in each pixel and assigning a false colour to each mineral.*

Corescan spectral analysis measures reflectance properties of minerals in the VNIR-SWIR (450 nm to 2500 nm) wavelength range of the electromagnetic spectrum. Minerals that are not active in this range or are low in reflectance do not produce distinctive and unique VNIR-SWIR spectra. For example, minerals such as feldspar and sulphides do not give VNIR-SWIR spectra with identifiable and characteristic absorption features and, therefore, are challenging to detect. Where VNIR-SWIR spectra with no absorption features are collected, the Corescan system assigns pixels as *aspectral*.

2.8 Hyperspectral principles

Spectroscopy has been applied to many fields including chemistry, biology, and materials engineering. It is especially suited to geological studies since the spectral properties of numerous mineral groups (including silicates, hydroxides, carbonates, nitrates and borates) are well established and diagnostic (Thompson, 1999). When light energy is directed at the surface of a target, it will interact with

the molecules of the target in a predictable way, reflecting the chemistry and arrangement of those molecules (ElMasry and Sun, 2010; Kortüm, 2012). The geological application of spectroscopy is based on the fundamental principles of molecular vibrational energies in minerals and the theory that molecules assume discrete and predictable energy levels (Burns, 1993). The electromagnetic radiation ranges most useful for mineral identification are the ultraviolet range (10 nm to 400 nm), the visible range (390 nm to 750 nm), and the infrared range (750 nm to 1 mm) (Figure 2.16) (Burns, 1993; Thompson, 1999). The hyperspectral characteristics of a material are captured by analysing the wavelengths of the signal that return to the spectrometer sensor (reflected energy) and the wavelengths that are not returned (absorbed energy). This information is displayed by a simple plot showing relative reflectance over a wavelength range (Figure 2.17).

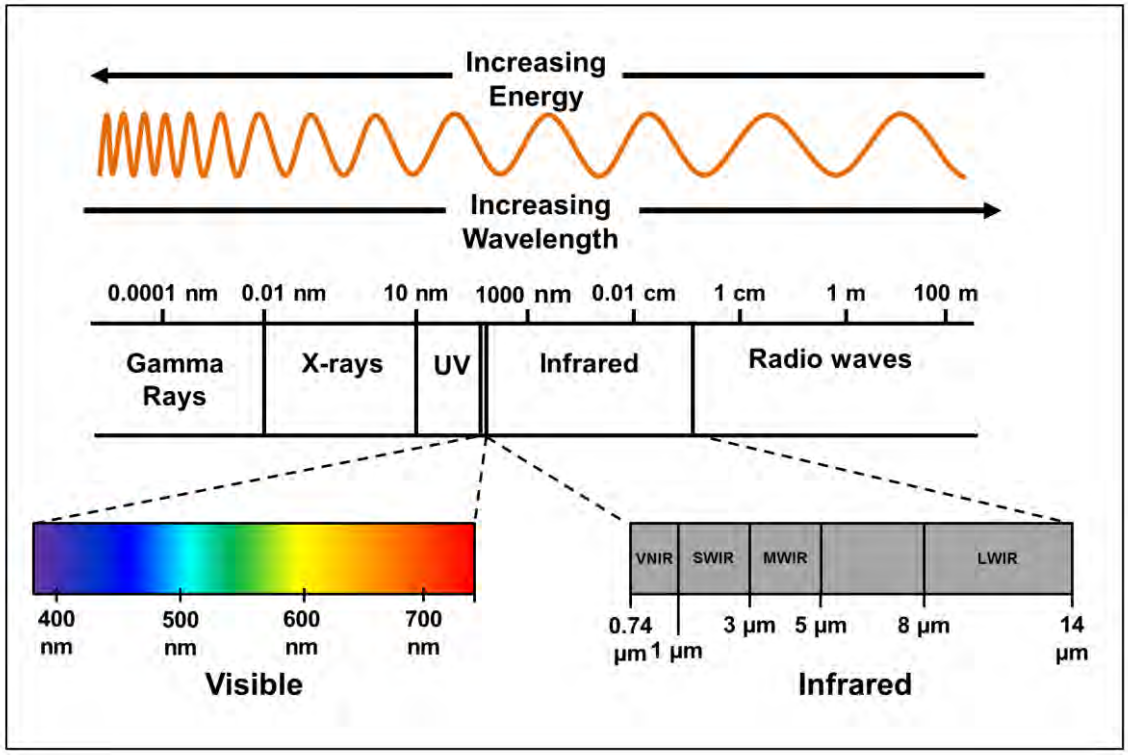

Figure 2.16. *Wavelengths of key ranges in the electromagnetic spectrum.*

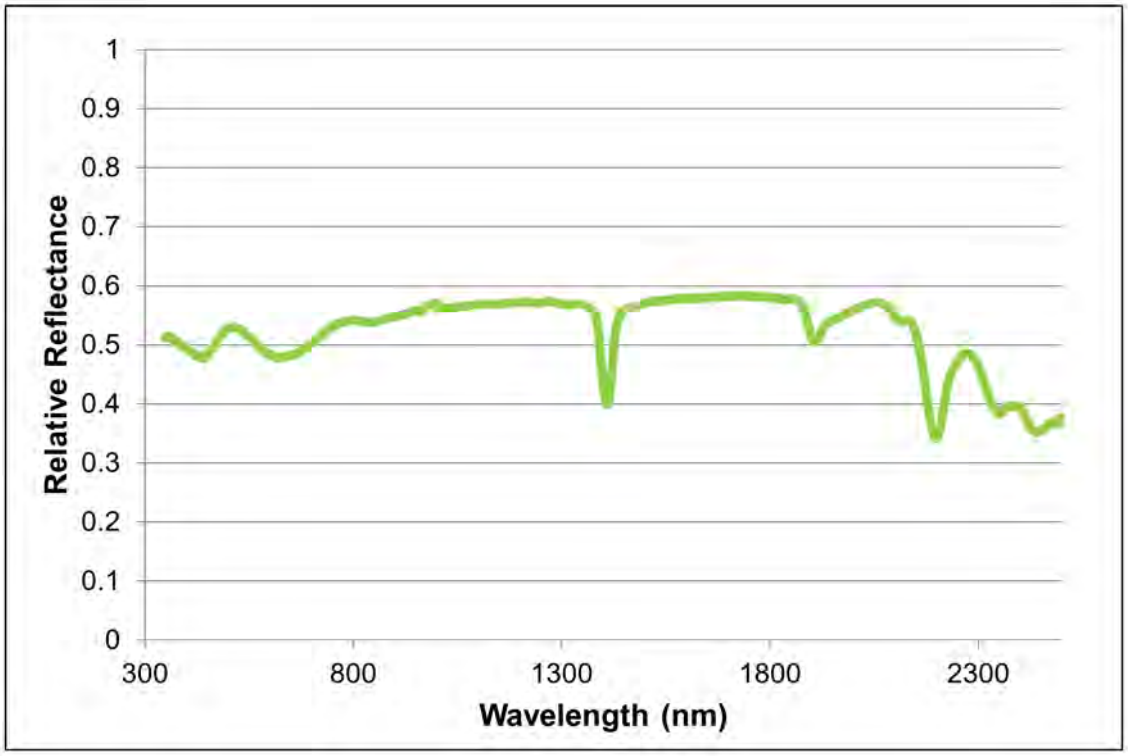

Figure 2.17. *Example of spectrum recorded from VNIR-SWIR spectra reflected from a pyrophyllite-altered granodiorite sample.*

Minerals suitable for VNIR-SWIR hyperspectral analysis exhibit distinctive absorption patterns over different wavelength values which can be used for identification. Since most hyperspectral spectrometers operate in the infrared range, it is important to consider which minerals are hyperspectrally active in this range. In general, hydroxide (OH), water (H_2O), and carbonate (CO_3) bonds are active in the infrared range (Figure 2.18). Minerals with very similar compositions and lattice structures (e.g. illite and sericite) may display similar absorption features, but can often be distinguished by subtle shifts in the positions, depths, or shapes of these features (Thompson et al., 1999).

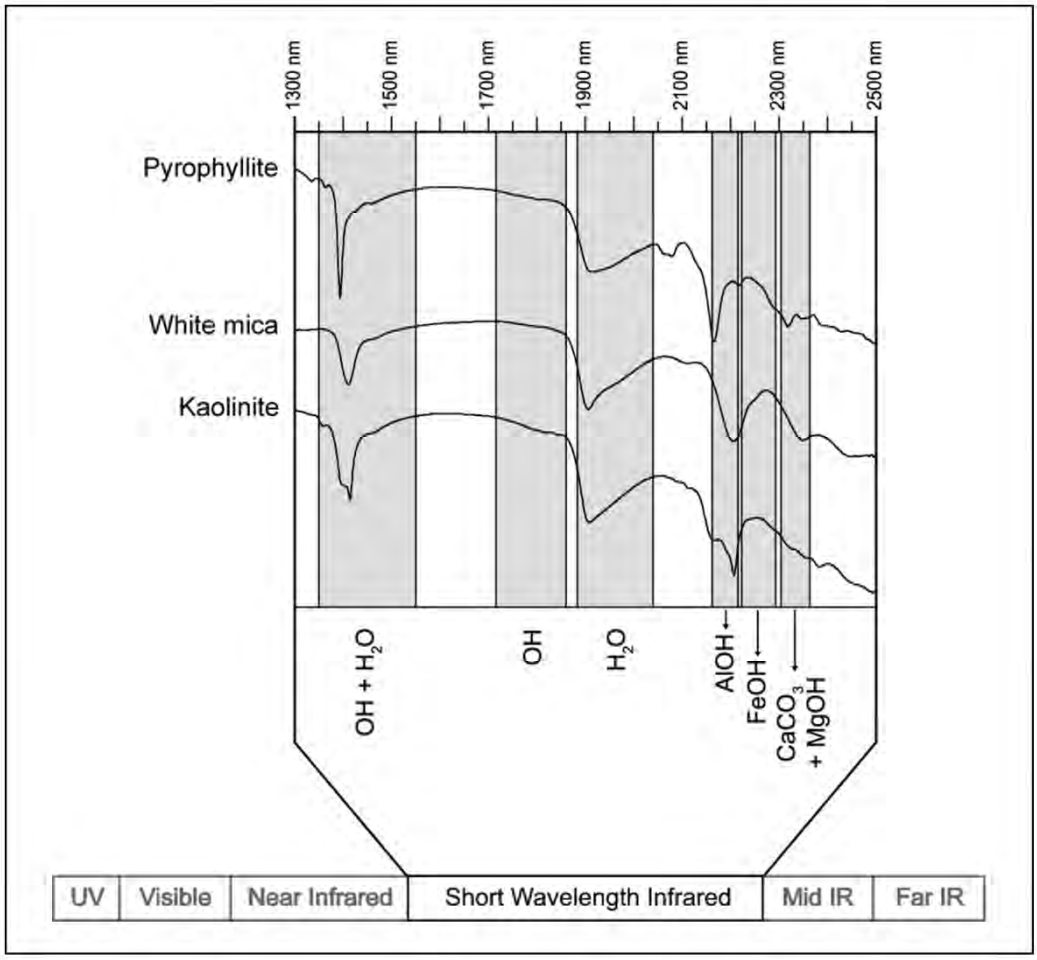

Figure 2.18. *Key molecular bond ranges of activity with reference phyllosilicate mineral spectra relative to the position of the visible, VNIR, and SWIR spectrum. Figure modified from Harraden et al. (2013).*

Phyllosilicate minerals are difficult to distinguish with confidence by visual examination of drill core, particularly where they are interlayered or in low abundances. VNIR-SWIR spectroscopy has been used successfully to differentiate subtle chemical changes in phyllosilicate minerals in numerous ore deposit case studies (e.g. Calvin and Pace, 2016; Harraden et al., 2013; Herrmann et al., 2001; Jones et al., 2005; Squire et al., 2007; Tappert et al., 2015; Thompson et al., 1999). The SWIR range provides the most information regarding the phyllosilicate minerals as this range encompasses molecular bonds matching the specific wavelengths for molecules such as H_2O, $CaCO_3$, AlOH, MgOH, and FeOH (Thompson et al., 1999).

Table 2.6 outlines the specific spectral characteristic features of minerals identified in Corescan hyperspectral analysis. An example of the spectrum for each of these minerals is presented in Figure 2.19.

Table 2.6. *Spectral characteristics of minerals detected by the Corescan system. Compiled from Kokaly et al. (2017), Laukamp (2011), and GMEX (2008).*

Mineral	Generic Mineral Formula	Key Spectral features
amphibole	$(Na,K)_{0\text{-}1}(Ca,Mg,Fe,Na)_2(Mg,Fe,Al)_5(Si,Al)_8O_{22}(OH)_2$	dominant absorption at 1400 nm; pair absorptions features near 2310 and 2380 nm; tremolite has a doublet at ~2315 nm
apophyllite	$(K,Na)Ca_4Si_8O_{20}(F,OH) \cdot 8H_2O$	dominant, deep absorption feature 1517 nm; broad doublet between ~2000 nm and ~2100 nm
carbonate	$CaCO_3$	dominant feature between 2340nm and 2345 nm, persists in mixed spectra; weaker features near 1880 nm, 1992 nm, and 2156 nm, but are not present in mixed spectra
clinochlore	$(Mg,Fe^{2+})_5Al(Si_3Al)O_{10}(OH)_8$	deep absorption feature ~2248 nm; chamosite closer to ~2260 nm;
chlorite	$(Mg,Al,Fe)_{12}[(Si,Al)_8O_{20}](OH)_{16}$	two major absorption features : 1) 2260 nm and 2350 nm for iron-rich chlorite, or 2) 2250 nm and 2330-2340 nm for Mg-chlorite; 2330-2350 nm feature typically asymmetric and broader than the symmetric feature at 2250-2260 nm
dickite	$Al_4(Si_4O_{10})(OH)_8$	distinguished from kaolinite by diagnostic OH doublet with two sharp, narrow features with lower wavelength values forming doublet near 1384 nm and 1418 nm; sharp, deep doublet with absorption values near 2178 nm and 2206 nm; shallower absorption near 2378 nm observed even in mixed spectra
epidote	$Ca_2Fe^{3+}(Al_2O)(OH)Si_2O_7(SiO_4)$	two intense, deep absorption features between 2335 nm and 2342 nm and one at 2256 nm; diagnostic OH absorption feature near 1545nm and 1830nm distinguish epidote from chlorite and help identify epidote in mixtures
gypsum	$CaSO_4$	three distinguishing water absorption features between 1400 nm and 1600 nm forming a 'triplet'; diagnostic absorption feature ~1750 nm (diagnostic of sulphate minerals); major absorption feature near 1948 nm persists when minor anhydrite is present; weak absorption feature sometimes present near 2215nm
iron carbonate	$Fe_{1\text{-}2}(CO_3)_{1\text{-}3}$	absorption feature at 2330 nm; deeper absorption at 2350 nm

Table 2.6 (cont).

Mineral	Generic Mineral Formula	Key Spectral features
iron oxide	$Fe_{1-3}O_{1-4}$	spectra often noisey; minor absorption feature ~2400 nm; weak absorption at 530 nm
kaolinite	$Al_2Si_2O_5(OH)_4$	diagnostic pair of doublets centred near 1400 nm and 2200 nm; first doublet composed of 1400 nm and 1450 nm features, 1450 nm usually deeper; second doublet composed of 2166 nm and 2206 nm features, 2206 nm usually deeper; additional features near 1360 nm and a triplet near 2320 nm, 2350 nm and 2380 nm; occasionally dimple or shoulder near 2240 nm in iron-bearing kaolinites; variations in crystallinity cause deviations in relative sharpness and depth of two doublets
laumontite	$Ca(Al_2Si_4)O_{12} \cdot 4H_2O$	diagnostic, deep and asymmetrical absorption features at 1420 nm and 1920 nm
montmorillonite	$(Na,Ca)_{0.33}(Al,Mg)_2(Si_4O_{10})(OH)_2 \cdot nH_2O$	deep and asymmetrical absorption features at 1410 nm, 1910 nm, and 2200 nm; changes in the Na and Ca cations shift the 2200 nm feature; rarely weak shoulder at 500 nm
nontronite	$Na_{0.3}Fe_2[(Si,Al)_4O_{10}](OH)_2 \cdot nH_2O$	diagnostic shoulder at 450 nm; absorption feature at 640 nm and broad absorption at 940 nm; AlOH absorption near ~2100 nm
phlogopite	$KMg_3(AlSi_3O_{10})(OH)_2$	two major features at 2245 nm and 2330 nm; well-developed feature near 2385 nm
prehnite	$Ca_2Al(AlSi_3O_{10})(OH)_2$	well-developed MgOH (at ~2330 nm)
quartz	SiO_2	broadens other absorption features in mixed spectra; pure quartz gives very broad reflectance signature
sericite	$K_2Al_4(Si_6Al_2)O_{20}(OH)_4$	fairly sharp absorption features near 1408 nm, 2200 nm, 2348 nm, and 2442 nm; variations in Na, K and Al cation substitution shift absorption of the 2200 nm feature; short-wavelength absorptions (near 2190 nm) more sodic (paragonitic), long-wavelength (near 2206 nm) more potassic
tourmaline	$Na(Mg,Fe,Li,Al)_3Al_6(Si_6O_{18})(BO_3)_3(OH,F)_4$	major absorption features at 2200 nm, 2245 nm, 2300 nm, and 2370 nm
vermiculite	$(Mg,Ca)_{0.3}(Mg,Fe^{2+},Fe^{3+},Al)_3(Si,Al)_4O_{10}(OH)_2 \cdot 4H_2O$	absorption feature near ~2100 nm; similar spectrum to nontronite, but vermiculite lacks 450 nm, 640 nm, and 940 nm features

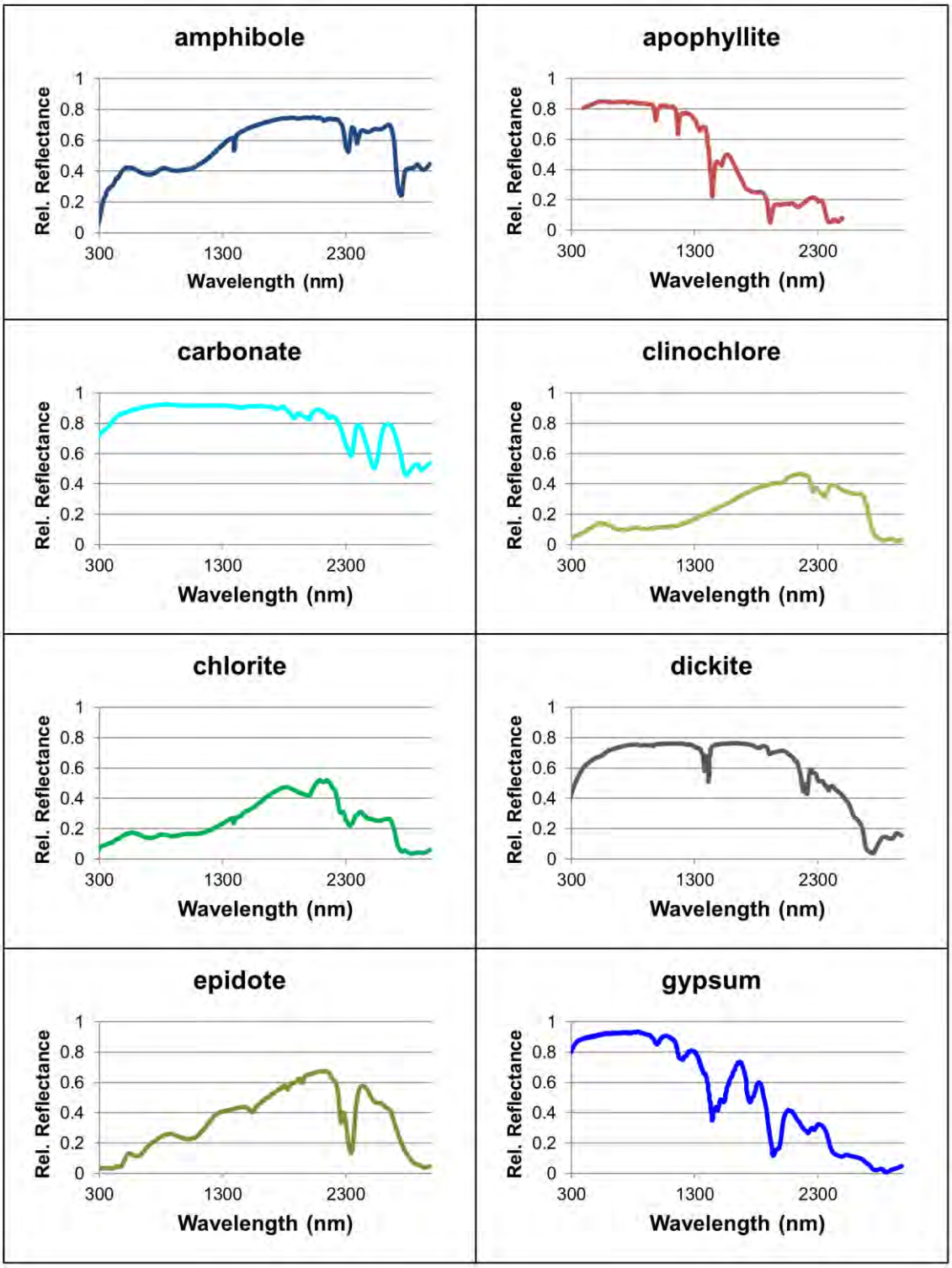

Figure 2.19. *Example spectra for minerals detected by the Corescan system. Spectra from Kokaly et al. (2017).*

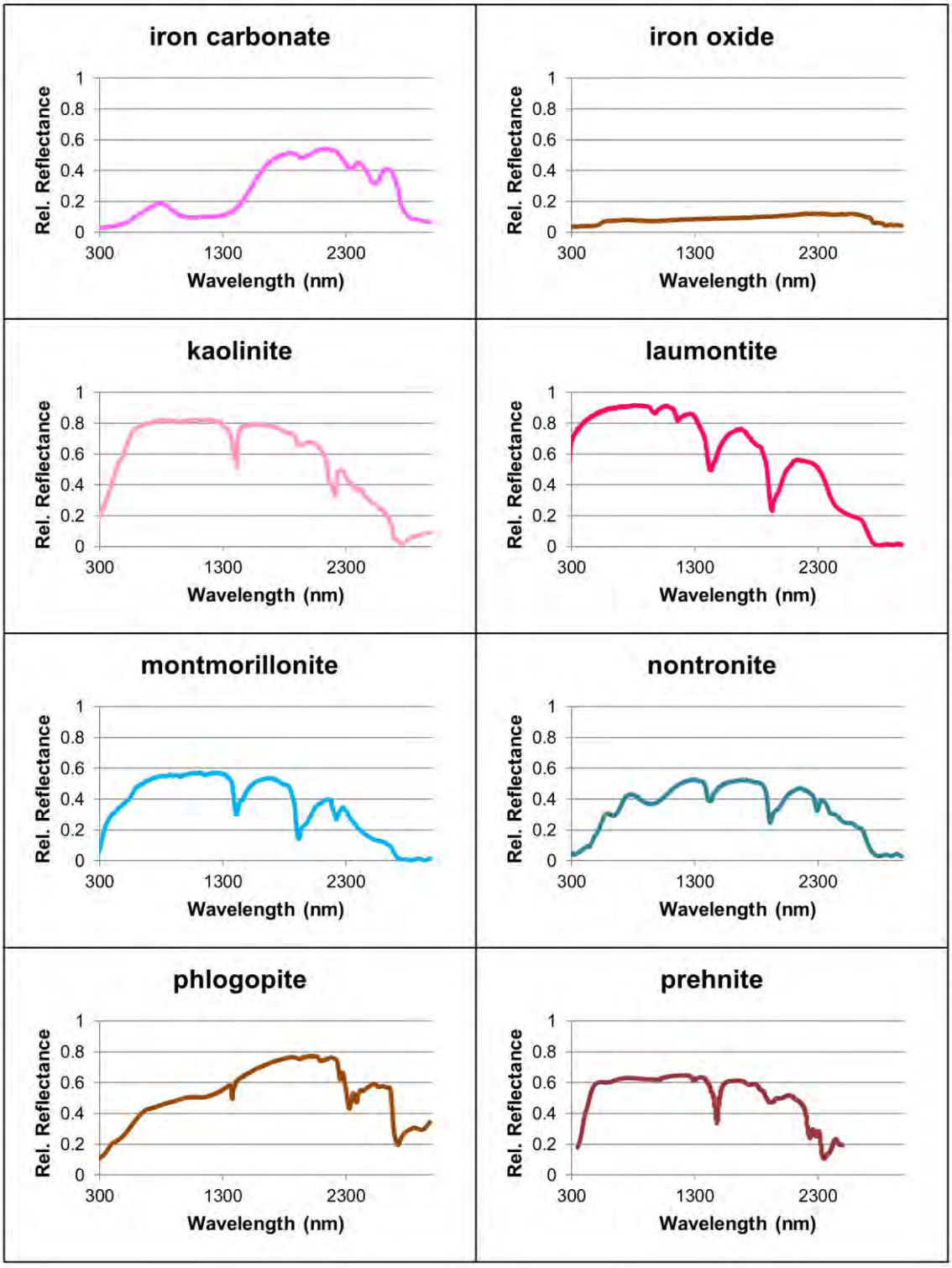

Figure 2.19 (cont.).

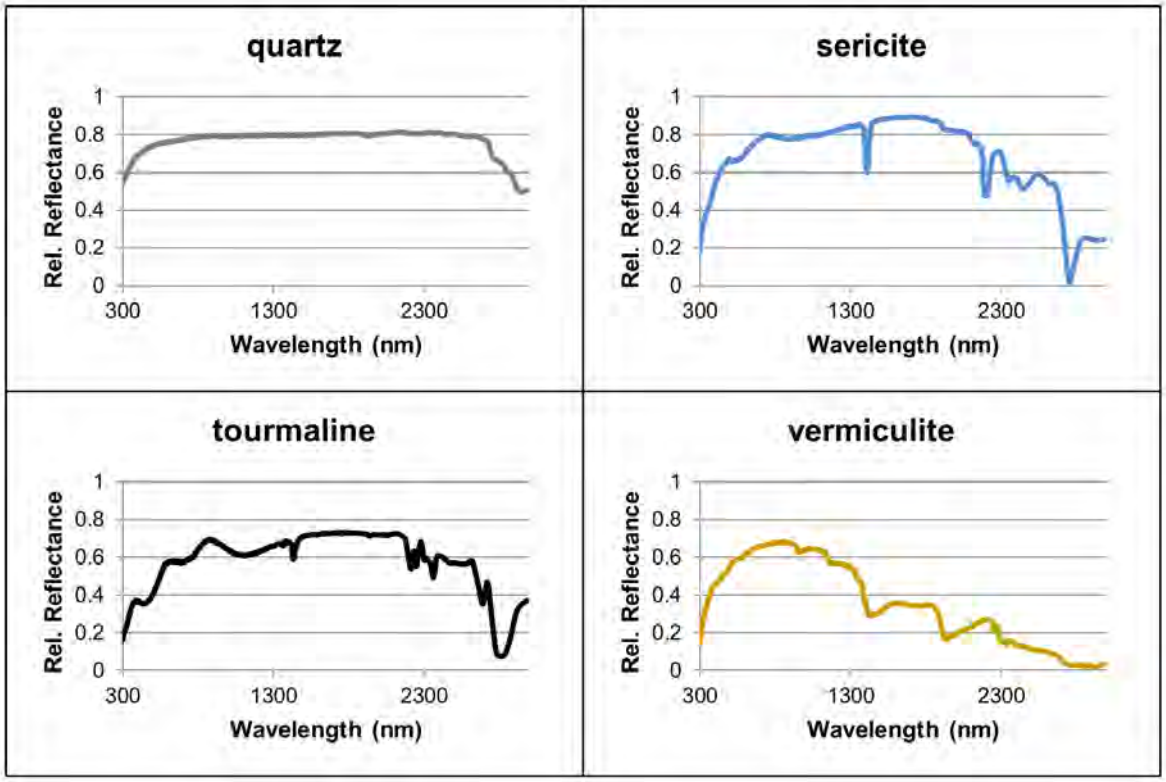

Figure 2.19 (cont.).

2.9 Outline of subsequent discussion chapters

A proof of concept study was designed to determine if protocols to extract morphological and mineralogical geotechnical parameters from Corescan data could be developed. A 76.3 metre interval of drill core from Cadia East containing 199 fractures was used to develop and test these protocols. The values calculated from Corescan data were compared to measured values, expected site values and/or core photographs to determine the ability of each technique to adequately assess geotechnical parameters.

Morphological geotechnical parameters are those that are related to the geometry, location, and orientation of the fractures, not the mineralogy. Morphological geotechnical parameters were extracted from the laser profiler and true colour image outputs of the Corescan system. Determining fracture parameters related to the mineralogy in and around the fracture surface requires the mineralogical outputs of the Corescan system. A discussion of how the geotechnical parameters were generated using Corescan technology is detailed in the chapters below:

- Chapter 3: Methods for morphological geotechnical assessment
- Chapter 4: Testing of methods for morphological geotechnical assessment
- Chapter 5: Methods and testing for mineralogical geotechnical assessment.

Chapter 12 contains a discussion of the implications of the results and the proposed future work in determining if these methods can be implemented as part of the current Corescan system for rapid, consistent geotechnical assessment.

Chapter 3

Methods for morphological geotechnical assessment

3.1 Introduction

The present industry standard method for geotechnical data acquisition and ground condition modelling in hard rock environments is manual logging of drill core by geologists and geotechnical engineers. While this approach has been successfully applied to mining in the past, it is often laborious and inconsistent. The scanning capabilities and sensor array of the Corescan system allows for the rapid, non-destructive analysis of drill core to produce high-resolution laser profile maps representing a digital profile model of the surface of the drill core (Figure 3.1). By utilizing the three image types collected, Corescan data can be applied to extract geotechnical input parameters as they relate to the key geotechnical indices and ground conditions in a mining environment. The goal of this study is to demonstrate that key geotechnical index parameters can be estimated rapidly from Corescan data at a scale and consistency that is superior to manually collected geotechnical data.

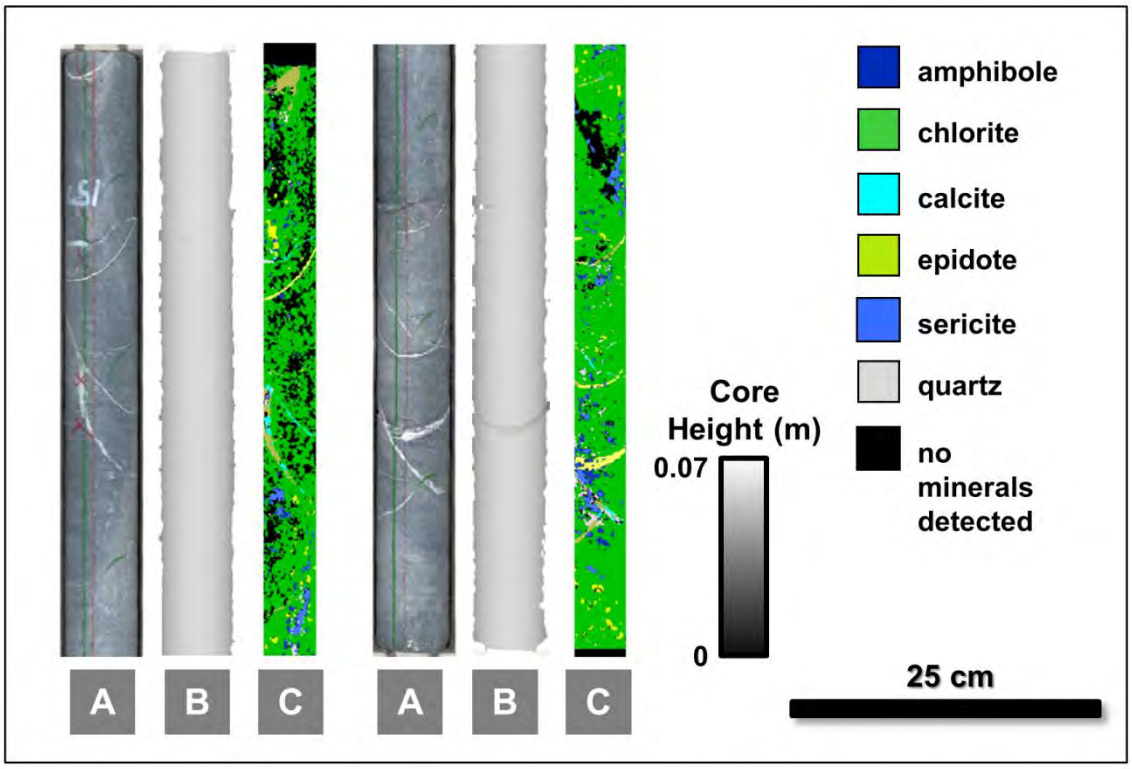

Figure 3.1. *Examples of Corescan data outputs: RGB imagery (A), laser profiler height data (B), and mineral map produced from SWIR data (C).*

A methodology that seeks to enhance and streamline the current, manual data collection techniques with the automated extraction of geotechnical parameters using Corescan's automated core logging technology is presented in the following sections. Data from Cadia East were used for the development and testing of these protocols.

The goal of this research is to develop a methodology that successfully extracts geotechnical index parameters, not to develop computer code that executes this workflow. As such, the reader should keep in mind that the protocols proposed here utilize manual steps, such as manually extracting points associated with each fracture and manually inputting those points into a Microsoft Excel workbook for orientation processing. It is assumed that a professional computer programmer would be able to code these steps into an automated process, but challenges might be encountered and some of the steps may require advanced data extraction methods and the intervention of a domain expert. Computer programing aspects of the protocols, as well as the associated challenges, will not be addressed in this thesis. This work is a proof of concept study only.

3.2 Geotechnical analysis using Corescan

In order to extract the morphological parameters for the RMR and the Q-index from Corescan data, the down hole location, orientation, and morphology of fractures need to be recognised and measured. The automation of this type of analysis requires that the mode of data collection be carefully considered. Corescan imaging is typically conducted on halved core, which provides a flat surface and constant core height. This ensures the focal length of the true colour photograph sensor and hyperspectral scanner is consistent for a given run. However, a fracture orientation cannot be calculated from a flat core surface and the cutting and sampling process induces rock breaks not related to natural fracture patterns. Additionally, the location of the orientation mark on the surface of the drill core is lost when the core is cut, so whole core imaging ensures that the orientation line can be located and used in fracture orientation measurements. For these reasons, Corescan analysis of whole, uncut core is required for geotechnical data collection.

The Corescan system automatically co-registers the pixels of the true colour photograph, the DSM laser data, and the hyperspectral image so that the pixels of all three data sets correspond to the same points in space. The images are spatially referenced so that the x-, y-, and z-values represent true measurements in metres. The x-values represent distance across the drill core with the centre line of the drill core located at x = 0 (Figure 3.2A). The y-values represent the down hole location in metres from the drill hole collar, e.g. 150 metres depth is given by y = -150.000 (Figure 3.2B). The z-values represent the height of the core off the bottom of the core tray in metres (Figure 3.2C).

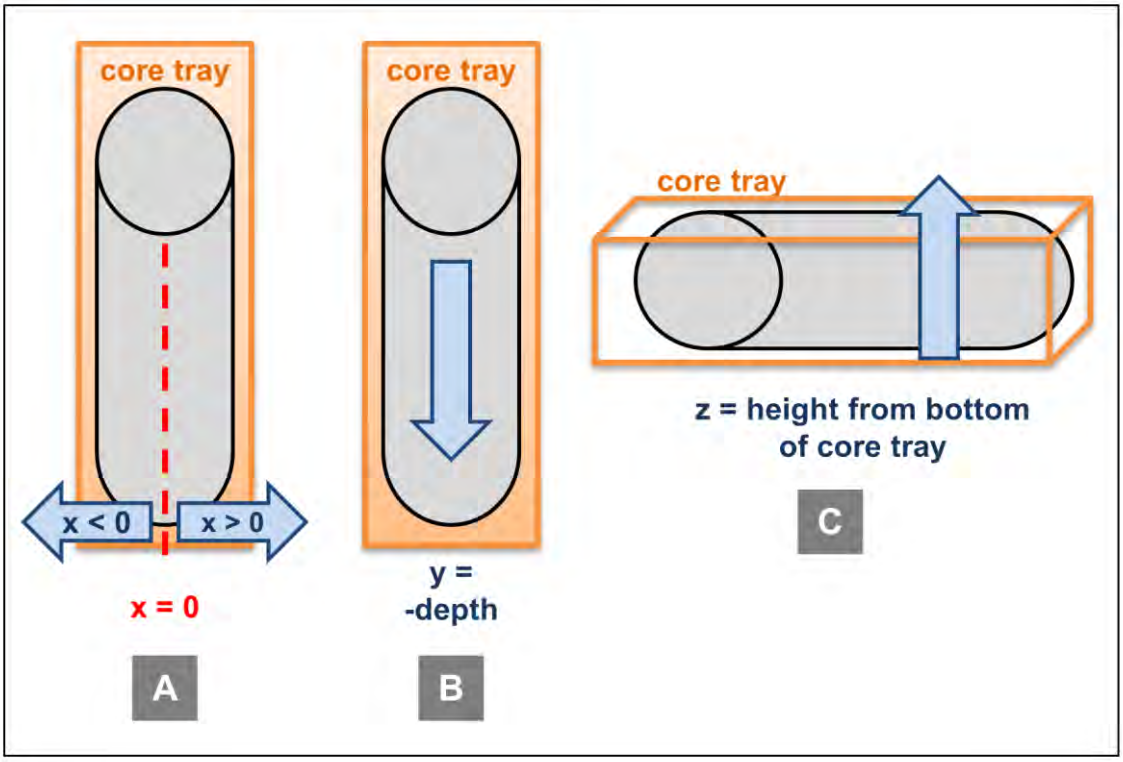

Figure 3.2. *The Corescan system's assignment of x-, y-, and z-coordinates (in metres). A. The x-values represent the location across the core with x = 0 representing the top centre of the core. B. The y-values represent the down hole depth (in negative numbers). C. The z-values measure the distance from the bottom of the core tray to the top of the drill core.*

For the purposes of developing the proof of concept protocols for the extraction of geotechnical parameters, spatial analysis tools available in ArcGIS were employed in conjunction with calculations in Excel workbooks. The general methodology includes the following steps which are illustrated in Figure 3.3:

1) recognise fractures;
2) remove mechanical breaks;
3) calculate orientation of selected fractures;
4) calculate fracture roughness;
5) determine number of fracture sets present; and
6) measure fracture spacing.

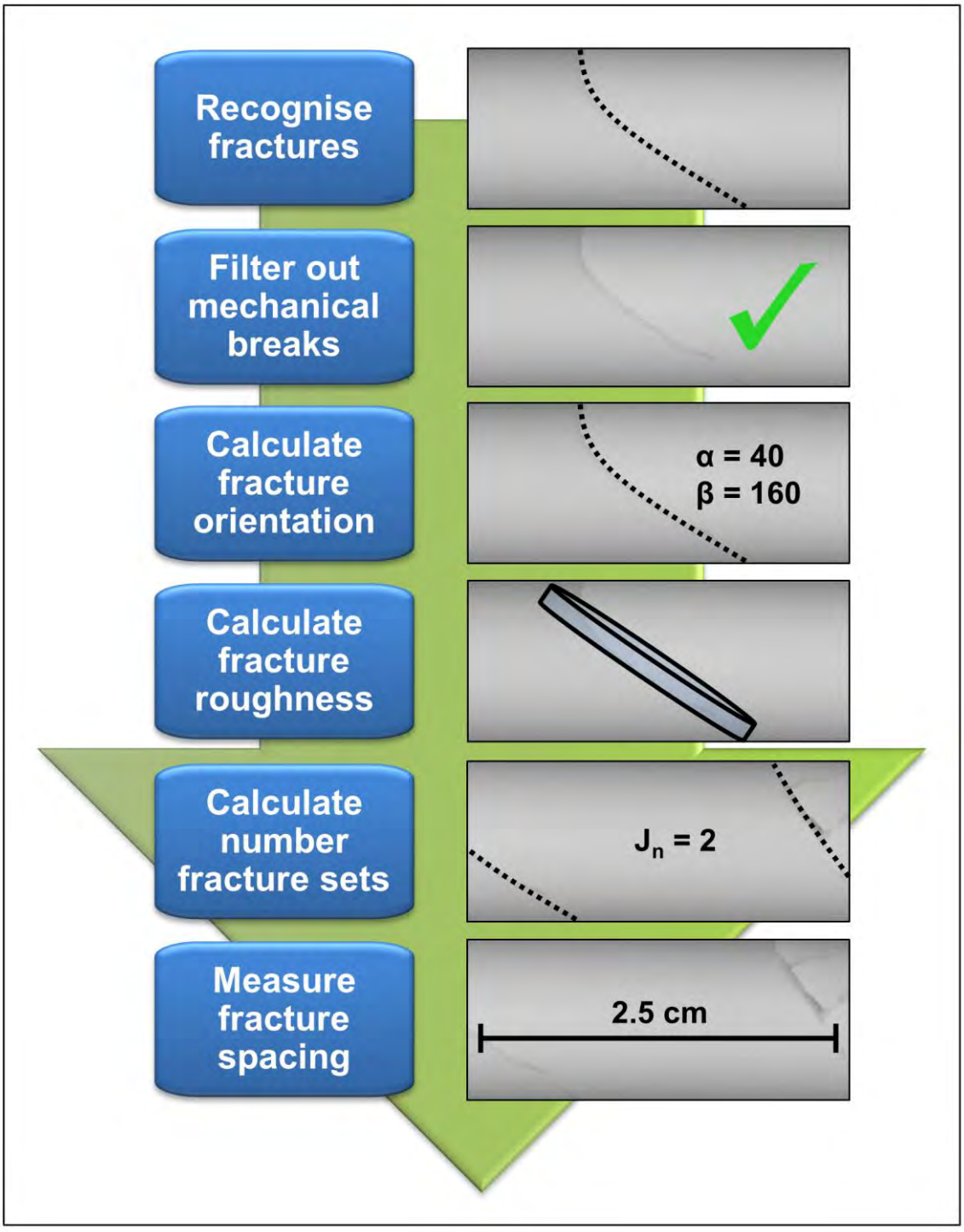

Figure 3.3. *General processing methodology for the automated extraction of morphological geotechnical index parameters.*

3.3 Recognise fractures

From the laser profiler data, the surface of the drill core can be modelled in three dimensions. Since any fracture represents a discontinuity in what should be a relatively consistent cylinder shape, any deviation from a typical cylinder represents a potential fracture. There are numerous ways to detect changes in the

continuity of a cylinder. These include tracking changes in slope, aspect (or facing-direction), and mean curvature value.

For the purpose of method development, the Corescan laser profiler data was treated as if it were a digital surface model (DSM), and analysed using the spatial data analysis tools in ArcGIS. Since these tools are based on fundamental mathematical and spatial modelling principles, the concepts can be used to develop future computer coding when this methodology is integrated into the Corescan software.

The general approach for recognising and exporting fracture pixels is outlined below:

1) clip the laser profile image to the extent of the true colour photograph to ensure core tray edges are not included in the analysis;
2) run analysis tool(s) and recognition parameters to segregate potential fracture pixels from non-fracture pixels (individual protocols outlined in the sub-sections below);
3) select pixels that meet the appropriate criteria for a given recognition protocol (individual recognition criteria outlined in the sections below);
4) manually group pixels that meet the recognition criteria in each core image into individual fractures; and
5) export the x-, y-, and z-coordinates of pixels associated with each individual fracture as a table.

Five different fracture selection protocols were evaluated to automatically detect pixels associated with fractures:

1) slope and aspect;

2) hillshade;

3) hillshade + slope and aspect;

4) high pass; and

5) combined.

Since the ability to extract geotechnical index parameters relies entirely on the ability to recognise fractures, these five recognition protocols were used to determine which method provides the best results. While all five recognition protocols were developed and tested, only three proved to be successful: the slope and aspect, hillshade, and combined protocols. In contrast, the hillshade +

slope and aspect and high pass recognition protocols provided very poor fracture recognition, orientation, and roughness. The details of these protocols are included in Appendix A, but will not be discussed in detail here.

The details of each recognition protocol are shown schematically in figures at the end of each section. Additionally, images demonstrating the visual outputs for the processing steps are included. These images are from an intersection with broken, rubbly core. While this example does not provide ideal conditions for fracture recognition, it was selected to show the relative performance of the fracture recognition protocols for a challenging core interval.

In order to set up an automated protocol and expedite testing, each fracture recognition protocol was developed within the ArcGIS platform using ModelBuilder. The ModelBuilder files for each protocol are included in Appendix B.

3.3.1 Fracture recognition by slope and aspect protocol

In spatial analysis, DSM slope derivatives can be obtained by calculating, on a pixel by pixel basis, the maximum rate of change of one pixel compared to its neighbours. Using the laser profiler data as a DSM base dataset, areas of drill core where the calculated slope is steeper than the curvature of the surface of the drill core represents a discontinuity (either a potential fracture or mechanical damage). In ArcGIS, the *Slope* tool fits a plane to the z-values of a 3 x 3 neighbourhood of pixels and calculates the maximum rate of change (Figure 3.4). A slope value (in degrees) is then assigned to each pixel based on this relationship (ESRI, 2011).

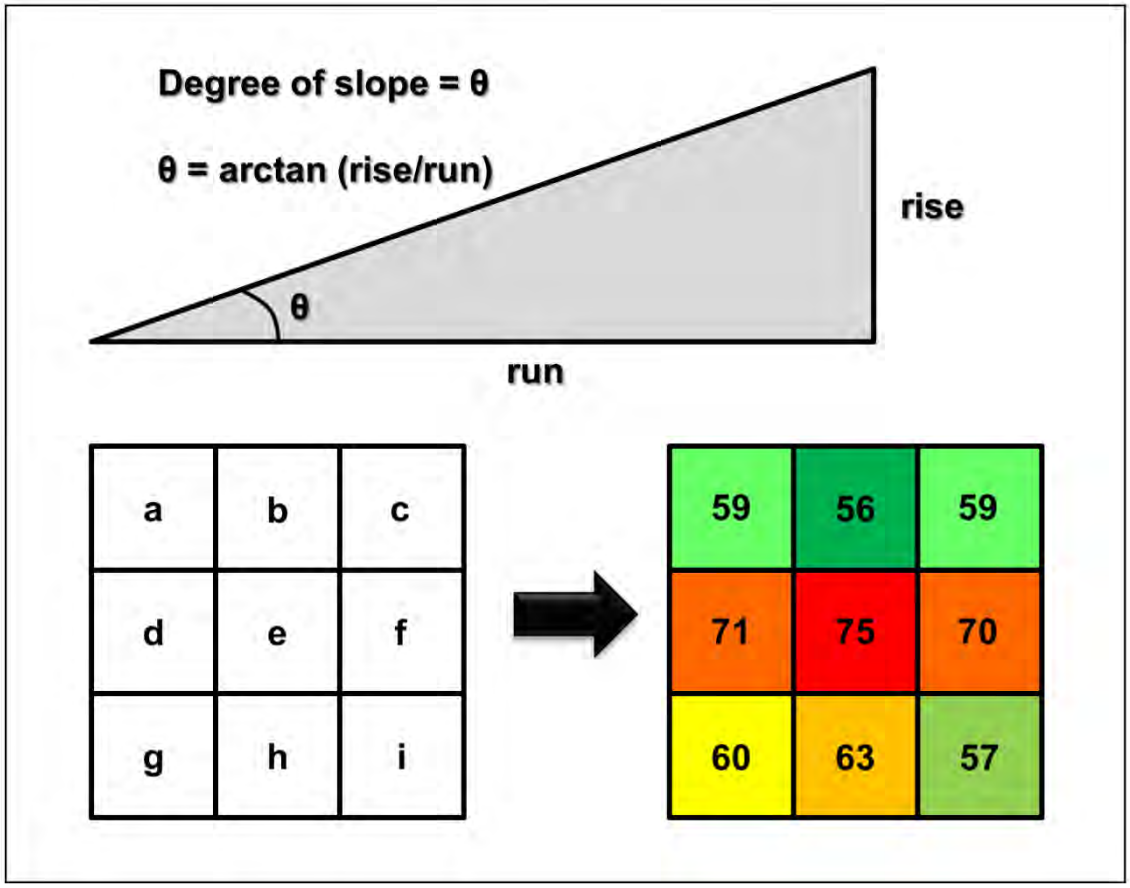

Figure 3.4. *Slope is a spatial analysis tool that calculates the maximum rate of change of each pixel relative to its neighbours. Figure modified from ESRI (2011).*

Because the surface of the drill core is cylindrical, the rounded margins of the drill core will also return steep slope values. To identify steep slope values associated with the edges of the drill core, the downslope direction (maximum rate of change) of the best-fit plane for a 3 x 3 neighbourhood of pixels (also known as aspect or facing direction) is calculated. The ArcGIS processing tool *Aspect* determines the facing direction of each pixel based on 360-degree cardinal direction system (Figure 3.5) (ESRI, 2011a). The edges of the core will have steep slopes and face either approximately right (90°) or left (270°) in the laser profiler image. Removing pixels with aspect values near 90° and 270° excludes those pixels with steep slope values that are associated with the curvature of the drill core and not fractures.

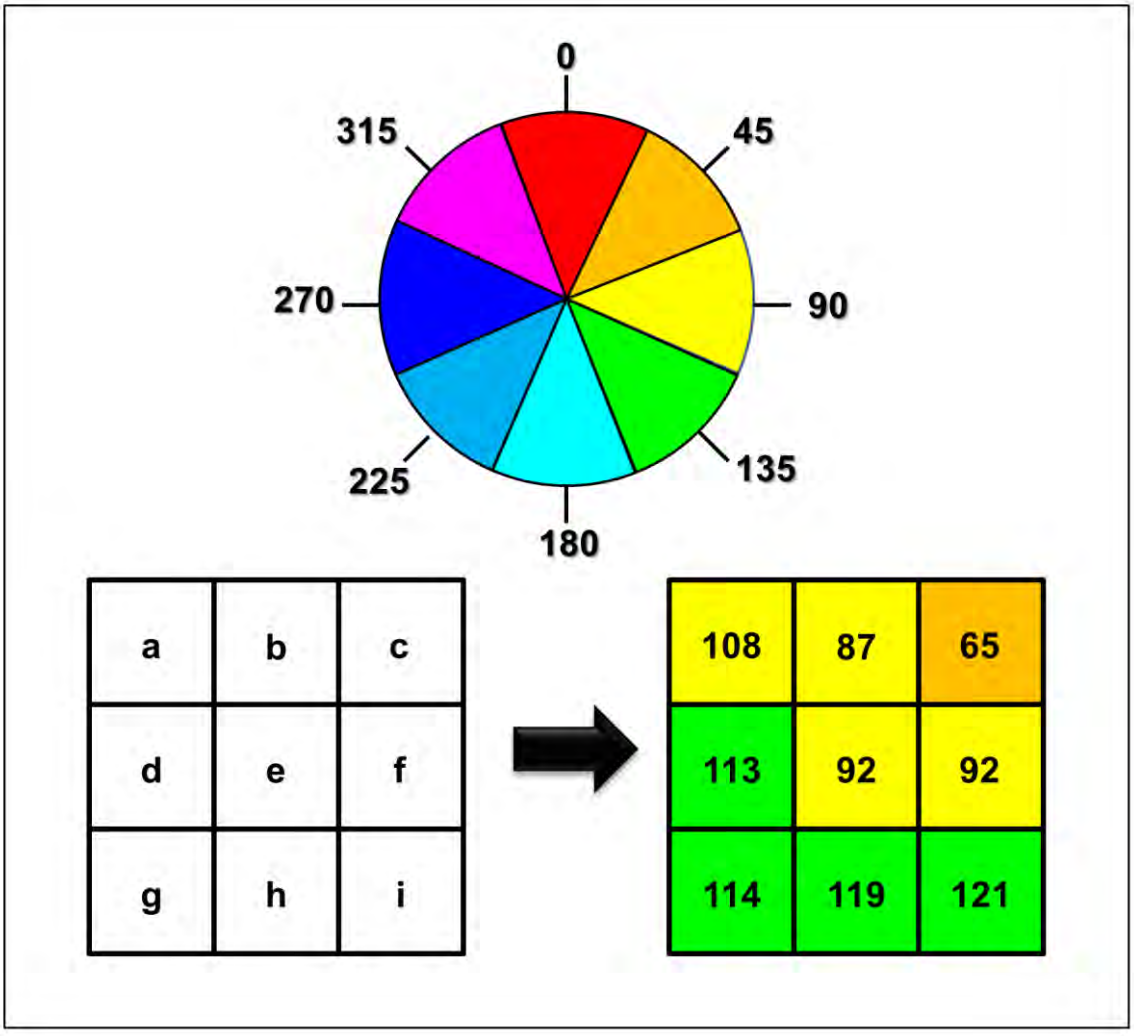

Figure 3.5. *Aspect is a spatial analysis tool that calculates the facing direction of each pixel relative to its neighbours. Figure modified from ESRI (2011a).*

By combining the slope and aspect analysis outputs, discontinuities can be automatically identified. The slope and aspect fracture selection protocol was built by applying thresholds to the slope and aspect pixel values calculated from the laser profile data. This recognition protocol also applies a height threshold to exclude pixels associated with the sides and bottom of the core tray. Table 3.1 outlines the criteria used to select fracture pixels using the slope and aspect values. Figure 3.6 shows a visual schematic of the steps used in the recognition protocol, while Figure 3.7 shows the visual outputs of the slope and aspect analysis process in ArcGIS.

Table 3.1. *Criteria used to select fracture pixels from the slope and aspect analysis outputs.*

Criteria for the Slope and Aspect Protocols	
Select Slope Values	> 70°
AND	
Select Aspect Values	0° to 60°
	120° to 240°
	300° to 360°
AND	
Pixel Height	> 0.03 m

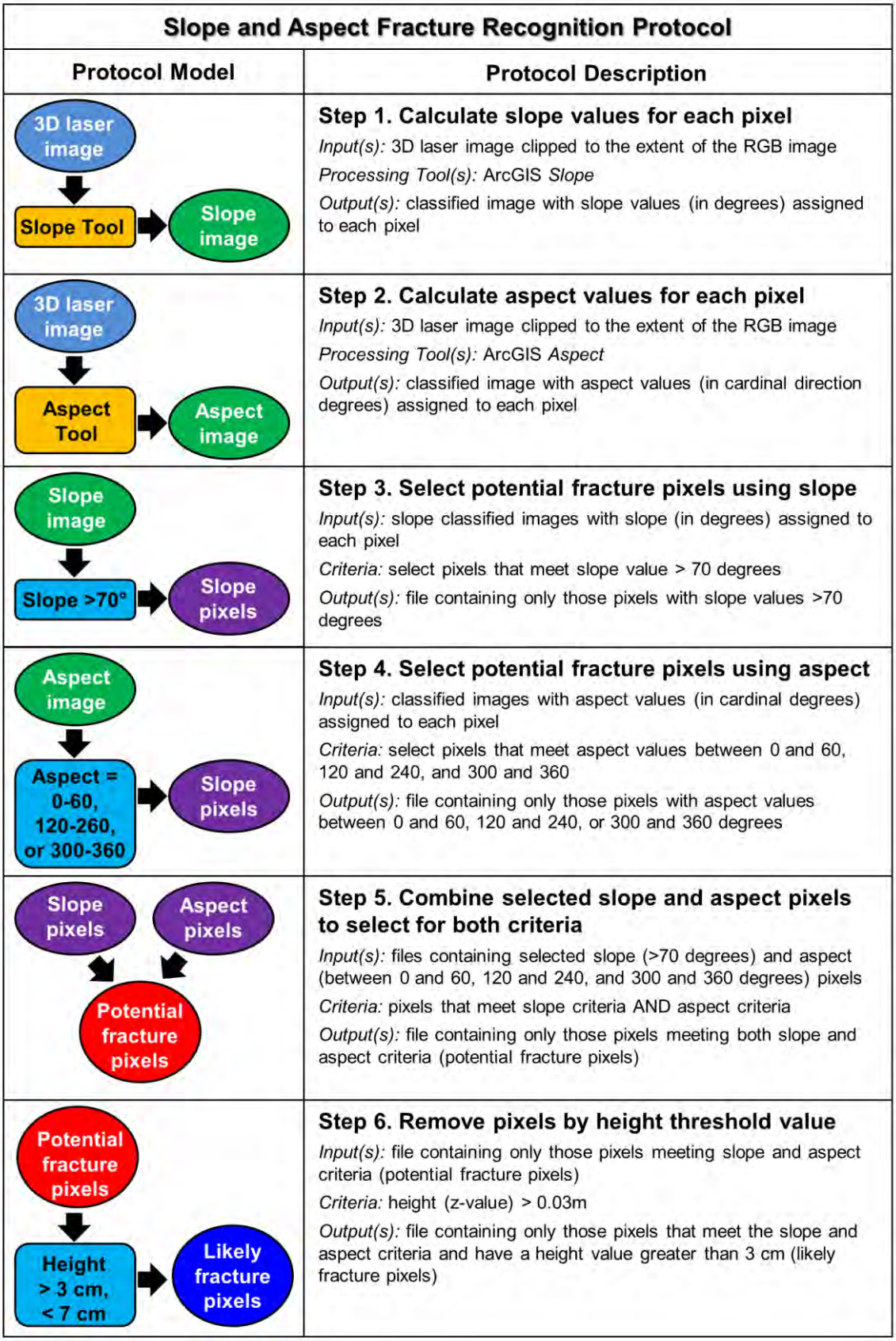

Figure 3.6. *Schematic of the processing steps for the slope and aspect recognition protocol.*

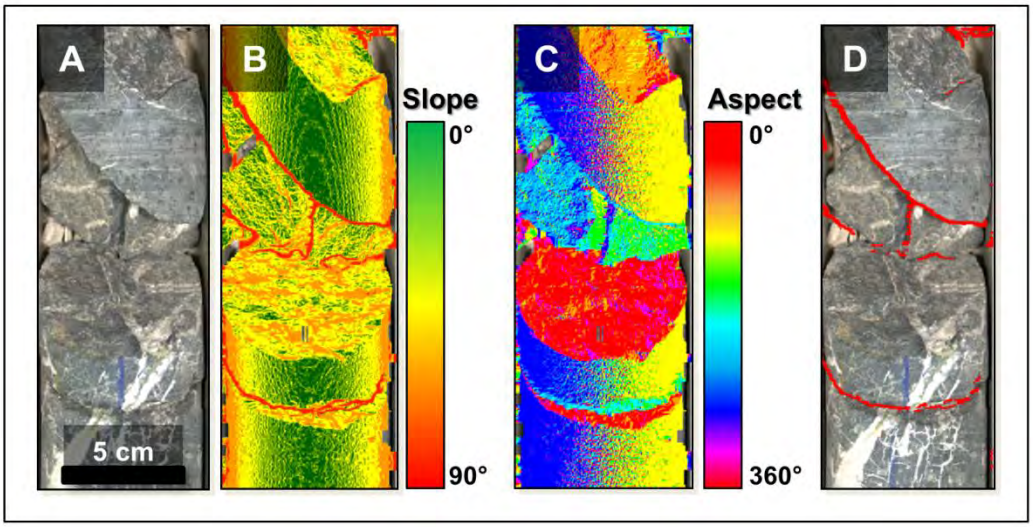

Figure 3.7. *Visualisations of the outputs of the slope and aspect processing steps in ArcGIS: core photograph (A), slope tool output (B), aspect tool output (C), selected fracture pixels (D).*

3.3.2 Fracture recognition by hillshade protocol

In hillshade analysis, a hypothetical light source of user-defined height and illumination angle is directed at a topographic surface and the estimated light intensity reflected from each pixel (a function of surface slope and aspect relative to the light source) is calculated. This method uses the relative height values of a DSM to determine which portions would be in shadow in the natural world. In ArcGIS, the *Hillshade* processing tool is used to calculate the relative illumination value for each pixel based on the height of the neighbouring pixels (Figure 3.8) (ESRI, 2011b).

Since fractures represent discontinuities in an otherwise consistent and fully illuminated cylindrical shape, areas with low hillshade light intensity may represent fractures. A light source positioned directly above the surface of the drill core surface would illuminate some, if not all, of the pixels associated with sharp changes in height (e.g. potential fractures). To overcome this for fracture recognition, the light source must be positioned to the side of the drill core, which puts the opposite side in shadow. To correct for this, two hillshade analysis steps need to be completed, one from each side of the drill core, to ensure that shadows related to the curvature of the core can be removed.

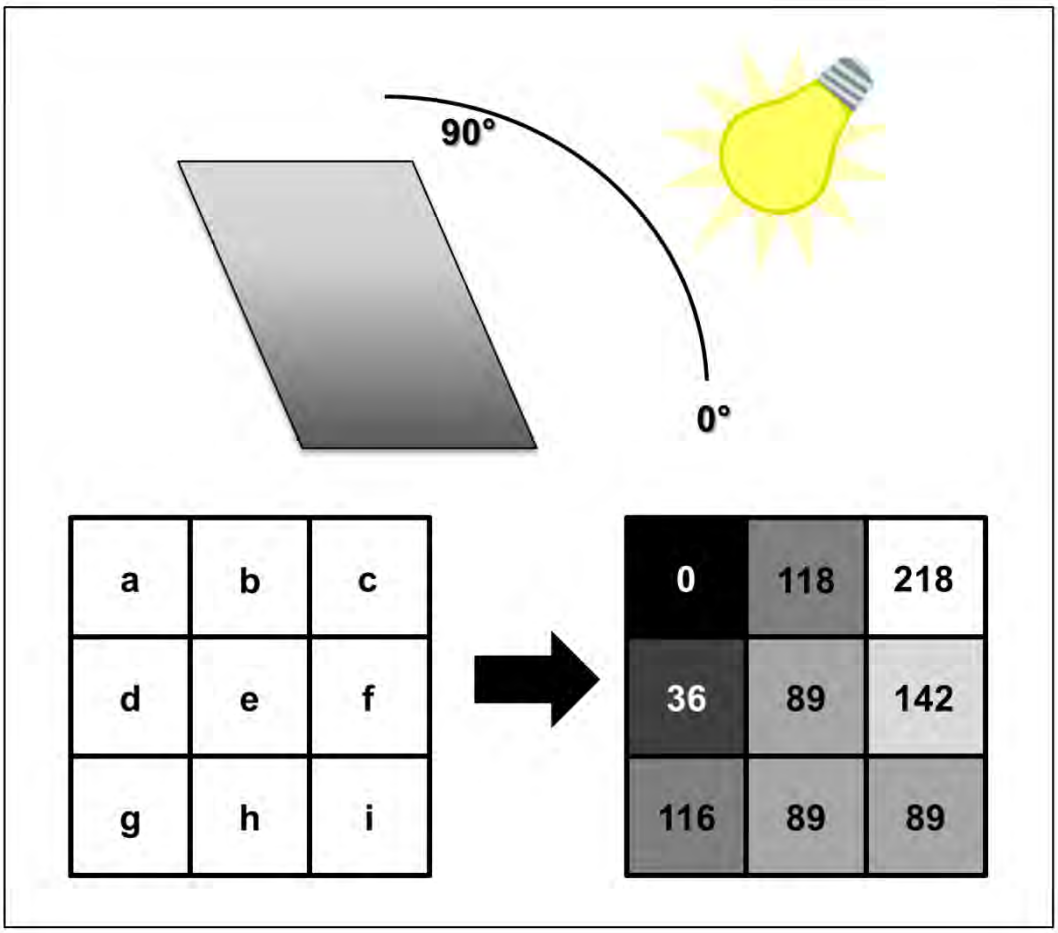

Figure 3.8. *Hillshade is a spatial analysis tool that calculates the relative light intensity of each pixel from a hypothetical illumination source. Figure modified from ESRI (2011b).*

By combining east- and west-facing hillshade analyses, discontinuities can be highlighted. The hillshade fracture recognition protocol was built by applying thresholds to the light intensity values calculated from the laser profiler data. This protocol also contains, as a final step, a height threshold to ensure that pixels associated with the sides and bottom of the core tray are not included. Table 3.2 contains the criteria used to identify fracture pixels in the hillshade fracture recognition protocol. Figure 3.9 shows a visual schematic of the processing steps used and Figure 3.10 shows the visual outputs of the hillshade recognition analysis process in ArcGIS.

Table 3.2. *Criteria used to select fracture pixels from the hillshade analysis outputs.*

Criteria for the Hillshade Protocols	
Light Source Azimuth - East	90°
Light Source Azimuth - West	270°
Light Source Height	45°
Select East-facing Values	< 100
AND	
Select West-facing Values	< 100
AND	
Pixel Height	> 0.03 m

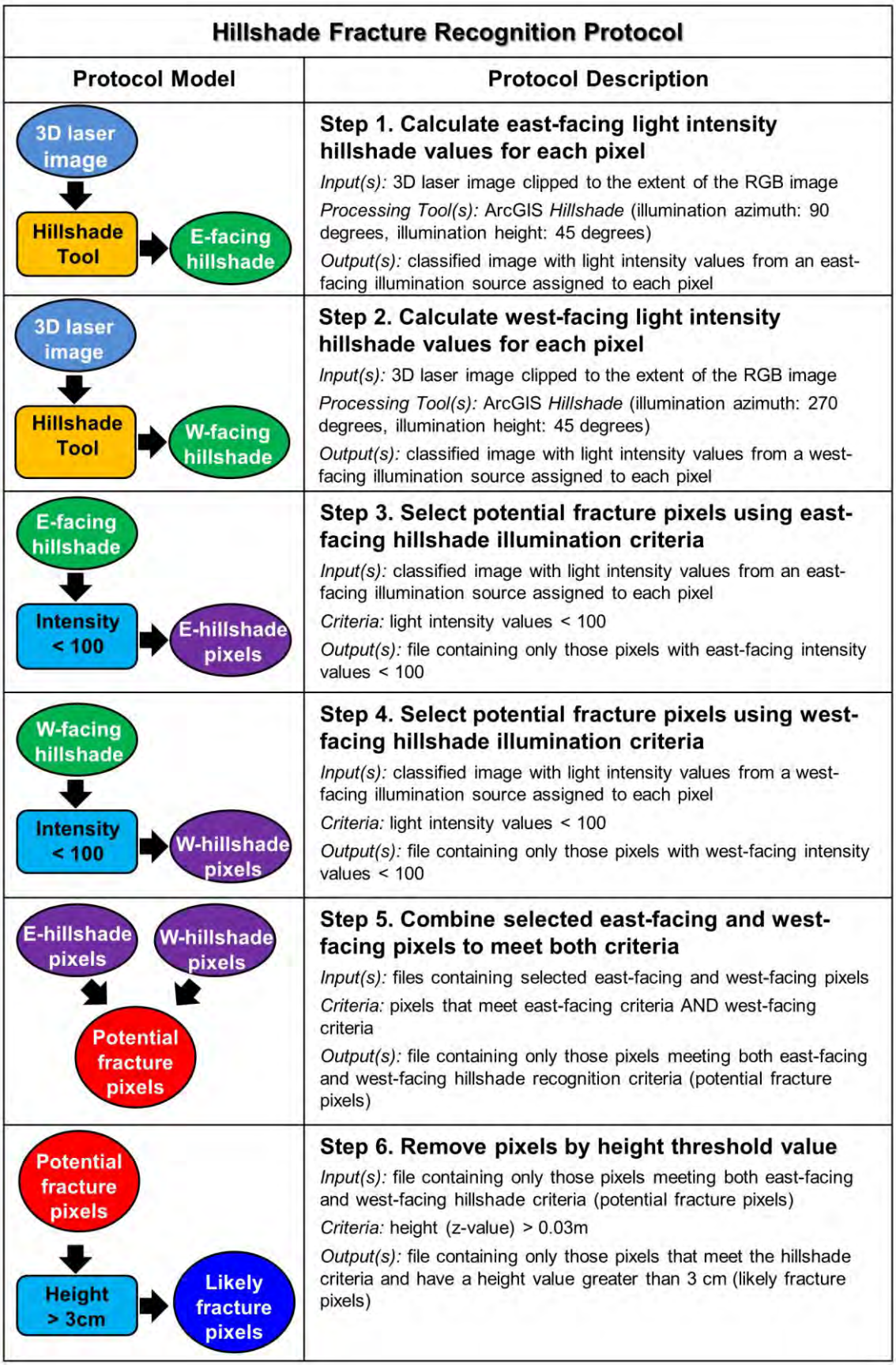

Figure 3.9. *Schematic of the processing steps for the hillshade recognition protocol.*

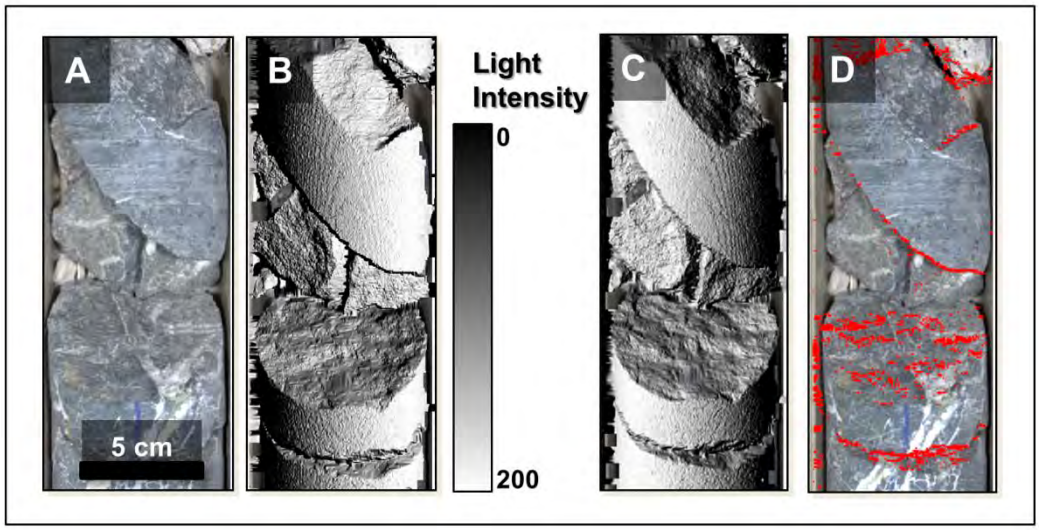

Figure 3.10. *Visualisations of the processing outputs of the hillshade processing steps in ArcGIS: core photograph (A), east-facing (90°) hillshade output (B), west-facing (270°) hillshade output (C), selected fracture pixels (D).*

3.3.3 Fracture recognition by combined protocol

The combined fracture recognition protocol incorporates all the selected fracture pixels identified by each of the other four protocols (including the hillshade + slope and aspect and high pass protocols discussed in Appendix A). This protocol was designed to test the overall performance when an increased number of fracture pixels were selected. Processing protocols for the combined recognition are outlined graphically in Figure 3.11. The visual outputs of each step of this analysis process are shown in Figure 3.12.

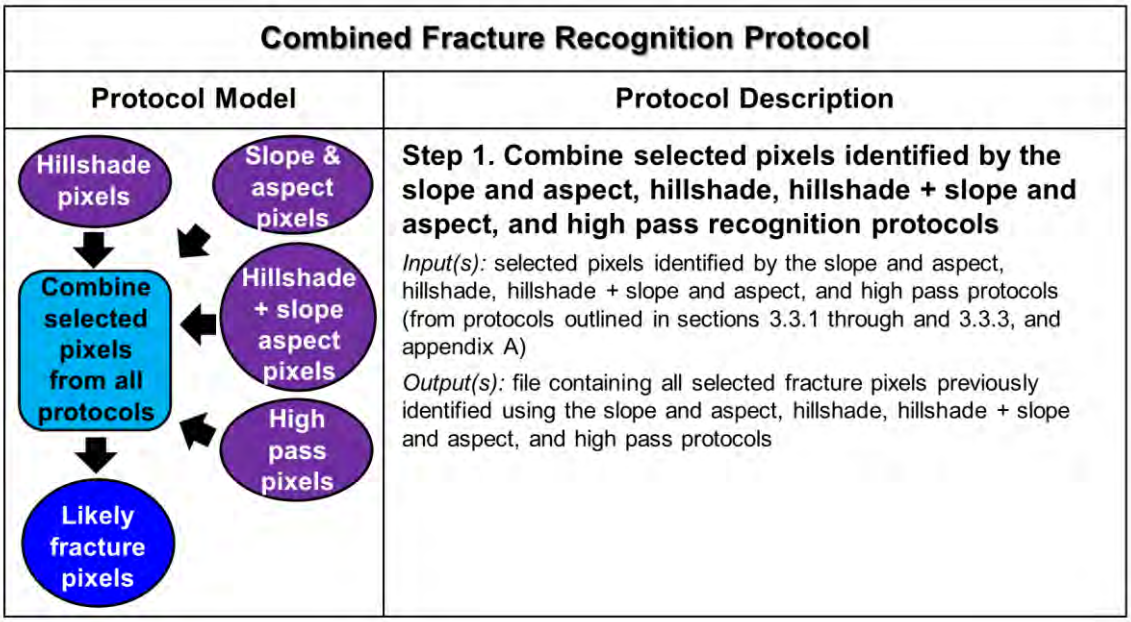

Figure 3.11. *Schematic of the processing steps for the combined recognition protocol.*

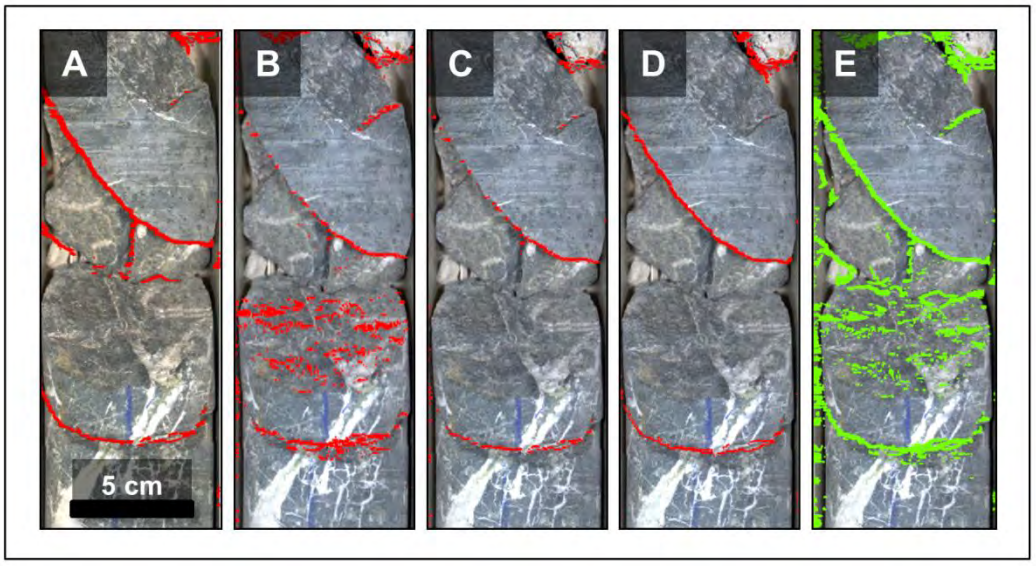

Figure 3.12. *Visualisations of the processing outputs of the combined processing steps in ArcGIS: slope and aspect pixels (A), hillshade pixels (B), hillshade + slope and aspect pixels (C), high pass pixels (D), and combined pixels (E).*

3.3.4 Criteria for a fracture to be deemed recognised

The fracture recognition protocols identify numerous pixels representing fractures. However, these protocols also identify pixels associated with chips and dents in the core, and not with fractures. To ensure that the fracture selection is as robust as possible, a series of further criteria can be applied after the fracture recognition protocols. For the purposes of this proof of concept study, a fracture is considered recognised if:

1) At least 20 pixels are identified;
2) the largest gap between pixels across the top of the drill core is less than 25 mm;
3) the pixels cover at least 50% of the distance across the top of the drill core (greater than 30 mm in the x-direction); and
4) the orientation line is clearly visible on the core surface.

The number of pixels identified is a simple count of each of the pixels selected by the fracture recognition protocols. The gap between pixels can be calculated using the distance formula where:

$$distance = \sqrt{\Delta x^2 + \Delta y^2} \quad [3.1].$$

The pixel coverage across the top of the drill core can be calculated by subtracting the minimum x-value and the maximum x-value giving the range in x-values. Any group of pixels identified by the recognition protocols that do not meet these criteria were discarded and not included in future processing steps.

3.3.5 Extraction of x-, y-, and z-values of recognised fracture pixels

Once the fractures are recognised, the geotechnical assessment protocols require the x-, y-, and z-coordinates of each fracture pixel. Since the Corescan laser profiler pixels are automatically referenced with these values in metres, exporting these coordinates is relatively straight forward. In this study, ArcGIS was used to convert fracture pixels to points and then automatically append the associated x-, y-, and z-coordinates of each pixel to the corresponding points. Grouping individual fracture pixels together as a single feature will be the most challenging step in automating fracture recognition and extraction. For the purposes of this study, this was completed manually by grouping the pixels corresponding to each fracture visible using the true colour image as a guide. The x-, y-, and z-coordinates for each group of fracture points was exported from ArcGIS as a single CSV file and used in further processing steps.

3.4 Remove mechanical breaks

Distinguishing between mechanical and other non-fracture breaks is important since not all drill core breaks represent true fractures. In order to adequately remove non-fracture breaks, some manually supervised decisions will need to be made by a geologist or geotechnical engineer. To accomplish this, we propose a

protocol that would flag potential mechanical breaks. Each flagged fracture could then be evaluated manually to determine whether it was natural or not. Previously identified fractures were flagged if they occurred:

1) at the beginning or end of a core tray row;
2) less than 3 cm away from a visible driller's mark (in this case, a red "x"); or
3) less than 3 cm away from a core block.

To identify the driller's marks (typically a red "x"), the red colour in the true colour image or the hyperspectral signature of the wax pencils used to make the marks would be identified. Then, any fracture within close proximity to these driller's marks would be flagged as a potential mechanical break. The Corescan system currently masks out core blocks and the end of the core tray as part of the hyperspectral data processing. Since the location of core blocks and core tray edges are already known, the proximity to each of these features could be easily calculated.

In addition to fractures occurring near core blocks and the end of core trays, the expected fracture roughness and orientation values for the deposit could also be used to flag potential mechanical breaks. A series of rulesets would include expected threshold values for natural fracture roughness and expected structural orientation based on observations and previous site knowledge from Cadia East. To tune these rulesets, a scoping study will need to be completed in collaboration with the Cadia geotechnical team to determine the range of roughness values measured in naturally occurring fractures and their expected orientations.

A manual review of flagged fractures by experienced site staff would ensure that site knowledge and human expertise is integrated into the fracture interpretation process. Practically, this manual inspection interface could be included in the existing Corescan online data portal (Coreshed, https://app.coreshed.com), encouraging data users to interact with the geotechnical data outputs online. Once the non-fractures are positively identified, they can be excluded from any geotechnical calculations. For this study, any fractures meeting the flagging criteria were manually examined and excluded if they were deemed mechanical breaks.

3.5 Calculate orientation of selected fractures

Calculating the orientation of selected fractures requires the exported CSVs containing the x-, y-, and z-coordinates of each group of fracture pixels identified by the fracture recognition protocols. The orientation of each fracture can be calculated by fitting an oriented three-dimensional plane through the pixels in 3D space (Olson, 2013; Quiniou et al., 2007). For the protocols described here, only one row of pixels on the extreme down hole edge of the fracture are used in the orientation calculations avoiding instances where numerous rows of pixels are selected from within the fracture itself (Figure 3.13). These orientations can then be used to determine the number of fracture sets required to calculate the RMR and the Q-index in future processing steps. Appendix C comprises an Excel workbook containing the 3D least squares linear regression and 2D linear transformation calculations used for fracture orientation in this study.

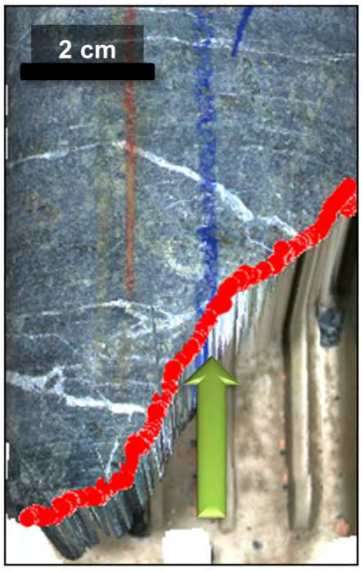

Figure 3.13. *Only those pixels on the most down hole edge of the fracture (identified by green arrow) were used in the fracture orientation protocols.*

3.5.1 Linear least squares regression

The equation of any plane in three-dimensional space is represented by the formula:

$$y = a + bx + cz \qquad [3.2].$$

This formula can then be optimized such that:

$$a + bx + cz - y = 0 \quad [3.3].$$

Using the x-, y- and z-coordinates of selected fracture pixels extracted from the laser profile image, coefficients a, b, and c can be optimized through linear least squares regression such that a plane best-fits these points (Figure 3.14). The specific calculations and mathematical proofs, as they pertain to 3D plane fitting for fracture orientation, are detailed in Appendix D.

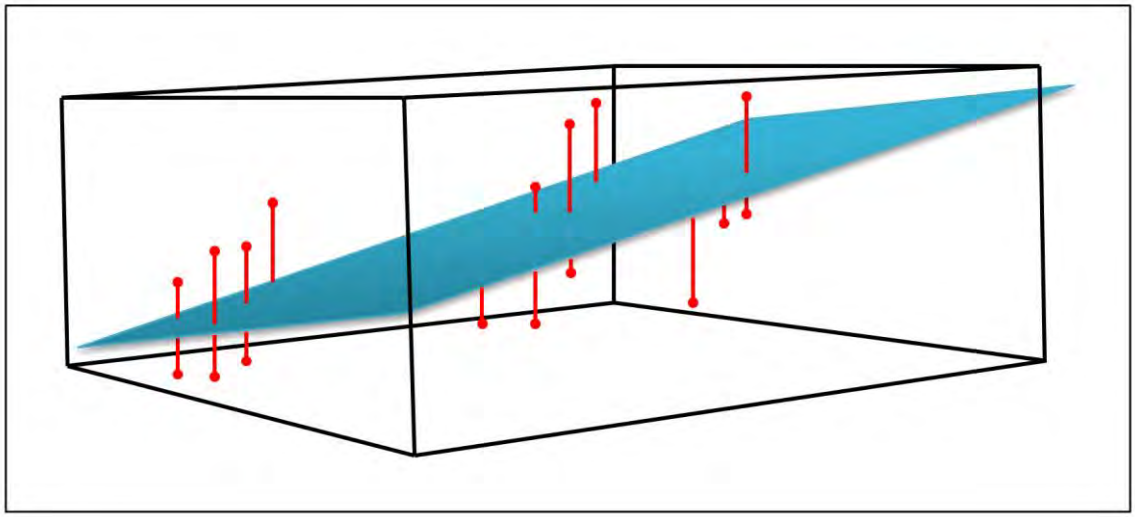

Figure 3.14. *Linear least squares regression allows for a flat, 3D plane (blue) to be fit to a series of three-dimensional points (red).*

3.5.2 Two-dimensional linear transformations

To account for the trend and plunge of the drill hole, the core must first be rotated so that the orientation line is at the bottom of the drill hole. It is possible that the location could be detected using either the RGB imagery or the hyperspectral signature of the wax pencils used to draw the line, but for the purposes of this thesis, the location of this line was extracted manually.

Once the orientation of the apparent fracture plane is calculated, it must then be rotated to account for the trend and plunge of the drill hole (Figure 3.15). This is accomplished by a series of three, 2D linear transformations: (1) about the x-axis, (2) about the y-axis, and (3) about the z-axis. The mathematical calculations and proofs behind these transformations are provided in Appendix E.

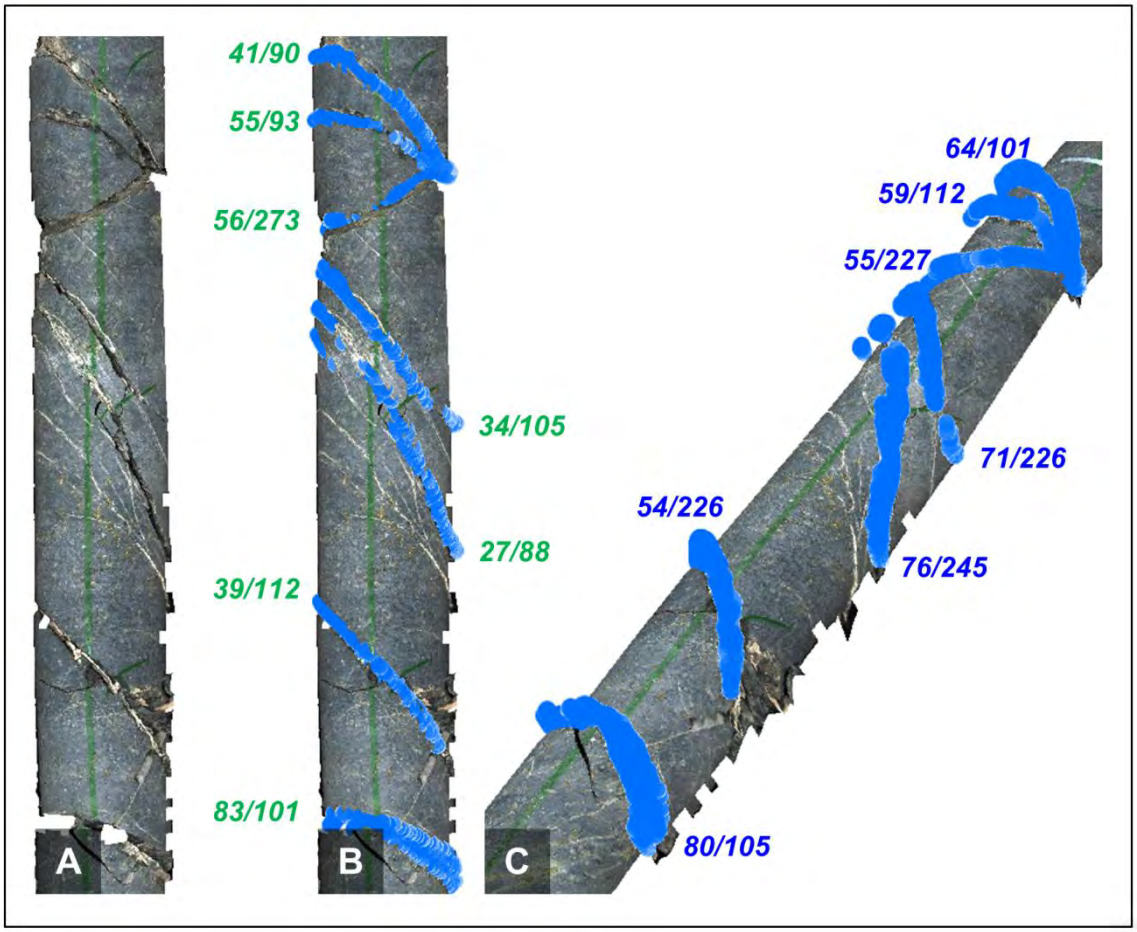

Figure 3.15. *A series of 2D linear transformations are used to rotate the apparent plane into the true orientation. From the drill core data (A), the apparent orientations are calculated (B. The apparent orientations are then rotated to account for the trend and plunge of the drill hole (C). Figure modified from Harraden et al. (2016).*

3.6 Calculate fracture roughness

In the Q-index system, Barton (1976) defines six general classifications of fracture roughness characteristics based on geometry and general roughness of the fracture surface. The 2D RL (real length profile) value is calculated by comparing the true length of a fracture profile to the nominal length and is commonly used in fracture roughness calculations (Yu and Vayssade, 1991). By modelling the 3D fracture surface using the recognised fracture pixels, a modified version of the RL value is calculated by comparing the calculated, 3D surface area of the fracture to the nominal area (or 2D footprint area) of the fracture (Figure 3.16). For this study, the RL value is calculated by:

$$\mathrm{RL} = \frac{\text{true 3D surface area}}{\text{nominal area}} \qquad [3.4].$$

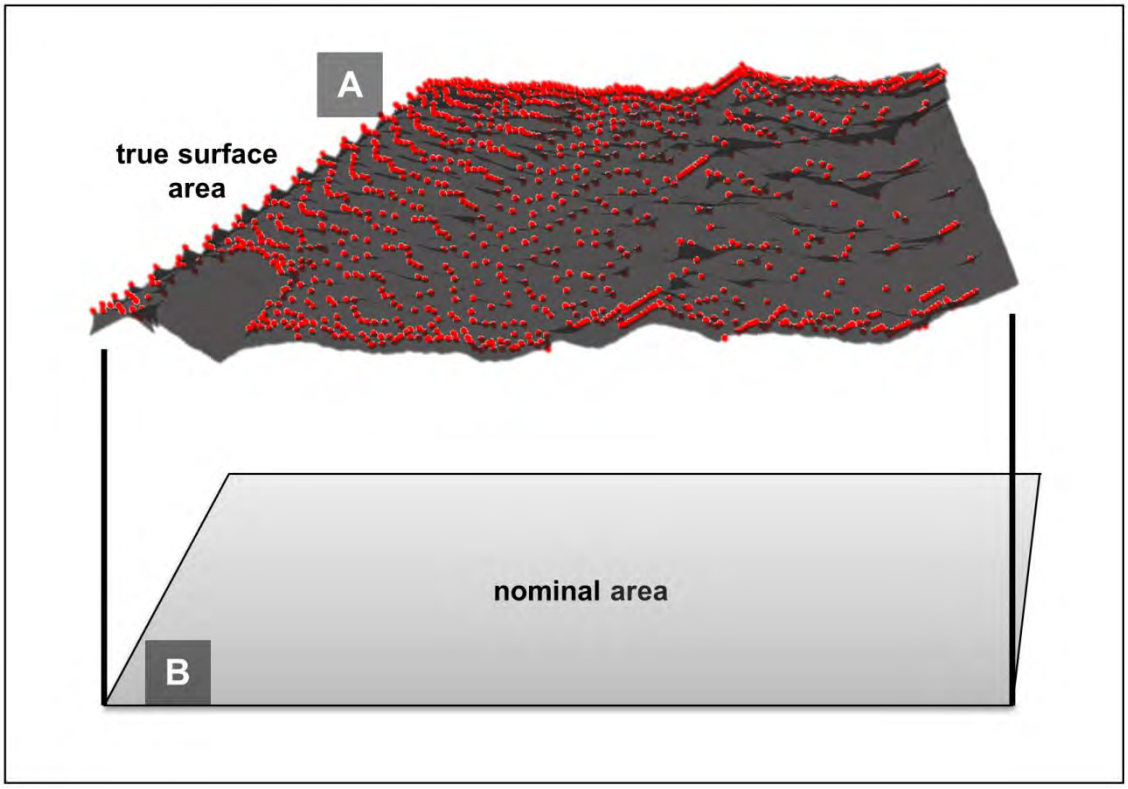

Figure 3.16. *Example of a 3D surface created from the recognised fracture points. The red points represent the fracture pixels used to create the 3D surface. By comparing the true, three-dimensional surface area (A) to the nominal area (or 2D footprint area, B) of the fracture, a roughness proxy can be calculated.*

Since the fracture pixels contain 3D information, it is possible to calculate the modified RL using the 3D fracture point locations. The roughness of the fracture must be measured from the surface perpendicular to the core axis (y-axis), so the surface and nominal areas need to be calculated from the y-value data. In order to accomplish this, the original coordinates of the fracture need to be converted so that changes in the y-coordinates of the drill core become the "height" data for future analysis steps. Functionally, this means that when importing the points into ArcGIS, the (x, y, z) coordinates are translated into (x, z, y) coordinates (Figure 3.17). Using the ArcGIS processing tool *Spline,* a three-dimensional surface through the fracture points is then created (Figure 3.16A). This surface is created strictly from the input points and is interpolated over an area that covers a rectangle stretching over the limits of the data (e.g. span of x-values and y-values). Occasionally, edges of the core tray or erroneous pixels were selected as part of the fracture selection causing issues with the *Spline* function. To address this, any points considered to be outliers (greater than 1 standard deviation away from points in the y-direction) were removed from the points file prior to

running the 3D calculations. All of the pixels recognised for each fracture were used to create the surface, reducing the extrapolation errors of the *Spline* algorithm. Using the *Surface Volume* tool in ArcGIS, the true 3D surface area of the fracture surface is calculated in m^2. This analysis tool analyses the surface topography from the height model of the fracture surface and measures both the true 3D surface area and the nominal 2D surface area. Once the true and nominal surface areas are determined, the RL can then be calculated by equation [3.4].

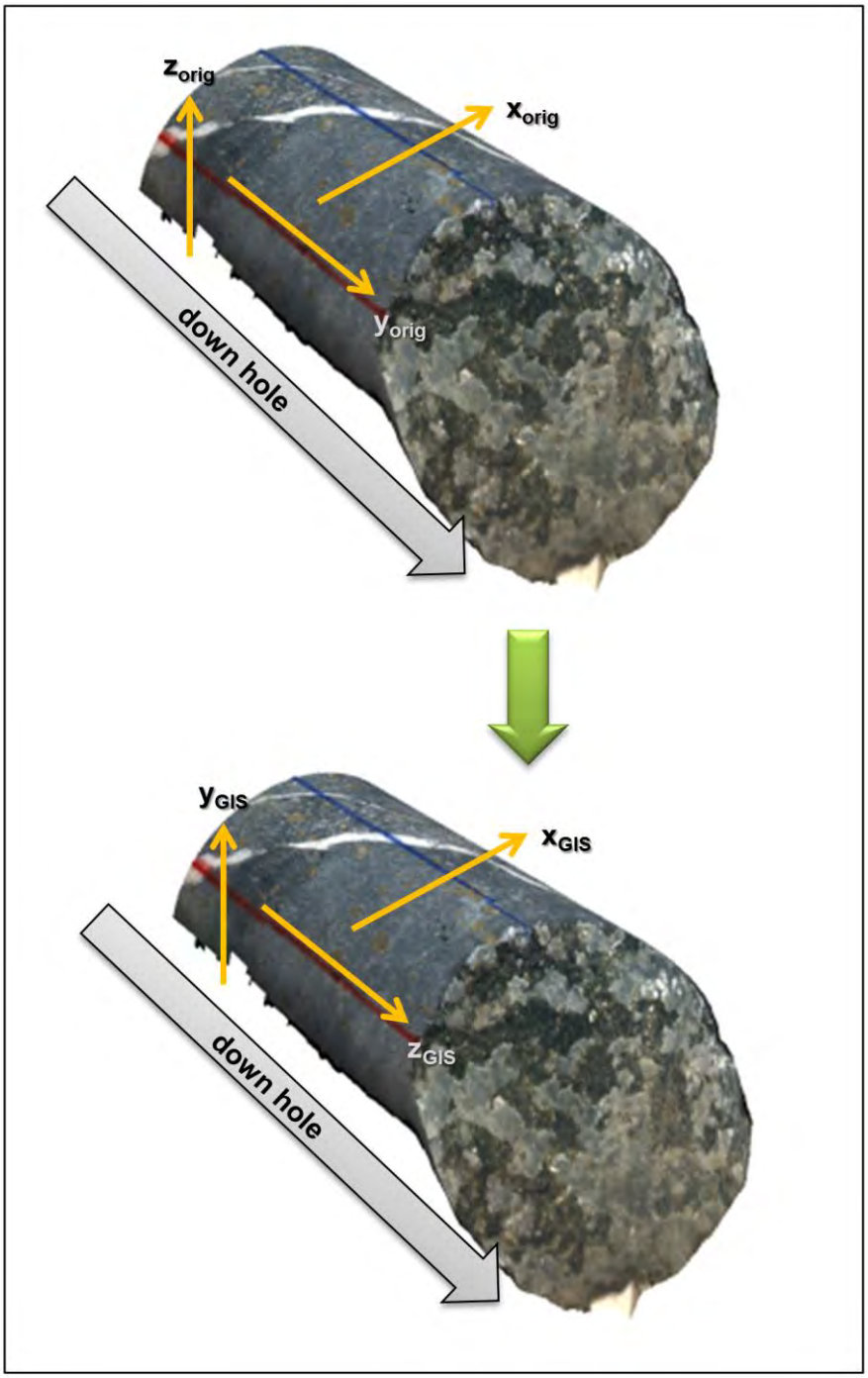

Figure 3.17. *The laser profile data coordinates must be translated prior to fracture roughness calculations to ensure the surface topography of the fracture is modelled as a surface.*

For the workflow outlined here, ArcGIS was used for the spatial processing steps; however, the methods are common mathematical and spatial algorithms that could be developed within the Corescan system if required. To summarise the entire process, the specific processing protocols for the 3D roughness calculations are outlined graphically in Figure 3.18.

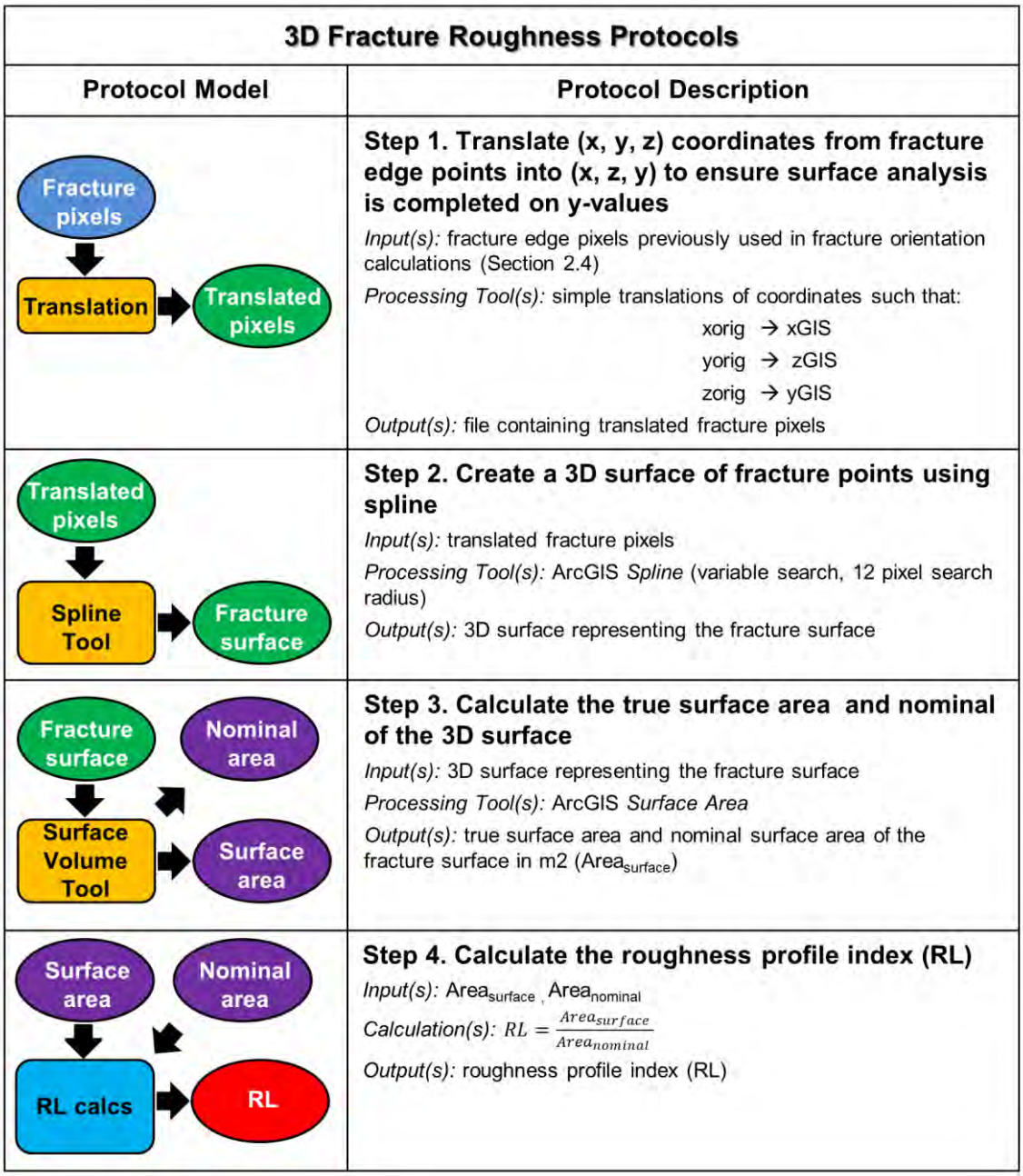

Figure 3.18. *Schematic of the processing steps for the fracture roughness protocol.*

The roughness parameters must be corrected to account for the increased data density and spacing variability by taking the cube root of the JRC equation. The JRC equation by Maerz et al. (1990) has been modified to suit the Corescan data where:

$$JRC_{3D} = \sqrt[3]{411 * RL} \qquad [3.5].$$

3.7 Determine number of fracture sets present

The number of fracture sets present in a given interval of drill core is a key geotechnical parameter for the Q-index. A comparison of the automated fracture orientation calculations over selected intervals can be used to group the data into distinct fracture sets. Since the orientations of fractures were previously calculated, these orientations can be plotted on a polar diagram to determine the number of primary fracture sets present in a given interval. An example of this type of polar plot is shown in Figure 3.19.

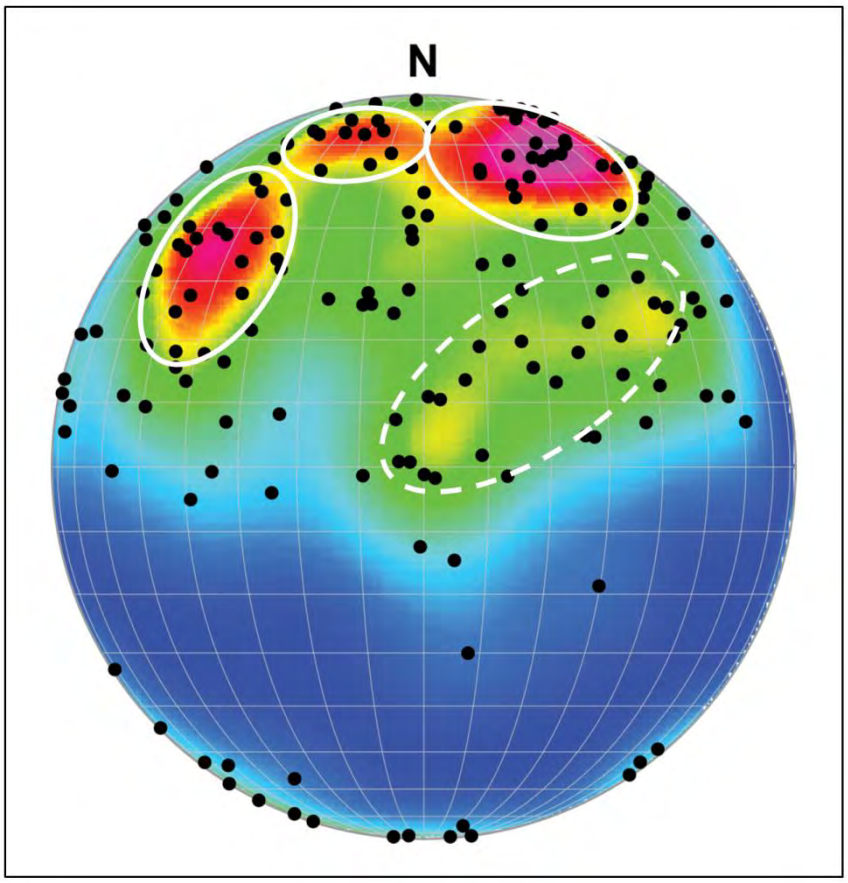

Figure 3.19. *An example of a polar plot projected on an equal area stereonet. Polar plots show the primary orientations of a group of data and can be used to determine the number of fracture sets present. In this example, 3 fracture sets (solid, white ellipses) and a possible 4th fracture set (dashed, white ellipse) can be identified.*

Determining the number of fractures sets using polar plots is somewhat subjective, and depends on the distribution of the structural data. The orientation of the drill hole relative to the primary orientation can affect the determination of the number of fracture sets present (Berg, 2012). Robust, multi-dimensional statistical techniques by k-means clustering and principle component analysis (PCA) have been applied to determining the number of fracture sets using

multiple fracture characteristics (such as orientation, thickness, and mineralogy) (Marcotte and Henry, 2002; Slob et al., 2005; Tokhmechi et al., 2011). This approach will be discussed further in chapter 5.

3.8 Measuring fracture spacing

Average fracture spacing is required for the calculation of the RMR value. The fracture spacing is the simplest calculation of the entire methodology. The site geotechnical team at Cadia uses a fracture frequency per metre (F/m) method where the number of fractures per metre is measured. The downhole location (y-value) of each fracture in metres is determined in the fracture identification steps, so the fracture spacing values can easily be calculated by determining the average distance between fractures for a given interval. The F/m can be calculated by taking an average number of fractures per metre over a given interval.

3.9 Conclusions

The specific protocols outlined in sections 3.4 – 3.8 were designed to replicate the industry-standard manual data collection methods for geotechnical index parameters. Six specific protocols were designed to accomplish this: 1) identify and extract fractures, 2) remove mechanical breaks, 3) calculate the orientation of the fractures, 4) determine the roughness of the fractures, 5) determine the number of fracture sets, and 6) determine the fracture spacing.

Calculating fracture orientations, roughness, sets, and spacing is impossible without the ability to first recognise the fractures. The proposed fracture recognition protocols selected different pixels for each fracture which ultimately affect the morphological fracture calculations. While the hillshade + slope and aspect and high pass recognition protocols proved to be poor recognition protocols, the slope and aspect, hillshade, and combined protocols were assessed. The fracture recognition, orientation, roughness, sets, and spacing using the pixels derived from each protocol were assessed and compared. This assessment is discussed in detail in chapter 4.

The goal of this research was to design a set of protocols that could replicate, as closely as possible, the current manual method of geotechnical core logging. There is no expectation that the proposed methodology will improve on the

quality of the data, but rather that the speed, consistency, and volume of data collection could be increased. This proof of concept study uses a combination of spatial analysis tools in ArcGIS, manual data handling, and mathematical calculations to show that fractures can be recognised and morphological features such as orientation, roughness, number of fracture sets, and fracture spacing can be determined using computer analysis of Corescan-derived data. Since the application of this work will be applied to Corescan data, it is assumed that Corescan will complete the computer programming and integration of these protocols into their proprietary software. To assess the individual protocols and proposed methodology, the performance of these protocols were tested using a manually-derived geotechnical dataset from Cadia East. The detailed results and discussion of the testing and assessment are outlined in chapter 4.

Chapter 4

Testing of methods for morphological geotechnical assessment

4.1 Introduction

The methodology and protocols presented in chapter 3 were designed to replicate the manual geotechnical logging procedures considered standard practice for geologists and geotechnical engineers. To assess the performance of these automated protocols, calculated values for fracture orientation, roughness, number of fracture sets, and spacing were compared to a set of manually measured fractures from one drill hole. The sections that follow outline the results of this assessment and discuss the strengths, and challenges of the automated extraction of morphological geotechnical index parameters from Corescan data.

4.2 Test data set

To assess the performance of each step of the proposed methodology, the processing results from a test data set were compared to expected values, photographs of the fractures or measured values in the case of orientations. The test data set contained 23 core trays (76 metres of drill core) and 199 fractures from the Cadia East drill hole UE276. Details of the core intervals used as the comparison data set are listed in Table 4.1.

Table 4.1. *Core intervals used to test the geotechnical data calculation protocols.*

Drill hole ID	Tray Number	Depth From (m)	Depth To (m)	Metres	Number Measured Fractures	Rock Type*^
UE276	1	0	3.5	3.5	14	FRV
UE276	2	3.5	6.7	3.2	5	FRV
UE276	3	6.7	10.1	3.4	8	FRV
UE276	25	80.1	83.3	3.2	15	FRV
UE276	26	83.3	84.3	1	3	FRV
UE276	26	84.3	86.6	2.3	17	CIC
UE276	27	86.6	89.9	3.3	12	CIC
UE276	46	148.7	152	3.3	5	FRV
UE276	47	152	155.3	3.3	6	FRV
UE276	48	155.3	158.7	3.4	11	FRV
UE276	49	158.7	162.1	3.4	11	FRV
UE276	50	162.1	165.5	3.4	7	FRV
UE276	51	165.5	168.8	3.3	9	FRV
UE276	70	228.5	231.8	3.3	5	FRV
UE276	71	231.8	234.9	3.1	5	FRV
UE276	72	234.9	238.2	3.3	8	FRV
UE276	73	238.2	241.5	3.3	4	FRV
UE276	74	241.5	244.9	3.4	12	FRV
UE276	75	244.9	248.2	3.3	7	FRV
UE276	97	317.7	320.9	3.2	6	FRV
UE276	98	320.9	324.1	3.2	7	FRV
UE276	99	324.1	327.4	3.3	7	FRV
UE276	121	396.7	400.1	3.4	6	FRV
UE276	123	403.2	406.7	3.5	9	FRV
Total	*23*			*76.3*	*199*	

*FRV = Forest Reef Volcanics

^CIC = Cadia Intrusive Complex

During a site visit to Cadia in October 2015, numerous core trays waiting to be scanned using the Corescan system were examined and the orientation of observed fractures was measured. This dataset forms the baseline observations for the fracture orientation comparisons described in section 4.5. The natural fractures identified in the drill core were measured using the manual alpha and beta methodology. The industry standard procedures for manual core orientation measurements are outlined in Holcombe (2013) and discussed in detail in Chapter 2.

The errors associated with measuring alpha and beta angles manually can be difficult to quantify since they can be the result of an incorrectly placed orientation line, inaccurate selection of the apical trace (especially as the fracture

approaches 90° to the core axis), and rounding to the nearest 5° on both the protractor and wrap-around beta ruler. Vearncombe (2013) assumes a typical error of less than 5° for manual alpha and beta measurements, but notes that this error can increase up to 25° as the alpha angle approaches 90°. For the test dataset, every effort was made to reduce measurement errors when measuring orientations but, in practice, errors of up to 10° for dip and 20° for dip direction are expected.

Since the alpha and beta angles represent the apparent orientations of fractures, the true measured orientations need to be determined to account for the trend and plunge of the drill hole. Geocalculator© was used to convert the measured alpha and beta angles to true orientations. The 199 measured alpha and beta values from the test dataset were converted into dip and dip direction based on the orientation of the drill hole. Appendix F contains the details of software procedures and conventions used for the alpha and beta angle conversions. Appendix G documents the measured alpha, beta, and true orientation value for each fracture in the test dataset.

No roughness values were measured manually while on site. As a result, the roughness values determined using the calculation protocols were compared to a visual assessment of the fractures from photographs as well as the expected roughness values for the rock units encountered in the test dataset. Since the test dataset is hosted in the Forest Reef Volcanics (FRV) and the Cadia Intrusive (CIC) units, the expected fracture roughness values range from JRC = 2.5 to JRC = 14 (Rossimel and Lett, 2012).

With respect to fracture sets and spacing, Rossimel and Lett (2012) define the average number of fracture sets to be 3 and the average fracture spacing (reported as F/m) to be between 2 and 4 for both the FRV and CIC.

While five fracture recognition protocols were developed and tested, only three proved to be successful. The hillshade + slope and aspect and high pass recognition protocols provided very poor fracture recognition, orientation, and roughness results. The results from these protocols are included in Appendix H, but will not be discussed in detail here.

4.3 Assessment of fracture recognition protocols

The fracture recognition protocols were used to identify pixels matching the criteria outlined in section 3.3. In general, the slope and aspect, hillshade, and combined fracture recognition protocols were successful in recognising a majority of fractures that were previously identified through manual logging. Table 4.2 summarises the fracture recognition rates for recognised true fractures for each of the five fracture recognition protocols.

Table 4.2. *Summary of fracture recognition rates for each fracture recognition protocol.*

	Slope and Aspect Recognition Protocol	**Hillshade Recognition Protocol**	**Combined Recognition Protocol**
# Fractures Measured in Drill Core	199	199	199
# Fractures Correctly Identified	150	138	157
% Fractures Correctly Identified	75%	69%	79%

Using the recognition criteria that must be met in order for a fracture to be identified (section 3.4.4), a number of fractures were discarded. In some cases, two of the three selection criteria were met, but the third criterion failed (Figure 4.1). Many of the fractures that were not detected were instances where there was very little space between the two core pieces. Figure 4.2 shows an example of a tight fracture that was not detected by any of the recognition protocols. The laser profiler on the Corescan system is used to construct images with a 200 μm pixel resolution, making it difficult to recognise fractures with gaps of less than 200 μm. Table 4.3 shows the distribution of criteria leading to fractures not being recognised by each recognition protocol. Where the core is highly fractured, or blocky, fractures are often recognised, but cannot be distinguished from the overall broken nature of the drill core, causing a high number of false positives (Figure 4.3).

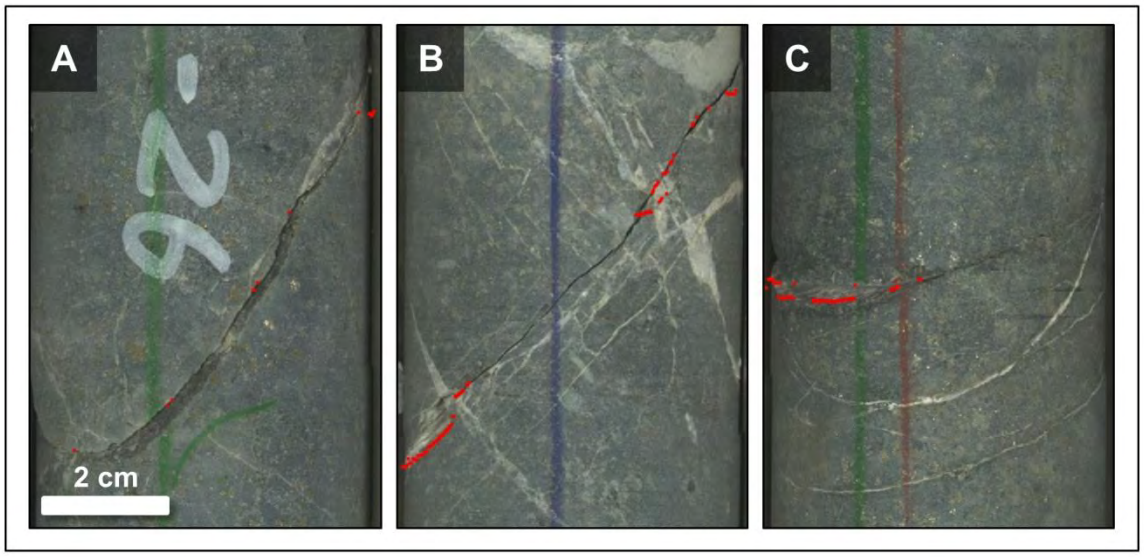

Figure 4.1. *Examples of fractures that met two of the three fracture recognition criteria but were not considered recognised as they failed to meet the third criterion. Fracture pixels shown in red. A. Fracture that failed to have more than 20 pixels identified. B. Fracture with gaps greater than 25 mm between pixels. C. Fracture with less than 50% coverage across the surface of the drill core.*

Table 4.3. *Summary of fractures failing to meet recognition criteria for each fracture recognition protocol.*

	Slope and Aspect Recognition Protocol	**Hillshade Recognition Protocol**	**Combined Recognition Protocol**
Fractures failing to meet <25 mm gap	23	26	12
Fractures failing to meet > 50% coverage	8	8	4
Fractures failing to meet >20 pixels criteria	2	1	0
Total number of fractures not meeting all 3 fracture detection criteria	23	28	16
Tight or blocky core fractures not detected by recognition protocol	28	33	31

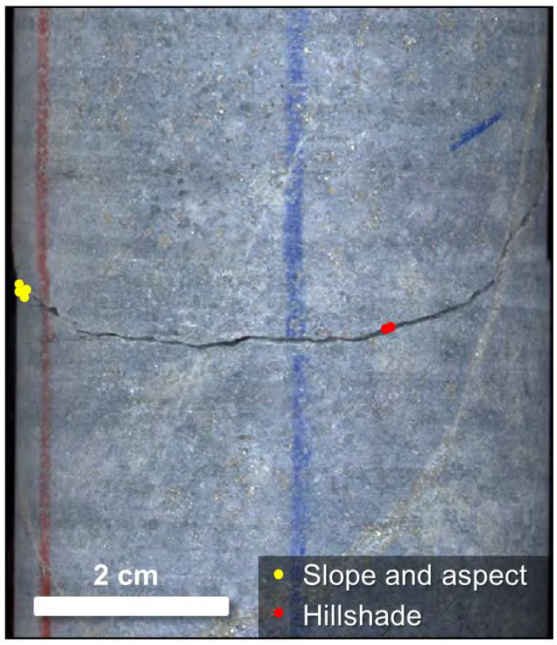

Figure 4.2. *Example of a tight fracture which was not detected by any of the fracture recognition protocols. Only a few fracture pixels were identified, but were insufficient for fracture recognition.*

Figure 4.3. *Example of a fracture in blocky core that was not detected by any of the fracture recognition protocols. Where the core is blocky, the true fracture (green) cannot be distinguished from the other breaks (red), so the fracture is not recognised.*

One major challenge in automatically recognising fractures is that the recognition protocols were set up to detect discontinuities in an otherwise cylindrical shape. This means that mechanical breaks, edges of core blocks, and other non-fracture features are also detected (Figure 4.4). As discussed in section 3.4, manual criteria were used to flag any fractures occurring:

1) at the beginning or end of a core tray row;
2) less than 3 cm away from a visible driller's mark (in this case, a red "x"); or
3) less than 3 cm away from a core block.

Flagged fractures were then manually reviewed to determine if they were, in fact, natural fractures. After removing fractures that were deemed to result from non-natural mechanisms, some false fractures were still automatically detected by the fracture detection protocols. Typically, these represented mechanical breaks where the driller's mark has been rotated out of the field of view (Figure 4.5). Table 4.4 summarises the false fracture recognition details for each fracture detection protocol.

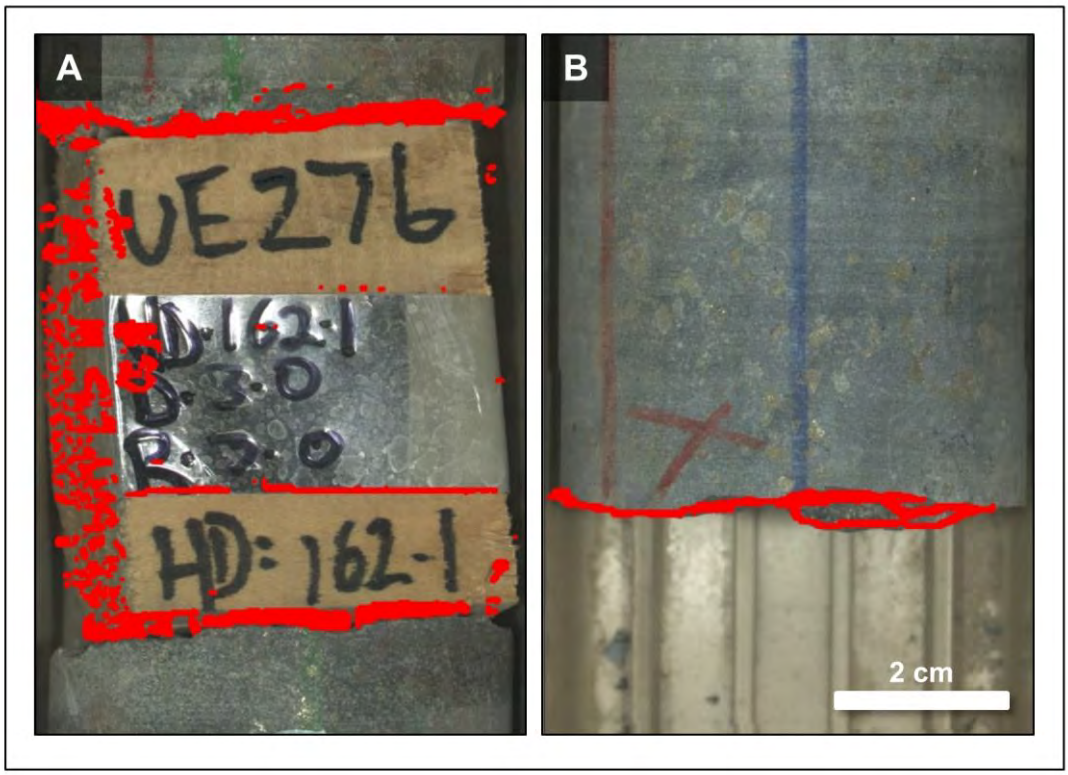

Figure 4.4. *An example of core block edges (A) and mechanical breaks (B) falsely identified as fractures.*

Figure 4.5. *An example of a mechanical break at the end of a drill core tray where the driller's mark has rotated out of the field of view (driller's mark on bottom of drill core).*

Table 4.4. *Summary of false fracture recognition for each fracture recognition protocol.*

	Slope and Aspect Recognition Protocol	**Hillshade Recognition Protocol**	**Combined Recognition Protocol**
Total # Non-fractures detected	144	180	240
# Fractures manually excluded by criteria	113	156	178
# Fractures falsely identified (false positives)	31	25	62

When evaluating the application of automated protocols for large datasets, analysis time is a key consideration. Since the complexity of each detection protocol varies, the analysis time for each detection protocol is also variable. It is also important to consider that the fracture detection protocols were constructed using ArcGIS software, and the exact analysis time per metre will depend on the

coding of the individual protocols. While exact times may vary, the overall analysis time in ArcGIS should be proportional between the protocols. Table 4.5 outlines the proportion of analysis time for each fracture recognition protocol relative to the slope and aspect recognition protocol (fastest analysis time of all the recognition protocols).

Table 4.5. *Proportion of analysis time by recognition protocol in ArcGIS relative to the slope and aspect recognition protocol (fastest analysis time of all the recognition protocols).*

Recognition Protocol	Proportion Analysis Time Relative to Fastest
Slope and Aspect	1.00
Hillshade	1.45
Combined	1.86

4.4 Assessment of fracture orientation protocols

It should be noted that only those fractures that were detected by each recognition protocol had orientations calculated. As a result, each recognition protocol only reports those orientations that were recognised.

To determine the difference in angle between the measured and calculated fracture orientations, vector geometry is used. As shown in Figure 4.6, the angle between two, 3D fracture planes is calculated by the dot product of two unit vectors representing the orientation of those planes (Groshong, 2006; Thomas, 1960). The cumulative results of the angle between the measured and calculated orientations of the test dataset are shown graphically in Figure 4.7. A complete table of the measured orientation of fractures, calculated orientation and the dot product difference between the two measurements is given in Appendix I.

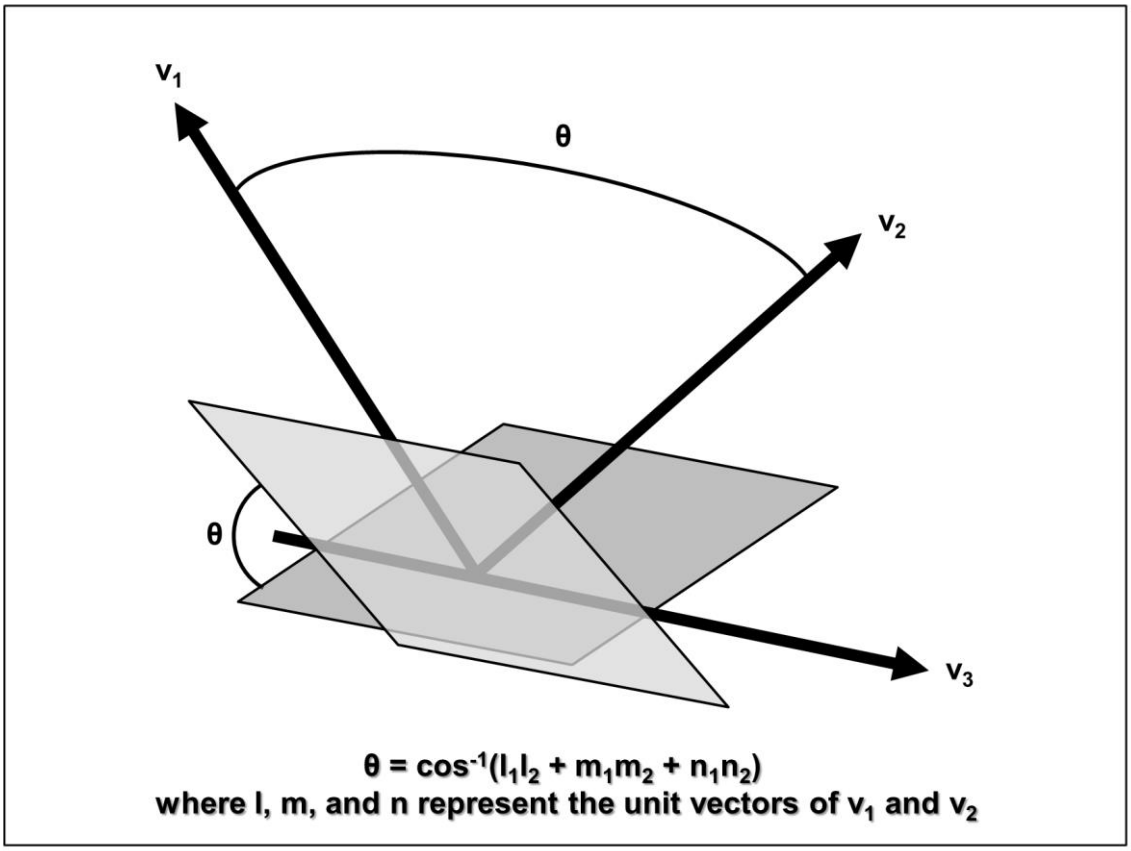

Figure 4.6. *Visualisation of the dot product where the darker plane is perpendicular to v1, and the lighter plane is perpendicular to v2. θ is the angle between v1 and v2, as well as the angle between the two planes. Figure modified from Groshong (2006).*

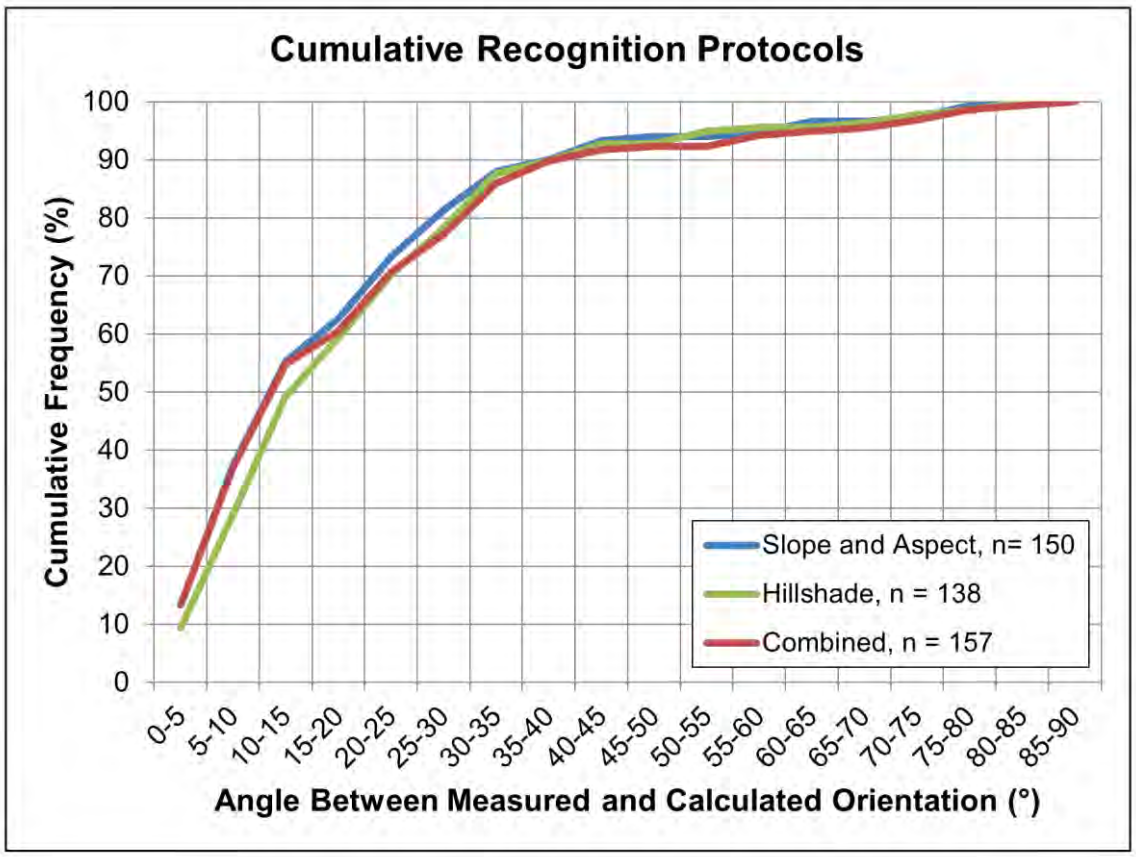

Figure 4.7. *Frequency distribution of the angle between the measured orientation values and the calculated orientation values, by recognition protocol, for the test dataset fractures.*

The highest acceptable error between the calculated and measured orientations should be 25° (Vearncombe, 2013). For all three protocols, over 70% of the calculated orientation values are within the expected maximum difference of 25°. While each fracture recognition protocol shows a general agreement between the measured and calculated orientation values, the difference varies depending on the individual fracture identification protocol. Each fracture recognition protocol will be assessed separately for orientation performance.

The slope and aspect recognition protocol uses a combination of the maximum slope relative to the surrounding pixels and the general facing direction to identify discontinuities in the surface of the drill core. This recognition protocol produced 119 calculated orientations of the 150 recognised fractures (or 79%) that were within 25° of the measured orientation value (Figure 4.8).

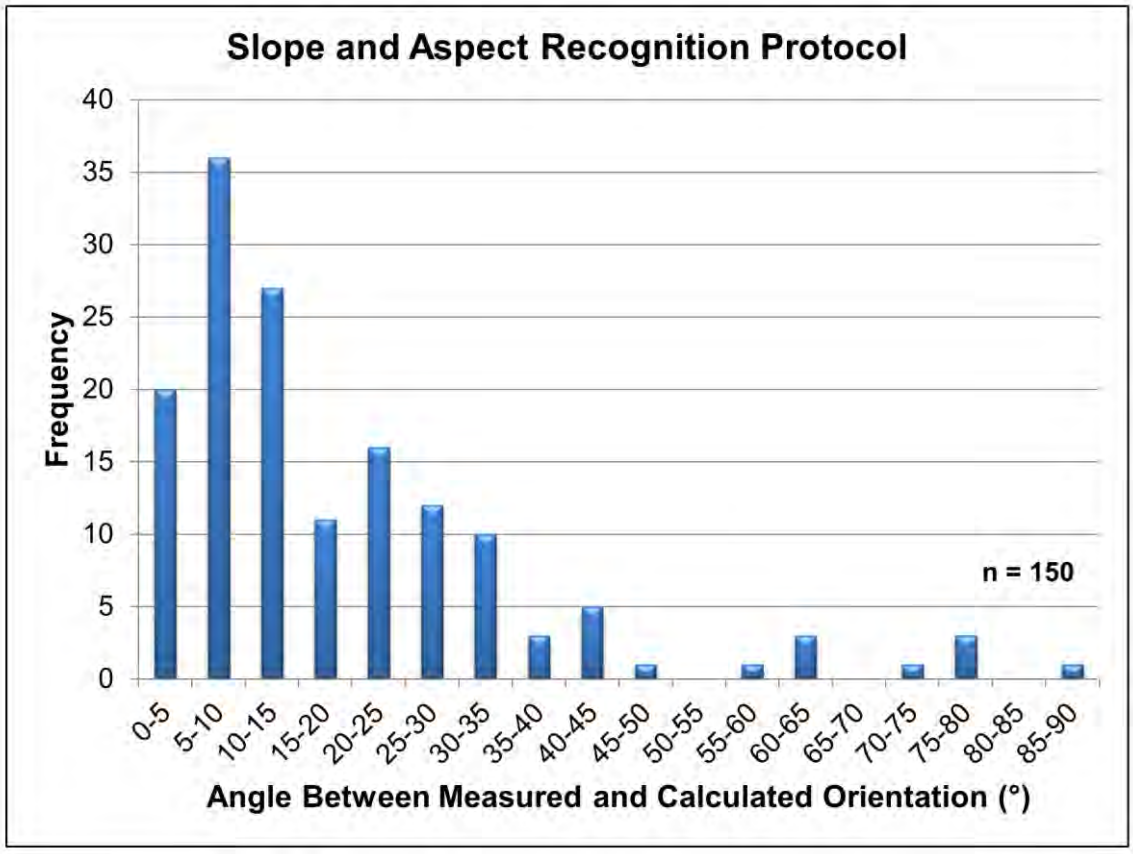

Figure 4.8. *Distribution of the angle between the measured and the calculated orientation values as calculated from pixels selected by the slope and aspect fracture recognition protocol for detected test dataset fractures.*

Using the expected light intensity values produced when the surface of the drill core is illuminated by a theoretical light source, the hillshade recognition protocol is designed to highlight discontinuities in the surface of the drill core. Of the 138 recognised fractures, 113 calculated orientations (or 82%) were within 25° of the measured orientation value (Figure 4.9).

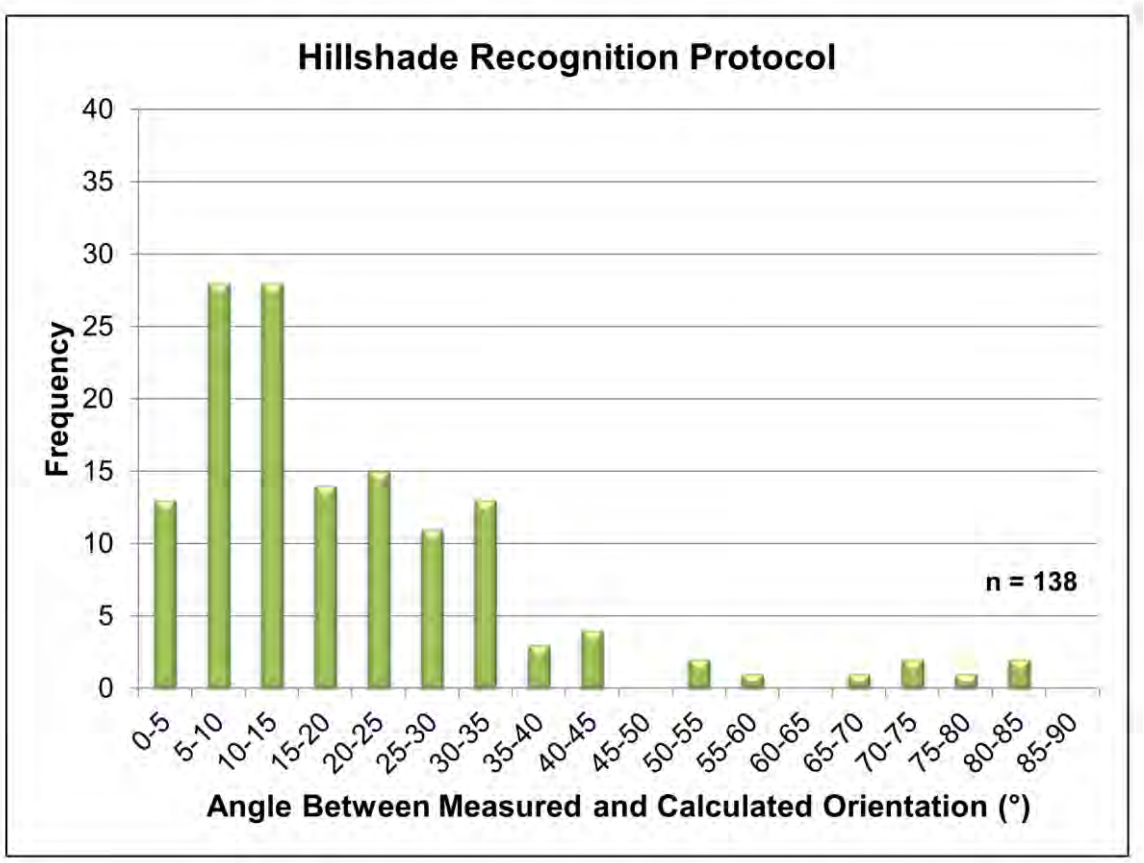

Figure 4.9. *Distribution of the angle between the measured and the calculated orientation values as calculated from pixels selected by the hillshade fracture recognition protocol for detected test dataset fractures.*

By combining the fracture pixels identified by all four of the other recognition protocols, the combined protocol was designed to provide an increased number of identified fracture pixels. The angle between the calculated and measured orientation values for the fracture pixels selected using this fracture recognition protocol are plotted in the histogram shown in Figure 4.10. One hundred and eighteen of the 157 recognised fracture orientations (or 75%) were within 25° of the measured orientation value.

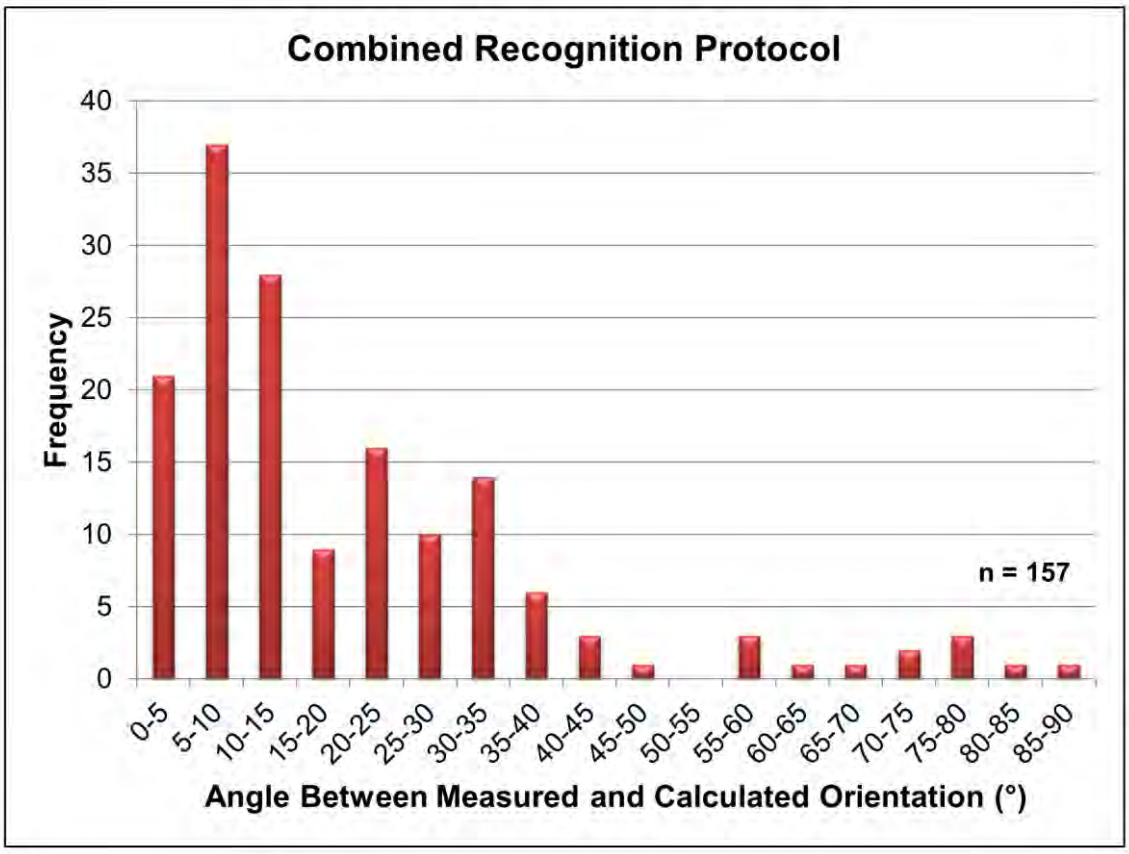

Figure 4.10. *Distribution of the angle between the measured and the calculated orientation values as calculated from pixels selected by the combined fracture recognition protocol for detected test dataset fractures.*

4.5 Assessment of fracture roughness protocols

The 3D roughness calculation protocols outlined in section 3.6 were assessed by comparing the calculated values to a visual inspection of the fractures from the Corescan RGB photographs. While roughness values for all identified fractures were calculated, a subset consisting of approximately 10% of the total test dataset was used to compare the calculated roughness to a visual estimate of the roughness from the RGB photograph. The test dataset has limited down hole extent and only dominant roughness values for a given logging interval are recorded by the Cadia geotechnical team. The test dataset intervals have JRC values ranging from 2.5 to 14. The assignment of roughness values visually can be highly subjective. In practice, an error of ± 2 JRC values outside of the range assigned would be reasonable. A photograph of each fracture in the subset annotated with the estimated roughness and a reference roughness profile for visual comparison is shown in Figure 4.11.

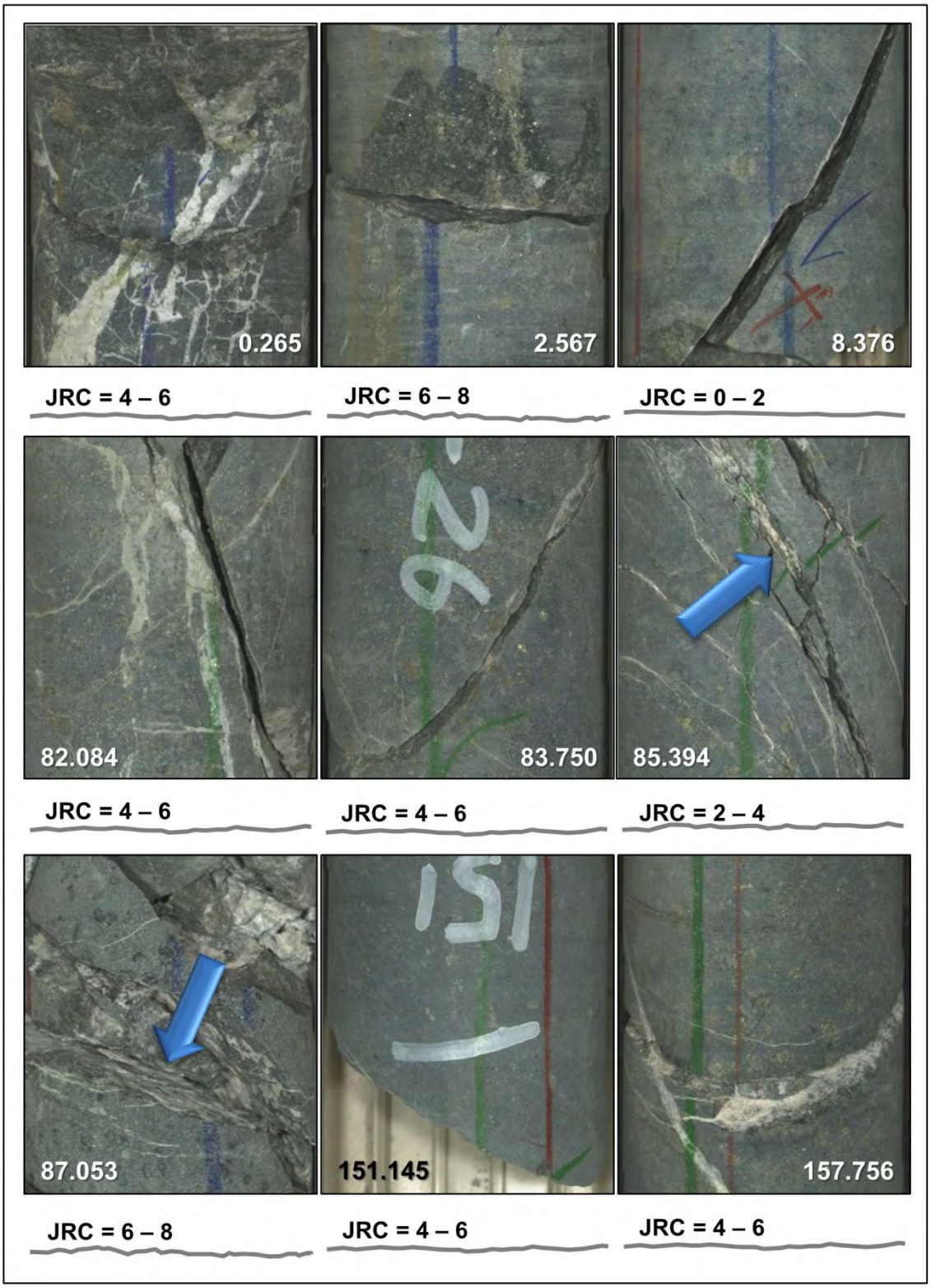

Figure 4.11. *Photographs of each fracture in the test subset with the corresponding visual roughness estimate below. The numbers on each fracture image represent the downhole meterage of the fracture.*

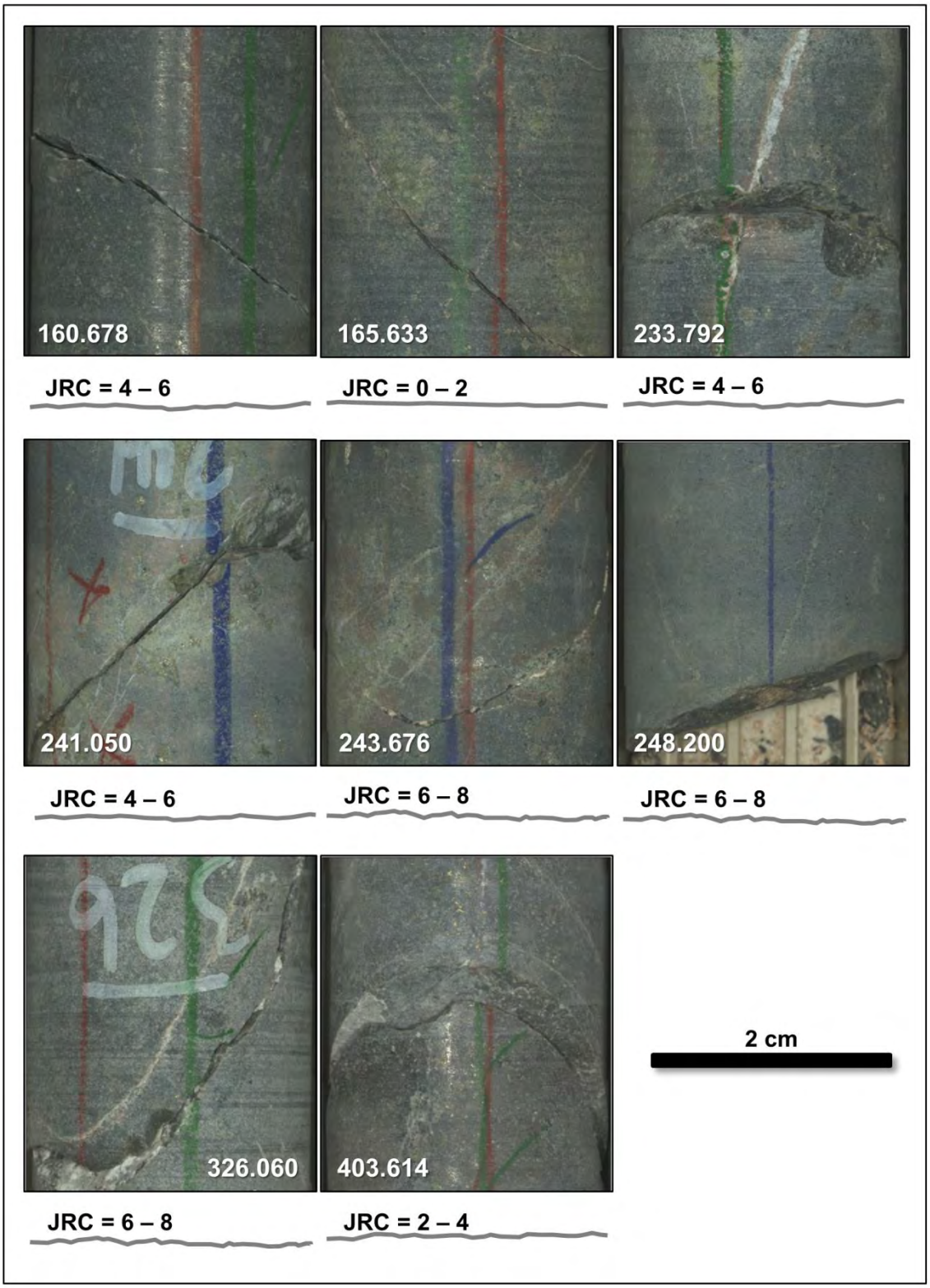

Figure 4.11 (cont.).

An assessment of the 3D roughness protocols was completed by comparing calculated roughness values of the test subset to the visual estimates from photos and the values expected for the Cadia East rock types in the test interval. Table 4.6 summarises the results of these comparisons.

Table 4.6. *Comparison of expected site roughness values and roughness estimated from photographs to the calculated 3D roughness for each recognition protocol for the roughness fracture subset.*

Meterage	Cadia East JRC Range	Visual Roughness Estimate	Slope & Aspect Calculated JRC_{3D}	Hillshade Calculated JRC_{3D}	Combined Calculated JRC_{3D}
0.265	2.5 -14	4 – 6	5.4	4.8	5.5
2.567	2.5 -14	6 – 8	5.2	4.5	5.1
8.376	2.5 -14	0 – 2	9.2	7.9	9.1
82.069	2.5 -14	4 – 6	12.6	11.3	12
83.749	2.5 -14	4 – 6	7.1	7.2	7.2
85.392	2.5 -14	6 – 8	10.4	9.8	9.9
87.051	2.5 -14	2 – 4	8	7	7.9
151.145	2.5 -14	4 – 6	4.5	4.6	4.6
157.756	2.5 -14	4 – 6	5.9	6.6	6.4
160.678	2.5 -14	4 – 6	7.6	6.6	7.3
165.633	2.5 -14	0 – 2	7.5	6.9	7.7
233.792	2.5 -14	4 – 6	5.6	5.3	28.1
241.05	2.5 -14	4 – 6	8.5	6.9	8.3
243.676	2.5 -14	6 – 8	10.1	9.6	9.8
248.2	2.5 -14	6 – 8	3.9	3.8	3.9
326.06	2.5 -14	6 – 8	8.4	7.7	8.4
403.614	2.5 -14	2 – 4	7.4	7.5	8.3

For the test subset of fractures, the slope and aspect and hillshade recognition protocols produced roughness values that are all within the expected Cadia East site values (between 2.5 and 14). The combined protocol returned 88% of the test subset roughness values within the expected values. Compared to the visual estimates of the test subset, the slope and aspect and hillshade recognition protocols produce reasonable JRC values. For the slope and aspect protocol, 47% of the roughness values are ± 2 JRC values of the visual estimate, while the hillshade protocol produces 65% roughness values within 2 JRC of the estimated value.

A complete table of the calculated 3D roughness for each fracture identified by the slope and aspect, hillshade, and combined recognition is given in Appendix J.

For all of the fractures identified by the slope and aspect protocol, 146 (or 97%) of the roughness values were within the expected site values. The hillshade protocol calculated 136 (or 99%) and the combined protocol calculated 129 (or 82%) JRC values between 2.5 and 14. In general, the 3D roughness calculations produce reasonable JRC results within the range expected for Cadia East.

4.6 Assessment of fracture set protocols

The number of fracture sets present in a given interval of drill core is dependent on the calculated orientation of the fractures in that interval. It is expected that fracture recognition protocols that performed well for fracture orientations would also perform well in calculating the number of fracture sets. All of the test dataset fractures occur within the FRV and the CIC units. Fractures in the FRV and the CIC are expected to have approximately 3.5 fracture sets, including three primary sets and one random set (Rossimel and Lett, 2012). The number of fractures present in a given interval needs to be sufficient to show a representative number of orientations. The measured fracture orientations are compared to the calculated fracture orientations of the FRV and the CIC. For the fractures detected by the slope and aspect, hillshade, and combined fracture recognition protocols, contoured polar plots are shown in Figures 4.12 through 4.14.

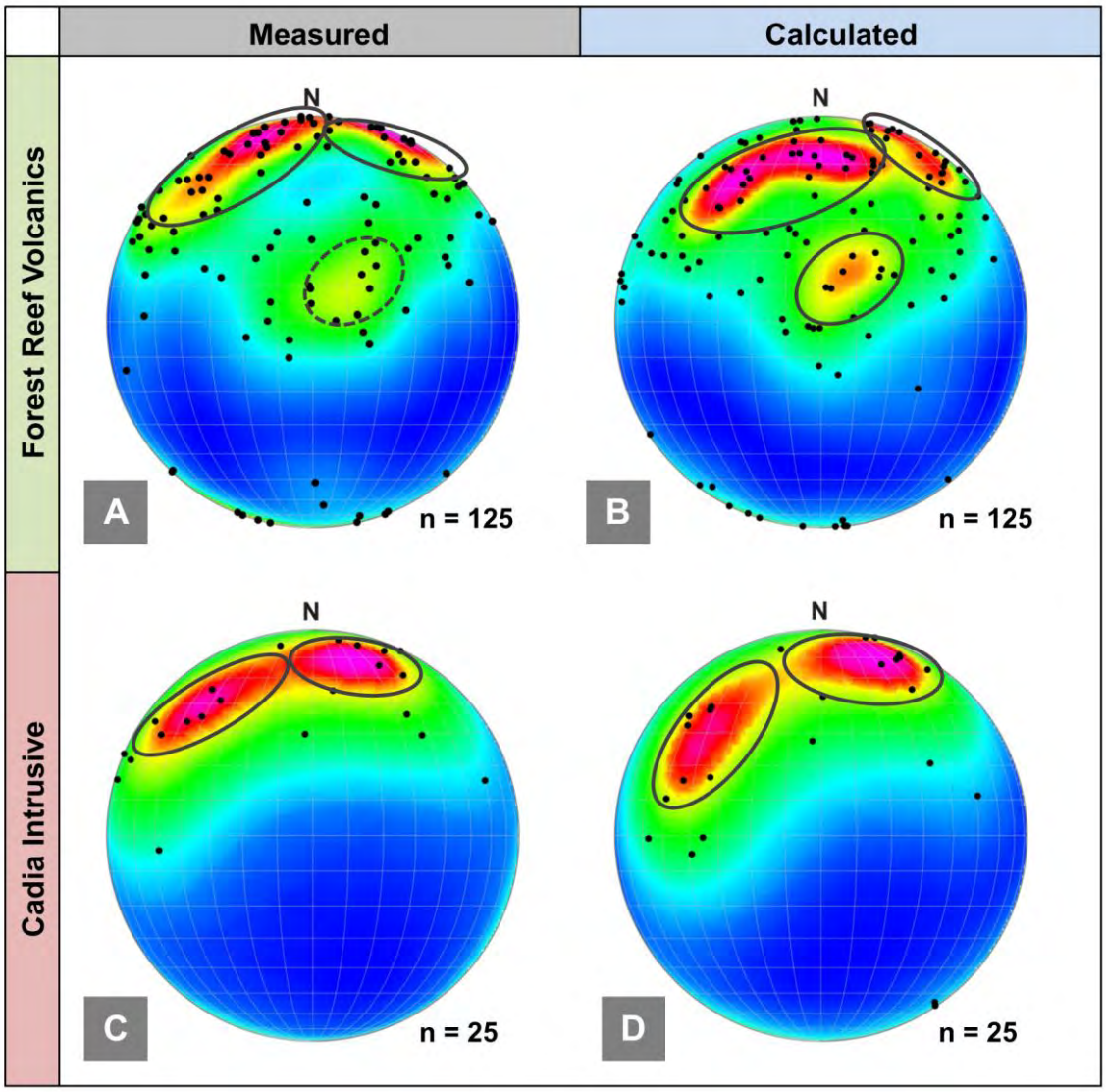

Figure 4.12. *Heat map showing the distribution of poles to fracture surfaces on a lower hemisphere equal area stereographic projection using the orientations derived from the slope and aspect fracture recognition protocols. Measured (A) and calculated (B) fracture orientations for fractures in the FRV, and measured (C) and calculated fracture orientations (D) for detected fractures in the CIC. Solid grey ellipses indicate a fracture set. Dashed ellipses represent a possible fracture set. FRV: measured = 2 plus a possible third, calculated = 3. CIC: measured = 2, calculated = 2.*

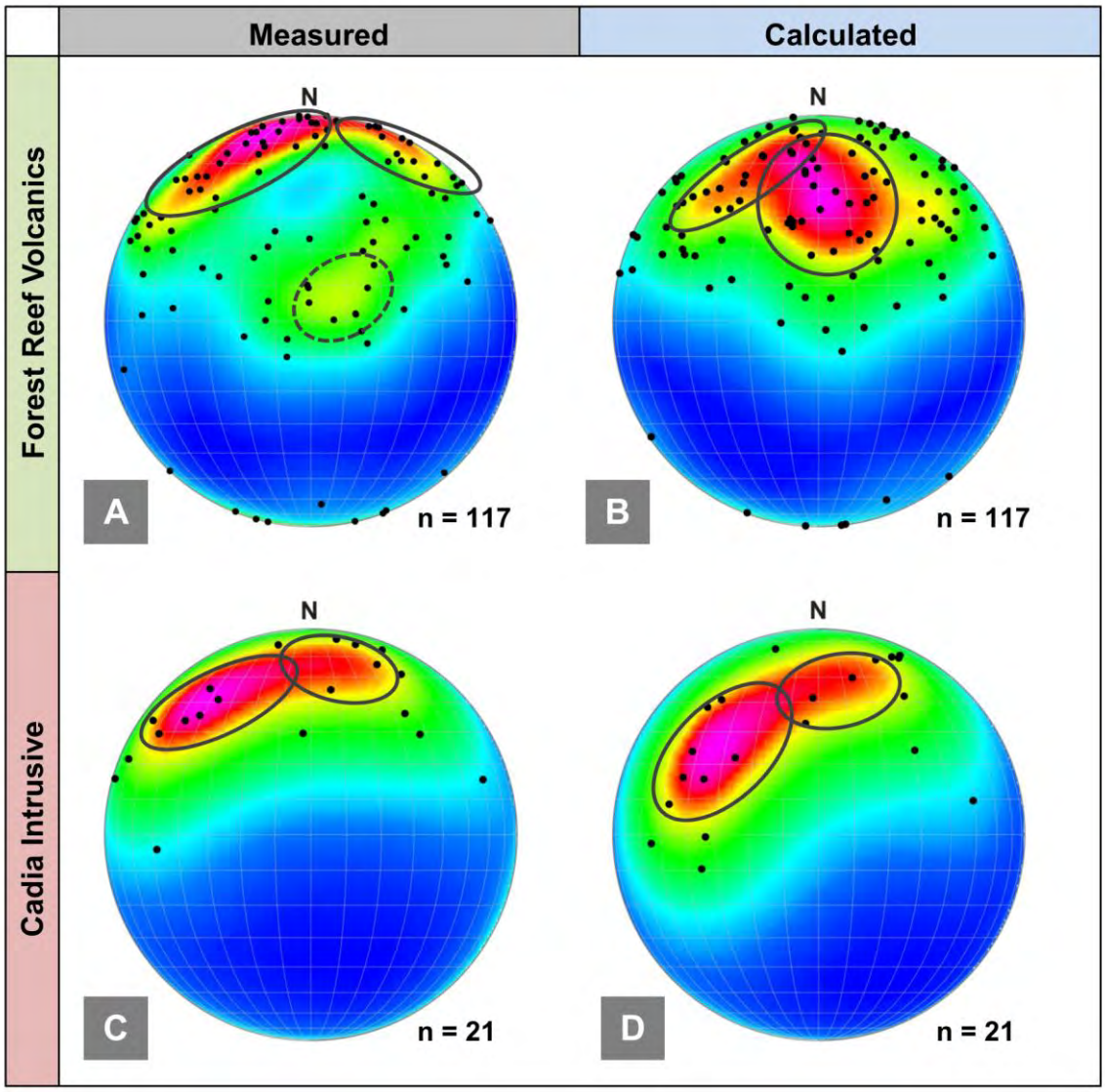

Figure 4.13. *Heat map showing the distribution of poles to fracture surfaces on a lower hemisphere equal area stereographic projection using the orientations derived from the hillshade fracture recognition protocols. Measured (A) and calculated (B) fracture orientations for fractures in the FRV, and measured (C) and calculated fracture orientations (D) for detected fractures in the CIC. Solid grey ellipses indicate a fracture set. Dashed ellipses represent a possible fracture set. FRV: measured = 2 plus a possible third, calculated = 2. CIC: measured = 2, calculated = 2.*

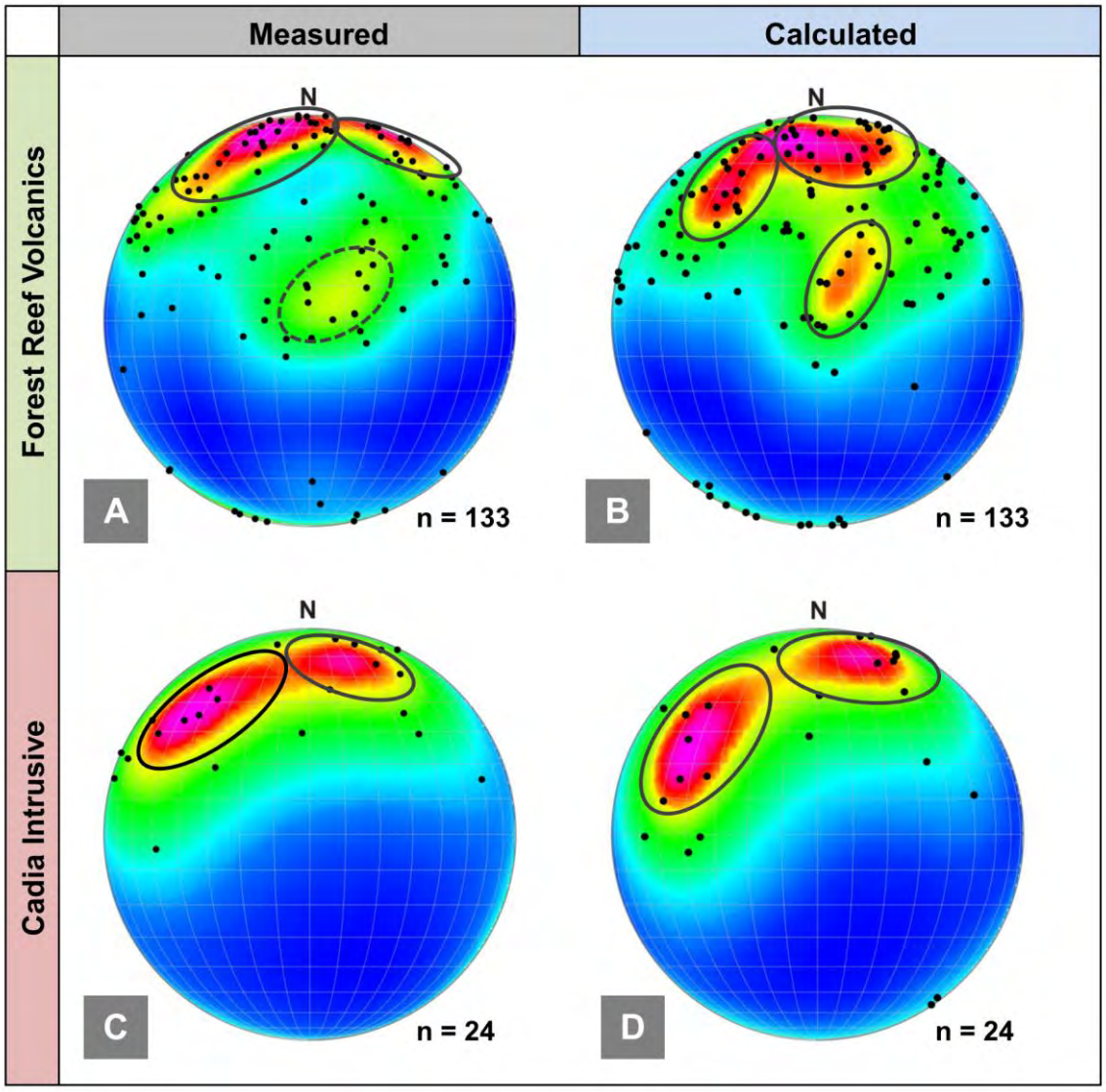

Figure 4.14. *Heat map showing the distribution of poles to fracture surfaces on a lower hemisphere equal area stereographic projection using the orientations derived from the combined fracture recognition protocols. Measured (A) and calculated (B) fracture orientations for fractures in the FRV, and measured (C) and calculated fracture orientations (D) for detected fractures in the CIC. Solid grey ellipses indicate a fracture set. Dashed ellipses represent a possible fracture set. FRV: measured = 2 plus a possible third, calculated = 3. CIC: measured = 2, calculated = 2.*

The measured orientations of the fractures recognised by the slope and aspect and combined protocols produced two fracture sets with a possible third for the FRV. The calculated orientations from these two protocols produced three fracture sets in the FRV, and the heat maps appear to be very similar between the measured and calculated orientations. For both the slope and aspect and combined protocols, the measured and calculated orientations produced two fracture sets in the CIC. The calculated orientation values for the slope and aspect and combined protocols produce a number of fracture sets equivalent to the

expected site value of three with an additional, random set expected for the FRV and CIC units (Rossimel and Lett, 2012).

The measured orientations of fractures recognised by the hillshade recognition protocol produced three with an additional, random set for the FRV and two fracture sets for the CIC. The calculated orientation values produced two fracture sets in both the FRV and the CIC. This value is lower than the expected site value of three with an additional, random set expected for the FRV and CIC units (Rossimel and Lett, 2012).

Since all three of the fracture recognition protocols tested here returned over 70% fracture orientations within 25° of the measured values, it follows that the calculated orientations from the fracture recognition protocols would produce heat maps that correlate well with the measured heat maps. A visual comparison of these results shows that the measured and calculated orientations produce similar patterns when plotted on a stereographic projection. To adequately assess the number of fracture sets present, a large number of fracture orientations covering a large spatial extent are required. Despite the comparison dataset being limited in its spatial extent, these results show a similar pattern to the measured fracture orientations for the same dataset and return values close to the expect Cadia East site values.

4.7 Assessment of fracture spacing and RQD protocols

The number of fractures per metre can be easily measured by extracting the down hole distance between each fracture. As a proxy for the fracture spacing value required by the RMR calculation, the Cadia site geotechnical team uses the fracture frequency per metre (F/m) measure. Rossimel and Lett (2012) define the average F/m for FRV to be 2 to 6, and the CIC to be between 2 F/m and 4 F/m. Table 4.7 outlines the measured and calculated average F/m for the test dataset, by rock type. The results of the RQD calculations for each fracture recognition protocol, by rock type, are compared to the measured RQD% in Table 4.8. Rossimel and Lett (2012) report that the RQD for the FRV is variable throughout the deposit and is typically between 90% and 100% for the CIC.

Table 4.7. *Average fractures per metre for all detected fractures.*

Average F/m	Measured Fractures (n = 170 FRV, n = 29 CIC)	Slope and Aspect Recognition Protocol (n = 126 FRV, n = 25 CIC)	Hillshade Recognition Protocol (n = 117 FRV, n = 21 CIC)	Combined Recognition Protocol (n = 133 FRV, n = 24 CIC)
Forest Reef Volcanics (FRV)	2.4	1.9	1.8	2
Cadia Intrusive (CIC)	5.7	4.9	4.1	4.7
Average for All Trays	*2.6*	*2.1*	*2*	*2.2*

Table 4.8. *Average RQD% for all detected fractures.*

Average RQD%	Measured Fractures	Slope and Aspect Recognition Protocol	Hillshade Recognition Protocol	Combined Recognition Protocol
Forest Reef Volcanics (FRV)	97%	98%	99%	97%
Cadia Intrusive (CIC)	86%	90%	93%	90%
Average for All Trays	*95%*	*98%*	*98%*	*96%*

Since this workflow relies heavily on the success of the fracture detection methodology, the performance of the fracture spacing calculations should be directly proportional to the fracture detection results outlined in section 4.3. All three fracture recognition protocols produced F/m values between the expected values of 2 and 6 for the CIC. The combined recognition protocol calculated 2 F/m for the FRV. This value is within the range expected by the Cadia East site team. The slope and aspect and hillshade recognition protocols slightly underestimated the F/m for the FRV. Given that the F/m is a measure of the average trend over an interval of drill core and the test data set covers less than 80 metres, this underestimation seems reasonable. In general, the calculated F/m values are systematically lower than the measured values, but follow the same general trends. The calculated RQD% values are consistent with the expected site values and correspond well with the measured RQD values.

4.8 Discussion

The goal of assessing the morphological geotechnical calculation protocols was to show that key geotechnical index parameters could be estimated from Corescan laser profiler data and a series of specifically-designed protocols with a precision similar to manual logging methods. These include calculation protocols for fracture detection, orientation, roughness, fracture sets and fracture spacing. To assess the performance of each of the geotechnical index calculation protocols, the calculated values were compared to either measured, observed or expected values for those parameters. A summary of the overall performance of the three successful fracture recognition protocols for the geotechnical index parameters is outlined in Table 4.9. Overall, the slope and aspect recognition protocol is the top performing fracture recognition protocol for the five geotechnical index parameter calculations.

Table 4.9. *Summary of the fracture recognition protocol performance for each of the calculated geotechnical index parameters.*

Index Parameter	Expected Value	Slope and Aspect Recognition Protocol	Hillshade Recognition Protocol	Combined Recognition Protocol
Fracture Recognition	*199*	150	138	157
% Fractures Recognised	*100%*	75%	69%	79%
# Fractures falsely identified	*0*	31	25	62
Fracture Orientation (within 25° measured)	*> 75%*	79%	82%	75%
3D Fracture Roughness	*JRC = 2.5 to 14 (100% within range)*	97%	99%	82%
Fracture Sets (FRV*)	*3.5*	3	2	3
Fracture Sets (CIC*)	*3.5*	2	2	2
Fracture Spacing (average Fracs/m, FRV*)	*2 to 4*	1.8	1.7	1.9
Fracture Spacing (average Fracs/m, CIC^)	*2 to 6*	4.9	4.1	4.7
RQD% (average, FRV*)	*97% (measured)*	98%	99%	97%
RQD% (average, CIC^)	*86% (measured)*	90%	93%	90%

**Forest Reef Volcanics*

^Cadia Intrusive Complex

The results from the fracture recognition protocols show that an automated fracture recognition protocol is possible. The slope and aspect and combined recognition protocols produced high fracture detection rates of 75% and 79%, respectively, but the combined protocol also identified many false positives. The combined recognition protocol produced the highest fracture detection rate of 79% but also had a high rate of false fracture identification. Overall, the best fracture recognition protocol was the slope and aspect. This demonstrates that detecting fractures from Corescan laser profiler data is possible.

The calculated orientations from the slope and aspect, hillshade, and combined recognition protocols showed good agreement with the measured orientation values. Over 75% of the detected fractures produced calculated orientations within 25° of the measured value. The hillshade recognition protocol provides the best calculated orientations with 82% of the 138 calculated fracture orientations within 25° of the measured orientations. The results from the assessment of the fracture orientation protocols clearly show that the orientation of fractures from fracture pixels selected by the proposed recognition protocols is possible.

In general, the 3D roughness protocols produce reasonable roughness values that are within 2 JRC values of the visual estimate for the test subset. When all of the recognised fractures for each recognition protocol are considered, the slope and aspect and hillshade protocols produce more than 90% roughness values within the expected range for Cadia East. The 3D roughness protocols used in this study are laborious and unlikely to be programmed into the Corescan system, although alternative roughness calculations based on the same principles should be investigated as the protocols are up scaled. Overall, the challenge with roughness calculations is that the Corescan system images very little, if any of the surface of the fracture, particularly where the fracture is tight. Despite this challenge, the results of this study demonstrate the potential to use Corescan laser data in calculating fracture roughness values.

Calculating the number of fracture sets relies entirely on calculating the correct fracture orientation values. Since all three recognition protocols produced over 70% of the recognised fractures within 25° of the measured orientation values, the calculated number of fracture sets were reasonable. The slope and aspect and combined protocols slightly underestimated the number of fracture sets for the Forest Reef Volcanics, and produced values below the expected range for the Cadia Intrusive. The hillshade recognition protocol calculated two fracture sets

for both units, underestimating the expected site value by 1.5. Determining the number of fracture sets from a polar plot requires a large number of orientation values. Given the small size of the test dataset, the minor underestimation of the number of fracture sets is reasonable. Overall, the slope and aspect and combined recognition protocols produced the best calculated number of fracture sets. These results show the potential to use Corescan data to determine the number of fracture sets. Section 5.12 of this thesis discusses a more robust method for determining the number of fracture sets using a number of fracture parameters including orientation and fracture mineralogy.

To accurately determine a fracture spacing value, fractures must be correctly recognised. Since the slope and aspect, hillshade, and combined protocols did not identify 20% of the fractures present, the fact that these protocols underestimated the average F/m values for the FRV is anticipated. These protocols did, however, identify fracture spacing within the expected range for the CIC unit. With a larger dataset, it is likely that the Corescan laser profiler data can be used to determine the fracture spacing.

RQD is a current output from the Corescan laser profile data, but does not discriminate between natural discontinuities (fractures) and mechanically induced breaks from the drilling process. Including these mechanical breaks greatly decreases the RQD values and falsely degrades the overall RMR and Q-index values. The or RQD can be directly derived from the fracture spacing output. The protocols outlined here remove mechanical breaks, and produce RQD values very close to the measured values. The current RQD methods used in the Corescan post-processing routines could be greatly improved using the protocols outlined here.

Overall, the slope and aspect recognition protocol showed the most consistent performance for all the geotechnical index parameters tested here.

Comparing the calculated values for the fracture orientation, fracture roughness, number of fracture sets, RQD, and fracture spacing demonstrates the ability of the Corescan system to collect geotechnical data at a precision similar to current manual methods. The Corescan system offers the opportunity to collect consistent geotechnical fracture information over a large volume of drill core. As discussed previously (chapter 2), only selected intervals of key drill holes at Cadia East are geotechnically logged. To demonstrate the increased data resolution opportunity provided by the Corescan system, the fracture index

parameters calculated from the slope and aspect recognition protocol used in this study are compared to the data collected manually on site over the same interval (Figure 4.15). The automated protocols developed in this study can be used to assess geotechnical indices of numerous fractures rapidly and consistently over the entire length of the drill core. The accuracy of these methods could be improved if a higher resolution laser scanning system was attached to the Corescan logging system.

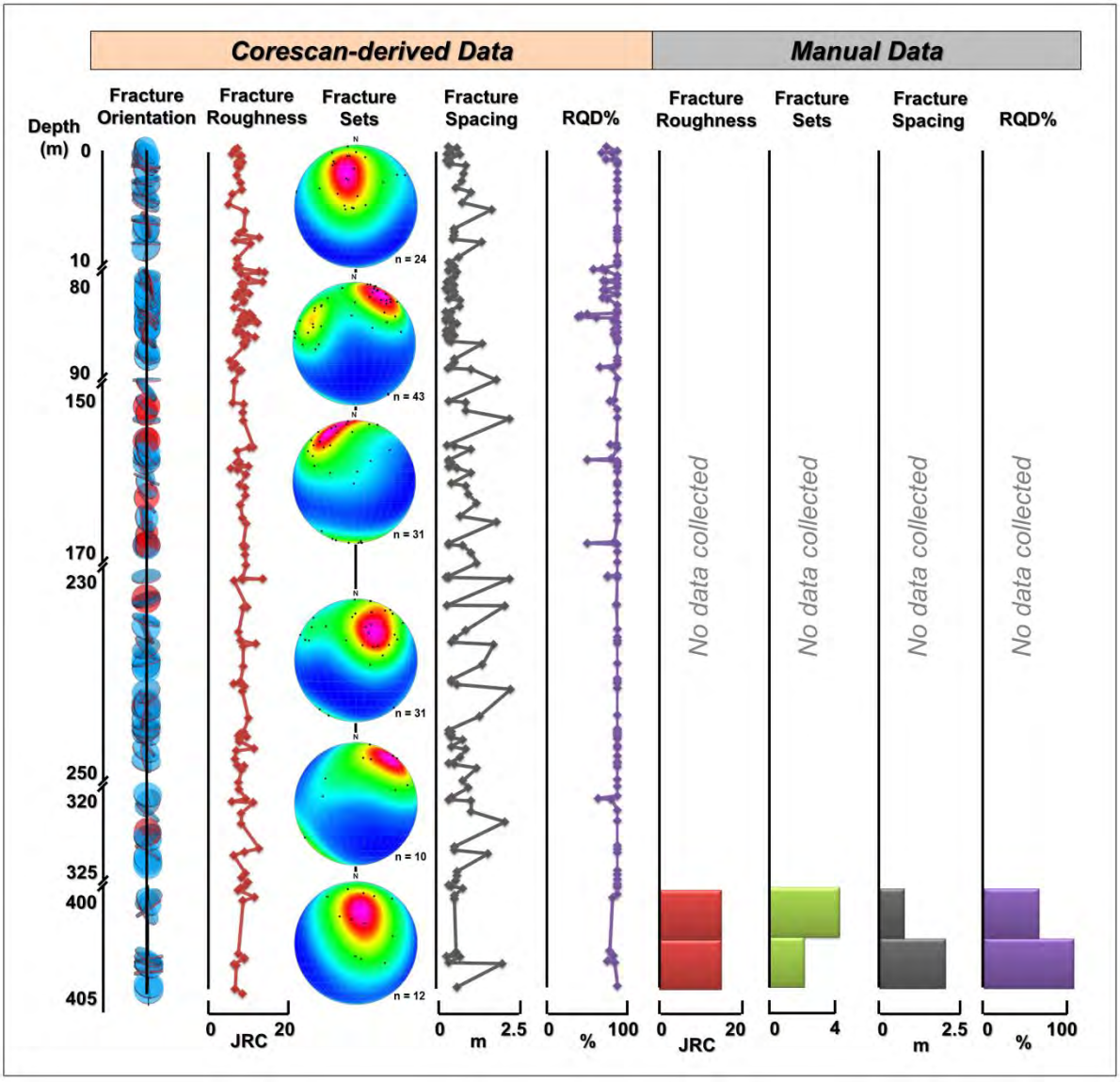

Figure 4.15. *Comparison of the morphological geotechnical parameters derived from Corescan data (orange) using the slope and aspect recognition protocol and the data collected manually on site (grey) over the same interval for the test fracture set (n = 150 fractures).*

A comparative study by Morelli (2015) evaluated the relative influence that each geotechnical index parameter used in the RMR and Q-index calculations has on the final calculated value. With respect to morphological parameters, this study determined that the RMR is most heavily influenced by the RQD and UCS values. The fracture spacing and roughness each contribute less than 10% to the overall variance of the RMR (Figure 4.16A). The RQD and fracture roughness contribute the most variance to the Q-index calculations, with the number of fracture sets contributing less than 10% to the overall variance (Figure 4.16B). The RQD, fracture roughness, spacing, and number of fractures sets are assessable by Corescan, but UCS will need to be measured outside of the Corescan system perhaps using a point load test (Momeni et al., 2015), Equotip survey (Verwaal and Mulder, 1993), sonic velocity (Chang et al., 2006) or measurement while drilling (Kalantari et al., 2018). The RQD protocols outlined here perform well and provide a more reasonable estimate of rock quality than the current RQD outputs from the Corescan system. The fracture roughness contributes the second largest variance in the final geotechnical index calculations and the 3D roughness protocol performs adequately overall. It is therefore expected that RMR and Q-index calculations derived from these protocols will provide reasonable values comparable to the current, manually derived values.

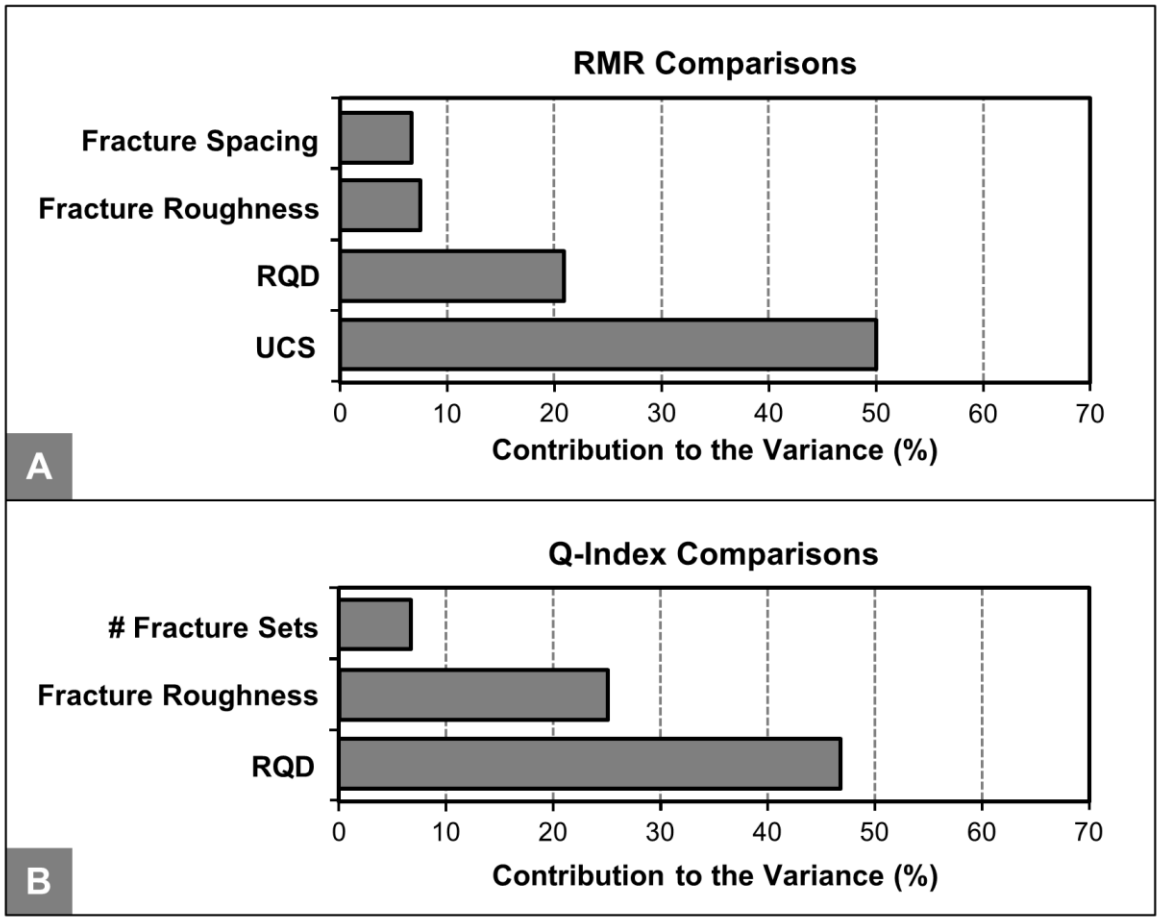

Figure 4.16. *Summary of the contribution of morphological geotechnical index parameters to the overall variance of the geotechnical index. A. contribution of fracture spacing, roughness, RQD, and Uniaxial Compression Strength (UCS) to the overall variance of the RMR. B contribution of fracture sets, roughness, and RQD geotechnical index parameters to the overall variance of the Q-index. Figure modified from Morelli (2015).*

The protocols proposed in this thesis could be up scaled and programmed to automatically calculate these key parameters from Corescan data. The determination of mineralogical geotechnical index parameters from Corescan data, such as fracture alteration and infill, will be addressed in Chapter 5. Other parameters such as UCS, groundwater conditions, and stress reduction factor (SRF) will need to be evaluated separately from the Corescan data.

One major challenge with fracture recognition is that the current Corescan procedure is to push the pieces of drill core together in the core tray so that gaps between the core pieces are minimised. Since the 3D laser outputs 200 μm pixels, and closed or tight fractures could have gaps of less than 200 μm, automatically recognising closed and tight fractures is challenging. To improve the detection rates, it is recommended that a small gap is left between core pieces before Corescan analysis. A gap would allow more of the surface of the fracture to be

imaged and improve the roughness calculations, but would artificially inflate the fracture aperture (discussed in detail in section 5.8). Additionally, decreasing the laser profiler pixel size would improve the performance of the fracture recognition protocols.

While the assessment presented in this chapter shows a general agreement between calculated and expected or measured values, the test dataset is limited and includes less than 80 metres of drill core, covering two rock types from one drill hole. Given these limitations, the trends presented here may not hold true when compared to a larger interval of drill core. It is recommended that these protocols be tested on a larger dataset before implementation into the Corescan data analysis and post-processing software.

4.9 Conclusions

The logistics, accessibility and time required to manually collect geotechnical data necessitate that not all drill holes are completely examined from top to bottom. Selected drill hole intervals are targeted to ensure that sufficient and representative data is available for input into the geotechnical model. Unfortunately, discrepancies in manual core logging techniques mean that not all data collected can be used in the geotechnical model. Inconsistencies in the data collected manually from drill core require that the underground geotechnical observations are weighted heavily in determining the RMR and Q-index values. While these observations are robust, it would be advantageous if geotechnical characteristics are assessed prior to underground development.

The continuous high-resolution down hole surface topography produced by the Corescan system provides an opportunity to capture a large volume of geotechnical data. The protocols proposed in chapter 3 produce results comparable to expected values, photographs of the fractures, or measured values (in the case of orientations). If these protocols were to be up scaled and incorporated into the Corescan data processing routines, morphological geotechnical parameters could be extracted from the laser profiler data. One advantage of the automated protocols developed in this study is the ability to collect high density data over the same interval. This increased data density is collected rapidly and consistently, increasing the underlying statistical support for rock mass characterisation.

Chapter 5

Methods and testing for mineralogical geotechnical assessment

5.1 Introduction

The geotechnical characteristics of the minerals present within and proximal to a fracture determine how that fracture will behave in the mining process. Fracture mineralogy data provides input into the construction of stress models, caveability models, ground support design, and fragmentation analysis. Current practice is to collect mineralogical geotechnical data from drill core by visual inspection and manual logging by a geologist or geotechnical engineer. This method is effective, but it is often laborious and has the potential to generate inconsistent results. Utilising automated core logging systems, such as Corescan, provides the opportunity to rapidly and consistently collect large volumes of mineralogical data from drill core. Data derived from Corescan's digital surface models (DSM) and mineralogical information can then be used to extract mineralogy and estimate the fracture condition parameters required by the RMR and Q-index systems.

A methodology that seeks to enhance and streamline the current manual data collection techniques using Corescan technology is presented in the sections that follow. The aim of this chapter is to discuss the use of automated core logging systems to extract fracture aperture, infill mineralogy, and weathering information to calculate fracture condition and alteration parameters as they relate to the RMR and Q-index geotechnical calculations. Additionally, by combining the fracture mineralogy information with the morphological fracture features, more robust calculations can be used to determine the number of fracture sets. Determining geotechnical properties of the minerals present in and around a fracture require the input of the mineralogical data collected by Corescan. The assessment of fracture condition using automated core logging technology provides an opportunity to capture rapid and consistent geotechnical data at a scale that is time-consuming to achieve via manual data collection. This approach has the potential to efficiently collect accurate information which can then be used in the Cadia East geotechnical model.

5.2 Mineralogical geotechnical analysis using Corescan

The Corescan system collects three high resolution data sets: 1) true colour core photography (50 μm pixel size), 2) DSM profiles (200 μm pixel size and 15 μm vertical resolution), and 3) visible near-infrared and short wave infrared (VNIR-SWIR) spectra (3.84 nm spectral resolution, 0.5 mm pixel size) (SGS, 2014). These datasets are co-registered, such that images of the core surface and mineralogy are spatially coincident (Figure 5.1).

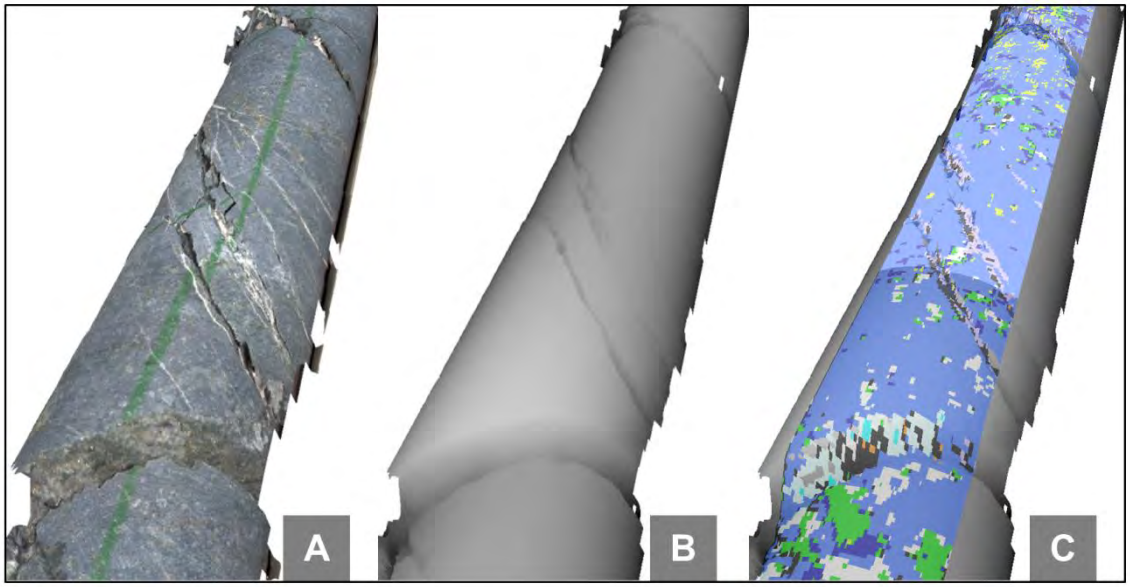

Figure 5.1. *Image showing Corescan outputs for 0.5 m of whole, uncut HQ core. The Corescan system simultaneously collects RGB imagery (A), a DSM image of surface topography (B), and mineralogical information (C). The mineralogical data (C) can be draped over the DSM to observe the relationship between the fractures and mineralogy. Modified from Harraden et al. (2017).*

The mineralogy reported for each pixel is represented by a spectral match value for each mineral based on how well the unknown spectrum matches the known library spectrum (detailed in section 2.7). The Corescan system measures reflectance properties of minerals in the VNIR-SWIR (450 nm to 2500 nm) wavelength range of the electromagnetic spectrum. Minerals that are not active in this range, or are low in reflectance, do not produce distinctive and unique VNIR-SWIR spectra. For example, minerals such as feldspar and sulphides do not give VNIR-SWIR spectra with identifiable and characteristic absorption features and, therefore, are challenging to detect using the VNIR-SWIR signal alone. In the Cadia East deposit, the mineralogy is dominated by feldspar minerals, therefore, it is likely that some pixels identified as *aspectral* represent feldspar. However, testing for the presence of feldspars associated with *aspectral*

pixel classifications has not been completed, hence no assumptions about the mineralogy of *aspectral* pixels are made and they are omitted from the fracture mineralogy estimations.

Pixels associated with a given fracture are identified by applying the fracture recognition methodologies outlined in section 3.4. Since the mineralogy, DSM, and RGB images are co-registered, fracture pixel locations can be queried against interpreted mineralogy. The spectral match values are used here for the mineralogical geotechnical analysis since these represent the relative proportion of each IR-active mineral reported in a spectrum.

In the RMR geotechnical system, fracture condition is calculated by assigning values for three mineralogy-related fracture parameters: 1) separation (aperture), 2) infilling, and, 3) weathering. Table 5.1 outlines the RMR fracture condition guidelines for these three parameters as established by Bieniawski (1989). The Q-index requires an input of the fracture alteration (J_a) value which is used to describe the mineralogy and weathering of a fracture. Table 5.2 outlines the J_a criteria defined by Barton et al. (1974).

Table 5.1. *Criteria for determining the fracture condition in the RMR system. Modified from Bieniawski (1989).*

RMR Fracture Condition Guidelines					
Separation (aperture)		Infilling (gouge)		Weathering	
Description	Rating	Description	Rating	Description	Rating
None	6	None	6	Unweathered	6
< 0.1 mm	5	Hard filling < 5 mm	4	Slightly weathered	5
0.1 - 1.0 mm	4	Hard filling > 5 mm	2	Moderately weathered	3
1 - 5 mm	1	Soft filling < 5 mm	2	Highly weathered	1
> 5 mm	0	Soft filling > 5 mm	0	Decomposed	0

Table 5.2. *Criteria for determining the fracture alteration values in the Q-index system. Modified from Barton et al. (1974).*

Q-index J_a Guidelines	
Rock wall contact	
Description	J_a value
Tightly healed, hard, high-friction, filling	0.75
Unaltered fracture walls, surface staining only	1
Slightly altered fracture walls, high-friction mineral coatings, clay-free disintegrated rock, etc.	2
Small clay-fraction (high-friction)	3
Low-friction clay mineral coatings	4

5.3 Geotechnical properties of Corescan minerals

Fracture geotechnical behaviour is strongly influenced by the properties of the minerals present. The mineralogy within and immediately surrounding fractures is particularly important since fractures represent planes of weakness. Any degradation of the integrity of the rock near this weakness due to the presence of soft, swelling, or low-friction minerals greatly affects the overall geotechnical properties of the rock mass (Pitts, 1985). Understanding properties, such as hardness, swelling potential, and friction potential, of minerals in and near fractures and the relative proportion of these minerals is vital to understanding the geotechnical properties of a rock mass. These properties are discussed in detail in section 2.5.

The Corescan system is capable of detecting minerals that are geotechnically significant with respect to their hardness, swelling potential, and friction potential properties (Table 5.3). Based on their geotechnical properties, the minerals detected by the Corescan system can be divided into three main groups: (1) hard, high-friction, non-swelling minerals (H); (2) soft, moderate- to low-friction, non-swelling minerals (S); and, (3) very soft, low-friction, swelling clays (V).

Table 5.3. *Geotechnical properties of minerals detected by the Corescan VNIR-SWIR system.*

Geotechnical Properties of Minerals Detected in Corescan					
Mineral Name	Mineral Abbreviation	Mohs Hardness	Swelling Potential	Low-friction Potential	Geotechnical Mineral Group
amphibole	amp	5 – 6			H
apophyllite	apo	4.5 – 5			H
epidote	epd	6 – 7			H
prehnite	pre	6 – 6.5			H
quartz	sil	7			H
tourmaline	tor	7 – 7.5			H
carbonate	car	4		X	S
clinochlore	clc	2 – 2.5		X	S
chlorite	chl	2 – 2.5		X	S
iron carbonate	fecar	3.5 – 4.5		X	S
iron oxide	feox	4.5 – 5.5		X	S
kaolinite	kao	2 – 2.5		X	S
phlogopite	phl	2 – 2.5		X	S
sericite	ser	2.5		X	S
dickite	dik	1.5 – 2		X	S
gypsum	gyp	2	X	X	V
laumontite	lau	3.5 – 4	X	X	V
montmorillonite	mon	1 – 2	X	X	V
nontronite	non	1.5 – 2	X	X	V
vermiculite	ver	1.5 – 2	X	X	V
H = hard, high-friction, non-swelling minerals					
S = soft, moderate- to low-friction, non-swelling minerals					
V = very soft, low-friction, swelling minerals					

The mineral groups summarised in Table 5.3 were created to simplify the protocols for defining RMR and Q-index parameter values. Some of the minerals identified by Corescan are not specific minerals, but rather mineral groups (in the case of amphibole) or field terms (in the case of sericite). In the case of laumontite, the site geotechnical team at Cadia East has observed that the zeolite mineral is very unstable and may degrade a fracture surface in the same way as a swelling mineral (Rossimel and Lett, 2012). For the purpose of geotechnical assessment at Cadia East, laumontite is considered to have high swelling potential. Given that the geotechnical properties of these mineral groups are similar, geotechnical index assignments should be robust. Details and descriptions of the minerals in each group and the reasoning behind the grouping are outlined in the following sections.

5.3.1 Geotechnical properties of group H minerals

Group H minerals include the amphibole group, apophyllite, epidote, prehenite, quartz, and tourmaline. These minerals are very hard, with Mohs hardness values greater than five. In addition, group H minerals have high internal cohesion (high friction potential) and cannot accommodate water (H_2O^-) in their crystal structure, thus, they have no swelling potential. These minerals are considered to be primary minerals and do not represent weathering as it relates to geotechnical index calculations. Group H minerals are geotechnically stable.

A number of minerals present in the Cadia East rocks that would otherwise be included in group H (including minerals of the feldspar group) are not detected by the Corescan VNIR-SWIR system. The fact that group H minerals generally give poor VNIR-SWIR spectra compared to minerals in groups S and V means that the Corescan data generally under reports the group H minerals.

5.3.2 Geotechnical properties of group S minerals

S group minerals include the carbonate group (not including iron carbonate), chlorite, dickite, iron carbonate, iron oxide, kaolinite, phlogopite, and sericite. The spectral signature of iron carbonate allows this mineral to be distinguished from other, non-iron bearing carbonate minerals, so they are reported as separate minerals by the Corescan system. S group minerals are soft, ranging from 2 to 5.5 on the Mohs hardness scale. Unlike mineral group H, group S minerals have moderate to low internal cohesion and are considered to have moderate- to low-friction potential. Iron carbonate and iron oxide have low swelling potential. The group S minerals dickite and kaolinite have the T-O structures and cannot accommodate water (H_2O^-). Chlorite, phlogopite, and sericite have T-O-T structures, but generally do not contain interlayer water, and, therefore, have little to no swelling potential.

5.3.3 Geotechnical properties of group V minerals

Minerals in group V are the most influential in the degradation of the condition of a rock mass. This group contains gypsum, laumontite, montmorillonite, nontronite, and vermiculite. With the exception of laumontite (hardness 3.5 – 4), this mineral group contains minerals with Mohs hardness values of less than three. In addition to being very soft, these minerals are capable of absorbing

water, giving them the potential to swell up to many times the original mineral volume. This property gives this mineral group a high swelling potential. V minerals are considered to be secondary and likely reflect the weathering or alteration of primary minerals. Group V mineral represent the most geotechnically unstable minerals of those detectable by Corescan.

5.4 Development of automated alteration methodology

Minerals present in and around the fractures can be determined by combining fracture locations extracted from the DSM data with hyperspectral mineralogical data. The mineralogy of each fracture is extracted by querying the mineralogy pixels coincident with the selected fracture pixels. The RMR and Q-index input parameters list specific mineral properties and, in the case of the Q-index, specific minerals in the classification schemes. The extent of weathering away from the fracture and fracture aperture are also required by the RMR system. To assess weathering effects beyond the extent of the fracture surface, the mineralogy as the distance from the fracture increases is also queried. The aperture of the fracture is calculated by measuring the apparent thickness from the fracture pixels, and then converting this apparent thickness to a true thickness based on the fracture orientation. Using the relative proportion of minerals from the VNIR-SWIR hyperspectral mineralogy and fracture aperture in combination with a series of experience-based, logical, ordered processing steps, the fracture condition and J_a values required in the RMR and Q-index calculations can be estimated by the following steps:

1) extract fracture mineralogy;
2) extract mineralogy adjacent to fracture (at 5 mm and 10 mm distances);
3) calculate relative mineral abundance;
4) calculate fracture aperture;
5) assign RMR infill values;
6) assign RMR weathering values; and,
7) assign Q-index J_a values.

The details of the methods in each step of the mineralogical geotechnical analysis are outlined in the following sections. To set up an automated protocol and expedite testing, each fracture mineralogy extraction protocol was developed within ArcGIS using ESRI spatial analysis tools within ModelBuilder. The

ModelBuilder files for extracting fracture mineralogy are included in Appendix K.

The goal of this study was to propose a workflow that could successfully extract mineralogical geotechnical index parameters, not to develop the computer code behind it. While some of the processing steps are completed manually, it is assumed that once the work flow is defined, these steps can be programmed into an automated process. As with the methods proposed in chapter 3, the specific computer programing aspects of the protocols, as well as the associated challenges, will not be addressed and this work is considered to be a proof of concept study only.

5.5 Extract fracture mineralogy

Extracting the mineralogy of each fracture requires querying the spectral match values for each identified fracture pixel. The ArcGIS tool S*patial Join* is used to query the mineralogy raster pixels nearest to each fracture pixel. The spectral match values are then appended to a table containing the mineralogical data for each fracture pixel (Figure 5.2).

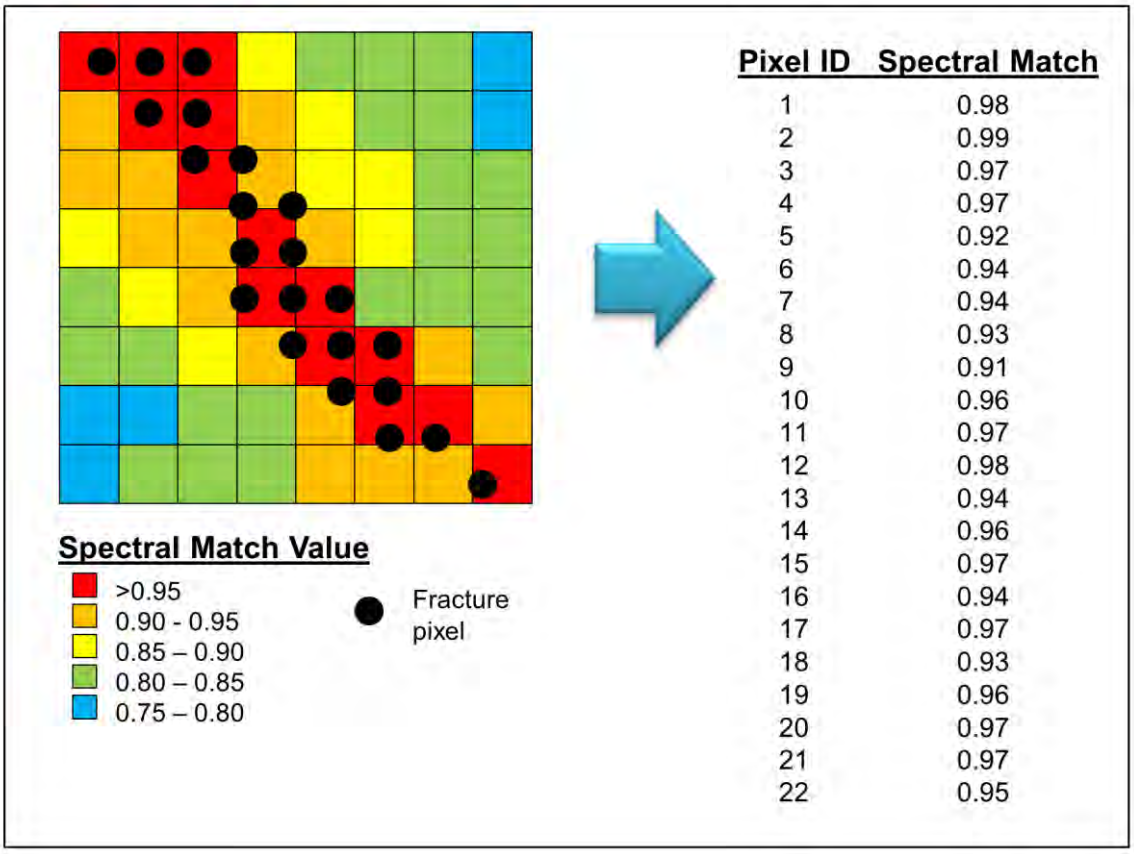

Figure 5.2. *Simplified example of calculating the spectral match values within a fracture (note, pixels not to scale). By extracting the spectral match value for a given mineral from the mineralogy pixel closest to each fracture pixel, a table of spectral match values can be exported.*

5.6 Extract mineralogy adjacent to fracture

Weathering can affect both fracture surfaces and the wall rock surrounding the fracture. The weathering characteristics of fracture minerals are estimated by evaluating changes in the abundance of minerals adjacent to the fracture surface. This change is monitored by comparing the proportion of mineral groups within the fracture to those within the 5 mm and 10 mm buffers. These buffer distances were selected because both the RMR and Q-index systems use 5 mm as a threshold for infill thickness, and this value was deemed to be geotechnically significant for fracture condition. The 5 mm buffer is meant to represent minerals immediately adjacent to the fracture surface while the 10 mm buffer represents more distal mineralogy. The fracture pixels are buffered using the *Buffer* tool to create 5 mm and 10 mm buffer polygons. The 5 mm buffer area contains both the fracture area and the 5 mm buffer area, while the 10 mm buffer consists of the fracture, 5 mm, and 10 mm buffer areas. The outlines of these polygons are then used to clip the mineralogy pixels to the extent of the buffer. The buffer mineralogy is then exported to a table containing the spectral match values for

each mineral within the area. The output is a table for each of the buffer distances containing the spectral match values for each mineral for every pixel intersected by the buffer region. The general process is shown visually in Figure 5.3. Figure 5.4 shows an example of a Corescan mineral map with buffers used to track weathering away from a fracture surface.

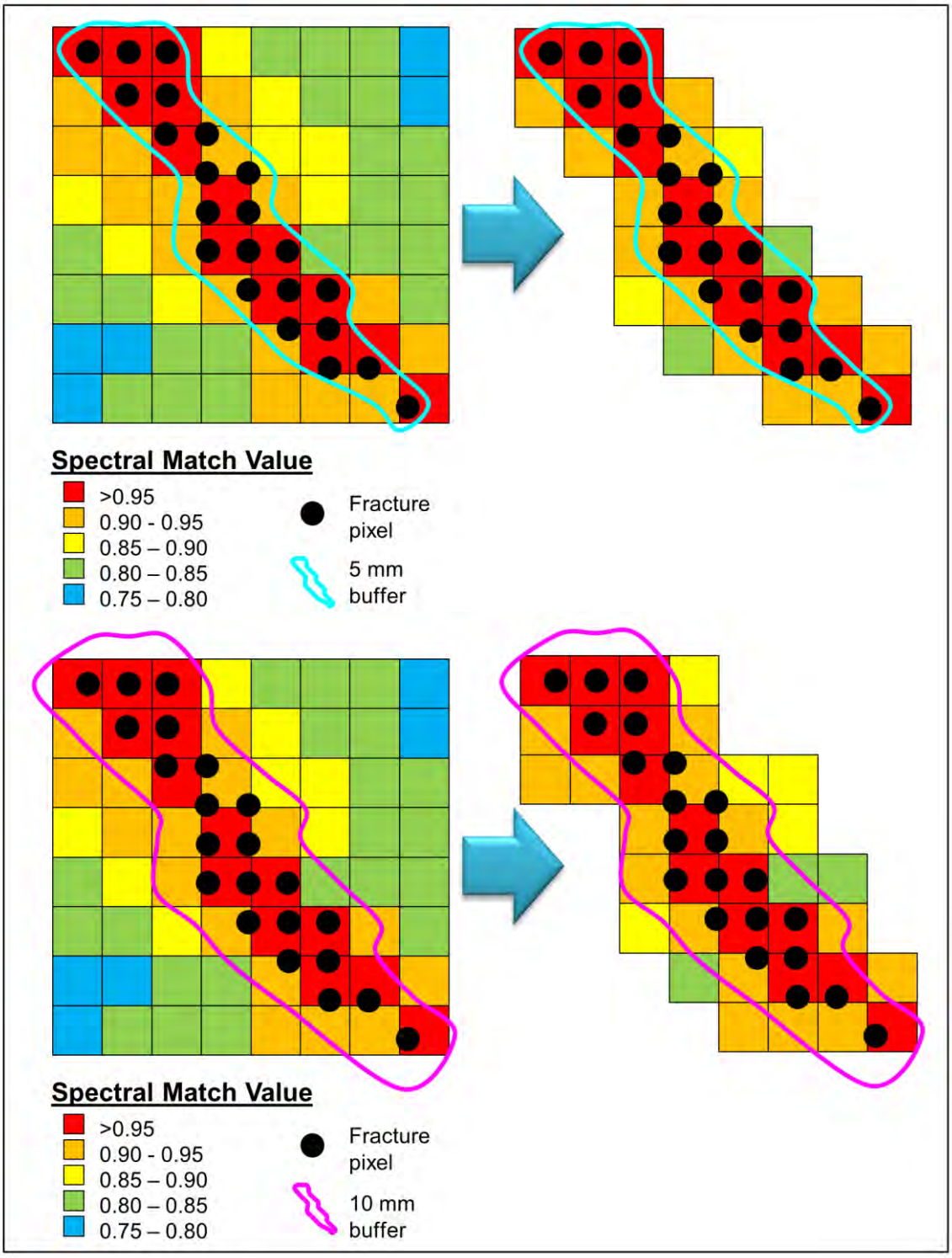

Figure 5.3. *Simplified example of extracting the spectral match values from the hyperspectral data within the 5 mm and 10 mm buffers away from the fracture (note, pixels not to scale). By clipping each mineralogy raster by the 5 mm and 10 mm buffers, the spectral match values for these areas can be extracted.*

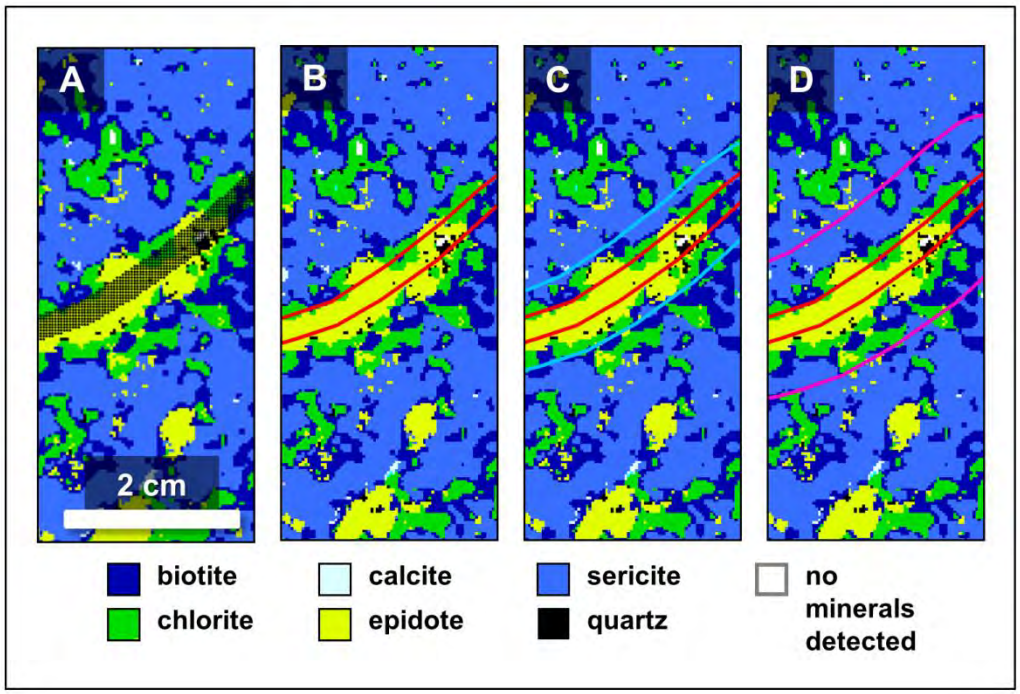

Figure 5.4. *The identified fracture pixels (A) are co-registered with the mineralogy. The mineralogy (as spectral match values) can be extracted for the fracture itself (B, red line), the 5 mm buffer (C, blue line) and the 10 mm buffer (D, pink line).*

5.7 Calculate relative mineral abundance

Calculating relative mineral abundance was achieved by first averaging the spectral match values for each mineral identified within the fracture and the 5 mm and 10 mm buffers. The average spectral match values within each mineral group were then summed. The summed group results were then normalised so that the sum of all minerals was 100%. This value was used as a relative proportion of minerals present for the three areas of interest: (1) within the fracture; (2) within 5 mm of the fracture; and, (3) within 10 mm of the fracture. For method testing, these processing steps were completed in Excel. Appendix L comprises an Excel workbook containing the relative mineral abundance calculations using the ArcGIS output tables.

Previous studies at Cadia East estimate that these rocks average approximately 60% group H minerals (primarily quartz and feldspar) (Berry et al., 2008; Bonnici, 2012). The Corescan system reports up to 10% quartz for the test interval, underestimating group H minerals by a factor of six. Since these minerals are not adequately accounted for in the Corescan data, the group H mineral result is multiplied by a factor of six. The other mineral group values were then re-normalised so that the sum of all mineral groups was 100%.

While the mineralogy from the three analysis areas (within the fracture and 5 mm and 10 mm buffers) can be reported as a metric for fracture mineralogy, these values can also be used to estimate the RMR infill, RMR weathering, and Q-index J_a values. A series of logical rules are used to assign geotechnical index parameter values to each fracture using the mineral proportion values extracted from the Corescan data.

5.8 Calculate fracture aperture

The apparent aperture of the fracture is calculated by multiplying the number of pixels across the fracture parallel to the long axis of the drill core (y-direction) by the DSM pixel size of 200 μm. In most cases, a fracture is intersected by the drill core at an oblique angle, so this approach calculates apparent aperture. To measure the true aperture, the orientation of the fracture is required. Using the orientation values derived from methods outlined in section 3.5, trigonometry can be used to calculate true aperture by:

$$t = L \cos \rho \qquad [5.1]$$

where,

t = true aperture,
L = apparent aperture
ϱ = angle between the pole to fracture plane and the drill hole
(Charlesworth and Kilby, 1981).

This method assumes the core has been pushed together as close as it will fit before the scanning starts. The protocol used at Cadia was to push core together, but the estimated aperture will have a bias to high values where this packing was not effective.

5.9 Assign RMR infill values

Determining the RMR infill value requires the fracture aperture and relative hardness of the infill minerals. The aperture value is assigned by comparing the estimated true fracture aperture (calculated in section 5.8) to the RMR aperture criteria (Table 5.1). Any fracture with a true aperture of less than 0.1 mm was assigned an RMR infill value of 6, regardless of the fracture mineralogy. Since any fracture pixels selected on such a tight fracture likely represent the

mineralogy of the surrounding wall rock, this assignment is reasonable. The mineral groups already account for the mineral hardness, so the criteria for assigning the remaining RMR infill values are based on the relative abundance of the group H minerals present in the fracture. Where group H minerals dominate (greater than 60%), the fracture is considered to contain hard infilling. Where a fracture contains less than 60% group H minerals, the fracture is considered to have soft infill. A series of logical rules that account for the infill aperture and hardness are then used to assign the RMR infill values (Table 5.4).

Table 5.4. *Decision criteria for the infill RMR parameter using Corescan mineralogical data.*

Decision Criteria for RMR Infill Value		
RMR Infill Value	Measured Aperture	Group H Proportion
6	0 mm	-
4	0 – 5 mm	> 60%
2	> 5 mm	> 60%
2	0 – 5 mm	< 60%
0	> 5 mm	< 60%

5.10 Assign RMR weathering values

Criteria for estimating the RMR weathering value were developed by comparing the abundance of mineral groups for the fracture and the 5 mm and 10 mm buffers. When group H exceeds 65%, primary (group H) minerals dominate and minimal weathering is present. Group H proportions between 50% and 65% represent a mixture of primary and weathering minerals (moderate weathering). The presence of less than 50% group H minerals indicates that a high proportion of weathering minerals are present. Fractures dominated by group H minerals (> 60%) are automatically assigned an RMR weathering value of 6, regardless of the mineralogy in the 5 mm and 10 mm buffers. An RMR weathering value of 0 is assigned where at least 50% geotechnically unstable weathering minerals (groups S and V) are present within the fracture and 5 mm and 10 mm buffers. An RMR weathering value between 5 and 1 is assigned by tracking the changes in the mineral group proportions away from the fracture and within the buffers. The criteria used to assign the RMR infill value is summarised in Table 5.5.

Table 5.5. *Decision criteria for the RMR weathering parameter using Corescan mineralogical data.*

Decision Criteria for RMR Weathering Parameter			
RMR Weathering Value	Within Fracture (group H)	5 mm Buffer (group H)	10 mm Buffer (group H)
6	> 65%	-	-
5	50% - 65%	> 50%	-
3	<50%	50% - 65%	> 50%
1	<50%	50% - 65%	50% - 65%
0	< 50%	< 50%	< 50%

For method testing, the rule sets used in assigning the RMR infill and weathering values were calculated in Excel. Appendix M includes an Excel workbook containing the RMR calculations from mineral proportions calculated for each fracture in the test set and the associated 5 mm and 10 mm buffer.

5.11 Assign Q-index J_a values

In order to calculate the J_a parameter, the Q-index requires a single value that accounts for fracture aperture, mineral hardness, friction potential, swelling potential, and weathering effects. For this parameter, only the mineralogy of the fracture itself is considered. By evaluating the abundance of less geotechnically stable groups (groups S and V) within the fracture, J_a can be estimated. Group S accounts for minerals with moderate- to high-friction and no swelling potential, while group V contains low-friction high-swelling potential minerals. Fractures with an aperture less than 0.1 mm were automatically assigned a J_a value of 0.75 regardless of the fracture mineralogy as it is likely that the mineralogy represents minerals in the rock itself, not those inside the fracture. Where soft, low-friction minerals are greater than 20%, these fractures are automatically assigned a value of 4.0 since these minerals greatly impact the geotechnical stability of the fracture. The remaining J_a values are assigned based on the criteria outlined in Table 5.6.

Table 5.6. *Decision criteria for the Q-index J_a parameter using Corescan mineralogical data.*

Decision Criteria for Q-index J_a Parameter			
Q-index J_a Value	Fracture Aperture (mm)	Within Fracture (group S)	Within Fracture (group V)
0.75	< 0.1	-	-
1	> 0.1	< 20%	< 10%
2	> 0.1	> 20%	< 10%
3	> 0.1	-	10 – 20%
4	> 0.1	-	> 20%

For method testing, the criteria used in assigning the Q-index J_a value were calculated in Excel. Appendix M includes an Excel workbook containing the Q-index calculations from the averaged mineral abundance calculated for each fracture.

5.12 Robust statistical determination of number of fracture sets

Determining the number of fractures sets using polar plots can be subjective, and depends on the distribution of the structural data. The orientation of the drill hole relative to the primary orientation can affect the determination of the number of fracture sets present (Berg, 2012). Robust, multi-dimensional statistical techniques by k-means clustering and principle component analysis (PCA) have been applied to determining the number of fracture sets using multiple fracture characteristics (such as orientation, thickness, and mineralogy) (Marcotte and Henry, 2002; Slob et al., 2005; Tokhmechi et al., 2011). The k-means clustering algorithm uses the values of numerous variables to separate the data into *k* number of groups. The expected number of clusters is defined by the user and the k-means algorithm randomly assigns, then adjusts the location of the cluster centre until the sum of the squared distances is minimised for the sample population (Marsland, 2015; Ripley, 2007; Witten et al., 2016). To test the ability of Corescan-derived data to determine the number of fracture sets using robust statistical methods, the k-means clustering tools in ioGAS were used. Corescan-derived fracture orientation, fracture roughness, and RMR infill, RMR weathering, and J_a values were used to determine the number of fracture sets by k-means clustering.

5.13 Results and method assessment

The slope and aspect filtering protocol recognised 75% of the fractures in the test dataset with 79% of the orientation values within 25° of the measured orientation (see summary table 4.9, section 4.9). Since the mineralogy-related geotechnical calculations rely on the fracture recognition and orientation results, the fractures identified by the slope and aspect filtering protocols were used to assess the methods outlined in this chapter. All of the fracture pixels identified by the filter (not just the fracture edge pixels used in the orientation calculations) were used to calculate the mineralogical geotechnical values. No fracture mineralogy information was manually collected on the test dataset, so a visual comparison to photographs was used. While the RMR and J_a values for every identified fracture were calculated, a subset consisting of seventeen fractures representing approximately 10% of the fractures identified in the total test dataset were used to assess the methods. While the test interval of core is limited in spatial extent and many of the fractures are in good condition, the subset was selected to represent a range of RMR and J_a values. Table 5.7 contains a compilation of the visual fracture condition that can be observed in the photograph with a qualitative ranking of “good”, “fair”, or “poor” for each. Figure 5.5 shows the mineralogy results for each fracture, as well as, the 5 mm and 10 mm buffers.

Table 5.7. *Visual fracture assessment from photographs of selected fractures.*

Fracture Meterage (m)	Fracture Infill Present?	Fracture Weathering Present?	Qualitative Fracture Condition
0.265	minor	none	good
3.197	minor	none	good
5.609	minor	none	good
8.376	minor	none	good
9.652	minor	none	good
81.171	yes	none	fair
82.223	minor	none	good
82.459	minor	none	good
85.517	yes	none	fair
85.587	none	none	good
86.788	minor	none	good
87.053	yes	none	good
87.136	minor	none	good
156.559	minor	none	good
157.756	minor	none	good
164.99	yes	none	fair
231.66	none	none	fair

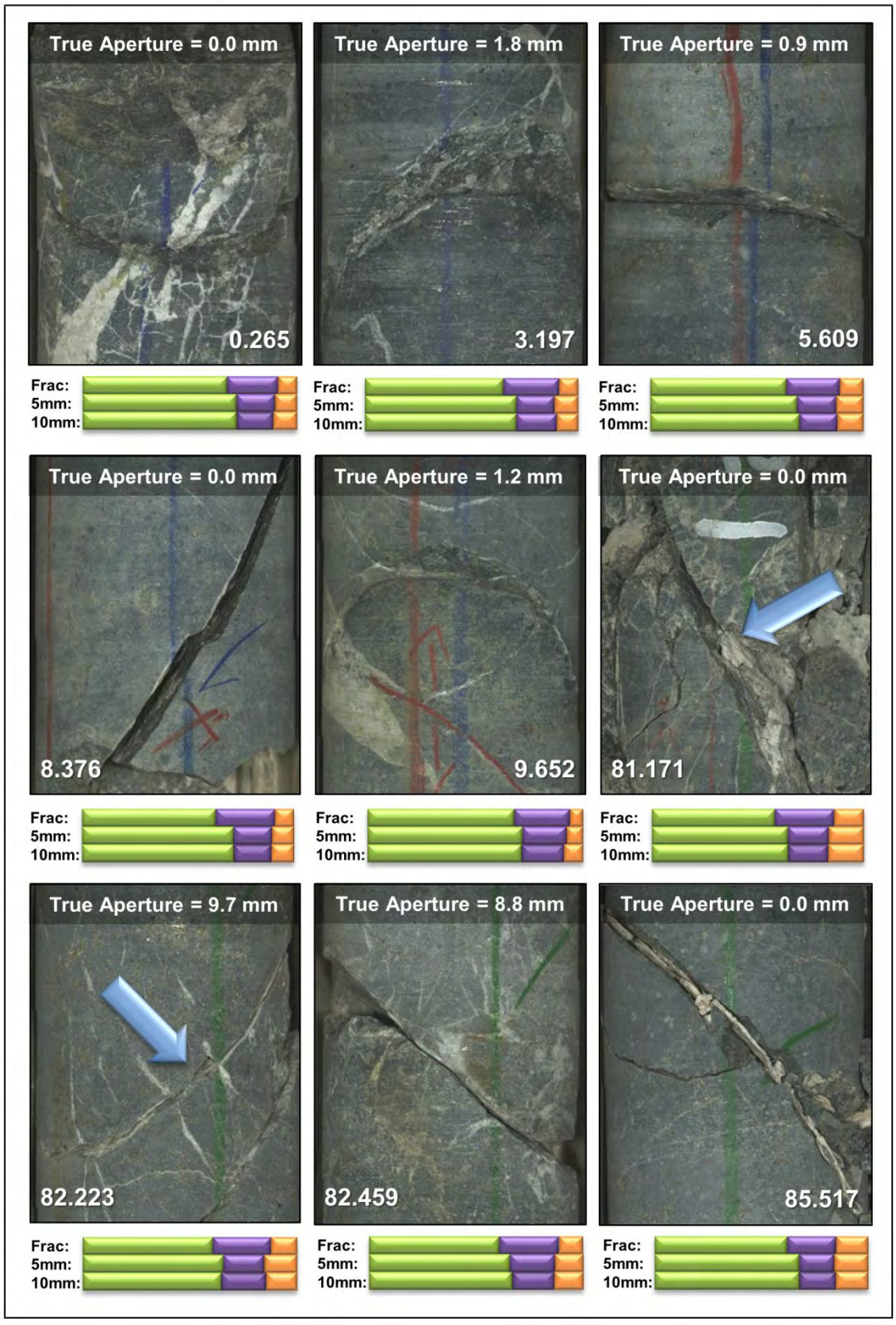

Figure 5.5. *Photographs of each fracture in the test subset (meterage in white text). Bars below each image indicate mineral abundance derived from Corescan data: in the fracture (upper bar, Frac), in the wall rock adjacent (within 5 mm) to the fracture (middle bar, 5 mm), and distal to the fracture (lower bar, 10 mm). The blue arrows point to the fracture measured in each photograph.*

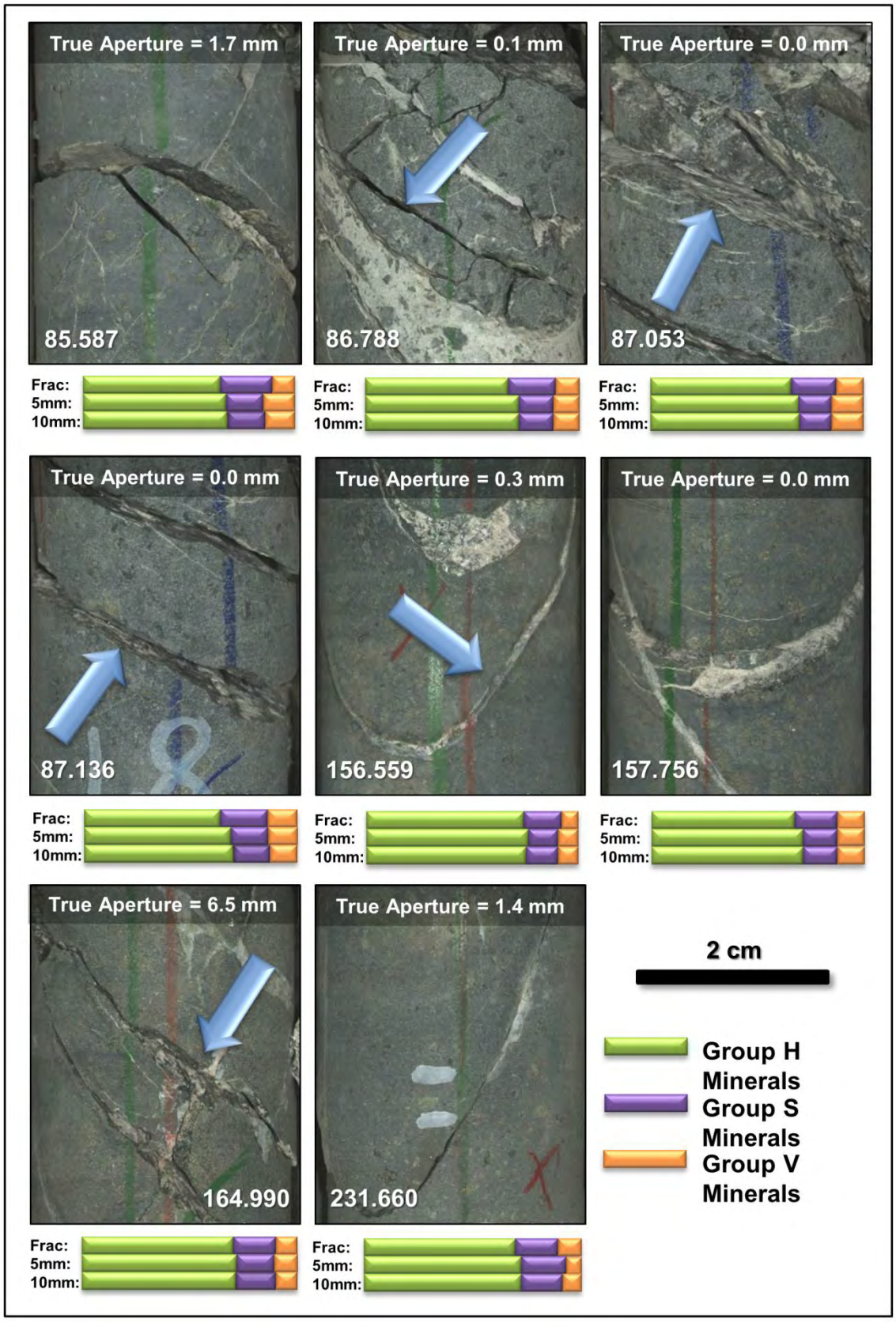

Figure 5.5 (cont.).

The hyperspectral mineralogy for each fracture is generally in agreement with the minerals observed in the drill core photographs. The mineralogy within the 5 mm and 10 mm buffers, in most cases, is similar which is consistent with the majority of fractures lacking significant weathering away from their surface. The true fracture apertures are variable. In some cases, they do not correlate with the aperture visible in the photo, while in other cases, the calculated values correlate well with the photograph.

Each of the fractures in the test data subset was assigned an RMR infill and weathering value, as well as a Q-index J_a value using the protocols outlined in this chapter. Figure 5.6 contains the photographs of each fracture in the test subset annotated with the calculated RMR infill, RMR weathering, and Q-index J_a values using the proposed criteria.

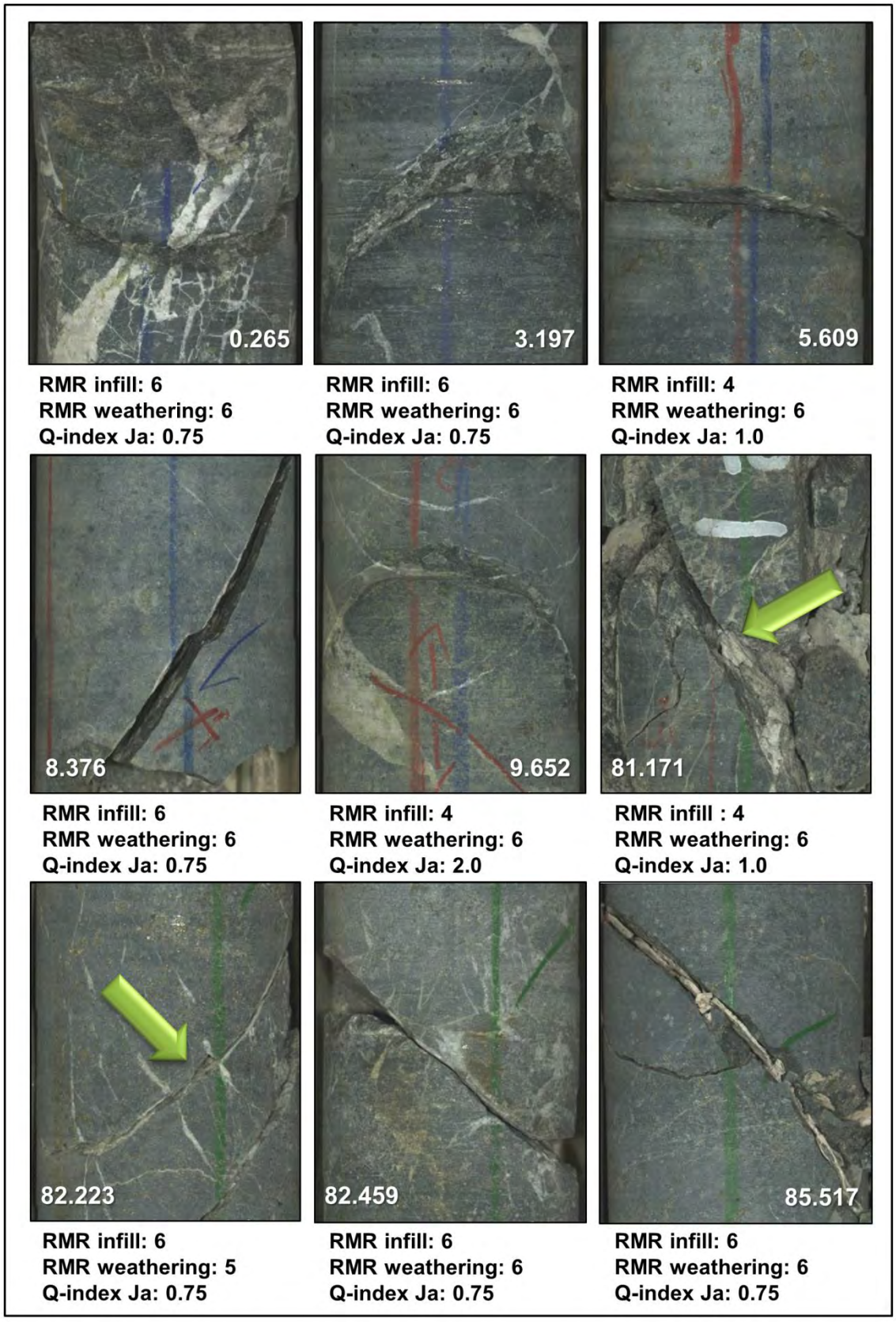

Figure 5.6. *Photographs of each fracture in the test subset with the calculated RMR infill, RMR weathering, and Q-index J_a ranking values. The green arrows indicate the location of the fracture in each photograph. The white numbers represent the down hole meterage of the fracture.*

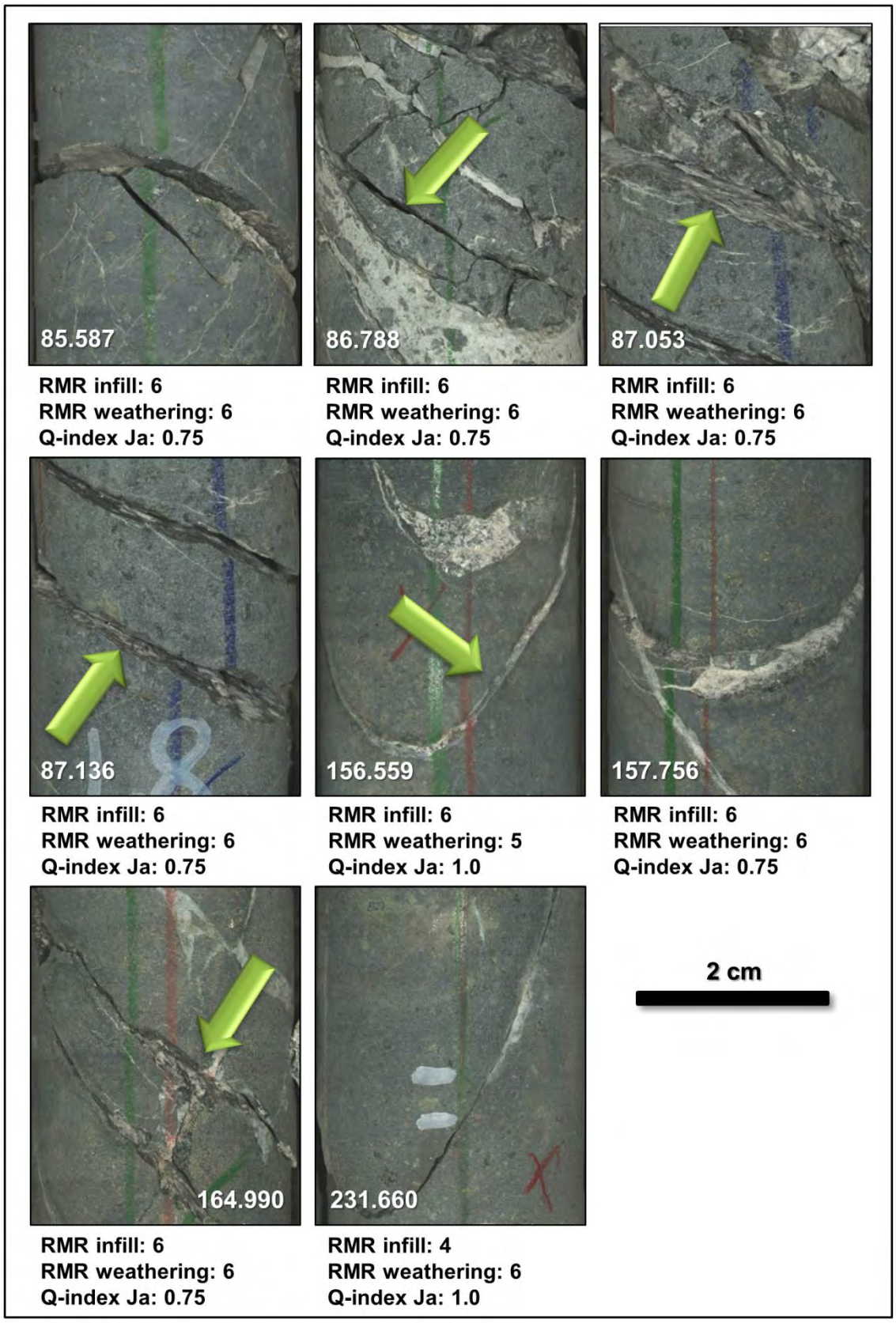

Figure 5.6 (cont.).

When compared to the fracture photograph, the mineralogical geotechnical calculations generally provide reasonable RMR infill, RMR weathering, and Q-index J_a estimates. Some fractures show a higher quality designation than what is visible in the photograph. The fracture at 85.517 m appears to have an aperture greater than 0.1 mm and be filled with group S and V minerals. This fracture appears to be in fair condition based on the photograph (see Table 5.7), but was assigned high quality RMR and J_a values of 6 and 0.75, respectively. The proposed criteria calculated an aperture less than 0.1 mm and determined that the fracture contained less than 15% group S and V minerals. In this case, the protocols are not adequately capturing the key parameters to determine fracture condition. Other fractures, such as those at 8.376 m and 85.587 m, appear to be high quality (see Table 5.7) and were assigned high quality RMR and Q-index values. The fracture at 81.171 m was assigned an RMR infill value of 6, an RMR weathering value of 6, and a J_a value of 1.0, accurately reflecting an infill less than 5 mm thick and lack of weathering (fair condition, see Table 5.7) of the fracture. A complete table of each fracture's calculated RMR infill, RMR weathering, and Q-index J_a values from Corescan data are given in Appendix N.

Using the k-means clustering algorithm in ioGAS, Corescan-derived fracture orientation, fracture roughness, RMR infill, RMR weathering, and J_a values were used to determine the number of fracture sets present in the Forest Reef Volcanics (FRV) and the Cadia Intrusive (CIC) units. The sum of squares and delta values for each rock unit compared to the number of clusters (k) are shown in Figure 5.7. Using the elbow method, the FRV and CIC units produced optimised clustering values of 4 and 3, respectively. Assigning each fracture to a cluster, the k-means groupings of the fracture sets can be observed on an equal area stereographic diagram (Figure 5.8). The expected number of fracture sets for the FRV is 3, and the expected number for the CIC is 2 plus one random set of orientations. The k-means methods are slightly overestimating the number of fracture sets compared to the expected site values.

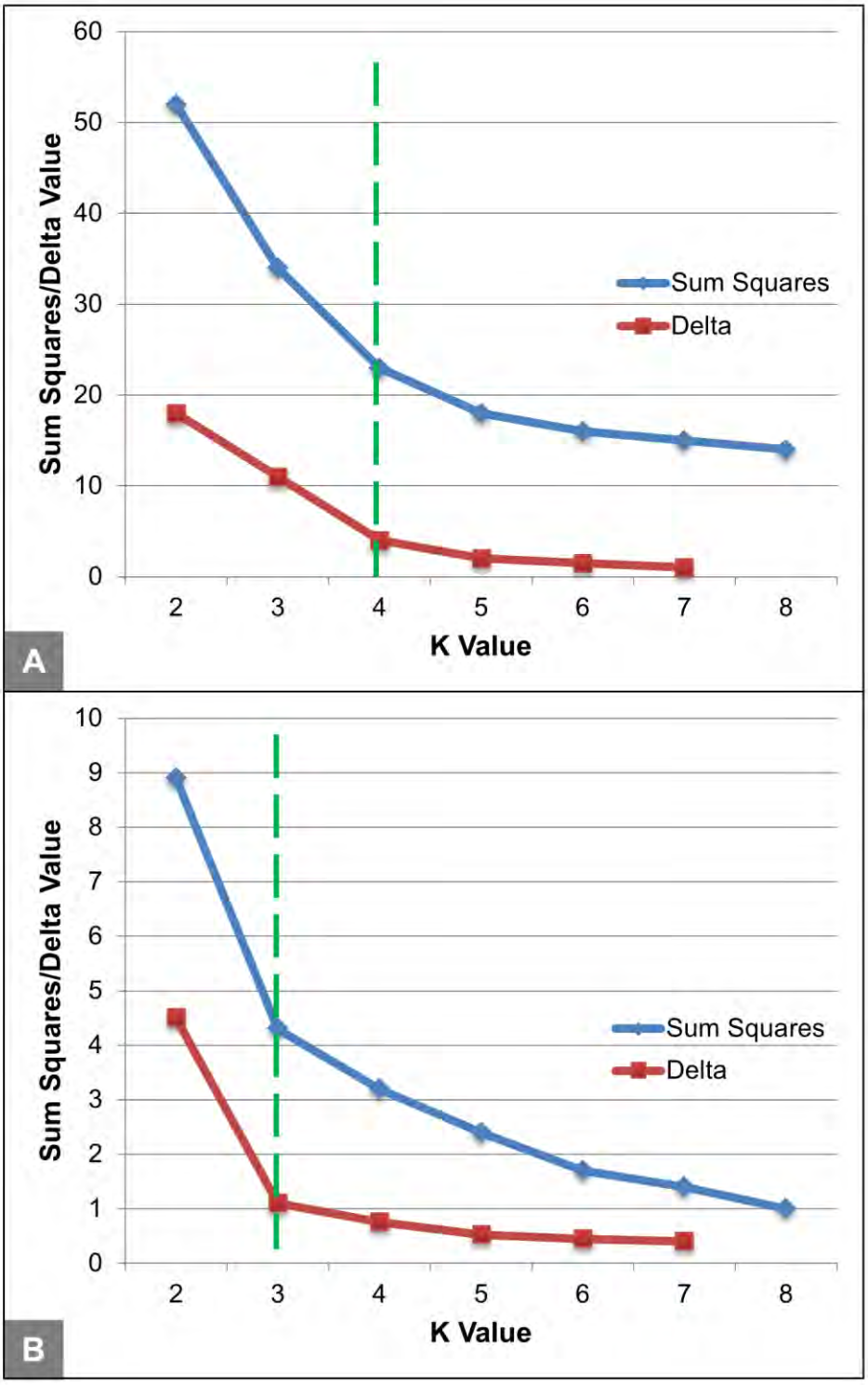

Figure 5.7. *Comparison of the calculated delta and sum of squares (SS) results for each k clustering value for the Forest Reef Volcanics (A) and the Cadia Intrusive (B). The green line shows the k value chosen using the elbow method.*

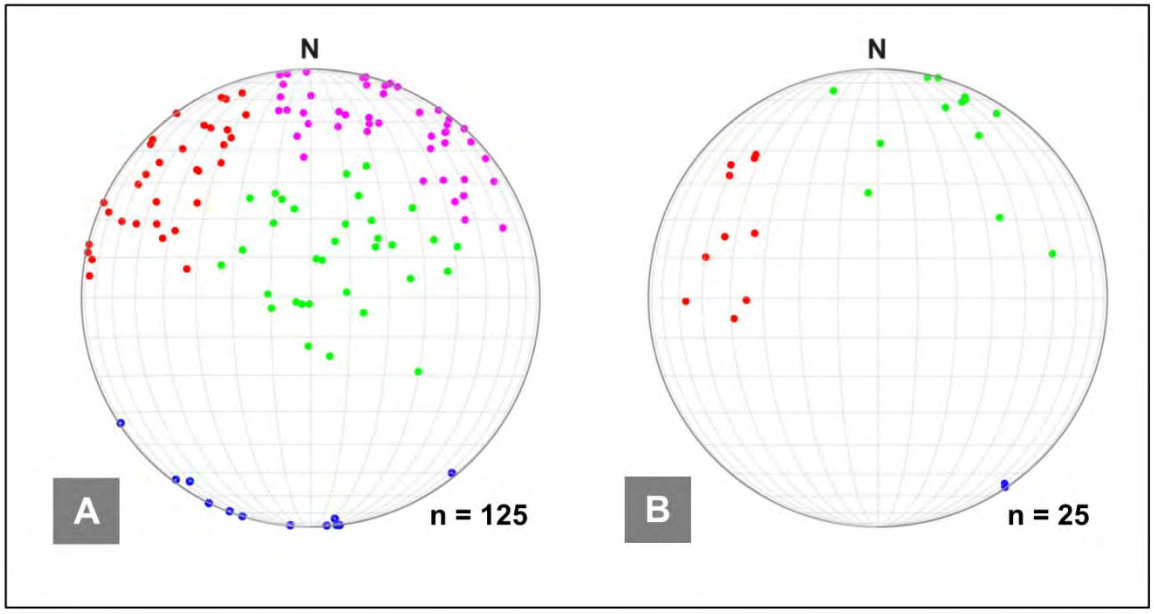

Figure 5.8. *Fractures detected by the slope and aspect protocols, projected on a on a lower hemisphere equal area stereographic projection, coloured by k-means cluster for the FRV (A) and the CIC (B).For these clusters, k-values of 4 and 3 were used for the FRV and CIC, respectively.*

5.14 Discussion

Both the RMR and Q-index geotechnical indices are designed to utilise mineral properties to determine fracture condition, indicating the clear relationship between mineralogy and fracture condition. Comparing the mineralogy of the fracture and 5 mm and 10 mm buffers appears to correlate reasonably well with the minerals visible in the photographs on a fracture by fracture basis. The proposed methods appear to generally produce reasonable RMR infill, RMR weathering, and Q-index J_a values. This comparison was completed on only a few fractures, but the positive results show the potential to upscale these methods to provide fracture condition information on a larger data set.

The k-means method for determining the number of fracture sets produces a slightly higher number of fracture sets than are expected and those calculated from Figure 4.20, section 4.6. Both of these comparison values are determined using the orientations of fractures only, while the k-means methods take into account the geotechnical parameters derived from fracture mineralogy. It may be that the k-means methods are producing a more realistic number of fracture sets. To test this, a larger dataset covering a larger spatial extent should be used.

While the comparison of the fracture mineralogy information and the photograph on a fracture by fracture basis seems reasonable, the Corescan system offers the opportunity to collect consistent fracture mineralogy

information over a large volume of drill core. As discussed previously (chapter 2), only selected intervals of key drill holes at Cadia East are geotechnically logged. To demonstrate the increased data resolution opportunity provided by the Corescan system, the fracture condition parameters derived from Corescan data are compared to the data collected manually on site over the same interval (Figure 5.9). The automated protocols developed in this study can be used to assess the mineralogy and geotechnical indices of numerous fractures rapidly and consistently over the entire length of the drill core.

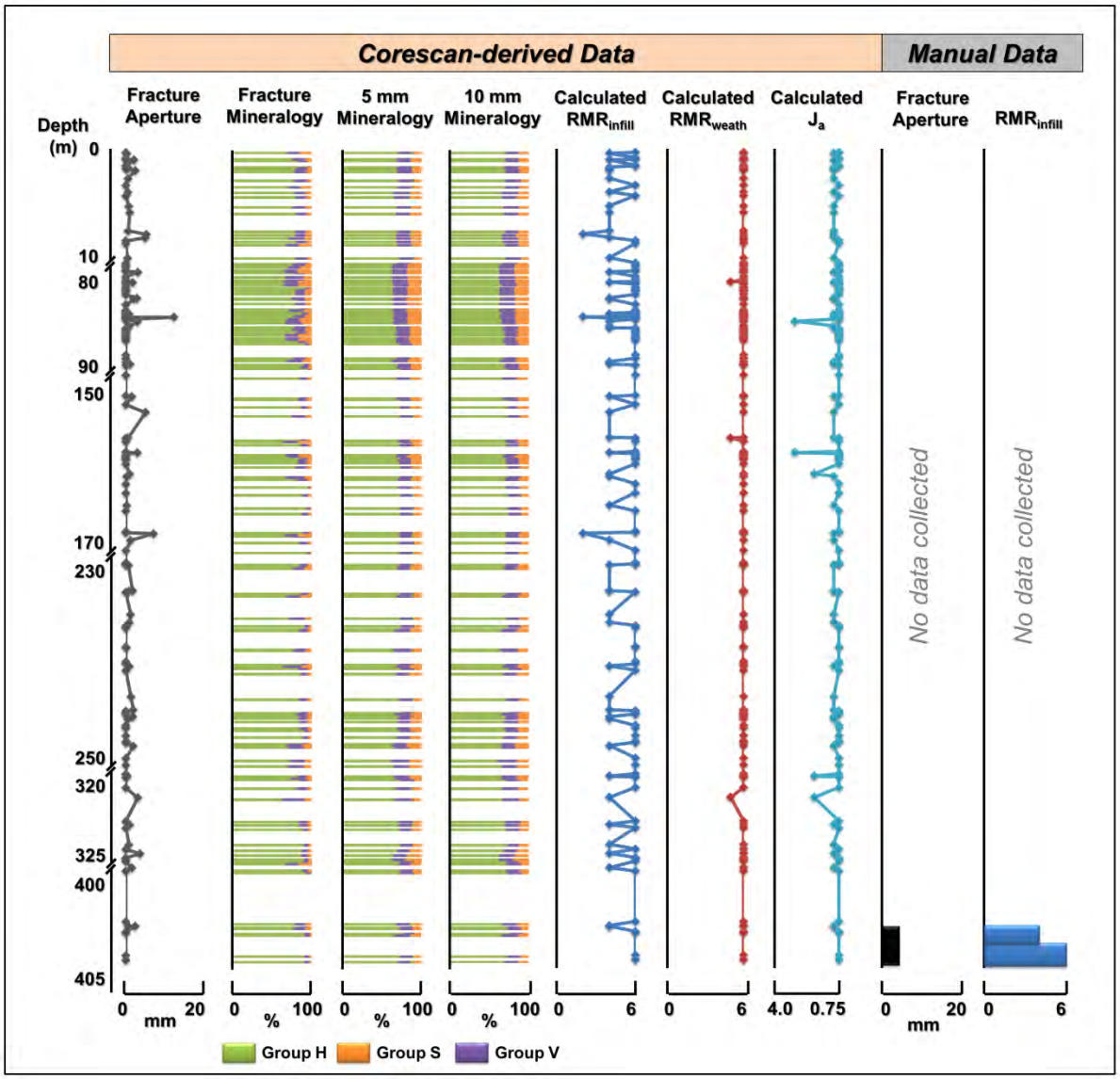

Figure 5.9. *Comparison of the mineralogical geotechnical parameters derived from Corescan data (orange) using the slope and aspect recognition protocol and the data collected manually on site (grey) over the same interval over the same interval for the test fracture set (n = 150 fractures).*

The Corescan system provides the opportunity to rapidly and consistently collect large volumes of mineralogical data from drill core. Currently, Cadia East mineralogical/geotechnical data is collected manually over a few metres of drill core and is assumed to be representative of nearby, un-sampled intervals. The Corescan system is capable of providing mineralogical information for individual fractures. This increased data density provides the opportunity to see small-scale trends that would be lost when logging these parameters on metre-scale intervals. Additionally, the Corescan system is able to detect numerous minerals that are difficult to distinguish visually. Both the RMR and Q-index geotechnical indices utilise mineral properties to determine fracture condition. Often, geotechnically unstable (group V) minerals, such as montmorillonite, are difficult to distinguish visually from more stable minerals (group S), such as kaolinite. Since the Corescan VNIR-SWIR system easily distinguishes these minerals, this approach provides a much more robust estimate of mineral proportions than visual inspection, particularly where the minerals are mixed, or in low quantities.

The increased data density and ability to detect fine-grained minerals via the Corescan automated core logging system provides a fantastic opportunity for fracture condition and mineralogical assessment. The Corescan system is capable of collecting data at a scale and consistency that is challenging when collecting the same data manually. Utilising this automated data and the geotechnical methods outlined here provide an advantage over manual logging methods.

One challenge with using fracture pixels selected from the DSM data in conjunction with the mineralogical data is that the DSM pixel resolution is 200 μm, whereas the mineralogical pixel resolution is 500 μm. This means that while the pixels are co-registered in space, there are 2.5 times more fracture pixels than there are mineralogical pixels in the same area, resulting in a 2.5 times increase in the spectral match values contributing to the overall mineral proportions for fractures compared to the buffers. However, since the overall mineralogy is an estimate based on relative proportions, this should not impact the overall mineral group proportion calculations.

A comparative study by Morelli (2015) evaluated the relative influence that each geotechnical index parameter has on the final calculated RMR and Q-index values. For the RMR value, fracture weathering and infill contribute less than 5% variance combined (Figure 5.10A). In the Q-index, the J_a values contribute approximately 20% to the total variance (Figure 5.10B). The estimated RMR infill, RMR weathering, and Q-index J_a values on the test subset show good agreement

with the fracture condition observed in photographs. Since the fracture condition is a relatively small contribution to the variance of the two geotechnical parameters, it is expected that an automated fracture mineralogy protocol would produce reasonable RMR and Q-index calculations.

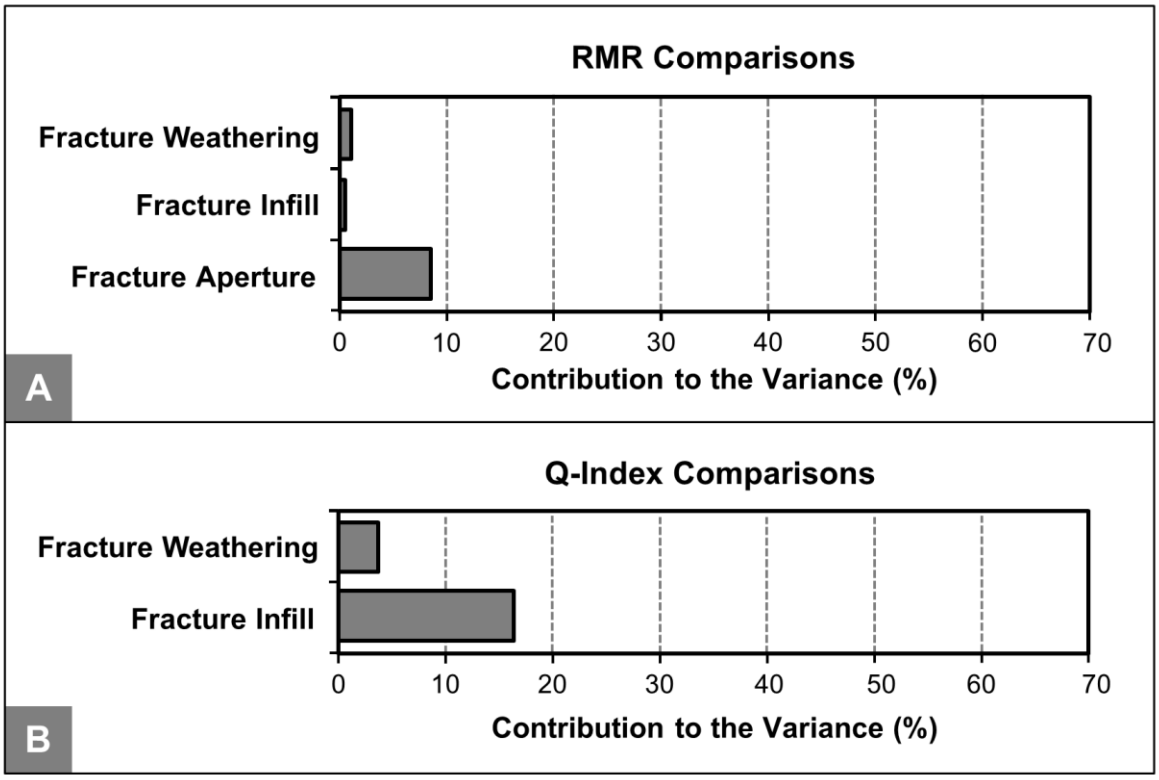

Figure 5.10. *Summary of the contribution of mineralogical geotechnical index parameters to the overall variance of the geotechnical index. A. contribution of fracture weathering, infill, and aperture to the overall variance of the RMR. B contribution of fracture weathering and infill to the overall variance of the Q-index. Figure modified from Morelli (2015).*

5.15 Conclusions

Manually assessing the mineralogical properties of fractures as they relate to geotechnical indices is time consuming and can be challenging where minerals are mixed or occur in small quantities. Since the assignment of RMR infill, RMR weathering, and Q-index J_a values is subjective, manual methods often provide inconsistent results. These factors often lead to irregularities when modelling the geotechnical characteristics of a deposit. Since the mineralogical properties of a rock mass dictate rock behaviour, understanding these properties is vital for the production of robust geotechnical models. Recent advances in automated core logging technology provide an opportunity to rapidly and consistently collect coincident surface topography (DSM data) and mineralogical information

(hyperspectral data) from exploration and production drill core. By combining surface topography and mineralogical data obtained from the Corescan automated core logging system, fracture infill aperture, infill mineralogy, and degree of weathering of the wall rock surrounding the fracture can be estimated. Key mineralogical and weathering properties affect the geotechnical response of a rock mass, so applying logical, ordered image processing steps allows mineralogical geotechnical index parameters to be rapidly and consistently calculated. The results of this small-scale study show the potential to apply automated core logging to geotechnical rock mass characterisation. In general, the mineralogical and fracture condition parameters produce results similar to those that can be observed in core photographs.

The Corescan system provides the opportunity to rapidly collect detailed fracture condition information over large volumes of drill core, increasing the underlying statistical support for rock mass characterisation. Improved rock mass characterisation models will greatly improve the efficiency and accuracy of rock stress and caveability prediction, ground support design, and fragmentation analysis. If the methods outlined here were up scaled and applied to a large volume of drill core, it would be possible to estimate key fracture mineralogical parameters from Corescan data at a scale and consistency that is currently impossible using manual data collection methods.

Chapter 6

Introduction to grain size assessment

6.1 Introduction

Geometallurgy is the process of integrating geological observations with liberation and recovery data to predict the behaviour of ore material in the mining process (Dunham and Vann, 2007; Dunham et al., 2011; Hoal, 2008; Lamberg, 2011). Ore processing parameters such as comminution, liberation, and recovery depend on the physical properties of ores (Bonnici, 2012; Lamberg, 2011). Specifically, the liberation, and ultimately, recovery of economic minerals is directly linked to the grain size of these minerals (Tungpalan et al., 2015). If rapid and broad-scale assessment of grain size can be achieved at reasonable cost, robust proxies for liberation and recovery can be implemented. Mine scale predictions of variation in recovery can contribute to improved mine planning and design.

Prior to the development of advanced mineral mapping software packages, grain size was measured manually by using reflected light microscopy. More modern reflected light microscopy techniques rely on image analysis software to identify mineral phases of interest in a reflected light image (Hunt et al. 2011; Berry 2008a). Grain size assessment of sulphides is commonly conducted by reflected light microscopy or scanning electron microscopy (SEM) in conjunction with advanced mineralogical interpretation software packages (Fandrich et al., 2007; Goodall and Butcher, 2012; Gu, 2003). While reflected light and SEM-based systems are effective, they require polished grain mounts, and have a high unit cost. These challenges make the application of the current grain size assessment methods inadequate for broad-scale liberation and recovery modelling.

The VNIR-SWIR Corescan system is effective in rapidly detecting a number of minerals important to geometallurgical and geotechnical assessment on a broad scale. Properties related to mineral hardness (for both comminution and fracture stability) can be determined using the Corescan mineralogical data derivatives. Since most metallic minerals are not IR-active, they cannot be readily detected using VNIR-SWIR techniques alone. To fully optimise the mineralogical capabilities of the Corescan system for geometallurgical assessment, an additional analysis system capable of detecting and assessing economic, metallic

minerals could be added to the existing configuration. As a preliminary investigation of these possibilities, a scoping study was designed to compare numerous, currently commercially available microanalytical techniques to determine which methods provide accurate, rapid assessment of grain sizes at a data acquisition rate similar to that of the Corescan system (3 minutes per metre).

A number of factors need to be considered in grain size assessment. The intent of this chapter is to introduce grain size assessment as it is commonly used in geometallurgical studies. A number of methods and considerations for grain size assessment are also discussed. Finally, the details of the grain size assessment study is presented including a description of the test samples used and the grain size results from the MLA analysis for these samples.

6.2 Geometallurgical studies at Cadia East

A number of geometallurgical studies have been completed on the Cadia East deposit over the last decade (Berry, 2012; Bonnici et al., 2008; Keeney, 2010; Keeney et al., 2011; Vatandoost and Fullagar, 2009; Walters, 2006). These studies have provided an excellent foundation for the understanding of the geometallurgical characteristics of the deposit. The AMIRA P843 GeM project addressed numerous aspects of the geometallurgy at Cadia East including textural analysis and mineralogy as it relates to processing behaviour (Bonnici et al., 2008), predictive recovery modelling (Berry, 2012), geometallurgical characterization and modelling using petrophysical characteristics (Vatandoost and Fullagar, 2009) as well as the mapping and modelling of comminution performance as it related to geologic properties (Keeney et al., 2011). These studies show that the physical rock properties clearly relate to the geometallurgical properties observed at the Cadia East deposit.

Cadia East is currently operating a flotation circuit for the recovery of copper and gold (Newcrest, 2011). Since recovery by flotation is a function of the flotation chemistry and hydrodynamic properties of the material, flotation is directly related to the texture and mineralogy of the ore in addition to the chemical and physical conditions at the particle surface (Wills, 2011). Additionally, flotation response is directly affected by the size, chemistry, and surface morphology of the particle in the flotation circuit. Evans (2010) developed an approach to predicting flotation response at Cadia East using detailed particle analysis. This work was based on an analysis of the composition and size of particles, and

effectively predicted flotation behaviour in the Cadia East deposit. This study highlights the importance of evaluating and modelling the grain size distribution at Cadia East.

6.3 Grain size and recovery

Numerous case studies have demonstrated the important relationship between grain size and recovery (e.g. Berry and Hunt, 2013; Feng and Aldrich, 1999; Sutherland, 2007; Trahar, 1981). While many factors affect the recovery of economic minerals (including mineral texture and paragenesis), the size of the grains is a key parameter. The predominant grain size of economic minerals in a given rock volume dictates the size that the material will need to be crushed and ground to in order to liberate the mineral of interest. Successful grain liberation is vitally important in extraction by techniques such as gravity separation, flotation, leaching, and magnetic and electrical separation and dictates the overall recovery (Wills, 2011). If grain liberation is unsuccessful, recovery will be poor. Since grain size dictates crushing and grinding which, in turn, affects overall liberation and recovery, grain size directly affects recovery.

6.4 Current grain size measurement techniques

Grain size assessment is traditionally completed by reflected light microscopy or scanning electron microscopy (SEM) in conjunction with advanced mineralogical interpretation software packages (Fandrich et al., 2007; Goodall and Butcher, 2012; Gu, 2003). Prior to the development of advanced software packages, grain size was measured manually using reflected light microscopy. More modern reflected light microscopy techniques rely on image analysis software to identify mineral phases of interest in a reflected light image (Berry, 2008; Hunt et al., 2011). While both manual and automated reflected light microscopy techniques produce robust grain size measurements, both techniques require a mounted, polished sample and, traditionally, analysis across the entire sample surface.

Automated SEM systems equipped with advanced mineral identification software, such as the "mineral liberation analyser" (MLA) and the "quantitative evaluation of mineral by scanning electron microscopy" (QEMSCAN), are now commonly implemented in grain size assessment (Coetzee et al., 2011; Fandrich et al., 2007; Goodall and Butcher, 2012; Gu, 2003; Lamberg, 2011). These systems identify minerals of interest, define the boundaries of the interested minerals, and

then calculate the grain size of each mineral. These systems scan the entire sample surface, and typically cost hundreds of dollars per sample. This unit cost restricts the rollout of this type of analysis to a few tens to hundreds of analyses for a given rock volume.

Currently, advances in micro-computed tomography (micro-CT) analysis allow for the 3D mapping and measurement of grains *in situ* (Cnudde and Boone, 2013; Ketcham, 2005; Mees et al., 2003). This technique has obvious advantages since it allows for mapping of the entire grain surface, regardless of complexity, and therefore provides much more accurate grain size measurements (Figure 6.1). While more accurate, this technique has its own unique challenges in physically correlating measured mineral densities to the expected mineralogy (Becker et al., 2016). This technique is also extremely data intensive, requiring high level computational power making it challenging to implement on a broad scale (Becker et al., 2016).

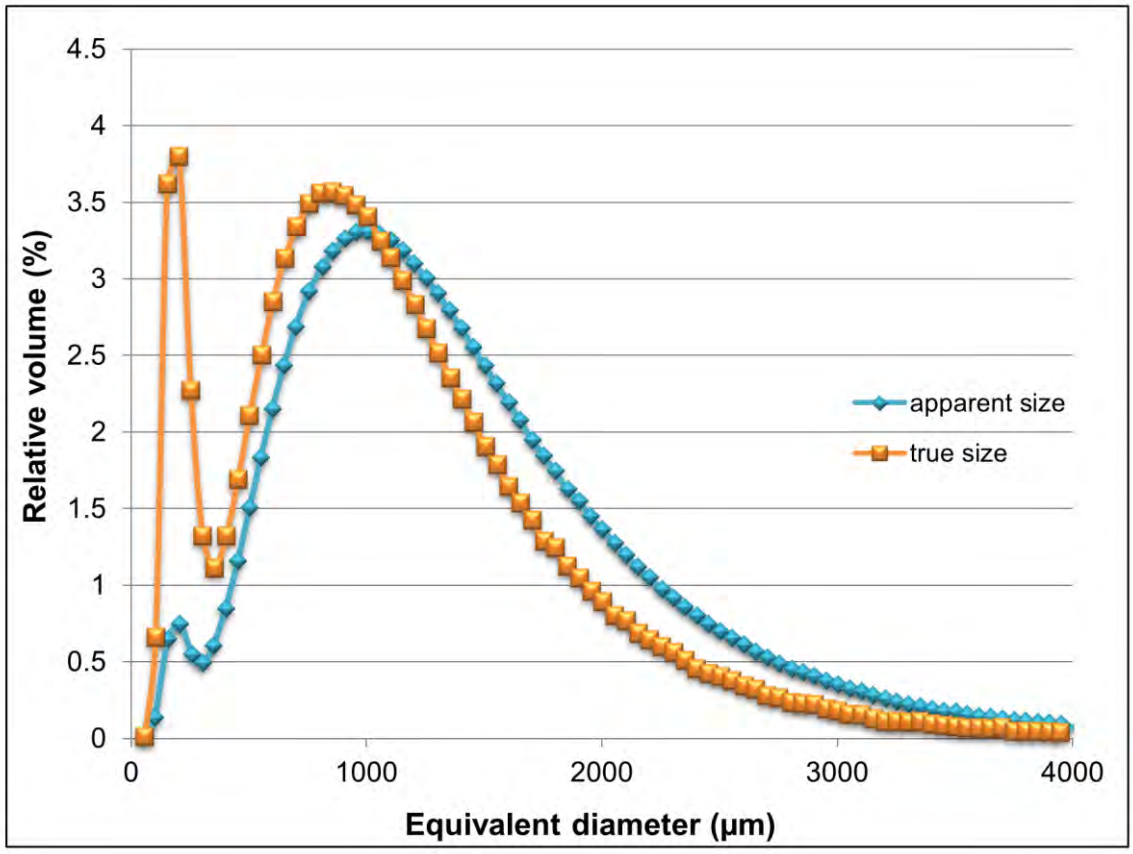

Figure 6.1. *Comparison of size distributions from apparent (2D measurements) and true (3D measurements) using micro-CT analysis. Figure modified from Van Dalen and Koster (2012).*

While 3D measurement of grains has obvious advantages, it is far more practical to measure grains as 2D objects (areas) or 1D objects (line intercept lengths). Two-dimensional areas are often measured by mapping the surface of a sample using microanalytical techniques such as reflected light imagery or a scanning electron microscope (SEM). These techniques produce maps of the surface of the sample that can then be used to measure the grain size. Line intercepts are measured by running a series of continuous analysis lines across a sample (e.g. LA-ICP-MS).

6.5 Challenges with grain size assessment

Measuring grain size presents a number of challenges, including:

- Sample surfaces expose random sections cut through grains of unknown size, orientation, spatial distribution, and geometry. This causes inherent bias in any measurement of these exposed grain surfaces.
- Assigning a single proxy value to represent the grain size of an entire population with variable distributions of grain sizes is challenging. The distribution of the grain sizes within a sample will affect whether an arithmetic average of the population provides a better proxy than an area weighted average.
- Little data currently exists on the sampling error and sampling statistics associated with grain size measurement. Evans and Napier-Munn (2013) calculated the typical error due to sampling statistics alone was ~15%. Both sampling error and sampling statistics must be carefully considered to ensure the grain size measurements are representative.

The challenges presented in this section are discussed in detail in sections 6.5.1 through 6.5.3. Each challenge has varying effects depending on the microanalytical technique being used for grain size assessment, so these considerations are also addressed individually in each of the subsequent microanalytical technique chapters (chapters 7 through 11).

6.5.1 Stereological complexities

Previous authors have noted that the estimation of grain size is inherently biased by the effects of cutting a random section through a particular grain of unknown orientation and geometry (Higgins, 2006; Sutherland, 2007; Ueda et al., 2018). Stereology is the study of using lower dimensional measurements to estimate

higher dimensional information (Baddeley and Jensen, 2004). Previous authors have noted that there are numerous stereological complexities in the estimation of grain size from a sample surface since it is inherently biased by the effects of cutting a random section through grains of unknown orientation and geometry (Sutherland 2007; Higgins 2006). Take the example of cutting a series of random, 2D sections through a volume containing spheres of the same diameter, randomly distributed throughout the volume. In this case, it is unlikely that the spheres will be cut exactly through the centre, causing the exposed surface to show a distribution of grain sizes smaller than or equal to the actual diameter (Figure 6.2).

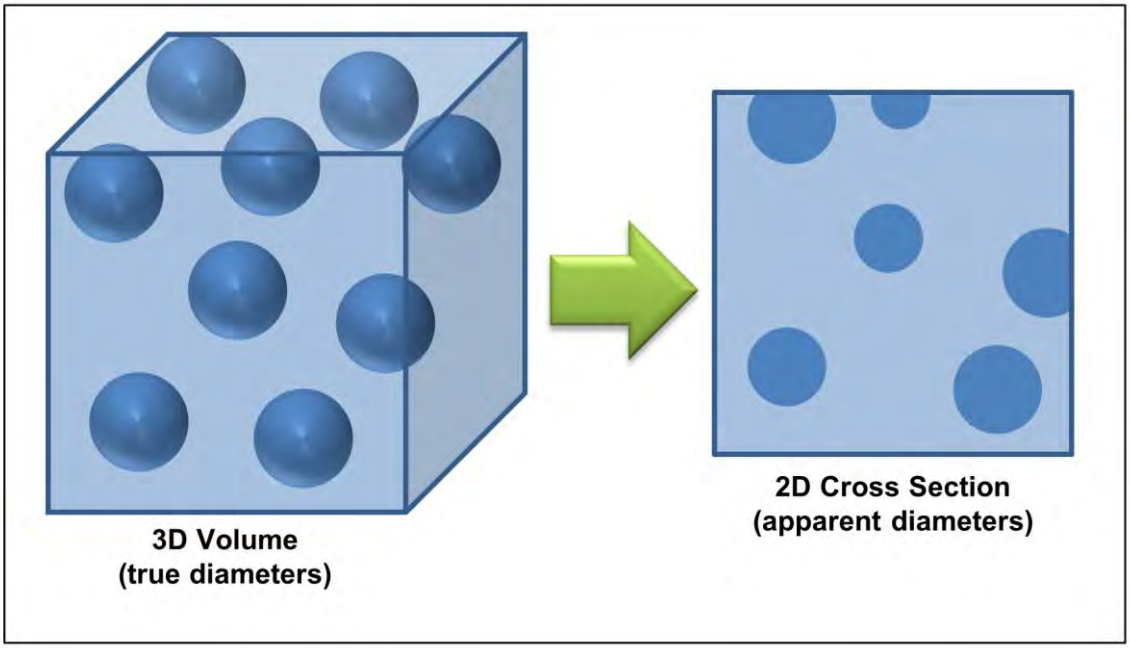

Figure 6.2. *Example of a 2D cross section compared to a 3D volume. By taking a 2D cross section through a 3D volume with randomly distributed spheres of the same size, it is unlikely that the spheres will be intersected exactly in the centre. This causes the apparent diameters to be smaller than the true diameter of the spheres.*

In the example above, the distribution of the grain sizes is known, but generally the true size and shape distribution of the grains present in a sample are unknown. Without this information, it is challenging to extract unbiased measurement parameters. For 2D area measurements, if it is assumed that the area proportion of the mineral of interest present on the sample surface reflects the volume proportion within the 3D sample volume, then measuring the 2D area proportion gives a proxy for true, dominant grain size (Berry and Hunt, 2011). Assuming that the interface density also accurately reflects the volume

proportion in 3D, Sutherland (2007) proposes that line intercept lengths from 1D data can be used to determine the surface interface density.

6.5.2 Challenges with representing a grain size population

To ensure that the grain size population is adequately represented by a grain size proxy, as many grains as possible should be measured and a statistical calculation for grain size should be used to reflect the population of grain sizes encountered in each sample. Any technique used to measure grain size will have a lower limit of grain sizes that can be detected ("limit of detectable grain size"). This means that, no matter how many grains are measured, the distribution of the grain sizes will always be truncated, ignoring the smallest grain sizes (Figure 6.3). Additionally, most samples contain a high number of small grain sizes and a low number of larger grain sizes causing a skewed grain size distribution. Commonly, a log normal distribution is assumed for grain size causing the geometric mean and average of the same distribution to be quite different. This relationship needs to be considered when evaluating a representative proxy for the dominant grain size of a given sample.

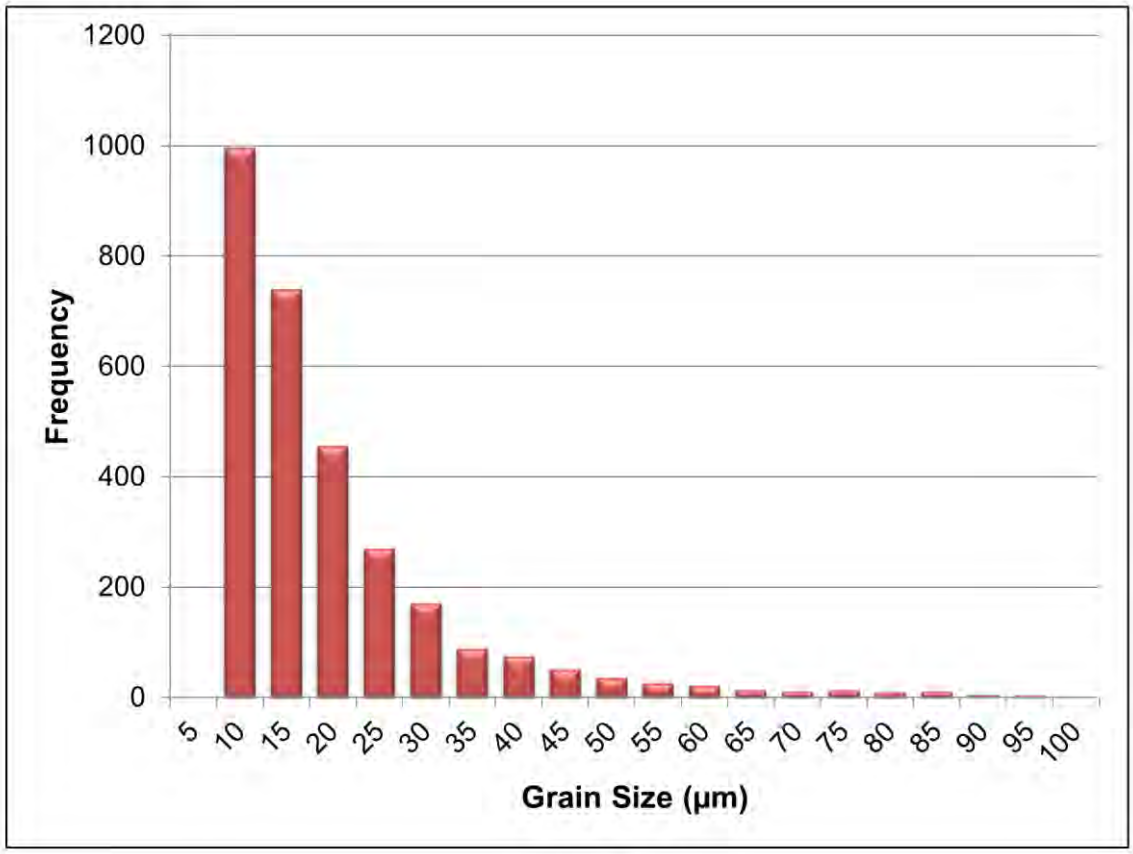

Figure 6.3. *Example of a truncated distribution. The analysis technique cannot detect grains below 5 microns, so this portion of the grain size distribution is not represented.*

In geometallurgical studies, the processing behaviour and characteristics of a rock mass, not a single sample, are considered. This means that knowing the absolute grain size distribution within a sample is less important than knowing the relative difference between grain sizes over a large interval. Often, this requires broad-scale measurements that cover numerous lithological and geometallurgical domains. Assigning a single value to represent the distribution of grain sizes within an individual sample can be challenging. Most authors describe the dominant grain size as a good proxy for the distribution (e.g. Berry and Hunt, 2011 and Sutherland, 2007). By extracting multiple grain size proxy measurements over a spatially large area, the key changes in grain size across a deposit can be tracked. In practice, grade is often used as a proxy for grain size, so grain size estimates are commonly reported on the same interval as the assay interval (1 to 2 metres).

6.5.3 Challenges with sampling error and sampling statistics

It is common for samples to contain a large number of smaller grains and significantly fewer larger grains. This poses challenges with the sampling statistics since smaller grains are more likely to be intersected by the sample surface. Most measurement programs use Gy's 1979 formula to calculate sampling errors on grain size calculations. This principle states that the minimum possible sampling variance for an individual sample can be calculated using information about particle shape, range of particle sizes, liberation, mineralogical composition of the particles, typical particle size, and mass of the sample (Gy, 1979). This approach is suitable for determining sampling errors for independently selected samples, but provides variance estimates that are unrealistic for dependent samples (Geelhoed, 2011). Since rock samples often represent only one sample population (e.g. ore material from one ore deposit), independent sample selection can be challenging, and Gy's formula often overestimates the variance (Berry and Hunt, 2011).

Other approaches to calculating sampling error include using the overall grade of a sample or testing the variance within a single sample. In a study by Evans (2010b), the relationship between sample grade and relative error was demonstrated. This study showed that the typical error for a specific size range of chalcopyrite was about 20% at approximately 1% copper grade. Evans and Napier-Munn (2013) determined that the typical error due to sampling statistics alone was approximately 15% for a series of grain mounts coarse enough to preserve the original grain size. Berry and Hunt (2011) used a method where 2D images of the sample surface were divided into four equal sections. The grain size parameters were then calculated for each of these four sections separately, and the standard error on the mean was estimated. This approach showed that single measurements had relative errors of 5 – 10% for grains of chalcopyrite with errors increasing as the grade of the sample decreases or the grain size increases (Berry and Hunt, 2011). While relatively few studies addressing specific guidelines to minimise sampling errors in grain size measurement have been completed, it is generally accepted that sampling 5,000 to 10,000 grains minimises the overall sampling error.

Calculating gold grain sizes is especially challenging since these grains are typically small and rare. Commonly this creates a critical sampling issue in that not enough gold grains are measured to adequately represent the grain size population. Berry and Hunt (2011) determined that gold grain population

statistics only become meaningful when at least 50 gold grains are included in the grain size proxy calculation (Figure 6.4).

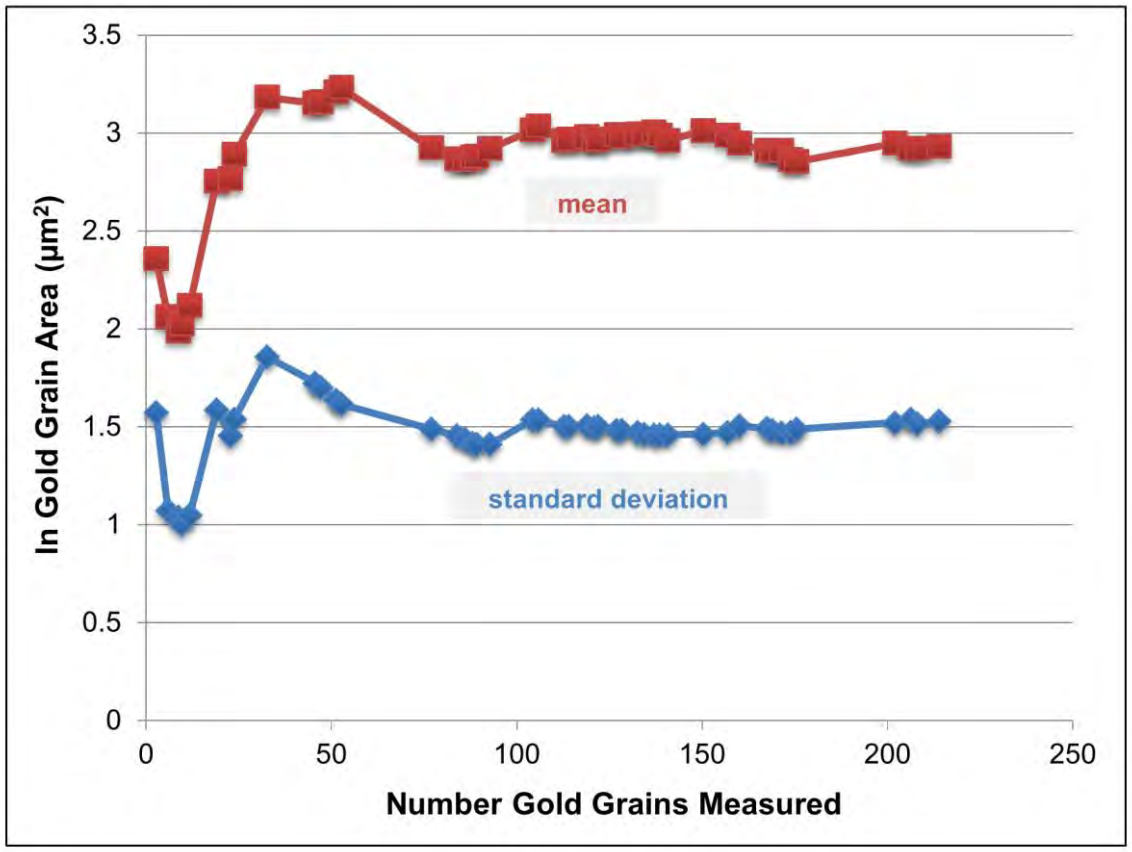

Figure 6.4. *Changes in population statistics compared to the number of gold grains measured. Figure modified from Berry and Hunt (2011).*

6.6 Grain size proxy values

It has been proposed by many authors that 2D and 1D grain size measurements in addition to bulk chemical data can be used to produce a proxy for a grain size distribution (e.g. Berry and Hunt, 2013, Sutherland 2007). Two-dimensional measurements are collected by mapping a sample surface, isolating the phase of interest, then measuring the grains. One-dimensional measurements are collected by running a series of lines through the sample and determining the average intercept length of the minerals of interest. Bulk chemical composition techniques use the chemical data from a large portion of the sample (e.g. assay or pXRF) then compare this to the abundance of elements of interest detected in a given volume.

There are numerous methods to represent the grain size of a population with a single value, but most methods involve averaging the grain diameters of the population. The distribution of the grain sizes within a sample will affect whether an arithmetic average of the population provides a better proxy than an area weighted average. Where an arithmetic average is used, the calculated grain size value is heavily influenced by smaller (and likely more abundant) grains. Using an area- weighted or volume-weighted average provides the opportunity to for larger grains to more heavily influence the grain size than small grains. Since very small grains do not contribute significantly to the overall grade, area-weighted and volume-weighted averages are used in this study. For these measurements, Berry and Hunt (2011) propose a method that uses the measured 2D grain boundary lengths and 2D areas to calculate a phase specific surface length (PSSL) of a population of grains by:

$$\mathrm{PSSL}_{\mathrm{population}} = \frac{\sum \text{boundary lengths}}{\sum \text{intercept areas}} \quad [6.1].$$

Assuming a spherical shape for the grains, the grain size measurement proxy (diameter by phase specific surface length, or D_{PSSL}) is given by:

$$\mathrm{D_{PSSL}} = \frac{4.7}{\mathrm{PSSL}_{population}} \quad [6.2]$$

(Berry and Hunt, 2011).

The 4.7 coefficient was derived by taking random cross sections through a simulated sphere of known diameter. Using a random number generator, random slices are selected and the diameter of the resulting circle from each cross section is calculated.

Assuming the constant value is unknown (z), the D_{PSSL} equation can be solved for z and rearranged such that:

$$\mathrm{z} = \mathrm{D_{PSSL}} * \frac{\sum \text{boundary lengths}}{\sum \text{intercept areas}} \quad [6.3].$$

This simulated sphere of known radius was sliced multiple times to derive the constant value (z) in the D_{PSSL} calculation. A series of experiments were run 10 times, each using 5,000 random slices of grains with diameters of 10 μm, 50 μm, 100 μm, and 1000 μm to calculate the average radius, circumference, and area of each resulting slice. The constant value (z) for the D_{PSSL} was then calculated for each experiment. The results are outlined in Figure 6.5.

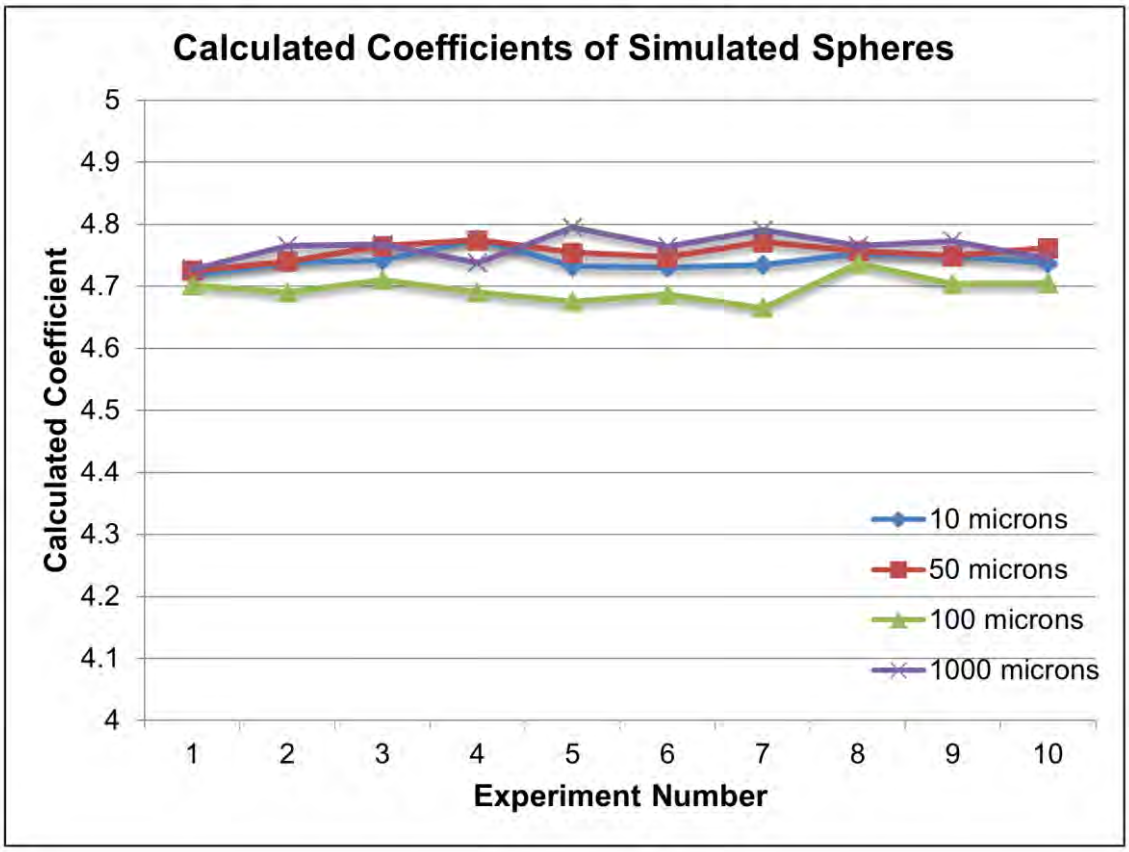

Figure 6.5. *Calculated coefficients for the D_{PSSL} equation using 10 experiments on simulated spheres with diameters of 10 μm, 50 μm, 100 μm, 1000 μm. The experiments converge on a coefficient of approximately 4.7.*

Each experiment converges on a constant near 4.7 for the D_{PSSL} equation, regardless of the grain size used. The D_{PSSL} is an area-weighted mean, ensuring that the larger, more significant grains are weighted more heavily in the proxy calculations. For grain size proxy measurements in this study, the D_{PSSL} will be calculated using equation [6.2].

6.7 Individual grain size detection versus bulk analysis

Where the analytical method provides a bulk analysis (e.g. assay, whole rock, portable XRF, etc.) and the measurement of individual grains to determine the population is not possible, elemental concentrations can be used to calculate a proxy for grain size. In this case, some assumptions about the sample are made. Two grain size proxy methods, proposed by Cohen (1990) and Smee and Stanley (2005), use the variability in elemental concentrations taken from a sample to calculate a proxy for grain size. Both authors assume that the grain size within a single sample is uniform. Cohen (1990) modelled the elemental variability using

a binomial distribution, whereas Smee and Stanley (2005) used a Poisson distribution. Both calculations were compared on a series of samples by Berry and Hunt (2011) and were found to produce almost identical results. While both authors applied these methods in gold grain analysis, similar techniques can be used to develop copper sulphide grain size proxies.

Where the microanalytical technique provides sufficient spatial and analytical resolution, the amount of contained copper and gold can be compared to the analysis volume or area to estimate the grain size present in each analysis pixel. Whether an analysis volume or surface area is used depends on the typical grain size of the minerals of interest and the depth of analysis for the microanalytical technique used. If a microanalytical technique is capable of detecting elements at a depth greater than the typical grain size, an analysis volume can be used. In this case, a 3D grain of the typical grain size could be detected in the analysis volume. If the typical grain size is greater than the depth of analysis, a 3D grain of the typical analysis size would not be completely detected, so the analysis must be treated as a surface measurement.

6.8 Grain size assessment study objectives

When defining the objectives of this study, three main factors were considered: (1) the ability of each technique to assess copper sulphide and gold grain sizes, (2) the acquisition rates and resolution required to adequately assess copper sulphide and gold grain sizes, and (3) the data acquisition rate compared to the Corescan system's rate. For Cadia East drill core, the Corescan system currently has an acquisition rate of 3 minutes per metre with an analysis resolution of 500 μm for the VNIR-SWIR data. Any complementary analysis system used in tandem would need to have similar acquisition rates. With respect to grain size assessment, previous studies of the Cadia East deposit show that the expected characteristic grain size for copper sulphides and gold is between 20 μm and 50 μm (Berry, 2012). Keeping these factors in mind, the objective of this research was to use various microanalytical techniques to test the ability of each method to adequately assess a grain size proxy for copper sulphides and gold at a rate similar to 3 minutes per metre.

To establish a baseline grain size measurement, each sample was analysed using the scanning electron microscope (SEM) coupled with the mineral liberation

analyser (MLA) software package. The details and results of this analysis are outlined in section 6.9.

6.9 Sample selection and comparison methods

Samples were selected from an existing set of 77 pre-prepared, cut and polished 3 cm by 3 cm tiles used in the AMIRA P843A GeM project from Cadia East drill hole CE143. This drill hole was selected because it intersected deep, high grade copper sulphide and gold in one of the main quartz monzonite porphyry bodies (CIC) and surrounding host volcanic units (FRV) in Cadia East (Figure 6.6). Twenty six samples total were selected using the following criteria:

- Samples previously analysed by MLA for gold in the AMIRA P843A GeM project were selected first.
- Six samples with pXRF values greater than 0.5 ppm gold (considered "high detectable gold") were selected.
- Six samples with pXRF values less than 0.5 ppm gold (considered "low detectable gold") were selected.
- The remaining 14 samples were selected using a random number generator – seven from the "high detectable gold" list and seven from the "low detectable gold" list.

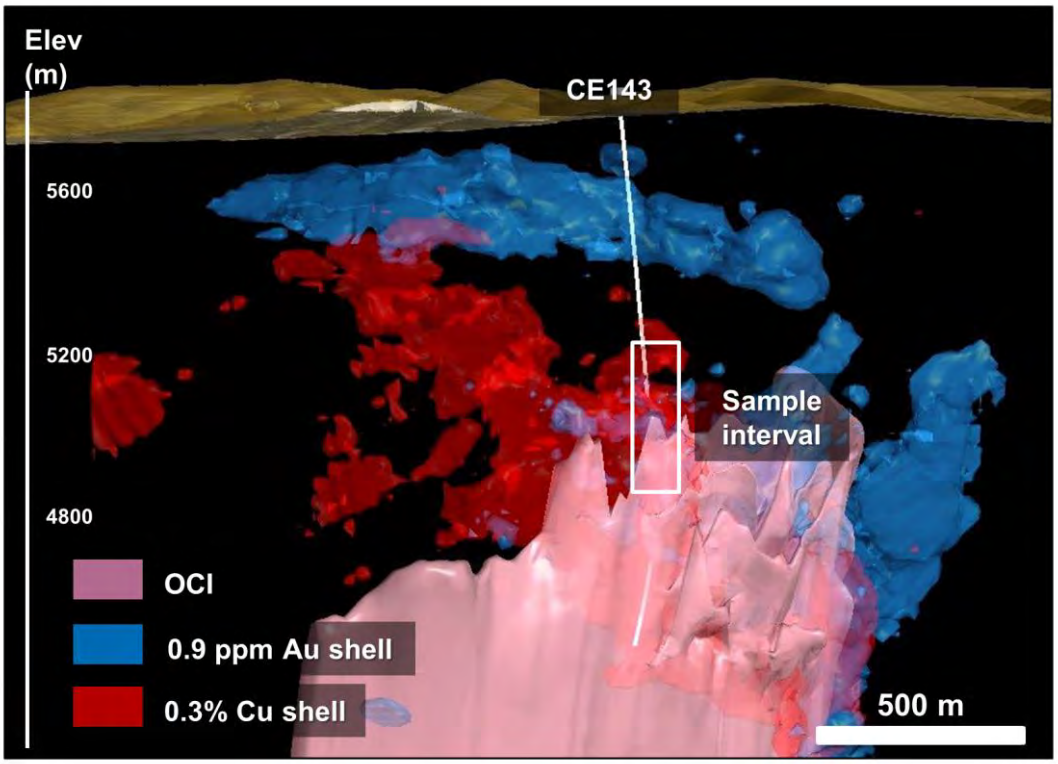

Figure 6.6. *Location of the CE143 drill hole relative to copper and gold grade shells and the main quartz monzonite porphyry (CIC) within the Cadia East deposit (cross section, looking north).The quartz monzonite porphyry is hosted within the volcanic units of the Forest Reef Volcanics (FRV).*

The final sample list is outlined in Table 6.1. Images of each of the tiles used in the study are included in Figure 6.7.

Table 6.1. *Details of samples selected for this grain size assessment study.*

Sample ID	pXRF Result (Au)	AMIRA P843A GeM project pXRF Complete	AMIRA P843A GeM project MLA Gold Analysis Complete
1185.0	high	X	X
1193.0	high	X	X
1207.0	low	X	X
1265.5	low	X	X
1269.0	low	X	X
1283.0	high	X	X
1283.5	high	X	X
1292.5	high	X	X
1306.5	low	X	X
1307.5	low	X	X
1356.5	low	X	X
1362.7	high	X	X
1380.5	high	X	X
1381.0	low	X	X
1392.5	high	X	X
1393.0	low	X	X
1400.5	high	X	X
1401.0	high	X	X
1409.0	low	X	X
1420.0	high	X	X
1420.5	low	X	X
1421.0	high	X	X
1431.0	low	X	X
1431.5	low	X	X
1448.5	high	X	X
1461.5	low	X	X

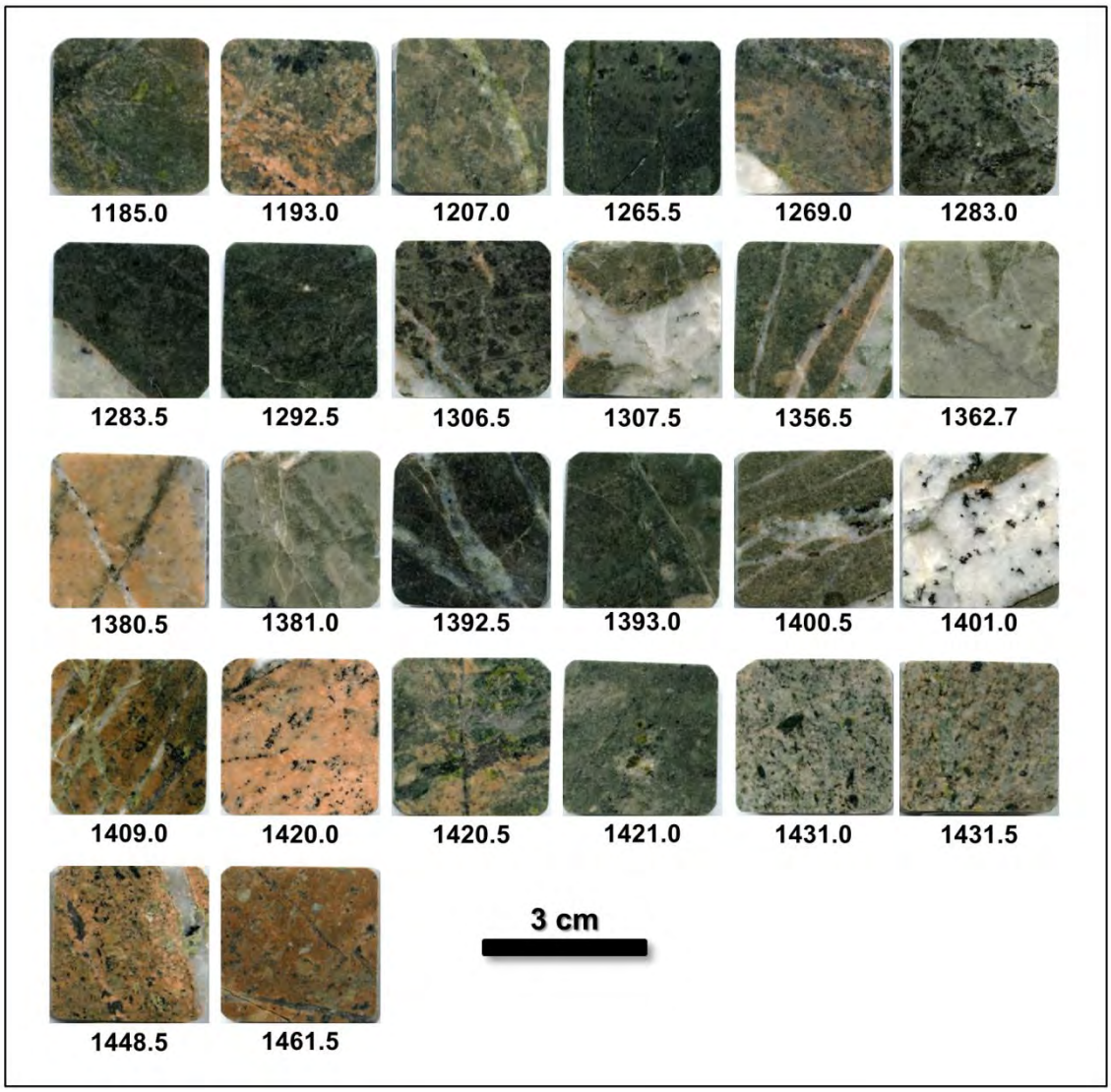

Figure 6.7. *Scanned images of the twenty-six test samples used in this grain size assessment study.*

6.10 MLA comparison data

The scanning electron microscope (SEM) is a specific type of electron microscope that focuses a beam of electrons at a sample surface. These electrons interact with the atoms of the sample and produce various responses including secondary electrons, backscattered electrons (BSE), and x-rays that are then detected by the sensors attached to the SEM unit (Goldstein et al., 2017). The SEM technique is non-destructive and is commonly used to detect gold and copper sulphide ore minerals. Gold has a diagnostic X-ray energy Lα peak at 9.7 keV, while copper shows diagnostic Kα and Lα peaks at 8.05 and 0.93 keV, respectively. While copper sulphide species can be difficult to distinguish from one another, the height of the copper peaks relative to the sulphur peak at 2.31 keV can be used to differentiate bornite from chalcopyrite.

The Mineral Liberation Analyser (MLA) is an automated analysis tool that uses SEM data to conduct copper sulphide and gold grain searches as well as quantify grain sizes and mineral associations (Coetzee et al., 2011; Lamberg, 2011). This system can be used to automatically calculate the size distribution of minerals of interest within a given sample. The sparse phase liberation (SPL-Lt) method is a type of MLA analysis that utilises a user defined threshold for BSE grey scale values to locate minerals of interest. Once the software locates grains matching the BSE ranges for the minerals of interest, the grain is divided into phases by BSE value, and a spectrum is collected for each phase. The collected spectra are then compared to a library of mineral spectra and assigned a mineral name.

All samples within the sample set were first prepared with 20 nm carbon coating, then analysed using the SPL-Lt routine for copper sulphide and gold. The analysis was completed on a tungsten source FEI MLA650 SEM located in the Central Sciences Laboratory (CSL) at the University of Tasmania, Australia. The specific parameters used in the SPL-Lt analysis are outlined in Table 6.2 for the gold and the copper sulphide search. For each of the twenty six samples, SPL-Lt analysis for gold, chalcopyrite, and bornite was performed and the grain areas and boundary lengths for each mineral in each sample were then exported. The grain size results from the microanalytical techniques tested in this study were compared to the MLA D_{PSSL} grain size data. Because gold grains present in the sample set are small and rare, only 40 grains of gold were identified in the AMIRA P843A GeM SPL-Lt gold search. To ensure that enough gold grains were measured to adequately represent the gold grain population, the samples were polished down ~20 μm, and then re-analysed by gold search on the MLA software an additional two times. The total of the three SPL-Lt gold searches from the three different exposed sample surfaces were used to calculate the D_{PSSL} values from MLA which are used for gold comparisons in this study.

To calculate grain size from the MLA data, the D_{PSSL} was calculated using the sum of the boundary lengths divided by the sum of the grain areas. The results of the grain size calculations using the MLA data are outlined in Table 6.3. Since MLA analysis is commonly used in grain size assessment studies for geometallurgical applications, these results were used as the "correct" value for calculated grain size. This data set was compared to the calculated grain size proxy values to determine the ability of each microanalytical technique to produce a reasonable grain size proxy.

Table 6.2. *SPL-Lt measurement parameters used in this study for the gold and copper sulphide mineral search.*

	Gold Search	**Copper Sulphide Search**
Pixel Size	0.88 μm	2 μm
Magnification	270	136
# of frames	900	256
Grey low	180-190	200-215
Grey high	255	255
Brightness & contrast standard	Au	Ni

Table 6.3. *D_{PSSL} results calculated from MLA analysis of the twenty-six samples used in this study.*

		Chalcopyrite		Bornite		Combined Cu Sulphide		Gold	
Sample ID	Rock Type	Number Grains	D_{PSSL} (μm)	Number Grains	D_{PSSL} (μm)	Number Grains	D_{PSSL} (μm)	Number Grains (in 3 runs)	D_{PSSL} (μm)
1185.0	FRV*	16	21	3159	36	3085	35	7	17
1193.0	FRV*	152	33	2400	70	2463	71	2	1
1207.0	FRV*	175	17	424	67	564	58	1	1
1265.5	FRV*	9998	33	4	6	9849	32	4	10
1269.0	FRV*	141	21	286	17	419	18	0	-
1283.0	FRV*	4532	68	25,006	23	26239	42	22	14
1283.5	FRV*	155	17	3098	31	3201	31	7	6
1292.5	FRV*	13	12	1711	27	1700	27	10	8
1306.5	FRV*	204	21	2638	20	2779	21	4	5
1307.5	FRV*	800	66	1190	24	1634	53	0	-
1356.5	FRV*	1734	38	1530	33	3022	39	9	14
1362.7	FRV*	2562	51	0	-	2509	52	0	-
1380.5	FRV*	9998	46	4	16	9831	46	1	5
1381.0	FRV*	1887	21	27	7	1912	21	0	-
1392.5	FRV*	1	8	7130	29	7093	29	17	10
1393.0	FRV*	10	17	1213	13	1218	13	0	-
1400.5	FRV*	5596	81	3134	38	7218	79	10	13
1401.0	FRV*	2255	95	2365	149	3552	152	38	27
1409.0	CIC**	592	22	52	21	623	23	8	3
1420.0	CIC**	3329	102	2862	77	4078	111	54	18
1420.5	CIC**	31	19	10	17	39	19	0	-
1421.0	CIC**	19389	29	34	17	18949	29	1	3
1431.0	CIC**	59	17	107	13	164	15	1	4
1431.5	CIC**	368	19	447	13	788	17	1	2
1448.5	CIC**	298	26	3166	36	3377	36	223	5
1461.5	CIC**	3546	24	397	15	3852	24	3	5
Total		*67,841*		*62,394*		*120,158*		*423*	

*Forest Reef Volcanics

^ Cadia Intrusive

Eighteen of the samples are from the Forest Reef Volcanics (FRV) and the remaining eight samples are from the Cadia Intrusive (CIC) unit. All twenty-six of the samples contained grains of chalcopyrite, and all but one contained grains of bornite. While discrete grains identified by the MLA may actually represent intergrown or composite grains of copper sulphide, this complexity is ignored in this study. Only twenty of the twenty-six samples contained grains of gold.

It should be noted that most of the gold grains identified in the sample set contain some amount of silver (typically less than 10%) and should therefore be classified as electrum (Figure 6.8) (Kamenetsky and Berry, 2010). For bulk proxy methods, this was addressed by assuming a density of 17 g/cm^3, slightly less than the pure gold density of 19.25 g/ cm^3. Kraut and Stern (2000) calculated that 17 g/cm^3 represents the expected value for an alloy of approximately 85% gold with 15% silver. For grain size proxy calculations that rely on the direct detection of gold, small electrum grains containing less than 15% silver would return negligible silver values (likely near or below the detection limit for silver). In these cases, it was assumed that any gold identified was contained in a pure gold grain. While this assumption could produce grain sizes lower than expected for gold, they should still be proportional to the grain size proxy values.

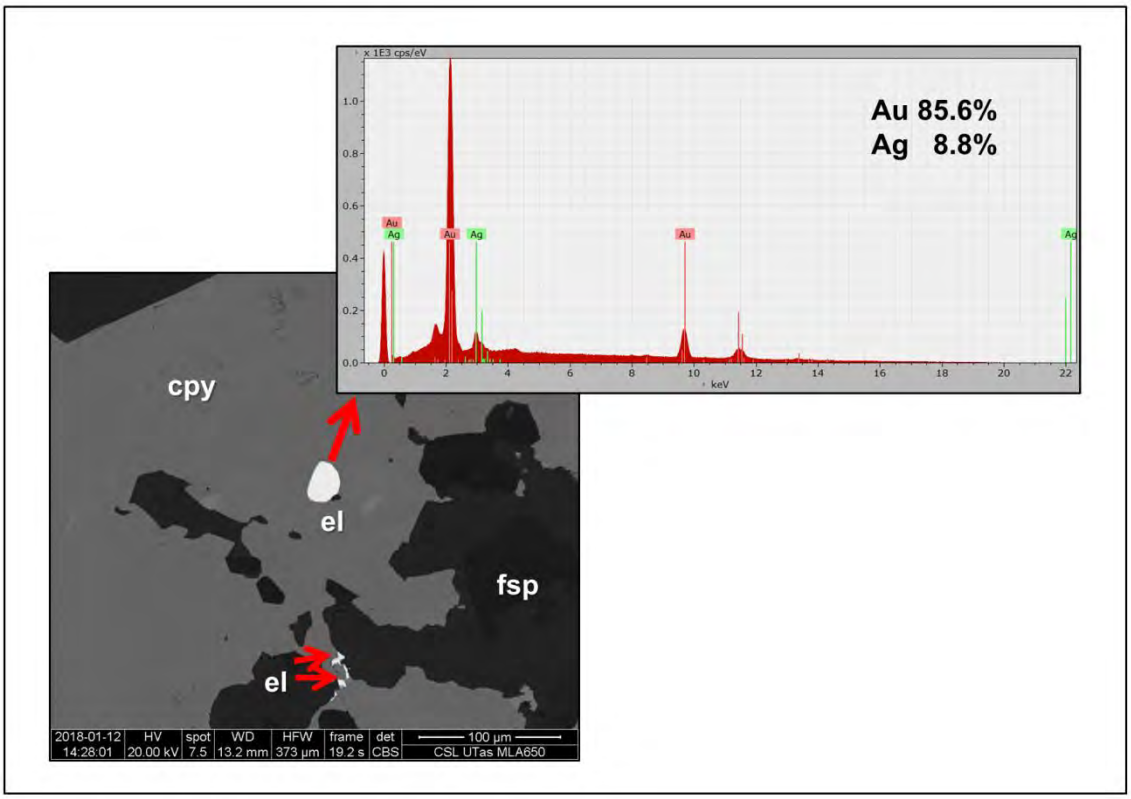

Figure 6.8. *BSE image of an electrum grain hosted in chalcopyrite (A). An x-ray spectrum collected from this grain shows it is approximately 86% gold with 9% silver (B).*

6.11 Outline of subsequent discussion chapters

A scoping study was designed to test a number of microanalytical techniques that could complement the current Corescan system by rapidly determining proxies for copper sulphide and gold grain sizes on the same interval as a typical assay (1 to 2 metres). A series of commercially available microanalytical systems were tested using a set of twenty-six, 3 cm by 3 cm rock tile samples from Cadia East. The traditional grain size measurement method of MLA analysis was used as the comparison grain size data. These samples were then analysed using portable x-ray fluorescence (pXRF), micro-x-ray fluorescence (μXRF), laser ablation inductively coupled mass spectrometry (LA-ICP-MS), laser induced breakdown spectroscopy (LIBS), and laser Raman. The grain size proxy calculations using each technique were then compared to the grain sizes from MLA to determine the ability of each technology to calculate copper sulphide and gold grain sizes. This assessment was completed by comparing the MLA and calculated D_{PSSL} values, then calculating the Pearson correlation coefficient (R^2) and the Spearman ranking coefficient (r_s). The number of analyses required to produce adequate grain size proxies was determined for each technique. Finally, the amount of time required to complete this critical number of analyses to produce a grain size assessment for each metre of drill core was compared to the Corescan data acquisition rate.

For each method tested, the scientific principles and ability of each technique to detect gold and copper sulphide minerals are summarised. The specific methods used to calculate grains size proxies using the data derived from each technique are then outlined. Finally, the results of the grain size assessment are presented. This includes a comparison of the calculated grain size proxies to the measured MLA grain sizes and the number of analyses required to provide sufficient grain sizes. For methods where using all of the available analyses provides a good grain size proxy, bootstrapping was conducted to determine how many analyses are required to get repeatable grain size proxy results. Bootstrapping is a method that runs a series of experiments, each using randomly selected analyses, to calculate multiple grain size proxy values. The standard error of these experiments compared to the number of analyses in each experiment is used to determine the number of analyses required to produce an adequate grain size proxy. Finally, the amount of time required to collect an adequate number of analyses is compared to the Corescan acquisition rate of 3 minutes per metre.

Each microanalytical technique is discussed separately in Chapters 7 through 11 as outlined below:

- Chapter 7: Grain size assessment by portable X-ray fluorescence (pXRF) spectroscopy
- Chapter 8: Grain size assessment by microscopic X-ray fluorescence (μXRF) spectroscopy
- Chapter 9: Grain size assessment by laser ablation inductively coupled plasma mass spectrometry (LA-ICP-MS)
- Chapter 10: Grain size assessment by laser-induced breakdown spectroscopy (LIBS)
- Chapter 11: Grain size assessment by laser Raman spectroscopy.

Chapter 12 contains a discussion of the implications of the results and proposes future work to determine if these technologies can be up scaled and used to complement the current Corescan system in providing rapid copper sulphide and gold grain size proxies on the same interval as a typical assay (1 to 2 metres).

Chapter 7

Grain size assessment by portable X-ray fluorescence (pXRF) spectroscopy

7.1 Introduction

Portable X-ray fluorescence (pXRF) spectroscopy is a common analytical technique used in geological investigations. Studies characterising lithology, alteration, and mineralisation in ore deposits have utilised pXRF analysis to provide rapid chemical information in the field (Gazley et al., 2014; Gazley et al., 2011; Mauriohooho et al., 2016; Morris, 2009; Piercey and Devine, 2014). Environmental geology has also benefited from the use of this technology as a rapid, on-site screening tool for the selection of costly off-site laboratory test samples (Gazley et al., 2014; Parbhakar-Fox and Lottermoser, 2015). Recent technological advancements in high sensitivity silicon drift detectors, semi-conductors, and the miniaturisation of X-ray sources have given rise to portable XRF systems in recent years (Hall et al., 2014). This technique requires little to no sample preparation, is non-destructive, and can identify elements over a dynamic range of concentrations, from ppm to percent level (Innov-X, 2010). The system is capable of rapid data collection and conversion from raw counts to elemental concentrations. These features, combined with the field durability, light weight, and portability of the pXRF instrument make it a useful tool in field geological investigations.

The aim of this study was to investigate the potential for pXRF technology to be used in conjunction with the Corescan system to rapidly assess gold and copper sulphide grain sizes. Currently, the Corescan system collects data at a rate of 3 minutes per metre. The acquisition rates and analytical conditions for pXRF analysis are compared to this rate to determine how many pXRF analyses can be completed in the same amount of time and if these analyses provide adequate grain size assessment. To determine if pXRF can provide a fit for purpose grain size assessment, the gold and copper grades from pXRF data were compared to the grain sizes measured from MLA data.

The grain sizes of gold and copper sulphides present in a sample are indirectly related to the concentration of gold and copper in the pXRF analysis volume. In this study, the capability of pXRF analysis to determine gold and copper sulphide grain sizes was tested. Since the analysis window is larger than the typical grain size, indirect grain size proxy methods were used. Methods proposed by Berry and Hunt (2013) which are based on the principles of Cohen (1990) and Smee and Stanley (2005) were used to calculate grain size from the pXRF element concentrations. These methods were successful for gold; however, copper grain size calculations were not successful and this approach was not applied to copper sulphide minerals.

7.2 Scientific principles of pXRF technology

In XRF analysis, a sample is bombarded by an X-ray source causing some electrons to be elevated to a higher energy orbital position. This vacant orbital is then re-occupied when an electron from a higher energy moves down to fill the vacant space. This causes a cascade of electrons achieving lower energy positions until the atom reaches the original ground energy state. As electrons cascade from outer orbits to fill the empty orbital, X-ray energy equal to the difference between the two orbits is emitted (Figure 7.1). Since the energy gap between atomic orbits is different for each element, the energy given off during the electron transition is characteristic of that particular element. These changes in energy can be measured as an X-ray spectrum (Bertin, 1975; Jenkins, 1976).

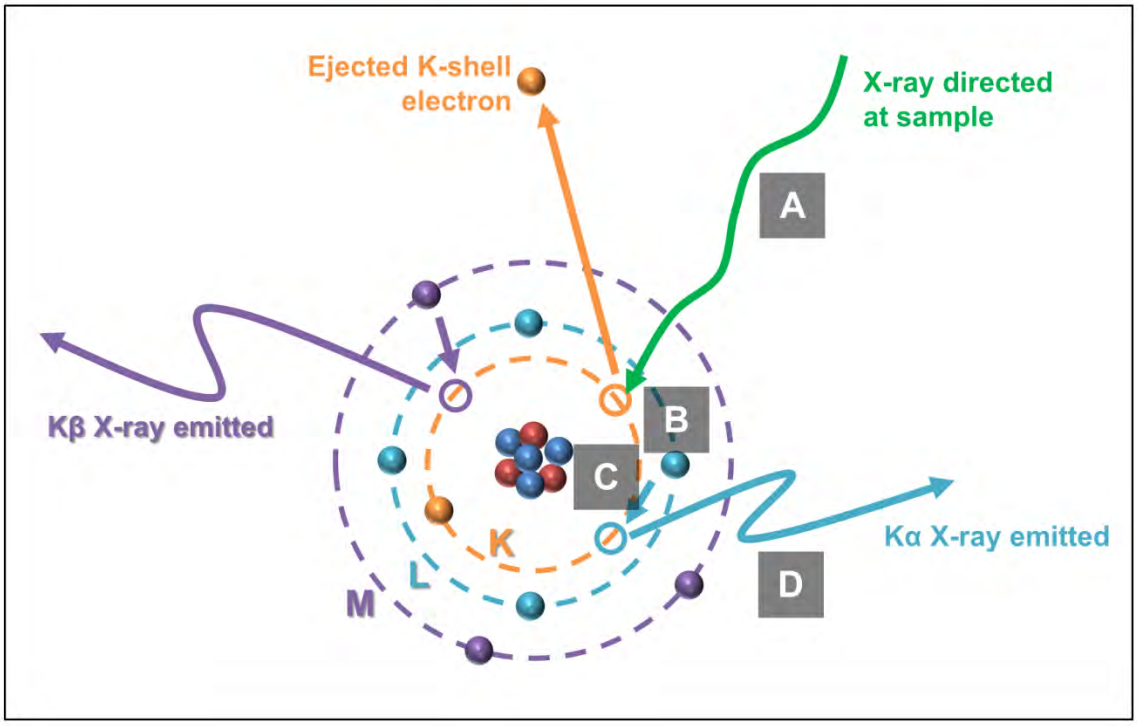

Figure 7.1. *Typical movement of energy within an atom during XRF analysis. X-rays are directed at the sample (A), an electron is ejected from its inner orbit (B) (K shell: 1s). An electron from a higher orbit (L or M shell) moves down to fill the vacant orbital position (C). The X-ray emitted during this transition (D) is characteristic of the element being analysed.*

Depending on which electron was ejected and which electron filled the vacancy, the energy will be different for atoms of the same element. For example, if a K-shell electron is ejected and replaced by an L-shell electron, the energy released produces a Kα X-ray. If a K-shell electron is replaced by an M-shell electron, the resulting energy is greater than that of the Kα, and gives rise to a Kβ X-ray photon (Figure 7.1) (Bertin, 1975; Jenkins, 1976).

7.3 Portable XRF instrument

Portable XRF systems are designed with a portable X-ray tube as the excitation source to bombard the sample with X-rays. A detector then measures the energy of the X-ray photons released by the atoms within the sample and a computer-based processing routine converts the X-ray spectrum to elemental concentrations. A schematic diagram of a typical μXRF system design is shown in Figure 7.2. This technique is non-destructive and can be used to quantify a range of elements, but is particularly suited to higher atomic number elements (e.g. calcium, atomic number = 20, and above). Copper has a diagnostic Kα peak at 8.046 keV with a minor Kβ peak at 8.910 keV. Gold has two diagnostic peaks at

9.713 keV (Lα) and 11.440 keV (Lβ). Figures 7.3 and 7.4 show reference XRF spectra for pure copper and pure gold, respectively.

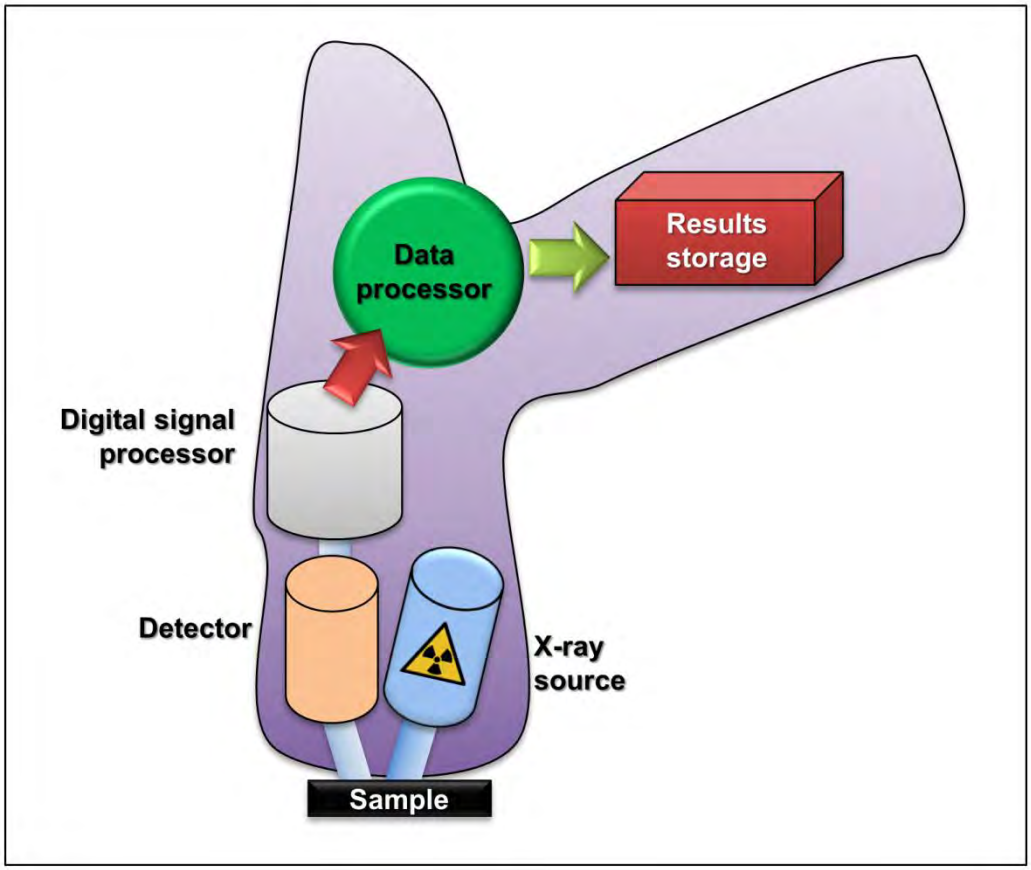

Figure 7.2. *Schematic design of a typical pXRF instrument setup.*

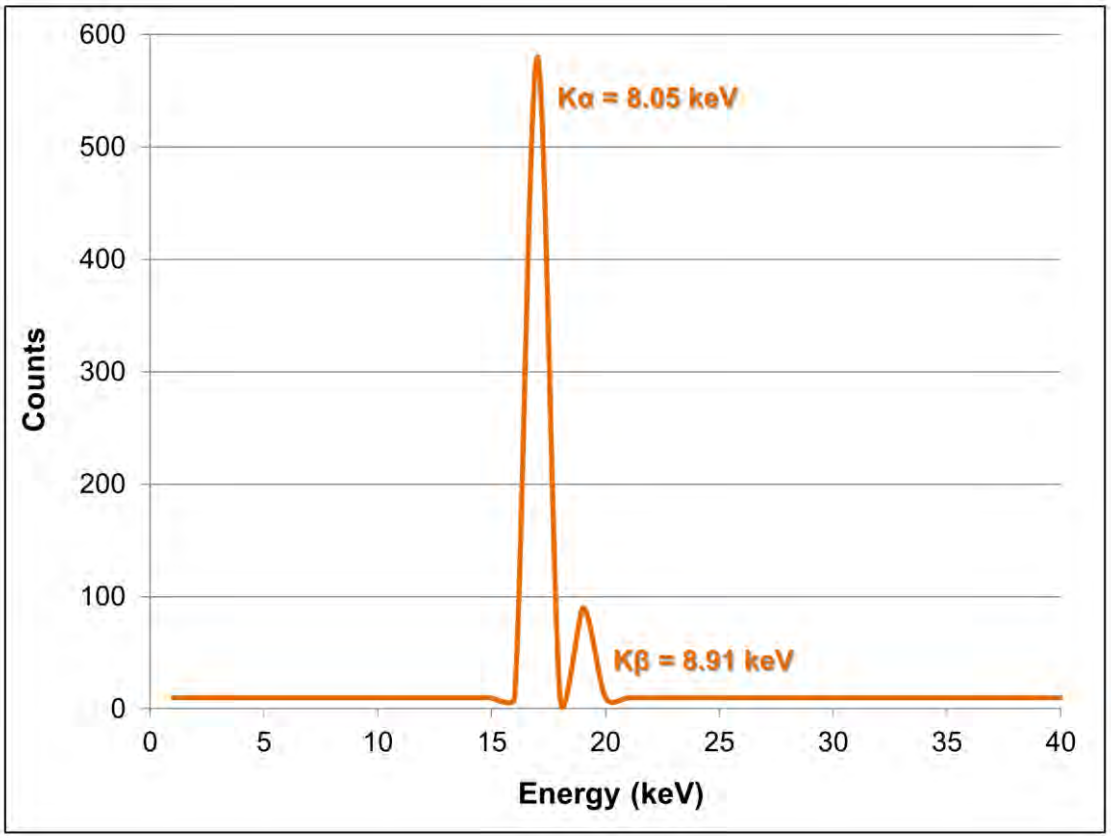

Figure 7.3. *XRF spectra for pure copper from Henke et al. (1993).*

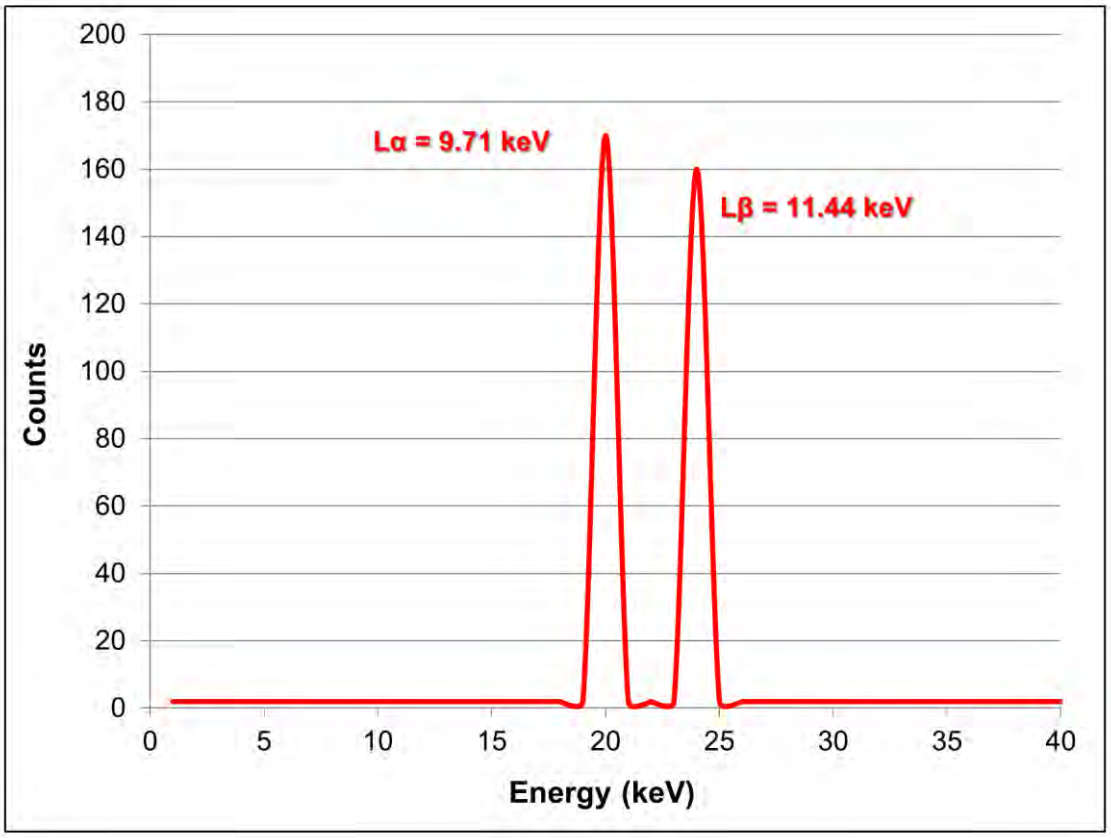

Figure 7.4. *XRF spectra for pure (99.9% fineness) gold from Henke et al. (1993).*

While it did not appear to affect the gold analyses in this study, it should be noted that lead has a Lα peak at 10.5 keV that can interfere with the Lα energy of gold at 9.7 keV. Since the test samples contained very little lead, this was not a factor for this study, but these types of interferences should be carefully considered when analysing gold by pXRF.

7.4 Data collection methodology

The twenty-six samples in the test set were previously analysed by pXRF as part of the AMIRA P843A GeM project in 2011. This data was used in the study outlined here. Copper and gold concentrations were measured using an Innov-X Premium Delta DP-6000 handheld XRF with a rhodium tube as the X-ray source. The irradiated area for this instrument was measured by incrementally moving the pXRF analysis window across a piece of steel fused to aluminium until the steel could be detected by the pXRF. These experiments showed that the Innov-X pXRF used in this study has an effective scan area of 33 mm^2 per spot. X-ray absorption spectra were collected between 8 keV and 40 keV using scanning mode. Each spot was analysed for 2 minutes with reported detection limits of 5 ppm for gold and 10 ppm for copper. The data was processed through the Innov-X software using "soil mode" which includes a background correction for solid samples and converts absorption values to elemental concentrations (Innov-X, 2010). Each of the 3 cm by 3 cm tile-shaped samples were analysed (Figure 7.5). Both the polished and unpolished sides of each sample were analysed using nine spots, for a total of eighteen pXRF analyses per sample.

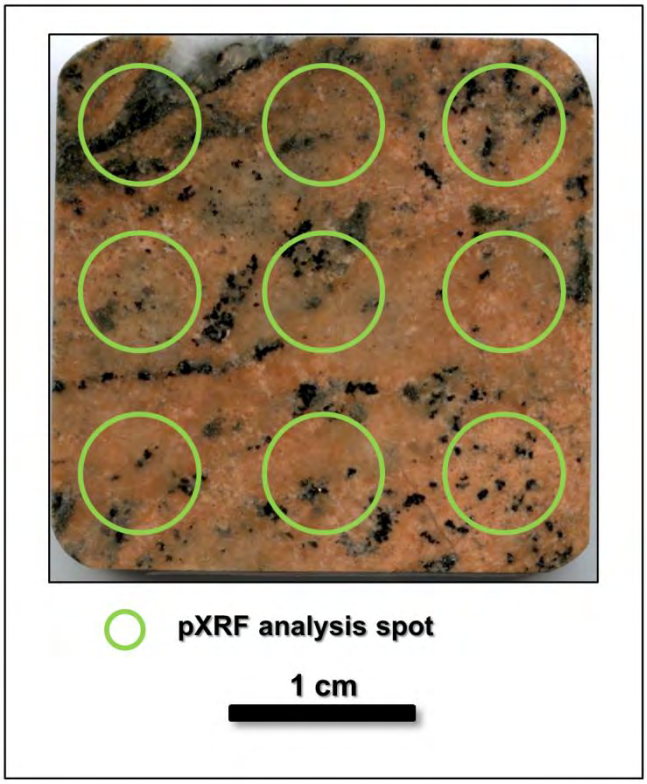

Figure 7.5. *Configuration of pXRF analysis spots on each test sample. Nine analyses were completed on each side, for a total of eighteen pXRF analyses per sample.*

7.5 Grain size proxy calculations

Since the gold and copper sulphide grain sizes present in the test samples are much smaller than the 33 mm^2 diameter spot size of the pXRF, direct detection of the individual grains by pXRF is not possible. Instead, the reported gold and copper values are compared to the pXRF analysis volume and used as an indirect proxy for grain size. The details of these proxy calculations and assumptions used are outlined in section 7.5.1 for gold and section 7.5.2 for copper.

7.5.1 Indirect gold grain size calculations

The indirect grain size calculation methods proposed by Berry and Hunt (2013) (and discussed in detail in section 6.7) were used to calculate gold grain size from the pXRF gold concentrations. These methods are based on the principles of Cohen (1990) and Smee and Stanley (2005) suggesting that gold nugget size is the primary reason for poor reproducibility in gold analyses. The variability of multiple pXRF gold analyses on the same sample can thus be used as a measure of free gold assuming a single dominant grain size. Cohen modelled this system using the binomial distribution while Smee and Stanley (2005) argued the

Poisson distribution was a better model for rare gold grains. Berry and Hunt (2011) reported that the binomial and Poisson methods yield almost identical grain size estimates. The difference between the two calculated values in this study was less than 30% for gold. The binomial method calculations for gold provide slightly higher correlation coefficients than the Poisson method, so only the binomial results will be presented here.

Assuming that all gold within a sample is distributed in a single dominant grain size and the distribution of these grains follows a binomial distribution, grain size proxies for gold can be calculated. The calculations involve using the arithmetic mean and standard deviation of multiple pXRF gold analyses of the same sample. The analysis volume, the density of gold, and the density of the rock itself are required. The assumptions used in the indirect grain size calculations for gold are outlined in Table 7.1. The mathematical calculations used for gold grain size assessment assuming a binomial distribution based on the principles of Cohen (1990) are included in Appendix O.

Table 7.1. *Assumptions used to calculate gold grain sizes by the binomial methods of Cohen (1990).*

Assumptions for pXRF Gold Data	
Spot diameter	6.5 mm
Spot radius	3.3 mm
Penetration depth	100 μm
Density gold	17 gm/cm^3
Density rock	2.7 gm/cm^3

Assuming a penetration depth of 100 μm for gold, each 33 mm^2 pXRF analysis measures an equivalent of approximately 8 mg of sample material. Eighteen analyses on each sample equates to 144 mg, while nine analyses equates to 72 mg, well below the typical fire assay for gold completed on a 40-50 g sample. Because of this, the eighteen pXRF analyses taken on each sample may not adequately represent the grain size trends within the sample, and would provide poor sampling statistics. To address this, multiple samples were grouped together by down hole location to determine how many pXRF analyses are required to adequately assess grain size. Dividing the test sample set into 3 groups (153 analyses) and 2 groups (234 analyses) greatly improves the sampling statistics.

7.5.2 Indirect copper sulphide grain size calculations

For copper, a 50 μm penetration depth was assumed since the energy of copper is approximately 8 keV and the escape depth of copper is less than that of gold (~10 keV). A 50 μm penetration depth means that each pXRF analysis represents approximately 4 mg of material, well below the typical ICP-MS analysis completed on a sample weighing less than 1 g. The 33 mm^2 analysis spot size of the pXRF is too large to detect the variability in copper values related to copper sulphide grain sizes in the test sample set. Comparing the calculated grain sizes from pXRF and the MLA results show that the approach consistently overestimates copper sulphide grain sizes, in some cases, by an order of magnitude. The D_{PSSL} values for chalcopyrite and combined copper sulphide grains measured from MLA are typically 50 μm or less. The binomial methods of Cohen (1990) use the standard deviation of multiple analyses to calculate an effective grain size. Assuming the pXRF spots average 0.25% copper, a standard deviation of 0.05 would be expected due to sampling error assuming a 50 μm copper sulphide grain size. Smee and Stanley (2005) indicated that 15-20% variability in multiple analyses is expected from other analytical errors not related to the grain size. In addition the model used here assumes randomly distributed grains. Many of the copper sulphide grains are in clusters of smaller grains, especially in small veins (Figure 7.6). This will lead to an overestimate of the dominant grain size when using bulk analysis methods.

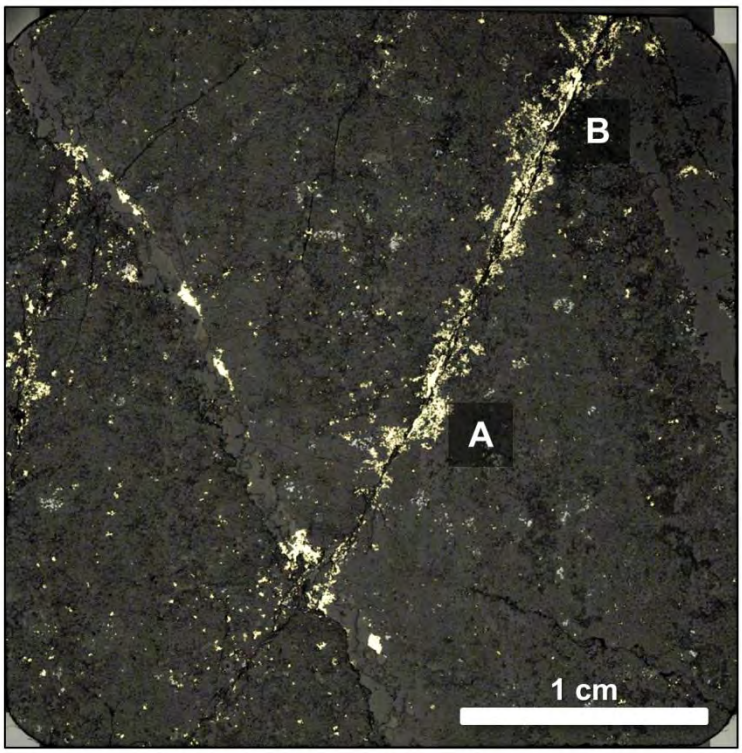

Figure 7.6. *Reflected light image of sample 1380.5 from the test sample set. Example of copper sulphide grains occurring as clusters of smaller grains (A) and small veins (B).*

The variability of multiple pXRF copper analyses is dominated by analytical errors and natural variability. The analyses cannot be used to recognise the grain size of copper minerals near the 50 μm diameter required. The statistics are improved if a smaller volume is analyses at each spot. However, this limitation could not be overcome using the pXRF data collected, so copper sulphide grain sizes were not assessed using pXRF data in this study.

7.6 Gold grain size proxy results

Using the gold results of pXRF analysis and the variability of multiple analyses on each sample as a proxy for grain size, the methods proposed by Berry and Hunt (2013) were used to calculate the grain size proxies from the eighteen pXRF analyses for each sample assuming a binomial distribution. The grain size proxy values calculated from pXRF data for gold are shown in Table 7.2. The D_{PSSL} of gold measured from MLA analysis was compared to the calculated grain size proxies using all eighteen pXRF analyses for each sample. A scatterplot of these comparisons are shown in Figure 7.7.

Table 7.2. *Grain size proxies calculated from pXRF gold values using the binomial methods based on principles from Cohen (1990) compared to the measured gold grain D_{PSSL} from MLA for each sample in the test set.*

Sample	D_{PSSL} from MLA (µm)	Calculated D_{PSSL} Grain Size Proxy (µm)
1185.0	17	14
1193.0	2	16
1207.0	1	-
1265.5	10	-
1269.0	-	-
1283.0	14	16
1283.5	6	16
1292.5	8	15
1306.5	5	-
1307.5	-	-
1356.5	14	13
1362.7	-	15
1380.5	5	16
1381.0	-	-
1392.5	10	21
1393.0	-	-
1400.5	13	22
1401.0	27	22
1409.0	3	-
1420.0	18	17
1420.5	-	-
1421.0	3	15
1431.0	4	-
1431.5	2	-
1448.5	5	24
1461.5	5	-

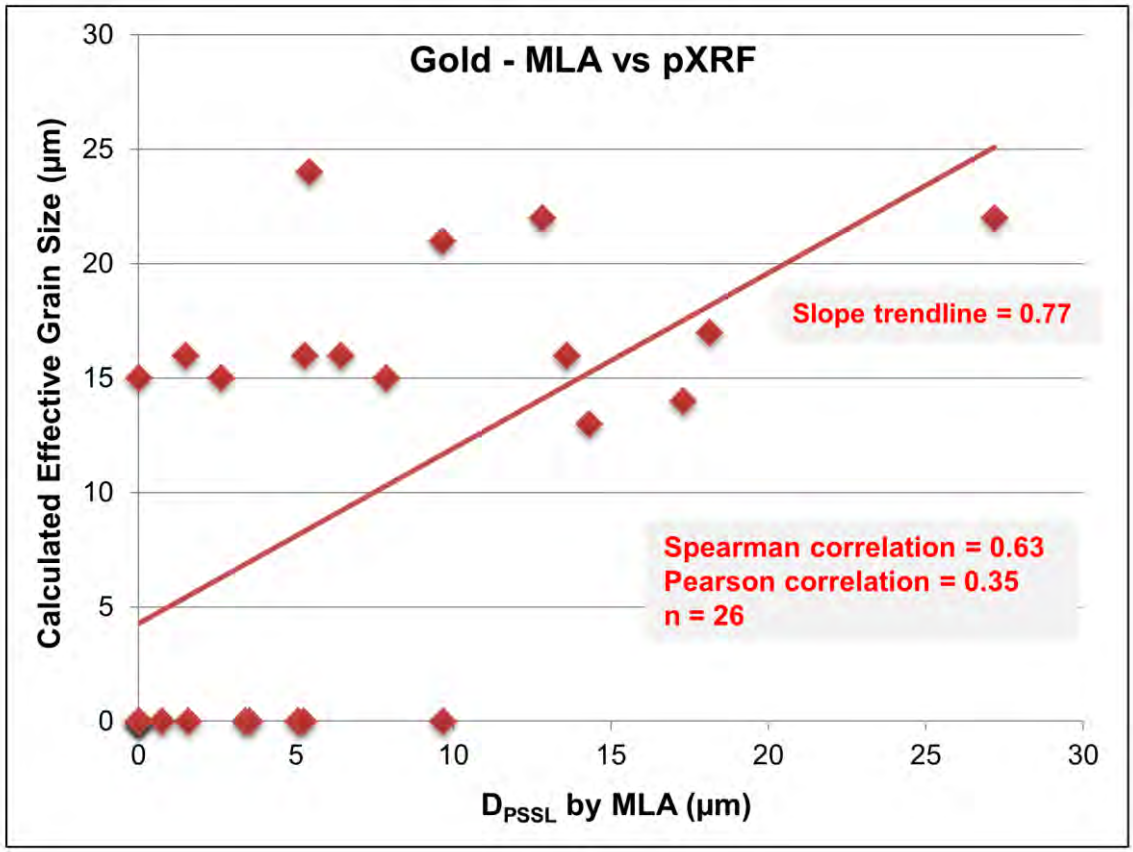

Figure 7.7. *Comparison of the* D_{PSSL} *for gold measured from MLA data and the grain size calculated using the binomial methods of Cohen (1990) for each of the twenty-six samples in the test set.*

By grouping multiple samples, the sampling statistics are greatly improved. The calculated and measured gold grain values for the twenty-six test samples were combined into 4, 3, and 2 groups by down hole location. These groupings provide a grain size estimate based on 112 pXRF analyses (4 groups), 156 pXRF analyses (3 groups) and 234 pXRF analyses (2 groups), equivalent to 0.9 g, 1.3 g, and 1.8 g samples, respectively. The combined D_{PSSL} of gold measured from MLA analysis was compared to the combined calculated grain size proxies from pXRF for each group. It should be noted that not all of the samples in the test set contain gold, and many of the pXRF analyses for gold returned a value below detection. For the grouping by MLA, all samples where no gold was detected by MLA were grouped together, even though this causes some groups to have more samples, and therefore more pXRF analyses, than others. A table of these comparisons and the calculated Pearson and Spearman correlation coefficients for grouping by down hole location is shown in Table 7.3.

Table 7.3. *Comparison of the D_{PSSL} for gold measured from MLA data and the grain size calculated using the binomial methods of Cohen (1990) (assuming binomial distribution) for samples grouped by down hole location.*

Grouping Criteria	Number Groups	Samples in Group	Pearson Correlation Coefficient (R^2)	Spearman Ranking Correlation Coefficient (r_s)
Down Hole Location	4	1185.0 – 1283.0	0.28	0.4
		1283.5 – 1362.7		
		1380.5 – 1409.0		
		1420.0 – 1461.5		
	3	1185.0 – 1292.5	0.4	0.5
		1306.5 – 1400.5		
		1401.0 – 1461.5		
	2	1185.0 – 1380.5	-	1
		1381.0 – 1461.5		

By comparing the average number of analyses to the Spearman and Pearson correlation coefficients, the performance of the grain size proxy as the number of analyses increases can be tracked. These results show that for all groups with more than 156 pXRF analyses, a Spearman ranking coefficient of r_s = 1.00 is produced for gold (Figure 7.8).

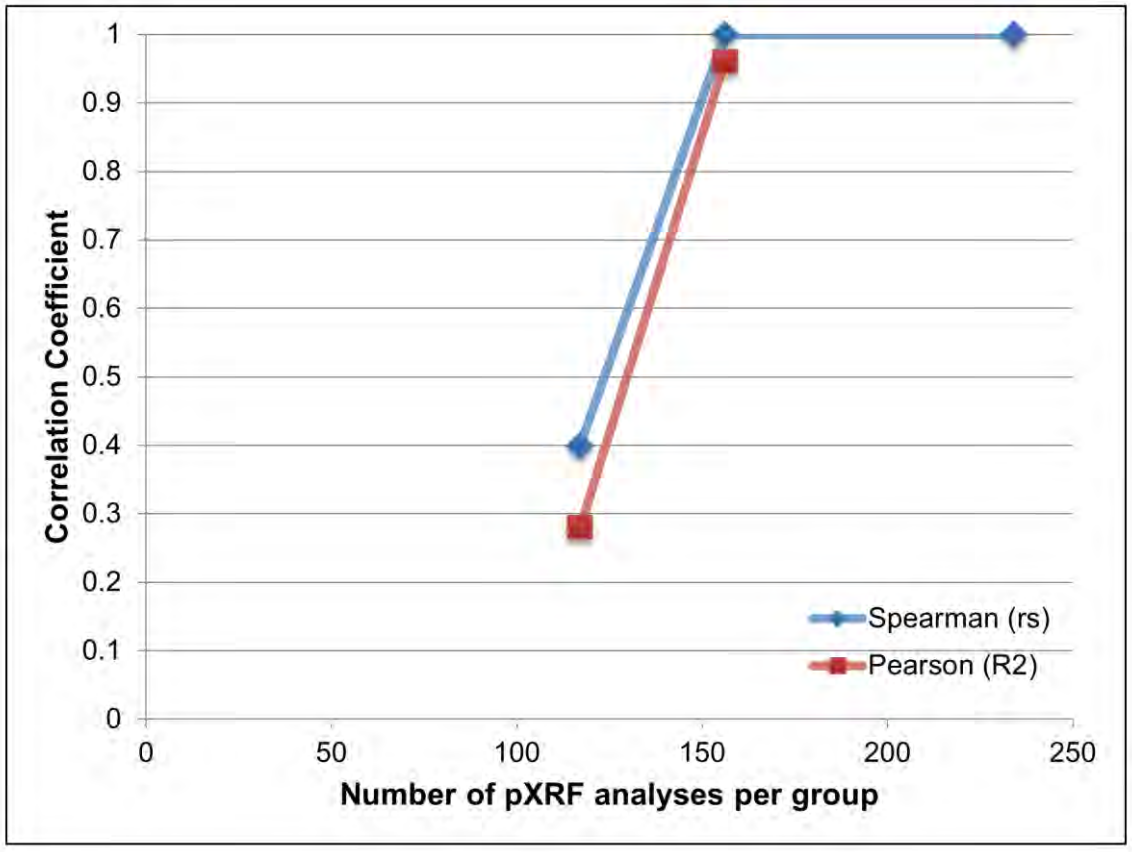

Figure 7.8. *Comparison of the average number of analyses per group compared to the Spearman and Pearson correlation coefficients for all grouped gold data. This trend shows that at least 156 pXRF analyses are required to adequately assess gold grain sizes.*

7.7 Discussion

For gold, the methods proposed by Berry and Hunt (2013) for calculating grain size proxies were used to determine the grain size of each sample using pXRF gold values. For these calculations, the gold grain size was assumed to be constant and the probability controlling the inclusion of gold grains in the analysed volume was assumed to be binomial. The grain sizes calculated by the binomial method show a poor correlation with the measured D_{PSSL} values from MLA on a sample by sample basis. The gold results, while within 10 μm of the measured MLA values, return a Pearson correlation coefficient value of $R^2 = 0.35$ with a slightly better Spearman coefficient of $r_s = 0.63$. The ability of the MLA to detect smaller gold grain sizes than the pXRF means that the calculated distribution is truncated and this affects the correlation value.

With eighteen analyses per sample, each sample is being represented to the equivalent of a 150 mg sample. This value is well below the 40-50 g sample weight typically used in a fire assay to assess gold. Berry and Hunt (2011)

determined that gold grain population statistics only become meaningful when at least 50 gold grains are included in the D_{PSSL} calculation (section 6.5.3). Only two of the samples in the test sample set contain more than 50 gold grains, so most of the D_{PSSL} values from MLA on a sample by sample basis are not adequately representing the gold grain size population. The poor correlation between the pXRF and MLA grain sizes reflects this challenge with population statistics and demonstrates that this sample size is not sufficient for reliable measurement using these techniques. The correlation between MLA results and grain sizes calculated from pXRF data using the binomial method improves when samples are combined to increase the number of analyses and the number of grains recognised by MLA. By grouping multiple test samples, both the number of analyses and gold grains measured by MLA were increased. These experiments show that for adequate gold grain size assessment, at least 156 pXRF analyses (equivalent to a 1.3 g sample) are required.

Some key considerations in using pXRF need to be addressed when applying indirect grain size proxies. First, for both gold and copper sulphide minerals, the MLA is a surface measurement technique while the pXRF measures a sample volume. It is possible that the pXRF is detecting gold and copper mineral grains that are just below the surface that would not be detectable by MLA surface analysis. Additionally, MLA analysis was completed on the entire polished sample surface (9 cm^2), and the eighteen pXRF analyses have a total analysis area of 5.9 cm^2. With respect to gold, only 400 gold grains were detected in all twenty-six samples meaning that less than two grains of gold were detected per square centimetre. Since the scan area of the pXRF is significantly lower than that of the MLA, the likelihood of encountering gold grains is greatly decreased causing challenges with sampling statistics. The 400 gold grains detected by MLA may not adequately represent the gold grain populations contained in the samples causing additional challenges when comparing the pXRF data to the MLA surface analysis grain size data.

7.8 Conclusions

While the test data set used in this study is small, the results show that increasing the number of pXRF analyses on a combined sample group greatly improves the ability to characterise gold grain sizes by indirect proxies. Using the average and standard deviation of at least 156 pXRF gold analyses produces a good proxy for

gold grain size when compared to the gold grain size obtained using MLA. While pXRF analysis rates have improved beyond the system used in this study, an analytical time of 30 seconds per spot would still be too slow. At this rate, a representative data set for a single point gold grain size proxy could be acquired in 78 minutes. It is unlikely that this rate is economic in any realistic environment. Due to the large spot size of the pXRF the grain size effect on copper assay variance is too small to be detected above other sources of variability. There are pXRF systems currently available with a much smaller irradiation area (down to a 1 mm spot size), but these were not compared in this study.

The objective of this study was to investigate the potential for pXRF technology to be used in conjunction with Corescan analysis to rapidly and adequately assess copper sulphide and gold grain sizes. Specifically, the number of pXRF analyses required to adequately assess grain size was tested and compared to the number of pXRF analyses achievable within the Corescan data acquisition rate of 3 minutes per metre. The pXRF system collects bulk elemental data over an analysis spot measuring approximately 33 mm^2 in two minutes. At this rate, a single point gold grain size proxy from 180 pXRF analyses could be acquired in 90 minutes. This analysis rate is far too slow when compared to the Corescan system. The resolution and analysis time of this technique using the Innov-X Premium Delta DP-6000 pXRF system is not capable of assessing detailed gold and copper sulphide grain sizes.

COX Analytical Systems has developed a drill core XRF scanning system called the Itrax Drillcore Scanner with a data acquisition rate of one step per second. Steps can be adjusted from 200 μm to 1 cm, depending on the required resolution (COX Analytical Systems, 2014). Huang et al. (2016) tested this system to compare the analytical results from multiple Itrax analyses using various analysis times. The results of this study suggest that 1 second is sufficient time for XRF analysis in this environment and saw no improvement in lead analytical results at 15 to 170 ppm from 1 to 100 seconds analysis time. At 1 second analysis time and a required acquisition speed of 3 minutes per metre, the step size required is about 3 mm. The Itrax sample area is 0.2 mm wide which gives an analytical area of 0.6 mm^2. This area is much smaller than the 33 mm^2 area of the pXRF system, and may be able to provide enough variability in copper results to calculate copper sulphide grain sizes using the methods outlined here. This technology operates at a rate close to that required to keep up with the Corescan acquisition

rate and would require minimal changes to be integrated into the existing Corescan system. Using the Itrax technology, the methods outlined here could be used to ascertain early gold grain size information from drill core using a non-destructive analysis method that could scan all mineralised drill core at a practical speed.

Chapter 8

Grain size assessment by microscopic X-ray fluorescence (μXRF) spectroscopy

8.1 Introduction

Recent technological advancements in microscopic X-ray fluorescence (μXRF) spectroscopy have allowed for the conventional XRF analysis methods to be applied at a much higher resolution. Unlike conventional XRF methods, μXRF uses optic fibres to focus the excitation beam on a small spot on the sample surface. This focused beam allows for very small portions of the sample to be analysed independently, reducing the number of minerals that interact with the X-rays and providing simpler X-ray spectra. Micro-XRF spectroscopy has recently been applied to a number of geological investigations, primarily for elemental and mineralogical studies of rock samples (Behrends and Kleingeld, 2009; Buehn et al., 1999; Flude et al., 2017; Jackson et al., 2018; Janssens et al., 2000). This technique is attractive as it is relatively low cost, simple to operate, and requires little to no sample preparation (Behrends and Kleingeld, 2009).

The aim of this study was to investigate the potential for μXRF technology to be used in conjunction with Corescan analysis to rapidly and adequately assess copper sulphide and gold grain sizes. To match the current Corescan acquisition rates, data would need to be collected at a rate of 3 minutes per metre of drill core. Here, we compare the acquisition rates and analytical conditions of μXRF analysis to those of the Corescan system.

Micro-XRF analysis is an *in situ* technique that measures elemental concentrations on small, discrete portions of the sample. The concentrations of copper and gold present in each μXRF analysis reflect the size of copper and gold grains present in the spot. This can be used to develop proxies for copper and gold grain sizes using elemental values from μXRF. Grain size estimates using the expected proportion of elements present in a given spot were used to calculate grain size proxies from μXRF data. To assess if μXRF can provide adequate grain size assessment, the results of copper sulphide and gold grain size proxies using μXRF data are compared to the grain sizes measured from MLA data. A series of bootstrapping experiments where completed to determine

the minimum number of μXRF analyses required to produce a representative grain size proxy result. The number of μXRF analyses required for adequate grain size assessment and the rate at which these analyses are acquired are compared to the data collection rate of the Corescan system.

8.2 Scientific principles of μXRF technology

Like conventional and pXRF analysis, μXRF uses an X-ray source to bombard the sample surface causing electrons to be elevated to higher energies in the orbital shells. The movement of an electron to fill the resulting vacancy causes a characteristic energy to be emitted which can then be used to quantify the elements present in the sample (see section 7.2 for more detail) (Bertin, 1975; Jenkins, 1976). While conventional and pXRF systems typically have an analysis spot size ranging from 1 to 10 millimetres, μXRF uses specialised optics to focus the X-ray beam resulting in spot size of 25 to 1000 μm. This reduced spot size allows for higher spatial resolution of elemental concentrations. The smaller spot size also decreases the number of minerals interacting with the X-rays in a single spot providing cleaner, less-mixed X-ray spectra. The technique is non-destructive and can be used to quantify a range of elements. Micro-XRF is better suited to lighter elements than pXRF and can detect elements with atomic masses as low as 22 (sodium) with detection limits less than 100 ppm (Bruker, 2015a). Figure 8.1 shows the typical limits of detection for μXRF over a range of atomic masses. Copper has a diagnostic Kα peak at 8.046 keV with a minor Kβ peak at 8.91 keV, while gold has two diagnostic peaks at 9.713 keV (Lα) and 11.44 keV (Lβ).

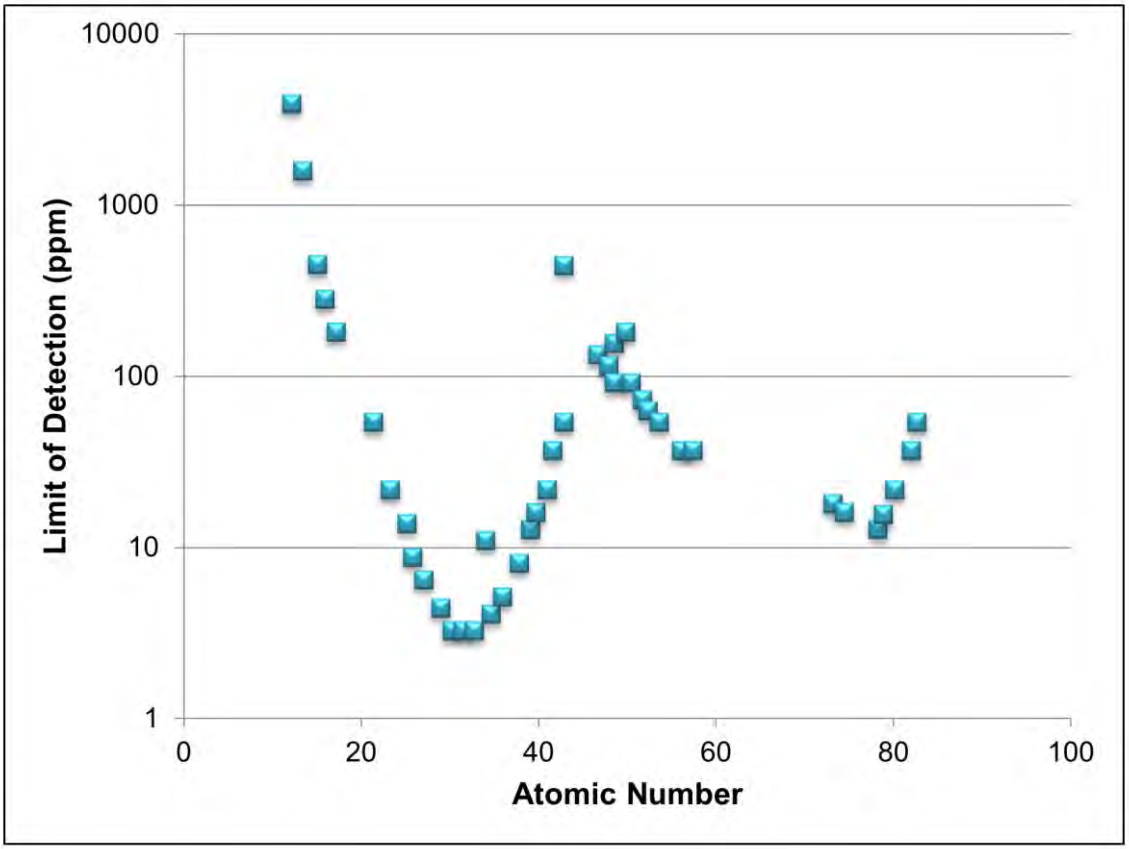

Figure 8.1. *Typical limits of detection for μXRF analysis over a range of atomic masses. Diagram modified from Bruker (2015a).*

8.3 Micro-XRF instrument

The instrumentation that comprises a μXRF system includes an X-ray source, specialised focusing optics, silicon drift detector (SDD) attached to an X-ray spectrometer, a specialised stage that records the coordinates of the analysis locations, and a computer interface system for programming and data processing (Behrends and Kleingeld, 2009). A schematic diagram of a typical μXRF system design is shown in Figure 8.2.

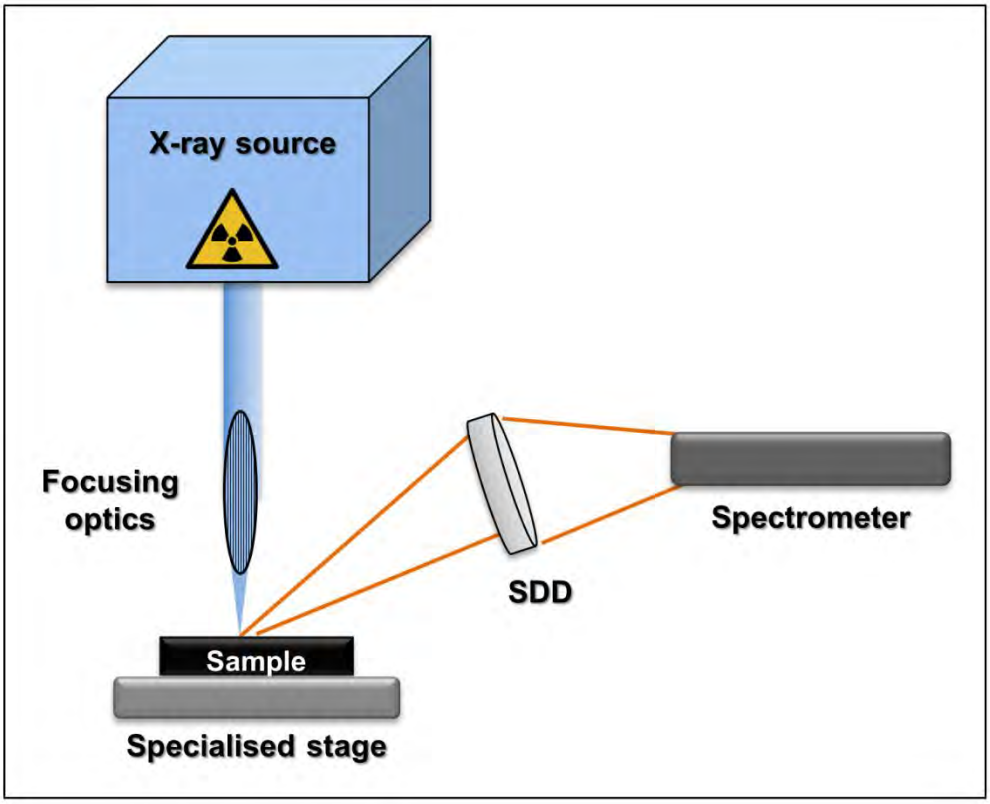

Figure 8.2. *Schematic design of a typical μXRF instrument setup.*

8.4 Data collection methodology

The twenty-six samples in the test set were analysed by μXRF using a Bruker M4 Tornado benchtop μXRF spectrometer at CSIRO's Advanced Characterisation Facility in Kensington, Western Australia. This system uses a rhodium X-ray tube as the source, with an acceleration voltage of 50 keV at 500 mA coupled with a Bruker Nano silicon drift detector operating at 100 to 150 kcps (Bruker, 2015). The irradiated area for this instrument was set to a nominal 35 μm spot size, but was measured by the research group at CSIRO to be closer to 40 μm in diameter, so a 50 μm step size was used (M. Pearce, written communication, 2016). Each spot was analysed for 5 milliseconds. The data was processed with the Bruker M4 TORNADO software ESPRIT using the oxide routine which acknowledges that most elements in rock samples occur in silicates rather than as individual elements (Bruker, 2015a). This software includes background correction for solid samples, elemental deconvolution to separate overlapping elemental energies, and conversion of X-ray counts to elemental concentrations (Bruker, 2015a). Each of the 3 cm by 3 cm samples were covered with a 2.5 cm by 2.5 cm μXRF mapping area for a total of 250,000 μXRF spots per sample. Element concentration maps for each sample were produced (Figure 8.3). The abundance

of each element within each analysis pixel was exported and used in the grain size proxy calculations.

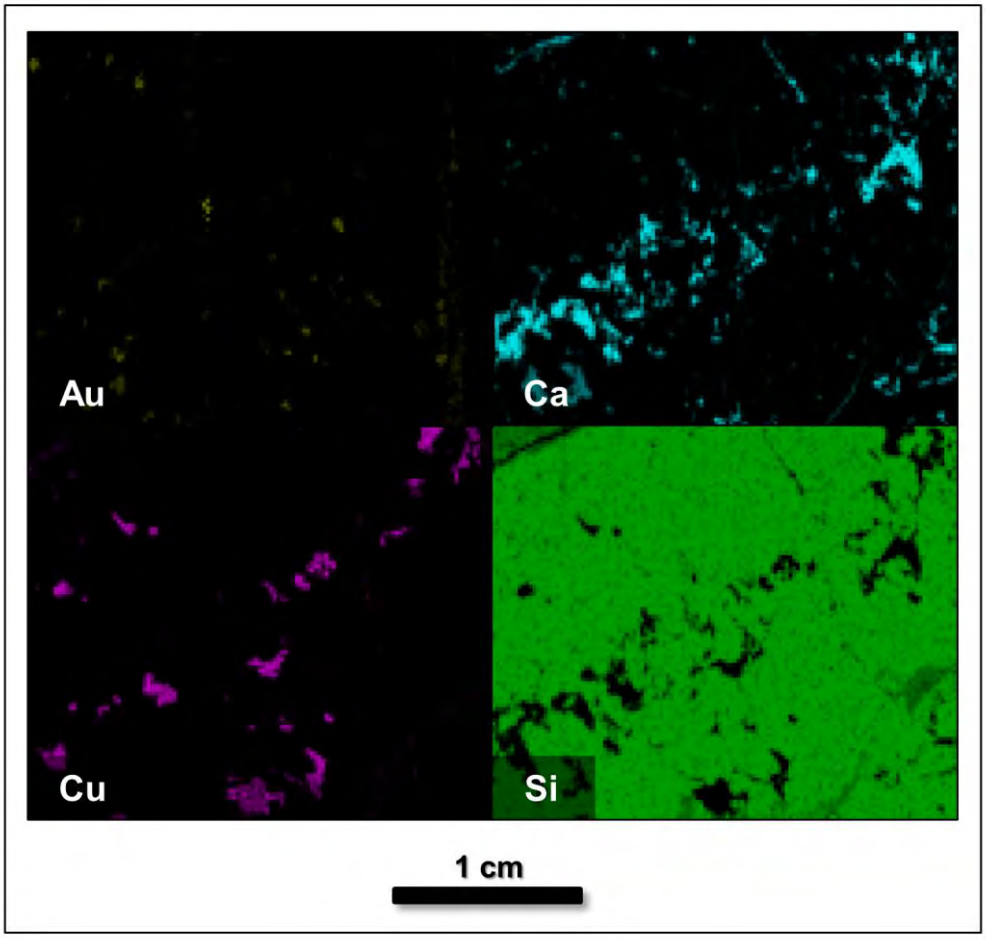

Figure 8.3. *Example of a series of elemental abundance maps produced from the μXRF data by the Bruker M4 TORNADO software ESPRIT.*

8.4.1 Combining μXRF analysis pixels

While the μXRF captures data at 40 μm spots with a 50 μm step size, the highest counts produced for a single spot in 5 milliseconds are relatively low (less than 500), producing inconsistent gold and copper elemental results. To address this, the μXRF data was binned so that X-ray spectra from neighbouring spots were combined to increase the total X-ray counts. The average weight percent of each element for all pixels within a subset of four samples was then compared. A test of different binning resolutions determined that 4 pixels by 4 pixels produced consistent elemental results while minimising the analysis spot size (Figure 8.4). This binning was used to quantify the elemental concentrations for the test samples. This binning increased the counts to over 3,500, increased the spot area

to 1257 μm², and decreased the number of pixels per sample to 15,625. Since the irradiated area of each spot is 40 μm in diameter, the total irradiated area for the binned pixels is a circle approximately 160 μm in diameter (Figure 8.5).

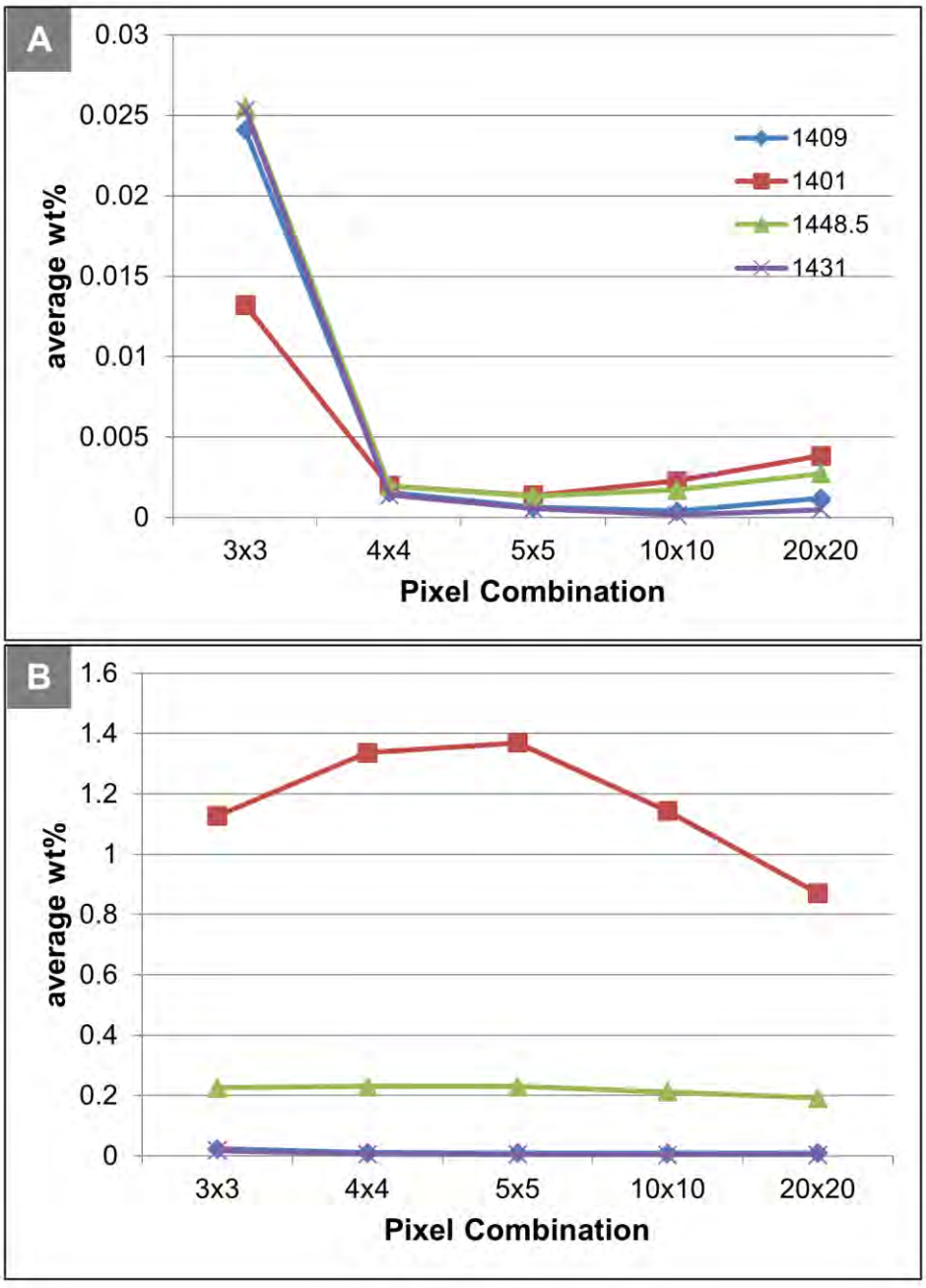

Figure 8.4. *Comparison of different pixel bin options for a subset of four samples from the test set for gold (A) and copper (B). At a 4 pixel by 4 pixel bin combination, copper and gold show a levelling off trend. Binning of 4 pixels by 4 pixels was used in this study.*

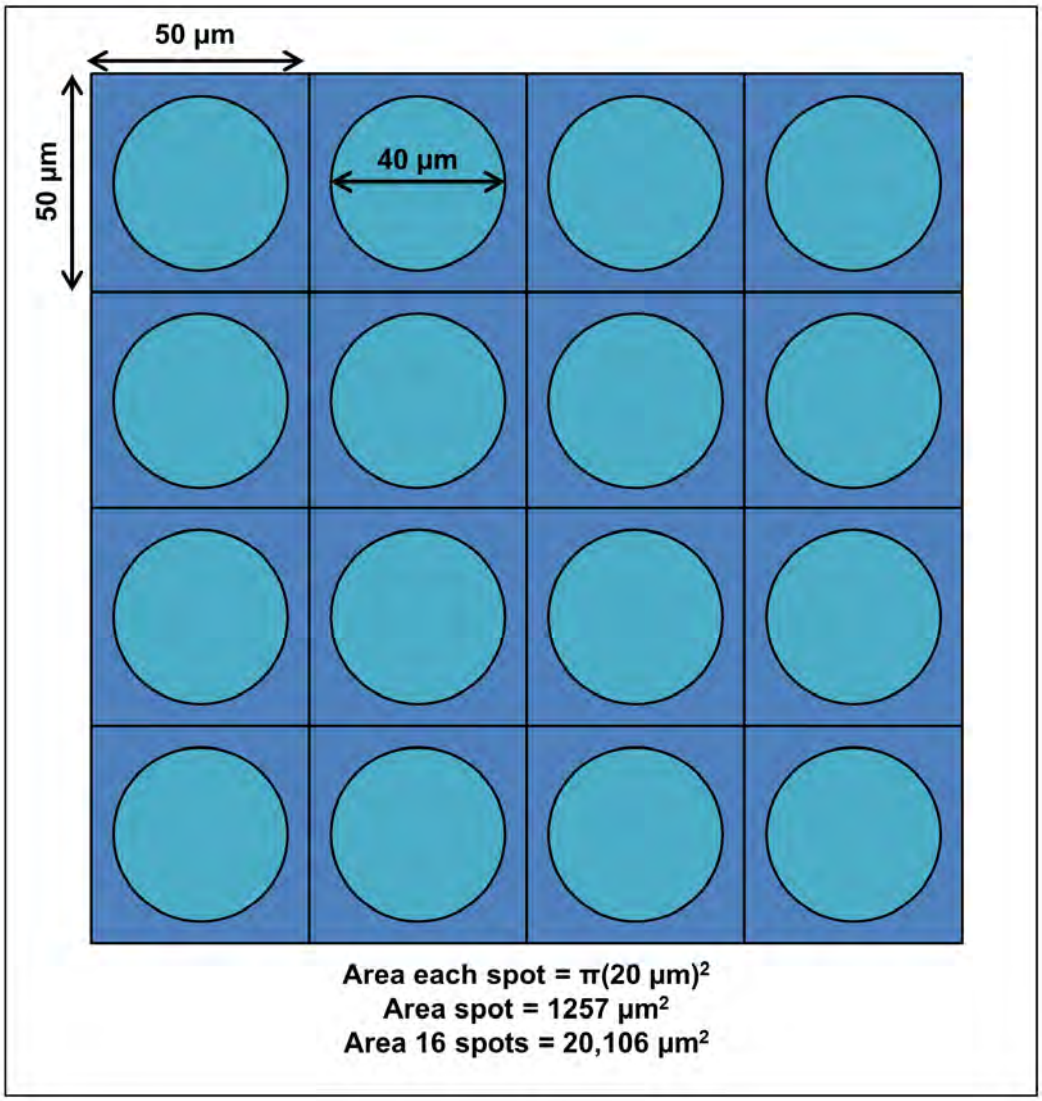

Figure 8.5. *Irradiated area for 4x4 binned μXRF pixels.*

8.4.2 Correction of μXRF gold values

A review of the gold concentration values shows that the quantification process produces inflated gold values. The inflated gold results may be caused by peak interferences between the lead Lα peak at 10.5 keV and the Lα energy of gold at 9.7 keV, but the exact cause was not investigated in detail. In order to ensure that these inflated values did not compromise the gold grain size proxy calculations, 1,500 ppm gold was subtracted from each analysis containing over 1,500 ppm gold prior to each grain size proxy calculation. This correction was required to bring the average grade of gold across all tiles to 0.3 ppm, the average calculated gold assay from MLA analysis for the samples. If this analysis is to be up scaled and included as part of the Corescan system, the background values for the gold Lβ 11.44 keV peak need to be further calibrated.

8.5 Grain size proxy calculations

Elemental concentrations of copper and gold from μXRF were used to determine if this technology is a viable option for online, rapid grain size assessment. Since most of the gold and copper grains are much smaller than the 160 μm binned spot size, a single spot could contain a number of different mineral grains. No attempt was made to distinguish between chalcopyrite and bornite grains. The grain size proxy calculations were completed assuming that copper is contained in combined copper sulphides (50% chalcopyrite and 50% bornite).

8.5.1 Assumptions for grain size proxy calculations

Unlike the pXRF analysis which provides elemental concentrations over a large analysis spot (>30 mm^2), the smaller spot size of the μXRF (0.0013 mm^2) allows the system to better detect elemental changes across a sample surface, improving the opportunity to capture gold and copper element concentrations at a scale comparable to the grain size. Grain size estimates using the expected proportion of elements present in a given spot were used to calculate grain size proxies from μXRF data. For this method, assumptions about the μXRF spot size, penetration depth, and density of both the mineral of interest and the rock mass are required (Table 8.1 and 8.2). The penetration depths of 100 μm for gold and 50 μm for copper were selected by determining the source depth at which 60% of the cumulative X-rays were detected assuming a rock attenuation equivalent to potassium feldspar (a primary rock-forming mineral for the test samples; Figures 8.6 and 8.7).

Table 8.1. *Assumptions used to calculate gold grain size proxies.*

Assumptions for μXRF Gold Data	
Binned spot diameter	160 μm
Effective analysis radius	80 μm
Penetration depth	100 μm
Density gold	17 gm/cm^3
Density rock	2.7 gm/cm^3

Table 8.2. *Assumptions used to calculate combined copper sulphide grain size proxies.*

Assumptions for μXRF Copper Data	
Binned spot diameter	160 μm
Effective analysis radius	80 μm
Penetration depth	50 μm
Density rock	2.7 gm/cm^3
Density 50/50 combined copper sulphides	4.5 gm/cm^3
Expected Cu in 50/50 combined copper sulphides	49.0%

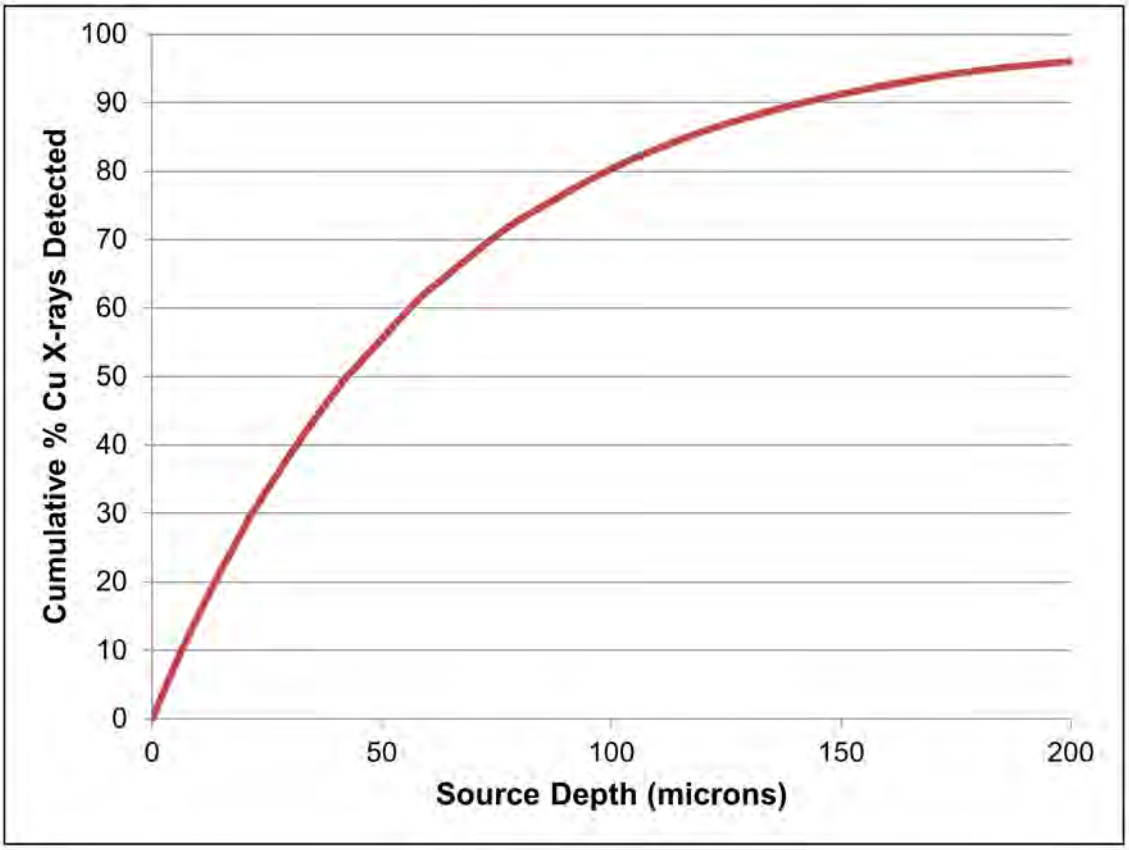

Figure 8.6. *Calculated source depth of characteristic copper X-rays from a Rh tube at 50 keV assuming a rock attenuation equivalent to potassium feldspar. Assuming a uniform distribution of Cu, 60% of the copper X-rays detected are sourced from within 50μm of the surface. Curve calculated using calculator from Kuznetsov (2016).*

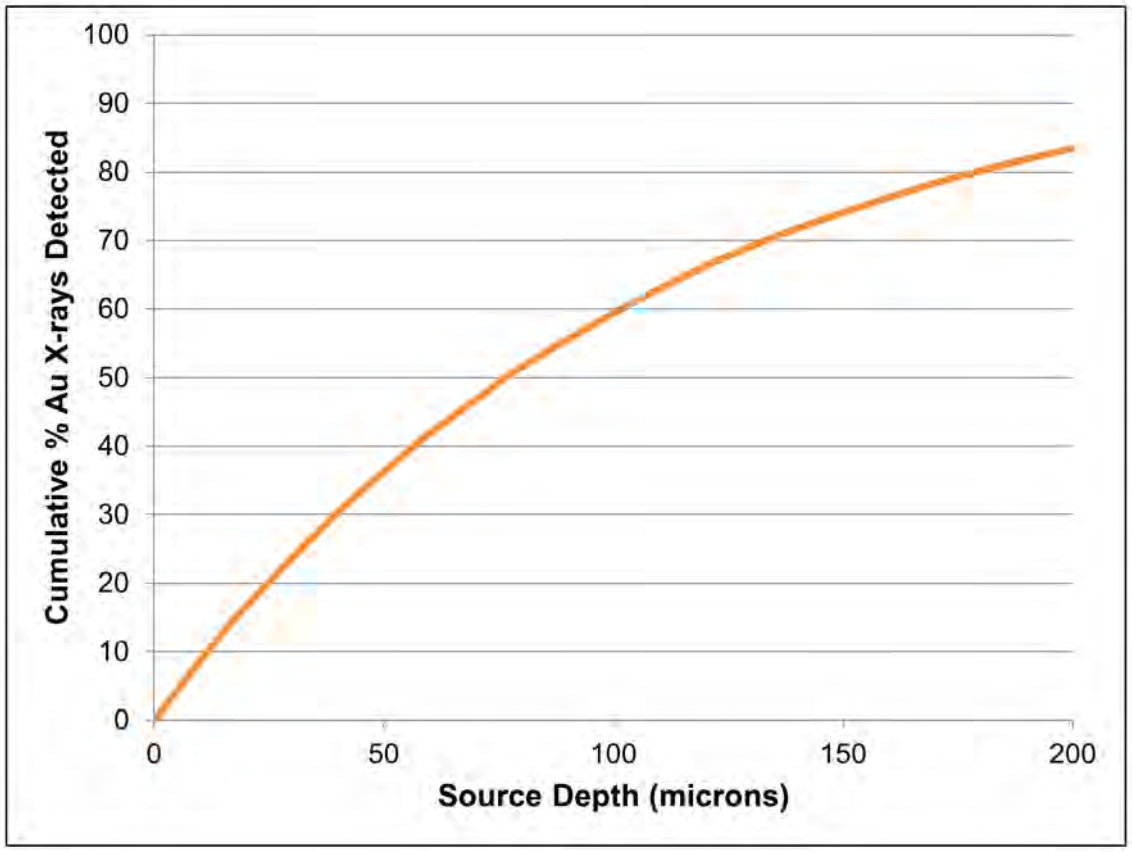

Figure 8.7. *Calculated source depth of characteristic gold X-rays from a Rh tube at 50 keV assuming a rock attenuation equivalent to potassium feldspar. Assuming a uniform distribution of Au, 60% of the Au X-rays detected are sourced from within 100μm of the surface. Curve calculated using calculator from Kuznetsov (2016).*

8.5.2 Copper sulphide and gold grain size proxy calculations

The concentration of gold and copper reflects the size of the gold or copper sulphide grain encountered by the μXRF analysis within the pixel. Assuming that all of the copper or gold in a single pixel is contained in a single grain, the expected copper and gold values for grains of different sizes were calculated. In the case of copper, it was assumed that the pixels could be treated as surface areas and not volumes. This was done because many of the copper grains are close in size to the 50 μm penetration depth of the μXRF, so comparing the proportion of copper to the pixel area was deemed sufficient for grain size proxy calculations. For gold, the grains are much smaller and the penetration depth is larger. Therefore, these calculations were completed on the total μXRF analysis volume for each pixel. Grain sizes for a mixture of 50% chalcopyrite and 50% bornite (combined copper sulphides) and gold ranging from 1 μm to the spot size of 160 μm were calculated using the following equations:

$$Expected\ Cu_{CuSulph}\ wt\%\ in\ pixel = \frac{\left(wt\%\ Cu_{CuSulph} * grain\ size^2\right)}{pixel\ diameter^2} \quad [8.1]$$

and

$$Expected\ Au\ Vol\%\ in\ pixel = \frac{\frac{4}{3}\pi\left(\frac{grain\ size}{2}\right)^3}{pixel\ volume} \quad [8.2].$$

The copper and gold values for each pixel were compared to the expected values. For pixels with copper or gold above detection, a grain size for combined copper sulphides or gold was assigned based on the calculated expected values. Where consecutive pixels exceeding 95% copper sulphide or gold were identified, they were combined these into a single, large grain. Assuming that the grains are spheres, each calculated grain size was then converted into a circle so that the boundary length and area could be calculated. These values were then used to determine the D_{PSSL} for all of the grains detected in each sample (see section 6.4 for details). The specific formulas and calculations used to complete the expected elemental proportion grain size proxies are included as an Excel workbook in Appendix P.

The detection limits for gold and copper are approximately 100 ppm and 20 ppm, respectively (Bruker, 2011). For gold, 0.01% (or 100 ppm) of the total μXRF analysis volume equates to a spherical gold grain with a diameter of 7.2 μm. For copper, 0.002% (or 20 ppm) of the total μXRF analysis area equates to 0.003% combined copper sulphide. Comparing this concentration to the μXRF analysis area produces a combined copper sulphide circle with a diameter of 6.3 μm. For gold grain size calculations, 7.2 μm is considered the "limit of detectable grain size". For copper, 3.6 μm was calculated as the "limit of detectable grain size". Any calculated gold or copper sulphide grain sizes below these limits were discarded from the D_{PSSL} calculations.

8.6 Grain size proxy results

The grain size proxy results produced by the methods outlined in section 8.5 were compared to the MLA results. These results are presented in the following sections.

8.6.1 Copper sulphide grain size proxy results

The μXRF grain size proxy calculation results for copper sulphide are shown in Table 8.3 and compared with the D_{PSSL} results from MLA analysis. The copper sulphide calculations produce an R^2 value of 0.83 and an r_s rank value of 0.78 (Figure 8.8).

Table 8.3. *Grain size calculated from μXRF expected copper proportions assuming combined copper sulphides. These values are compared to the measured combined sulphide grain D_{PSSL} from MLA for each sample in the test sample set.*

Sample	D_{PSSL} from MLA (μm)	Calculated D_{PSSL} Grain Size Proxy (μm)
1185.0	35	51
1193.0	71	100
1207.0	58	60
1265.5	32	44
1269.0	18	12
1283.0	42	64
1283.5	31	42
1292.5	27	28
1306.5	21	22
1307.5	53	36
1356.5	39	27
1362.7	52	34
1380.5	46	46
1381.0	21	13
1392.5	29	49
1393.0	13	20
1400.5	79	47
1401.0	152	191
1409.0	23	9
1420.0	111	78
1420.5	19	4
1421.0	29	43
1431.0	15	8
1431.5	17	11
1448.5	36	61
1461.5	24	17

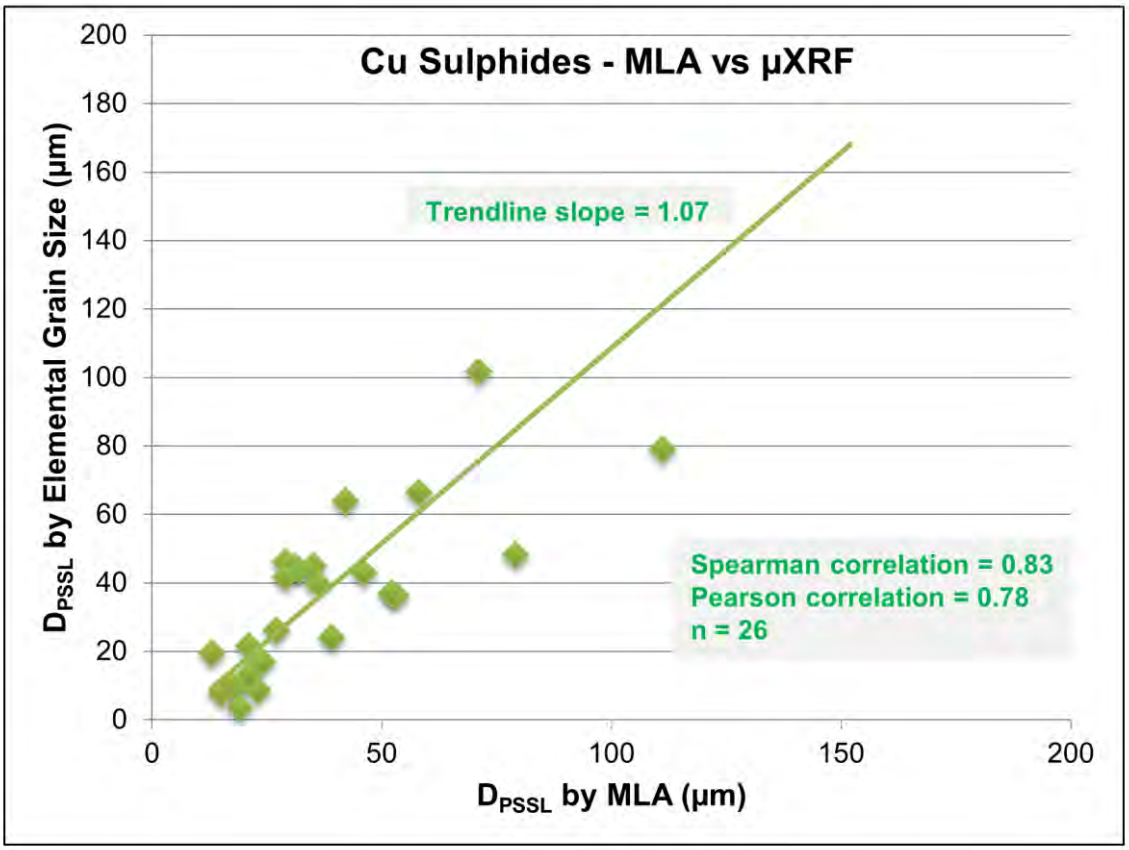

Figure 8.8. *Comparison of the D_{PSSL} for combined copper sulphides measured from 2D MLA data and the grain size calculated using the expected proportion of copper assuming that 50% of the copper is contained in chalcopyrite and 50% is contained in bornite for each of the twenty-six samples in the test set.*

8.6.2 Gold grain size proxy results

The µXRF gold grain size proxy calculation results are shown in Table 8.4. When compared to the D_{PSSL} results from MLA analysis, the gold results produce an R^2 value of 0.41 and an r_s rank value of 0.26 (Figure 8.9).

Table 8.4. *Grain size calculated from μXRF expected gold proportions compared to the measured gold grain* D_{PSSL} *from MLA for each sample in the test sample set.*

Sample	D_{PSSL} from MLA (μm)	Calculated D_{PSSL} Grain Size Proxy (μm)
CE143-1185.0	17	-
CE143-1193.0	1	19
CE143-1207.0	1	-
CE143-1265.5	10	15
CE143-1269.0	-	14
CE143-1283.0	14	17
CE143-1283.5	6	22
CE143-1292.5	8	17
CE143-1306.5	5	-
CE143-1307.5	-	-
CE143-1356.5	14	-
CE143-1362.7	-	-
CE143-1380.5	5	-
CE143-1381.0	-	-
CE143-1392.5	10	-
CE143-1393.0	-	-
CE143-1400.5	13	12
CE143-1401.0	27	51
CE143-1409.0	3	-
CE143-1420.0	18	25
CE143-1420.5	-	14
CE143-1421.0	3	18
CE143-1431.0	4	-
CE143-1431.5	2	-
CE143-1448.5	5	37
CE143-1461.5	5	-

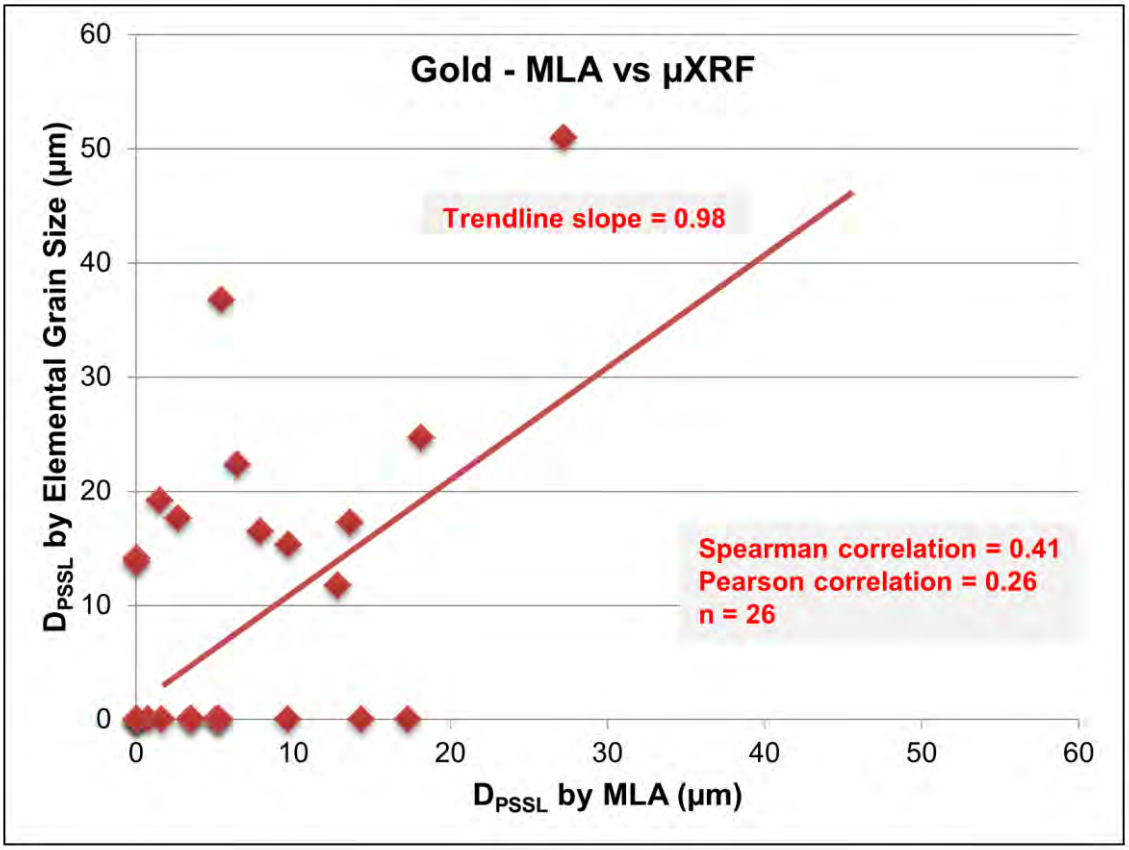

Figure 8.9. *Comparison of the DPSSL for gold measured from 2D MLA data and the grain size calculated using the expected proportion of gold for each of the twenty-six samples in the test set.*

As discussed in chapter 6, gold poses multiple challenges related to sampling statistics and distribution (see section 6.5.3). Berry and Hunt (2013) suggested that at least 50 grains of gold must be measured by MLA to produce a reliable grain size. Grouping the samples increases the number of gold grains present and improves the sampling statistics. The calculated gold grain size proxy values for each sample were grouped by down hole location and a grain size proxy for the group was calculated (Table 8.5). These calculated values were compared to the combined DPSSL gold measured from MLA analysis calculated for each group.

Table 8.5. *Comparison of the D_{PSSL} for gold measured from 2D MLA data and the grain size calculated using expected gold proportions from μXRF. Samples are grouped by down hole location.*

Grouping Criteria	Number Groups	Samples in Group	Pearson Correlation Coefficient (R^2)	Spearman Ranking Correlation Coefficient (r_s)
Down Hole Location	4	1185.0 – 1283.0	0.5	0.4
		1283.5 – 1362.7		
		1380.5 – 1409.0		
		1420.0 – 1461.5		
	3	1185.0 – 1292.5	0.78	1
		1306.5 – 1400.5		
		1401.0 – 1461.5		
	2	1185.0 – 1380.5	-	1
		1381.0 – 1461.5		

Figure 8.10 shows the evolution of the correlation coefficients as the number of μXRF analysis pixels increases. These results show that at least 135,000 μXRF analysis pixels are required to adequately assess gold grain sizes.

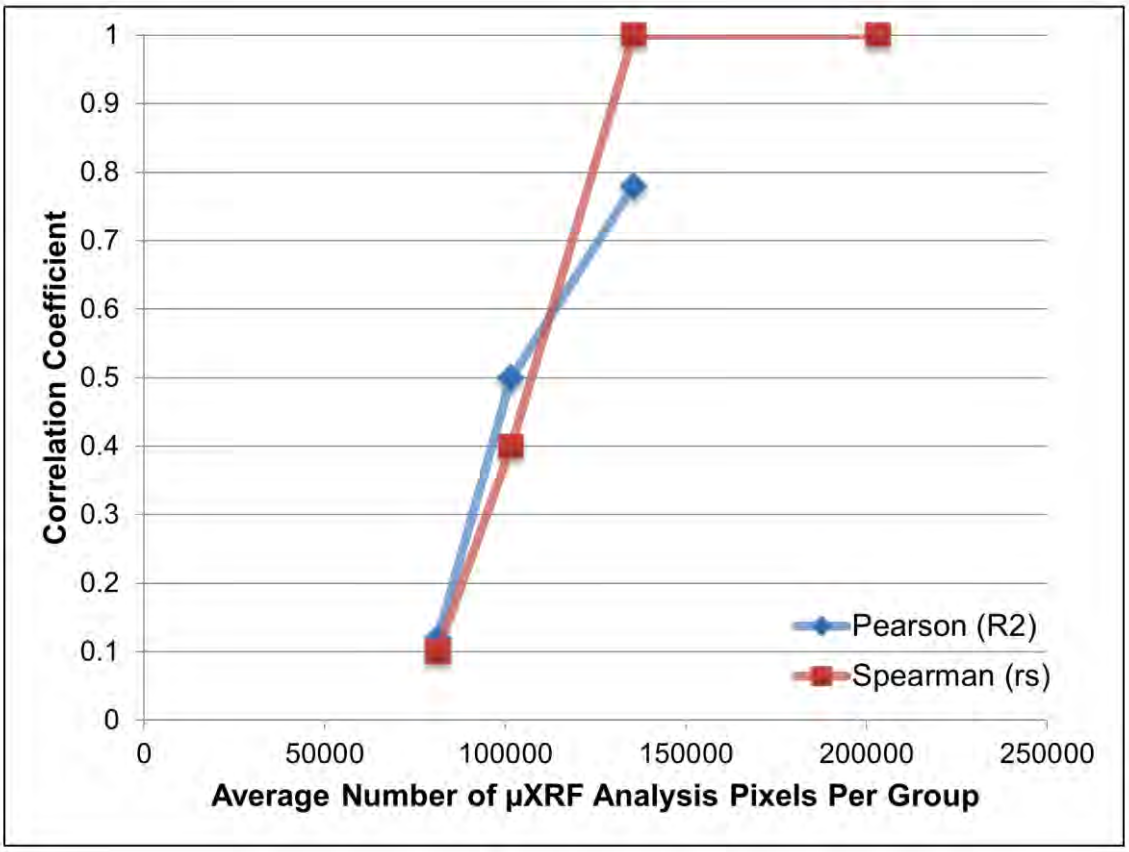

Figure 8.10. *Comparison of the average number of analyses per group compared to the Spearman and Pearson correlation coefficients for all grouped gold data using the expected elemental proportion proxy. This trend shows that at least 135,000 μXRF analysis pixels are required to adequately assess gold grain sizes.*

8.7 Bootstrapping of copper results

For copper minerals, using all 15,625 pixels from the surface of the sample provides a good estimate of the grain size using the proposed calculation methods (Figure 8.7). However, since the goal of this study is to investigate the potential for rapid grain size assessment, the minimum number of pixels required to produce a reasonable grain size estimate was investigated. A series of bootstrapping experiments were designed to randomly select rows of μXRF pixels from each sample, and use these results to calculate the expected elemental proportion grain size proxy. Fifty iterations of randomly selected groups of 100 lines, 75 lines, 50 lines, 25 lines, and 1 line were used to calculate the copper sulphide grain size proxy.

To assess the variability of the grain size estimates from μXRF as the number of analysis lines decreases, a series of box and whisker plots containing the bootstrapping results for combined copper sulphides were plotted (Figures 8.11

through 8.16). In general, as the number of lines used to calculate the μXRF grain size proxy decreases, the mean bootstrapped D_{PSSL} values and the second and third quartile range of D_{PSSL} values increase.

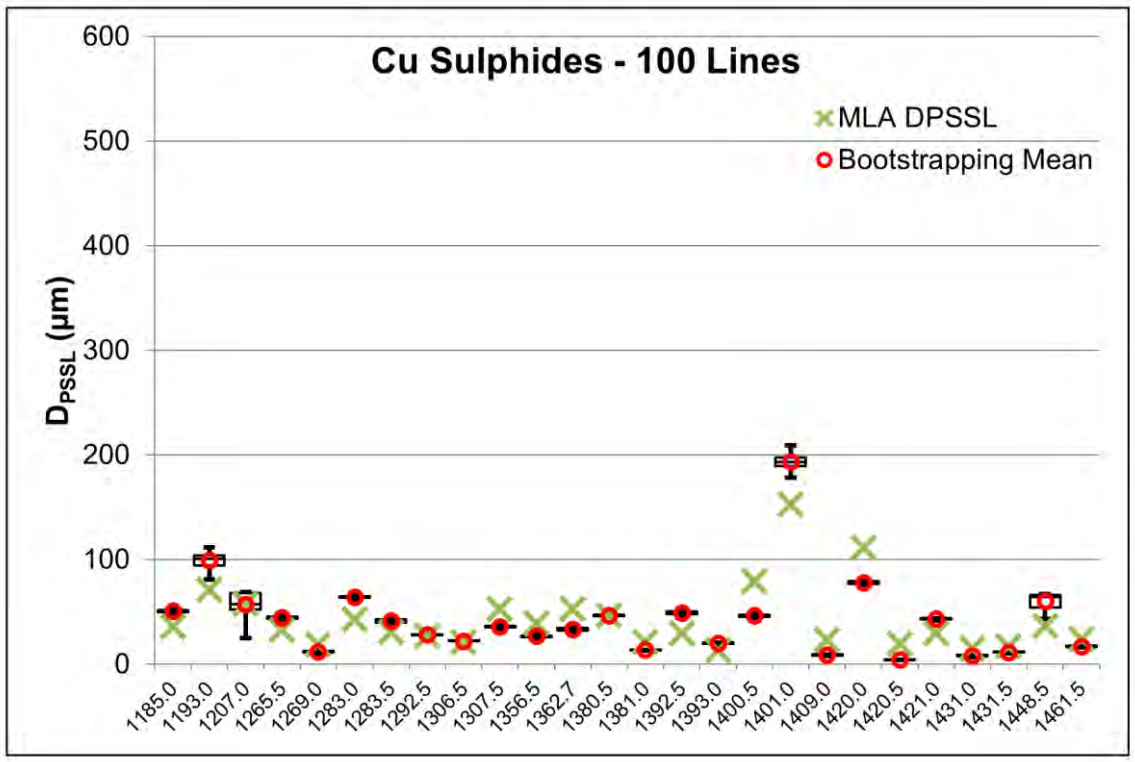

Figure 8.11. *Box and whisker plot showing the bootstrapping results for combined copper sulphides using 100 random lines per sample. The whiskers represent the minimum and maximum values.*

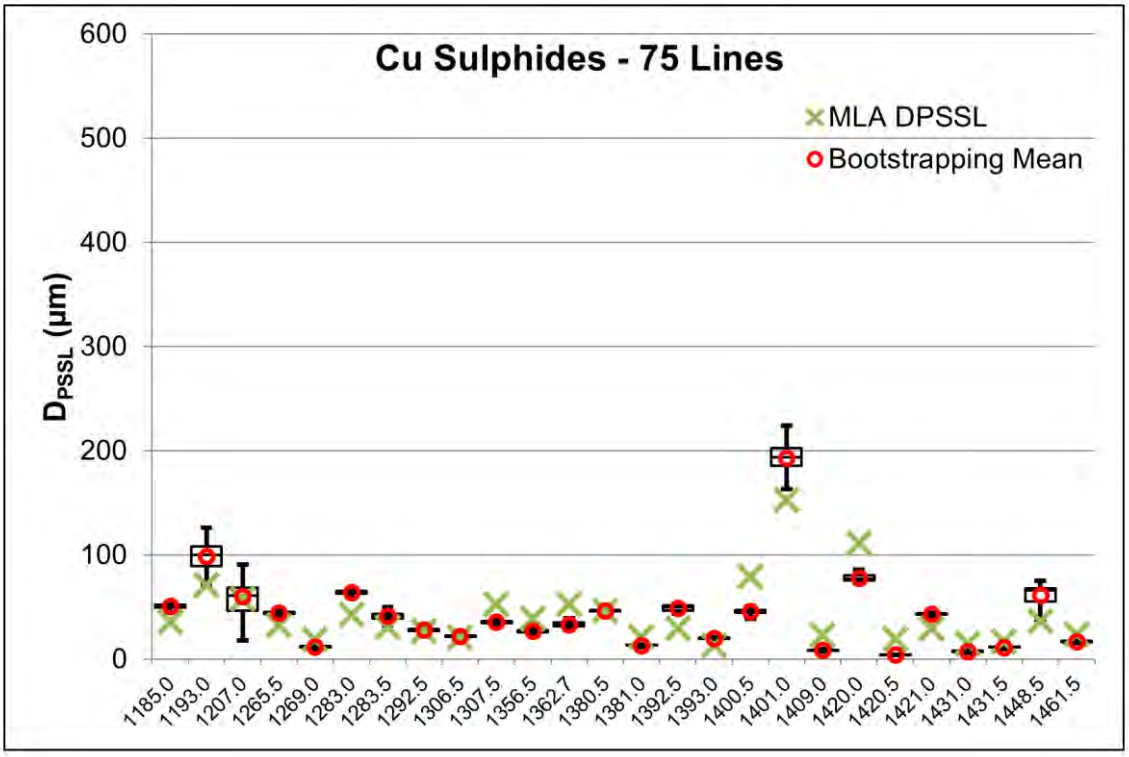

Figure 8.12. *Box and whisker plot showing the bootstrapping results for combined copper sulphides using 75 random lines per sample. The whiskers represent the minimum and maximum values.*

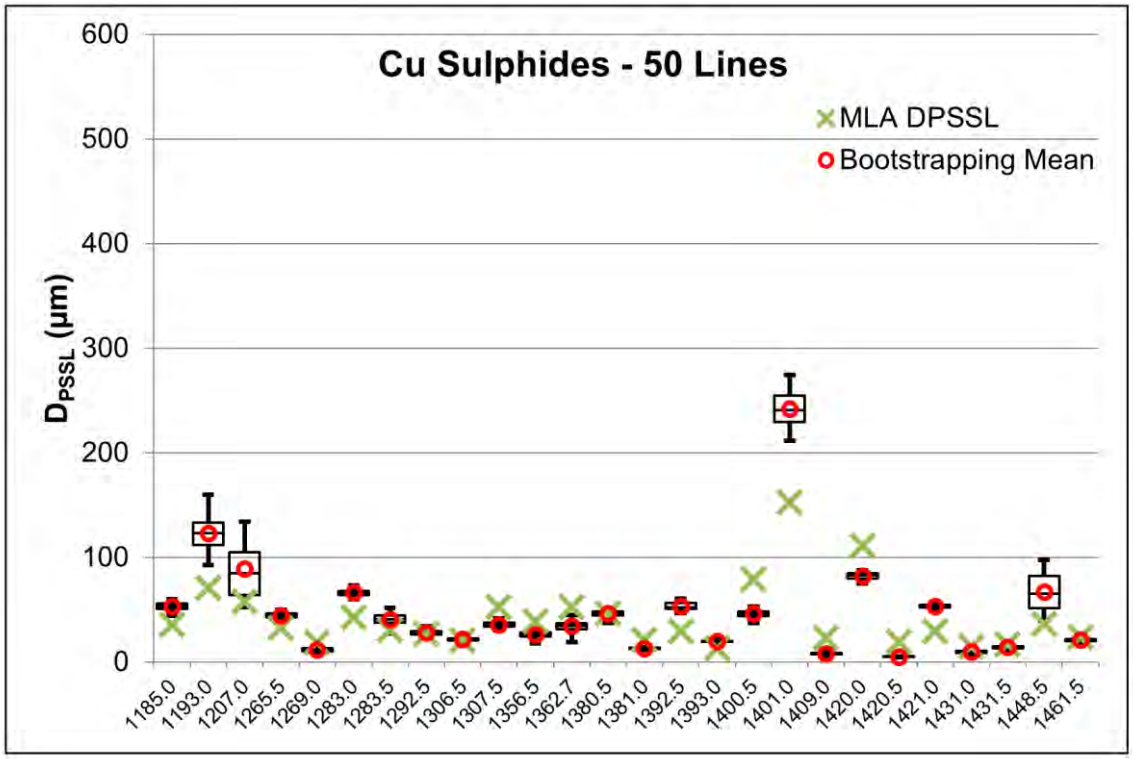

Figure 8.13. *Box and whisker plot showing the bootstrapping results for combined copper sulphides using 50 random lines per sample. The whiskers represent the minimum and maximum values.*

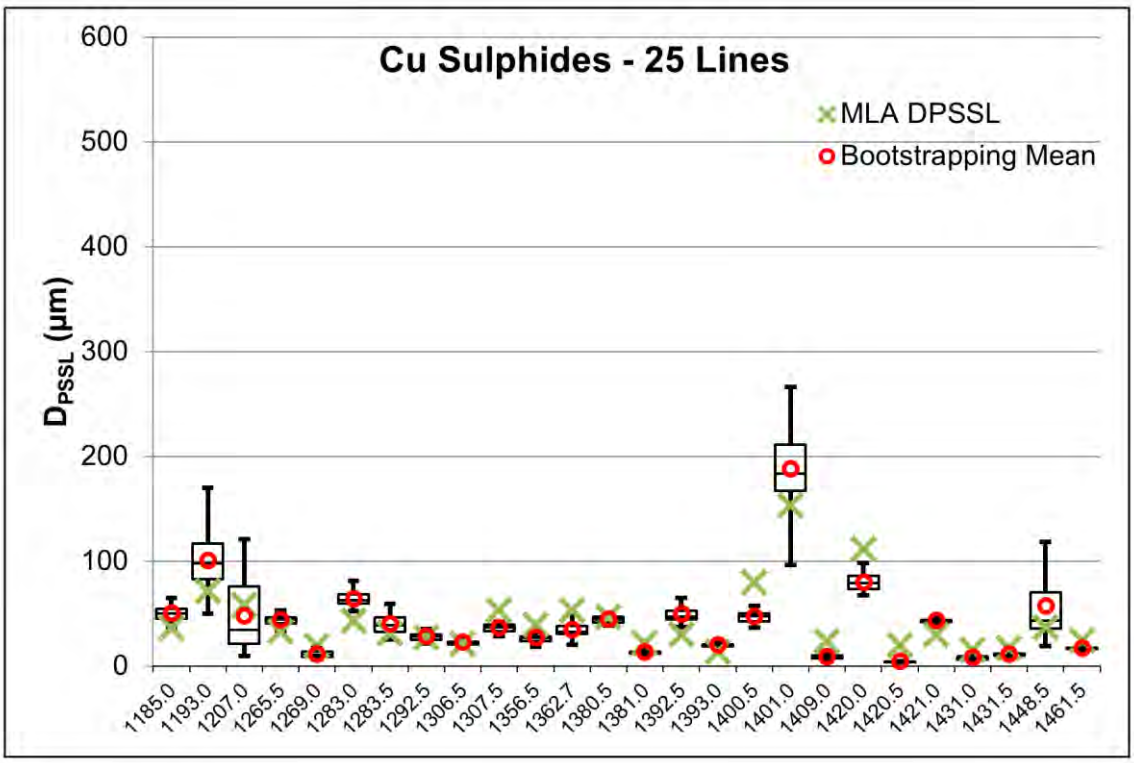

Figure 8.14. *Box and whisker plot showing the bootstrapping results for combined copper sulphides using 25 random lines per sample. The whiskers represent the minimum and maximum values.*

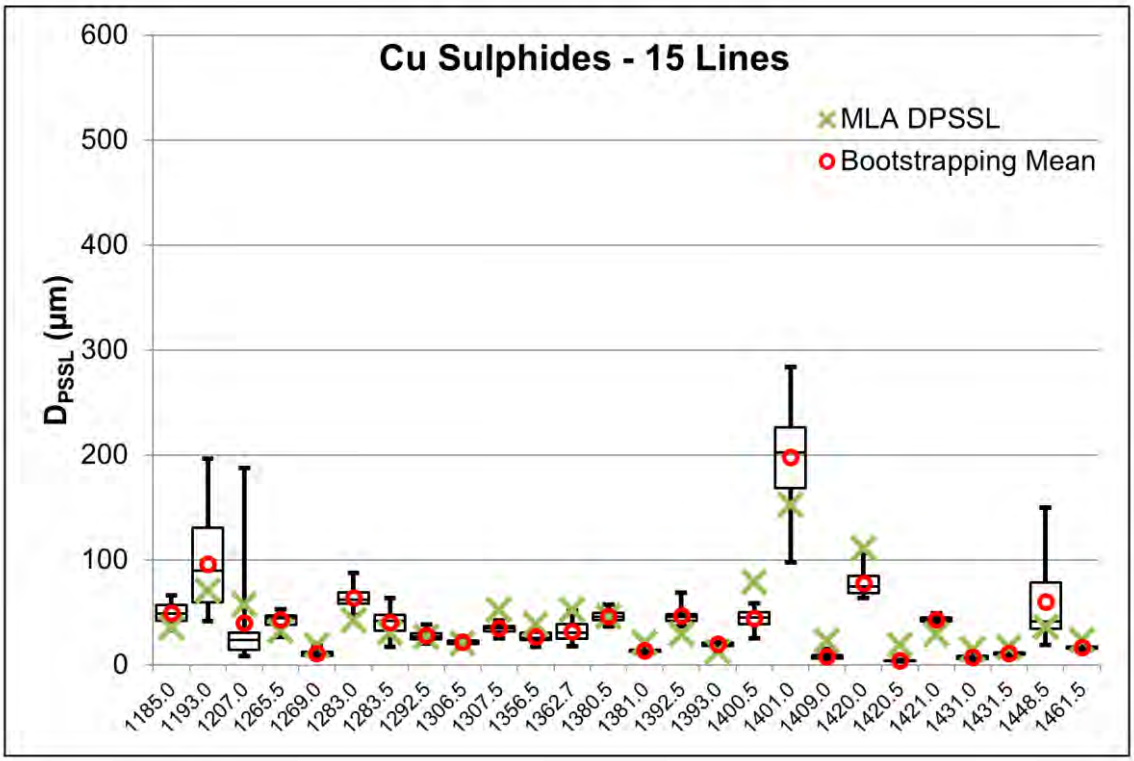

Figure 8.15. *Box and whisker plot showing the bootstrapping results for combined copper sulphides using 15 random lines per sample. The whiskers represent the minimum and maximum values.*

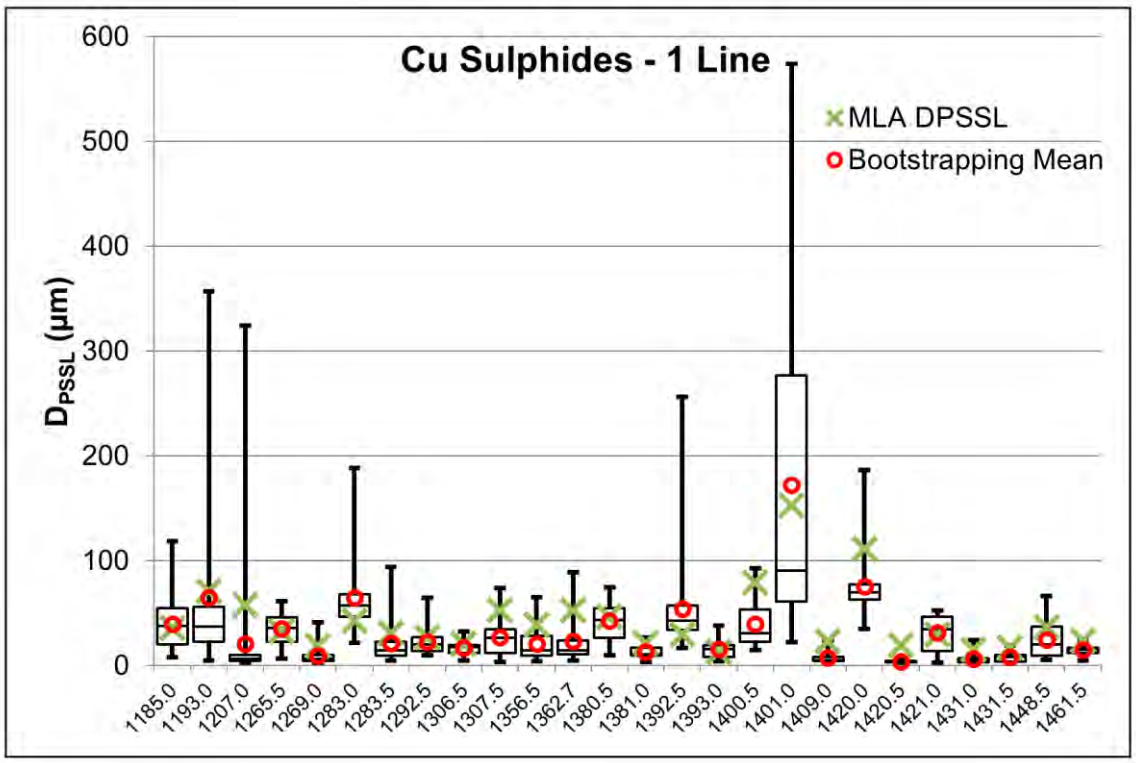

Figure 8.16. *Box and whisker plot showing the bootstrapping results for combined copper sulphides using 1 random line per sample. The whiskers represent the minimum and maximum values.*

The calculated D_{PSSL} proxy values for combined copper sulphides have a standard error of less than 1.5 in 50 experiments when at least 15 of the total 125 analysis lines are used. Fifteen lines contain 1,875 μXRF analysis pixels. With fewer analyses, the standard error of proxy values for all bootstrapped samples increases to more than 2 for combined copper sulphides (Figure 8.17). A standard error value of 1.5 indicates that using 1,875 random μXRF analyses will provide D_{PSSL} values within 1.5 μm in 50 repeated experiments, with 95% confidence.

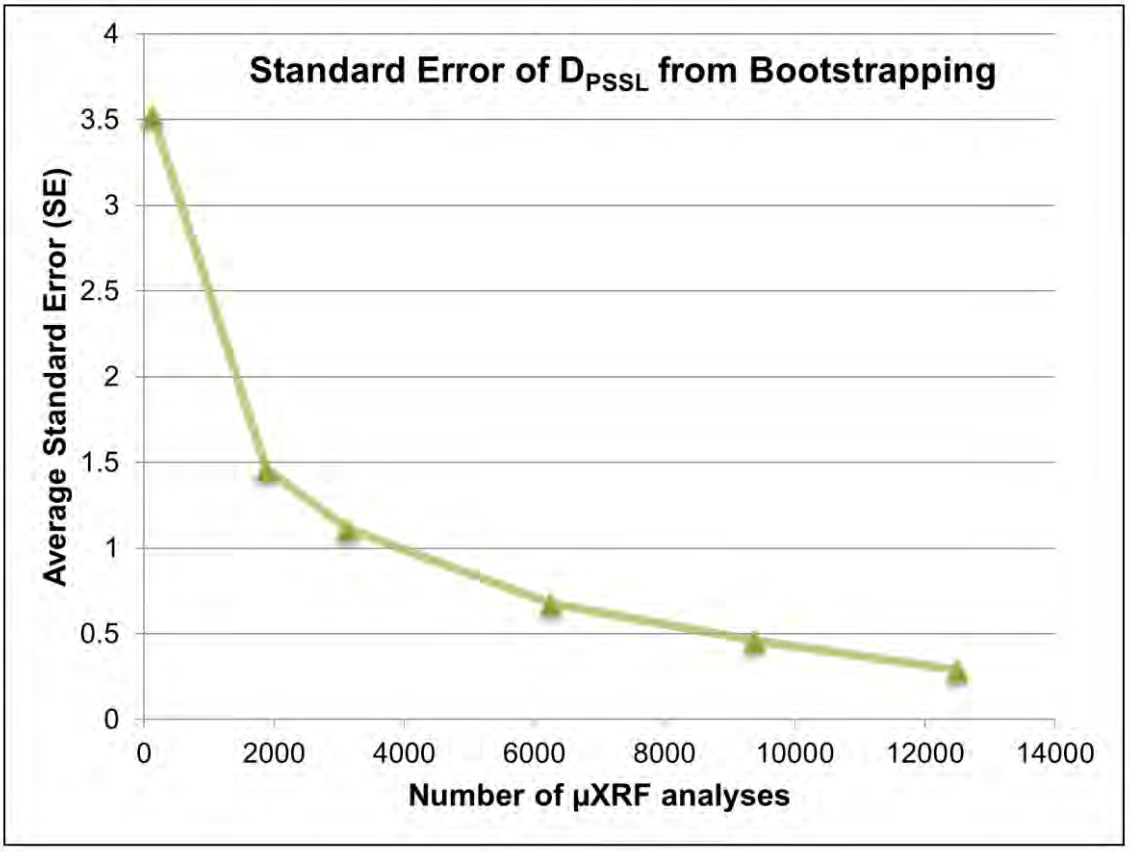

Figure 8.17. *Comparison of the number of μXRF analysis lines used and the standard error of grain size proxy values calculated using the expected elemental proportion for all twenty-six test samples. This trend shows that about 2000 μXRF analysis pixels are required to rank samples in terms of copper mineral grain size proxies to a satisfactory precision.*

8.8 Discussion

The copper and gold concentrations from μXRF analysis were used to calculate a grain size proxy for each pixel using the expected copper and gold proportions. When compared to the MLA grain size data on a sample by sample basis, the D_{PSSL} values for combined copper sulphides produce correlation coefficients of $R^2 = 0.78$ and $r_s = 0.83$. The slope of the trendline produced by the Pearson correlation graph is 1.07, indicating that the copper sulphide proxy grain sizes are similar to those measured by MLA. These results indicate that the elemental proportion grain size calculations can successfully be used to assess grain size on a sample by sample basis using μXRF data.

Comparing the individual gold grain size results for each sample to the D_{PSSL} from MLA produced poor correlation values of $R^2 = 0.26$ and $r_s = 0.41$ using the expected elemental proportion proxy methods. Berry and Hunt (2011) determined that gold grain population statistics only become meaningful when

at least 50 gold grains are included in the D_{PSSL} calculation (section 6.5.3). Only two of the samples in the test sample set contain more than 50 gold grains. As such, most of the D_{PSSL} values from MLA on a sample by sample basis are not adequately representing the gold grain size population. The poor correlation between the μXRF and MLA grain sizes when comparing individual sample results reflects this challenge and demonstrates that this sample size is not sufficient for reliable gold measurements using these techniques.

Because the gold grains in the test sample set are small and rare, they provide a unique challenge related to sampling statistics and grain size distributions. These challenges can be addressed by combining multiple samples together in groups. For the expected elemental proportion proxy, this grouping improves the correlation coefficients. When the twenty-six sample are divided into 3 groups (average of approximately 135,000 analysis pixels), the R^2 value improves to 0.78 and the r_s value to 1.0. When the samples are split into 2 groups (an average of 203,125 analysis pixels), the proxy method ranks the grain size of gold in the two groups correctly. Here the test is strongly affected by the sampling error in the MLA analyses. It may be that the μXRF is a much better assessment of the gold grain size than the MLA as it samples a larger volume. Unfortunately we have no independent method better than the MLA to check the validity of the grain size assessment.

For gold grain size calculations, the "limit of detectable grain size" is 7.2 μm, while the MLA can detect grains as small as 1 μm. Only nine of the twenty-six samples returned D_{PSSL} values from MLA data greater than 7 μm. As a result, many of the gold grains are discarded and not included in the D_{PSSL} grain size calculations. As such, the μXRF grain size proxy population statistics are different compared to the MLA data, which results in poor correlation coefficients. As with pXRF grain size assessment, comparing the surface analysis grain size calculations from MLA to grain sizes derived from μXRF volume analyses may not provide a good comparison. In the case of gold, it is possible that the μXRF is detecting grains that are just below the surface that would not be detectable by MLA surface analysis. Additionally, only 400 gold grains were detected in all twenty-six samples by MLA analysis meaning that less than two grains of gold were detected per square centimetre. Since the scan area of the μXRF is lower than that of the MLA, the likelihood of encountering gold grains is greatly decreased causing challenges with sampling statistics. The 400 gold grains detected by MLA may not adequately represent the gold grain

populations contained in the samples, causing additional challenges when comparing the volumetric μXRF data to the MLA surface data.

8.9 Conclusions

While the test data set used in this study is small, the results show that the μXRF copper mineral grain size proxy is successful. The expected elemental proportion proxy calculations produced values that are generally within 20 μm of the measured D_{PSSL} values from MLA data. The slope of the R^2 trendline is 1.07, indicating that the proxy values are reporting results close to the measured MLA grain sizes. Bootstrapping analysis indicates that this method requires about 2,000 μXRF analysis pixels to achieve repeatable grain size results with an average standard error of less than 1.5.

With respect to gold, the proxy produced poor correlations on a sample by sample basis, but reasonable correlations when the samples were grouped into 3 groups and 2 groups. Three groups represent an average of approximately 135,000 analysis pixels and approximately 203,000 analysis pixels for two groups. However, it is likely that the limitations of the MLA method and the low number of gold grains present in the test dataset are a significant challenge. For the samples measured, μXRF analysis detected a total of 44 gold grains in 406,250 μXRF analyses. This is the best estimate available of the minimum number of analyses required for an effective grain size proxy.

The objective of this study was to investigate the potential of μXRF technology to be used in conjunction with Corescan analysis to rapidly and adequately assess copper-sulphide and gold grain sizes. Specifically, the number of μXRF analyses required to adequately assess grain size was tested. The Bruker M4 TORNADO used in this study can analyse 1,875 μXRF pixels in 2.5 minutes. Corescan acquires data at a rate of 3 minutes per metre; nearly 2,250 μXRF analysis pixels measuring 160 μm in diameter can be measured in the same amount of time. At this rate, a copper grain size proxy could be calculated for every metre of drill core, the same resolution as a typical assay interval.

While the current acquisition rate of the M4 TORNADO μXRF system is sufficient to calculate a copper grain size proxy, increasing the μXRF data acquisition rate could be achieved by: (1) installing a second X-ray source with a different target and collimator to double the analysis rate, or (2) by installing a second detector to increase the X-ray counts without increasing the dwell time.

Both of these options are currently available from Bruker as upgrades to the M4 TORNADO system (Bruker). If the μXRF data acquisition rates were increased, copper sulphide grain size proxies could be calculated on drill core intervals of less than one metre. In either case, currently available μXRF technology shows great promise to acquire early copper sulphide grain size information using a rapid, non-destructive technique at an acquisition rate similar to the current Corescan system.

For gold, the sampling statistics are much more challenging. If the detection of 50 grains is required for a good proxy, the results of this study show that over 406,000 μXRF analyses are required. Assuming the μXRF sampling rate is capable of 2,250 analyses per metre, the minimum resolution for a gold grain size proxy is approximately 180 metres of drill core. This interval is much larger than a typical 1 to 2 metre assay interval, but could provide low resolution, large scale gold grain size discrimination. A dedicated high power XRF for drill core measurement optimised for gold and copper could realistically be expected to work 2 to 5 times faster than the μXRF used in this study. At this rate, a gold grain size proxy may be achievable in the next decade.

Chapter 9

Grain size assessment by laser ablation inductively coupled plasma mass spectrometry (LA-ICP-MS)

9.1 Introduction

Laser ablation inductively coupled plasma mass spectrometry (LA-ICP-MS) technology is capable of precise trace elemental analysis of rock samples in spot, line, or rastering analytical modes. For geological and geochemical applications, LA-ICP-MS analysis has been a commonly used microanalytical technique for more than a decade (Ridley and Lichte, 1998; Thompson et al., 1990). Recent developments in LA-ICP-MS technology have improved the ability to detect trace elements, particularly in sulphide minerals (Danyushevsky et al., 2011). Numerous metal deportment studies (e.g. Cabri et al., 2017, Belousov et al., 2016, Cook et al., 2016) have also been conducted using LA-ICP-MS analysis, showing the potential of this technology to be used in geometallurgical assessment.

The advantage of the LA-ICP-MS system is that up to six orders of magnitude of concentration can be analysed simultaneously. This technology may allow for the detection and quantification of sub-micron to sub-millimetre mineral grains on unpolished rock samples. This study aims to investigate the potential to rapidly assess copper sulphide and gold grain sizes using LA-ICP-MS technology. Unlike the other microanalytical techniques discussed in this thesis, LA-ICP-MS analysis cannot currently be carried out in air, and must be conducted in a helium atmosphere in an ablation cell. Therefore, it could not be attached to an automated core logging system, but could be used for the rapid scanning of selected core samples outside of the Corescan sample analysis stream. To keep pace with the Corescan system, this technology would need to analyse a sufficient number of selected samples from one metre of drill core in 3 minutes.

The capabilities of LA-ICP-MS analysis were tested to determine if this technology can assess copper sulphide and gold grain sizes. This *in situ* technique measures elemental concentrations on small, discrete portions of the sample. The concentrations of copper and gold present in each LA-ICP-MS analysis line reflect the size of copper and gold grains encountered. Grain size estimates using the proportion of elements present in a given spot along the analysis line were

used to calculate grain size proxies from LA-ICP-MS data. Here, we compare the acquisition rates of LA-ICP-MS analysis to those of the Corescan system. The results of copper sulphide and gold grain size proxies using LA-ICP-MS data are compared to the grain sizes measured from MLA data. The minimum number of LA-ICP-MS line analyses required to produce a representative grain size proxy was determined by running a series of bootstrapping experiments. These results were then used to calculate data acquisition rates compared to those of the Corescan system.

9.2 Scientific principles of LA-ICP-MS technology

LA-ICP-MS analysis is an analytical technique that measures major and trace element concentrations *in situ* by a process involving laser ablation, ionization in a plasma, and, finally, measurement by mass spectrometry. Like other ICP-MS techniques, LA-ICP-MS is a type of plasma torch mass spectrometry based on the principles that different elements have different atomic masses. The laser is used to ablate sample material which is, in turn, ionised into a plasma. This plasma is then pumped through a mass spectrometer designed to count atoms of different masses as they move through a specialised instrument (mass spectrometer) designed to segregate the atoms by atomic mass (Ridley and Lichte, 1998). The specific details of the LA-ICP-MS instrumentation are discussed in section 9.3.

9.3 LA-ICP-MS instrument

In LA-ICP-MS analysis, an ultraviolet laser is combined with an inductively coupled plasma mass spectrometer (ICP-MS). The ultraviolet laser fires multiple pulses into a sealed ablation cell continuously purged with helium gas, removing approximately 0.1 μm to 0.2 μm in depth of material from the surface of the sample (Arrowsmith and Hughes, 1988; Gilbert et al., 2014; Thompson et al., 1990). Argon is pumped into the system where it functions as a carrier gas and transports the sample material as an aerosol from the ablation cell to a plasma stream. This plasma is induced by a rapidly oscillating electrical current, and functions to simultaneously melt, dissociate, and ionise the ablated material (Ridley and Lichte, 1998). A series of pumps then introduce the ions from the plasma to a mass spectrometer where a rapid scan (0.1 to 0.5 seconds for 30 to 60 elements) sequentially measures the masses of contained ions as the material

passes through the mass spectrometer (Ridley and Lichte, 1998). A schematic diagram of the LA-ICP-MS system design is shown in Figure 9.1.

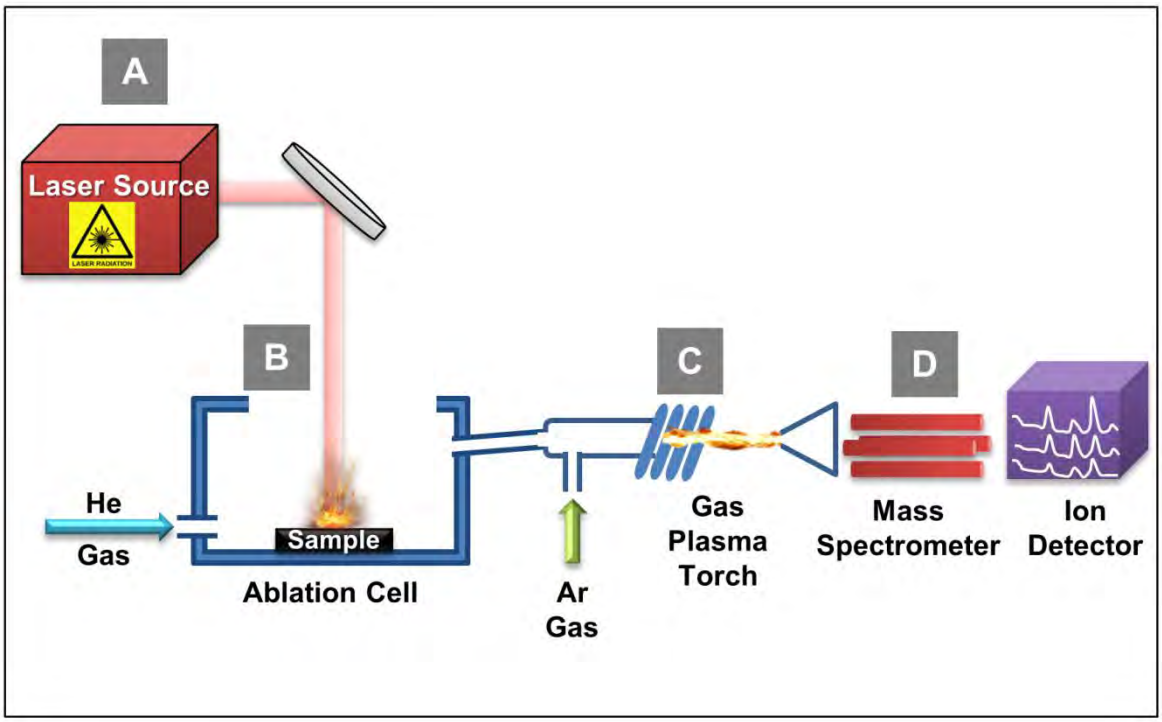

Figure 9.1. *Schematic design of the LA-ICP-MS instrument setup including four principle systems: (A) laser source, (B) ablation cell, (C) gas plasma torch, and (D) mass spectrometer (modified from Ridley and Lichte, 1998).*

9.3.1 Data output of LA-ICP-MS analysis

The data output from the mass spectrometer system is a series of lines representing counts of each element as a function of time (Figure 9.2). To quantify elemental concentrations based on the raw counts, glass standards are normally analysed for calibration, but matrix matched standards provide more realistic standard values (Danyushevsky et al., 2011). For this study, a series of matrix-matched standards in addition to glass standards were analysed and used to quantify elements. Matrix effects cause challenges in converting raw ICP-MS counts to concentrations and calibrating these values based on the standards. These effects add to the complexity of a general line scan method since the counts must be used to classify the source material that has been ablated before the correct calibration can be applied. Most commonly, more than one mineral is ablated causing the correction factors and calibration to be less accurate.

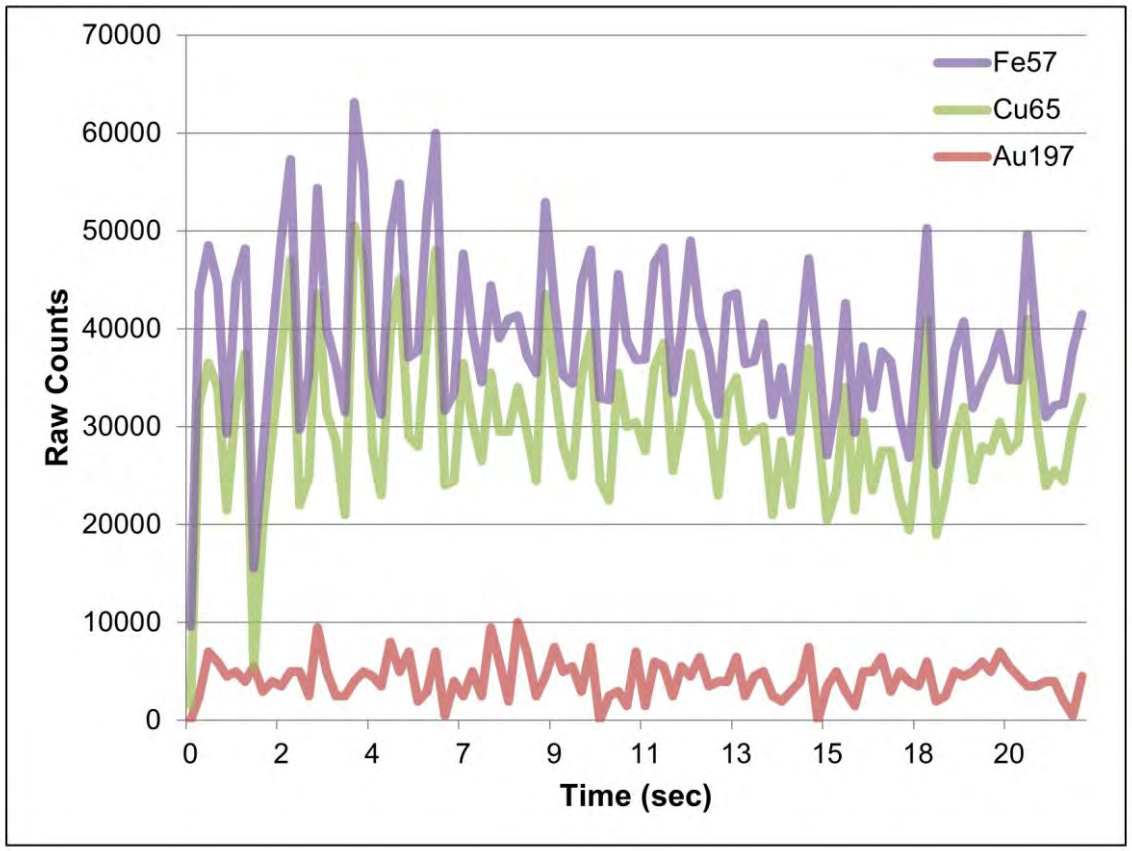

Figure 9.2. *Data output of the LA-ICP-MS system: raw counts for each element measured as a function of time.*

9.3.2 Sample requirements for LA-ICP-MS analysis

Geochemical analysis by LA-ICP-MS requires that the sample surface be relatively flat and clean. The ablation process causes minimal surface damage to the sample. LA-ICP-MS analysis has been applied to numerous geological studies over the past 20 years, with recent studies focused on the analysis of sulphide minerals (Belousov et al., 2016; Danyushevsky et al., 2011; Large et al., 2009; Steadman et al., 2015). While many sulphide studies use either targeted spot analyses or sample imaging by spot rastering, the LA-ICP-MS system is also capable of line scan analysis. In line scan mode, the system fires the laser at a set repetition rate while moving the sample stage at a constant speed. This analysis can be challenging for the measurement of major elements and has high running costs, but it has a number of advantages including: (1) better detection limits than most other microanalytical techniques (ppt to ppm), and (2) the capability for rapid, precise chemical analysis. With the notable exceptions of N, O, and noble gases, almost all elements can be detected by the LA-ICP-MS system. Some

elements such as Hg, S, C, and the halogens are detectable but they are either difficult or impossible to quantify.

9.3.3 Consideration for LA-ICP-MS analysis

There are numerous factors that should be considered when utilising LA-ICP-MS elemental data. First, elements in different minerals display different fractionation behaviours which can affect both the ablation and the transport of the ablated material within the LA_ICP-MS system (Fryer et al., 1995). For example, sulphides tend to melt and ablate well, while silicates like quartz tend to fragment with uneven, irregular ablation craters. Additionally, the speed at which data can be collected is limited by both the ICP-MS sequential scan times and the time it takes the ablated material in the ablation cell to reach the plasma (known as the washout time). The more elements that are being analysed, the more time it takes the ICP-MS system to scan for the selected range. Similarly, the washout time is limited by the setup of the LA-ICP-MS system and directly affects the speed at which the analysis can be completed. Both the ICP-MS scan time and the washout times are currently being assessed and new technologies are being developed (e.g. Gundlach-Graham and Günther, 2016; Van Malderen et al., 2015).

9.4 Data collection methodology

The goal of this study was to investigate if LA-ICP-MS analysis could be used to effectively detect and assess copper sulphide and gold grain sizes using a series of LA-ICP-MS line scans. The twenty-six test samples were analysed using a Resolution/ASI S155 laser ablation cell coupled to a 193 nm Coherent COMPex excimer laser and Agilent 7700 quadrupole ICP-MS system at CODES, University of Tasmania, Australia. A series of 20 lines (each 23 mm long), spaced approximately 1.4 mm apart were analysed across each sample (Figure 9.3). The line scan analyses were completed using a laser fluence of 3 J/cm^2, at 20 Hz, and a 34 μm^2 square-shaped beam moving at 300 μm per second. The mass spectrometer measures the elements sequentially every 0.22 seconds along the length of the analysis line, with each ICP-MS analysis sweep representing one pixel of data. A list of 44 elements was analysed. For copper and iron, LA-ICP-MS detection limits are reported in the literature as typically less than 10 ppb (Ridley and Lichte, 1998). Detection limits for gold are variable, with some

studies reporting detection limits between 1 and 10 ppb, but typically less than 50 ppb (Piña et al., 2012; Sylvester and Eggins, 1997). The detection limits were calculated for the LA-ICP-MS analysis completed in this study and are presented in Table 9.1. Initial data analysis and reduction of raw data was completed using the methodology outlined in Longerich et al. (1996) and Danyushevsky et al. (2011). The line signal data was then converted to quantified elemental data for each pixel of LA-ICP-MS analysis along each analysis line using techniques similar those used at the University of Tasmania to quantify trace element images of pyrite (e.g. Steadman et al., 2015). Further data processing was performed to correct for mineral specific laser ablation effects using algorithms developed at the University of Tasmania (Meffre et al., 2017). The post-processed, quantified analysis line results were then used in the grain size proxy calculations.

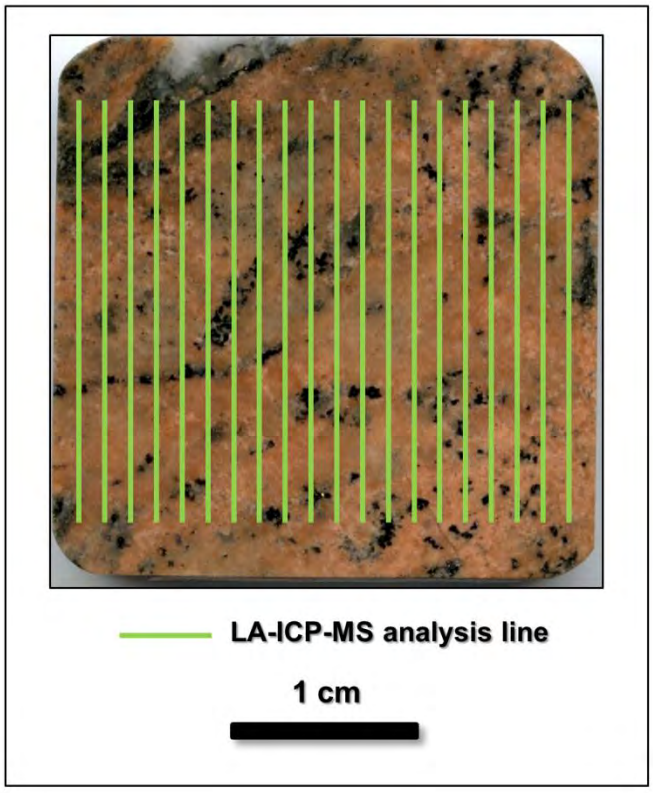

Figure 9.3. *Configuration of LA-ICP-MS analysis lines across each test sample. Twenty lines were completed on each sample.*

Table 9.1. *Average calculated detection limits for iron, copper, and gold in silicates and sulphides using the data collected from the test samples.*

Matrix	Element	Calculated Detection Limit (ppb)
Silicate	Fe	1197.0
	Cu	34.0
	Au	0.8
Sulphide	Fe	3012.0
	Cu	104.0
	Au	2.1

9.4.1 Determining LA-ICP-MS pixel size

The LA-ICP-MS analysis results represent the chemical composition of the total area ablated by the laser in a given analysis pixel. Any grains encountered that were larger than the spot size would produce concentrations equal to those of pure gold or pure copper sulphide minerals. If grains less than the spot size are encountered, the elemental concentrations were then compared to the ablation area to estimate the grain size. While the spot size used for analysis was 34 μm, the laser was running at 300 μm per second with the spectrometer sweeping every 0.22 seconds. This causes the length of each laser analysis spot to be approximately 67 μm, producing a rectangular analysis pixel measuring 34 μm by 67 μm (Figure 9.4).

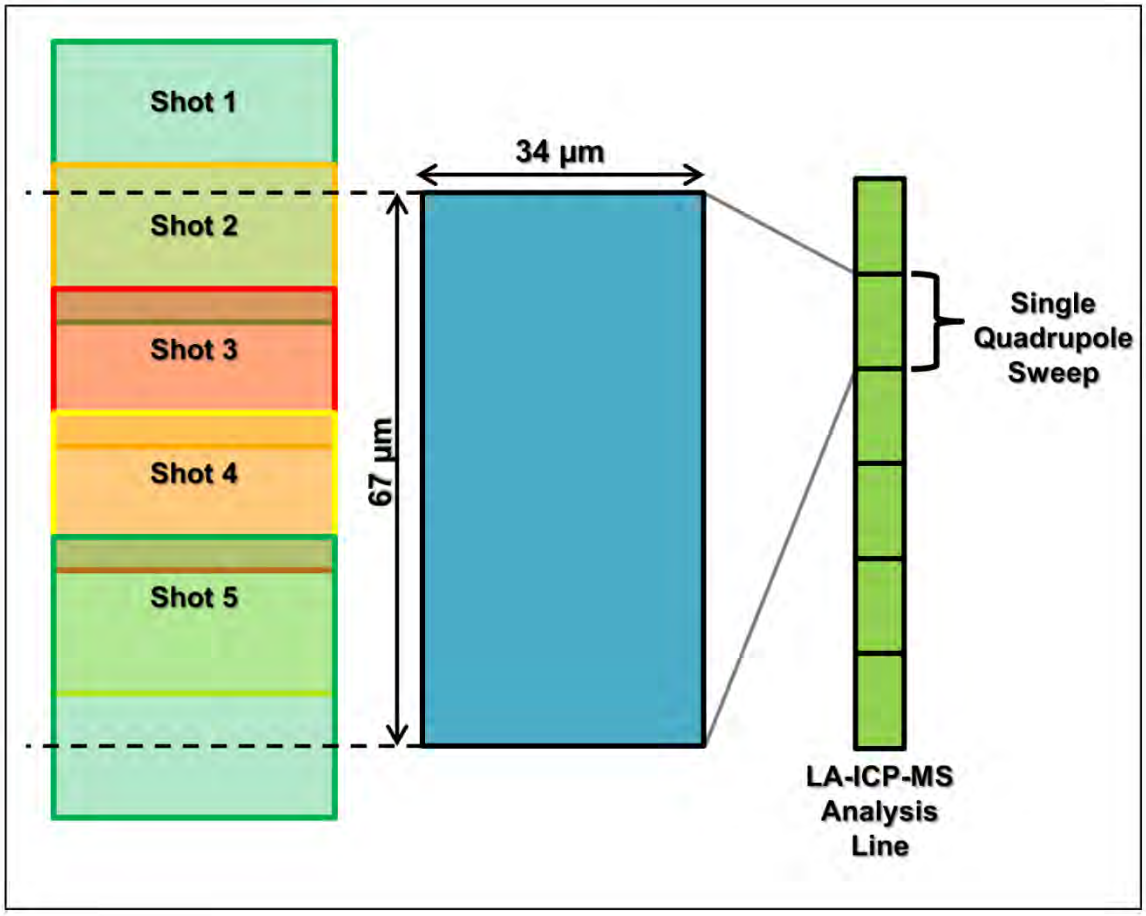

Figure 9.4. *Dimensions of the LA-ICP-MS analysis spots used in this study. Each pixel represents a single sweep of the quadrupole. In a single sweep, the laser (operating at 20Hz) fires nearly 4.5 shots. These 4.5 shots make up the total analysis of the LA-ICP-MS pixel.*

A select number of ablation crater depths were measured using a reflected petrographic microscope with an automated stage (Figure 9.5). Laser lines ablated across numerous minerals (such as quartz, feldspar, chalcopyrite, and bornite) were measured and the average depth of the analysis lines in copper sulphides was approximately 0.5 µm. This ablation depth is much smaller than the majority of gold and copper sulphide grains encountered in the samples making the analysis footprint essentially a surface measurement. To address this, it was assumed that the analysis results represent an area rather than an ablation volume. Pure gold or copper sulphide LA-ICP-MS signals represent mineral grains greater than 67 µm long. Any grains less than 67 µm would produce diluted concentrations of gold, copper, and iron while the relative proportions of these elements would remain constant. Therefore, gold and copper sulphide mineral grains less than 67 µm long can be estimated using the proportion of elements relative to the total analysis area.

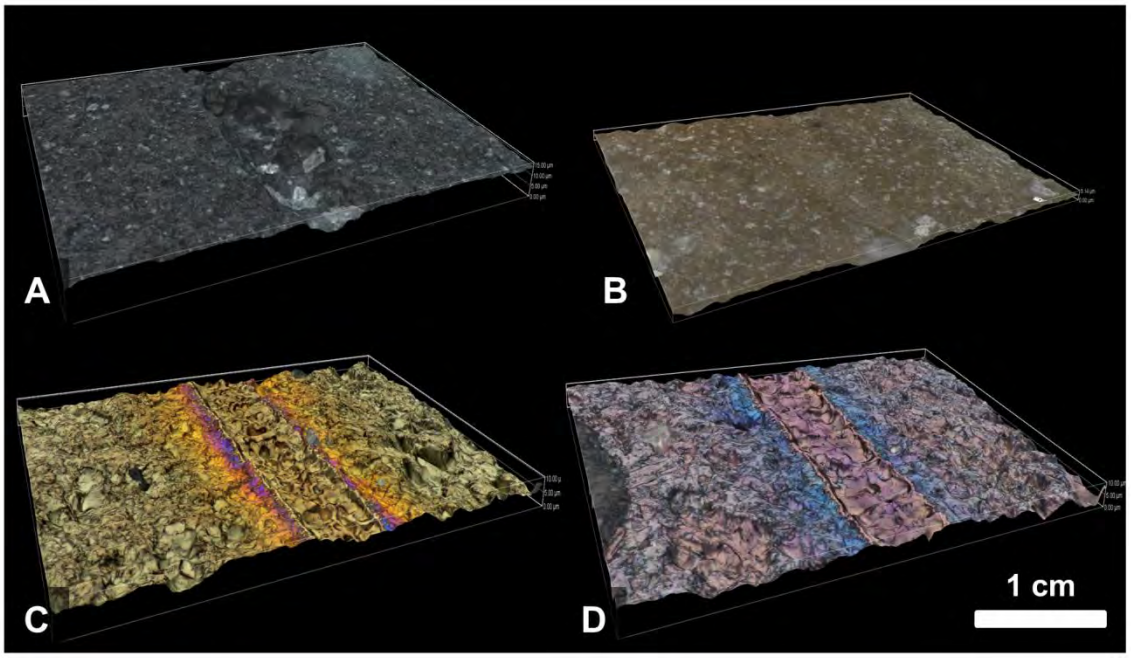

Figure 9.5. *Reflected light 3D step image of LA-ICP-MS line through quartz (A), feldspar (B), chalcopyrite (C) and bornite (D). The average ablation depth in copper sulphide minerals was measured to be approximately 0.5 μm.*

9.4.2 Background copper and gold

A number of minerals can contain trace amounts of background copper and gold. These background values are not associated with copper sulphide and gold grains, and can range from a few ppb to a few percent. Wilkinson et al. (2015) reported a range of 0 to 24 ppb gold and 0 to 1100 ppm copper in over 80 chlorite spots using LA-ICP-MS spot analysis. A series of calcite samples were analysed by LA-ICP-MS and reported 1 to 2 ppm copper (Strnad et al., 2009). Because the LA-ICP-MS system is capable of precise trace element detection, it is likely to detect background copper and gold. To account for any potential background values, thresholds were used in the grain size calculations (section 9.5).

9.5 Grain size proxy calculations

Elemental concentrations of iron, copper, and gold from LA-ICP-MS line scans were used to determine if this technology could provide rapid grain size assessment. Since this technique is capable of precise elemental analysis, chalcopyrite and bornite can be distinguished and grain size proxies for these two minerals were calculated separately. Assuming that copper is contained in

combined copper sulphides consisting of 50% chalcopyrite and 50% bornite, a proxy for combined copper sulphides was also calculated.

9.5.1 Assumptions for grain size proxy calculations

The D_{PSSL} grain size for each sample with LA-ICP-MS data was calculated using the methods outlined in sections 9.4.1 and 9.4.2. For these methods, assumptions about the density of the mineral of interest and the rock mass are required. The assumptions used for grain size calculations are outlined in Tables 9.2 for copper sulphides and 9.3 for gold.

Table 9.2. *Assumptions used to calculate chalcopyrite, bornite, and combined copper sulphide grain size proxies.*

Assumptions for LA-ICP-MS Copper Data	
Analysis pixel length	67 μm
Analysis pixel width	34 μm
Analysis pixel area	2278 μm^2
Density rock	2.7 gm/cm^3
Density chalcopyrite	4.3 gm/cm^3
Density bornite	4.7 gm/cm^3
Density combined copper sulphides	4.5 gm/cm^3

Table 9.3. *Assumptions used to calculate gold grain size proxies.*

Assumptions for LA-ICP-MS Gold Data	
Analysis pixel length	67 μm
Analysis pixel width	34 μm
Analysis pixel area	2278 μm^2
Density gold	17 gm/cm^3
Density rock	2.7 gm/cm^3

9.5.2 LA-ICP-MS limits of detectable grain size

The LA-ICP-MS detection limits for gold and copper in sulphides are approximately 2 ppb and 100 ppb, respectively. The differences are related to the isotopic composition (100% for gold and 69% for copper), the mass bias of the instrument, and the fact that gold was counted for nearly 15 times longer than as copper. For gold, 2 ppb of the total LA-ICP-MS analysis area equates to a gold

grain with a diameter of 0.002 μm. One hundred ppb of copper would be produced by chalcopyrite, bornite, and combined copper sulphide grains with a diameter of less than 0.02 μm. These grain sizes are considered the "limit of detectable grain size" for the LA-ICP-MS grain size calculations. Any calculated gold or copper sulphide grain sizes below this limit were discarded from the D_{PSSL} calculations.

9.5.3 Measuring grains larger than 67 μm

The elemental concentrations in gold and copper sulphide minerals analysed by LA-ICP-MS can vary due to a number of factors including sample-dependent ablation behaviour and elemental fractionation (Fryer et al., 1995). To account for this, a threshold percentage was applied to the elemental concentrations. Studies comparing results from the LA-ICP-MS system to those of the solution ICP-MS system generally produce results within 10-30%, so ± 20% should be a reasonable threshold value (Limbeck et al., 2015; Sinclair et al., 1998). Any analysis greater than 70% gold was considered a gold grain. This threshold was selected to account for the ± 20% precision in LA-ICP-MS analysis, and the fact that most of the gold grains identified in the sample set contain some amount of silver (typically less than 10%). For copper sulphide analysis, the threshold percentages for iron and copper were set to ± 20% of the expected value (Table 9.4).

Table 9.4 *Threshold values for copper sulphide minerals used when grains are greater than the 67 μm data resolution.*

Mineral	Element	Expected Value (%)	Upper Threshold (%)	Lower Threshold (%)
Gold	Au	100.0	-	70.0
Chalcopyrite	Cu	34.6	41.6	27.7
	Fe	30.4	36.5	24.3
Bornite	Cu	63.3	76.0	50.6
	Fe	11.1	13.4	8.9

The total length of consecutive analysis pixels identified as chalcopyrite or bornite were summed to calculate the combined copper sulphide grain measurement. Since this length represents the length of the grain in some direction, and no assumptions about the geometry of the grain can be made with the spatially limited LA-ICP-MS line scan data, this intercept length was used as a grain diameter in the D_{PSSL} calculations. No gold grains larger than 67 μm were

encountered in the test samples. However, the calculations were designed to capture this data, if present.

9.5.4 Considerations for measuring grains smaller than 67 μm

Grains smaller than the 67 μm by 34 μm LA-ICP-MS pixel cannot be measured using the above methods. In this case, the iron, copper, and gold concentrations will be reduced, but the proportions of elements will remain the same. This relationship can be used to estimate the D_{PSSL}. For copper sulphide minerals, the ratio of iron to copper can be used to identify the copper sulphide species present. The elemental concentrations are then compared to the ablation area to estimate the size of the grain encountered in each pixel. In these calculations, it is assumed that all of the gold or copper sulphides present occur as a single grain since it is impossible to distinguish between multiple small grains and a single, larger grain in one analysis pixel.

9.5.5 Measuring copper sulphide grains smaller than 67 μm

Calculating the sub-pixel grain size for chalcopyrite and bornite grains requires first identifying pixels where copper is above a minimum value (set at 10,000 ppm for this analysis). The threshold of 10,000 ppm copper was selected to account for any copper contained as trace elements within other minerals and not associated with copper sulphide grains. Any pixels containing greater than 10,000 ppm copper that have not been previously recognized as a full-pixel copper sulphide grain are identified. To determine which species of copper sulphide is present, the ratio of iron to copper is assessed (Table 9.4). Half the distance between the two end member ratios was used as a threshold for the classification of each copper species (Table 9.5).

Table 9.5. *Expected ratios of iron to copper used to speciate copper sulphide minerals. The Fe:Cu criteria used in the grain size assessment methods are also stated. While bornite grain sizes were not calculated, the criteria are included to show how the combined copper sulphide criteria were derived.*

Mineral	Expected Fe:Cu Ratio	Fe:Cu Criteria
Chalcopyrite	0.88	>0.53
Bornite	0.18	<0.53

LA-ICP-MS lines through chalcopyrite and bornite were measured to be less than 1 μm deep, so it was assumed that the results from the LA-ICP-MS analysis pixels represent an area rather than an analysis volume. The grain size calculations were designed to use the mineral area to determine grain size. Once the species of copper sulphide was determined, the ppm value from the LA-ICP-MS data was converted into a density-corrected concentration by:

$$mineral_{density-corrected\ ppm} = \frac{Cu_{ppm}}{density_{mineral}/density_{rock}} \quad [9.1].$$

These density-corrected concentration values were then compared to the expected copper concentrations if a pixel was pure chalcopyrite, bornite, or combined copper sulphides to determine the area percentage of each mineral:

$$mineral_{area\%} = \frac{mineral_{density-corrected\ ppm}}{Cu\ \exp\ mineral_{ppm}} \quad [9.2].$$

Assuming that all of the copper sulphide minerals detected reside in a single, circular grain in the analysis pixel, the area percentage of each mineral is compared to the analysis area of each pixel to give the mineral area:

$$mineral_{area} = mineral_{area\%} * pixel\ area \quad [9.3].$$

The diameter of this grain is calculated by:

$$mineral_{diameter} = 2 * \sqrt{\frac{mineral_{area}}{\pi}} \quad [9.4].$$

9.5.6 Measuring gold grains smaller than 67 μm

To calculate the sub-pixel grain size for gold grains, a threshold value of 350 ppm gold was set. This threshold represents the concentration of gold expected from a 1 μm grain when using a 34 μm spot size. Since small gold grains do not significantly impact the D_{PSSL} grain size calculations and the MLA data was collected at a resolution of approximately 1 μm, any gold results below the 350 ppm threshold were rejected and not included in the grain size calculations. Assuming the densities outlined in Table 9.2, gold concentrations were converted into a density-corrected concentration by:

$$Au_{density-corrected\ ppm} = \frac{Au_{ppm}}{density_{Au}/density_{rock}} \quad [9.5].$$

The density-corrected concentration value was then compared to the expected gold concentration of a pure gold pixel to determine the area percentage of gold by:

$$Au_{area\%} = \frac{Au_{density-corrected\ ppm}}{1{,}000{,}000_{ppm}\ Au} \quad [9.6].$$

Assuming that all of the gold detected resides in a single, circular grain in the analysis pixel, the area percentage is compared to the pixel analysis area to derive the gold area:

$$Au_{area} = Au_{area\%} * pixel\ area \quad [9.7].$$

The diameter of this grain is calculated by:

$$Au_{diameter} = 2 * \sqrt{\frac{Au_{area}}{\pi}} \quad [9.8].$$

Because the sub-pixel gold calculation is completed on a density-corrected value, the fact that most of the gold grains identified in the sample set contain some amount of silver (typically less than 10%) is accounted for by using 17 gm/cm^3 as the density for gold.

9.5.7 Reporting D_{PSSL} values for copper sulphides and gold

The D_{PSSL} values for chalcopyrite, bornite, combined copper sulphides, and gold were calculated as a grain size proxy using all 20 of the LA-ICP-MS analysis lines for each of the twenty-six test samples. Assuming that the calculated grain size values represent the diameter of a spherical grain, the boundary length and area for each of the grains encountered was calculated. These values were used to determine the D_{PSSL} using all of the grains detected in each sample (see section 6.4 for details). This approach was used to provide an area weighted average size consistent with the methods used to calculate the D_{PSSL} from MLA data. The formulas and calculations used to calculate the gold and copper mineral grain

size proxies from LA-ICP-MS data are included as an Excel workbook in Appendix Q.

9.6 Grain size proxy results

To test the outlined in section 9.5, the grain size proxies using the LA-ICP-MS data are compared to the MLA D_{PSSL} values. These results are presented in the following sections.

9.6.1 Chalcopyrite grain size proxy results

The results for chalcopyrite are shown in Table 9.6. This comparison produces an R^2 value of 0.58 and an r_s rank value of 0.81 (Figure 9.6).

Table 9.6. *Grain size calculated from LA-ICP-MS assuming all of the copper is contained in chalcopyrite compared to the measured chalcopyrite grain* D_{PSSL} *from MLA for each sample in the test sample set.*

Sample	D_{PSSL} from MLA (μm)	Calculated D_{PSSL} Grain Size Proxy (μm)
1185.0	21	16
1193.0	33	21
1207.0	17	21
1265.5	33	25
1269.0	21	14
1283.0	68	26
1283.5	17	18
1292.5	12	16
1306.5	21	15
1307.5	66	45
1356.5	38	21
1362.7	51	25
1380.5	46	82
1381.0	21	21
1392.5	8	15
1393.0	17	15
1400.5	81	29
1401.0	95	134
1409.0	22	23
1420.0	102	83
1420.5	19	20
1421.0	29	25
1431.0	17	16
1431.5	19	19
1448.5	26	15
1461.5	24	24

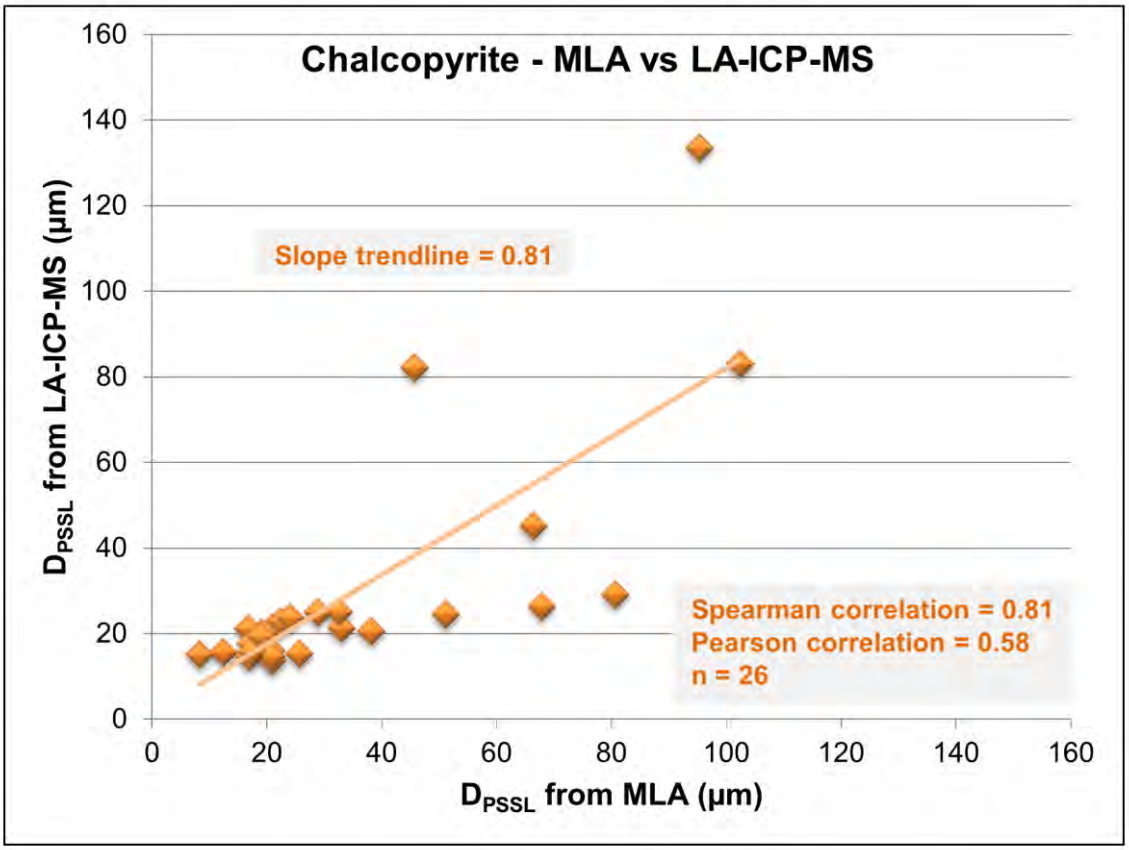

Figure 9.6. *Comparison of the D_{PSSL} for chalcopyrite measured from MLA data and the D_{PSSL} chalcopyrite grain size calculated using the LA-ICP-MS grain size methods.*

9.6.2 Bornite grain size proxy results

The calculated D_{PSSL} results for bornite using the LA-ICP-MS grain size methods are shown in Table 9.7. The grain size proxy methods from LA-ICP-MS compared to the MLA results produce an R^2 value of 0.88 and an r_s rank value of 0.92 (Figure 9.7).

Table 9.7. *Grain size calculated from LA-ICP-MS assuming all of the copper is contained in bornite compared to the measured bornite grain* D_{PSSL} *from MLA for each sample in the test sample set.*

Sample	D_{PSSL} from MLA (μm)	Calculated D_{PSSL} Grain Size Proxy (μm)
1185.0	36	30
1193.0	70	31
1207.0	67	48
1265.5	6	-
1269.0	17	19
1283.0	23	23
1283.5	31	29
1292.5	27	24
1306.5	20	23
1307.5	24	21
1356.5	33	28
1362.7	0	10
1380.5	16	18
1381.0	7	9
1392.5	29	29
1393.0	13	19
1400.5	38	45
1401.0	149	153
1409.0	21	14
1420.0	77	55
1420.5	17	-
1421.0	17	22
1431.0	13	15
1431.5	13	16
1448.5	36	29
1461.5	15	20

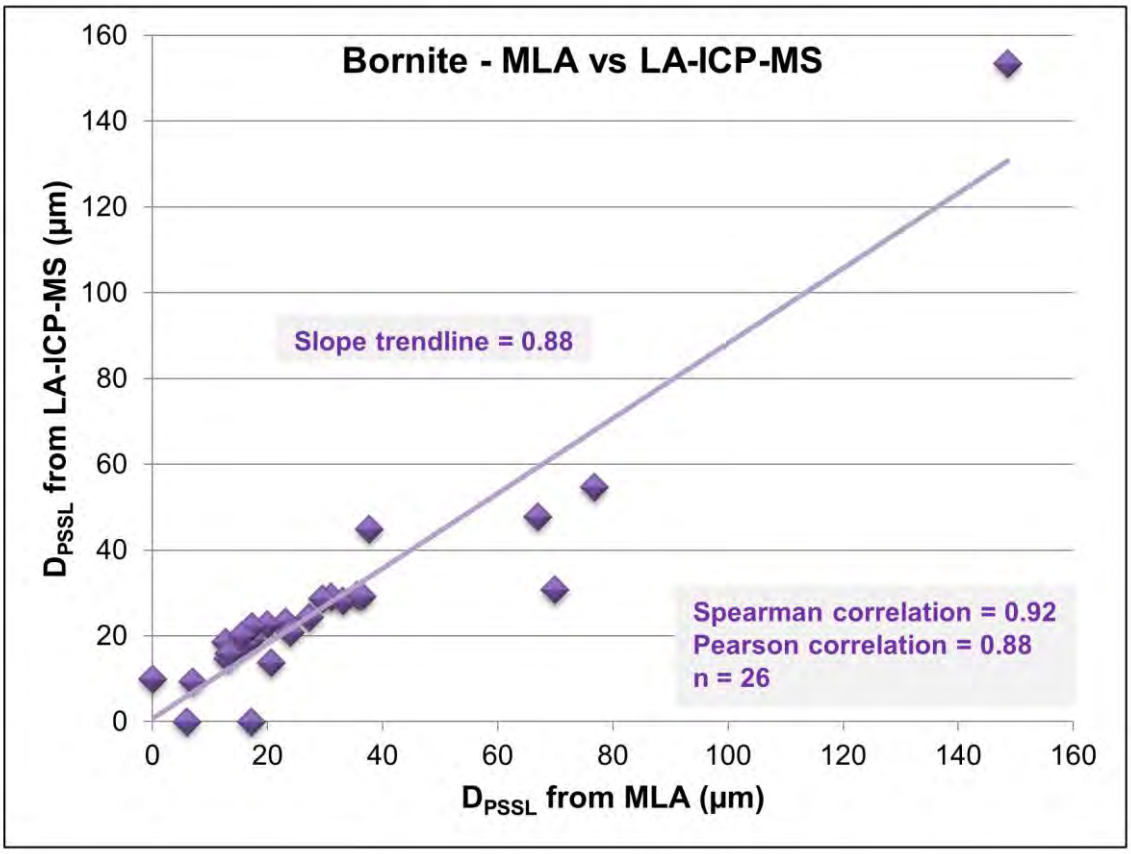

Figure 9.7. *Comparison of the D_{PSSL} for bornite measured from 2D MLA data and the D_{PSSL} bornite grain size calculated using the LA-ICP-MS grain size methods.*

9.6.3 Combined copper sulphides grain size proxy results

The LA-ICP-MS grain size results assuming that the copper is contained equally in chalcopyrite and bornite (combined copper sulphides) are shown in Table 9.8. When compared to the MLA results, the LA-ICP-MS combined copper sulphides grain size method results produce an R^2 value of 0.74 and an r_s correlation value of 0.87 (Figure 9.8).

Table 9.8. *Grain size calculated from LA-ICP-MS assuming combined copper sulphides. These values are compared to the measured combined sulphide grain* D_{PSSL} *from MLA for each sample in the test sample set.*

Sample	D_{PSSL} from MLA (μm)	Calculated D_{PSSL} Grain Size Proxy (μm)
1185.0	35	29
1193.0	71	32
1207.0	58	46
1265.5	32	21
1269.0	18	18
1283.0	42	25
1283.5	31	26
1292.5	27	21
1306.5	21	21
1307.5	53	40
1356.5	39	22
1362.7	52	20
1380.5	46	85
1381.0	21	17
1392.5	29	29
1393.0	13	16
1400.5	79	29
1401.0	152	144
1409.0	23	18
1420.0	111	78
1420.5	19	17
1421.0	29	20
1431.0	15	14
1431.5	17	17
1448.5	36	26
1461.5	24	20

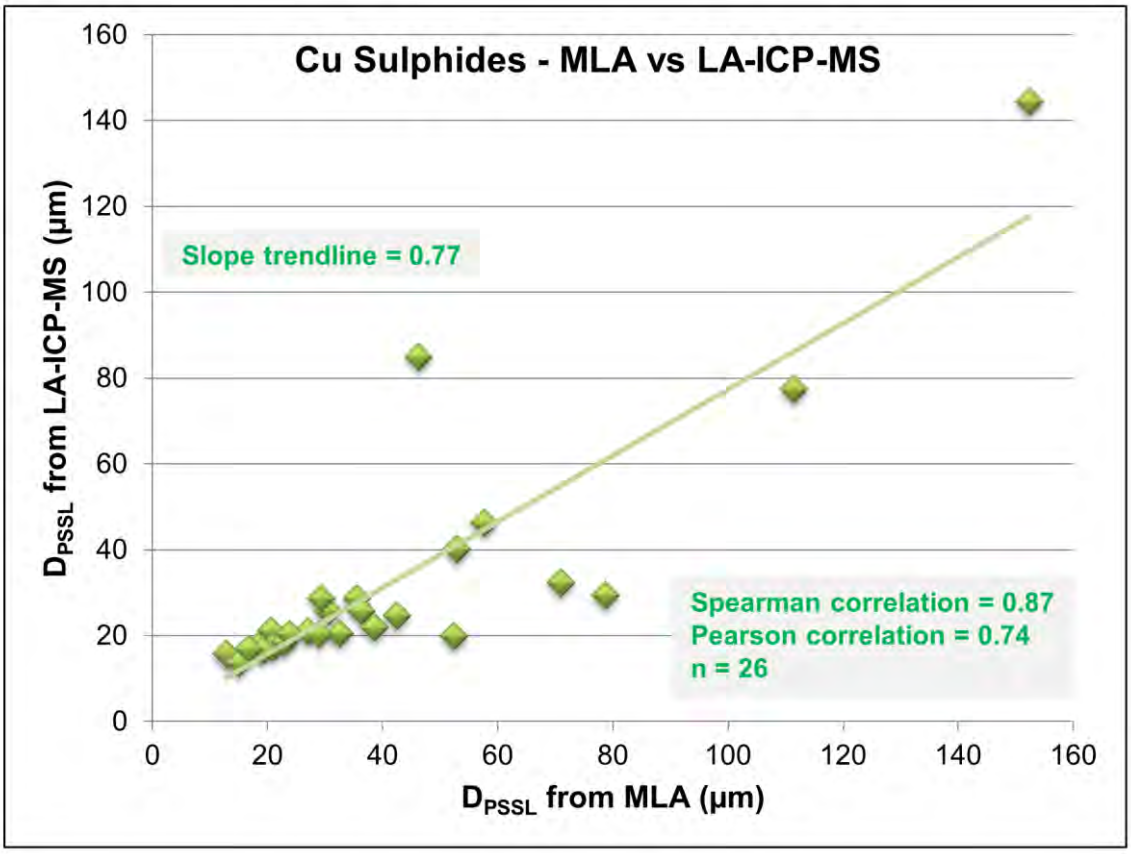

Figure 9.8. *Comparison of the D_{PSSL} for combined copper sulphide measured from 2D MLA data and the grain size calculated using LA-ICP-MS data. These calculations assumed that chalcopyrite and bornite equally occur as combined copper sulphides.*

9.6.4 Gold grain size proxy results

The gold grain size results calculated from LA-ICP-MS data are shown in Table 9.9. When compared to the MLA results, the LA-ICP-MS gold grain size methods produce an R^2 value of 0.25 and an r_s correlation value of 0.50 (Figure 9.9).

Table 9.9. *Gold grain sizes calculated from LA-ICP-MS. These values are compared to the measured gold grain* D_{PSSL} *from MLA for each sample in the test sample set.*

Sample	D_{PSSL} from MLA (μm)	Calculated D_{PSSL} Grain Size Proxy (μm)
1185.0	17	-
1193.0	1	1
1207.0	1	-
1265.5	10	-
1269.0	-	-
1283.0	13	8
1283.5	7	-
1292.5	8	-
1306.5	5	-
1307.5	-	-
1356.5	13	-
1362.7	-	-
1380.5	5	-
1381.0	-	-
1392.5	10	-
1393.0	-	-
1400.5	13	-
1401.0	27	3
1409.0	3	1
1420.0	17	6
1420.5	-	-
1421.0	3	-
1431.0	4	-
1431.5	2	-
1448.5	5	3
1461.5	5	-

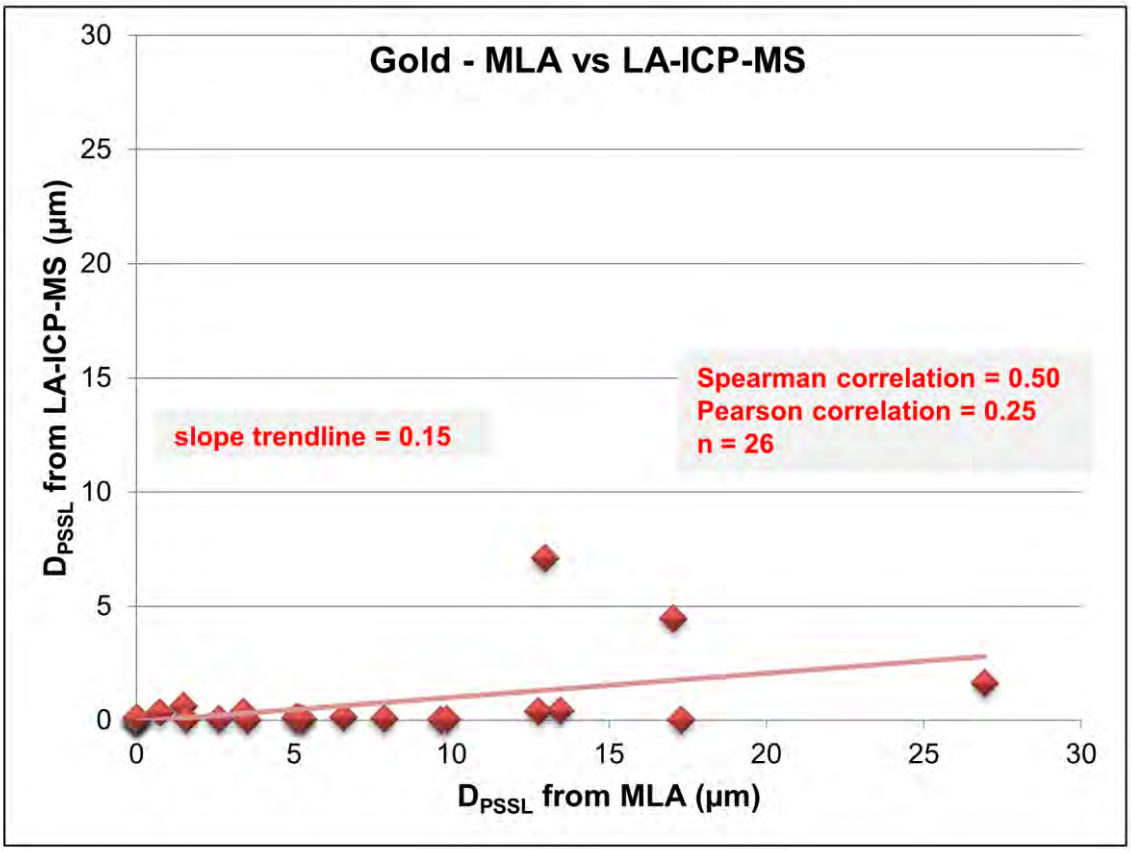

Figure 9.9. *Comparison of the D_{PSSL} for gold measured from 2D MLA data and the grain size calculated using LA-ICP-MS data.*

Gold poses multiple challenges related to sampling statistics and distribution (see section 6.4.1). At least 50 grains of gold must be measured to produce a reliable grain size estimate. In all twenty-six samples, only 8 grains of gold greater than the 1 µm threshold were identified in the LA-ICP-MS data. The D_{PSSL} calculations for gold suffer from a lack of sufficient grains to represent the population.

9.6.5 Sub-micron gold grains

The precise elemental analysis capabilities of the LA-ICP-MS allow for sub-micron grains to be detected. While they cannot be directly compared to the MLA grain sizes, grains between 0.002 µm (the limit of detectable grain size for gold) and 1 µm (the pixel size for the MLA analysis and lower threshold for LA-ICP-MS grain size calculations) are also detected. Very small gold grains or inclusions contribute almost nothing to the gold grade, so identifying grains less than 0.1 µm provides little value. The LA-ICP-MS grain size methods identified over 200 gold grains greater than 0.1 µm but less than 1 µm. While these grains are not useful in the area weighted D_{PSSL} grain size calculation, it is important to note that

these methods can detect sub-micron grains, which could be important for other geometallurgical applications. Table 9.10 outlines the number of grains between 0.1 μm and 1 μm identified in each sample.

Table 9.10. *Count of gold grains detected in each sample, including those between 0.1 μm and the 1 μm grain size calculation threshold.*

Sample	Total Number Grains	Number Grains 0.1 μm – 1 μm	Number Grains > 1 μm
1185.0	5	5	0
1193.0	6	5	1
1207.0	3	3	0
1265.5	0	0	0
1269.0	3	3	0
1283.0	17	14	3
1283.5	5	5	0
1292.5	9	9	0
1306.5	7	7	0
1307.5	4	4	0
1356.5	10	10	0
1362.7	2	2	0
1380.5	7	7	0
1381.0	2	2	0
1392.5	20	20	0
1393.0	5	5	0
1400.5	15	15	0
1401.0	16	15	1
1409.0	44	43	1
1420.0	19	17	2
1420.5	2	2	0
1421.0	0	0	0
1431.0	0	0	0
1431.5	0	0	0
1448.5	17	17	0
1461.5	0	0	0
Total	*218*	*210*	*8*

9.7 Bootstrapping of copper results

For copper minerals, using all 20 LA-ICP-MS line analyses provides a reasonable estimate of grain size. A series of bootstrapping experiments were completed to assess the minimum number of laser lines required to estimate grain size. These experiments were designed to randomly select groups of 15, 10, 5, and 1 LA-ICP-

MS lines from a sample, and calculate the corresponding D_{PSSL} grain size proxy using only the selected lines. Fifty iterations of each line group were computed. The sampling statistics of gold require that all of the available analyses from a group of samples are combined to calculate the grain size from LA-ICP-MS. As such, the gold results were not bootstrapped as this would decrease the overall sampling statistics.

A series of box and whisker plots showing the results of the bootstrapping experiments and measured grain size values from MLA were used to track the performance of the calculated grain size estimates as the number of analysis lines decreases. Figures 9.10 through 9.13 show the results for chalcopyrite, Figures 9.14 through 9.17 show the results for bornite, and Figures 9.18 through 9.21 show the results for combined copper sulphides. As the number of lines used to calculate the D_{PSSL} grain size proxy decreases, the mean bootstrapped D_{PSSL} values change and the second and third quartile range of D_{PSSL} values increases.

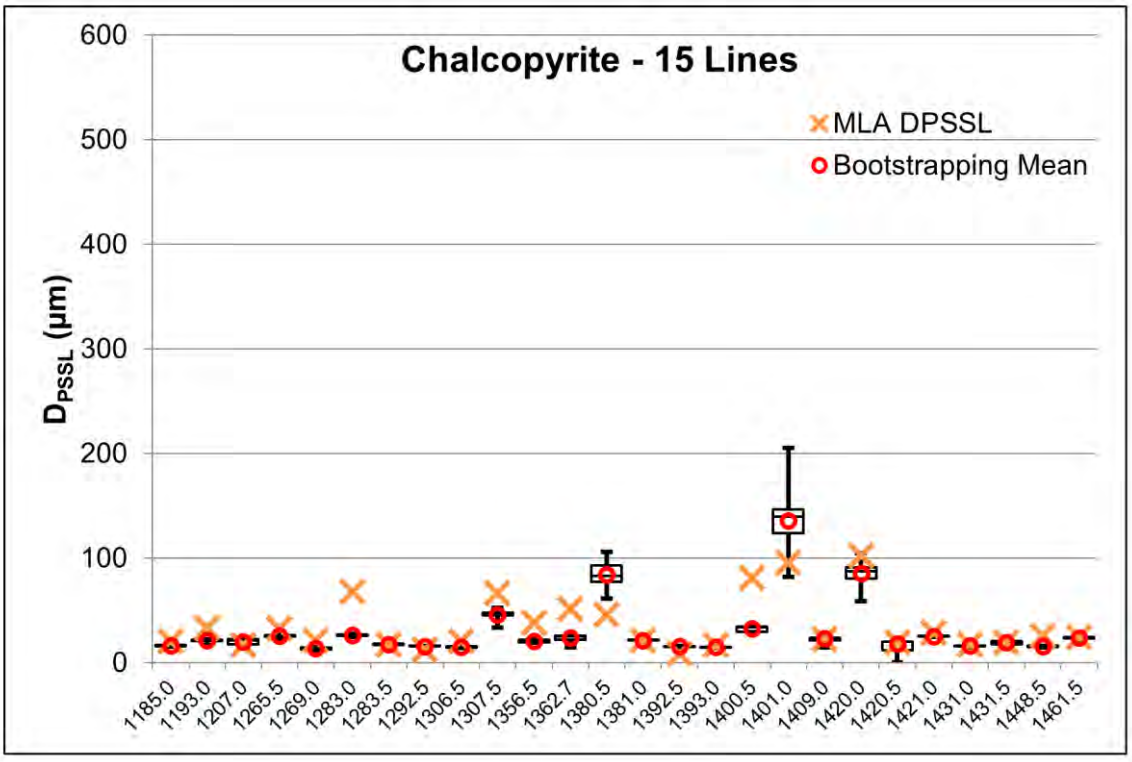

Figure 9.10. *Box and whisker plot showing the bootstrapping results for chalcopyrite using 15 random lines per sample. The whiskers represent the minimum and maximum values.*

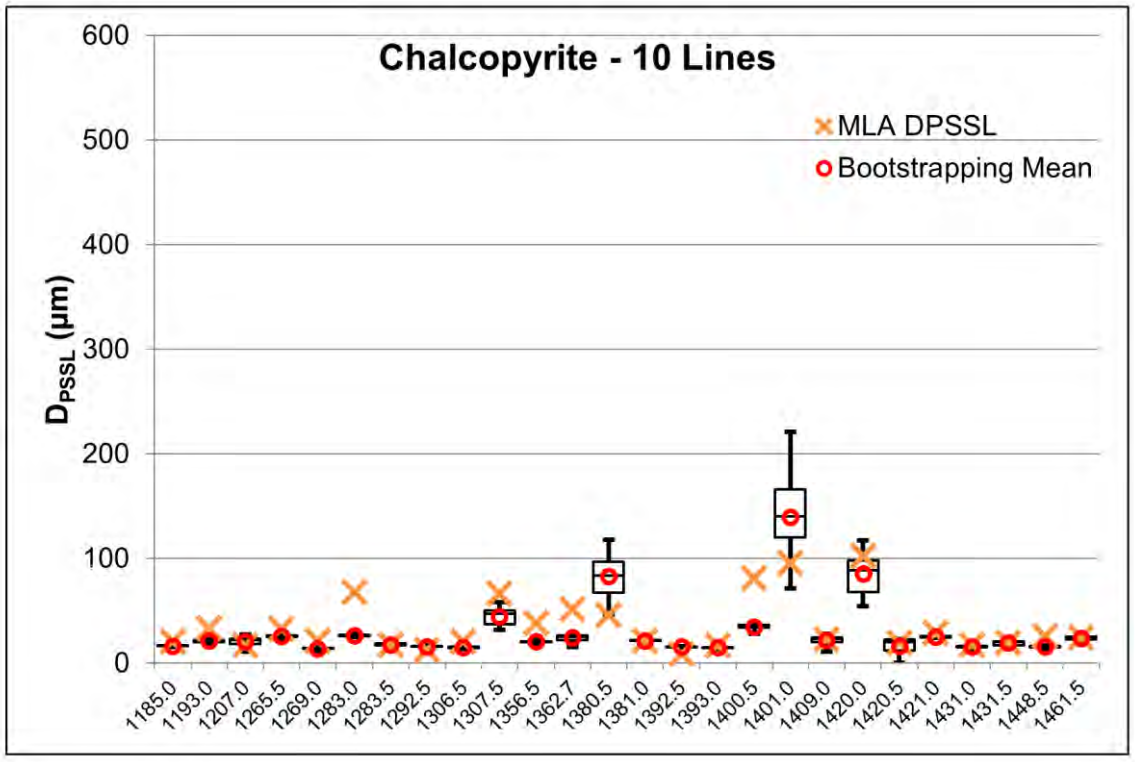

Figure 9.11. *Box and whisker plot showing the bootstrapping results for chalcopyrite using 10 random lines per sample. The whiskers represent the minimum and maximum values.*

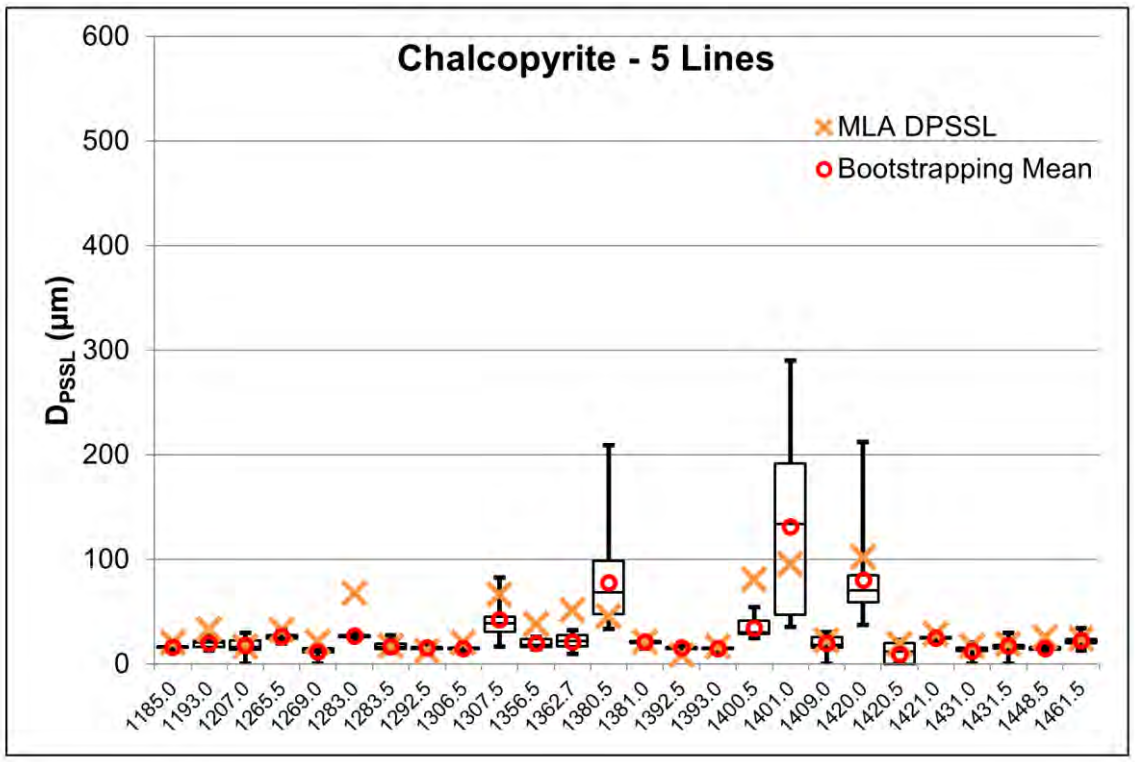

Figure 9.12. *Box and whisker plot showing the bootstrapping results for chalcopyrite using 5 random lines per sample. The whiskers represent the minimum and maximum values.*

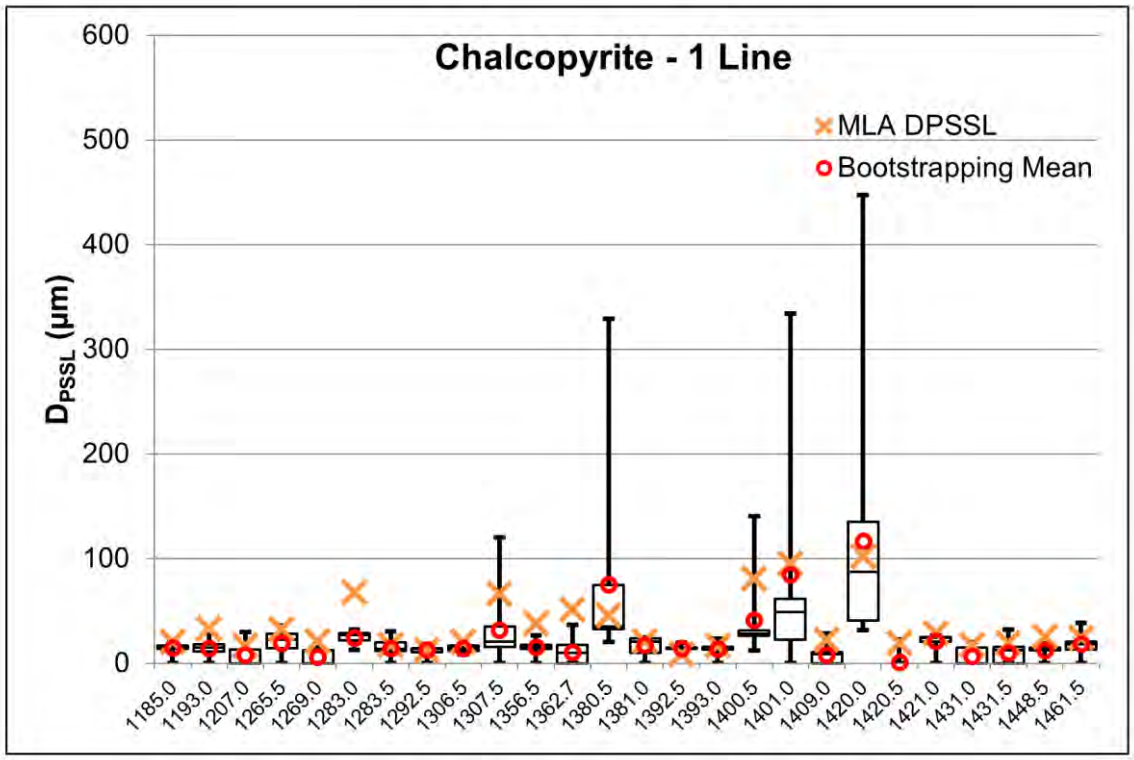

Figure 9.13. *Box and whisker plot showing the bootstrapping results for chalcopyrite using 1 random line per sample. The whiskers represent the minimum and maximum values.*

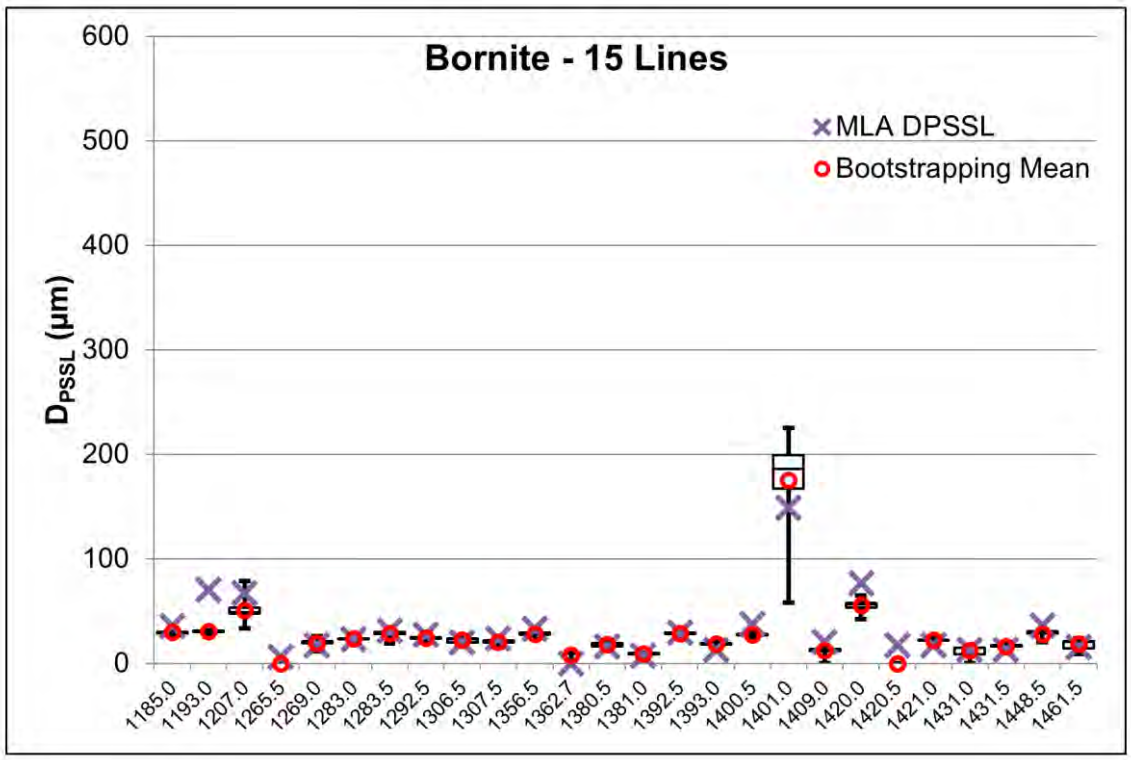

Figure 9.14. *Box and whisker plot showing the bootstrapping results for bornite using 15 random lines per sample. The whiskers represent the minimum and maximum values.*

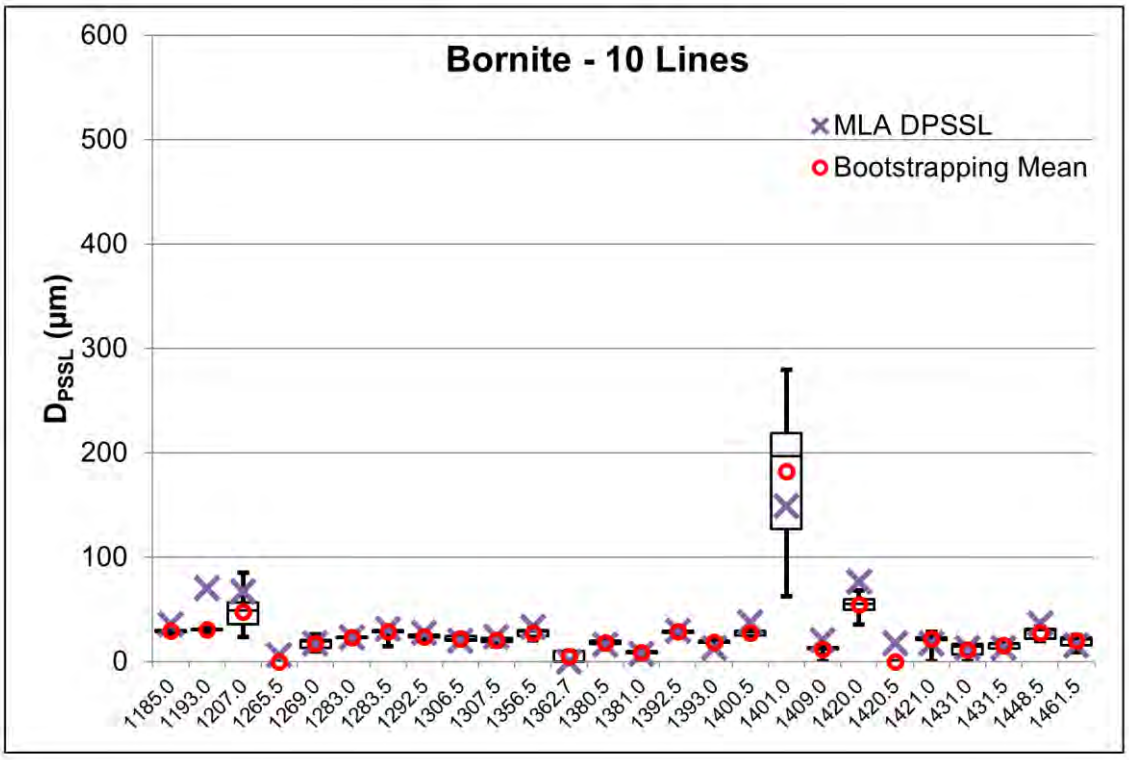

Figure 9.15. *Box and whisker plot showing the bootstrapping results for bornite using 10 random lines per sample. The whiskers represent the minimum and maximum values.*

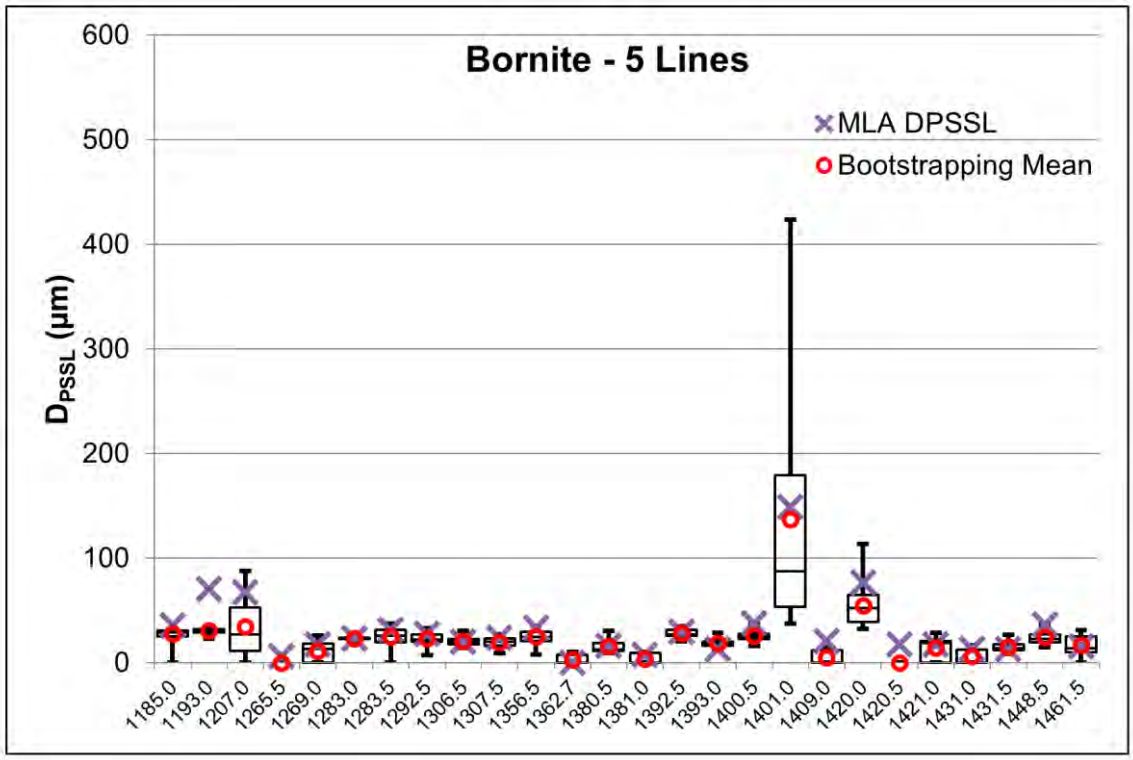

Figure 9.16. *Box and whisker plot showing the bootstrapping results for bornite using 5 random lines per sample. The whiskers represent the minimum and maximum values.*

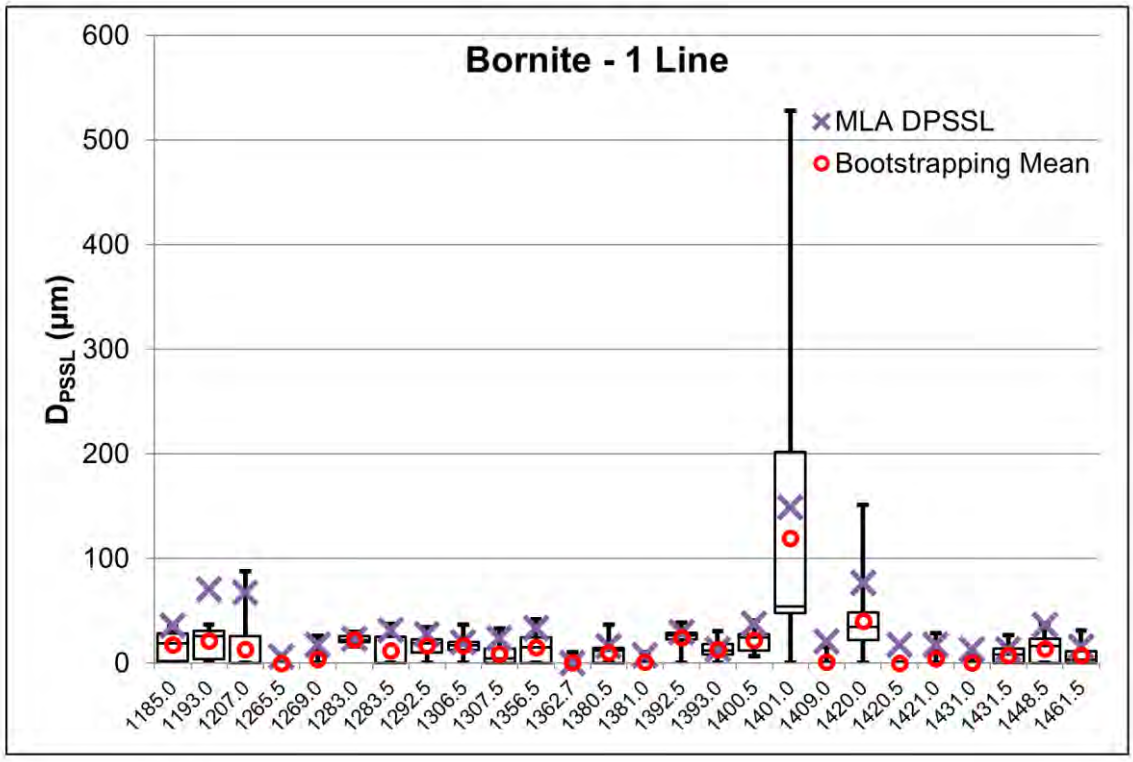

Figure 9.17. *Box and whisker plot showing the bootstrapping results for bornite using 1 random line per sample. The whiskers represent the minimum and maximum values.*

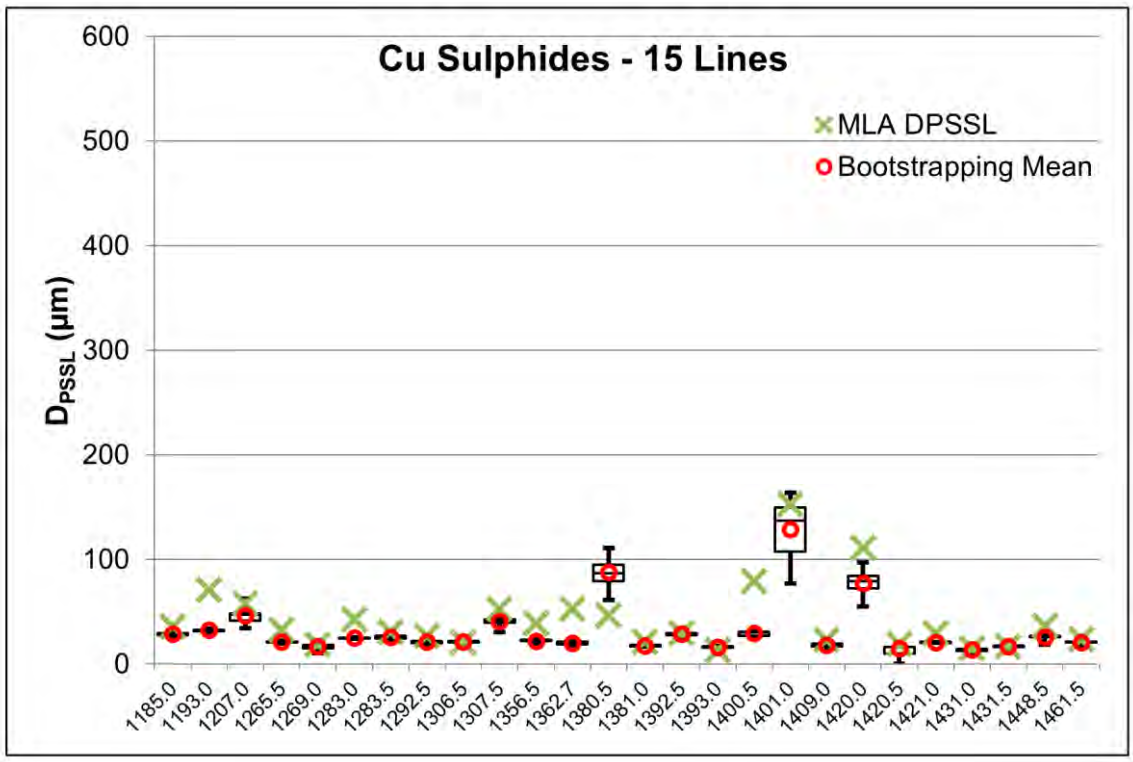

Figure 9.18. *Box and whisker plot showing the bootstrapping results for combined copper sulphides using 15 random lines per sample. The whiskers represent the minimum and maximum values.*

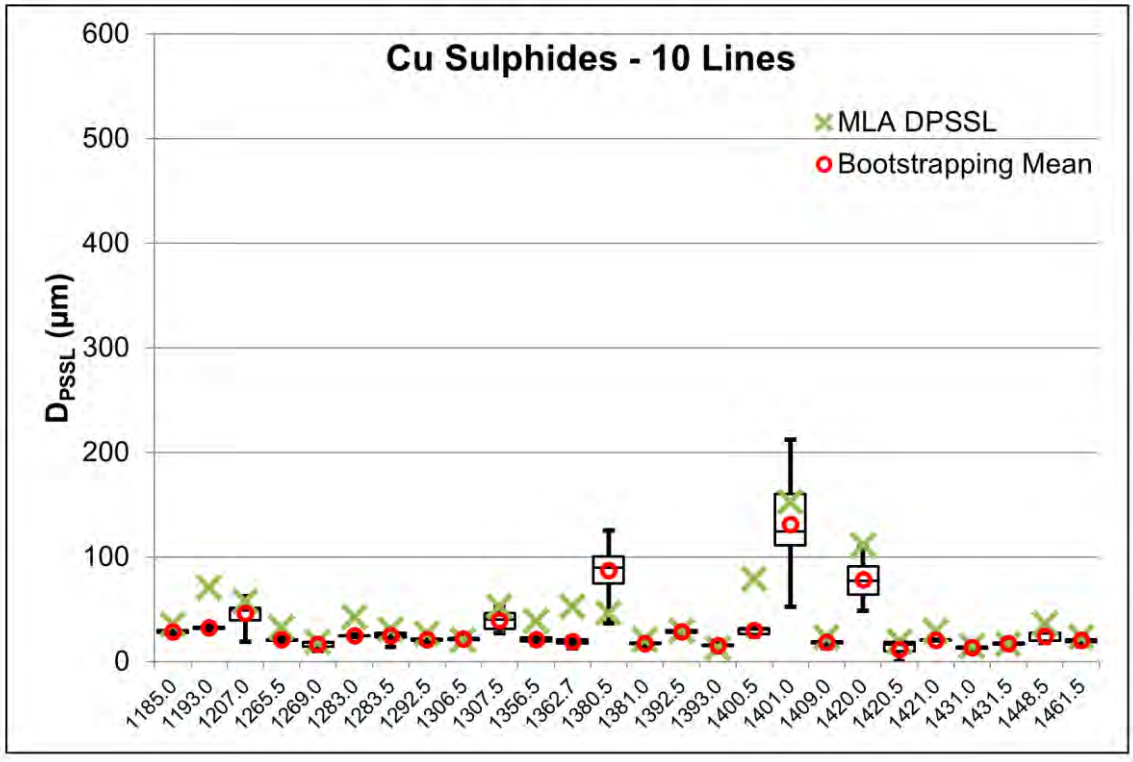

Figure 9.19. *Box and whisker plot showing the bootstrapping results for combined copper sulphides using 10 random lines per sample. The whiskers represent the minimum and maximum values.*

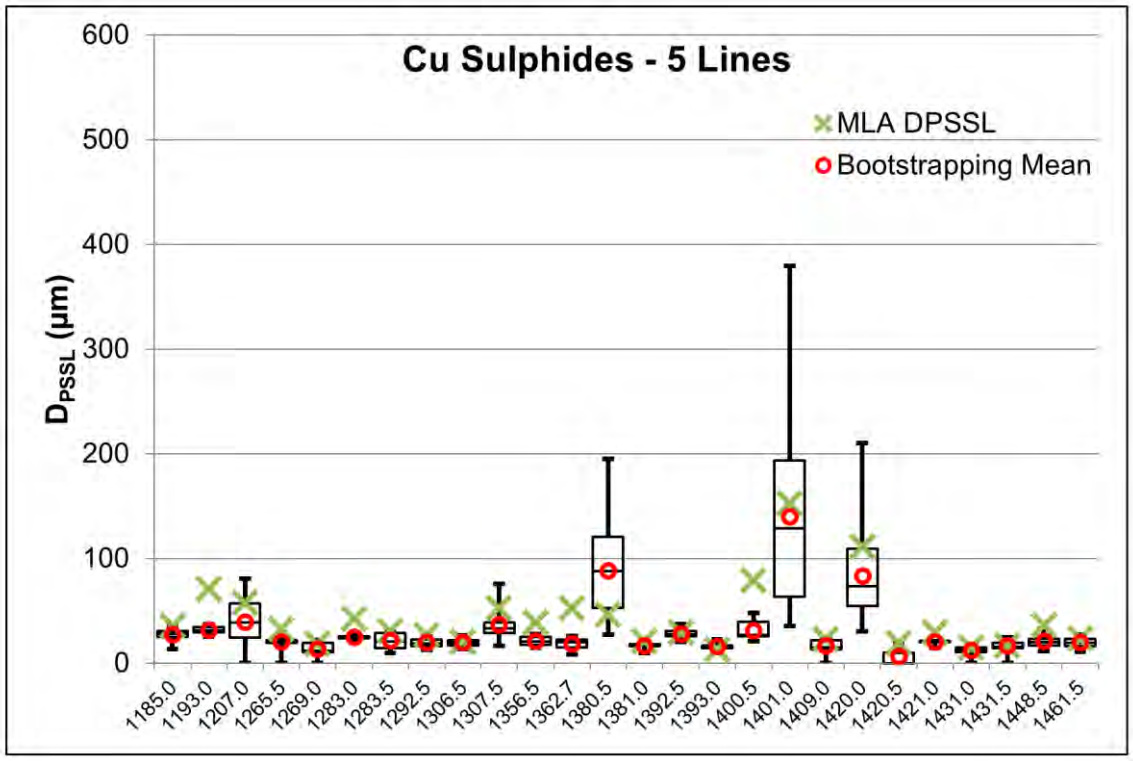

Figure 9.20. *Box and whisker plot showing the bootstrapping results for combined copper sulphides using 5 random lines per sample. The whiskers represent the minimum and maximum values.*

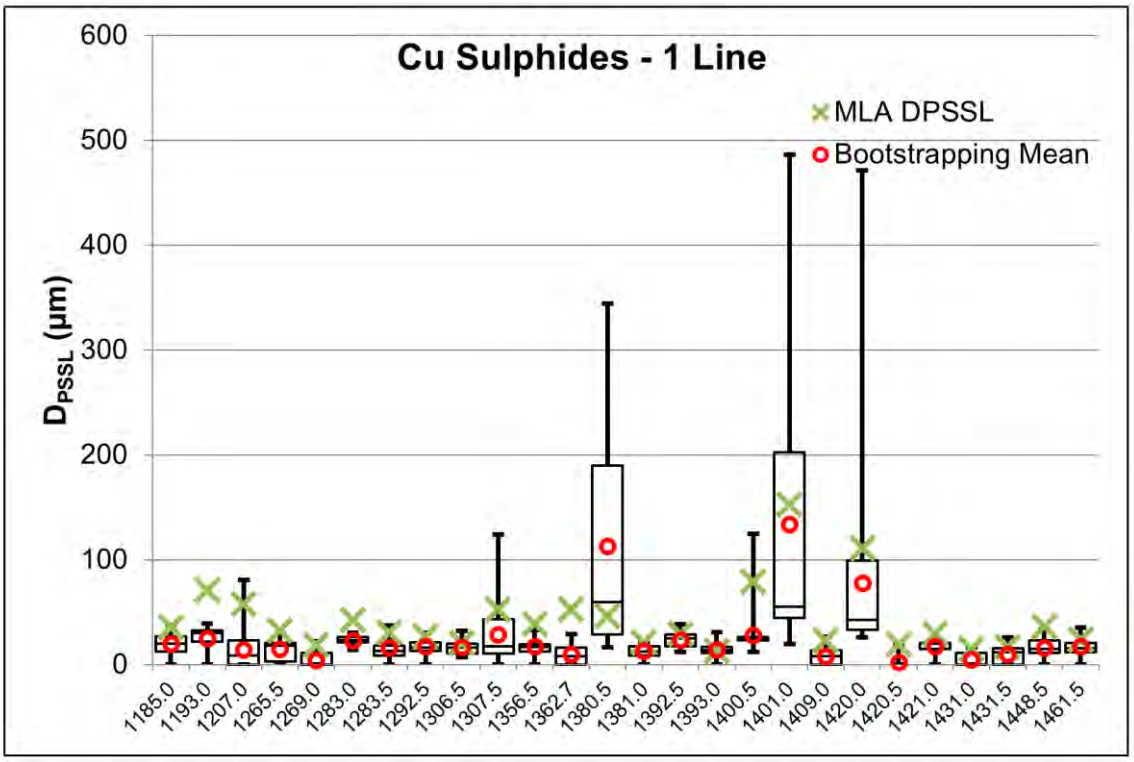

Figure 9.21. *Box and whisker plot showing the bootstrapping results for combined copper sulphides using 1 random line per sample. The whiskers represent the minimum and maximum values.*

To test the number of lines required to provide a reasonable grain size proxy, a series of bootstrapping experiments were designed to randomly select LA-ICP-MS analysis lines from each sample. D_{PSSL} grain size proxies for copper sulphide minerals calculated from LA-ICP-MS data produce an average standard error of less than 1.5 in 50 experiments when at least 5 of the total 20 analysis lines are used (Figure 9.22). Using 5 random LA-ICP-MS analysis lines will provide D_{PSSL} values within 1.5 µm in 50 repeated experiments (with 95% confidence) as indicated by a standard error value of 1.5.

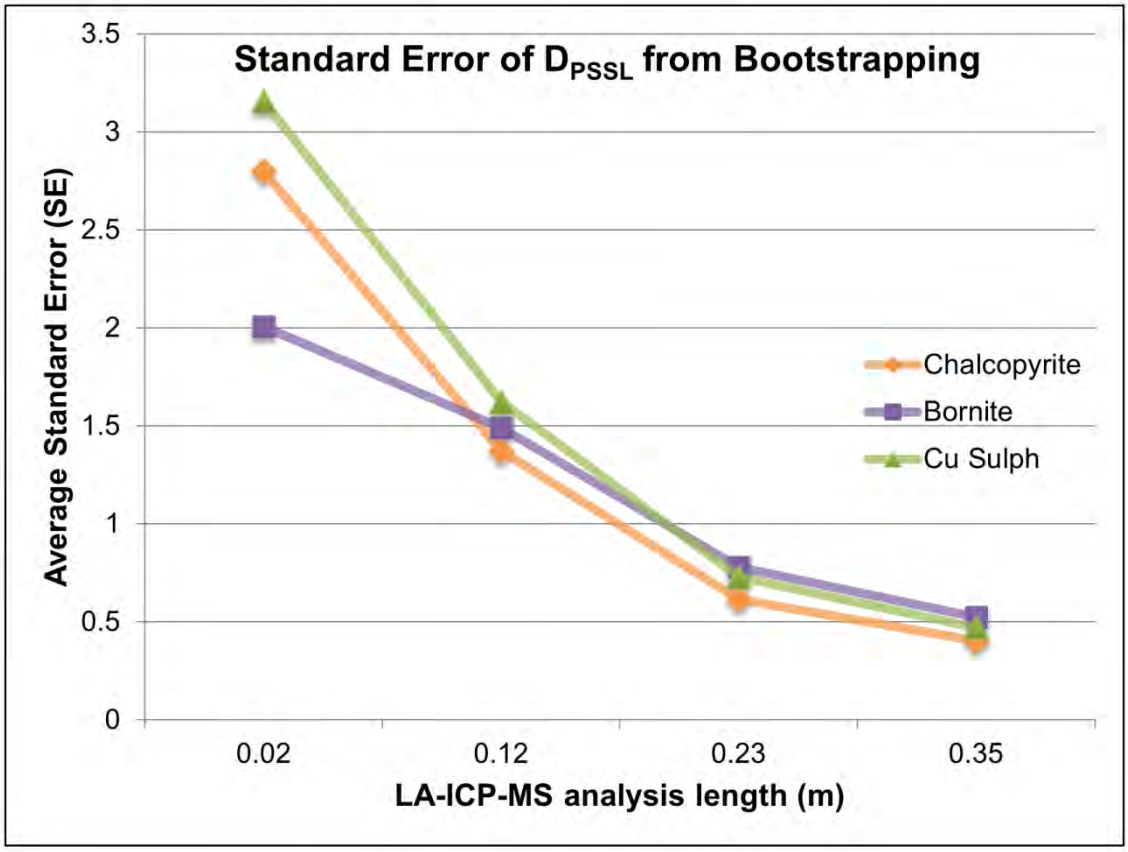

Figure 9.22. *Comparison of the length of LA-ICP-MS analysis used and the average standard error of grain size proxy values calculated for all twenty-six test samples. This trend shows that approximately 0.12 metres of LA-ICP-MS (or 5 analysis lines) are required to produce copper grain size values with a standard error of less than 1.5.*

9.8 Discussion

The elemental concentrations of gold, copper, and iron from LA-ICP-MS analysis were used to calculate the D_{PSSL} grain size proxies for chalcopyrite, bornite, combined copper sulphides, and gold. When including all 20 of the LA-ICP-MS line analyses, bornite and combined copper sulphides show the best correlation with the MLA values producing Pearson correlation coefficients greater than $R^2 = 0.7$. Using Spearman ranking coefficients, bornite gives an $r_s = 0.92$ and combined copper sulphides a $r_s = 0.87$, both very good ranking values. These results show that the LA-ICP-MS grain size proxy for bornite and combined copper sulphides produce sensible grain size estimates and properly rank the D_{PSSL} values. Chalcopyrite had a slightly lower correlation with the MLA data producing a Pearson correlation of $R^2 = 0.58$ and a Spearman ranking of $r_s = 0.81$. The slopes of the R^2 trendlines for chalcopyrite, bornite, and combined copper sulphides are reasonably close to 1 (ranging from 0.77 to 0.88), indicating that the calculated proxies are reporting grain sizes comparable to the measured MLA grain sizes.

Overall, the copper sulphide D_{PSSL} grain size proxies calculated from LA-ICP-MS data correlate well with the measured MLA values.

For copper minerals, using all 20 LA-ICP-MS analysis lines (equivalent to 46 cm of analysis) provides a good estimate of the grain size using the proposed grain size proxy methods. The acquisition time for this data is about 26 minutes and would provide reasonable copper mineral grain size assessment in that time. The bootstrapping results indicate that at least 5 LA-ICP-MS analysis lines are required to produce sufficient grain size proxies. Each LA-ICP-MS analysis line contains 23 mm of LA-ICP-MS analysis. If 5 lines are required to calculate a reasonable grain size proxy, this equates to approximately 0.12 metres of LA-ICP-MS analyses. Ten lines of LA-ICP-MS analysis have an acquisition time of 6.4 minutes which is nearly half the speed of the Corescan acquisition for one core tray (4 metres). At this rate, an LA-ICP-MS grain size proxy calculation on selected samples could be made for 2 metres of drill core in the same time that the Corescan system scans 1 metre.

The gold grain sizes calculated from laser data provided poor correlation values of $R^2 = 0.25$ and $r_s = 0.50$ when compared to the measured D_{PSSL} values from MLA on a sample by sample basis. Berry and Hunt (2011) determined that at least 50 grains of gold are required to assess gold grain size. Only two of the samples in the test sample set contain more than 50 gold grains measured by MLA, so most of the D_{PSSL} values from MLA on a sample by sample basis are not representing the gold grain size population. Because the gold grains in the test sample set are small and rare, they provide poor sampling statistics. In chapters 9 and 10, this was addressed by combining multiple samples together in groups to improve the sampling statistics and the resulting correlation coefficients. Since only 8 gold grains greater than 1 μm were detected in the entire test dataset, combining the sample results will not provide enough gold grains to determine a sufficient grain size. Here the test is strongly affected by the sampling error, as the likelihood of encountering rare gold grains is very low. Additionally, MLA analysis is a surface technique while the LA-ICP-MS system analyses a small volume of material. The LA-ICP-MS detects gold grains that are just below the surface that would not be detectable by MLA surface analysis. It may be that LA-ICP-MS analysis is a much better assessment of the gold grain size than the MLA as the sensitivity of this system is higher and the ability to detect minerals slightly below the sample surface is greater than the MLA. Unfortunately, no independent method is available to better check the validity of the grain size

assessment than the MLA. The poor sample by sample correlation between the LA-ICP-MS and MLA grain sizes reflects this challenge with population statistics and demonstrates that this sample size is not sufficient for reliable measurement using these techniques. These methods can, however, quantify sub-micron gold grains which are not useful for D_{PSSL} grain size calculations, but could be used in other geometallurgical applications.

9.9 Conclusions

The objective of this study was to investigate the potential for LA-ICP-MS technology to be used in conjunction with Corescan analysis to rapidly and sufficiently assess copper sulphide and gold grain sizes by rapid scanning selected core samples outside of the Corescan sample analysis stream. Specifically, the number of LA-ICP-MS analyses required to assess grain size was tested. Assessment of the laser data shows that the elemental concentrations of copper, iron, and gold collected along a line scan can be used to assess grain size.

While the test sample set is small, chalcopyrite, bornite, and combined copper sulphides show good correlation with the D_{PSSL} values calculated from MLA when 20 analysis lines are used. Bootstrapping of the copper minerals shows that this method requires about 0.12 metres of LA-ICP-MS analysis length to achieve grain size results that produce an average standard error of less than 1.5 in 50 experiments. The LA-ICP-MS data in this study was collected at a rate of 300 μm per second, or 18 mm per minute. The Corescan system collects data at a rate of 3 minutes per metre and 12 minutes per 4 metre core tray. In the same amount of time that the Corescan collects 4 metres of data (12 minutes), 0.22 metres of LA-ICP-MS data can be acquired, nearly the same length determined to produce good copper sulphide grain size proxies.

For gold, the proxy produced poor correlations on a sample by sample basis, and only identified 8 gold grains for the entire sample set. Even if all of the analysis lines from all twenty-six samples were used, there would not be enough gold grains to provide a suitable grain size estimate. Additionally, the analysis length of all 20 lines in each of the twenty-six samples represents approximately 12 metres of LA-ICP-MS analysis. At the rate of 300 μm per second, 12 metres of LA-ICP-MS analysis would take 11 hours to acquire. The current data acquisition rate of the LA-ICP-MS system makes this technology unsuitable for gold grain size assessment. As this technology develops, however, LA-ICP-MS systems may be

adapted to acquire data more rapidly making gold grain size assessment feasible. While it seems simple to increase the laser speed, numerous factors including ICP-MS sequential element scan times and ablation cell washout times will need to be considered before increasing the laser analysis speed. This study was completed by analysing for 44 elements simultaneously. These experiments should be repeated, limiting the element list to only gold to decrease the elemental sweep time in the ICP-MS and increase the data resolution.

Currently available LA-ICP-MS technology is capable of collecting data on selected samples for copper sulphide grain size calculations at a rate similar to the Corescan system. This analysis it is not rapid enough for gold grain size assessment. As this technology is constantly developing, the results of this study should be periodically reassessed. If future LA-ICP-MS technological developments significantly increase the analysis speed, elemental scan times, and washout times, the acquisition time could be decreased and this may prove to be a viable technique to acquire early gold grain size information outside of the Corescan system analysis stream. At the moment, this technology cannot be completed outside of an ablation cell. If increased data acquisition speed can be combined with the capability to analyse samples in atmospheric conditions and not in a laboratory setting, this technology may be developed to analyse online within or alongside the Corescan system.

Chapter 10

Grain size assessment by laser-induced breakdown spectroscopy (LIBS)

10.1 Introduction

Laser-induced breakdown spectroscopy (LIBS) is a surface analysis technique that measures the optical emission from a laser-induced plasma. This technology has been applied to numerous fields of study including manufacturing and forensic examination (Naes et al., 2008). This technique can provide rapid, *in situ* geochemical analysis of geologic materials in real time (Hark and Harmon, 2014). Advantages of LIBS analysis include minimal sample preparation, low analysis costs, and the ability to analyse samples in atmospheric conditions. Over the past 15 years, the number of publications demonstrating the potential of LIBS as a geochemical tool has been rapidly increasing (Hark and Harmon, 2014). These studies have applied LIBS analysis to a range of geochemical applications including extra-terrestrial rock analysis, provenance studies, mine waste characterisation, and drill core analysis (Bolger, 2000; Dalm and Buxton, 2016; Harmon et al., 2017; Kuhn et al., 2016; Senesi, 2014).

An investigation into the potential for LIBS technology to be used in conjunction with Corescan analysis to rapidly assess copper sulphide and gold grain sizes was completed. To evaluate if LIBS is capable of providing adequate grain size assessment data, the results of gold and copper sulphide grain size proxies using LIBS are compared to the MLA and μXRF grain size result datasets. Importantly, for LIBS technology to be successfully paired with the Corescan system, the acquisition rates of LIBS data need to be collected at an equivalent rate of 3 minutes per metre.

The LIBS *in situ* analytical technique captures a spectrum that reflects the relative proportions of elements in a given analysis spot. The proportions of copper and gold from LIBS data are linked to the size of copper minerals and gold grains present in the analysis spot. Therefore, this data can be used to develop proxies for determining grain sizes from the LIBS spectral signature. A combination of spectral matching and peak integration techniques were applied to identify gold and copper minerals and calculate grain size proxies from twenty-six samples. To

determine the minimum number of LIBS analyses required to produce a representative grain size proxy, a series of bootstrapping experiments were competed. The results of bootstrapping were then used to calculate data acquisition rates and compared to that of the Corescan system.

10.2 Scientific principles of LIBS technology

Laser induced breakdown spectroscopy is an optical spectroscopy technique based on the principles of plasma physics and is used to measure the chemical characteristics of a given material. When ionised in a plasma, each element in the periodic table emits photons between 200 nm and 1000 nm, so a complete chemical fingerprint of a material can be captured rapidly and simultaneously by the LIBS system (Connors et al., 2016; De Lucia and Gottfried, 2011; Harmon et al., 2005; Harmon et al., 2017; Somers, 2017).

In LIBS analysis, a focused laser ablates a small amount of sample to form a high-temperature plasma plume. This plasma is short-lived and temporarily elevates the electrons to higher orbitals. As the plasma cools, the excited electrons return to their ground state (Figure 10.1). This change in electron energy results in the emission of characteristic spectra representing the elements present in the plasma as a series of peaks (also known as emission lines). These characteristic emissions are detected by specialised optical spectrometers that collect light intensities over a series of wavelengths and convert these values into a LIBS spectrum.

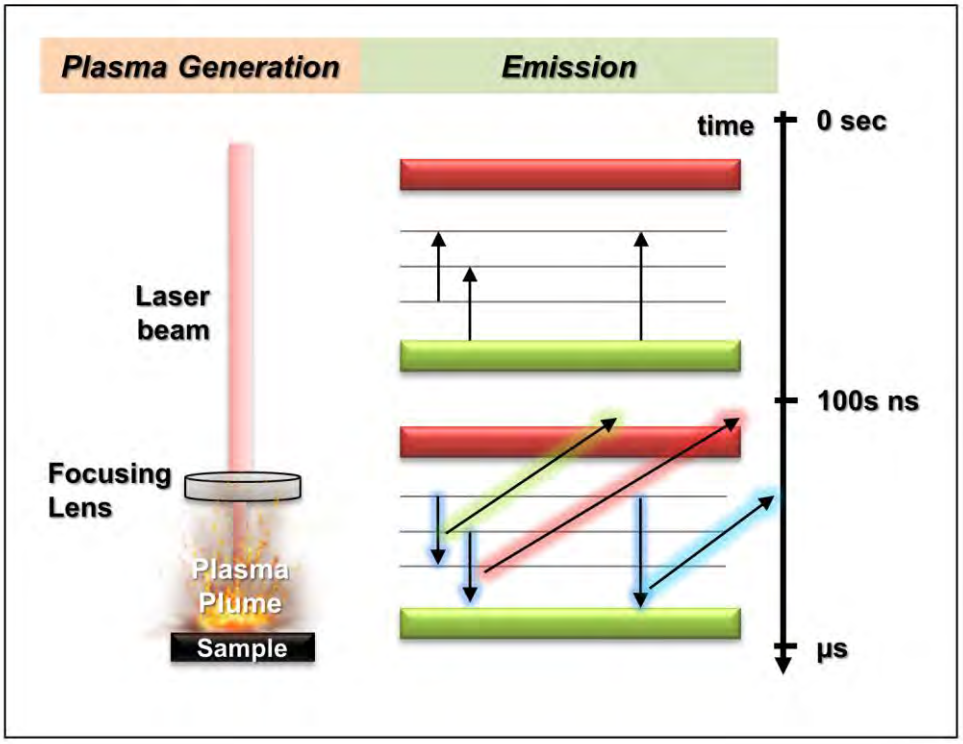

Figure 10.1. *Graphical representation of the excitation and optical emission of electrons in LIBS analysis. Modified from Lasertechnik (2018).*

10.3 LIBS instrument

LIBS instruments consist of a series of components that are designed for either benchtop laboratory use or ruggedized for use in the field (Hark and Harmon, 2014). These components include a laser source, optics to focus the laser, a spectrograph and detector (e.g. CCD or ICCD), and a computer control system for programming and data processing. A schematic diagram of the LIBS system design is shown in Figure 10.2.

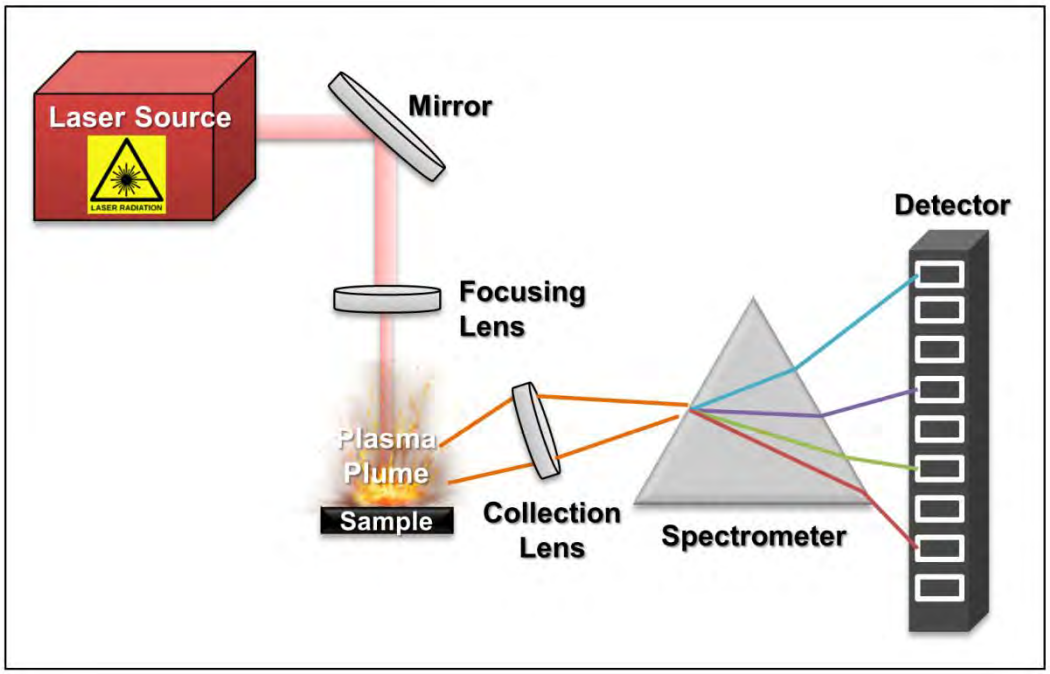

Figure 10.2. *Schematic design of the LIBS instrument setup. Modified from Somers (2017).*

Quantification of elemental abundances from LIBS spectra is difficult due to a number of factors. The likelihood of encountering multiple minerals, and therefore multiple elements, in a geological sample is high. There are additional challenges with multiple atomic emission peak overlaps resulting in signal interferences. The interactions between the laser and the sample material are complex and difficult to quantify (Ready, 1971; Senesi, 2014). Instead of attempting to quantify copper and gold concentrations for grain size assessment, a combination of spectral matching and peak integration was used to identify gold and copper minerals and develop grain size proxies based on the relative abundance of each mineral.

10.4 Data collection methodology

LIBS spectra from the twenty-six rock tiles in the test set were collected using an Applied Spectra RT100-HP laboratory system located at Juniata College in Huntingdon, Pennsylvania, USA. This system is fitted with a Q-switched Nd:YAG laser operating at 1064 nm and a Czerney-Turner spectrograph ICCD detector containing 600 grooves per nm to achieve 0.25 nm spectral resolution across the 200 nm to 1000 nm wavelength range. Spectra were collected with a 100 μm beam size at 65% laser power operating at a repetition rate of 20 Hz.

Typical detection limits reported in the literature for copper are in the range of 10s of ppm and 100 to 500 ppm for gold (Hark and Harmon, 2014).

Prior to LIBS analysis of the entire sample set, a series of measurements were collected on standard reference materials and an unknown sample to determine the effects of the laser on the sample surface and identify an appropriate analysis step size. While a 100 μm beam size was used, the ablation craters were measured to be approximately 150 μm across. A damage zone with deposits of ejecta was observed 20-50 μm outside the ablation craters (Figure 10.3). To avoid analysing material ejected from the previous analysis spot, a step size between analyses of 300 μm was used. Sixty percent of each of the 3 cm by 3 cm samples was covered in LIBS analysis spots. The analysis pattern consisted of 89 lines across the sample surface with 61 analysis spots per line, for a total of 5429 spot analyses per sample (Figure 10.4).

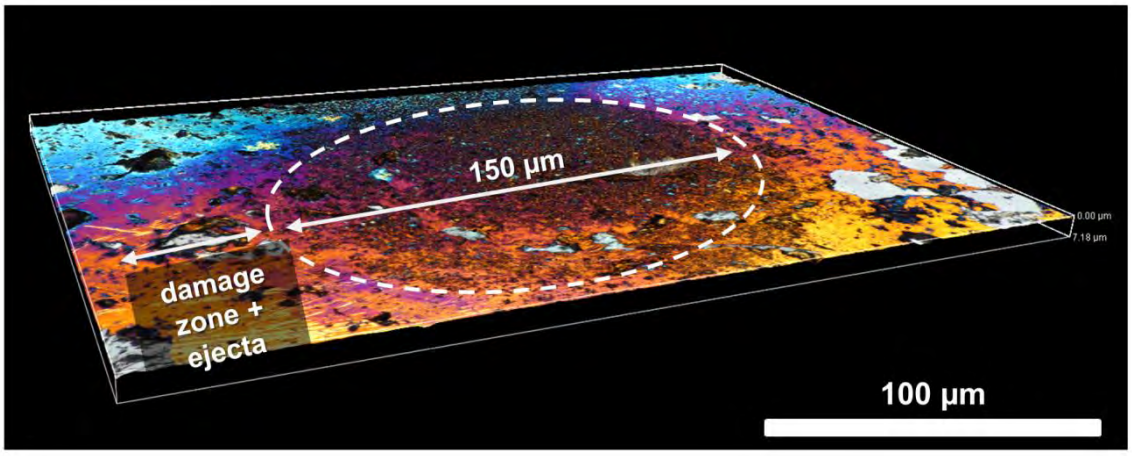

Figure 10.3. *Reflected light 3D step image of a LIBS crater in chalcopyrite (outlined in white). The ablation depth in copper sulphide minerals is 1-5 μm.*

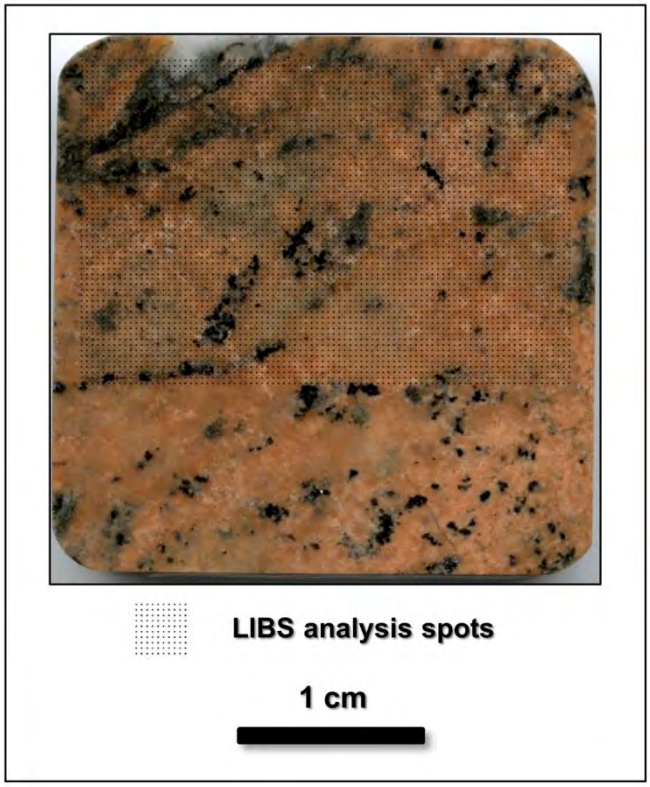

Figure 10.4. *Configuration of LIBS analysis spots on each test sample. The upper 60% of each analysis line was used, for a total of 5429 LIBS analyses per sample.*

10.4.1 Selection of copper and gold lines

Pure gold and copper sulphide samples were analysed to: (1) select diagnostic copper and gold emission lines, (2) determine background thresholds for data reduction, and (3) identify spectra that contain copper sulphide and gold using spectral matching. Pure chalcopyrite, bornite, and gold samples were analysed under the same LIBS conditions as used on the test samples to serve as standards for pure minerals. From the reference spectra copper and gold emission lines were selected to optimise peak intensity and minimise the effects of interferences from other element emission lines. For copper, the Cu 324.75 nm and Cu 327.40 nm emission lines were selected as the main copper peaks. These emission lines are commonly used to determine copper concentrations from LIBS spectra as they typically show high intensities relative to background and minimal interference from nearby lines (Bolger, 2000). For gold, a number of lines are commonly used, including the Au 242.73 nm, 267.59 nm, and the 312.24 nm lines, which exhibit a strong signal relative to the sample background (Diaz Ordonez, 2017; Harhira et al., 2017). In this study, the Au 312.4 nm line provided the best signal and was used as the main gold peak for grain size assessment. Figures 10.5

and 10.6 show the spectra collected on the pure copper sulphide and gold samples.

10.4.2 Selection of copper and gold background

Background values represent noise in the LIBS signal that is unrelated to the material being analysed. The pure chalcopyrite, bornite and gold mineral standards were used to assess the background levels near the diagnostic copper and gold emission lines. Copper and gold background levels were measured for the unknown LIBS analyses at the 329.9 nm and 314.00 nm wavelengths, respectively. The background must be removed from the spectrum to ensure that only the LIBS signal related to the chemistry of the sample is used for grain size proxy calculations.

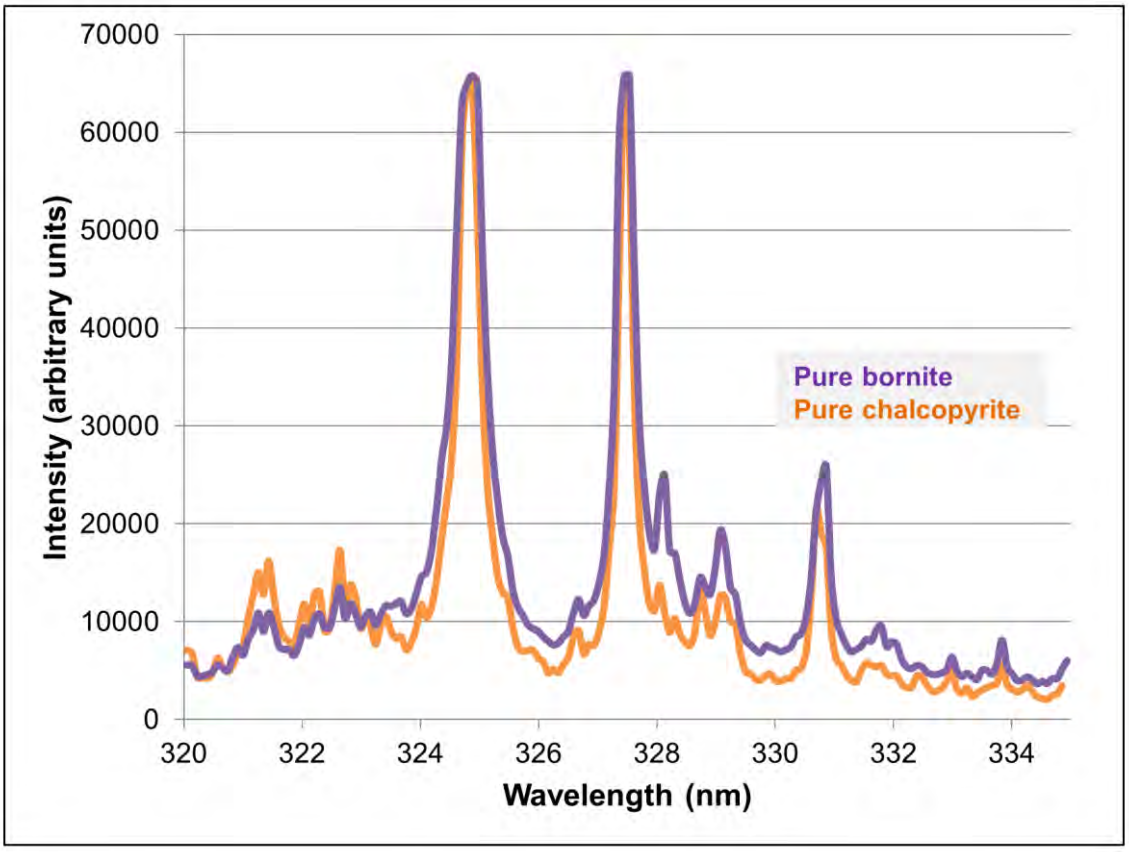

Figure 10.5. *Pure chalcopyrite and pure bornite spectra from 335 to 370 nm. The Cu 324.75 and Cu 327.40 lines were selected and a background value was taken at 329.9 nm.*

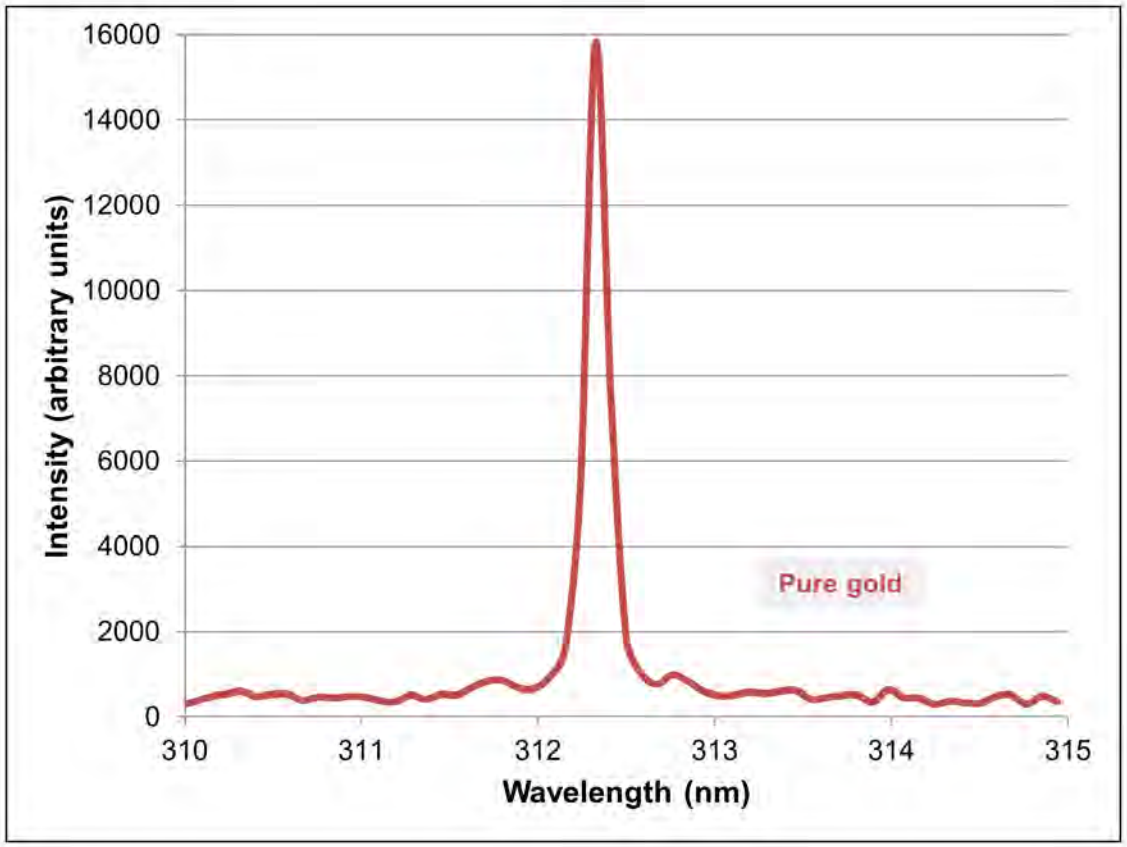

Figure 10.6. *Pure gold spectrum from 310 to 315 nm. The Au 312.24 nm line was selected and a background value was taken at 314.00 nm.*

10.5 Grain size proxy calculations

Elemental quantification from LIBS data can be challenging, so basic techniques were used here to determine if LIBS is a viable option for online, rapid grain size assessment. Since most of the gold and copper grains are much smaller than the 150 μm spot size, a single spot could contain a number of different mineral grains. No attempt was made to distinguish between chalcopyrite and bornite grains. Instead, the grain size calculations were completed assuming that copper is contained in combined copper sulphides consisting of 50% chalcopyrite and 50% bornite.

10.5.1 Identification of copper sulphide and gold grains

As a first pass, the spectral analysis software TSG HotCore was used to compare each unknown LIBS spectrum to the pure mineral reference spectra. Copper was identified using the wavelength range of 320 to 335 nm and the 310 to 315 nm range was used for gold. A Pearson correlation value between the unknown and

the standard reference spectra was used to identify those spectra that were likely to contain copper sulphides or gold. Pearson correlation cut-offs were selected by visually assessing numerous unknown spectra over a range of spectral correlation values to limit false positives (Figure 10.7). For copper, a cut-off of 0.3 Pearson correlation spectral match value was used and any spectra with a lower value were discarded from the copper sulphide grain size calculations. For gold, a Pearson correlation spectral match value of 0.7 was used and results below this were discarded from the gold grain size calculations. This value is significantly higher than the 0.3 threshold value used for copper sulphides because the relative intensity of the Au 312.24 nm line is significantly lower than that of the copper lines.

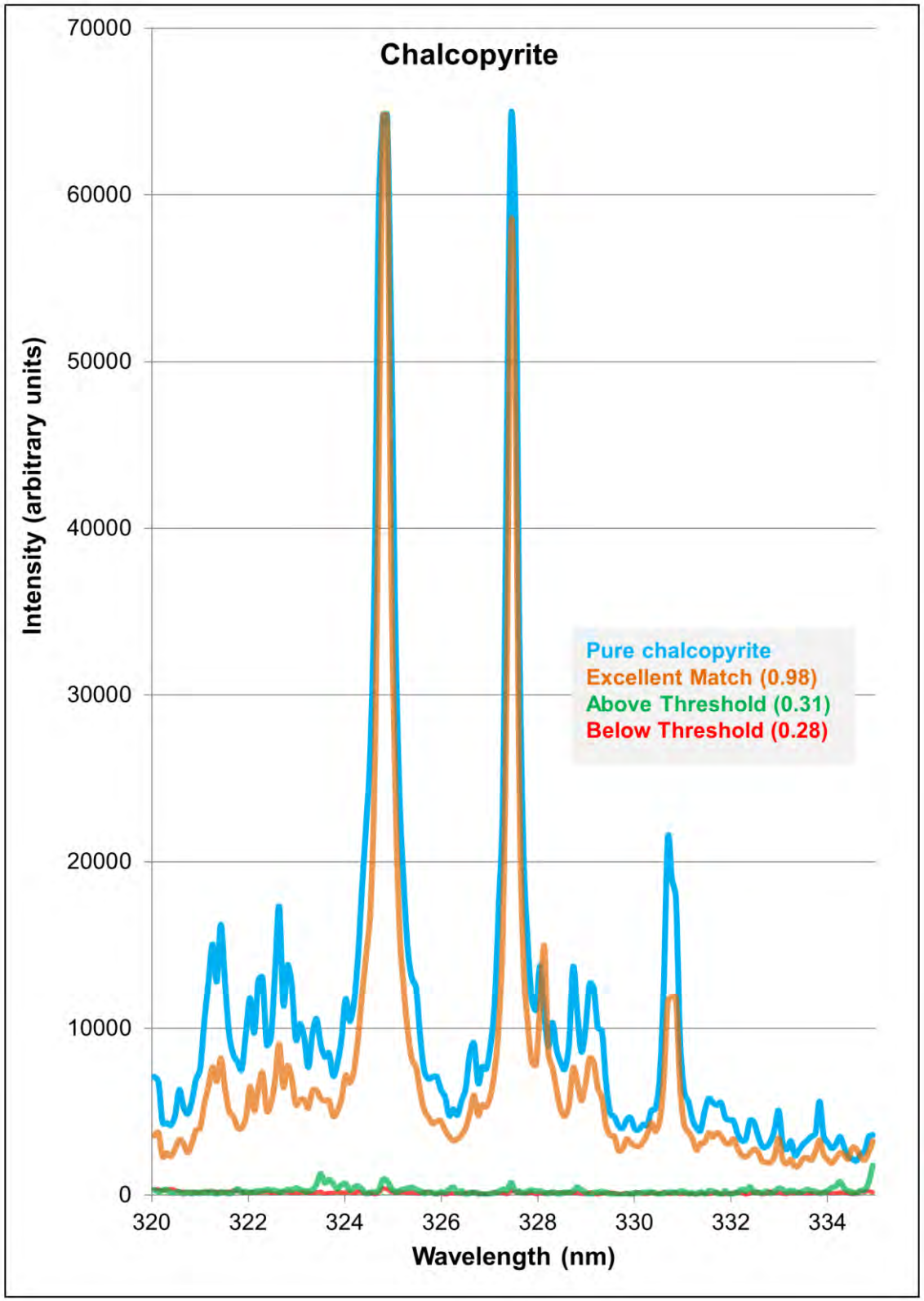

Figure 10.7. *Example of a Pearson spectral match value for a series of unknown spectra with spectral matches just above the 0.3 cut-off threshold (green), just below the cut-off (red), and well above the cut-off (orange) compared to a pure chalcopyrite mineral spectrum (blue). The Pearson spectral match threshold values were selected by analysing this relationship for numerous unknown spectra.*

10.5.2 Copper and gold line integration

Peak integration of the key emission lines was used to determine the proportion of copper sulphide minerals or gold present in spots exceeding the Pearson match criteria. To estimate the area under the emission lines, the area of multiple trapezoids drawn between the spectral channels to fit under the curve were summed by:

$$integration\ value = \sum_{i=0}^{n} \frac{intensity_i + intensity_{i+1}}{2 * (wavelength_{i+1} - wavelength_i)} \quad [10.1].$$

The proportion of combined copper sulphides contained in an individual LIBS analysis spot was calculated by first background correcting the integration value (IV) for a sum of both copper peaks:

$$IV_{Cu\ Sulph} = (IV_{Cu\ 324.75} + IV_{Cu\ 327.40}) - (2 * IV_{BG\ 329.9}) \quad [10.2].$$

For gold, the background corrected integration value was calculated by:

$$IV_{gold} = IV_{Au\ 312.3} - IV_{BG\ 314.0} \quad [10.3].$$

The integration intervals for copper peaks and background, gold peaks and background as well as the expected values for pure minerals are outlined in Table 10.1. Appendix R contains the calculated integration values for each spectrum in the test sample set.

Table 10.1 *Integration intervals used to calculate the proportion of copper minerals and gold present in each LIBS analysis spot.*

Mineral	Chalcopyrite	Bornite	Combined Cu Sulphides	Gold
Mineral Integration Interval 1	324.62 nm - 325.13 nm	324.62 nm - 325.13 nm	324.62 nm - 325.13 nm	312.06 nm - 312.50 nm
Mineral Integration Interval 2	327.19 nm - 327.70 nm	327.19 nm - 327.70 nm	327.19 nm - 327.70 nm	-
Background Integration Interval	329.67 nm - 330.18 nm	329.67 nm - 330.18 nm	329.67 nm - 330.18 nm	313.90 nm - 314.24 nm
Pure Mineral Integration Value 1	26239.92	29919.83	-	194.34
Pure Mineral Integration Value 2	21116.59	24962.61	-	-
Pure Mineral Background Integration Value (same interval used for 1 & 2)	2156.21	3159.25	-	11.90
Background Corrected Expected Integration Value (sum of interval 1 & 2 minus background)	43044.09	48563.93	45804.01	182.44

Since the background signal was variable from spectrum to spectrum, an individual "limit of detectable grain size" for each spectrum was determined by taking three times the square root of the IV_{BG}. This limit was then used to ensure that gold and copper could be qualitatively distinguished from the background signal (Potts, 1993). Any spectrum with a gold or copper integration value less than the limit of detectable grain size was discarded from the grain size calculations.

10.5.3 Copper sulphide and gold grain size proxy calculations

For LIBS analysis spots that had not been discarded to this point, the calculated integration value was then compared to the expected value for pure combined copper sulphide or gold from the reference spectra:

$$Cu\ Sulph_{prop} = \frac{IV_{Cu\ Sulph}}{IV_{Pure\ Cu\ Sulph}} \quad [10.4].$$

$$Au_{prop} = \frac{IV_{Au}}{IV_{Pure\ Au}} \quad [10.5].$$

LIBS craters in chalcopyrite and bornite were measured to be less than 2 μm deep, so it was assumed that the LIBS spot is an analysis area rather than an analysis volume. As such, the proportion by area of copper sulphide and gold present in a spot can be easily converted into a grain size by:

$$Grain\ Size = Mineral_{prop} * 150\ \mu m \quad [10.6].$$

Assuming that the reported grain size values represented the length of a square grain, this length was then used to calculate the boundary length and area for each of the grains encountered in each sample. These values were used to determine the diameter by phase-specific surface area (D_{PSSL}) for all of the grains detected in each sample (see section 6.4 for details). The formulas and calculations used to calculate the grain size proxies from LIBS data are included as an Excel workbook in Appendix S.

10.6 Grain size proxy results

The grain size proxy results produced by the methods outlined in section 10.5 were compared to the MLA results and, in the case of copper sulphides, the μXRF results. These results are presented in the following sections.

10.6.1 Copper sulphide grain size proxy results

The grain size results calculated from LIBS data assuming that the copper is contained in combined copper sulphides are shown in Table 10.2. The LIBS combined copper sulphides grain size results compared to the MLA results have an R^2 value of 0.57 and an r_s correlation value of 0.69 (Figure 10.8).

Table 10.2. *Grain size calculated from LIBS assuming combined copper sulphides. These values are compared to the measured combined sulphide grain* D_{PSSL} *from MLA for each sample in the test sample set.*

Sample	D_{PSSL} from MLA (μm)	Calculated D_{PSSL} Grain Size Proxy (μm)	D_{PSSL} from μXRF (μm)
1185.0	35	43	51
1193.0	71	41	100
1207.0	58	19	60
1265.5	32	46	44
1269.0	18	20	12
1283.0	42	64	64
1283.5	31	40	42
1292.5	27	39	28
1306.5	21	31	22
1307.5	53	39	36
1356.5	39	32	27
1362.7	52	45	34
1380.5	46	54	46
1381.0	21	25	13
1392.5	29	59	49
1393.0	13	31	20
1400.5	79	64	47
1401.0	152	106	191
1409.0	23	17	9
1420.0	111	63	78
1420.5	19	12	4
1421.0	29	60	43
1431.0	15	16	8
1431.5	17	21	11
1448.5	36	54	61
1461.5	24	30	17

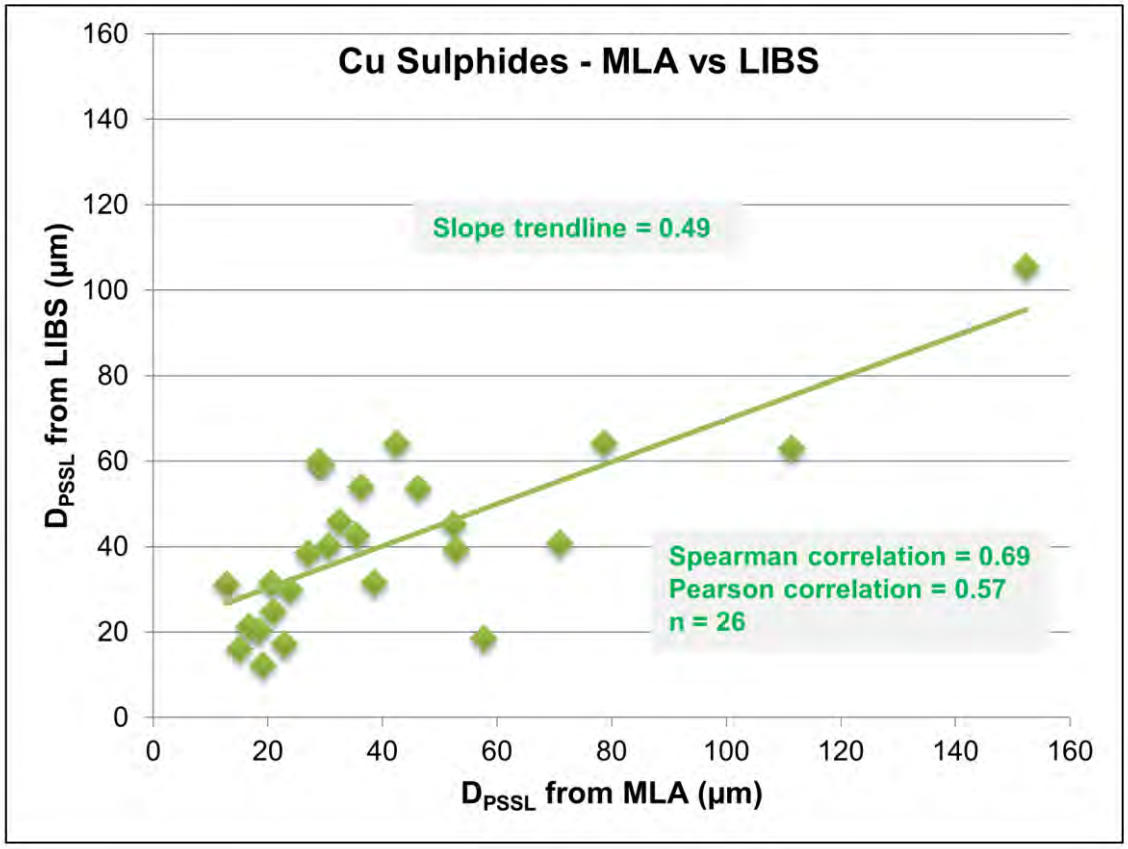

Figure 10.8. *Comparison of the D_{PSSL} for combined copper sulphide measured from MLA data and the grain size calculated using LIBS data. These calculations assumed that chalcopyrite and bornite equally occur as combined copper sulphides.*

Because the μXRF analysis was also completed assuming that the data was capturing a surface area and the results represent a calculated proxy value, the LIBS grain size results were compared to the μXRF calculated grain size results (Table 10.2, Figure 10.9). The combined copper sulphides grain size results from LIBS compared to the μXRF results have an R^2 value of 0.68 and an r_s correlation value of 0.81.

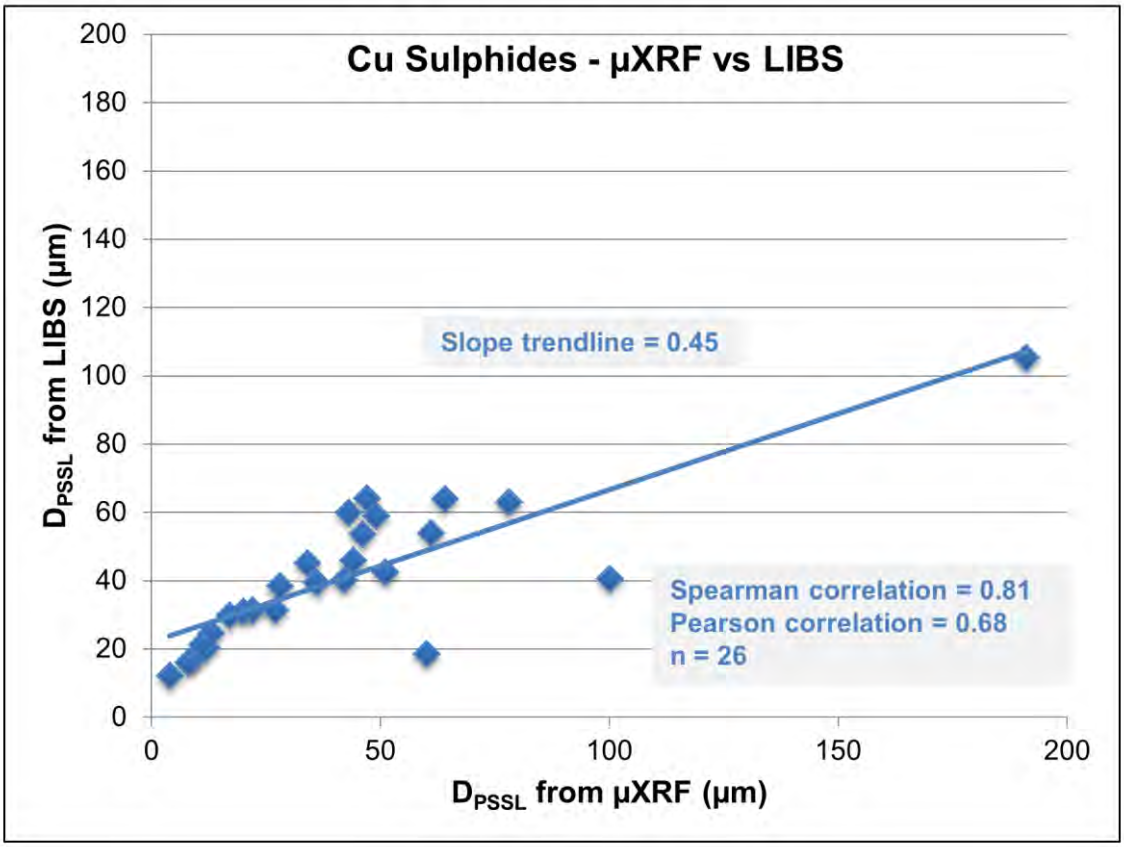

Figure 10.9. *Comparison of the D_{PSSL} for combined copper sulphide calculated from the µXRF data and the grain size calculated using LIBS data. These calculations assumed that chalcopyrite and bornite equally occur as combined copper sulphides.*

10.6.2 Gold grain size proxy results

Gold proved to be challenging to detect in the LIBS data. The integration values on pure gold are two orders of magnitude lower than the copper in chalcopyrite (Table 10.1), which leads to a much higher detection limit. This increased detection limit means that gold grains must be at least 20 µm to be detected above background. In the MLA dataset, less than 20 grains of gold identified were greater than 20 µm. The grain size of interest for gold is also much lower than the grain size for copper sulphides. The ability to detect these smaller, less common gold grains is challenging given the large spot size of 150 µm and the low peak counts, even in pure spectra. From 140,000 spots, only one LIBS analysis spot in the test sample set produced a Pearson spectral match value above the 0.7 threshold (Figure 10.10). Based on the Au 312.3 nm integration value, this gold grain has a calculated grain size of 17 µm. However, the spectrum for this analysis spot had a limit of detectable grain size of 20µm for gold, so this grain was discarded from the grain size calculations. No gold grains

met the criteria for acceptance. By comparison the μXRF method can detect 7.2 μm grains of gold and located 72 grains from this sample set (section 8.4).

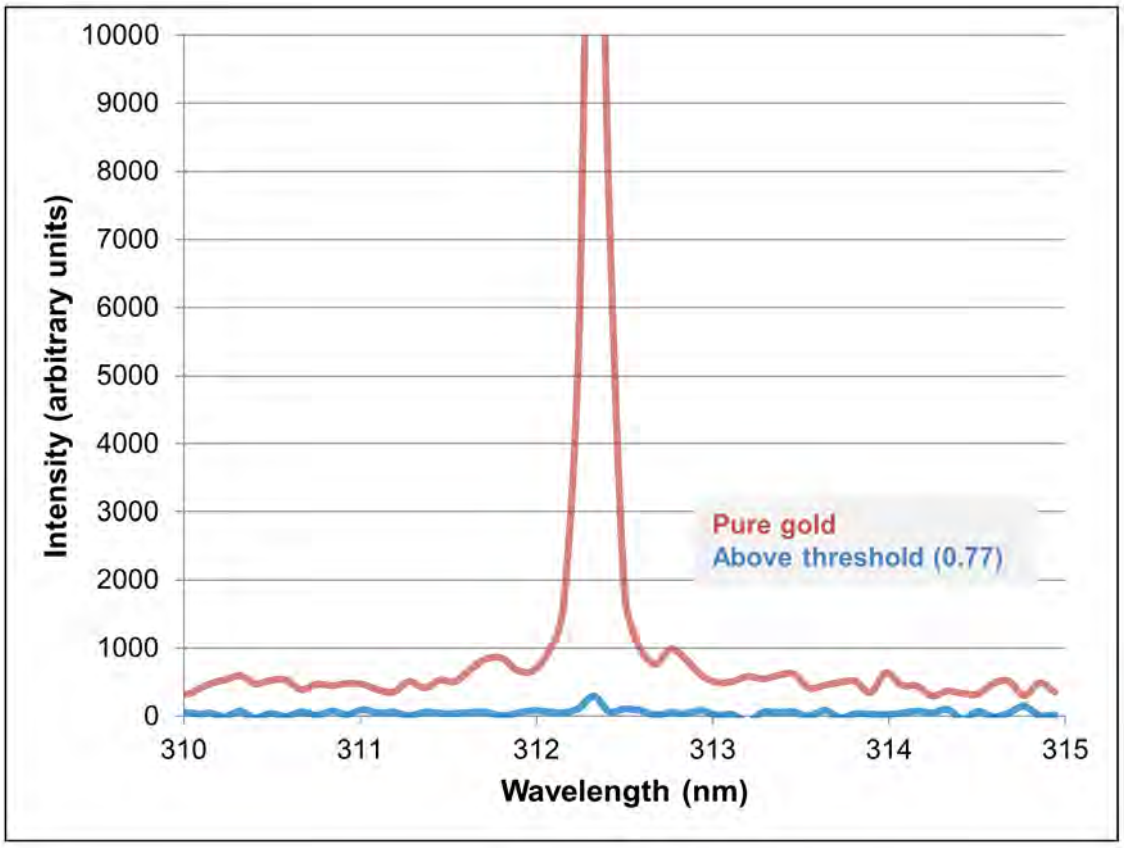

Figure 10.10. *Spectrum of single LIBS analysis that returned a Pearson spectral match greater than the 0.7 threshold (red line) compared to a pure gold spectrum (blue line).*

10.7 Bootstrapping of copper results

For copper sulphide minerals, using all 5429 LIBS analysis spots provides a reasonable estimate of grain size. A series of bootstrapping experiments were completed to assess the minimum number of LIBS spots required to adequately estimate a grain size proxy. These experiments were designed to randomly select groups of 75, 50, 25, 10, and 1 line of LIBS analysis spots from each sample, and calculate the corresponding D_{PSSL} grain size proxy. Fifty iterations of each bootstrapping experiment were completed.

To compare the performance of the calculated grain size estimates as the number of analysis lines decreases, a series of box and whisker plots containing the bootstrapping results for combined copper sulphides were plotted (Figures 10.11 through 10.15). In general, as the number of lines used to calculate the D_{PSSL} grain

size proxy from LIBS decreases, the mean bootstrapped D_{PSSL} values change and the second and third quartile range of D_{PSSL} values increases.

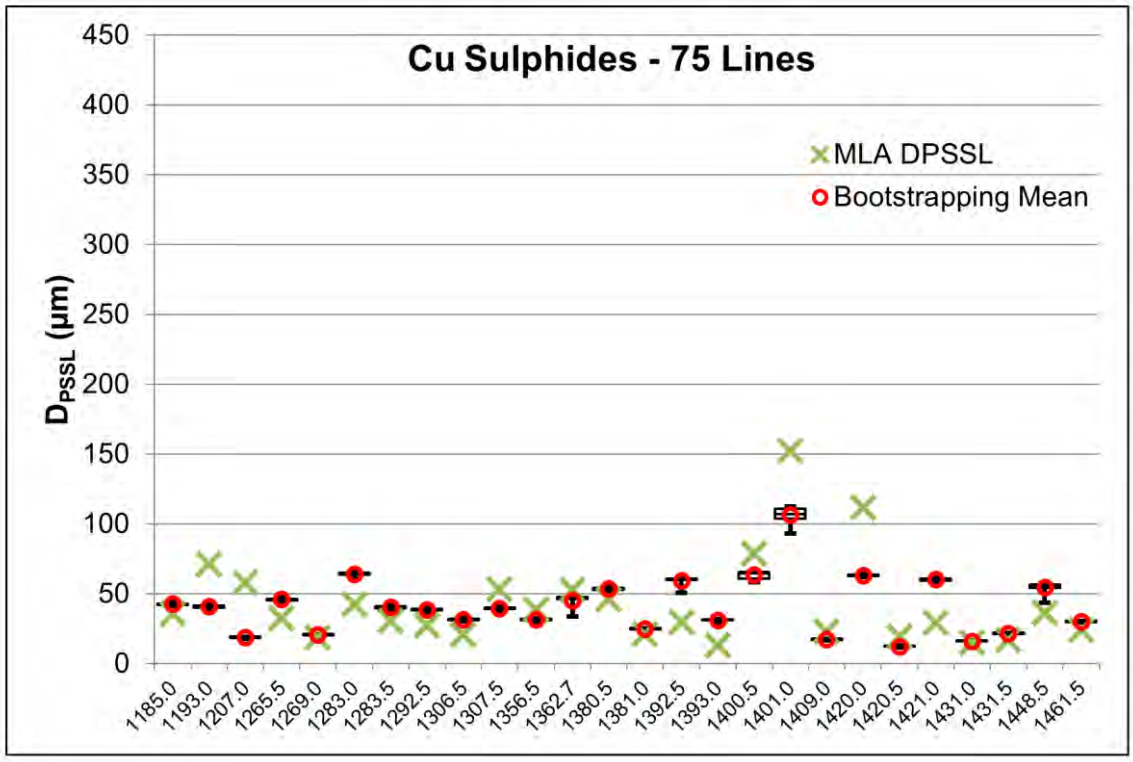

Figure 10.11. *Box and whisker plot showing the bootstrapping results for combined copper sulphides using 75 random LIBS lines per sample. The whiskers represent the minimum and maximum values. These are compared with the MLA results on the same tiles.*

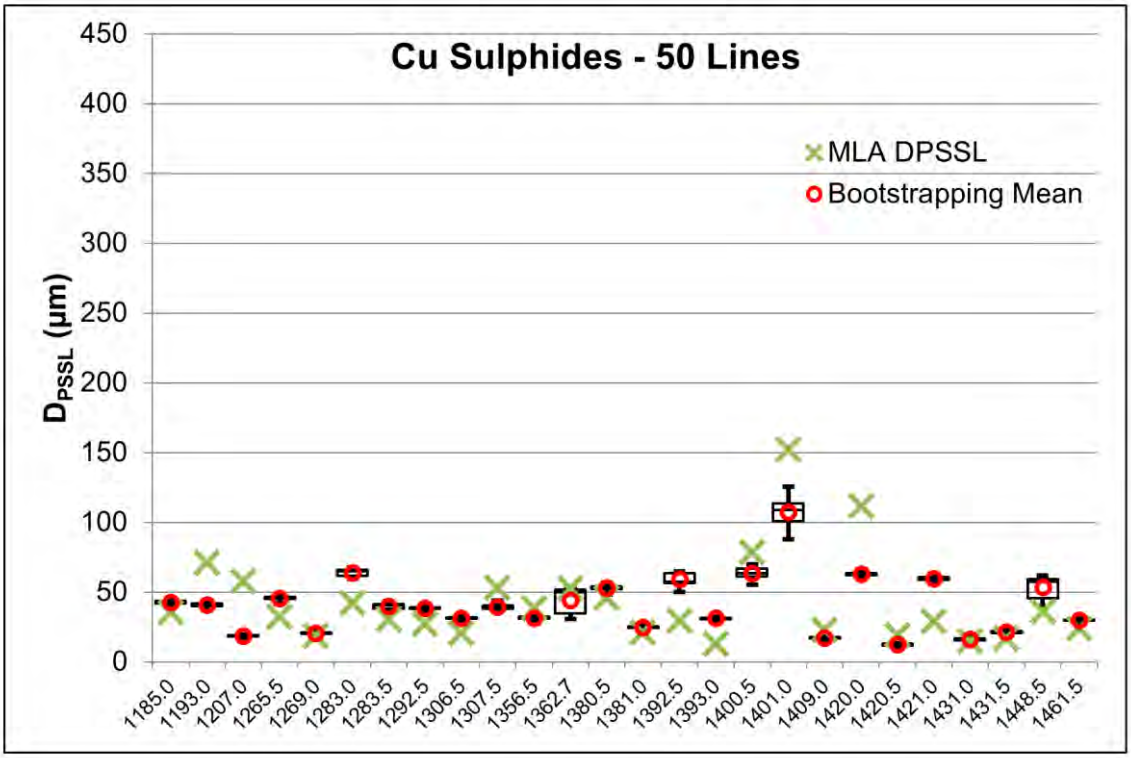

Figure 10.12. *Box and whisker plot showing the bootstrapping results for combined copper sulphides using 50 random LIBS lines per sample. The whiskers represent the minimum and maximum values. These are compared with the MLA results on the same tiles.*

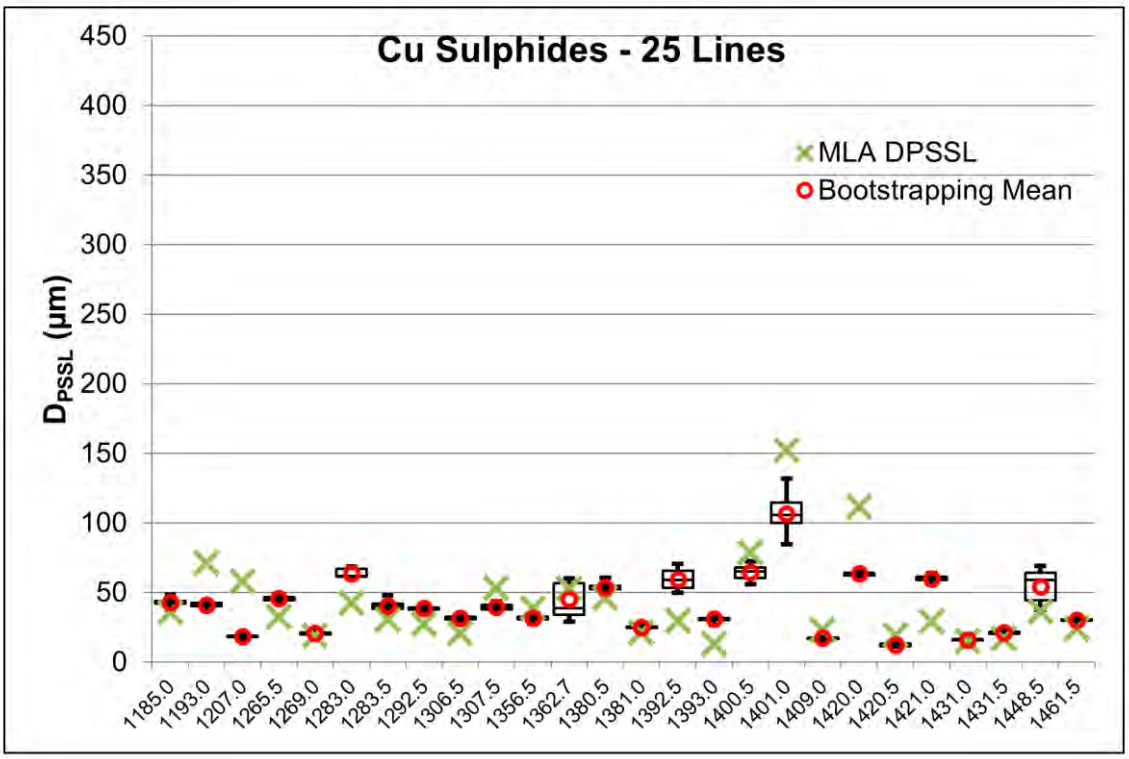

Figure 10.13. *Box and whisker plot showing the bootstrapping results for combined copper sulphides using 25 random LIBS lines per sample. The whiskers represent the minimum and maximum values. These are compared with the MLA results on the same tiles.*

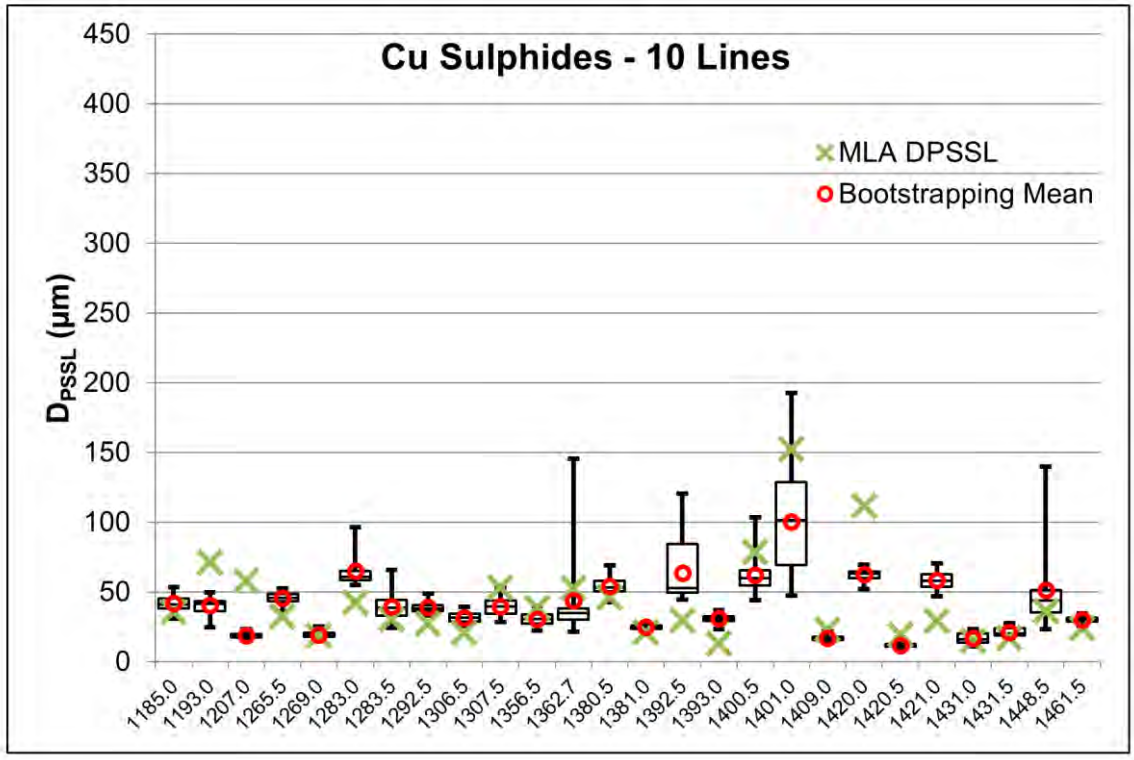

Figure 10.14. *Box and whisker plot showing the bootstrapping results for combined copper sulphides using 10 random LIBS lines per sample. The whiskers represent the minimum and maximum values. These are compared with the MLA results on the same tiles.*

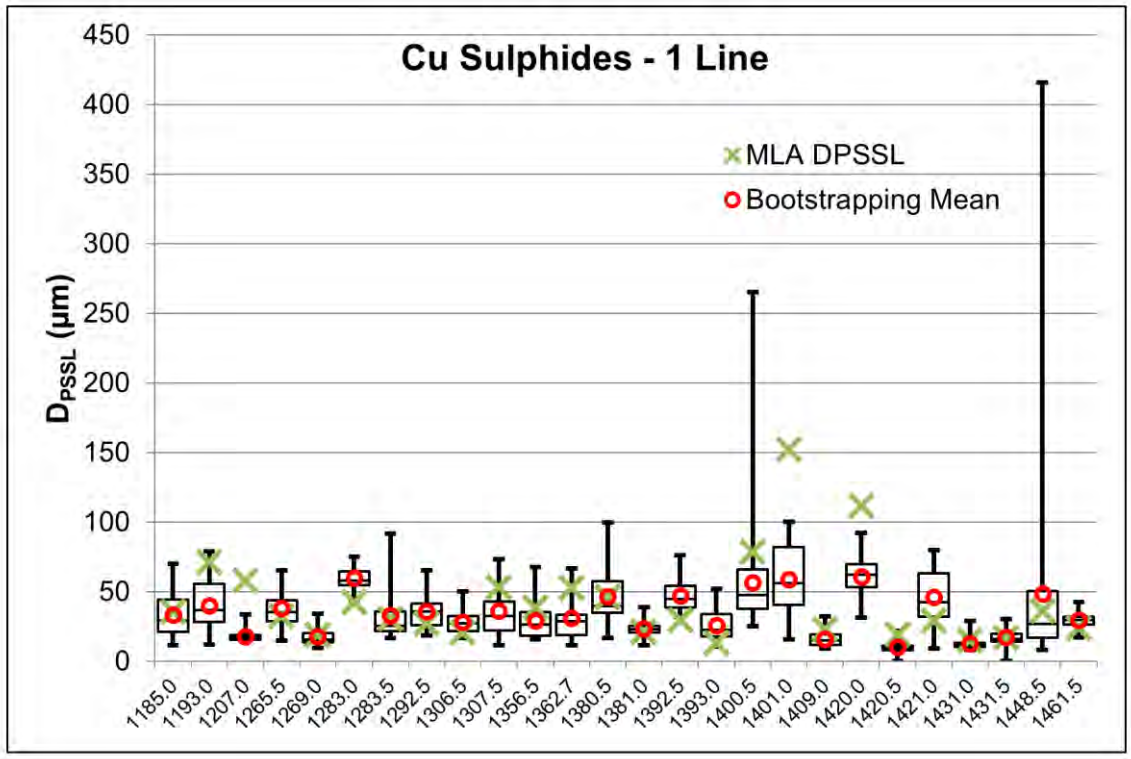

Figure 10.15. *Box and whisker plot showing the bootstrapping results for combined copper sulphides using 1 random LIBS lines per sample. The whiskers represent the minimum and maximum values. These are compared with the MLA results on the same tiles.*

D_{PSSL} grain size proxy values for combined copper sulphide calculated from LIBS data have an average standard error of less than 1.5 in 50 experiments when at least 620 of the total 5429 analysis spots are used for grain size assessment (Figure 10.16). A standard error value of 1.5 indicates that, with 95% confidence, using 620 random LIBS analyses will provide D_{PSSL} values within 1.5 μm in 50 repeated experiments.

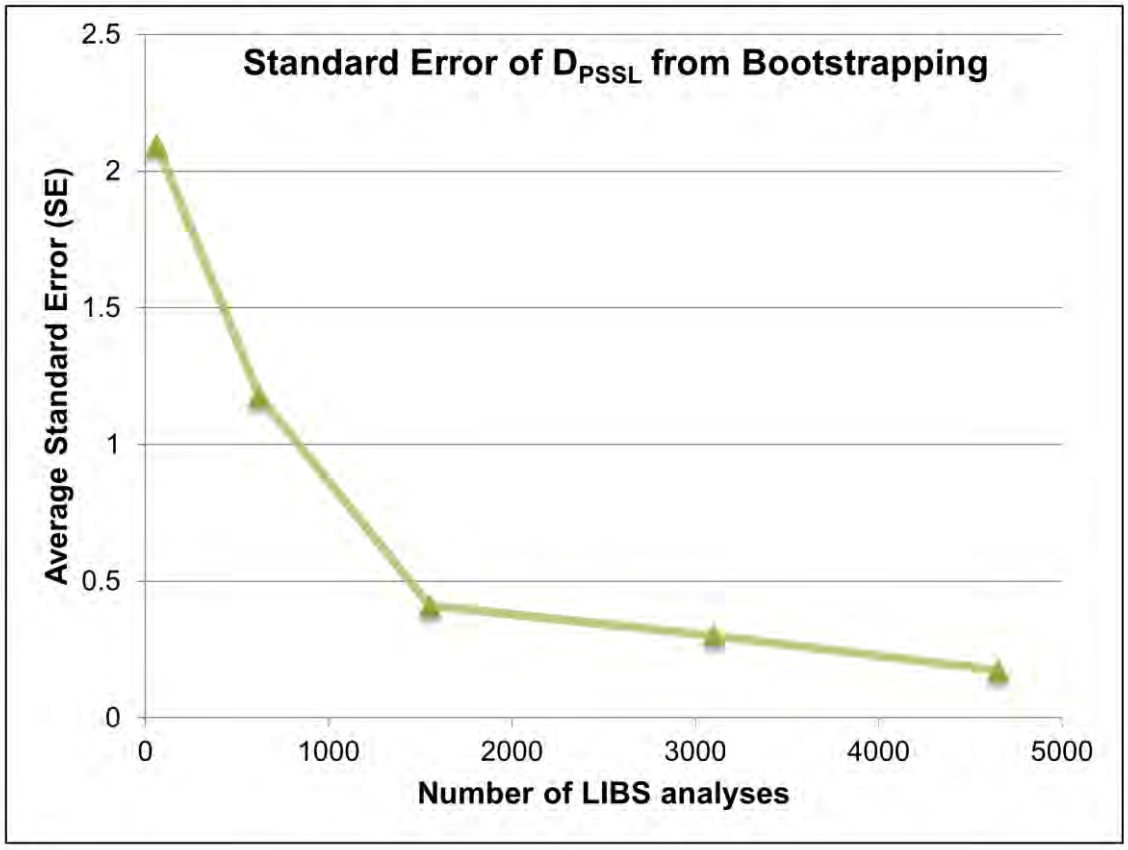

Figure 10.16. *Comparison of the number of LIBS analysis spots used and the average range of grain size proxy values calculated for all twenty-six test samples. This trend shows that about 620, 150 μm LIBS analysis pixels (or 10 analysis lines) are required to rank samples in terms of copper mineral grain size proxies to a satisfactory precision.*

10.8 Discussion

A combination of spectral matching and peak integration was used to identify gold and combined copper sulphides from LIBS spectra. Gold grains were challenging to detect using LIBS analysis. Only a single LIBS analysis spot in the entire test sample set produced a Pearson spectral match value above the 0.7 threshold. This analysis spot, however, did not meet the limit of detectable grain size of 20 μm for that analysis spot and was discarded from the grain size proxy

calculations. In the pure gold reference spectrum, the background integration value is 6% of the Au 312.3nm integration value meaning that a pure gold LIBS analysis spot must contain over 6% gold (equivalent to a 36 μm grain) to be detectable above the background signal. The average limit of detectable gold grain size for the entire dataset is 29 μm. Less than 10 of the 400 gold grains identified by MLA in the test sample set are larger than the 29 μm detectable limit, so over 98% of the grains detected by MLA in the test sample set are too small to be detected using the LIBS data. Gold also suffers from poor sampling statistics. The chances of encountering one of the 10 gold grains greater than 29 μm in the sample set using LIBS are very low. A smaller spot size and greater sample coverage would increase the likelihood of adequately detecting and measuring gold grains.

LIBS analysis was successful in detecting and measuring combined copper sulphide grains. When including all 89 LIBS analysis lines, combined copper sulphides show a Pearson correlation coefficient of $R^2 = 0.57$ with a Spearman correlation coefficient of $r_s = 0.69$ when compared to the D_{PSSL} from MLA. These correlation coefficients are lower than other microanalytical methods investigated, but show that the LIBS data can be used to rank samples by grain size. When compared to the calculated μXRF D_{PSSL} grain sizes, the LIBS data produces correlation coefficients of $R^2 = 0.68$ and $r_s = 0.81$ for copper sulphides, indicating that the μXRF and LIBS grain size proxy calculations are measuring the same parameters. The slopes of the correlation trendlines when compared to MLA and μXRF are both below 0.5. These low slope values indicate that the LIBS grain size proxy is underestimated by approximately 50%.

There are numerous complexities of LIBS analysis that should be investigated before implementing this technology as a grain size assessment tool. The LIBS ablation craters are not uniform or symmetrical, making an estimation of the surface area or ablation volume challenging (Figure 10.17). While the ablation depth in quartz is more than 75 μm, the ablation depth in copper sulphide minerals is 1-5 μm. The variation in LIBS ablation craters show that different minerals ablate at different rates and behave differently under laser power. Figure 10.18 shows an SEM image of a LIBS ablation crater in calcite and copper sulphide, both of which display brittle (Figure 10.18A) and melting behaviour (Figure 10.18B). Additionally, the depth of ablation varies depending on the mineral present in the laser spot. Minerals such as quartz and feldspar produce very deep ablation craters (>100 μm) while sulphide minerals produce very

shallow LIBS ablation craters (<5 μm) (Figure 10.19). These changes in mineral behaviour and ablation crater depth will impact the ablation volume in a given spot. If copper sulphide or gold grains are smaller than the spot size and hosted in other minerals, the ablation volume will be higher than it would be if only copper sulphide or gold were ablated. For this study, it was assumed that all ablation craters are shallow, and that the LIBS spectra represent a surface area as opposed to a volume. If a grain of copper sulphide or gold smaller than the 150 μm spot size were hosted in quartz, the ablation would be a volume not an area. By assuming this volume is an area, the grain size proxy calculation is underestimated. On the other hand, where the ablated volume is large much of the material is likely in the surrounding ejecta so the actual volume of material that enters the plasma is impossible to estimate. If the methods developed here are going to be used for LIBS grain size proxies, further testing to account for the variable ablation behaviour will be required. A visible light laser (e.g. double YAG laser) or a UV laser such as the one used in LA-ICP-MS analysis (discussed in chapter 12) would reduce the cratering, but these lasers have lower output power and may require smaller spot sizes (Delmdahl and Paetzel, 2009; Tamura et al., 2002).

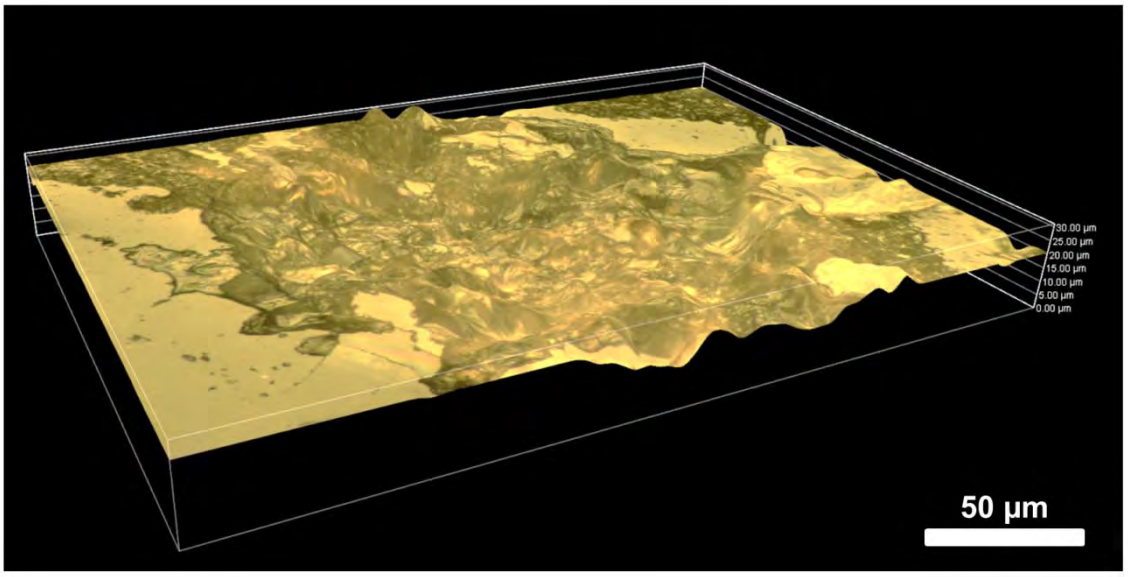

Figure 10.17. *Example of a reflected light 3D step image of a LIBS crater in feldspar. The crater is not uniform or symmetrical, making an estimation of area or ablation volume challenging.*

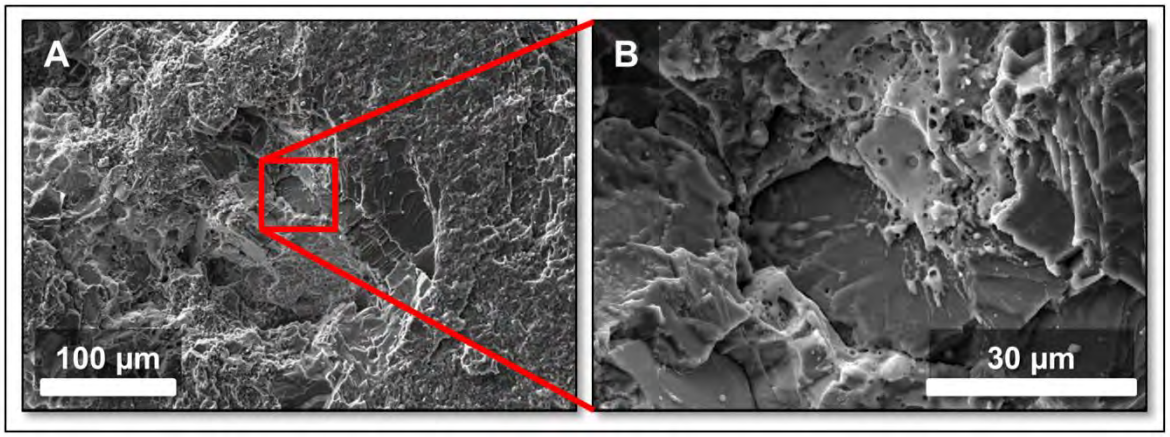

Figure 10.18. *SEM images of a LIBS ablation crater in calcite (darker grey) and copper sulphide (brighter grey).The ablations crater generally shows brittle behaviour (A), but up close, both calcite and copper sulphide also display melting behaviour (B).*

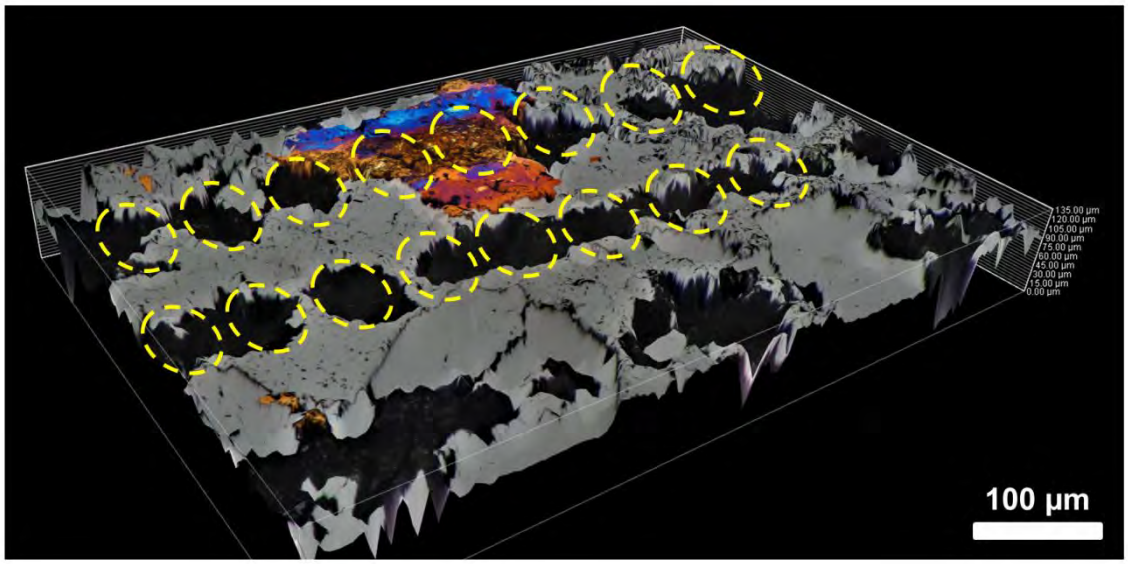

Figure 10.19. *Reflected light 3D step image of LIBS craters (outlined in yellow circles) in quartz (grey) and chalcopyrite (coloured). While the ablation depth in quartz is more than 50 µm, the ablation depth in copper sulphide minerals is 1-5 µm.*

10.9 Conclusions

While the test data set used in this study is small, the results show that copper sulphide grain size proxies developed from LIBS data can be used to adequately assess grain size. Calculated D_{PSSL} values are generally within 20 µm of the measured D_{PSSL} values from MLA data, although the slope of the correlation trendline (0.49) indicates that the LIBS underestimates the MLA grain size by approximately 50%. Bootstrapping experiments show that this method requires only 620 LIBS analysis pixels to achieve repeatable copper sulphide grain size results with an average standard error of less than 1.5. In the case of copper, 620,

150 μm LIBS analyses are required to adequately estimate combined copper sulphide grain sizes using proxy calculations developed from LIBS data.

If gold grain sizes are to be extracted from LIBS data, the analysis spot size should be decreased and the system should be optimised to specifically collect high resolution spectra near the Au 312.3 nm line. Additionally, more advanced spectral matching algorithms (such as full spectral stripping) would provide better spectral matching for improved gold grain identification.

The objective of this study was to investigate the potential for LIBS technology to be used in conjunction with Corescan analysis to rapidly and adequately assess copper-sulphide and gold grain sizes. Specifically, the number of LIBS analyses required produce a reasonable grain size proxy was tested. The Applied Spectra RT100-HP LIBS system used in this study can analyse 620 spots in 31 seconds when operating at 20 Hz. Currently, the Corescan system acquires data at a rate of 3 minutes per metre. In the same amount of time, nearly 3600 LIBS analysis spots measuring 150 μm in diameter can be collected. Since only 620 LIBS analyses are required for a copper sulphide grain size proxy, nearly 6 representative grain size proxy values can be calculated in the same amount of time as one metre of Corescan analysis. Therefore, LIBS analysis can easily collect enough data to provide a robust grain size proxy over a one metre core interval (typical assay interval). In the case of combined copper sulphides, currently available LIBS technology shows great promise to acquire early grain size information using a rapid, minimally destructive analytical technique at an acquisition rate similar to the current Corescan system.

While not the focus of this study, a LIBS system running at a rate of nearly 3600 spots per metre could also be used to provide additional mineral recognition capability by spectral matching of other minerals (e.g. McMillan et al., 2007, McMillan et al., 2014). This data would help in the determination of the abundance of *aspectral* minerals that cannot be easily detected using the existing hyperspectral logging system.

Chapter 11

Grain size assessment by laser Raman spectroscopy

11.1 Introduction

Raman spectroscopy is commonly applied to biological and chemical investigations, as well as geologic applications (Hope et al., 2001; Qian et al., 2015). Raman analysis provides direct observation of the vibrational excitations of samples and, therefore, the bonding state of molecules that make up that material (Born and Huang, 1954). This information can be utilized to determine crystalline phases and atomic structures of minerals within a geologic sample (Lin et al., 2014). Raman spectroscopy is not dependent on the atomic number of elements. This means that minerals containing light elements (e.g. C, H, N, O, etc.) which are challenging to detect using electron based techniques can be characterized using Raman analysis (Hope et al., 2001). Additionally, polymorphs and the influence of trace elements integrated into the crystal lattice of minerals can be examined (Hope et al., 2001). Raman spectroscopy is an inexpensive, non-destructive, rapid, *in situ* analysis method that requires little to no sample preparation making it especially applicable to geologic samples (Hope et al., 2001; Lin et al., 2014; Qian et al., 2015).

The aim of this chapter is to discuss the potential for laser Raman analysis to be used for rapid copper sulphide and gold grain size assessment in tandem with Corescan analysis at a similar rate. The sections that follow will present the results of a prelminary investigation of these possibilities.

11.2 Scientific principles of laser Raman spectroscopy

Raman spectroscopy is an analytical technique based on the vibrational energy levels of specific molecules when a substance is exposed to monochromatic light energy (typically from a laser source) between ultraviolet and NIR wavelengths (Grasselli et al., 1980; Lin et al., 2014). A monochromatic light source ensures that the sample only interacts with a single wavelength of light. When this light is directed at a sample surface, it interacts with and is scattered by the molecules in the sample (Hanson and Vargis, 2015). During elastic (Rayleigh) scattering, the frequency of the scattered light remains at the incident frequency (Figure 11.1). In

contrast, when inelastic or Raman scattering occurs, the frequency of scattered light is higher or lower than the incident frequency (Hanson and Vargis, 2015; Lin et al., 2014). This change in frequency is the result of either a loss (Stokes) or gain (anti-Stokes) of energy (Figure 11.1) (Lin et al., 2014). These frequency and energy changes directly correlate to the photon excitation energy in the material being interacted with and are, therefore, diagnostic for specific minerals (Lin et al., 2014).

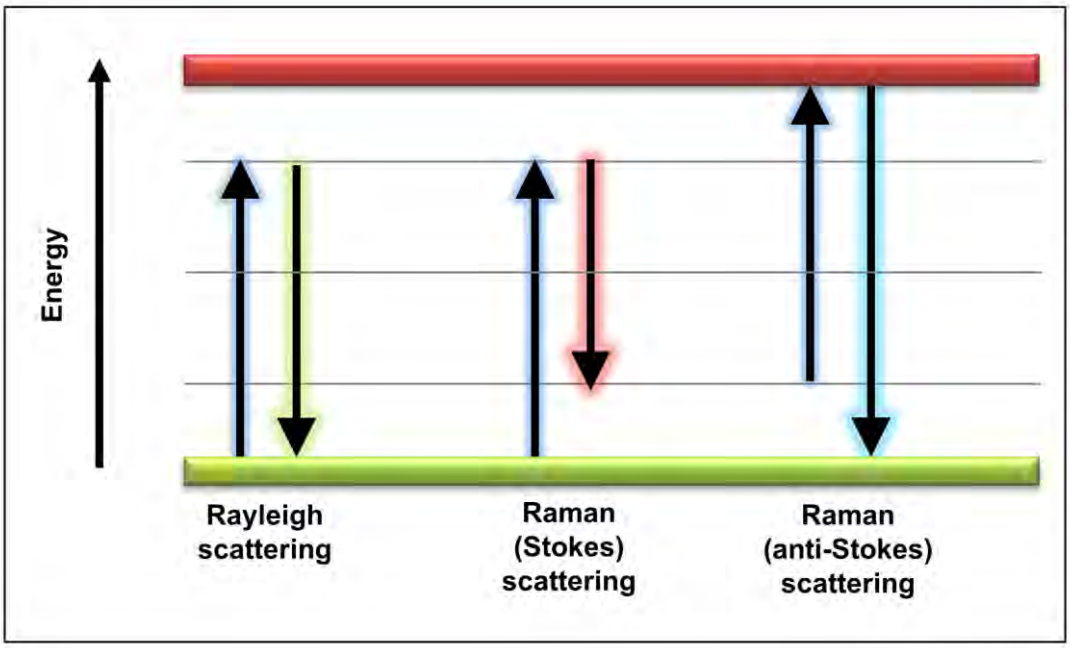

Figure 11.1. *Typical vibrational energy levels experienced by a molecule when interacting with light. Excitation energy from a laser source is shown by upward arrows; the resulting emitted photons (downward arrows) can then be measured as a Raman response.*

Raman spectroscopy can be used to classify a wide range of minerals. In laser Raman analysis, a single-frequency laser beam is directed at a sample surface and the inelastic scattering response is measured. While this technique has been shown to successfully detect common gangue minerals such as carbonates, silicates, and oxides, sulphides can me more challenging to identify (Hope et al., 2001; Mernagh and Trudu, 1993). Although it is a poor overall Raman scatterer and tends to produce low Raman counts, chalcopyrite shows a diagnostic Raman band between ~300 cm^{-1} and 400 cm^{-1} (Pasteris, 1998). Mernagh and Trudu (1993) found that Raman spectra could not be obtained from bornite because this mineral was easily damaged by the laser before adequate spectra can be collected. Other authors, however, have indicated that bornite can in fact be identified in Raman spectra (Lafuente et al., 2016; Pasteris, 1998). Figure 11.2

shows the best-effort reference spectra for bornite and chalcopyrite from the RRUFF™ database; a free database of high quality Raman spectra of reference materials (Lafuente et al., 2016). Metals like elemental gold show almost no Raman response (Lafuente et al., 2016; Lewis and Edwards, 2001), so the ability for laser Raman to detect gold grains was not assessed in this study.

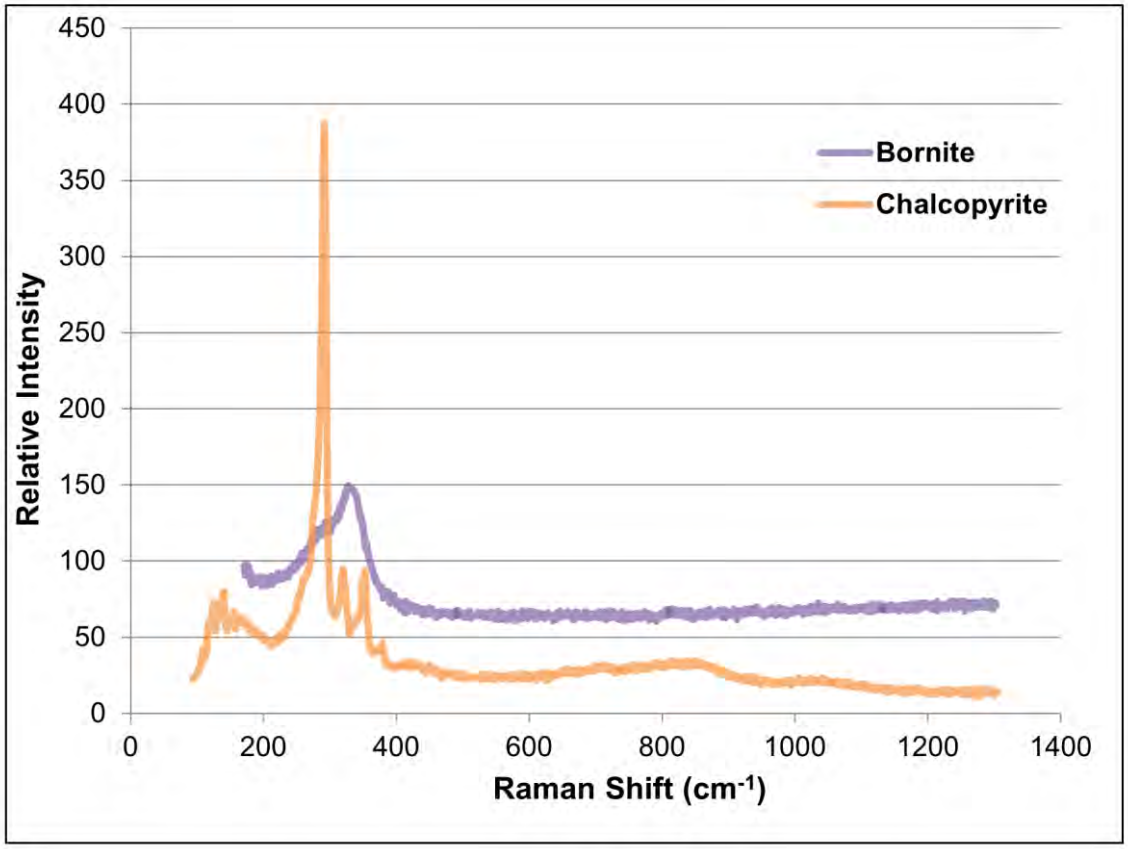

Figure 11.2. *Raman spectra for bornite and chalcopyrite from the RRUFF™ database collected under optimised conditions (Lafuente et al., 2016).*

11.3 Data collection methodology

Laser Raman analysis was completed using a Renishaw inVia Raman microscope fitted with a 4X objective attached to a 532 nm (visible light) diode-pumped laser system located in the Central Sciences Laboratory (CSL) at the University of Tasmania, Australia. The spectra were recorded from 100-1360 cm^{-1} using a grating of 2400 l/mm resulting in a spectral resolution of about 1.2 cm^{-1}. This system is capable of analysing in streamline (a pseudo-line scan continuous analysis) and point modes. Using a 4X objective, the laser energy was measured to be 1 mW at 5% laser power and 20 mW at 100% laser power. Sample 1400.5 was chosen to conduct initial testing of the laser Raman technology to determine

if large copper sulphide grains would return adequate spectra. This sample was selected because it contains a number of chalcopyrite and bornite grains greater than 200 μm, which provides the best chance for identifying copper sulphides.

The laser Raman system has two primary modes of data collection: spot and streamline analysis. In spot analysis, discrete analysis spots are collected on the sample at a given laser power. Using a 4X objective produces a spot size of 16 μm. In streamline mode, the 16 μm spot is stretched over an area measuring approximately 800 μm by 16 μm or 50 analysis pixels. Streamline mode is used so that all of the laser power is not focussed on a single spot which is especially important when analysing minerals that burn easily (e.g. bornite). As the streamline moves in the y-direction, laser Raman spectra from 50 pixels are acquired at the same time. Binning the data from two consecutive pixels creates an effective pixel size of 32 μm by 16 μm.

An initial experiment was completed in point mode at 5% laser power with a 5 second dwell time and 16 μm spot size using both 16 μm and 32 μm step sizes. These conditions were chosen to determine if adequate Raman spectra could be collected under optimal conditions for the Raman microscope system. A second experiment using 21 analysis lines (each 3 cm long) spaced evenly across the sample was completed using three different dwell times: 2 seconds, 4 seconds, and 10 seconds. In streamline mode, the 4X objective produces a laser analysis line measuring 31.5 μm in length (y-direction) and 16.25 μm in width (x-direction). To increase the Raman counts, 100% laser power was used and this laser power was distributed over an 800 μm by 16 μm streamline area. This test was conducted to determine if adequate Raman spectra could be collected rapidly at a pixel size near 50 μm.

Spectral processing was completed using Renishaw's WiRE™ data processing and analysis software. All spectra had cosmic rays removed prior to data analysis. Since copper sulphide spectra are noisy, a smoothing algorithm (Savitsky-Golay smooth window of 19 using a polynomial order of 2) was applied to smooth the spectra. A direct classical least squares (DCLS) component analysis was then used on the first derivative of the spectra. This analysis determines if the unknown spectra is similar to chalcopyrite and bornite reference spectra collected from the test sample. A lack of fit category was used in the DCLS analysis for spectra that did not fit either the chalcopyrite or bornite reference spectra.

11.4 Results

The two point mode tests, one with a 16 μm step size (42 spots) and one with a 32.5 μm step size (18 spots), were completed across a 450 μm grain of intergrown bornite and chalcopyrite surrounded by quartz and calcite (Figure 11.3a). At the 32 μm step size, the Raman analysis incorrectly identifies quartz and calcite as bornite and bornite as chalcopyrite (Figure 11.3b). The 16 μm step point analysis correctly identifies the location of the bornite and chalcopyrite (Figure 11.3c). As shown in Figure 11.3d, the bornite suffered heat damage under 5% laser power spot and 100% laser power streamline analysis, while the chalcopyrite appears to be stable under these analysis conditions. Representative chalcopyrite, bornite, calcite, and quartz Raman spectra collected from this grain are shown in Figure 11.4.

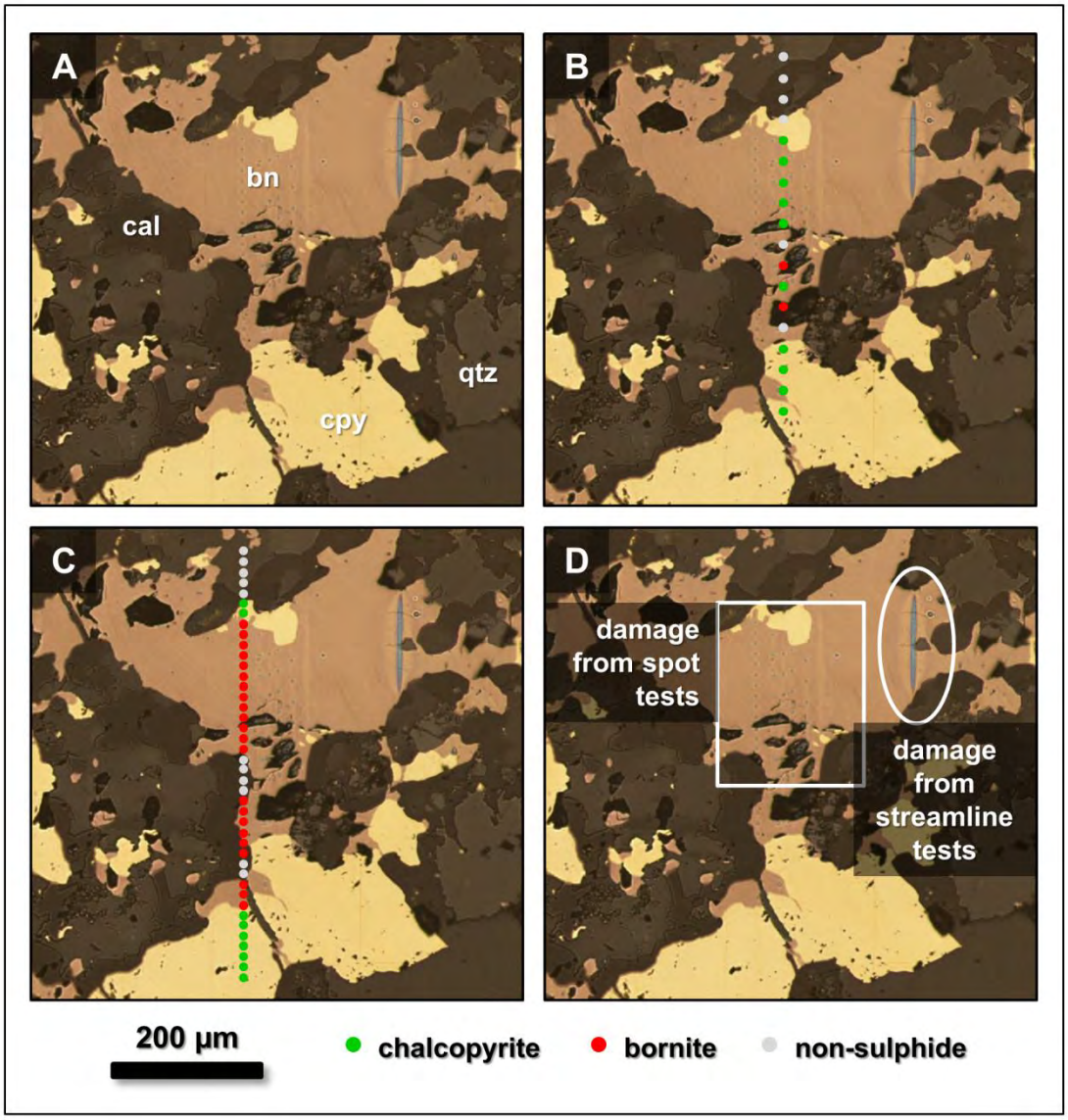

Figure 11.3. *Results of the point mode laser Raman tests. A. 450 µm grain of intergrown bornite and chalcopyrite surrounded by quartz and calcite. B. 32 µm step analysis line results. C. 16 µm step analysis line results Spots present the site of analysis and the mineral classification from the software. D. Bornite grain suffered heat damage during the analysis under 5% laser power in spot mode, and 100% laser power in streamline mode.*

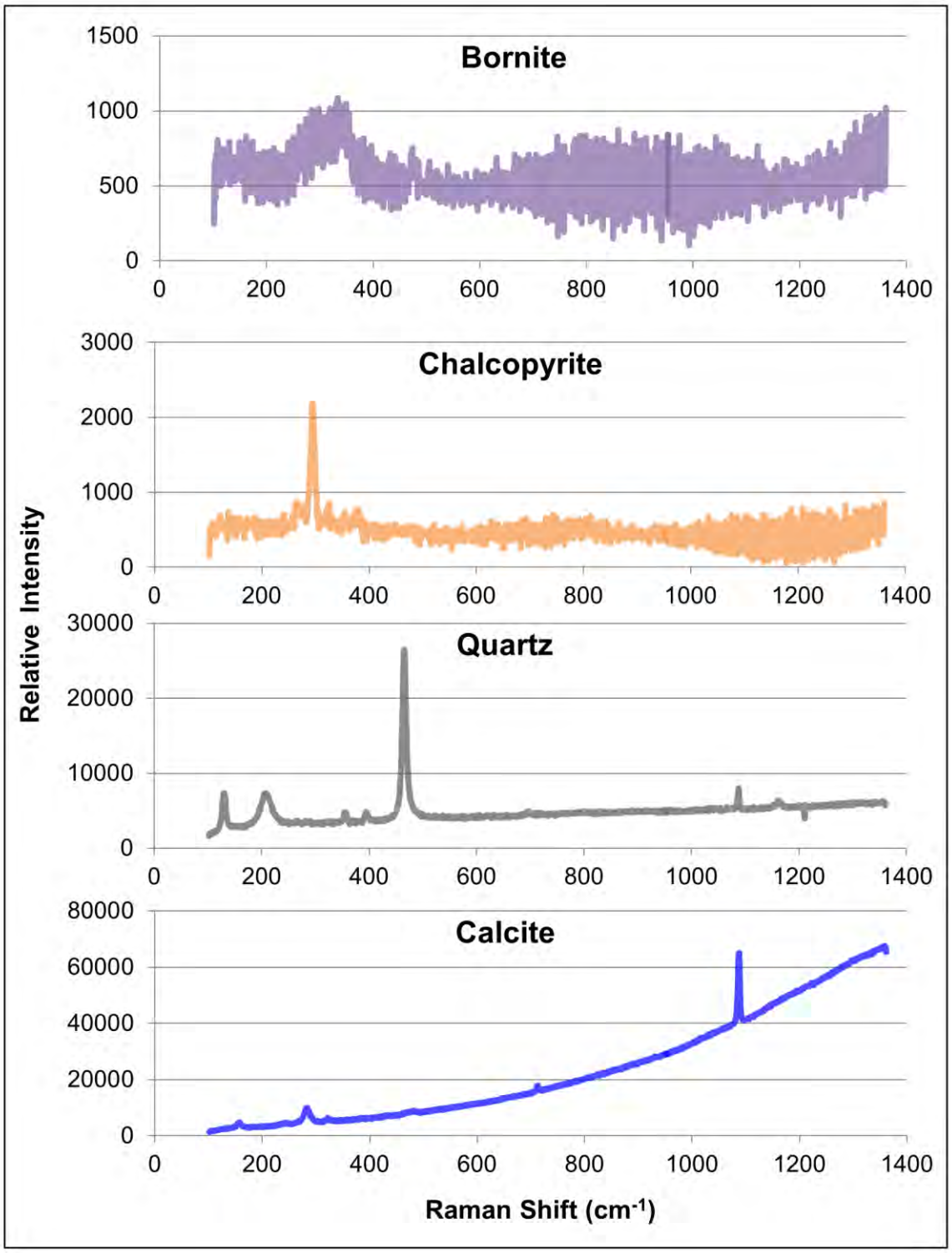

Figure 11.4. *Representative Raman spectra of bornite, chalcopyrite, quartz, and calcite collected from sample 1400.5.*

In all three streamline experiments, no bornite and less than twenty grains of chalcopyrite were detected in the sample. The results of the three streamline experiments are outlined in Table 11.1.

Table 11.1. *Results of three laser streamline Raman experiments (4X objective, 31.5 μm line scans, 100% laser power). Bn = bornite, cpy = chalcopyrite.*

Dwell Time (sec)	Analysis time per 3 cm line (min)	Approx. analysis time per pixel (ms)	Number of Bn Grains Detected	Number of Cpy Grains Detected	Bn Grains Expected	Cpy Grains Expected
2	1.4	110	0	1	> 50	> 15
4	3	230	0	3		
10	7.2	550	0	11		

11.5 Discussion

The results of the spot mode experiments using 16 μm spots with 16 μm and 32 μm steps revealed two major challenges: (1) chalcopyrite and bornite are poor Raman scatterers and provide low counts, and (2) bornite is thermally unstable and burns easily under low laser power. The relative Raman counts for calcite and quartz are 20 – 40 times higher than the counts for chalcopyrite and bornite causing these sulphides to be masked by the high Raman response of quartz and calcite (Figure 11.5). Since mixed spectra cause major challenges in identifying copper sulphides, only spot sizes smaller than or equal to the primary grain size in the sample will detect chalcopyrite and bornite. The average grain size of chalcopyrite and bornite in the test dataset (as measured by the MLA) is approximately 30 μm (very close to the 31.5 μm spot size). Thus, the likelihood of encountering grains near or intergrown with gangue minerals resulting in mixed Raman spectra is high. It is unlikely that the detection of chalcopyrite and bornite can be improved unless the spot size is greatly reduced. The streamline analysis also shows challenges in identifying copper sulphides. Over 15 grains of chalcopyrite and 50 grains of bornite greater than 200 μm were identified in the test sample by MLA analysis. The Raman streamline analysis identified no bornite and less than 15 grains of chalcopyrite in the sample. The streamline analysis reports an underestimation of both chalcopyrite and bornite grains.

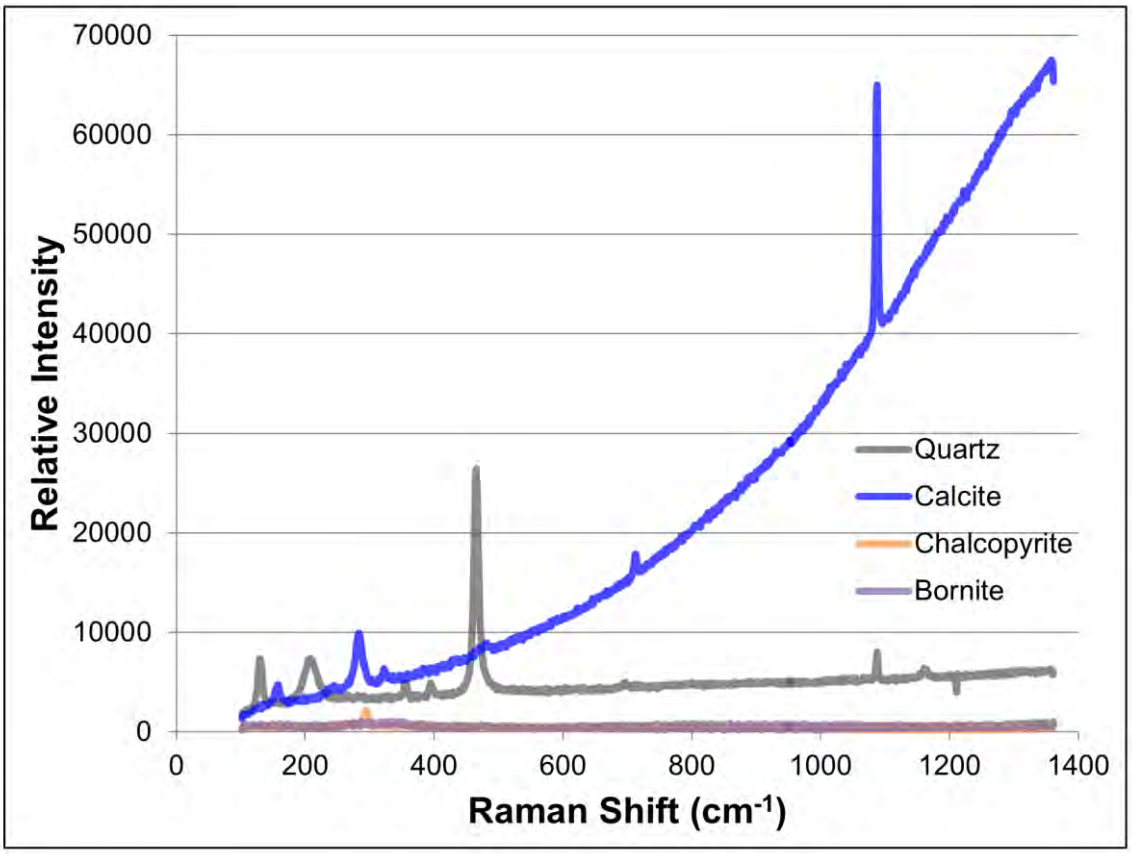

Figure 11.5. *In mixed spectra, bornite (purple) and chalcopyrite (orange) are masked by common gangue minerals including quartz (grey) and calcite (blue) making copper sulphide detection challenging.*

11.6 Conclusions

An initial test of the application of Raman spectroscopy for sulphide grain size assessment was completed on a single 3 cm by 3 cm rock sample (1400.5). Under the conditions of the initial experiments, long dwell times combined with small spot sizes are able to detect chalcopyrite and bornite. When the scanning rate or spot size is increased, copper sulphides occurring near or intergrown with gangue minerals produce mixed spectra and are often misidentified. This greatly underestimates grain size and imposes a bias toward larger grain sizes. In addition to being poor Raman scatterers (and therefore difficult to detect in mixed spectra), sulphide minerals (especially bornite) also burn easily under laser power limiting the application of this technique for sulphide detection.

Typically, challenges in identifying sulphides in laser Raman analysis are overcome by striking a balance between increased laser power and reduced spot size; however, decreasing the spot size increases the analysis time and increasing the laser power will cause further heat damage to the bornite. Even at the

optimised microscope conditions, the laser Raman is unable to accurately differentiate chalcopyrite and bornite from calcite and quartz. While 16 μm step spot experiment showed reasonable results with respect to mineral identification and grain size determination, these settings produce a spot acquisition rate of 6 seconds per 16 μm spot, far exceeding the goal of an acquisition rate near 3 minutes per metre. If this technique is unable to correctly identify copper sulphides, any grain size estimates resulting from this analysis will be inaccurate. The results of the initial experiments show that laser Raman is not suitable to quantify copper sulphide sizes at the required spot size and acquisition rates to be used in tandem with the Corescan system. Gold cannot be identified using laser Raman analysis alone. Testing of the laser Raman technique was terminated after the initial experiments as the results indicated that there was no operational window that could meet the aim of a grain size proxy at rates close to the Corescan data acquisition rate.

Chapter 12

Research conclusions and recommendations

12.1 Overview

The current data outputs obtained from the Corescan automated core logging system allow for key properties that affect the geotechnical response of a rock mass to be rapidly and consistently estimated. Integration of the existing Corescan data outputs with a complementary microanalytical system to assess grain size provides an opportunity to generate large volumes of consistent geometallurgical data. Both the geotechnical and grain size results show the potential application of automated core logging technology in assessment of parameters that are vital to the prediction of mining and processing responses of a rock mass. The application of multi-sensor automated systems, like the Corescan, provides the mineral resource sector an opportunity to optimize drill core data collection and increase the value gained from drill core assessment.

12.2 Geotechnical assessment conclusions

Geotechnical models provide the foundation for the construction of stress models, caveability models, ground support design, and fragmentation analysis. While not all industry standard geotechnical parameters can be derived from Corescan data, this research focuses on calculating fracture orientation, fracture roughness, number of fracture sets, fracture spacing, fracture condition, and fracture alteration. The results from the Cadia East small-scale test showed that the proposed methods performed well, overall. Over 75% of the calculated orientations were within 25° of their measured orientation value. When compared to photographs, measured values, or expected site values, the fracture protocols produced comparable calculated values. Over 90% of the calculated roughness values were within the expected range for Cadia East. The methods slightly underestimated the number of fracture sets and fracture spacing, and produced fracture condition and alteration values consistent with the fracture condition observed in photographs.

Traditionally, geotechnical assessment is completed using manual geotechnical logging procedures which are time-consuming and subjective. By utilizing laser profile data in conjunction with RGB imagery and hyperspectral mineralogical data collected by Corescan, large volumes of consistent, continuous down hole geotechnical data can be calculated automatically. The morphological geotechnical parameters that can be derived from Corescan data are the RQD, fracture spacing, fracture orientation, number of fracture sets, fracture roughness, fracture condition and fracture alteration. Other essential input parameters such as UCS, groundwater conditions, and SRF will need to be evaluated separately, using alternate datasets.

One advantage of the automated protocols developed in this study is the ability to collect a higher density of data than is feasible by manual methods. A comparison of all geotechnical parameters collected on the test dataset using the developed methods and those logged by the site team over the same interval is shown in Figure 12.1. The data density is greatly increased and can be collected in a much shorter amount of time. Manual geotechnical drill core logging can take 15 minutes to an hour per metre, depending on the condition of the drill core and level of detail required. The Corescan system is able to capture data at a rate of 3 minutes per metre, with minimal additional processing time, regardless of the level of detail or condition of the drill core. The scanning rate of the Corescan system combined with the increased data density ensures that geotechnical data is collected rapidly and consistently, providing major advantages over manual geotechnical logging methods.

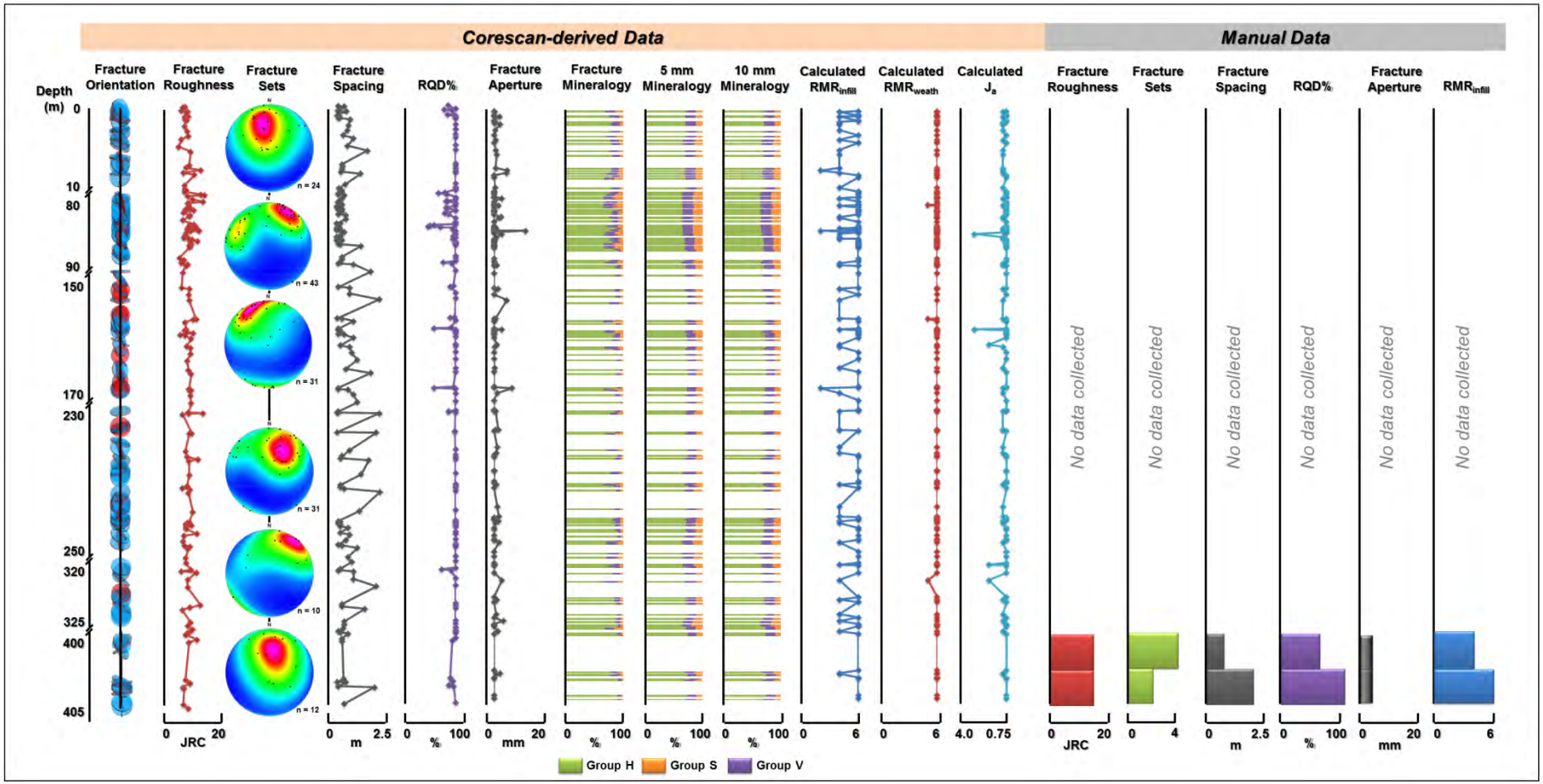

Figure 12.1. *Comparison of all of the morphological and mineralogical geotechnical parameters derived from Corescan data (orange) using the slope and aspect recognition protocol and the data collected manually on site (grey) over the same over the same interval for the test fracture set (n = 150 fractures).*

Whole, oriented drill core is required to extract fracture orientations (and the number of fracture sets). It may be possible, however, to collect fracture roughness, fracture spacing, fracture condition, and fracture alteration on whole, un-oriented drill core. The work by Morelli (2015) shows that the number of fracture sets contributes less than 10% to the variability of the RMR and Q-index calculations, so it may be possible to calculate a partial RMR or Q-index values without calculating the number of fractures sets (using whole, un-oriented drill core). This potential should be investigated, as it may provide meaningful geotechnical information without the cost and logistics of obtaining oriented drill core.

The automation of geotechnical data collection has the potential to increase both the efficiency and precision of geotechnical models. This novel approach to geotechnical assessment may provide rapid, reliable, continuous down hole geotechnical data, and become a key data source for geotechnical models and their application to the construction of stress models, caveability models, ground support design, and fragmentation analysis.

12.3 Grain size assessment conclusions

Of the five microanalytical techniques tested, μXRF, LA-ICP-MS, and LIBS were capable of producing reasonable grain size proxies for copper sulphide minerals. Determining grain size proxies for gold proved challenging due to limitations imposed by sampling statistics, but, in general, when a sufficient number of gold grains were analysed, pXRF and μXRF produced reasonable gold grain size proxies. LA-ICP-MS line scan analysis was unable to overcome the challenges of sampling statistics for gold, but this is the only technique with high enough precision to detect sub-micron gold grains, which could have broader geometallurgical applications. The laser Raman system was unable to detect gold and copper minerals under relevant conditions and further testing of this technique was terminated. A summary table of the grain size performance, analysis time, and relative cost of each microanalytical technique tested are presented in Table 12.1.

Table 12.1. *Comparison of the grain size assessment performance, analysis time, and relative cost of the 5 microanalytical techniques tested in this study. Compiled from Hark and Harmon (2014); Naes et al. (2008).*

	Experimental Parameters		**Copper**		**Gold**		**Copper**		**Gold**		
Technology	Spot Size	Analysis Time per Spot	R^2	r_s	R^2	r_s	Critical Analyses	Time to Collect	Critical Analyses	Time to Collect	Approx. Cost*
pXRF	33 mm^2	2 min	-	-	0.35	0.63	-	-	180 spots	90 min	~$30,000
μXRF	160 μm	80 ms	0.78	0.83	0.26	0.41	2000 spots	2.5 min	406,000 spots	180 min	~$120,000
LA-ICP-MS	34 μm	220 ms	0.74	0.87	0.25	0.5	0.12 m line	12 min	-	-	~$210,000
LIBS	150 μm	50 ms	0.57	0.69	-	-	620 spots	31 sec	-	-	~$100,000

* In USD, cost of complete system setup

Currently available μXRF and LIBS technologies are able to collect a sufficient number of analyses to produce robust copper sulphide grain size proxies at a rate comparable to the Corescan system throughput. These technologies are also relatively low cost (less than $150,000). Recent developments in core scanning XRF systems suggest that this approach will have data acquisition rates sufficient for gold grain size proxy calculations to become feasible within a decade. At the moment, LA-ICP-MS technology cannot be completed outside of an ablation cell, but, it could be used for the rapid scanning of selected core samples outside of the Corescan sample analysis stream. This technology, however, is quite expensive (more than $200,000) to implement. Of all the methods tested, μXRF and LIBS show the most promising potential for future development and integration into the current Corescan system for geometallurgical grain size assessment.

Current grain size assessment methods are time-consuming and expensive. Often, grain size assessment prior to mining is insufficient, leading to costly modifications of existing processing infrastructure. If the ability to capture rapid grain size proxies could be incorporated into the Corescan system, grain size values could be assessed and reassessed throughout the life of a deposit (e.g. exploration, feasibility, mining). This technology would provide the opportunity to collect rapid, consistent grain size data at a much lower cost than current grain size analysis methods. This will allow for a much higher data density than is often utilised, providing a better statistical sampling of a rock mass from drill core, leading to more robust geometallurgical models.

12.4 Recommendations for future work

Both the geotechnical and the grain size methods proposed here provide positive results and demonstrate the ability of these methods to be used broadly for geotechnical and grain size assessment. Both studies, however, represent small-scale proof of concept studies on rock samples from one drill hole in one deposit. These methods should be up scaled and tested on larger, more diverse data sets.

For geotechnical assessment, the methods should be rolled out through a few thousand metres of drill core at Cadia East, covering a broad spatial extent of the deposit. This up scaling will require that the methods be coded into the proprietary Corescan data analysis software. The methods should then be re-evaluated and any necessary changes should be made. A large-scale test of the methods over all available whole drill core data from Cadia East should follow. These methods

should then be tested on a different deposit type to identify any potential challenges with different rock types, structures, or mineralisation than the porphyry Au-Cu case study presented here.

For grain size assessment, the methods presented here should first be up scaled to include a few hundred drill core samples. The effects of sample surface roughness and drill core curvature were not specifically addressed in this thesis and will need to be investigated as drill core samples are rough and cylindrical. Prototypes of the microanalytical methods showing the most promise for grain size assessment will need to be developed to work in tandem with the Corescan automated core logging system. Additionally, the grain size proxy calculations will need to be coded into the Corescan propriety software. Like the geotechnical methods, the grain size methods should then be tested on a different deposit type to identify any potential challenges with different mineralisation styles than the porphyry Au-Cu case study presented here.

12.5 Key research outcomes

Two fundamental questions were address in this research:

(1) Can the methods currently used in manual geotechnical data collection be automated using data derived from automated core logging technology?

(2) Are currently available microanalytical methods capable of producing robust grain size proxies at a rate similar to current automated core logging systems? Addressing these research questions through method development and testing, the results of this research lead to two primary conclusions:

(1) Geotechnical assessment using automated core logging technology is possible and has the potential to provide rapid and consistent geotechnical assessment at a scale and consistency that is not feasible by manual logging methods.
(2) Currently available microanalytical techniques are capable of assessing copper grain size proxies at a rate comparable to the Corescan system throughput, but gold proved challenging due to limitations of sampling statistics.

The application of automated core logging systems increases the value gained from drill core assessment, particularly in the collection of geotechnical and grain size data. Through the methods developed in this thesis for geotechnical and geometallurgical assessment, the underlying statistical support for rock mass

characterisation and liberation and recovery modelling can be greatly increased. These outcomes have the capacity to substantially contribute to better geotechnical and geometallurgical models that will improve mine planning and ore recovery, which in turn will improve mine safety and profitability.

References

Arqué Armengol, A., 2015, Towards automated logging of ore: positive identification of sulphides in the ores of Agnico Eagle Kittilä and New Boliden Mines: M.S. thesis, Luleå, Sweden, Luleå University of Technology, 64 p.

Arrowsmith, P., and Hughes, S. K., 1988, Entrainment and transport of laser ablated plumes for subsequent elemental analysis: Applied Spectroscopy, v. 42, p. 1231-1239.

Baddeley, A., and Jensen, E. V., 2004, Stereology for statisticians, Chapman & Hall/CRC Monographs on Statistics and Applied Probability, 412 p.

Barton, N., 1973, Review of a new shear-strength criterion for rock joints: Engineering Geology, v. 7, p. 287-332.

Barton, N., 1976, Unsupported underground openings: Rock Mechanics Meeting, Stifrelsen Bergteknisk Forskning, Stockholm, 1976, Proceedings, p. 62-94.

Barton, N., 1987, Predicting the behavior of underground openings in rocks: The 4th Manuel Rocha Memorial Lecture, Lisbon, Portugal, 1987, p. 1-21.

Barton, N., and Choubey, V., 1977, The shear strength of rock joints in theory and practice: Rock Mechanics, v. 10, p. 1-54.

Barton, N., Lien, R., and Lunde, J., 1974, Engineering classification of rock masses for the design of tunnel support: Rock Mechanics, v. 6, p. 189-236.

Becker, M., Jardine, M., Miller, J., and Harris, M., 2016, X-ray computed tomography–a geometallurgical tool for 3D textural analysis of drill core?: Third AusIMM International Geometallurgy Conference, Perth, WA, Australia, 2016, p. 231-240.

Behrends, T., and Kleingeld, P., 2009, Bench-top micro-XRF–a useful apparatus for geochemists: Geochemical News, v. 138, p. 1-5.

Bell, F. G., 2013, Engineering properties of soils and rocks, Oxford, Elsevier, 344 p.

Belousov, I., Large, R., Meffre, S., Danyushevsky, L., Steadman, J., and Beardsmore, T., 2016, Pyrite compositions from VHMS and orogenic Au deposits in the Yilgarn Craton, Western Australia: Implications for gold and copper exploration: Ore Geology Reviews, v. 79, p. 474-499.

Berg, C., 2012, The effect of fracture and borehole orientation on fracture frequency and density: RDA Dip Interpretation Suite tutorial (http://www.resdip.com/docs/fracture%20orientation.pdf).

Berry, R., 2012, Cadia East case study report: (AMIRA Project P843 Geometallurgical Mapping and Mine Modelling), 90 p.

Berry, R., and Hunt, J., 2011, Grain size in geometallurgy - review of progress: Technical Report 8 (AMIRA Project P843 Geometallurgical Mapping and Mine Modelling), p. 61-75.

Berry, R., and Hunt, J., 2013, Proxy methods for domaining ore deposits for Au grain size: Technical Report (AMIRA Project P843 Geometallurgical Mapping and Mine Modelling), 30 p.

Berry, R., Hunt, J., and McKnight, S., 2008, Estimating mineralogy in bulk samples: (AMIRA Project P843 Geometallurgical Mapping and Mine Modelling), 12 p.

Berry, R., and Nguyen, K., 2016, Structure from photographs of oriented core: STORC: Economic Geology, v. 111, p. 1525-1527.

Berry, R., Walters, S., and McMahon, C., 2008a, Automated mineral identification by optical microscopy: Ninth AusIMM International Congress for Applied Mineralogy, Brisbane, Queensland, Australia, 2008, p. 91-94.

Bertin, E. P., 1975, Principles and practice of X-ray spectrometric analysis: Springer US, 1080 p.

Bieniawski, Z. T., 1976, Exploration for rock engineering: Symposium on Exploration for Rock Engineering, Johannesburg, South Africa, 1976, Proceedings, p. 97-106.

Bieniawski, Z. T., 1989, Engineering rock mass classifications: a complete manual for engineers and geologists in mining, civil, and petroleum engineering: John Wiley & Sons, 257 p.

Bolger, J., 2000, Semi-quantitative laser-induced breakdown spectroscopy for analysis of mineral drill core: Applied Spectroscopy, v. 54, p. 181-189.

Bonnici, N., Hunt, J., Walters, S., Berry, R., and Collett, D., 2008, Relating textural attributes to mineral processing: Developing a more effective approach for the Cadia East Cu-Au porphyry deposit: Ninth AusIMM International Congress for Applied Mineralogy, Brisbane, Queensland, Australia, 2008, p. 415-418.

Bonnici, N. K., 2012, The mineralogical and textural characteristics of copper-gold deposits related to mineral processing attributes: Ph.D. thesis, Hobart, Tasmania, Australia, University of Tasmania, 248 p.

Born, M., and Huang, K., 1954, Dynamical theory of crystal lattices: Clarendon, Oxford, 430 p.

Brady, B. H., and Brown, E. T., 2013, Rock mechanics for underground mining: Springer Science & Business Media, 570 p.

Broz, M. E., Cook, R. F., and Whitney, D. L., 2006, Microhardness, toughness, and modulus of Mohs scale minerals: American Mineralogist, v. 91, p. 135-142.

Bruker, M4 Tornado Specifications (https://www.bruker.com/products/x-ray-diffraction-and-elemental-analysis/micro-xrf-and-txrf/m4-tornado/overview.html).

Bruker, 2011, Webinar: μ-XRF - Fast and sensitive spatially resolved elemental analysis (https://www.bruker.com/service/education-training/webinars/xrf/xrf-archive.html).

Bruker, 2015, M4 Tornado User Manual (https://www.bruker.com/fileadmin/user_upload/8-PDF-Docs/X-rayDiffraction_ElementalAnalysis/mXRF/Brochures/Bro_m4_tornado_8p_en_rev3_3_lores.pdf).

Bruker, 2015a, Lab Report XRF 442 - Analytical performance of the M4 Tornado (https://www.bruker.com/fileadmin/user_upload/8-PDF-Docs/X-rayDiffraction_ElementalAnalysis/mXRF/LabReports/LR_m4_tornado_xrf_442_analyt_perform_rev1_1_lores.pdf).

Buehn, B., Rankin, A. H., Radtke, M., Haller, M., and Knoechel, A., 1999, Burbankite, a (Sr, REE, Na, Ca)-carbonate in fluid inclusions from carbonatite-derived fluids: Identification and characterization using Laser Raman spectroscopy, SEM-EDX, and synchrotron micro-XRF analysis: American Mineralogist, v. 84, p. 1117-1125.

Burns, R. G., 1993, Mineralogical applications of crystal field theory, Cambridge University Press, 576 p.

Cabri, L. J., Kelvin, M., Yang, Z., Jackson, S. E., and Altun, O., 2017, Application of LA-ICP-MS trace-element analysis for precious metal deportment: a case study of the Kevitsa mine, Finland: European Journal of Mineralogy, v. 29, p. 635-644.

Calvin, W. M., and Pace, E. L., 2016, Mapping alteration in geothermal drill core using a field portable spectroradiometer: Geothermics, v. 61, p. 12-23.

Chang, C., Zoback, M. D., and Khaksar, A., 2006, Empirical relations between rock strength and physical properties in sedimentary rocks: Journal of Petroleum Science and Engineering, v. 51, p. 223-237.

Charlesworth, H., and Kilby, W., 1981, Calculating thickness from outcrop and drill-hole data: Bulletin of Canadian Petroleum Geology, v. 29, p. 277-292.

Cnudde, V., and Boone, M. N., 2013, High-resolution X-ray computed tomography in geosciences: A review of the current technology and applications: Earth Science Reviews, v. 123, p. 1-17.

Coetzee, L. L., Theron, S. J., Martin, G. J., Van der Merwe, J.-D., and Stanek, T. A., 2011, Modern gold deportments and its application to industry: Minerals Engineering, v. 24, p. 565-575.

Cohen, D., 1990, GOLDCALS—a FORTRAN program for estimating the number and size of gold particles in geological samples: Computers & Geosciences, v. 16, p. 153-161.

Connors, B., Somers, A., and Day, D., 2016, Application of handheld laser-induced breakdown spectroscopy (LIBS) to geochemical analysis: Applied Spectroscopy, v. 70, p. 810-815.

Cook, N., Ciobanu, C. L., George, L., Zhu, Z.-Y., Wade, B., and Ehrig, K., 2016, Trace element analysis of minerals in magmatic-hydrothermal ores by laser ablation inductively-coupled plasma mass spectrometry: approaches and opportunities: Minerals, v. 6, p. 111.

Coulomb, C., 1773, Essay on the rules of maximis and minimis applied to some problems of equilibrium related to architecture: Academy of Royal Science Memorial Physics, v. 7, p. 343-382.

COX Analytical Systems, 2014, XRF scanner for elements in drill cores - Itrax Drillcore Scanner (http://www.coxsys.se/wp-content/uploads/2016/02 /Itrax-Corescanner-brochure.pdf).

Cummings, R., Kendorski, F., and Bieniawski, Z., 1982, Caving rock mass classification and support estimation: US Bureau of Mines Contract Report #J100103 (https://www.rocscience.com/documents/hoek/corner/ 04_Rock_mass_classification.pdf).

Dalm, M., and Buxton, M., 2016, Characterizing the economic value of an epithermal Au-Ag ore with Laser Induced Breakdown Spectroscopy (LIBS): The 7th Sensor-Based Sorting and Control, Aachen, Germany, 2016, Proceedings, p. 1-13.

Danyushevsky, L., Robinson, P., Gilbert, S., Norman, M., Large, R., McGoldrick, P., and Shelley, M., 2011, Routine quantitative multi-element analysis of sulphide minerals by laser ablation ICP-MS: standard development and consideration of matrix effects: Geochemistry: Exploration, Environment, Analysis, v. 11, p. 51-60.

De Lucia, F. C., and Gottfried, J. L., 2011, Rapid analysis of energetic and geo-materials using LIBS: Materials Today, v. 14, p. 274-281.

Deere, D. U., Hendron, A., Patton, F., and Cording, E., 1967, Design of surface and near-surface construction in rock: in "Failure and Breakage of Rock", Society of Minerals Engineering, p. 237-302.

Delmdahl, R., and Paetzel, R., 2009, The Midas Touch: Surface processing with the UV excimer laser: Lasertechnik Journal, v. 6, p. 24-29.

Diaz Ordonez, D. H., 2017, Laser-induced breakdown spectroscopy (LIBS) for analysis of precious metals in minerals: Ph.D. thesis, Medellín, Columbia, Universidad Nacional de Colombia, 117 p.

Dunham, S., and Vann, J., 2007, Geometallurgy, geostatistics and project value—does your block model tell you what you need to know: Project Evaluation Conference, 2007, Melbourne, Victoria, Australia, p. 19-20.

Dunham, S., Vann, J., and Coward, S., 2011, Beyond geometallurgy—gaining competitive advantage by exploiting the broad view of geometallurgy: Proceedings of the first AusIMM international geometallurgy conference, Brisbane, Queensland, Australia, 2011, p. 5-7.

ElMasry, G., and Sun, D.W., 2010, Principles of hyperspectral imaging technology: Hyperspectral imaging for food quality analysis and control: Elsevier, p. 3-43.

ESRI, 2011, How Slope (Spatial Analyst) works, webhelp: (http://desktop.arcgis.com/en/arcmap/10.3/tools/spatial-analyst-toolbox/how-slope-works.htm).

ESRI, 2011a, How Aspect (Spatial Analyst) works, webhelp: (http://desktop.arcgis.com/en/arcmap/10.3/tools/spatial-analyst-toolbox/how-aspect-works.htm).

ESRI, 2011b, How Hillshade (3D Analyst) works, webhelp: (http://desktop.arcgis.com/en/arcmap/10.3/tools/spatial-analyst-toolbox/how-hillshade-works.htm).

Evans, C., 2010, Development of a methodology to estimate flotation separability from ore microtexture: Ph.D. thesis, Brisbane, Queensland, Australia, University of Queensland, 303 p.

Evans, C. L., and Napier-Munn, T. J., 2013, Estimating error in measurements of mineral grain size distribution: Minerals Engineering, v. 52, p. 198-203.

Fandrich, R., Gu, Y., Burrows, D., and Moeller, K., 2007, Modern SEM-based mineral liberation analysis: International Journal of Mineral Processing, v. 84, p. 310-320.

Feng, D., and Aldrich, C., 1999, Effect of particle size on flotation performance of complex sulphide ores: Minerals Engineering, v. 12, p. 721-731.

Flude, S., Haschke, M., and Storey, M., 2017, Application of benchtop micro-XRF to geological materials: Mineralogical Magazine, v. 81, p. 923-948.

Fox, N., 2012, Controls on alteration and mineralisation at the Cadia East alkalic porphyry Au-Cu deposit, NSW: Ph.D. thesis, Hobart, Tasmania, Australia, University of Tasmania, 222 p.

Fryer, B. J., Jackson, S. E., and Longerich, H. P., 1995, The design, operation and role of the laser-ablation microprobe coupled with an inductively coupled plasma; mass spectrometer (LAM-ICP-MS) in the earth sciences: The Canadian Mineralogist, v. 33, p. 303-312.

Fresia, B., Ross, P.-S., Gloaguen, E., and Bourke, A., 2017, Lithological discrimination based on statistical analysis of multi-sensor drill core logging data in the Matagami VMS district, Quebec, Canada: Ore Geology Reviews, v. 80, p. 552-563.

Gazley, M. F., Tutt, C. M., Brisbout, L. I., Fisher, L. A., and Duclaux, G., 2014, Application of portable X-ray fluorescence analysis to characterize dolerite dykes at the Plutonic Gold Mine, Western Australia: Geochemistry: Exploration, Environment, Analysis, v. 14, p. 223-231.

Gazley, M. F., Vry, J. K., du Plessis, E., and Handler, M. R., 2011, Application of portable X-ray fluorescence analyses to metabasalt stratigraphy, Plutonic Gold Mine, Western Australia: Journal of Geochemical Exploration, v. 110, p. 74-80.

Geelhoed, B., 2011, Is Gy's formula for the fundamental sampling error accurate? Experimental evidence: Minerals Engineering, v. 24, p. 169-173.

Gilbert, S., Danyushevsky, L., Goemann, K., and Death, D., 2014, Fractionation of sulphur relative to iron during laser ablation-ICP-MS analyses of sulphide minerals: implications for quantification: Journal of Analytical Atomic Spectrometry, v. 29, p. 1024-1033.

GMEX, 2008, Spectral interpretation field manual, 3rd ed.: AusSpec International Ltd., v. I, II, III.

Goldstein, J. I., Newbury, D. E., Michael, J. R., Ritchie, N. W., Scott, J. H. J., and Joy, D. C., 2017, Scanning electron microscopy and X-ray microanalysis, Springer, 689 p.

Goodall, W., and Butcher, A., 2012, The use of QEMSCAN in practical gold deportment studies: Mineral Processing and Extractive Metallurgy, v. 121, p. 199-204.

Grasselli, J. G., Snavely, M. K., and Bulkin, B. J., 1980, Applications of Raman spectroscopy: Physics Reports, v. 65, p. 231-344.

Groshong, R. H., 2006, 3-D structural geology: A practical guide to quantitative surface and subsurface map interpretation, Springer, 400 p.

Gu, Y., 2003, Automated scanning electron microscope based mineral liberation analysis an introduction to JKMRC/FEI mineral liberation analyser: Journal of Minerals and Materials Characterization and Engineering, v. 2, p. 33.

Gundlach-Graham, A., and Günther, D., 2016, Toward faster and higher resolution LA–ICPMS imaging: on the co-evolution of LA cell design and ICPMS instrumentation: Analytical and Bioanalytical Chemistry, v. 408, p. 2687-2695.

Gy, P., 1979, Sampling of particulate materials theory and practice, Amsterdam, Elsevier, 431 p.

Hall, G. E., Bonham-Carter, G. F., and Buchar, A., 2014, Evaluation of portable X-ray fluorescence (pXRF) in exploration and mining: Phase 1, control reference materials: Geochemistry: Exploration, Environment, Analysis, v. 14, p. 99-123.

Hanson, C., and Vargis, E., 2015, Open-system Raman microscopy: (https://www.laserfocusworld.com/articles/print/volume-51/issue-05/biooptics-world/biooptics-features/microscopy-and-raman-imaging-open-system-raman-microscopy.html).

Harhira, A., Bouchard, P., Rifai, K., El Haddad, J., Sabsabi, M., Blouin, A., and Laflamme, M., 2017, Advanced laser-induced breakdown spectroscopy (LIBS) sensor for gold mining: COM2017, Conference of Metallurgists, Vancouver British Columbia, 2017, Proceedings, 12p.

Hark, R. R., and Harmon, R. S., 2014, Geochemical fingerprinting using LIBS, Laser-Induced Breakdown Spectroscopy (Chapter 12), Springer, p. 309-348.

Harmon, R. S., De Lucia, F. C., Miziolek, A. W., McNesby, K. L., Walters, R. A., and French, P. D., 2005, Laser-induced breakdown spectroscopy (LIBS)–an emerging field-portable sensor technology for real-time, in-situ geochemical and environmental analysis: Geochemistry: Exploration, Environment, Analysis, v. 5, p. 21-28.

Harmon, R. S., Hark, R. R., Throckmorton, C. S., Rankey, E. C., Wise, M. A., Somers, A. M., and Collins, L. M., 2017, Geochemical Fingerprinting by Handheld Laser-Induced Breakdown Spectroscopy (LIBS): Geostandards and Geoanalytical Research, v. 41, p. 563-584.

Harraden, C. L., Berry, R., and Lett, J., 2016, Proposed methodology for utilising automated core logging technology to extract geotechnical index parameters: Third AusIMM International Geometallurgy Conference, Perth, Australia,2016, Proceedings, p. 119-124.

Harraden, C. L., Cracknell, M. J., Lett, J., and Berry, R., 2017, The use of automated core logging technology to improve estimation of fracture mineralogy and weathering for geotechnical index calculations: AIG Drilling for Geology II, 2017, Brisbane, Queensland, Australia, p. 73-80.

Harraden, C. L., McNulty, B. A., Gregory, M. J., and Lang, J. R., 2013, Shortwave infrared spectral analysis of hydrothermal alteration associated with the Pebble porphyry copper-gold-molybdenum deposit, Iliamna, Alaska: Economic Geology, v. 108, p. 483-494.

Harris, A., Cooke, D. R., Fox, N., Cuison, A., Tosdal, R., Groome, M., Percival, I., Dunham, P. D., Collett, D., Holliday, J. R., and Allen, C., 2010, Architectural controls on Paleozoic porphyry Au-Cu mineralisation in the Cadia Valley, NSW: Mines and Wines Symposium 2010, Mudgee, New South Wales (http://citeseerx.ist.psu.edu/viewdoc/download?doi=10.1.1.869.4703&rep=rep1&type=pdf).

Henke, B. L., Gullikson, E. M., and Davis, J. C., 1993, X-ray interactions: photoabsorption, scattering, transmission, and reflection at E= 50-30,000 eV, Z= 1-92: Atomic Data and Nuclear Data Tables, v. 54, p. 181-342.

Herrmann, W., Blake, M., Doyle, M., Huston, D., Kamprad, J., Merry, N., and Pontual, S., 2001, Short wavelength infrared (SWIR) spectral analysis of hydrothermal alteration zones associated with base metal sulfide deposits at Rosebery and Western Tharsis, Tasmania, and Highway-Reward, Queensland: Economic Geology, v. 96, p. 939-955.

Higgins, M. D., 2006, Quantitative textural measurements in igneous and metamorphic petrology: Cambridge University Press, 276 p.

Hoal, K. O., 2008, Getting the geo into geomet: SEG Newsletter, Society of Economic Geologists, n. 73, p. 1, 11-15.

Hoek, E., Kaiser, P. K., and Bawden, W. F., 2000, Support of underground excavations in hard rock: CRC Press, 225 p.

Holcombe, R., 2013, Oriented drillcore: measurement, conversion, and QA/QC procedures for structural and exploration geologists: (http://www.hcovglobal.com/#!downloads/lf947).

Holliday, J. R., Wilson, A. J., Blevin, P. L., Tedder, I. J., Dunham, P. D., and Pfitzner, M., 2002, Porphyry gold–copper mineralisation in the Cadia district, eastern Lachlan Fold Belt, New South Wales, and its relationship to shoshonitic magmatism: Mineralium Deposita, v. 37, p. 100-116.

Hope, G. A., Woods, R., and Munce, C. G., 2001, Raman microprobe mineral identification: Minerals Engineering, v. 14, p. 1565-1577.

Huang, J. J., Löwemark, L., Chang, Q., Lin, T. Y., Chen, H. F., Song, S. R., and Wei, K. Y., 2016, Choosing optimal exposure times for XRF core-scanning: Suggestions based on the analysis of geological reference materials: Geochemistry, Geophysics, Geosystems, v. 17, p. 1558-1566.

Hunt, J., Berry, R., and Bradshaw, D., 2011, Characterising liberation and flotation potential using image analysis, simulated fragmentation and small-scale flotation: First AusIMM International Geometallurgy Conference, Brisbane, Queensland, Australia, 2011, p. 331-333.

Huntington, J. F., Mauger, A. J., Skirrow, R. G., Bastrakov, E. N., Connor, P., Mason, P., Keeling, J. L., Coward, D. A., Berman, M., and Phillips, R., 2006, Automated mineralogical core logging at the Emmie Bluff iron oxide-copper-gold prospect: MESA Journal, v. 41, p. 38-44.

Innov-X, 2010: Delta TM Family: Handheld XRF analyzers user manual (https://usenvironmental.com/download/manuals/Olympus+-+Delta+User+Manual.pdf).

Jackson, L., Parbhakar-Fox, A., Fox, N., Cooke, D., Harris, A., Meffre, S., Danyushevsky, L., Goemann, K., Rodemann, T., and Gloy, G., 2018, Assessing geo-environmental risk using intact materials for early life-of-mine planning–a review of established techniques and emerging tools: in From Start to Finish, AusIMM Publication, P. 9-26.

Janssens, K. H., Adams, F., and Rindby, A., 2000, Microscopic X-ray fluorescence analysis: John Wiley & Sons Inc, 420 p.

Jenkins, R., 1976, An introduction to X-Ray spectrometry: London, John Wiley & Sons Ltd, 174 p.

Jones, S., Herrmann, W., and Gemmell, J. B., 2005, Short wavelength infrared spectral characteristics of the HW horizon: Implications for exploration in the Myra Falls volcanic-hosted massive sulfide camp, Vancouver Island, British Columbia, Canada: Economic Geology, v. 100, p. 273-294.

Kalantari, S., Hashemolhosseini, H., and Baghbanan, A., 2018, Estimating rock strength parameters using drilling data: International Journal of Rock Mechanics and Mining Sciences, v. 104, p. 45-52.

Kamenetsky, M., and Berry, R., 2010, Report on a scoping study for gold characterisation of 77 Cadia East samples from DDH CE143 using MLA techniques: Technical Report (AMIRA Project P843 Geometallurgical Mapping and Mine Modelling), 6 p.

Keeling, J., Mauger, A., and Huntington, J., 2004, Spectral core logger update—preliminary results from the Barns gold prospect: MESA Journal, v. 33, p. 32-36.

Keeney, L., 2010, The Development of a novel method for integrating geometallurgical mapping and orebody modelling, Ph.D. thesis, Brisbane, Queensland, Australia, University of Queensland, 309 p.

Keeney, L., Walters, S., and Kojovic, T., 2011, Geometallurgical mapping and modelling of comminution performance at the Cadia East porphyry deposit: First AusIMM International Geometallurgy Conference, Brisbane, Queensland, Australia, 2011, p. 73-83.

Kendorski, F., Cummings, R., Bieniawski, Z., and Skinner, E., 1983, Rock mass classification for block caving mine drift support: 5th International Congress of Rock Mechanics, Melbourne, Victoria, Australia, 1983, in Proceedings, p. 51-63.

Ketcham, R. A., 2005, Computational methods for quantitative analysis of three-dimensional features in geological specimens: Geosphere, v. 1, p. 32-41.

Kitto, J., 2005, Lithostratigraphy, Alteration and Geochemistry at the Cadia East Gold-Copper Porphyry Deposit, NSW, B.Sc. Honours thesis, Hobart, Tasmania, Australia, University of Tasmania, 136 p.

Kokaly, R., Clark, R., Swayze, G., Livo, K., Hoefen, T., Pearson, N., Wise, R., Benzel, W., Lowers, H., and Driscoll, R., 2017, USGS Spectral Library Version 7 Data: US Geological Survey data release 1035, 61 p. (https://dx.doi.org/10.5066/F7RR1WDJ).

Kortüm, G., 2012, Reflectance spectroscopy: principles, methods, applications: Springer Science & Business Media, 366 p.

Kraut, J., and Stern, W., 2000, The density of gold-silver-copper alloys and its calculation from the chemical composition: Gold Bulletin, v. 33, p. 52-55.

Kuhn, K., Meima, J. A., Rammlmair, D., and Ohlendorf, C., 2016, Chemical mapping of mine waste drill cores with laser-induced breakdown spectroscopy (LIBS) and energy dispersive X-ray fluorescence (EDXRF) for mineral resource exploration: Journal of Geochemical Exploration, v. 161, p. 72-84.

Kuznetsov, S., 2016, X-ray optics calculator: Institute of Microelectronics Technology and High Purity Materials, Russian Academy of Sciences (IMT RAS), (http://purple.ipmt-hpm.ac.ru/xcalc/xcalc_mysql/airtrans.php).

Lafuente, B., Downs, R., Yang, H., and Stone, N., 2016, The power of databases: the RRUFF project: Highlights in Mineralogical Crystallography, p. 1-29.

Lamberg, P., 2011, Particles–the bridge between geology and metallurgy: Conference in Minerals Engineering, Luleå, Sweden, 2011, in Proceedings, p. 8-9.

Large, R. R., Danyushevsky, L., Hollit, C., Maslennikov, V., Meffre, S., Gilbert, S., Bull, S., Scott, R., Emsbo, P., and Thomas, H., 2009, Gold and trace element zonation in pyrite using a laser imaging technique: implications for the timing of gold in orogenic and Carlin-style sediment-hosted deposits: Economic Geology, v. 104, p. 635-668.

Lasertechnik, 2018, How does LIBS work?, Lasertechnik Berlin (http://www.ltb-berlin.de/en/technologies/libs/).

Laubscher, D., 1977, Geomechanics classification of jointed rock masses-mining applications: Transactions of the Institute of Mining and Metallurgy, v. 86, p. A1-8.

Laubscher, D., 1984, Design aspects and effectiveness of support systems in different mining conditions: Transactions of the Institute of Mining and Metallurgy, v. 93, p. 70-81.

Laubscher, D., and Page, C., 1990, The design of rock support in high stress or weak rock environments: 92nd Canadian Institute of Mining and Metallurgy, AGM, Ottawa, Ontario, Canada, in Proceedings, Paper No. 91.

Laubscher, D., and Taylor, H., 1976, The importance of geomechanics classification of jointed rock masses in mining operations: Symposium on Exploration for Rock Engineering, Johannesburg, South Africa, 1976, in Proceedings, p. 119-128.

Lauffer, H., 1958, Gebirgsklassifizierung für den Stollenbau: Geologie und Bauwesen, v. 24, p. 46-51.

Laukamp, C., 2011, Short Wave Infrared Functional Groups of Rock-forming Minerals, CSIRO report EP115222, (https://publications.csiro.au/rpr/download?pid=csiro:EP115222&dsid=DS5).

Lewis, I. R., and Edwards, H., 2001, Handbook of Raman spectroscopy: from the research laboratory to the process line, CRC Press, 1072 p.

Limbeck, A., Galler, P., Bonta, M., Bauer, G., Nischkauer, W., and Vanhaecke, F., 2015, Recent advances in quantitative LA-ICP-MS analysis: challenges and solutions in the life sciences and environmental chemistry: Analytical and Bioanalytical Chemistry, v. 407, p. 6593-6617.

Lin, J. F., Alp, E. E., and Goncharov, A. F., 2014, Raman and nuclear resonant spectroscopy in geosciences: in Treatise on geochemistry, ch. 14, Amsterdam, Elsevier, 454 p.

Longerich, H. P., Jackson, S. E., and Günther, D., 1996, Laser ablation inductively coupled plasma mass spectrometric transient signal data acquisition and analyte concentration calculation: Journal of Analytical Atomic Spectrometry, v. 11, p. 899-904.

Maerz, N., Franklin, J., and Bennett, C., 1990, Joint roughness measurement using shadow profilometry: International Journal of Rock Mechanics and Mining Sciences & Geomechanics Abstracts, v. 27, p. 329-343.

Marcotte, D., and Henry, E., 2002, Automatic joint set clustering using a mixture of bivariate normal distributions: International Journal of Rock Mechanics and Mining Sciences, v. 39, p. 323-334.

Marinos, P., and Hoek, E., 2000, GSI: a geologically friendly tool for rock mass strength estimation: International Society of Rock Mechanics international symposium, Melbourne Australia, 2000, 19 p.

Marsland, S., 2015, Machine learning: an algorithmic perspective: CRC press, 457 p.

Mason, P., and Huntington, J., 2010, HyLogger 2 components and preprocessing: an overview: Northern Territory Geological Survey Technical Note, v. 1, p. 7.

Mauger, A., and Huntington, J., 2005, HyLogging applications in exploration: Mineral Exploration Through Cover, Adelaide, South Australia, Australia, 2005, in Proceedings, p. 20-21.

Mauriohooho, K., Barker, S. L., and Rae, A., 2016, Mapping lithology and hydrothermal alteration in geothermal systems using portable X-ray fluorescence (pXRF): A case study from the Tauhara geothermal system, Taupo Volcanic Zone: Geothermics, v. 64, p. 125-134.

McMillan, N. J., Harmon, R. S., De Lucia, F. C., and Miziolek, A. M., 2007, Laser-induced breakdown spectroscopy analysis of minerals: carbonates and silicates: Spectrochimica Acta Part B: Atomic Spectroscopy, v. 62, p. 1528-1536.

McMillan, N. J., Rees, S., Kochelek, K., and McManus, C., 2014, Geological Applications of Laser - Induced Breakdown Spectroscopy: Geostandards and Geoanalytical Research, v. 38, p. 329-343.

Mees, F., Swennen, R., Van Geet, M., and Jacobs, P., 2003, Applications of X-ray computed tomography in the geosciences: Geological Society, London, Special Publications, v. 215, p. 1-6.

Meffre, S., Danyushevsky, L., Harraden, C. L., Berry, R., Olin, P. H., and Fox, N., 2017, Scanning Unpolished Drill Cores with Laser Ablation Quadrupole ICPMS: Goldschmidt, Paris, France, 2017, in Abstracts, p. 2679.

Mernagh, T. P., and Trudu, A. G., 1993, A laser Raman microprobe study of some geologically important sulphide minerals: Chemical Geology, v. 103, p. 113-127.

Mohs, F., 1825, Treatise on mineralogy (translated by W. Haidinger): Edinburgh, Caledonian Mercury Press, 458 p.

Momeni, E., Nazir, R., Armaghani, D. J., and Mohamad, E., 2015, Prediction of unconfined compressive strength of rocks: a review paper: Jurnal Teknologi, v. 77, n. 11, p. 43-50.

Morelli, G. L., 2015, Variability of the GSI index estimated from different quantitative methods: Geotechnical and Geological Engineering, v. 33, p. 983-995.

Morris, P. A., 2009, Field-portable X-ray fluorescence analysis and its application in GSWA, Geological Survey of Western Australia Report, 23 p.

Naes, B. E., Umpierrez, S., Ryland, S., Barnett, C., and Almirall, J. R., 2008, A comparison of laser ablation inductively coupled plasma mass spectrometry, micro X-ray fluorescence spectroscopy, and laser induced breakdown spectroscopy for the discrimination of automotive glass: Spectrochimica Acta Part B: Atomic Spectroscopy, v. 63, p. 1145-1150.

Newcrest, 2011, Technical report on the Cadia Valley Operations property in New South Wales, Australia, 137 p.

Newcrest, 2018, Annual mineral resources and ore reserves statement – 31 December 2017, 11 p.

Nguyen, A., Jackson, J., Nguyen, K., and Manlapig, E., 2016, A new semi-automated method to rapidly evaluate the processing variability of the ore body: Third AusIMM International Geometallurgy Conference, 2016, Perth, Western Australia, Australia, in Proceedings, p. 145-51.

Olson, L., 2013, The 3-D imaging of drill core for fracture mapping, M.Sc. thesis, Ottawa, Ontario, Canada, Carleton University.

Parbhakar-Fox, A., and Lottermoser, B. G., 2015, A critical review of acid rock drainage prediction methods and practices: Minerals Engineering, v. 82, p. 107-124.

Pasteris, J., 1998, The Laser Raman Microprobe as a Tool for the Economic Geologist, in Applications of microanalytical techniques to understanding mineralizing processes: Reviews in Economic Geology, v. 7, 263 p.

Piercey, S. J., and Devine, M. C., 2014, Analysis of powdered reference materials and known samples with a benchtop, field portable X-ray fluorescence (pXRF) spectrometer: evaluation of performance and potential applications for exploration lithogeochemistry: Geochemistry: Exploration, Environment, Analysis, v. 14, p. 139-148.

Piña, R., Gervilla, F., Barnes, S.-J., Ortega, L., and Lunar, R., 2012, Distribution of platinum-group and chalcophile elements in the Aguablanca Ni–Cu sulfide deposit (SW Spain): evidence from a LA-ICP-MS study: Chemical Geology, v. 302, p. 61-75.

Pitts, J., 1985, A manual of geology for civil engineers: World Scientific, 228 p.

Potts, P., 1993, Laboratory methods of analysis, in Analysis of Geological Materials: New York, Marcel Dekker, 480 p.

Prensky, S. E., 1999, Advances in borehole imaging technology and applications: Geological Society, London, Special Publications, v. 159, p. 1-43.

Qian, G., Li, Y., and Gerson, A. R., 2015, Applications of surface analytical techniques in Earth Sciences: Surface Science Reports, v. 70, p. 86-133.

Quiniou, T., Selmaoui, N., Laporte-Magoni, C., and Allenbach, M., 2007, Calculation of Bedding Angles Inclination from Drill Core Digital Images: IAPR Conference on Machine Vision Applications, Tokyo Japan, 2007, in Proceedings, p. 252-255.

Railsback, L. B., 2006, Some fundamentals of mineralogy and geochemistry: Department of Geology, University of Georgia, Athens, Georgia (http://www.gly.uga.edu/railsback/FundamentalsIndex.html).

Rauh, F., and Thuro, K., 2007, Investigations on the swelling behavior of pure anhydrites: 1st Canada-US Rock Mechanics Symposium, Vancouver, British Columbia, Canada, 2007, 7 p.

Ready, J., 1971, Effects of high-power laser radiation: Elsevier, 433 p.

Ridley, W. I., and Lichte, F. E., 1998, Major, trace, and ultratrace element analysis by laser ablation ICP-MS: Reviews in Economic Geology, v. 7, p. 199-215.

Ripley, B. D., 2007, Pattern recognition and neural networks, Cambridge University Press, 416 p.

Ritter, W., 1879, Die Statik der Tunnelgewölbe: J. Springer, 66 p.

Rossimel, C., and Lett, J., 2012, Cadia East geotechnical block model for PC1-S1: Internal Newcrest Mining Limited report, 101 p.

Sabtan, A. A., 2005, Geotechnical properties of expansive clay shale in Tabuk, Saudi Arabia: Journal of Asian Earth Sciences, v. 25, p. 747-757.

Scott, R. J., and Berry, R. F., 2004, A new method for obtaining and quantifying the reliability of structural data from axially-oriented drill core using a fabric of known orientation: Journal of Structural Geology, v. 26, p. 643-658.

Senesi, G. S., 2014, Laser-Induced Breakdown Spectroscopy (LIBS) applied to terrestrial and extraterrestrial analogue geomaterials with emphasis to minerals and rocks: Earth-Science Reviews, v. 139, p. 231-267.

SGS, 2014, Automated Core Logging, SGS Minerals Services Report - T3 SGS 1344 (https://www.sgs.com/-/media/global/documents/flyers-and-leaflets/sgs-1344-automated-core-logging.pdf).

Shigematsu, N., Otsubo, M., Fujimoto, K., and Tanaka, N., 2014, Orienting drill core using borehole-wall image correlation analysis: Journal of Structural Geology, v. 67, p. 293-299.

Sinclair, D. J., Kinsley, L. P., and McCulloch, M. T., 1998, High resolution analysis of trace elements in corals by laser ablation ICP-MS: Geochimica et Cosmochimica Acta, v. 62, p. 1889-1901.

Sinclair, W., 2007, Porphyry deposits: Mineral deposits of Canada: A synthesis of major deposit-types, district metallogeny, the evolution of geological provinces, and exploration methods: Geological Association of Canada, Mineral Deposits Division, Special Publication, v. 5, p. 223-243.

Slob, S., Van Knapen, B., Hack, R., Turner, K., and Kemeny, J., 2005, Method for automated discontinuity analysis of rock slopes with three-dimensional laser scanning: Transportation research record, p. 187-194.

Smee, B., and Stanley, C., 2005, Sample preparation of 'nuggety'samples: dispelling some myths about sample size and sampling errors: Explore, Association of Applied Geochemists Newsletter, v. 126, p. 21-27.

Somers, A., 2017, Application of hand-held laser induced breakdown spectroscopy to drilling samples: new technology providing new in-field analytical capabilities: AIG Drilling for Geology II, 2017, Brisbane, Queensland, Australia, p. 89-96.

Specim, 2014, SisuRock Hyperspectral Core Logger (http://www.specim.fi/downloads/SisuROCK_Brochure-1_17_web.pdf).

Squire, R., 2001, The volcanological and tectono-magmatic evolution of the Cadia-Neville region, Lachlan Fold Belt, NSW: Ph.D. thesis, Hobart, Tasmania, Australia, University of Tasmania, 221 p.

Squire, R. J., Herrmann, W., Pape, D., and Chalmers, D. I., 2007, Evolution of the Peak Hill high-sulfidation epithermal Au–Cu deposit, eastern Australia: Mineralium Deposita, v. 42, p. 489-503.

Steadman, J. A., Large, R. R., Meffre, S., Olin, P. H., Danyushevsky, L. V., Gregory, D. D., Belousov, I., Lounejeva, E., Ireland, T. R., and Holden, P., 2015, Synsedimentary to early diagenetic gold in black shale-hosted pyrite nodules at the Golden Mile Deposit, Kalgoorlie, Western Australia: Economic Geology, v. 110, p. 1157-1191.

Strnad, L., Ettler, V., Mihaljevic, M., Hladil, J., and Chrastny, V., 2009, Determination of Trace Elements in Calcite Using Solution and Laser Ablation ICP-MS: Calibration to NIST SRM Glass and USGS MACS Carbonate, and Application to Real Landfill Calcite: Geostandards and Geoanalytical Research, v. 33, p. 347-355.

Sullivan, T., Duran, A., and Eggers, M., 1992, Use and abuse of oriented core in open pit mine design: Australasian Institute of Mining and Metallurgy Conference, 1992, Parkville, Victoria Australia, in Proceedings, p. 387-395.

Sutherland, D., 2007, Estimation of mineral grain size using automated mineralogy: Minerals Engineering, v. 20, p. 452-460.

Sylvester, P. J., and Eggins, S. M., 1997, Analysis of Re, Au, Pd, Pt and Rh in NIST glass certified reference materials and natural basalt glasses by laser ablation ICP-MS: Geostandards and Geoanalytical Research, v. 21, p. 215-229.

Tamura, S., Horisawa, H., Yamaguchi, S., and Yasunaga, N., 2002, Laser Ablation of Sapphire with a Pulsed Ultra-Violet Laser Beam, in Initiatives of Precision Engineering at the Beginning of a Millennium: Springer, p. 224-228.

Tappert, M., Rivard, B., Fulop, A., Rogge, D., Feng, J., Tappert, R., and Stalder, R., 2015, Characterizing Kimberlite Dilution by Crustal Rocks at the Snap Lake Diamond Mine (Northwest Territories, Canada) using SWIR (1.90–2.36 μm) and LWIR (8.1–11.1 μm) Hyperspectral Imagery Collected from Drill Core: Economic Geology, v. 110, p. 1375-1387.

Tappert, M., Rivard, B., Giles, D., Tappert, R., and Mauger, A., 2011, Automated drill core logging using visible and near-infrared reflectance spectroscopy: a case study from the Olympic Dam IOCG deposit, South Australia: Economic Geology, v. 106, p. 289-296.

TerraCore, 2014, View Core Logging in a New Light, TerraCore Report, (http://terracoregeo.com/wp-content/uploads/2014/11/TC_Hyperspectral-Core-Imaging.pdf).

Terzaghi, K., 1946, Rock defects and loads on tunnel supports: Harvard University Press, 95 p.

Thomas, G. B., 1960, Calculus and analytic geometry: Addison Wesley, 1264 p.

Thompson, A. J., Hauff, P. L., and Robitaille, A. J., 1999, Alteration mapping in exploration: application of short-wave infrared (SWIR) spectroscopy: SEG Newsletter, n. 39, p. 16-27.

Thompson, M., Chenery, S., and Brett, L., 1990, Nature of particulate matter produced by laser ablation—implications for tandem analytical systems: Journal of Analytical Atomic Spectrometry, v. 5, p. 49-55.

Tiu, G., 2017, Classification of drill core textures for process simulation in geometallurgy: Aitik Mine, New Boliden: M.S. thesis, Luleå, Sweden, Luleå University of Technology, 71 p.

Tokhmechi, B., Memarian, H., Moshiri, B., Rasouli, V., and Noubari, H. A., 2011, Investigating the validity of conventional joint set clustering methods: Engineering Geology, v. 118, p. 75-81.

Trahar, W., 1981, A rational interpretation of the role of particle size in flotation: International Journal of Mineral Processing, v. 8, p. 289-327.

Trofimczyk, K., and Du Pisani, P., 2009, Integration of borehole radar and acoustic televiewer data in geotechnical boreholes–a case study of the use of downhole geophysical data in mitigating risk to a new mning shaft development: 11th SAGA Biennial Technical Meeting and Exhibition, 2009, Swaziland, p. 149-154.

Tungpalan, K., Wightman, E., and Manlapig, E., 2015, Relating mineralogical and textural characteristics to flotation behaviour: Minerals Engineering, v. 82, p. 136-140.

Ueda, T., Oki, T., and Koyanaka, S., 2018, A general quantification method for addressing stereological bias in mineral liberation assessment in terms of volume fraction and size of mineral phase: Minerals Engineering, v. 119, p. 156-165.

Ureel, S., Momayez, M., and Oberling, Z., 2013, Rock core orientation for mapping discontinuities and slope stability analysis: International Journal of Research in Engineering and Technology, v. 2, p. 1-8.

Van Dalen, G., and Koster, M., 2012, 2D & 3D particle size analysis of micro-CT images: Bruker SkyScan User Meeting, 2012, Brussels, Belgium, 17p.

Van Malderen, S. J., van Elteren, J. T., and Vanhaecke, F., 2015, Development of a fast laser ablation-inductively coupled plasma-mass spectrometry cell for sub-μm scanning of layered materials: Journal of Analytical Atomic Spectrometry, v. 30, p. 119-125.

Vatandoost, A., and Fullagar, P., 2009, Characterisation of ore crushability using petrophysical properties: Seventh International Mining Geology Conference, 2009, Perth, Western Australia, Australia, p. 119-124.

Vearncombe, J. R., 2013, Structural Geology from oriented drill core, (http://www.sjsresource.com.au/blog-layout/structural-geology-from-oriented-drill-core).

Verwaal, W., and Mulder, A., 1993, Estimating rock strength with the Equotip hardness tester: International Journal of Rock Mechanics and Mining Sciences and Geomechanics, v. 30, p. 659-662.

Walters, S., 2006, Update report on Cadia East ore type definition and GeM core logging initiatives: Presentation (AMIRA Project P843 Geometallurgical Mapping and Mine Modelling), 61 p.

Wickham, G., Tiedemann, H., and Skinner, E. H., 1972, Support determinations based on geologic predictions: North American Rapid Excavation and Tunnelling, 1972, New York, New York, USA, in Conference Proceedings, p. 43-64.

Wilkinson, J. J., Chang, Z., Cooke, D. R., Baker, M. J., Wilkinson, C. C., Inglis, S., Chen, H., and Gemmell, J. B., 2015, The chlorite proximitor: a new tool for detecting porphyry ore deposits: Journal of Geochemical Exploration, v. 152, p. 10-26.

Wills, B. A., 2011, Wills' mineral processing technology: an introduction to the practical aspects of ore treatment and mineral recovery: Elsevier, 456 p.

Wilson, A., 2003, The genesis and exploration context of porphyry copper-gold deposits in the Cadia district, NSW: Ph.D. thesis, Hobart, Tasmania, Australia, University of Tasmania, 335 p.

Witten, I. H., Frank, E., Hall, M. A., and Pal, C. J., 2016, Data Mining: practical machine learning tools and techniques: Morgan Kaufmann, 654 p.

Yu, X., and Vayssade, B., 1991, Joint profiles and their roughness parameters: International Journal of Rock Mechanics and Mining Sciences, v. 28, p. 333-336.

Appendix A

Hillshade + slope and aspect and high pass fracture recognition protocols

The hillshade + slope and aspect and high pass fracture recognition protocols provided very poor fracture recognition, orientation, and roughness. The details of these protocols are outlined below.

A.1 Fracture recognition by hillshade + slope and aspect protocols

Combining the hillshade protocols with the slope and aspect protocols provides more rigorous fracture pixel criteria than the slope and aspect or hillshade filers alone. This approach was used to investigate the possibility of combining fracture selection techniques to provide alternative selection criteria. As with the previous protocols, a height threshold was used to exclude any selected pixels associated with the sides and bottom of the core tray

The processing protocols for the hillshade + slope and aspect fracture recognition protocols rely on the processing methods outlined in sections 3.3.1 and 3.3.2. The added selection criteria for the hillshade + slope and aspect protocols are shown graphically in Figure A.1. Figure A.2 shows the visual outputs of each step of the hillshade + slope and aspect analysis process in ArcGIS.

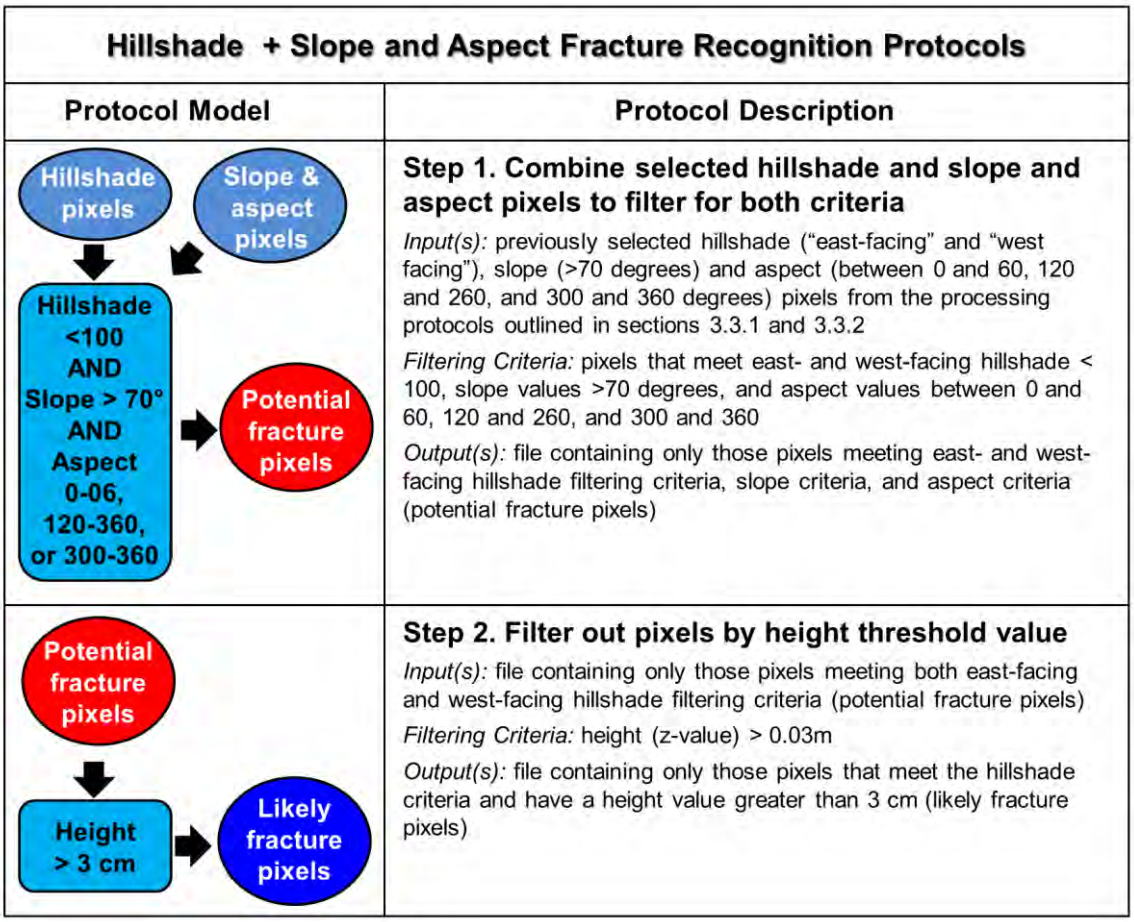

Figure A.1. *Protocol details for the hillshade + slope and aspect fracture recognition protocols.*

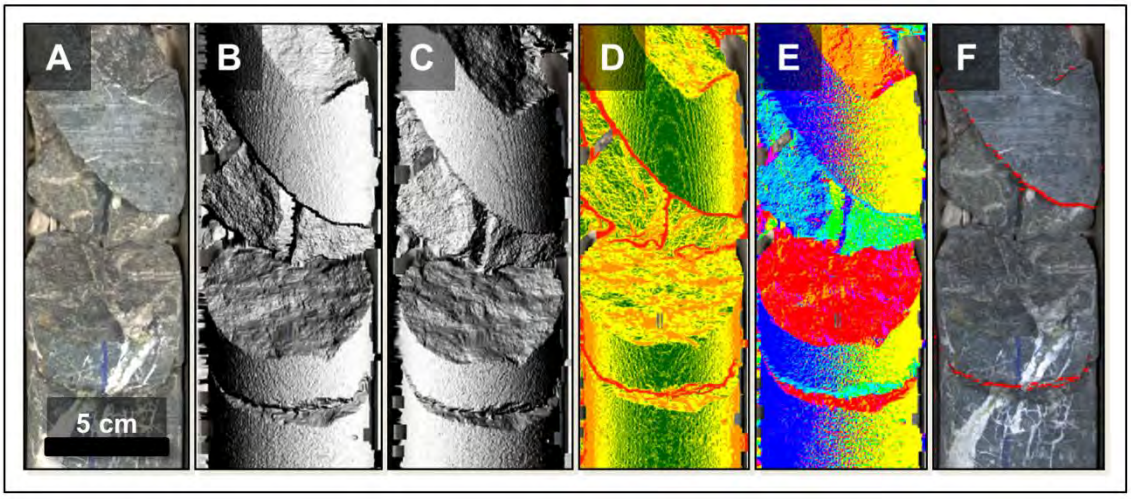

Figure A.2. *Visualisations of the processing outputs of the hillshade + slope and aspect fracture recognition protocols in ArcGIS: core photograph (A), east-facing hillshade output (90°) (B), west-facing hillshade output (270°) (C), slope tool output (D), aspect tool output (E), selected fracture pixels (F).*

A.2 Fracture recognition by high pass protocols

The high pass fracture recognition protocols outlined here was developed by Dr Matthew Cracknell (co-supervisor at the University of Tasmania) and is included for comparison.

The high pass protocols uses a two-step process that first calculates the mean height value (z) within a 3 pixel (in the x-direction) by a 33 pixel (in the y-direction) search window. This search window was designed to imitate the cylindrical surface of the drill core. The mean value of the search window is assigned to the centre pixel within the search window. The second step compares the height of each pixel to the calculated mean for that pixel. Since the cylindrical shape of drill core should deviate very little from the mean height value, fracture pixels can be identified by isolating pixels showing large deviations from the mean value.

The ArcGIS processing tool *Focal Statistics* was used to calculate the mean value of each centre pixel (Figure A.3) (ESRI, 2011b). This mean is then subtracted from the original height value from the laser profiler data. The standard deviation value of ± 2 mm was selected as a threshold for pixels considered to be substantially deviating from the mean. As the edges of the cylindrical core can cause noise in the mean deviation pixels, the slope and aspect recognition protocols as outlined in section 3.4.1 were applied as an additional step.

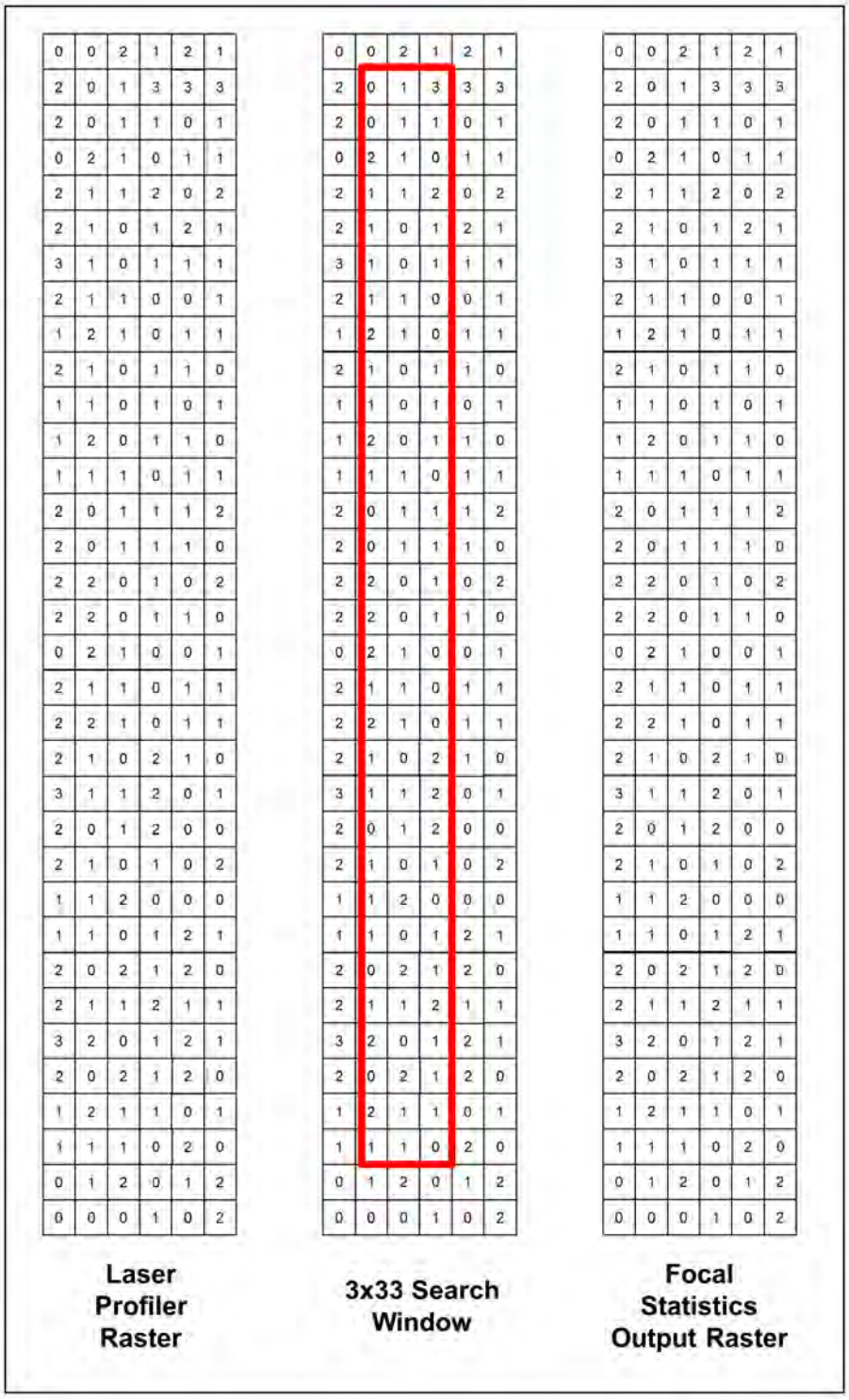

Figure A.3. *Focal statistics is a spatial analysis tool that calculates the mean height value in a user-defined search window (modified from ESRI 2011b).*

Specific processing protocols for the high pass recognition are outlined graphically in figure A.4. The visual outputs of each step of this analysis process are shown in figure A.5.

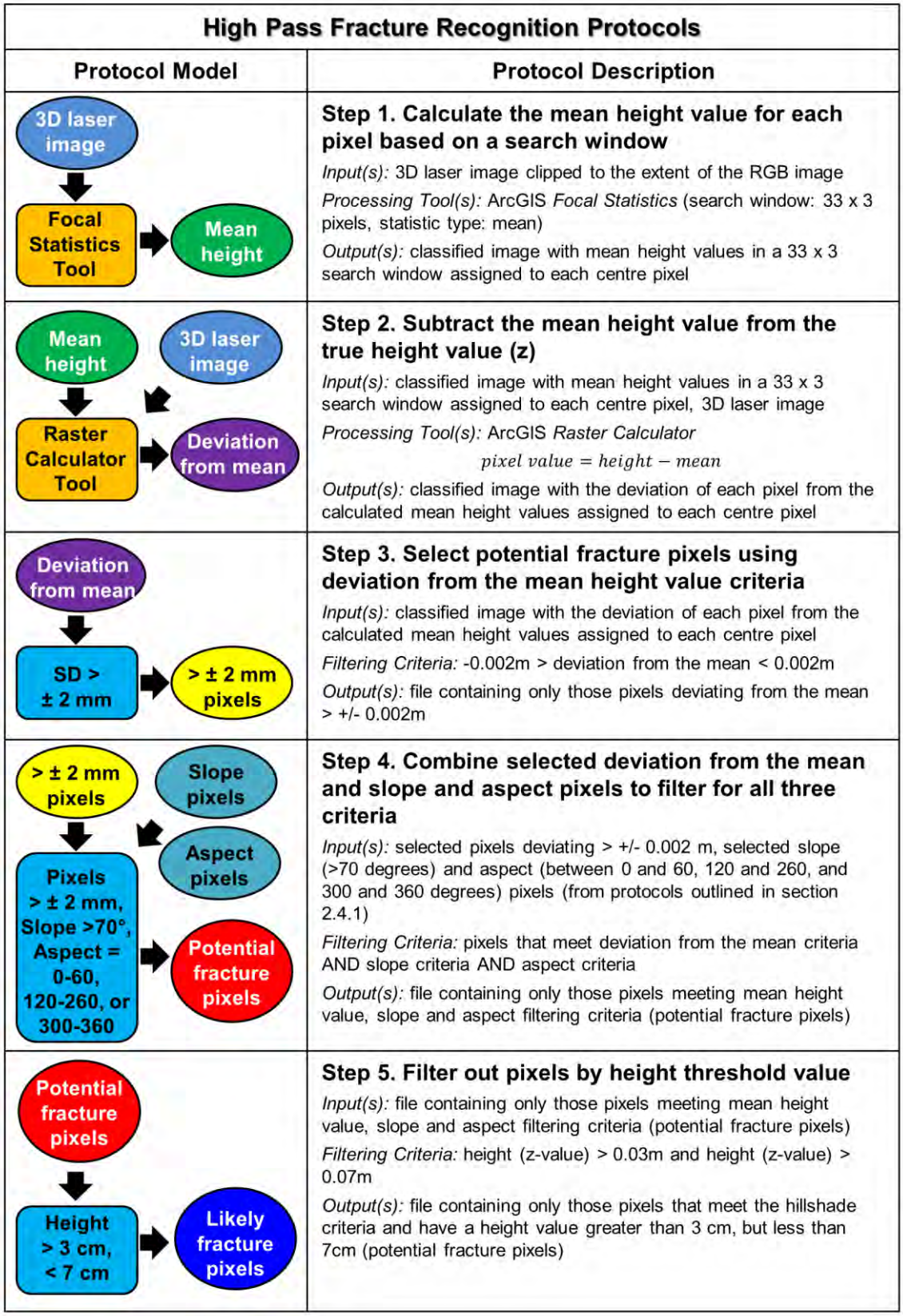

Figure A.4. *Protocol details for the high pass fracture recognition protocols.*

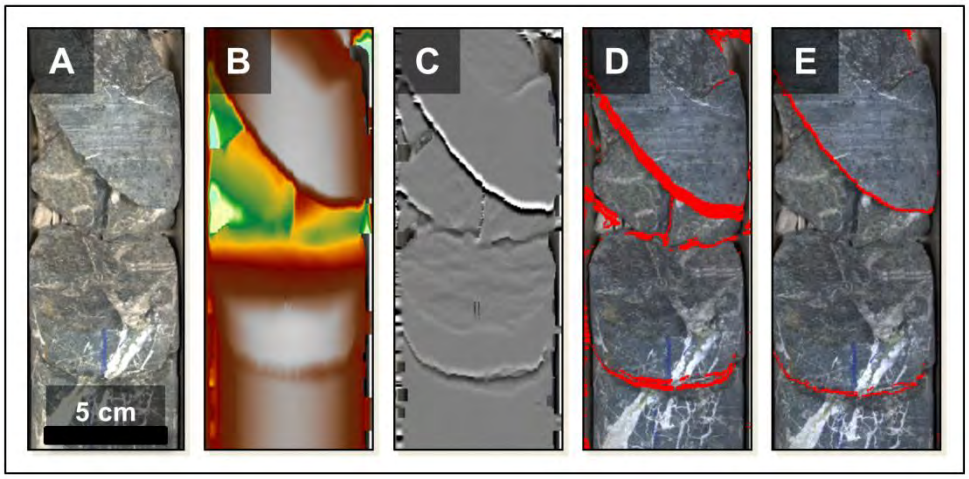

Figure A.5. *Visualisations of the processing outputs of the high pass fracture recognition protocols in ArcGIS: core photograph (A), focal statistics output (B), focal statistics minus the pixel height output (C), selected focal statistics pixels (D), selected fracture pixels after the height filter is applied (E).*

Appendix B

Fracture recognition ModelBuilder files

Appendix B is in a digital format supplied on the USB flash drive accompanying this thesis. The ArcGIS toolbox "Appendix_B_FractureRecognitionProtocols" contains the five ModelBuilder tools developed to execute the slope and aspect, hillshade, hillshade + slope and aspect, and high pass fracture recognition protocols. Each protocol is a separate tool that can be launched in ArcMap or ArcCatalog and executed to extract fracture pixels according to the methods outlined in sections 3.3.1 through 3.3.3 and appendix A.

To launch the tools, open the toolbox in ArcMap or ArcCatalog and double-click the protocol to execute. As inputs, the tools require the laser profiler file (.ers file) and the RGB image (.ers file). The user can specify the location and filename for the output fracture pixels (.shp file).

Appendix C

Fracture orientation calculation Excel workbook

The fracture orientation calculation Excel workbook (Appendix_C_FractureOrientation.xlsm) is a macro-enabled sheet that is set up to process numerous fracture files and report the orientation and pixel statistics for each. This sheet is set up for whole, un-cut HQ-sized drill core. The calculation sheet is set up to accept fracture pixel data in the following format:

- The x-, y-, and z-coordinates of the selected fracture pixels in a separate Excel file under a sheet called "calculation". The x-coordinates should be placed in A3:A2000, the y-coordinates in B3:B2000, and the z-coordinates in C3:C2000.
- A second sheet called "rotation_angle" contains information about the x- and y-value of the orientation line, the coordinates of the top of the drill core, and the bottom of the drill core. The average x-value of the orientation line is entered into cell B3, the average height of the orientation line is entered into cell C3.

Under the "filenames" sheet in the calculation workbook, the complete file path is entered into cell B1, and the names of the files containing the coordinates of the fracture pixels and the core rotation information in cells A3:A500 (cells highlighted in yellow).

After the information is entered, click the "Go" button in the "filenames" sheet. The results are reported in the "summary" sheet. The results of the fracture orientation calculations for the test dataset fractures are contained in the "summary" sheet.

Appendix D

Linear least squares regression calculations

The equation of any plane in three-dimensional space is represented by the formula:

$$y = a + bx + cz \quad \text{[D.1].}$$

This formula can then be optimized such that:

$$a + bx + cz - y = 0 \quad \text{[D.2].}$$

The specific details of the least squares linear regression calculations are included as Appendix 1.

The pixel x, y and z values selected from the 3D laser image should lie on a 3D plane where the optimum values for the coefficients a, b and c can be calculated using the least squares linear regression method.

For a given set of three-dimensional pixel values (x_1, y_1, z_1), (x_2, y_2, z_2),…, (x_n, y_n, z_n), where n = number of fracture pixels, n≥3, the best fit plane $f(x)$is represented by the following equation:

$$\Pi = \sum_{i=1}^{n}[y_i - f(x_i, z_i)]^2 \quad \text{[D.3]}$$

which equals:

$$\Pi = \sum_{i=1}^{n}\left[y_i - (a + bx_i + cz_i)\right]^2 \quad \text{[D.4].}$$

To solve for the optimized values of a, b and c that provide the best least squares fit, the first derivatives must equal zero, yielding the following system of equations:

$$\frac{\partial \Pi}{\partial a} = 2\sum_{i=1}^{n}\left[y_i - (a + bx_i + cz_i)\right] = 0 \quad \text{[D.5]}$$

$$\frac{\partial \Pi}{\partial b} = 2\sum_{i=1}^{n} x_i \left[y_i - (a + bx_i + cz_i)\right] = 0 \quad \text{[D.6]}$$

$$\frac{\partial \Pi}{\partial c} = 2\sum_{i=1}^{n} y_i \left[y_i - (a + bx_i + cz_i)\right] = 0 \quad \text{[D.7].}$$

By expanding this system of equations, the following linear equations result:

$$\sum_{i=1}^{n} y_i = a \sum_{i=1}^{n} 1 + b \sum_{i=1}^{n} x_i + c \sum_{i=1}^{n} z_i \quad [D.8]$$

$$\sum_{i=1}^{n} x_i y_i = a \sum_{i=1}^{n} x_i + b \sum_{i=1}^{n} x_i^2 + c \sum_{i=1}^{n} x_i z_i \quad [D.9]$$

$$\sum_{i=1}^{n} z_i y_i = a \sum_{i=1}^{n} y_i + b \sum_{i=1}^{n} x_i z_i + c \sum_{i=1}^{n} z_i^2 \quad [D.10].$$

Solving this system of equations for a, b and c gives:

$$a = \left[\left(\sum_{i=1}^{n} y_i \cdot \sum_{i=1}^{n} x_i^2 - \sum_{i=1}^{n} z_i y_i \cdot \sum_{i=1}^{n} x_i\right) \cdot \left(\sum_{i=1}^{n} x_i z_i \cdot \sum_{i=1}^{n} x_i z_i - \sum_{i=1}^{n} z_i^2 \cdot \sum_{i=1}^{n} x_i^2\right)\right]$$

$$- \left[\left(\sum_{i=1}^{n} x_i y_i \cdot \sum_{i=1}^{n} x_i z_i - \sum_{i=1}^{n} z_i y_i \cdot \sum_{i=1}^{n} x_i^2\right) \cdot \left(\sum_{i=1}^{n} z_i \cdot \sum_{i=1}^{n} x_i^2 - \sum_{i=1}^{n} x_i z_i \cdot \sum_{i=1}^{n} z_i\right)\right]$$

$$\div \left[\left(n \cdot \sum_{i=1}^{n} x_i^2 - \sum_{i=1}^{n} x_i \cdot \sum_{i=1}^{n} x_i\right) \cdot \left(\sum_{i=1}^{n} x_i z_i \cdot \sum_{i=1}^{n} x_i z_i - \sum_{i=1}^{n} z_i^2 \cdot \sum_{i=1}^{n} x_i^2\right)\right]$$

$$- \left[\left(\sum_{i=1}^{n} x_i \cdot \sum_{i=1}^{n} x_i z_i - \sum_{i=1}^{n} z_i \cdot \sum_{i=1}^{n} x_i^2\right) \cdot \left(\sum_{i=1}^{n} z_i \cdot \sum_{i=1}^{n} x_i^2 - \sum_{i=1}^{n} x_i z_i \cdot \sum_{i=1}^{n} x_i\right)\right] \quad [D.11]$$

$$b = \left[\left(\sum_{i=1}^{n} y_i \cdot \sum_{i=1}^{n} x_i - \sum_{i=1}^{n} x_i y_i \cdot n\right) \cdot \left(\sum_{i=1}^{n} x_i z_i \cdot \sum_{i=1}^{n} z_i - \sum_{i=1}^{n} x_i \cdot \sum_{i=1}^{n} z_i^2\right)\right]$$

$$- \left[\left(\sum_{i=1}^{n} x_i y_i \cdot \sum_{i=1}^{n} z_i - \sum_{i=1}^{n} z_i y \cdot \sum_{i=1}^{n} x_i\right) \cdot \left(\sum_{i=1}^{n} z_i \cdot \sum_{i=1}^{n} x_i - n \cdot \sum_{i=1}^{n} x_i z_i\right)\right]$$

$$\div$$

$$\left[\left(\sum_{i=1}^{n} x_i \cdot \sum_{i=1}^{n} x_i - n \cdot \sum_{i=1}^{n} x_i^2\right) \cdot \left(\sum_{i=1}^{n} x_i z_i \cdot \sum_{i=1}^{n} z - \sum_{i=1}^{n} x_i \cdot \sum_{i=1}^{n} z_i^2\right)\right]$$

$$-$$

$$\left[\left(\sum_{i=1}^{n} x_i^2 - \sum_{i=1}^{n} z_i \cdot \sum_{i=1}^{n} x_i \cdot \sum_{i=1}^{n} x_i z\right) \cdot \left(\sum_{i=1}^{n} z_i \cdot \sum_{i=1}^{n} x_i - n \cdot \sum_{i=1}^{n} x_i z_i\right)\right]$$

[D.12]

$$c =$$

$$\left[\left(\sum_{i=1}^{n} y_i \cdot \sum_{i=1}^{n} x_i - \sum_{i=1}^{n} x_i y_i \cdot n\right) \cdot \left(\sum_{i=1}^{n} x_i^2 \cdot \sum_{i=1}^{n} z_i - \sum_{i=1}^{n} x_i \cdot \sum_{i=1}^{n} x_i y_i\right)\right]$$

$$-$$

$$\left[\left(\sum_{i=1}^{n} x_i y_i \cdot \sum_{i=1}^{n} z_i - \sum_{i=1}^{n} z_i y_i \cdot \sum_{i=1}^{n} x_i\right) \cdot \left(\sum_{i=1}^{n} x_i \cdot \sum_{i=1}^{n} x_i - n \cdot \sum_{i=1}^{n} x_i^2\right)\right]$$

$$\div$$

$$\left[\left(\sum_{i=1}^{n} z_i \cdot \sum_{i=1}^{n} x_i - n \cdot \sum_{i=1}^{n} x_i z_i\right) \cdot \left(\sum_{i=1}^{n} x_i^2 - \sum_{i=1}^{n} z_i \cdot \sum_{i=1}^{n} x_i \cdot \sum_{i=1}^{n} x_i z_i\right)\right]$$

$$-$$

$$\left[\left(\sum_{i=1}^{n} x_i z_i \cdot \sum_{i=1}^{n} z_i - \sum_{i=1}^{n} x_i \cdot \sum_{i=1}^{n} z_i^2\right) \cdot \left(\sum_{i=1}^{n} x_i \cdot \sum_{i=1}^{n} x_i - n \cdot \sum_{i=1}^{n} x_i^2\right)\right]$$

[D.13].

The values of a, b and c can then be substituted back into the equation for a plane fitting a series of points (x, y, z):

$$y = a + bx + cz \qquad \text{[D.14].}$$

Appendix E

2D linear rotation calculations to adjust for trend and plunge of drill hole

For rotation θ of a plane in a clockwise direction about the origin, looking downhole:

$$\begin{bmatrix} x' \\ y' \end{bmatrix} = \begin{bmatrix} \cos\theta & \sin\theta \\ -\sin\theta & \cos\theta \end{bmatrix} \begin{bmatrix} x \\ y \end{bmatrix} \quad \text{[E.1].}$$

Written in equation form, the following equations result:

$$x' = x\cos\theta + y\sin\theta \quad \text{[E.2]}$$

$$y' = y\cos\theta - x\sin\theta \quad \text{[E.3].}$$

The direction cosine must be calculated in order to determine the current, three-dimensional location of the calculated plane in space relative to the coordinate system uncorrected for the trend and plunge of the drill hole (Figure E.1). For any plane $z = a + bx + cy$, the direction cosines are given by *l*, *m* and *n* where:

$$l = \cos\alpha = \frac{a}{\sqrt{a^2 + b^2 + c^2}} \quad \text{[E.4]}$$

$$m = \cos\beta = \frac{b}{\sqrt{a^2 + b^2 + c^2}} \quad \text{[E.5]}$$

$$n = \cos\gamma = \frac{c}{\sqrt{a^2 + b^2 + c^2}} \quad \text{[E.6].}$$

Once the location of the calculated plane in space is determined, the two-dimensional linear transformations must be completed to account for the trend and plunge of the drillhole. The first rotation is about the y-axis to rotate the orientation mark (which denotes the bottom of the drillhole) to the downward direction. This requires that the rotation angle to rotate the orientation line to the bottom of the drill core is determined.

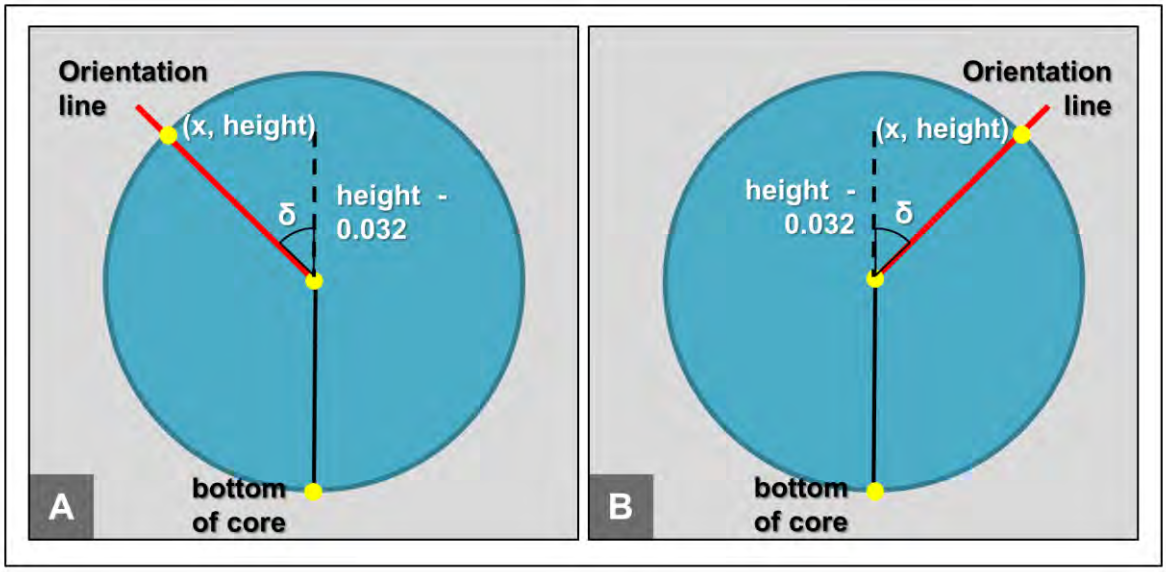

Figure E.1. *Two core rotation cases where the orientation line is left of x = 0 (A) and where the orientation line is right of x = 0 (B).*

In order to rotate the plane clockwise (looking downhole), the angle (δ) between the orientation line and x = 0 (the top of the drill core) is measured where,

$$\delta = \tan^{-1}\frac{x}{z-0.032} \quad \text{[E.7].}$$

In the case where the orientation line is left of x = 0 looking downhole (and therefore x < 0), the rotation angle (ω) is calculated by:

$$\omega = 180 + \delta \quad \text{[E.8].}$$

In the case where the orientation line is right of x = 0 looking downhole (and therefore x < 0), the rotation angle (ω) is calculated by:

$$\omega = 180 - \delta \quad \text{[E.9].}$$

In the case where the orientation line is located at x = 0, the rotation angle (ω) is always:

$$\omega = 180 \quad \text{[E.10].}$$

Once the core is rotated to move the orientation line to the bottom of the drill core, the rotations to correct for the plunge (θ_{plunge}) and trend (θ_{trend}) and trend of the plane must also be calculated.

In order to rotate the calculated plane about the y-axis looking downhole (to account for the plunge of the drill hole), the x-position and z-position must be translated by the following equations:

$$x' = l\cos\omega - n\sin\omega \quad \text{[E.11]}$$

$$z' = l\sin\omega + n\cos\omega \quad \text{[E.12].}$$

In order to rotate the calculated plane about the x-axis to correct the calculated plane for the drillhole plunge, the y-position and z-position must be translated by the following equations:

$$y' = m\cos\theta_{plunge} - (l\sin\omega + n\cos\omega)\sin\theta_{plunge} \quad \text{[E.13]}$$

$$z'' = l\sin\theta_{plunge} + (l\sin\omega + n\cos\omega)\cos\theta_{plunge} \quad \text{[E.14].}$$

Finally, to rotate the calculated plane about the z-axis looking downhole in order to correct the calculated plane for the drillhole trend, the x-position and y-position must be translated by the following equations:

$$x'' = (l\cos\omega - n\sin\omega)\cos\theta_{trend} - (m\cos\theta_{plunge} - (l\sin\omega + n\cos\omega)\sin\theta_{plunge})\sin\theta_{trend} \quad \text{[E.15]}$$

$$y'' = (l\cos\omega - n\sin\omega)\sin\theta_{trend} + (lm\cos\theta_{plunge} - (l\sin\omega + n\cos\omega)\sin\theta_{plunge})\cos\theta_{trend} \quad \text{[E.16].}$$

The final system of equations to rotate the calculated plane to adjust for the trend and plunge of the drillhole are given by:

$$x''' = (l\cos\omega - n\sin\omega)\cos\theta_{trend} - (m\cos\theta_{plunge} - (l\sin\omega + n\cos\omega)\sin\theta_{plunge})\sin\theta_{trend} \quad \text{[E.17]}$$

$$y''' = (l\cos\omega - n\sin\omega)\sin\theta_{trend} + (lm\cos\theta_{plunge} - (l\sin\omega + n\cos\omega)\sin\theta_{plunge})\cos\theta_{trend} \quad \text{[E.18]}$$

$$z''' = l \sin \theta_{plunge} + (l \sin \omega + n \cos \omega) \cos \theta_{plunge} \quad \text{[E.19].}$$

Once the x, y, and z-values are transformed to account for the trend and plunge of the drillhole, the orientation of this new plane can be calculated using simple geometry. The dip of the calculated plane is given by solving the following equation:

$$dip_{calculated} = 90 - |\sin^{-1}(z''')| \quad \text{[E.20].}$$

In order to calculate the dip direction, a series of equations must be calculated:

If

$$y''' < 0, \ dip\ direction_{initial} = 180 + \left(\tan^{-1}\frac{x'''}{y'''}\right) \quad \text{[E.21]}$$

but if

$$y''' > 0, \ dip\ direction_{initial} = \tan^{-1}\frac{x'''}{y'''} \quad \text{[E.22]}$$

then, if

$$\sin^{-1} z''' > 0, \ dip\ direction_{intermediate} = \left(\tan^{-1}\frac{x'''}{y'''}\right) + 180 \quad \text{[E.23]}$$

but if

$$\sin^{-1} z''' < 0, \ dip\ direction_{intermediate} = \left(\tan^{-1}\frac{x'''}{y'''}\right) \quad \text{[E.24].}$$

The final calculated strike is then given by the following equation:

$$dip\ calculated_{calculated} = (dip\ direction_{intermediate} + 180)\ mod\ 360 \quad \text{[E.25].}$$

Appendix F

GeoCalculator© calculation details

GeoCalculator© is a software program (developed by Rod Holcombe) capable of mathematically converting alpha and beta angles to true dip and dip directions based on the orientation of the drill hole. The convention for Cadia East drill core is that the orientation line marks the bottom of the drill hole. Alpha angles were measured parallel to the long axis of the ellipse, and beta angles were measured to the down hole (bottom) end of the ellipse. The conventions used in the conversions for the test dataset are shown in figure F.1.

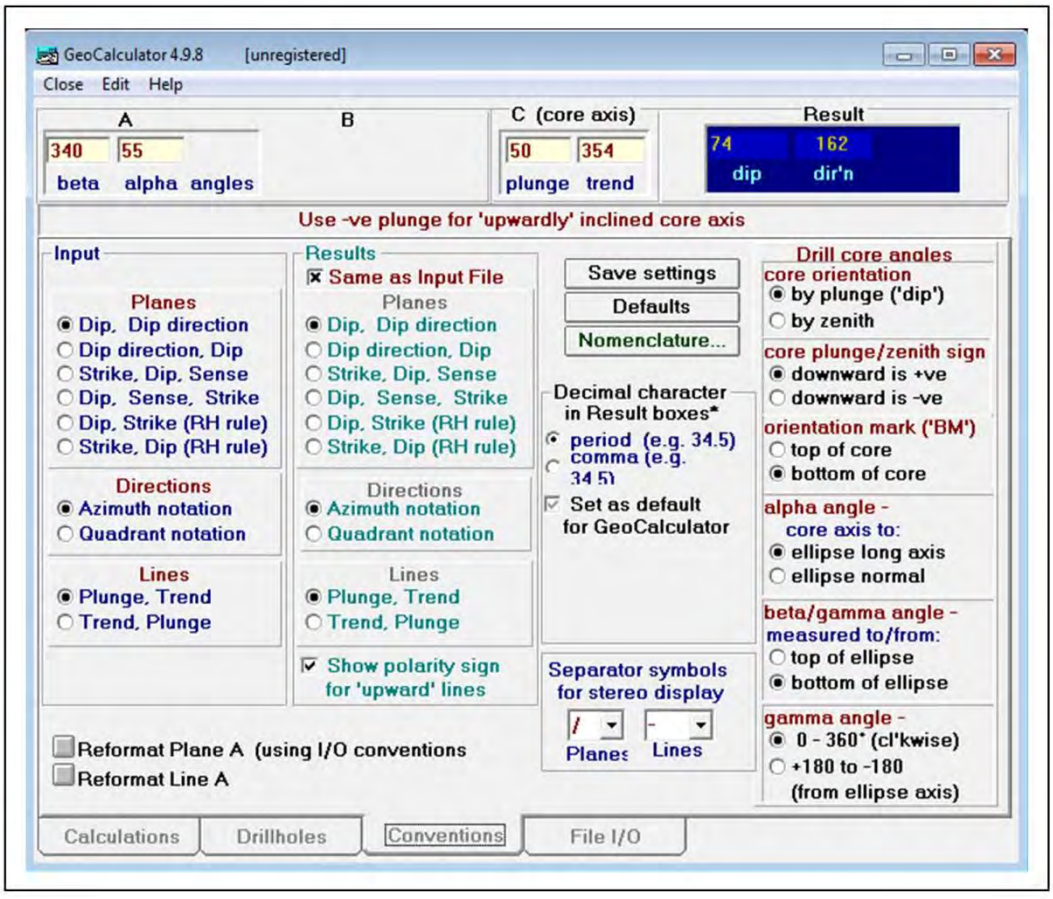

Figure F.1. *Conventions used to convert the alpha and beta values from the measured test dataset to true dip and dip direction, accounting for the trend and plunge of the drill hole.*

Appendix G

Measured fracture orientations

Drill hole	Tray	Row	Meterage	Measured alpha	Measured beta	Measured dip	Measured dip direction
UE276	1	0	0.265	55	340	74	163
UE276	1	0	0.351	60	320	65	154
UE276	1	0	0.744	55	10	75	180
UE276	1	0	0.848	45	180	5	354
UE276	1	1	0.876	50	260	49	117
UE276	1	1	0.922	70	330	58	163
UE276	1	1	1.428	55	240	36	116
UE276	1	1	1.456	60	300	60	144
UE276	1	1	1.576	70	210	25	150
UE276	1	2	1.735	45	190	8	52
UE276	1	2	1.854	55	180	5	174
UE276	1	3	2.567	65	340	64	165
UE276	1	3	2.842	50	70	64	217
UE276	1	3	3.197	40	160	17	292
UE276	2	0	3.773	55	120	36	232
UE276	2	0	4.133	60	290	57	140
UE276	2	2	4.972	55	200	13	115
UE276	2	2	5.029	85	160	35	177
UE276	2	2	5.609	75	210	28	158
UE276	3	0	7.236	60	180	10	174
UE276	3	0	7.528	50	20	79	187
UE276	3	1	7.834	10	250	70	75
UE276	3	1	8.133	60	20	69	185
UE276	3	1	8.202	60	30	84	223
UE276	3	1	8.376	30	80	73	237
UE276	3	3	9.652	40	190	12	34
UE276	3	3	10.115	35	70	75	227
UE276	25	0	80.691	55	150	19	240
UE276	25	1	81.013	30	320	88	322
UE276	25	1	81.171	30	290	79	120
UE276	25	1	81.292	25	300	88	124
UE276	25	1	81.391	45	100	51	239
UE276	25	1	81.761	45	110	46	244
UE276	25	2	82.084	25	310	87	222
UE276	25	2	82.223	50	80	59	223
UE276	25	2	82.254	45	80	62	228
UE276	25	2	82.459	55	290	60	137
UE276	25	3	82.764	50	80	59	223
UE276	25	3	82.798	60	60	59	206
UE276	25	3	83.017	50	70	63	218

Drill hole	Tray	Row	Meterage	Measured alpha	Measured beta	Measured dip	Measured dip direction
UE276	25	3	83.031	30	250	55	92
UE276	25	3	83.312	50	60	67	213
UE276	26	0	83.626	50	40	74	201
UE276	26	0	83.750	45	30	81	197
UE276	26	0	84.210	55	60	63	209
UE276	26	1	84.702	55	110	46	227
UE276	26	1	84.798	30	100	61	252
UE276	26	1	84.901	60	240	34	125
UE276	26	1	84.938	35	60	80	222
UE276	26	2	84.989	30	240	49	84
UE276	26	2	85.092	50	40	74	201
UE276	26	2	85.158	40	40	83	205
UE276	26	2	85.268	30	280	73	113
UE276	26	2	85.319	60	50	62	201
UE276	26	2	85.394	20	280	81	106
UE276	26	2	85.517	45	280	62	124
UE276	26	2	85.587	60	300	59	145
UE276	26	3	85.754	50	40	74	201
UE276	26	3	86.124	55	30	72	193
UE276	26	3	86.336	55	60	63	209
UE276	26	3	86.390	55	20	73	187
UE276	26	3	86.514	30	240	49	84
UE276	27	0	86.709	20	290	87	113
UE276	27	0	86.788	60	280	52	137
UE276	27	0	87.053	65	290	53	146
UE276	27	0	87.136	60	280	52	137
UE276	27	0	87.282	40	290	71	126
UE276	27	1	87.326	75	100	39	199
UE276	27	1	87.435	55	280	55	132
UE276	27	2	88.560	45	90	57	233
UE276	27	2	88.761	80	60	45	188
UE276	27	3	89.008	60	350	69	170
UE276	27	3	89.387	80	180	30	176
UE276	27	3	89.602	60	90	48	218
UE276	46	0	148.703	55	140	24	240
UE276	46	1	149.875	30	20	83	13
UE276	46	1	150.017	50	170	6	267
UE276	46	2	150.998	55	320	69	153
UE276	46	2	151.145	50	200	13	91
UE276	47	0	152.615	60	310	62	150
UE276	47	0	152.755	65	270	46	139
UE276	47	1	152.850	35	30	90	20
UE276	47	1	153.502	35	350	86	348
UE276	47	2	154.296	50	160	13	261
UE276	47	3	155.057	55	90	51	224
UE276	48	0	155.339	35	10	86	4

Drill hole	Tray	Row	Meterage	Measured alpha	Measured beta	Measured dip	Measured dip direction
UE276	48	1	156.508	25	350	76	346
UE276	48	1	156.559	35	20	87	12
UE276	48	1	156.855	60	330	67	160
UE276	48	2	157.583	60	20	68	186
UE276	48	2	157.756	55	340	73	164
UE276	48	3	157.878	55	340	73	164
UE276	48	3	157.971	60	330	67	160
UE276	48	3	158.153	50	270	54	123
UE276	48	3	158.324	75	310	50	161
UE276	48	3	158.469	60	180	9	176
UE276	49	0	158.869	55	110	41	231
UE276	49	0	158.950	45	350	84	169
UE276	49	1	159.775	65	270	46	139
UE276	49	1	159.967	40	270	60	114
UE276	49	1	160.105	60	120	34	226
UE276	49	1	160.350	40	170	13	319
UE276	49	2	160.563	65	110	38	216
UE276	49	2	160.678	65	280	49	142
UE276	49	3	161.364	60	350	69	170
UE276	49	3	161.423	60	350	69	170
UE276	49	3	161.751	55	10	74	182
UE276	50	0	162.151	45	0	84	176
UE276	50	0	162.564	30	30	85	22
UE276	50	1	163.099	50	300	67	139
UE276	50	3	164.717	40	240	42	95
UE276	50	3	164.843	60	330	67	160
UE276	50	3	164.990	55	300	63	142
UE276	50	3	165.014	35	280	69	116
UE276	51	0	165.539	65	290	53	146
UE276	51	0	165.633	35	290	75	123
UE276	51	1	166.596	35	340	87	340
UE276	51	1	166.932	55	340	73	164
UE276	51	2	167.661	30	340	83	338
UE276	51	2	167.733	35	30	90	20
UE276	51	2	167.818	40	30	86	198
UE276	51	3	168.771	75	330	53	166
UE276	51	3	168.805	65	310	58	153
UE276	70	0	229.351	65	140	25	217
UE276	70	1	230.055	40	350	89	169
UE276	70	3	231.634	20	50	83	43
UE276	70	3	231.660	45	160	14	282
UE276	70	3	231.791	60	150	19	226
UE276	71	0	231.883	40	310	79	140
UE276	71	2	233.792	50	160	13	262
UE276	71	3	234.494	55	60	63	357
UE276	71	3	234.781	20	320	79	319

Drill hole	Tray	Row	Meterage	Measured alpha	Measured beta	Measured dip	Measured dip direction
UE276	71	3	234.934	35	300	79	131
UE276	72	1	236.427	55	180	4	177
UE276	72	1	236.631	60	270	48	134
UE276	72	2	236.679	60	140	24	228
UE276	72	2	236.823	45	40	78	204
UE276	72	3	237.404	25	50	88	41
UE276	72	3	237.607	50	200	13	92
UE276	72	3	237.936	35	40	87	209
UE276	72	3	238.132	45	140	27	263
UE276	73	0	238.307	35	110	52	256
UE276	73	0	238.734	40	0	89	177
UE276	73	3	240.733	45	170	9	303
UE276	73	3	241.050	40	40	83	206
UE276	74	0	242.290	40	30	86	199
UE276	74	0	242.371	45	280	62	125
UE276	74	1	242.514	50	0	79	177
UE276	74	1	242.660	40	10	89	184
UE276	74	1	242.813	40	40	83	206
UE276	74	1	243.045	70	120	33	209
UE276	74	2	243.264	45	40	78	204
UE276	74	2	243.676	30	290	79	121
UE276	74	2	243.791	60	100	44	222
UE276	74	2	243.896	40	10	89	184
UE276	74	2	243.998	20	320	79	219
UE276	74	3	244.510	70	180	19	77
UE276	75	0	245.011	65	130	29	218
UE276	75	0	245.189	40	40	83	206
UE276	75	0	245.442	65	10	64	181
UE276	75	1	246.583	40	280	66	121
UE276	75	2	247.120	70	20	59	185
UE276	75	3	247.978	45	300	71	136
UE276	75	3	248.200	70	100	40	208
UE276	97	0	317.687	35	40	87	210
UE276	97	0	318.441	65	70	50	202
UE276	97	1	318.783	70	90	43	209
UE276	97	1	319.298	40	40	82	208
UE276	97	2	319.479	35	50	83	218
UE276	97	2	320.109	35	60	79	225
UE276	98	0	321.068	35	260	58	106
UE276	98	1	321.762	65	50	58	201
UE276	98	1	322.079	40	330	85	156
UE276	98	2	323.139	20	70	86	241
UE276	98	3	323.427	45	100	45	247
UE276	98	3	323.757	55	50	66	207
UE276	98	3	323.784	70	50	54	197
UE276	99	1	325.211	55	230	30	116

Drill hole	Tray	Row	Meterage	Measured alpha	Measured beta	Measured dip	Measured dip direction
UE276	99	1	325.674	50	350	79	172
UE276	99	2	326.060	30	60	83	227
UE276	99	2	326.274	45	120	39	253
UE276	99	2	326.438	40	50	73	114
UE276	99	2	326.497	35	170	18	330
UE276	99	3	327.093	40	180	11	358
UE276	121	1	397.617	25	50	88	43
UE276	121	1	397.657	40	170	13	323
UE276	121	1	397.826	70	350	58	175
UE276	121	2	398.494	30	180	51	359
UE276	121	2	398.791	50	340	77	166
UE276	121	3	399.992	50	340	77	166
UE276	123	0	403.294	65	220	24	138
UE276	123	0	403.614	65	330	61	165
UE276	123	0	403.664	45	0	84	179
UE276	123	1	404.197	40	40	82	209
UE276	123	1	404.255	75	180	24	179
UE276	123	1	404.918	65	290	52	149
UE276	123	3	406.042	55	100	45	232
UE276	123	3	406.215	75	90	41	202
UE276	123	3	406.662	35	20	88	15

Appendix H

Orientation results of hillshade + slope and aspect and high pass fracture recognition protocols

The hillshade + slope and aspect and high pass filters provided very poor fracture recognition, orientation, and roughness. The orientation results of these protocols are outlined below.

The hillshade + slope and aspect filter identifies discontinuities on the surface of the drill core by combining the filtering criteria for both the hillshade and slope and aspect filters. This protocol produced a 65% calculated orientation values (or 47 of the 72 fractures detected) within 25° of the measured orientation value (Figure H.1).

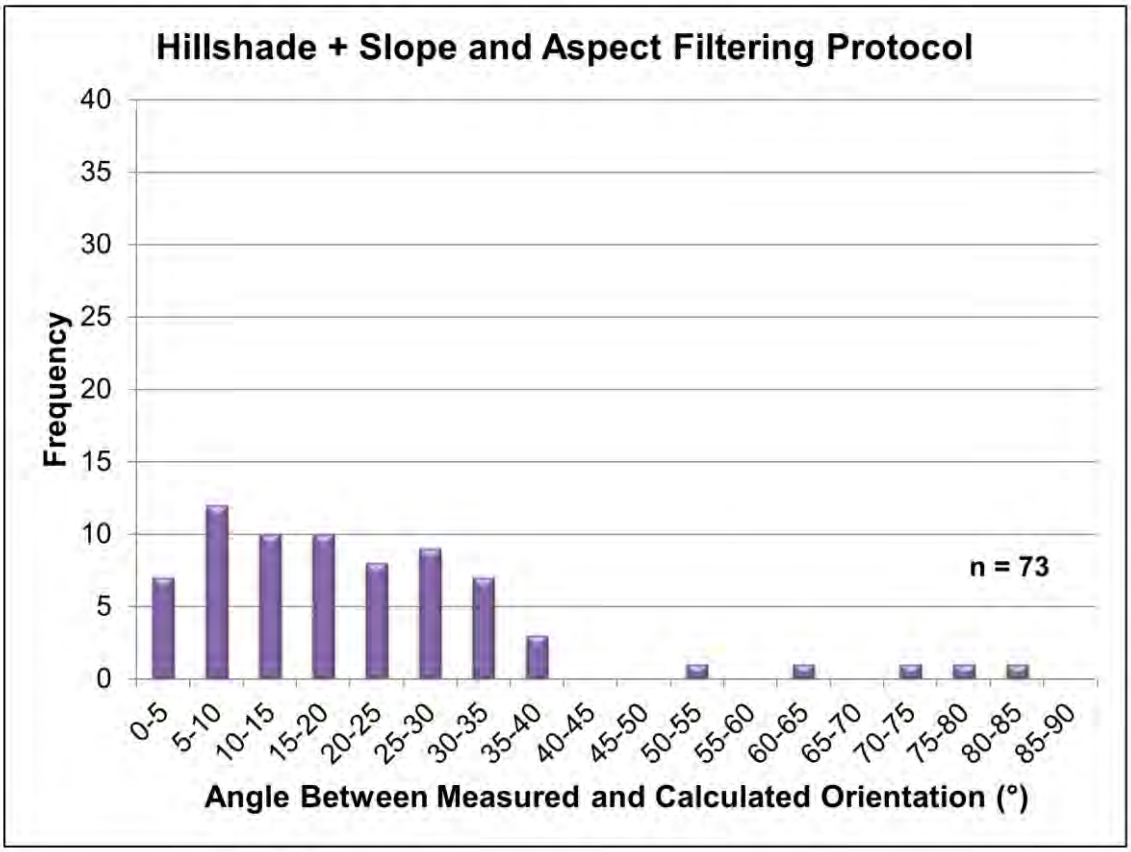

Figure H.1. *Distribution of the angle between the measured and the calculated orientation values as calculated from pixels selected by the hillshade + slope and aspect filtering protocol for detected test dataset fractures.*

The high pass filtering protocol searches for pixels whose heights deviate substantially from the mean height value to filter for discontinuities in the surface of the drill core. The pixels selected using this filtering protocol produced 50 calculated orientations of the 75 fractures detected (or 67%) that were within 25° of the measured orientation value (Figure H.2).

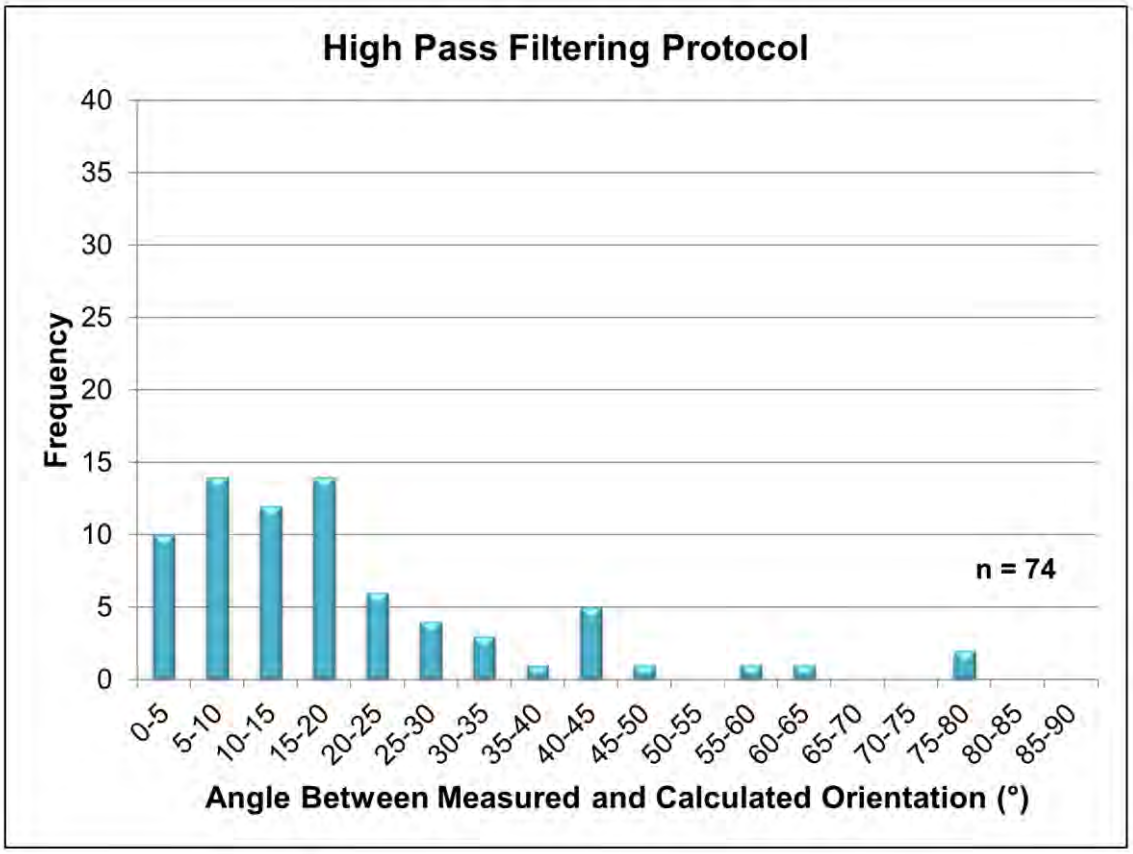

Figure H.2. *Distribution of the angle between the measured and the calculated orientation values as calculated from pixels selected by the high pass filtering protocol for detected test dataset fractures.*

Appendix I

Calculated and measured fracture orientations

Appendix I is in a digital format supplied on the USB flash drive accompanying this thesis. The Excel workbook (Appendix_I_CalcMeasFractureOrientations.xls) contains the calculated and measured fracture orientations and the angle between these values for the test dataset. The results for each protocol (presented in sections 3.3.1 through 3.3.3 and appendix A) are contained separately in individual sheets.

Appendix J

Calculated fracture roughness values

Drill hole	Tray	Row	Meterage	Slope Aspect Roughness	Hillshade Roughness	Combined Roughness
UE276	1	0	0.265	5.4	4.8	5.5
UE276	1	0	0.351	4.6	4.8	5.0
UE276	1	0	0.744	3.8	3.0	3.8
UE276	1	0	0.848	-	-	-
UE276	1	1	0.876	6.5	5.8	6.4
UE276	1	1	0.922	6.1	6.2	6.3
UE276	1	1	1.428	6.7	6.1	28.7
UE276	1	1	1.456	5.5	5.5	5.7
UE276	1	1	1.576	5.7	5.3	5.7
UE276	1	2	1.735	5.4	6.1	7.8
UE276	1	2	1.854	6.0	5.5	6.8
UE276	1	3	2.567	5.2	4.5	5.1
UE276	1	3	2.842	-	-	-
UE276	1	3	3.197	6.2	4.4	6.3
UE276	2	0	3.773	6.7	6.3	6.7
UE276	2	0	4.133	4.0	4.2	4.0
UE276	2	2	4.972	-	-	-
UE276	2	2	5.029	2.9	3.3	2.9
UE276	2	2	5.609	7.6	7.2	7.7
UE276	3	0	7.236	7.1	7.6	8.3
UE276	3	0	7.528	5.8	5.2	-
UE276	3	1	7.834	11.6	11.1	11.4
UE276	3	1	8.133	4.7	5.6	6.0
UE276	3	1	8.202	-	-	-
UE276	3	1	8.376	9.2	7.9	9.1
UE276	3	3	9.652	5.3	6.2	24.4
UE276	3	3	10.115	5.4	4.9	5.3
UE276	25	0	80.691	5.9	5.0	6.4
UE276	25	1	81.013	5.1	5.4	5.1
UE276	25	1	81.171	11.6	9.9	11.3
UE276	25	1	81.292	13.1	-	13.3
UE276	25	1	81.391	6.4	6.5	6.4
UE276	25	1	81.761	8.3	6.1	8.7
UE276	25	2	82.084	12.6	-	12.0
UE276	25	2	82.223	6.5	6.2	6.6
UE276	25	2	82.254	7.0	6.4	7.1
UE276	25	2	82.459	7.0	6.9	6.7
UE276	25	3	82.764	7.3	6.5	7.2
UE276	25	3	82.798	6.8	6.2	6.9
UE276	25	3	83.017	5.4	5.3	5.5

Drill hole	Tray	Row	Meterage	Slope Aspect Roughness	Hillshade Roughness	Combined Roughness
UE276	25	3	83.031	8.8	8.8	8.6
UE276	25	3	83.312	4.8	3.6	4.8
UE276	26	0	83.626	7.3	6.3	7.3
UE276	26	0	83.750	7.1	7.2	7.2
UE276	26	0	84.210	4.5	4.1	4.5
UE276	26	1	84.702	8.9	7.1	9.8
UE276	26	1	84.798	7.4	7.1	7.4
UE276	26	1	84.901	-	-	11.5
UE276	26	1	84.938	-	-	-
UE276	26	2	84.989	9.5	8.8	9.5
UE276	26	2	85.092	6.6	6.0	6.5
UE276	26	2	85.158	7.5	-	7.5
UE276	26	2	85.268	8.5	7.4	8.5
UE276	26	2	85.319	6.2	5.7	6.0
UE276	26	2	85.394	10.4	9.8	9.9
UE276	26	2	85.517	11.1	8.8	11.4
UE276	26	2	85.587	7.5	6.9	7.9
UE276	26	3	85.754	5.9	-	-
UE276	26	3	86.124	5.2	4.8	31.1
UE276	26	3	86.336	6.6	5.8	6.4
UE276	26	3	86.390	5.1	4.4	4.9
UE276	26	3	86.514	8.3	-	8.3
UE276	27	0	86.709	10.4	-	10.1
UE276	27	0	86.788	7.4	6.6	-
UE276	27	0	87.053	8.0	7.0	7.9
UE276	27	0	87.136	7.5	7.3	7.5
UE276	27	0	87.282	7.0	6.0	6.7
UE276	27	1	87.326	-	-	-
UE276	27	1	87.435	7.4	6.8	7.1
UE276	27	2	88.560	-	-	-
UE276	27	2	88.761	3.2	2.4	3.2
UE276	27	3	89.008	4.9	4.3	38.7
UE276	27	3	89.387	3.8	3.2	3.9
UE276	27	3	89.602	6.5	6.0	6.6
UE276	46	0	148.703	-	-	-
UE276	46	1	149.875	-	-	-
UE276	46	1	150.017	5.8	5.0	19.3
UE276	46	2	150.998	-	-	-
UE276	46	2	151.145	4.5	4.6	4.6
UE276	47	0	152.615	-	6.4	6.6
UE276	47	0	152.755	4.1	3.8	4.1
UE276	47	1	152.850	7.2	-	7.2
UE276	47	1	153.502	6.9	5.7	7.0
UE276	47	2	154.296	7.1	4.8	8.0
UE276	47	3	155.057	-	-	-
UE276	48	0	155.339	-	-	-

Drill hole	Tray	Row	Meterage	Slope Aspect Roughness	Hillshade Roughness	Combined Roughness
UE276	48	1	156.508	9.9	-	9.8
UE276	48	1	156.559	8.7	7.3	8.8
UE276	48	1	156.855	5.4	5.7	6.2
UE276	48	2	157.583	-	6.6	6.2
UE276	48	2	157.756	5.9	-	6.4
UE276	48	3	157.878	5.1	5.0	32.8
UE276	48	3	157.971	6.1	5.9	6.2
UE276	48	3	158.153	8.6	7.7	8.6
UE276	48	3	158.324	3.5	3.9	3.5
UE276	48	3	158.469	5.5	5.0	6.0
UE276	49	0	158.869	7.8	6.4	8.0
UE276	49	0	158.950	-	-	34.4
UE276	49	1	159.775	6.0	6.0	5.9
UE276	49	1	159.967	7.5	7.0	7.4
UE276	49	1	160.105	-	4.5	-
UE276	49	1	160.350	-	-	-
UE276	49	2	160.563	-	-	33.0
UE276	49	2	160.678	7.6	6.6	7.3
UE276	49	3	161.364	-	-	36.2
UE276	49	3	161.423	6.2	5.5	6.0
UE276	49	3	161.751	-	4.8	36.9
UE276	50	0	162.151	-	-	-
UE276	50	0	162.564	6.8	6.2	29.1
UE276	50	1	163.099	7.8	6.9	7.6
UE276	50	3	164.717	-	6.5	7.0
UE276	50	3	164.843	7.0	-	7.0
UE276	50	3	164.990	7.7	6.8	7.5
UE276	50	3	165.014	7.4	6.7	7.4
UE276	51	0	165.539	-	-	-
UE276	51	0	165.633	7.5	6.9	7.7
UE276	51	1	166.596	7.8	4.8	
UE276	51	1	166.932	-	5.6	26.4
UE276	51	2	167.661	6.8	5.6	6.8
UE276	51	2	167.733	12.5	-	11.9
UE276	51	2	167.818	6.9	6.4	6.4
UE276	51	3	168.771	-	-	-
UE276	51	3	168.805	-	-	-
UE276	70	0	229.351	4.4	4.6	4.4
UE276	70	1	230.055	-	-	-
UE276	70	3	231.634	8.1	-	8.4
UE276	70	3	231.660	7.1	6.9	7.4
UE276	70	3	231.791	-	-	-
UE276	71	0	231.883	-	-	-
UE276	71	2	233.792	5.6	5.3	28.1
UE276	71	3	234.494	6.3	5.7	6.4
UE276	71	3	234.781	10.6	9.2	10.1

Drill hole	Tray	Row	Meterage	Slope Aspect Roughness	Hillshade Roughness	Combined Roughness
UE276	71	3	234.934	7.0	-	7.0
UE276	72	1	236.427	-	-	-
UE276	72	1	236.631	-	-	-
UE276	72	2	236.679	7.0	6.4	7.1
UE276	72	2	236.823	-	-	-
UE276	72	3	237.404	-	-	-
UE276	72	3	237.607	-	-	-
UE276	72	3	237.936	6.2	-	6.7
UE276	72	3	238.132	4.3	5.4	30.8
UE276	73	0	238.307	7.4	6.7	7.4
UE276	73	0	238.734	6.8	6.3	6.7
UE276	73	3	240.733	-	-	-
UE276	73	3	241.050	8.5	6.9	8.3
UE276	74	0	242.290	7.1	7.0	7.3
UE276	74	0	242.371	6.3	5.9	6.3
UE276	74	1	242.514	5.7	5.1	5.6
UE276	74	1	242.660	8.0	7.0	8.2
UE276	74	1	242.813	5.9	6.2	6.2
UE276	74	1	243.045	5.9	5.1	6.0
UE276	74	2	243.264	-	-	-
UE276	74	2	243.676	10.1	9.6	9.8
UE276	74	2	243.791	-	-	-
UE276	74	2	243.896	5.0	4.6	24.3
UE276	74	2	243.998	4.6	7.6	-
UE276	74	3	244.510	4.6	3.7	26.8
UE276	75	0	245.011	5.3	5.3	5.7
UE276	75	0	245.189	7.3	6.5	33.7
UE276	75	0	245.442	6.5	6.2	6.2
UE276	75	1	246.583	5.7	5.4	5.4
UE276	75	2	247.120	5.8	5.5	5.9
UE276	75	3	247.978	7.7	7.9	7.8
UE276	75	3	248.200	3.9	3.8	3.9
UE276	97	0	317.687	-	-	-
UE276	97	0	318.441	-	-	-
UE276	97	1	318.783	-	-	-
UE276	97	1	319.298	9.9	-	-
UE276	97	2	319.479	-	-	8.6
UE276	97	2	320.109	6.5	6.1	6.2
UE276	98	0	321.068	6.5	6.7	6.7
UE276	98	1	321.762	-	-	-
UE276	98	1	322.079	-	-	-
UE276	98	2	323.139	11.5	11.5	260.6
UE276	98	3	323.427	7.4	6.8	7.4
UE276	98	3	323.757	4.3	4.6	4.8
UE276	98	3	323.784	-	-	-
UE276	99	1	325.211	7.6	6.1	31.9

Drill hole	Tray	Row	Meterage	Slope Aspect Roughness	Hillshade Roughness	Combined Roughness
UE276	99	1	325.674	6.5	8.3	8.0
UE276	99	2	326.060	8.4	7.7	-
UE276	99	2	326.274	-	-	9.3
UE276	99	2	326.438	7.2	6.9	7.2
UE276	99	2	326.497	-	-	-
UE276	99	3	327.093	-	-	-
UE276	121	1	397.617	6.3	-	-
UE276	121	1	397.657		5.5	27.7
UE276	121	1	397.826	5.6	4.8	6.0
UE276	121	2	398.494	10.2	-	9.5
UE276	121	2	398.791	6.9	5.9	6.5
UE276	121	3	399.992	-	-	27.5
UE276	123	0	403.294	5.6	5.2	5.3
UE276	123	0	403.614	7.4	7.5	8.3
UE276	123	0	403.664	7.3	7.0	8.9
UE276	123	1	404.197	4.5	5.7	31.2
UE276	123	1	404.255	5.1	4.2	27.9
UE276	123	1	404.918	-	-	-
UE276	123	3	406.042	-	-	-
UE276	123	3	406.215	4.7	5.0	5.2
UE276	123	3	406.662	6.8	4.5	6.8

Appendix K

Details of fracture mineralogy ModelBuilder files

Appendix K is in a digital format supplied on the USB flash drive accompanying this thesis. The ArcGIS toolbox "Appendix_K_FractureMineralogy" contains the ModelBuilder tool developed to execute the mineralogy extraction protocols for the fracture, 5 mm buffer, and 10 mm buffer. This tool that can be launched in ArcMap or ArcCatalog and executed to extract fracture mineralogy according to the methods outlined in sections 5.5 and 5.6.

To launch the tool, open the toolbox in ArcMap or ArcCatalog and double-click the "FractureMineralogy" protocol to execute. As inputs, the tool requires the fracture pixels (.shp file) for each individual fracture and the mineralogy raster images (.ers files). These tools are set up to have the following mineralogy rasters: amphibole (amp), apophyllite (apo), *aspectral* (asp), carbonate (car), chlorite (chl), clinochlore (clc), dickite (dik), epidote (epd), iron carbonate (fe-car), iron oxide (fe-ox), gypsum (gyp), kaolinite (kao), laumontite (lau), montmorillonite (mon), nontronite (non), phlogopite (phl), prehnite (pre), sericite (ser), quartz (sil), tourmaline (tor), and vermiculite (ver). The user can specify the location and filename for the three output files (.xls files): fracture mineralogy, 5 mm buffer mineralogy, 10 mm buffer mineralogy.

Appendix L

Fracture mineralogy compilation Excel workbook

Appendix L is in a digital format supplied on the USB flash drive accompanying this thesis. The fracture mineralogy compilation Excel workbook (Appendix_L_FractureMineralogyCompilation.xlsm) is a macro-enabled workbook that is set up to process the mineralogy outputs from the fracture mineralogy extracted from ModelBuilder (Appendix K). The fracture, 5 mm and 10 mm buffer outputs must be processed separately.

Under the "filenames" sheet in the calculation workbook, the complete file path is entered into cell B1, and the names of the files containing the mineralogy in cells A3:A500 (cells highlighted in yellow). After the information is entered, click the "Go" button in the "filenames" sheet. The results are reported in the "summary" sheet.

Appendix M

RMR_{infill}, $RMR_{weathering}$, and J_a calculation Excel workbook

Appendix M is in a digital format supplied on the USB flash drive accompanying this thesis. The RMR_{infill}, $RMR_{weathering}$, and J_a calculation Excel workbook (Appendix_M_RMR_QindexCalculations.xlsm) is set up to process the results of the fracture mineralogy protocols and report RMR_{infill}, $RMR_{weathering}$, and J_a values using the criteria outlined in sections 5.9 through 5.11. The normalised mineral results for the fracture, 5 mm buffer, and 10 mm buffer are entered in the "data" sheet. The calculations automatically run, and the RMR_{infill}, $RMR_{weathering}$, and J_a results are reported in the "results" sheet. The workbook currently contains the fracture mineralogy data for the test data set fractures used in this study.

Appendix N

Calculated RMR_{infill}, $RMR_{weathering}$, and J_a values

Drill hole	Tray	Row	Meterage	RMR_{infill}	$RMR_{weathering}$	J_a
UE276	1	0	0.265	6.0	6.0	0.8
UE276	1	0	0.351	4.0	6.0	1.0
UE276	1	0	0.744	6.0	6.0	0.8
UE276	1	0	0.848	-	-	-
UE276	1	1	0.876	6.0	6.0	0.8
UE276	1	1	0.922	4.0	6.0	1.0
UE276	1	1	1.428	6.0	6.0	0.8
UE276	1	1	1.456	6.0	6.0	0.8
UE276	1	1	1.576	4.0	6.0	1.0
UE276	1	2	1.735	4.0	6.0	1.0
UE276	1	2	1.854	4.0	6.0	1.0
UE276	1	3	2.567	4.0	6.0	1.0
UE276	1	3	2.842	-	-	-
UE276	1	3	3.197	6.0	6.0	0.8
UE276	2	0	3.773	4.0	6.0	1.0
UE276	2	0	4.133	6.0	6.0	0.8
UE276	2	2	4.972	-	-	-
UE276	2	2	5.029	4.0	6.0	1.0
UE276	2	2	5.609	4.0	6.0	1.0
UE276	3	0	7.236	4.0	6.0	1.0
UE276	3	0	7.528	2.0	6.0	1.0
UE276	3	1	7.834	4.0	6.0	1.0
UE276	3	1	8.133	6.0	6.0	0.8
UE276	3	1	8.202	-	-	-
UE276	3	1	8.376	6.0	6.0	0.8
UE276	3	3	9.652	4.0	6.0	1.0
UE276	3	3	10.115	6.0	6.0	0.8
UE276	25	0	80.691	6.0	6.0	0.8
UE276	25	1	81.013	6.0	6.0	0.8
UE276	25	1	81.171	6.0	6.0	0.8
UE276	25	1	81.292	6.0	6.0	0.8
UE276	25	1	81.391	4.0	6.0	1.0
UE276	25	1	81.761	6.0	6.0	0.8
UE276	25	2	82.084	6.0	6.0	0.8
UE276	25	2	82.223	6.0	5.0	0.8
UE276	25	2	82.254	4.0	6.0	1.0
UE276	25	2	82.459	6.0	6.0	0.8
UE276	25	3	82.764	6.0	6.0	0.8
UE276	25	3	82.798	6.0	6.0	0.8
UE276	25	3	83.017	6.0	6.0	0.8

Drill hole	Tray	Row	Meterage	RMR_{infill}	$RMR_{weathering}$	J_a
UE276	25	3	83.031	6.0	6.0	0.8
UE276	25	3	83.312	6.0	6.0	0.8
UE276	26	0	83.626	4.0	6.0	1.0
UE276	26	0	83.750	4.0	6.0	1.0
UE276	26	0	84.210	6.0	6.0	0.8
UE276	26	1	84.702	6.0	6.0	0.8
UE276	26	1	84.798	6.0	6.0	0.8
UE276	26	1	84.901	-	-	-
UE276	26	1	84.938	-	-	-
UE276	26	2	84.989	6.0	6.0	0.8
UE276	26	2	85.092	4.0	6.0	1.0
UE276	26	2	85.158	6.0	6.0	0.8
UE276	26	2	85.268	6.0	6.0	0.8
UE276	26	2	85.319	6.0	6.0	0.8
UE276	26	2	85.394	2.0	6.0	1.0
UE276	26	2	85.517	6.0	6.0	0.8
UE276	26	2	85.587	6.0	6.0	0.8
UE276	26	3	85.754	4.0	6.0	3.0
UE276	26	3	86.124	4.0	6.0	1.0
UE276	26	3	86.336	4.0	6.0	1.0
UE276	26	3	86.390	6.0	6.0	0.8
UE276	26	3	86.514	6.0	6.0	0.8
UE276	27	0	86.709	6.0	6.0	0.8
UE276	27	0	86.788	6.0	6.0	0.8
UE276	27	0	87.053	6.0	6.0	0.8
UE276	27	0	87.136	6.0	6.0	0.8
UE276	27	0	87.282	6.0	6.0	0.8
UE276	27	1	87.326	-	-	-
UE276	27	1	87.435	6.0	6.0	0.8
UE276	27	2	88.560	-	-	-
UE276	27	2	88.761	6.0	6.0	0.8
UE276	27	3	89.008	6.0	6.0	0.8
UE276	27	3	89.387	4.0	6.0	1.0
UE276	27	3	89.602	4.0	6.0	1.0
UE276	46	0	148.703	-	-	-
UE276	46	1	149.875	-	-	-
UE276	46	1	150.017	6.0	6.0	0.8
UE276	46	2	150.998	6.0	6.0	0.8
UE276	46	2	151.145	-	-	-
UE276	47	0	152.615	-	-	-
UE276	47	0	152.755	6.0	6.0	0.8
UE276	47	1	152.850	4.0	6.0	1.0
UE276	47	1	153.502	6.0	6.0	0.8
UE276	47	2	154.296	4.0	6.0	1.0
UE276	47	3	155.057	-	-	-
UE276	48	0	155.339	-	-	-

Drill hole	Tray	Row	Meterage	RMR_{infill}	$RMR_{weathering}$	J_a
UE276	48	1	156.508	4.0	6.0	1.0
UE276	48	1	156.559	6.0	5.0	0.8
UE276	48	1	156.855	6.0	6.0	0.8
UE276	48	2	157.583	-	-	-
UE276	48	2	157.756	6.0	6.0	0.8
UE276	48	3	157.878	4.0	6.0	3.0
UE276	48	3	157.971	6.0	6.0	0.8
UE276	48	3	158.153	6.0	6.0	0.8
UE276	48	3	158.324	6.0	6.0	0.8
UE276	48	3	158.469	6.0	6.0	0.8
UE276	49	0	158.869	6.0	6.0	0.8
UE276	49	0	158.950	-	-	-
UE276	49	1	159.775	4.0	6.0	2.0
UE276	49	1	159.967	4.0	6.0	1.0
UE276	49	1	160.105	-	-	-
UE276	49	1	160.350	-	-	-
UE276	49	2	160.563	-	-	-
UE276	49	2	160.678	6.0	6.0	0.8
UE276	49	3	161.364	-	-	-
UE276	49	3	161.423	6.0	6.0	0.8
UE276	49	3	161.751	-	-	-
UE276	50	0	162.151	-	-	-
UE276	50	0	162.564	4.0	6.0	1.0
UE276	50	1	163.099	6.0	6.0	0.8
UE276	50	3	164.717	-	-	-
UE276	50	3	164.843	6.0	6.0	0.8
UE276	50	3	164.990	6.0	6.0	0.8
UE276	50	3	165.014	2.0	6.0	1.0
UE276	51	0	165.539	-	-	-
UE276	51	0	165.633	4.0	6.0	1.0
UE276	51	1	166.596	6.0	6.0	0.8
UE276	51	1	166.932	-	-	-
UE276	51	2	167.661	6.0	6.0	0.8
UE276	51	2	167.733	6.0	6.0	0.8
UE276	51	2	167.818	6.0	6.0	0.8
UE276	51	3	168.771	-	-	-
UE276	51	3	168.805	-	-	-
UE276	70	0	229.351	4.0	6.0	1.0
UE276	70	1	230.055	-	-	-
UE276	70	3	231.634	4.0	6.0	1.0
UE276	70	3	231.660	4.0	6.0	1.0
UE276	70	3	231.791	-	-	-
UE276	71	0	231.883	6.0	6.0	0.8
UE276	71	2	233.792	4.0	6.0	1.0
UE276	71	3	234.494	4.0	6.0	1.0
UE276	71	3	234.781	6.0	6.0	0.8

Drill hole	Tray	Row	Meterage	RMR_{infill}	$RMR_{weathering}$	J_a
UE276	71	3	234.934	6.0	6.0	0.8
UE276	72	1	236.427	-	-	-
UE276	72	1	236.631	6.0	6.0	0.8
UE276	72	2	236.679	6.0	6.0	0.8
UE276	72	2	236.823	-	-	-
UE276	72	3	237.404	-	-	-
UE276	72	3	237.607	-	-	-
UE276	72	3	237.936	6.0	6.0	0.8
UE276	72	3	238.132	6.0	6.0	0.8
UE276	73	0	238.307	4.0	6.0	1.0
UE276	73	0	238.734	6.0	6.0	0.8
UE276	73	3	240.733	-	-	-
UE276	73	3	241.050	4.0	6.0	1.0
UE276	74	0	242.290	4.0	6.0	1.0
UE276	74	0	242.371	6.0	6.0	0.8
UE276	74	1	242.514	6.0	6.0	0.8
UE276	74	1	242.660	6.0	6.0	0.8
UE276	74	1	242.813	4.0	6.0	1.0
UE276	74	1	243.045	4.0	6.0	1.0
UE276	74	2	243.264	-	-	-
UE276	74	2	243.676	6.0	6.0	0.8
UE276	74	2	243.791	-	-	-
UE276	74	2	243.896	6.0	6.0	0.8
UE276	74	2	243.998	-	-	-
UE276	74	3	244.510	6.0	6.0	0.8
UE276	75	0	245.011	6.0	6.0	0.8
UE276	75	0	245.189	6.0	6.0	0.8
UE276	75	0	245.442	4.0	6.0	1.0
UE276	75	1	246.583	6.0	6.0	0.8
UE276	75	2	247.120	6.0	6.0	0.8
UE276	75	3	247.978	6.0	6.0	0.8
UE276	75	3	248.200	4.0	6.0	2.0
UE276	97	0	317.687	-	-	-
UE276	97	0	318.441	-	-	-
UE276	97	1	318.783	-	-	-
UE276	97	1	319.298	6.0	6.0	0.8
UE276	97	2	319.479	-	-	-
UE276	97	2	320.109	6.0	6.0	0.8
UE276	98	0	321.068	4.0	5.0	2.0
UE276	98	1	321.762	-	-	-
UE276	98	1	322.079	-	-	-
UE276	98	2	323.139	6.0	6.0	0.8
UE276	98	3	323.427	4.0	6.0	1.0
UE276	98	3	323.757	6.0	6.0	0.8
UE276	98	3	323.784	-	-	-
UE276	99	1	325.211	4.0	6.0	1.0

Drill hole	Tray	Row	Meterage	RMR_{infill}	$RMR_{weathering}$	J_a
UE276	99	1	325.674	6.0	6.0	0.8
UE276	99	2	326.060	4.0	6.0	1.0
UE276	99	2	326.274	-	-	-
UE276	99	2	326.438	6.0	6.0	0.8
UE276	99	2	326.497	-	-	-
UE276	99	3	327.093	-	-	-
UE276	121	1	397.617	6.0	6.0	0.8
UE276	121	1	397.657	-	-	-
UE276	121	1	397.826	6.0	6.0	0.8
UE276	121	2	398.494	4.0	6.0	1.0
UE276	121	2	398.791	6.0	6.0	0.8
UE276	121	3	399.992	-	-	-
UE276	123	0	403.294	6.0	6.0	0.8
UE276	123	0	403.614	4.0	6.0	1.0
UE276	123	0	403.664	4.0	6.0	1.0
UE276	123	1	404.197	6.0	6.0	0.8
UE276	123	1	404.255	6.0	6.0	0.8
UE276	123	1	404.918	-	-	-
UE276	123	3	406.042	-	-	-
UE276	123	3	406.215	6.0	6.0	0.8
UE276	123	3	406.662	6.0	6.0	0.8

Appendix O

Gold grain size calculations from pXRF Excel workbook

Appendix O is in a digital format supplied on the USB flash drive accompanying this thesis. The gold grain size calculation Excel workbook (Appendix_O_pXRFGoldGrainCalcs.xls) is designed to calculate the gold grain size (assuming a binomial grain size distribution) using the methods outlined in section 7.4. These calculations were developed by Berry and Hunt (2011) based on the methods proposed by Cohen (1990). The spot size and assumptions about the penetration depth, density of the rock, and density of gold must be entered in the "assumptions" tab (green cells). The sample ID, average gold (in ppm) and standard deviation should be entered in Cells A2:C100 (highlighted in yellow) in the "calcs" tab. The calculated grain size proxy result is reported in column D. The workbook currently contains the assumptions and pXRF grain size results for the Cadia East sample set used in this study.

Appendix P

Grain size calculations from μXRF Excel workbook

Appendix P is in a digital format supplied on the USB flash drive accompanying this thesis. The gold grain size calculation Excel workbook (Appendix_P_uXRFGrainSizeCalcs.xls) is designed to calculate the gold and copper sulphide grain sizes using the methods discussed in section 8.4.1. The grain size calculations for each sample are contained in separate sheets named by the sample ID. The relative x- and y-coordinates of each pixel and the gold and copper results from μXRF (in ppm) are entered in columns A through D in each individual sheet for each sample. Columns E through S contain the grain size calculation formulas. The calculated grain size proxy results are reported in the "summary" sheet. The workbook currently contains the μXRF grain size results for the Cadia East sample set used in this study.

Appendix Q

Grain size calculations from LA-ICP-MS Excel workbook

Appendix Q is in a digital format supplied on the USB flash drive accompanying this thesis. The gold and copper grain size calculation Excel workbook (Appendix_Q_LAICPMSGrainSizeCalcs.xlsm) is a macro-enabled sheet that is designed to calculate the gold and copper sulphide grain sizes using the methods discussed in section 9.4. In the "filenames" sheet in the calculation workbook, the complete file path is entered into cell B1, and the names of the files containing the processed LA-ICP-MS results are entered into cells A3:A500 (cells highlighted in yellow). The macros will automatically import the LA-ICP-MS data, calculate the grain sizes for each sample, and report the results in the "FinalSummary" sheet. The workbook currently contains the LA-ICP-MS grain size results for the Cadia East sample set used in this study.

Appendix R

LIBS copper and gold integration and spectral match values

Appendix R is in a digital format supplied on the USB flash drive accompanying this thesis. The Excel workbook (Appendix_R_LIBSCuAuIntegrationValues.xls) contains the integration and spectral match values for gold and copper sulphides for each analysis spot. and gold grain size calculation.

Appendix S

Grain size calculations from LIBS Excel workbook

Appendix P is in a digital format supplied on the USB flash drive accompanying this thesis. The gold grain size calculation Excel workbook (Appendix_S_LIBSCopperGrainSizeCalcs.xls) is designed to calculate the copper sulphide grain sizes using the methods discussed in section 10.4. The grain size calculations for each sample are contained in separate sheets named by the sample ID. The sample ID, line number, shot number, and spectral match values are entered in columns A through I. The integrated values from the Cu324.75 nm and Cu 327.40 nm lines, as well as, the Cu 329.90 nm background value are entered in columns O through Q in each individual sheet for each sample. Columns R through X contain the grain size calculation formulas. The calculated grain size proxy results are reported in the "results" sheet. The workbook currently contains the LIBS copper grain size results for the Cadia East sample set used in this study.